

Schubert, Gerlind (2014) *Manufacture, characterisation and modelling of magneto-rheological elastomers*. PhD thesis.

<http://theses.gla.ac.uk/5475/>

Copyright and moral rights for this thesis are retained by the author

A copy can be downloaded for personal non-commercial research or study, without prior permission or charge

This thesis cannot be reproduced or quoted extensively from without first obtaining permission in writing from the Author

The content must not be changed in any way or sold commercially in any format or medium without the formal permission of the Author

When referring to this work, full bibliographic details including the author, title, awarding institution and date of the thesis must be given

Manufacture, Characterisation and Modelling of Magneto-Rheological Elastomers

by
Gerlind Schubert

*A thesis submitted for the
degree of **Doctor of Philosophy***

Supervised by Dr Phil Harrison

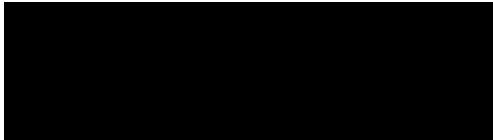
Submitted to the School of Engineering
College of Science and Engineering
University of Glasgow
Scotland

July 2014

Keywords: Magneto-Rheological Elastomers, Silicone Rubber - Iron Particle Composites, Magnetic Fields, Magneto-Rheological Effect, Stress-Strain Behaviour, Uniaxial Compression Tests, Uniaxial Tension Tests, Equi-Biaxial Tension Tests, Pure Shear Tests, Digital Image Correlation, Constitutive Modelling, Phenomenological Approach

Declaration

I declare that this thesis is a record of the original work carried out by myself, Gerlind Schubert, under the supervision of Dr. Philip Harrison in the School of Engineering at the University of Glasgow, United Kingdom. The copyright of this thesis therefore belongs to the author under the terms of the United Kingdom Copyright acts. Due acknowledgement must always be made of the use of any material contained in, or derived from, this thesis. The thesis has not been presented elsewhere in consideration for a higher degree.



Glasgow, July 2014

Abstract

This investigation is concerned with the large-strain characterisation of Magneto-Rheological Elastomers (MREs), with the main focus on experimental characterisation. Quasi-static uniaxial compression, uniaxial tension, pure shear and equi-biaxial tension experiments have been performed both in the absence and in the presence of magnetic fields. The experimental data generated during this investigation constitutes an extensive data set characterising MREs under various deformation modes. This is the first time that such a consistent data set has been produced, and such data are essential to develop accurate constitutive models characterising MREs under general deformations.

Isotropic and anisotropic MREs composed of silicone rubber and up to 40 *vol%* carbonyl iron powder were manufactured using a reliable and repeatable process. Specimens of different shapes were made in specially designed moulds and anisotropic samples were produced by placing the moulds inside a strong magnetic field during the curing process. Understanding the magnetic permeability of MREs is a prerequisite for both the development of constitutive models and for quantifying the magnetic flux applied to specimens during testing. Accordingly, the magnetic permeability of MREs has been characterised using a novel, simple and low-cost method. Large-strain experiments were conducted using test rigs specially designed for use in universal test machines, while incorporating permanent magnets. The magnetic flux was applied in the loading direction and samples were aligned with their direction of particle alignment both parallel and perpendicular to the loading direction. Where possible, strains were measured using a digital image correlation system. MREs were found to be very sensitive to the stress-softening Mullins effect as such a novel testing strategy was used: MRE samples were repeatedly used in several cyclic tests in a test series and tests conducted in the absence of magnetic fields were repeated twice in the test series in order to verify the stress-strain results and importantly, to eliminate the influence of the Mullins effect when interpreting the final stress-strain results. Cyclic fatigue tensile tests were conducted to determine stability strain limits of MREs, and specimens were not tested beyond these limits in the experiments.

The mechanical response of MREs was found to be strongly nonlinear when tested up to large strains. Anisotropic MREs with particle alignment in the loading direction are the stiffest specimens, followed by anisotropic MREs with their particle alignment perpendicular to the loading direction, while isotropic MREs are the softest type of MRE. Moduli were found to increase with increasing iron content and MREs preconditioned to larger levels of strain were measured to be softer than the same type of MRE tested to lower strain levels. The largest MR effects were found in the small-strain region for all MREs. Anisotropic MREs containing 30% volume iron fraction with particle chains aligned parallel to both the loading direction, and the direction of the magnetic field, were found to exhibit the greatest MR effect

of all specimens tested. MR effects generally decrease rapidly in the mid-strain region, but increase again at larger strain ($> 15\%$). MR effects can be enhanced by preconditioning the specimens to larger levels of strain. The largest relative MR effects were found in uniaxial and equi-biaxial tension tests.

Data fitting to pre-established hyperelastic constitutive models were conducted to evaluate their ability to characterise MREs. The parameters of the *Ogden* model describing isotropic MREs under general deformations in the absence of a magnetic field were successfully determined when experimental data obtained from tests up to the same strain level were combined in multi-deformation mode data fitting. The *Ogden-Roxburgh* model was found to describe the stress-softening well. Data fitting of several transversely isotropic constitutive models to experimental data of anisotropic MREs was not successful and none of the models employed in this investigation could accurately represent the data.

Acknowledgement

I would like to express my deep sense of gratitude to my supervisor Dr Philip Harrison for his continuous interest, encouragement, inspirational guidance, suggestions, unselfish help and support throughout this research. I also would like to thank my second supervisor Dr Zaoyang Guo for his introduction into the large field of continuum mechanics. Thanks to Brian Robb and to all the technicians in the School of Engineering for their expertise, guidance and creative ideas. They manufactured the moulds and experimental setups used to characterise this complex material. A special thanks to John Davidson; he guided me through my experimental investigation, had very supportive ideas, and was always there when needed. It was a pleasure working with him. Thanks also to Norbert Klauke and Ian Peden for helping me with micro-structural analysis and Kenny Roberts who conducted the laser diffraction analysis of the iron particles.

I am very grateful to Prof Raymond Ogden for the helpful discussions and for the advices he gave me on the data fitting procedure and suitable constitutive models. He enabled my participation in the summer school about 'Mechanics and Electrodynamics of Magneto- and Electro-Elastic Materials' in Italy, and also in the 'European Solid Mechanics Conference 2012' in Austria.

I am so thankful to Dr Robert Etges and again to my supervisor Dr Philip Harrison for reading and reviewing my thesis, improving the English writing style and checking all the grammar. For me, as a non-native English speaker this help was of invaluable importance. Thanks to the School of Engineering, and to the Glasgow Research Partnership in Engineering (GRPE) for their financial support of this PhD course, for the possibility to take two maternity leaves during my studies, and for allowing to finish this study from abroad which saved me from being far away from my lovely family. The Engineering and Physical Sciences Research Council (EPSRC) is acknowledged for providing the digital image correlation system.

On the personal side, I am so thankful to my partner Udo Hügler who always supported and encouraged me, helped me to relax, and always made me smile. Words alone cannot express what I owe him for his patient love that inspired me to finish this work. Thanks also to our two little children Lorna and Angus who have been so brave when Mama needed to work again on weekends, they both forced me to take breaks, which are of invaluable importance when working on such a project. I am thankful to my parents for their education in my early years, and so thankful that they always believed in me. A special thanks to my mum Dr Ilona Schubert, I cannot express how much she helped with her spontaneity. She was always supportive with the children, although she had so much work to do herself.

Contents

List of Figures	X
List of Tables	XII
List of Symbols	XIII
List of Abbreviations	XVII
1 Introduction	1
1.1 Objectives	2
1.2 Structure of the Thesis	2
2 Literature Review - Experimental Work	4
2.1 Classification of Smart Materials	4
2.2 Historical Overview	7
2.3 Manufacture and Microstructure of MREs	9
2.4 Applications	9
2.5 Large-Strain Experiments on MREs	14
3 Manufacture of MREs	25
3.1 Elastomeric Matrix	25
3.2 Magnetic Particles	26
3.3 Manufacture Process	27
3.4 Microscopic Analysis of MREs	30
4 Magnetic Permeability of MREs	32
4.1 Theoretical Overview	32
4.2 Magnetic Permeability of CIP and MREs	33
4.2.1 Magnetic Permeability of Carbonyl Iron Powder (CIP)	33
4.2.2 Permeability of Composite Structures	36
4.2.3 Comparison and Summary	39
4.3 Measurement of Magnetic Flux Density and Attractive Force	40
4.4 Simulation of the Magnetic Flux Density using Comsol	45
4.4.1 Permeability of Isotropic MREs	46
4.4.2 Permeability of Anisotropic MREs	50
4.5 Conclusions of Chapter 4	55

5	Large-Strain Experiments on MREs	57
5.1	Test and Analysis Method	57
5.1.1	General Test Method	57
5.1.2	Analysis Method	61
5.2	Uniaxial Compression Tests	65
5.2.1	Procedure of the Compression Tests	66
5.2.2	Compression Test Setup	66
5.2.3	Tests in the Absence of a Magnetic Field	73
5.2.4	Characterisation of the Magneto-Rheological Effect	78
5.2.5	Summary of Compression Tests	81
5.3	Uniaxial Tension Tests	82
5.3.1	Procedure of the Tension Tests	82
5.3.2	Tension Test Setup	84
5.3.3	Fatigue Tests	87
5.3.4	Strain Measurement - Digital Image Correlation	88
5.3.5	Tests in the Absence of a Magnetic Field	93
5.3.6	Characterisation of the Magneto-Rheological Effect	100
5.3.7	Summary of Tension Tests	106
5.4	Pure Shear Tests	107
5.4.1	Procedure of the Pure Shear Tests	108
5.4.2	Pure Shear Test Setup	110
5.4.3	Strain Measurement - Digital Image Correlation	113
5.4.4	Tests in the Absence of a Magnetic Field	117
5.4.5	Characterisation of the Magneto-Rheological Effect	122
5.4.6	Summary of Pure Shear Tests	125
5.5	Equi-Biaxial Tension Tests	125
5.5.1	Procedure of the Equi-Biaxial Tests	126
5.5.2	Equi-Biaxial Test Setup	127
5.5.3	Strain Measurement - Digital Image Correlation	134
5.5.4	Stress Calculation and Assumptions	135
5.5.5	Tests in the Absence of Magnetic Field (CASE1 and CASE3)	140
5.5.6	Characterisation of the Magneto-Rheological Effect	143
5.5.7	Future Improvements of the Setup and Test Procedure	147
5.5.8	Summary of the Equi-Biaxial Tension Tests	149
5.6	Conclusions of Chapter 5	149
5.6.1	Stress-Softening Behaviour	150
5.6.2	Mechanical Response in the Absence of a Magnetic Field	151
5.6.3	Mechanical Response when subject to a Magnetic Field	152

6	Constitutive Modelling of MREs	154
6.1	Introduction to Continuum Theory	155
6.1.1	Basic Definitions in Continuum Mechanics	155
6.1.2	Constitutive equations	157
6.2	Optimisation Methods	159
6.3	Modelling of Isotropic MREs	162
6.3.1	Ogden Model, Tests Kinematics and Stress Definitions	163
6.3.2	Fitting Procedure	167
6.3.3	Experimental Data Fitting for the Ogden Model	168
6.3.4	Ogden-Roxburgh Model for the Mullins Effect	173
6.3.5	Fitting of the Ogden Model to Data of Same Strain Level	179
6.3.6	Summary of the Modelling of Isotropic MREs	182
6.4	Modelling of Anisotropic MREs	182
6.4.1	Theory and Forms of Strain Energy Functions	183
6.4.2	Kinematics and Stress Definitions	187
6.4.3	Fitting Procedure	192
6.4.4	Experimental Data Fitting for Transversely Isotropic Models	193
6.5	Models to describe the MR effect	196
6.6	Conclusions of Chapter 6	198
7	Conclusions and Future Work	200
	Bibliography	219
	Appendix	219
A	Technical Data Sheets	220
B	Technical Drawings	233
C	Amounts of components used to manufacture MREs	251
D	Matlab Codes	252
E	Experimental Results	257
F	Results of Constitutive Modelling	286

List of Figures

2.1	Classification of Smart Materials	5
2.2	Experimental investigations on MREs up to 2013	8
2.3	Automotive suspension bushing developed by the Ginder (2004)	10
2.4	Tunable vibration isolation device developed by Hitchcock <i>et al.</i> (2006). .	10
2.5	AVA developed by Albanese Lerner and Cunefare (2006) and ATVA developed by Zhang <i>et al.</i> (2008a)	11
2.6	Scheme of the active vibrational damper invented by Crist (2009)	12
2.7	Design of the prosthetic foot (Gudmundsson, 2011)	12
2.8	Scheme of the actuator invented by Heier and Schubert (2010)	13
2.9	Results of the uniaxial tension tests performed by Stepanov <i>et al.</i> (2007). .	14
2.10	Results of the compression tests performed by Farshad and Le Roux (2005)	16
2.11	Results of the compression tests performed by Kallio (2005)	16
2.12	Results of the compression tests performed by Varga <i>et al.</i> (2006)	17
2.13	Results of the compression tests performed by Gudmundsson (2011) . . .	17
2.14	Results of the compression and simple shear tests performed by Gordaninejad <i>et al.</i> (2012)	18
2.15	Results of the simple shear tests performed by Shen <i>et al.</i> (2004)	19
2.16	Results of the simple shear tests performed by Stepanov <i>et al.</i> (2007) . .	19
2.17	Results of the shear tests performed by Yu and Wang (2010) and Zajac <i>et al.</i> (2010)	20
2.18	Results of the dynamic shear tests performed by Hu <i>et al.</i> (2011)	21
2.19	Absolute MR effects of large-strain experiments published in the literature	23
2.20	Relative MR effects of large-strain experiments published in the literature	23
3.1	Laser diffraction analysis of CIP	27
3.2	SEM image of CIP	27
3.3	Material and consumables to manufacture MREs	28
3.4	Moulds for preparing compression samples	28
3.5	Moulds for preparing tension samples	29
3.6	Moulds for preparing pure shear and biaxial samples	29
3.7	Electromagnet used to prepare anisotropic MREs	30
3.8	Microscopic images of isotropic MREs with 10 Vol% CIP	31
3.9	Microscopic images of anisotropic MREs with 10 Vol% CIP	31
4.1	Estimation of the magnetisation curve $B(H)$ of CIP	35
4.2	Magnetisation curve $B(H)$ of CIP with different initial permeability . . .	36

4.3	Permeability measurements performed by Vicente <i>et al.</i> (2002)	38
4.4	Effective permeability μ_e versus the volume particle concentration	40
4.5	Setup for magnetic flux density measurements	41
4.6	Scheme showing the positions of magnetic flux measurements	41
4.7	Measured magnetic flux versus VPC of isotropic and vert. aligned MREs	42
4.8	Measured magnetic flux versus VPC of horizontally aligned MREs	43
4.9	Measurements of attractive force versus VPC	43
4.10	Geometry defined in <i>Comsol</i>	45
4.11	Magnetic flux density versus permeability of isotropic MREs	47
4.12	Attractive force versus permeability of isotropic MREs	48
4.13	Magnetic flux density versus permeability of vertically aligned MREs . . .	50
4.14	Attractive force versus permeability of vertically aligned MREs	51
4.15	Magnetic flux density versus permeability of horizontally aligned MREs .	53
4.16	Attractive force versus permeability of horizontally aligned MREs	53
5.1	Four-cycle compression tests of an isotropic MRE with 30% CIP	59
5.2	Four-cycle compression test (magnification up to 10% strain) of an isotropic MRE with 30% CIP	62
5.3	4-cycle load-displacement curve up to 15 mm and down to -5 mm of an isotropic tension sample with 30% iron content	64
5.4	Test setup for compression tests	67
5.5	Test setup for compression tests with permanent magnets	67
5.6	Geometry of top and bottom rig structure modelled using <i>Abaqus</i>	68
5.7	Deformed geometry with values of vertical displacement	69
5.8	Comparison of stress-strain results achieved with different setups	70
5.9	Distribution of magnetic flux density B_Z in <i>Setup 450mT</i>	72
5.10	Distribution of magnetic flux density B_Z in <i>Setup 210mT</i>	72
5.11	Stress-strain curves comparing <i>NoField01</i> and <i>NoField02</i> compression tests	74
5.12	Stress-strain results comparing different types of MREs	76
5.13	Stress-strain results up to 10% strain comparing different types of MREs .	77
5.14	Tangent Moduli E_T versus strain	77
5.15	Moduli E_{0-5} and E_T versus the volume particle concentration	78
5.16	Absolute and relative MR effects achieved in the <i>Magnet35</i> tests	79
5.17	Absolute and relative MR effects achieved in the <i>Magnet62</i> tests	79
5.18	Relative MR effects versus particle content and versus magnetic induction	81
5.19	Test Setup for uniaxial tension tests with the DIC system	84
5.20	Test Setup for uniaxial tension tests with permanent magnets	85
5.21	Geometry of the <i>Comsol</i> model and vertical distribution of B_Z	86
5.22	Distribution of the magnetic flux density B_Z within the MRE sample . . .	87

5.23	Maximum load (relative value referring to 1st cycle) versus cycles	88
5.24	DIC system: pattern sprayed on the sample and vertical displacement field	90
5.25	Average strain calculated by the DIC system versus the time	91
5.26	Reference image and image of the stretched state of an MRE sample . . .	92
5.27	Comparison of strains obtained from the DIC analysis and from the pixel measurement method	92
5.28	Stress-strain curves comparing <i>NoField01</i> and <i>NoField02</i> tension tests . .	94
5.29	Mean values of the sample areas versus the performed tests	96
5.30	Stress-strain results of tension tests comparing different types of MREs . .	97
5.31	Stress-Strain results of tension tests of samples tested up to 15 mm	98
5.32	Tangent Moduli E_T versus strain of MRE samples tested up to 15 mm . .	98
5.33	Moduli E_{0-5} and E_T versus the volume particle concentration	100
5.34	MR effects achieved in the <i>Magnet63</i> tests	101
5.35	MR effect versus particle content and preconditioning level (<i>Magnet63</i>) .	102
5.36	MR effects achieved in the <i>Magnet73</i> tests	103
5.37	MR effects achieved in the <i>Magnet89</i> tests	103
5.38	MR effects versus applied magnetic induction	106
5.39	Pure shear sample clamped in the test rig	110
5.40	Test Setup for pure shear tests: DIC system and permanent magnets . . .	110
5.41	Model geometry used in <i>Comsol</i> (pure shear)	111
5.42	Distribution of the magnetic flux density B_Z and B_X	112
5.43	DIC system: pattern sprayed on the sample and vertical displacement field	114
5.44	Vertical and horizontal strains calculated by the DIC system	114
5.45	Horizontal strains calculated by the DIC software after post-processing . .	115
5.46	Average strains calculated by the DIC system versus time	115
5.47	Reference image and image of the stretched state of an MRE sample . . .	116
5.48	Comparison of strains obtained from the DIC analysis and from the pixel measurement method	117
5.49	Stress-strain curves comparing <i>NoField01</i> and <i>NoField02</i> pure shear tests	118
5.50	Stress-strain results comparing different types of MRE samples	118
5.51	Stress-strain results of MRE samples tested up to 6 mm and up to 3 mm .	119
5.52	Tangent moduli versus strain comparing different types of MRE samples .	120
5.53	Moduli versus particle content and preconditioning level	121
5.54	Strain in the horizontal versus vertical direction of MREs	122
5.55	Absolute and relative MR effects of MRE samples tested up to 6 mm . . .	123
5.56	Absolute and relative MR effects of MRE samples tested up to 3 mm . . .	123
5.57	Relative MR effect versus particle content and preconditioning level . . .	124
5.58	Biaxial test rig with an isotropic MRE (<i>CASE I</i>)	127

5.59	Biaxial test setup with and without permanent magnets (<i>CASE 2 - CASE 5</i>)	128
5.60	Geometry implemented into <i>Abaqus</i> and deformed geometry	129
5.61	Deformation U of the biaxial test rig	130
5.62	Contour plot of the vertical deformation of the clamps	130
5.63	Geometry implemented in <i>Comsol</i>	131
5.64	Magnetic flux density within the region occupied by the biaxial sample . .	132
5.65	Calculated and experimentally measured magnetic inductions B_Y	132
5.66	Contour plot of the DIC strains in x-direction	134
5.67	Strain of a pure rubber sample in both stretching directions versus time . .	135
5.68	Structural system of the biaxial test setup	136
5.69	Relative stress factor $f(\varepsilon)$ between anisotropic MREs in uniaxial tension .	138
5.70	Load-displacement and stress-strain curves of all MREs (<i>NoField</i>)	141
5.71	Tangent moduli E_T versus engineering strain	142
5.72	Low strain secant and tangent moduli versus iron volume fraction	142
5.73	Load-displacement curve of isotropic MREs tested without and with mag- netic field	144
5.74	Absolute and relative MR effects of isotropic MREs	144
5.75	Load-displacement curve of anisotropic MREs comparing <i>NoField</i> and <i>Magnet</i> tests with applied induction parallel to the particle alignment . . .	145
5.76	MR effects of anisotropic MREs with the magnetic flux applied parallel to the particle alignment	146
5.77	Load-displacement curve of anisotropic MREs comparing <i>NoField</i> and <i>Magnet</i> tests with the applied induction perp. to the particle alignment . .	146
5.78	MR effects of anisotropic MREs with the applied magnetic induction per- pendicular to the particle alignment	147
5.79	Relative MR effect versus volume particle concentration	148
5.80	Comparison of the mechanical response for all deformation modes	151
5.81	Comparison of absolute MR response for all deformation modes	152
5.82	Comparison of relative MR response for all deformation modes	153
6.1	Predictions of the <i>Ogden</i> model fitted to single deformation modes	169
6.2	Predictions of the <i>Ogden</i> model fitted to combined deformation modes . .	172
6.3	Predictions of the <i>Ogden</i> model fitted to combined deformation modes for isotropic 30% MREs	173
6.4	Predictions of the <i>Ogden-Roxburgh</i> model fitted to compression and pure shear data	176
6.5	Adjusted pure shear and compression data to a 10% preconditioning level	178
6.6	Predictions of the <i>Ogden</i> model fitted to combined deformation modes for pure rubber and isotropic 10% MREs (50% and 10% strain level)	180

6.7	Predictions of the <i>Ogden</i> model fitted to combined deformations for isotropic MREs with 20% and 30% iron content (50% and 10% strain level) .	181
6.8	Predictions of the <i>Qui-Pence</i> model fitted to uniaxial compression data . .	194
6.9	Predictions of the <i>Qui-Pence</i> model fitted to uniaxial tension data	194
6.10	Predictions of the <i>Qui-Pence</i> model fitted to pure shear data	195
6.11	Predictions of the <i>Qui-Pence</i> model fitted to equi-biaxial tension data . . .	195
A.1	Technical information of the silicone rubber <i>MM 240 TV</i>	221
A.2	Technical information of the silicone fluid <i>ACC 34</i> (Page 1)	222
A.3	Technical information of the silicone fluid <i>ACC 34</i> (Page 2)	223
A.4	Technical information of <i>CIP-SQ</i>	224
A.5	Technical information of the silicone rubber heaters (Page 1)	225
A.6	Technical information of the silicone rubber heaters (Page 2)	226
A.7	Technical information of the DC amplifier (Page 1)	227
A.8	Technical information of the DC amplifier (Page 2)	228
A.9	Technical information of the Gaussmeter (Page 1)	229
A.10	Technical information of the Gaussmeter (Page 2)	230
A.11	Technical information of the probe	231
A.12	Technical information of the permanent magnets	232
B.1	Technical drawing of the moulds used for the compression samples	234
B.2	Technical drawing of the moulds used for the tension samples	235
B.3	Technical drawing of the moulds used for the tension samples	236
B.4	Technical drawing of the moulds used for the pure shear samples	237
B.5	Technical drawing of the moulds used for the biaxial samples	238
B.6	Technical drawing of the top rig structure used for compression tests . . .	239
B.7	Technical drawing of the compression setup without magnetic induction .	240
B.8	Technical drawing of the compression <i>Magnet35</i> test setup	241
B.9	Technical drawing of the compression test setup with permanent magnets 62 mm apart creating 210 mT magnetic induction.	241
B.10	Technical drawing of the top rig used for tension and pure shear tests . . .	242
B.11	Technical drawing of the bottom rig used for tension and shear tests . . .	243
B.12	Technical drawing of the tension test setup without magnetic induction . .	244
B.13	Technical drawing of the tension test setup with permanent magnets . . .	245
B.14	Technical drawing of the pure shear test setup with permanent magnets . .	246
B.15	Technical drawing of the top and bottom part of the biaxial test rig	247
B.16	Technical drawing of the connectors to the aluminium rods, and the sliding clamps for the biaxial test rig	248
B.17	Technical drawing of the equi-biaxial setup in the reference configuration	249

B.18	Technical drawing of the equi-biaxial setup in the deformed configuration	250
E.1	Stress-strain curves, tangent moduli, and relative MR effect of pure rubber and isotropic 10% MREs tested in uniaxial compression	258
E.2	Stress-strain curves, tangent moduli, and relative MR effect of isotropic 20% and 30% MREs tested in uniaxial compression	259
E.3	Stress-strain curves, tangent moduli, and relative MR effect of vertically aligned 10% and 20% MREs tested in uniaxial compression	260
E.4	Stress-strain curves, tangent moduli, and relative MR effect of vertically aligned 30% MREs and horizontally aligned 10% MREs	261
E.5	Stress-strain curves, tangent moduli, and relative MR effect of horizontally aligned 20% and 30% MREs tested in compression	262
E.6	Comparison between <i>NoField01</i> and <i>NoField02</i> tension tests of pure rubber and isotropic MREs	263
E.7	Comparison between <i>NoField01</i> and <i>NoField02</i> tension tests of anisotropic MREs with vertical particle alignment	264
E.8	Comparison between <i>NoField01</i> and <i>NoField02</i> tension tests of anisotropic MREs with horizontal particle alignment	264
E.9	Stress-strain curves, tangent moduli, and relative MR effect of pure rubber samples tested in uniaxial tension	265
E.10	Stress-strain curves, tangent moduli, and relative MR effect of isotropic 10% MREs tested in uniaxial tension	266
E.11	Stress-strain curves, tangent moduli, and relative MR effect of isotropic 20% MREs tested in uniaxial tension	267
E.12	Stress-strain curves, tangent moduli, and relative MR effect of isotropic 30% MREs tested in uniaxial tension	268
E.13	Stress-strain curves, tangent moduli, and relative MR effect of vertically aligned 10% MREs tested in tension	269
E.14	Stress-strain curves, tangent moduli, and relative MR effect of vertically aligned 20% MREs tested in tension	270
E.15	Stress-strain curves, tangent moduli, and relative MR effect of vertically aligned 30% MREs tested in tension	271
E.16	Stress-strain curves, tangent moduli, and relative MR effect of horizontally aligned 10% MREs tested in tension	272
E.17	Stress-strain curves, tangent moduli, and relative MR effect of horizontally aligned 20% MREs tested in tension	273
E.18	Stress-strain curves, tangent moduli, and relative MR effect of horizontally aligned 30% MREs tested in tension	274

E.19	Comparison between <i>Preconditioning</i> , <i>NoField01</i> , and <i>NoField02</i> pure shear tests of pure rubber and isotropic MREs	275
E.20	Comparison between <i>Preconditioning</i> , <i>NoField01</i> , and <i>NoField02</i> pure shear tests of anisotropic MREs with vertical particle alignment	276
E.21	Comparison between <i>Preconditioning</i> , <i>NoField01</i> , and <i>NoField02</i> pure shear tests of anisotropic MREs with horizontal particle alignment	276
E.22	Stress-strain curves, tangent moduli, and relative MR effect of pure rubber and isotropic 10% MREs tested in pure shear	277
E.23	Stress-strain curves, tangent moduli, and relative MR effect of isotropic 20% and 30% MREs tested in pure shear	278
E.24	Stress-strain curves, tangent moduli, and relative MR effect of MREs with 10% and 20% vertically aligned particles tested in pure shear	279
E.25	Stress-strain curves, tangent moduli, and relative MR effect of MREs with 30% vertically and 10% horizontally aligned particles tested in pure shear	280
E.26	Stress-strain curves, tangent moduli, and relative MR effect of MREs with 20% and 30% horizontally aligned particles tested in pure shear	281
E.27	Stress-strain curves, tangent moduli, and relative MR effect of pure rubber and isotropic MREs tested in equi-biaxial tension	283
E.28	Stress-strain curves, tangent moduli, and relative MR effect of anisotropic MREs with the magnetic induction parallel to the alignment	284
E.29	Stress-strain curves, tangent moduli, and relative MR effect of anisotropic MREs with the magnetic induction perpendicular to the alignment	285
F.1	Predictions of the <i>Merodio-Ogden</i> model fitted to compression data	291
F.2	Predictions of the <i>Merodio-Ogden</i> model fitted to tension data	292
F.3	Predictions of the <i>Merodio-Ogden</i> model fitted to pure shear data	292
F.4	Predictions of the <i>Merodio-Ogden</i> model fitted to equi-biaxial tension data	293
F.5	Predictions of the <i>Holzapfel-Gasser</i> model fitted to compression data	294
F.6	Predictions of the <i>Holzapfel-Gasser</i> model fitted to tension data	294
F.7	Predictions of the <i>Holzapfel-Gasser</i> model fitted to pure shear data	295
F.8	Predictions of the <i>Holzapfel-Gasser</i> model fitted to equi-biaxial tension	295
F.9	Predictions of the <i>Guo</i> model fitted to uniaxial compression data	296
F.10	Predictions of the <i>Guo</i> model fitted to uniaxial tension data	297
F.11	Predictions of the <i>Guo</i> model fitted to pure shear data	297
F.12	Predictions of the <i>Guo</i> model fitted to equi-biaxial tension data	298

List of Tables

2.1	Uniaxial tension tests published in the literature	15
2.2	Uniaxial compression tests published in the literature	18
2.3	Uniaxial compression tests published in the literature	18
2.4	Simple shear tests published in the literature	21
2.5	Simple shear tests published in the literature	21
3.1	Properties of silicone rubber <i>MM 240 TV</i>	26
3.2	Properties and composition of <i>CIP-SQ</i>	26
4.1	Coordinates of the positions of magnetic flux measurements	42
4.2	Measured magnetic flux at <i>Top</i> and <i>Bottom</i> positions	44
4.3	Measured magnetic flux at <i>Mid-Height</i> positions and attractive force . . .	44
4.4	Dimensions of MRE samples used for the <i>Comsol</i> model	46
4.5	Identification process to find the permeability of isotropic 30% MREs . .	49
4.6	Permeability of isotropic MREs	49
4.7	Permeabilities μ_Z and μ_X of anisotropic MRE samples with vertical particle alignment in z-direction	52
4.8	Permeabilities μ_X and μ_Z of anisotropic MRE samples with particle alignment in the x-direction	54
4.9	Permeabilities μ_Y and μ_Z of anisotropic MRE samples with particle alignment in the y-direction	54
4.10	Permeabilities μ_{\parallel} and μ_{\perp} of anisotropic MREs	55
4.11	Permeabilities of isotropic and anisotropic MREs	56
5.1	Material Properties of Aluminium and Brass	69
5.2	Magnetic flux densities calculated and measured (compression)	71
5.3	Differences in the magnetic flux distribution of B_Z ($\mu_r = 1$)	73
5.4	Comparison between <i>NoField01</i> and <i>NoField02</i> compression tests	75
5.5	Moduli obtained from <i>NoField02</i> compression tests	78
5.6	MR effects achieved with 450 <i>mT</i> and 210 <i>mT</i> applied magnetic flux . .	80
5.7	Types of MRE samples tested under uniaxial tension	83
5.8	Magnetic flux densities calculated and measured (tension)	86
5.9	Differences in the magnetic flux distribution of B_Z ($\mu_r > 1$)	87
5.10	Results of the fatigue tests	89
5.11	Differences in strain comparing the DIC analysis and the pixel analysis . .	93
5.12	Comparison between <i>NoField01</i> and <i>NoField02</i> tension tests	95

5.13	Moduli E_{0-5} and E_T from <i>NoField02</i> tension tests	99
5.14	MR effects achieved in the <i>Magnet63</i> tests	102
5.15	MR effects achieved in the <i>Magnet73</i> tests	104
5.16	MR effects achieved in the <i>Magnet89</i> tests	105
5.17	Types of MRE samples tested under pure shear	109
5.18	Averaged dimensions of pure shear samples	109
5.19	Differences in the magnetic flux distribution of B_Z and B_X)	113
5.20	Moduli E_{0-5} and E_T from no-field pure shear tests	120
5.21	MR effects achieved with 290 mT magnetic induction	124
5.22	Differences in the magnetic flux distribution of B_Y and B_X	133
5.23	Moduli E_{0-5} and E_T from no-field equi-biaxial tests	143
5.24	MR effects measured with 67.5 mT average magnetic induction	148
6.1	Results of the <i>Ogden</i> model fitted to single deformation modes	170
6.2	Results of the <i>Ogden</i> model fitted to combined deformation modes	171
6.3	Results of the <i>Ogden-Roxburgh</i> data fitting to single deformation modes	177
6.4	Results of the <i>Ogden</i> model fitted to combined deformation modes of same preconditioning level	180
6.5	Results of the <i>Qui-Pence</i> model fitted to data of each deformation mode	196
A.1	List of materials used to manufacture MRE materials	220
A.2	List of equipment used to manufacture MRE materials, to measure magnetic flux densities, and to perform experiments with magnetic fields.	220
C.1	Amounts of the components used to manufacture compression, tension, pure shear, and equi-biaxial tension specimens.	251
F.1	Identified model parameters of the <i>Ogden Model</i> fitted to single deformation modes	287
F.2	Different sets of start parameters and resulting identified model parameters of the <i>Ogden Model</i> fitted to uniaxial compression test data of pure rubber	288
F.3	Identified model parameters of the <i>Ogden Model</i> fitted to combined deformation modes	289
F.4	Identified model parameters of the <i>Ogden Model</i> fitted to combined deformation modes of same preconditioning level	290
F.5	Results of the <i>Merodio-Ogden</i> model fitted to each deformation mode	293
F.6	Results of the <i>Holzapfel-Gasser</i> model fitted to each deformation mode	296
F.7	Results of the <i>Guo</i> model fitted to each deformation mode	298

List of Symbols

α_p	Model parameter of the <i>Ogden Model</i> [–]
b	Left Cauchy-Green Tensor
B	Magnetic induction, Unit Tesla $T = Vs/m^2$ (SI units)
$B(H)$	Magnetisation curve
B_{lin1}	Initial part of the magnetisation curve described as linear function
B_{lin1}	Saturation part of the magnetisation curve as linear function
B_{max}	Maximum magnetic flux density in a defined region
B_{mean}	Average magnetic flux density in a defined region
B_{min}	Minimum magnetic flux density in a defined region
B_S	Saturation induction, level where the material saturates
B_{trans}	Function describing the transition part of the magnetisation curve
B_X, B_{\perp}	Magnetic flux perpendicular to the main magnetic field direction
B_Z, B_{\parallel}	Magnetic flux in the main magnetic field direction
B_{\parallel}/B_{\perp}	Magnet factor, relation between the flux in the two directions
β	Contrast factor within the self-consistent point-dipole theory, dimensionless
C	Right Cauchy-Green Tensor
χ	Susceptibility of a material, dimensionless
χ_p	Susceptibility of particles, dimensionless
d	Displacement, measured by the test machine, in <i>mm</i>
d_{50}	Particle size read from the cumulative distribution curve, in <i>mm</i>
E	Modulus or Young's Modulus of stress-strain data, in <i>MPa</i>
E_0	Modulus of stress-strain data achieved without magnetic induction
E_{0-5}	Linear Modulus of stress-strain data from 0% to 5% strain
E_M	Modulus of stress-strain data achieved with magnetic induction
E_T	Tangent Modulus, calculated with linear fits to 1% stress-strain increments
E_m	Modulus of the matrix material
erf	Error function of the Gaussian distribution

ε	Engineering strain (reference configuration), dimensionless
$\varepsilon_y, \varepsilon_x$	Engineering strains in y- and x-direction, dimensionless
η	Damage parameter of the <i>Ogden-Roxburgh Model</i> , dimensionless
$d\mathbf{f}$	Infinitesimal force
\mathbf{f}	Force, in N
\mathbf{F}	Deformation Gradient
$f(\varepsilon)$	Relative stress factor as a function of strain, obtained from uniaxial tension tests
Φ, Φ_p	Volume particle concentration in composites, dimensionless
Φ_m	Volume concentration of the matrix material in composites, dimensionless
$\Phi(\eta)$	Damage function of the <i>Ogden-Roxburgh Model</i>
g	Shape factor of the <i>Guth Model</i> , dimensionless
G	Shear Modulus known from the linear theory, in MPa
\mathfrak{g}	General constitutive equation for a hyperelastic material describing the Cauchy stress
\mathfrak{G}	General constitutive equation for a hyperelastic material describing the Piola-Kirchhoff stress
h	Height of MRE samples, in mm
H	Magnetic field, Units A/m (SI units)
k	Shape factor of the <i>Mooney Model</i> , dimensionless
I	Intensity of magnetisation M , Units Tesla $T = Vs/m^2$ (SI units)
I_1, I_2, I_3	Strain invariants, dimensionless
J	Jacobian Determinant, dimensionless
l	Length, usually in mm
l_0, l_1	Distance between lines in the reference and the stretched state
$l_{v,0}, l_{v,1}$	Vertical distance between lines, reference and stretched state
$l_{h,0}, l_{h,1}$	Horizontal distance between lines, reference and stretched state
λ	Stretch $\lambda = \varepsilon + 1$, dimensionless
$\lambda_1, \lambda_2, \lambda_3$	Principal stretches

λ_i	Vector of stretches, experimental data
M	Magnetisation, Units A/m (SI units)
M	Moment at the fixed support of the biaxial rig, in Nmm
MR_{rel}	Relative MR effect defined with E_M/E_0 , dimensionless
M_S	Saturation magnetisation, Units A/m (SI units)
μ	Magnetic permeability of a material, Units Vs/Am (SI units)
μ_0	Magnetic permeability of vacuum, $\mu_0 = 4\pi \times 10^{-7} Vs/Am$
μ_e, μ_{eff}	Relative effective permeability of composites
μ_{in}	Relative initial permeability of a non-linear magnetic material
μ_{iso}	Relative effective permeability of isotropic composites
μ_m	Relative permeability of the matrix material
μ_p	Relative permeability of the particle material
μ_r	Relative permeability of a material, dimensionless
$\mu_{ }$	Permeability of anisotropic materials in direction of particle alignment
μ_{\perp}	Permeability of anisotropic materials perpendicular to the particle alignment
μ	Modulus of the <i>Neo-Hookean Model</i> , or determined from the <i>Ogden Model</i> , in MPa
μ_p	Model parameter of the <i>Ogden Model</i> , in MPa
μ_{prim}	Modulus determined with a constitutive equation of the primary loading path
N	Model order of the <i>Ogden Model</i> $[-]$
ν	Poisson's ratio, dimensionless
p	Lagrange multiplier required for incompressible materials
P, P_V	Vertical force, measured by the test machine, in N
$P_{increase}$	Increased vertical force due to the applied magnetic induction
$P_{V,CASE1}$	Vertical force recorded in <i>CASE 1</i> , mean value
$P_{V,CASE3}$	Vertical force recorded in <i>CASE 3</i> , mean value
P_H	Horizontal force at the fixed support of the biaxial rig, in N
\mathbf{P}	First Piola-Kirchhoff Stress (Engineering Stress), in MPa
Ψ	Strain-energy function of an hyperelastic material, in MPa
$\tilde{\Psi}$	Strain-energy function of the primary loading path
Ψ_2	Structural parameter of composite structures, dimensionless

R_2	Coefficient of determination, dimensionless
$d\mathbf{s}, d\mathbf{S}$	Surface elements defined in the current and reference configuration
$\mathbf{S}_{\mathfrak{S}}$	Objective function to be minimised
σ	Confidence interval provided by the DIC system, in <i>pixels</i>
σ	Cauchy Stress defined in the current configuration, in <i>MPa</i>
σ_A, σ_{AW}	Stress obtained from uniaxial tension tests
σ_x	Stress in the stretching direction x , in <i>MPa</i>
σ_y	Stress in the stretching direction y , in <i>MPa</i>
$\sigma_{x, \text{increase}}, \sigma_{y, \text{increase}}$	Increased stress in the stretching directions due to a magnetic induction
t	Thickness of MRE samples, in <i>mm</i>
$\boldsymbol{\tau}_i$	Vector of experimental stress data, in <i>MPa</i>
U_1, U_2, U_3	Deformation of a test setup in the 1, 2 and 3-direction, in <i>mm</i>
w	Width of MRE samples, in <i>mm</i>
w	Length of the clamps in the biaxial rig, in <i>mm</i>
w_c, w_{ps}, w_{eb}	Weight factors used in Piola stress functions to scale the compression (<i>c</i>), pure shear (<i>ps</i>), and equi-biaxial tension (<i>eb</i>) deformation mode
\mathbf{x}, \mathbf{X}	Material positions in the current and the reference configuration

List of Abbreviations

A	Anisotropic MREs with particle alignment in the loading direction
AC	Alternating current
AW	Anisotropic MREs with particle alignment along the sample width perpendicular to the loading direction
ACC 34	Silicone Fluid provided by the company <i>ACC Silicones</i>
AOI	Area of interest, used for the DIC analysis
ATMD	Adaptively tuned mass damper
ATVA	Adaptively tuned vibration absorber
AVA	Adaptive vibration absorber
BR	Cis-polybutadiene Rubber
CIP	Carbonyl Iron Powder
CIP-SQ	Specific type of Carbonyl Iron Powder, provided by the company <i>BASF</i>
Co	Cobalt particles
CPVC	Critical particle volume concentration
c	Uniaxial compression deformation mode
DC	Direct current
DIC	Digital Image Correlation
DMA	Dynamic mechanic analysis
DOF	Degree of freedom
EPU	Urea-urethane Elastomer
EPSRC	Engineering and Physical Sciences Research Council
ERF	Electro-Rheological Elastomers
eb	Equi-biaxial tension deformation mode
Fe	Iron particles
MDOF	Multi-degree of freedom
MM 240 TV	Silicone Rubber provided by the company <i>ACC Silicones</i>
MR	Magneto-Rheological

MRE	Magneto-Rheological Elastomer
MRF	Magneto-Rheological Fluid
MSMA	Magnetic Shape Memory Alloy
NR	Natural Rubber
PCL	Polycaprolactone
PDMS	Poly-dimethyl-siloxane / Silicone rubber
PTFE	Polytetrafluorethylen, known as Teflon
PU	Polyurethane
PVA	Polyvinyl alcohol / Hydrogel
ps	Pure Shear deformation mode
RTV	Room Temperature Vulcanizing Silicone
SEBS	Styrene- β -ethylene-co-butylene- β -styrene
SEM	Scanning electron microscopy
SEEPS	Polystyrene- β -ethylene-ethylene-propylene- β -styrene
SI	International System of Units
SMA	Shape Memory Alloy
SMP	Shape Memory Polymers
SSA	State-switched absorber
TVA	Tuned vibration absorber
t	Uniaxial tension deformation mode
VPC	Volume particle concentration
VR	Vinyl-containing rubber
VSM	Vibration Sample Magnetometer

1 Introduction

Magneto-Rheological Elastomers (MREs) are composite materials made of an elastomer as the matrix and usually iron particles as the magnetic component. The magnetic particles are dispersed in the matrix material, and are locked in position after the elastomeric material is cured. Both isotropic and anisotropic materials can be prepared. The latter can be manufactured by exposing the uncured composite mixture to a magnetic field during the curing process. This aligns the particles into chains, resulting in both mechanical and magnetic anisotropy. MREs belong to a class of smart materials that can change their properties reversibly and almost instantaneously by the application of an external magnetic field. Not only mechanical properties such as stiffness, natural frequency and damping coefficient can be altered, but also the shape and electrical properties of MREs can change. This behaviour is caused by the magnetic interaction of the particles within the matrix material. MREs can potentially be used as vibration absorbers, adaptive stiffness devices, actuators to control the flow of a fluid or a gas, or sensors measuring changes in electrical resistance or recognising the change in dimensions. Thus, MREs are promising materials that can potentially be used for a wide range of applications. Research on MREs is still relatively immature even though several research groups have been working on them since 1983. Experimental analysis and constitutive models are required to describe the material behaviour and to advance the development of applications using MREs.

Since the behaviour of MREs is very complex, experimental data characterising MREs under various deformation modes, both without and with the application of external magnetic fields, are essential to develop accurate constitutive models. Understanding the magnetic properties of MREs is required in order to predict the material behaviour under magnetic fields. So far, no consistent experimental data set is available, and no accurate constitutive model describing the behaviour of MRE materials has yet been formulated and verified.

The work presented in this thesis is concerned with the large-strain properties of MREs, with the main focus on experimental characterisation. Isotropic and anisotropic MREs with various amounts of iron particles are manufactured and used for characterisation under uniaxial tension, uniaxial compression, pure shear, and equi-biaxial tension deformation both in the absence and in the presence of magnetic fields. The aim is to generate an extensive experimental data set for evaluation and development of constitutive models able to describe the behaviour of MREs under general deformations and arbitrary magnetic fields. The ultimate goal is to facilitate the design of large-strain applications employing MREs.

1.1 Objectives

The main objectives to be achieved in this work are to:

- Manufacture MREs using a reliable and repeatable process.
- Determine the magnetic permeability of both isotropic and anisotropic MREs.
- Characterise the mechanical response of both isotropic and anisotropic MREs in the absence of a magnetic field and study their non-linear large-strain behaviour under various deformation modes.
- Study the influence of the *Mullins* effect on the stress-strain behaviour of MREs. The experimental procedure and method of data analysis has to account for this stress-softening effect to ensure that reliable and comparable data are used for the MRE characterisation.
- Characterise the mechanical response of isotropic and anisotropic MREs in the presence of magnetic fields. The MR effect is determined as the increase in tangent moduli using experimental data from tests without and with the application of external magnetic fields.
- Generate an extensive experimental data set from tests conducted using various deformation modes, on the same type of MRE material, and using samples preconditioned to the same strain level. Such consistent data are required to develop constitutive equations describing the behaviour of MRE materials.
- Conduct data fitting to pre-established hyperelastic constitutive models. Combined experimental data sets, obtained under different deformations, are to be used to characterise the MREs under more general deformations.

1.2 Structure of the Thesis

The thesis is structured in seven chapters. The main content and motivation of each chapter is given below:

Chapter 2 is a literature review on experimental investigations conducted on MREs. The classification of MREs as a smart material emphasises the diversity of MREs. Further, the review provides a historical overview of research carried out so far and discusses the common choices of material components used to manufacture MREs. Several potential applications proposed for MREs are discussed. Large-strain experiments conducted on MREs are an important focus of the review, the latter exposes a lack of comparable experimental data necessary for the development of accurate constitutive models.

Chapter 3 describes the material components and manufacturing process used to produce isotropic and anisotropic MREs. In this investigation MREs composed of silicone rubber and up to 40 *vol%* Carbonyl Iron Powder (CIP) are manufactured. Specimens of different shapes are manufactured in specially designed moulds and anisotropic samples were produced by placing the moulds inside a strong magnetic field during the curing process. The microscopic structure of isotropic and anisotropic MREs is briefly studied using optical and confocal microscopy.

Chapter 4 discusses the magnetic properties of CIP and composite materials, and examines the magnetic permeabilities of the produced MREs. The magnetic permeabilities of MREs are identified using a novel, simple and low-cost method. Magnetic flux and attractive force measurements are conducted and the permeabilities are identified using an inverse approach involving finite element calculations performed using the multi-physics software *Comsol*. Understanding magnetic permeability of MREs is a necessary requirement for the future development of constitutive models for MREs subject to magnetic fields.

Chapter 5 contains experimental results from large-strain uniaxial compression, uniaxial tension, pure shear, and equi-biaxial tension experiments up to various levels of strain. Tests are performed both without and with the application of an external magnetic field. The importance of the Mullins effect and the level of preconditioning strain are examined. A novel testing strategy is developed and used throughout this investigation. The approach is designed to eliminate the influence of the stress-softening *Mullins* effect from the final stress-strain results in order to isolate and characterise the MR response of the material. The non-linear large-strain behaviour of MREs is characterised at first in the absence of a magnetic field. MR effects are then studied and quantified by measuring the increase in tangent moduli when samples are subjected to a magnetic field. In this chapter an extensive experimental data set is generated that can be used to evaluate and develop constitutive models for MREs.

Chapter 6 presents various constitutive models designed to describe the non-linear behaviour of materials under large strain. A short introduction to continuum mechanics and constitutive equations relevant to this investigation are presented. Model parameters of the *Ogden* model, suitable for describing isotropic MREs under general deformations in the absence of a magnetic field, are successfully fitted to the experimental data. The performance of several transversely isotropic constitutive models (available in the literature) in describing the response of anisotropic MREs under general deformations in the absence of a magnetic field is then assessed. The theoretical framework used to model magneto-elastic materials is presented.

Chapter 7 summarises the main results and conclusions of this thesis and gives suggestions for future work.

2 Literature Review - Experimental Work

Magneto-Rheological Elastomers (MREs) belong to the class of smart materials with manifold characteristics. MREs are known to change their mechanical properties such as stiffness and natural frequency, but also their shape and electrical properties by the application of an external magnetic field. Research on MREs has been conducted since 1983 but is still at an early stage. Thus far, the properties of MREs in the small-strain region and their performance as vibration absorbers is studied extensively. Some prototypes of applications were developed but MREs are not yet used in industrial applications. Experimental data characterising the behaviour of MREs under large-strain are relatively few, and the multi-axial behaviour of MREs was never studied. Only recently the magnetostriction and electrical properties were discovered. This chapter provides a literature review concentrating on the experimental investigations previously performed by other researchers. MREs are classified into the group of smart materials in Section 2.1. A historical overview is provided in Section 2.2 covering experimental investigations. The common choices of materials to manufacture MREs, and the microstructure are discussed in Section 2.3. Potential applications and prototypes are presented in Section 2.4. Finally, the large-strain experiments conducted on MREs are discussed in detail in Section 2.5. The classification of MREs into smart materials is important to understand the great capability of MREs, and their potential use in a wide range of applications. The study of investigations performed previously on MREs is important to focus future research. The large-strain experiments are discussed in detail to emphasise the difficulties in comparing them, and to clarify that there is still a lack of experimental data that can be used to develop constitutive models in future.

2.1 Classification of Smart Materials

‘Smart’ or ‘intelligent’ materials are those that can alter their properties under the influence of external stimuli. The range of smart materials is very large and can be broadly distinguished between property-changing, energy-exchanging, and matter-exchanging smart materials (Ritter, 2007). Piezoelectrics, shape memory alloys, electro-active, and magneto-active materials are all examples of property-changing smart materials. Electrical properties such as resistance or capacitance, magnetic properties such as permeability, mechanical properties such as stiffness or viscosity, and material shape can all be altered when the property-changing materials are exposed to external stimuli. Examples of external stimuli include mechanical pressure, temperature, electrical current, or magnetic flux. Various property-changing materials are classified in Figure 2.1.

Some materials work in two directions, for example piezoelectric devices generate an elec-

Stimuli Response	Electrical Current	Magnetic Fields	Mechanical Loading	Temperature
Electrical (i.e. Resistance, Capacitance)	Ferroelectrics	Magnetoresistor, Capacitors, (i.e. MRE)	Electrostrictive Materials Piezo-electric, Piezo- resistive devices Magnetostrictive Materials (i.e. MRE)	Thermoelectric and Electrocaloric Materials
Magnetic (i.e. Permeability)	Magnetic Materials, Paramagnetic, Diamagnetic		MRE	
Mechanical (i.e. Stiffness, Frequency, Viscosity)	Electro-Rheological Fluids (ERF)	Magneto-Rheological Fluid (MRF), Magneto-Rheological Elastomer (MRE)	Auxetics, Thixotropics	
Shape Change	Electrostrictive Materials: Piezo-electric, Piezo- resistive devices, ERF	Magnetostrictive Materials: Ferrofluid, Ferrogel, MRE Magnetic Shape Mem- ory Alloy (MSMA)		Shape Memory Alloy (SMA) Shape Memory Polymers (SMP)

Figure 2.1: Classification of property-changing smart materials (Choi, 2009).

tric field when subject to a mechanical strain, and change their shape when exposed to an electric field. Likewise, ERFs, MRFs, and MREs not only change their shape when exposed to an electrical or magnetic field (electro- and magnetostrictive materials), but also change their resistance when a mechanical strain is applied (Bica, 2012; Wang and Gordaninejad, 2009). Additionally, MREs also alter their resistance or capacitance when exposed to a magnetic field (Li *et al.*, 2009). Electro- and magneto-active materials are very similar and only differ in the way they are activated. They both consist of an insulating or non-magnetic matrix material (either a fluid, a foam, or an elastomer), into which polarisable but non-conductive particles or magnetic particles are mixed. The size of these particles can range from nanometers to several micrometers. Electro-active materials require quite high voltages for activation (Choi, 2009). Magneto-active materials have clear advantages compared to the electro-active materials, since, for example, they can be activated by permanent magnets, implying that they can be used in the absence of external power sources (Carlson and Jolly, 2000). Depending on the type of matrix material, MRFs, ferro-fluids, MR foams, MREs, and ferro-gels can all be distinguished. MRFs and ferro-fluids are composed of a fluid matrix, which is usually a low-viscosity silicone fluid or oil. MRFs change their viscosity, yield stress, and natural frequency when exposed to a magnetic field. They work in the post-yield regime (Carlson and Jolly, 2000), and find use in vibration control devices (Jolly *et al.*, 1999; Klingenberg, 2001). MRFs are the best known magnetoactive materials, finding widespread applications (Klingenberg, 2001). MREs and ferro-gels are comprised of elastomeric matrix material in which magnetic particles are dispersed. It is often said that

MREs are the solid analogue of MRFs (Carlson and Jolly, 2000), although there are distinctive differences. In MREs, particles are locked in position, and further, anisotropic MREs can be prepared by exposing the fluid mixture to a magnetic field during the curing process. This forces the magnetic particles to align in chains, resulting in both strong mechanical and magnetic anisotropy. MREs change their stiffness and natural frequency when subjected to magnetic fields, and are employed in the pre-yield regime (Jolly *et al.*, 1996a). The size of magnetic particles distinguishes MRFs from ferro-fluids, and MREs from ferro-gels. Ferro-fluids and ferro-gels tend to consist of nano-sized particles which are effectively magnetic mono-domains, whereas MREs and MRFs consist of micron-sized magnetic particles which “support hundreds of magnetic domains” (Carlson and Jolly, 2000). Ferro-gels and ferro-fluids are strongly magnetostrictive materials that dramatically alter their shape in response to a magnetic flux. MREs and MRFs are also magnetostrictive, although the magnitude of shape change is much smaller; nevertheless, they exhibit a range of magnetostriction similar to that of the giant magnetostrictive material, *Terfenol-D* (Aga and Faidley, 2008). Aside from these general definitions, instances in the literature describing nano-sized particles embedded in an elastomeric matrix referred to by the authors as MREs have been published, potentially causing some confusion in the accepted terminology (Bica, 2012; Filipcsei *et al.*, 2007; Stepanov *et al.*, 2013a). Further, ferro-gels were originally manufactured using nano-sized particles embedded in matrix materials much softer than those used to manufacture MREs. However, more recently, micron-sized particles have also been mixed into silicone gels (Varga *et al.*, 2006), effectively blurring the distinction between the accepted terminology for ferro-gels and MREs.

This study is concerned with the properties of Magneto-Rheological Elastomers (MREs). Their classification into smart materials has shown that MREs are able to change several properties, making them suitable for a wide range of possible applications. Magnetic fields, mechanical properties, and the material shape can be external stimuli for MREs, but can also be internal responses. MREs can be used as vibration control elements, as adaptive stiffness devices, as actuators due to their ability to change their shape, and also as resistors that alter their resistance due to an applied magnetic flux or due to an applied mechanical strain. They can also potentially be used as electric or force sensors. The research which was conducted on MREs over the past few years is detailed in the following sections, including potential and prototyped applications of MREs. The main focus in this study are the changes of mechanical stiffness under the influence of a magnetic flux when large strains are applied to the material.

2.2 Historical Overview

To provide an historical overview, past experimental investigations on MREs are presented in a time-line in Figure 2.2. Researchers are sorted into research groups according to their locations and research partners. Descriptions of the working area of each specific research group, the material used, the main results, and the applications developed are described in this graphical overview. Colours are used to identify the working area of the groups indicating the following categories: static large-strain experiments (red), dynamic tests under small strain (yellow), magnetostriction of MREs (blue), microstructure studies (orange), magnetic and electrical properties of MREs (purple), and proposed applications (green). References are given within Figure 2.2.

The MR effect was first explored by Rabinow (1948) while working on MRFs, but it was not until 1983 that Rigbi and Jilken (1983) conducted preliminary tests on MREs. Initial investigations on MREs were concerned with the dynamic small strain properties; the change of storage modulus and the shift of natural frequency were investigated by Jolly *et al.* (1996b) and Ginder *et al.* (1999). Interest in MREs increased significantly from 2002, with the main focus remaining on dynamic small strain shear properties (see Figure 2.2).

Magnetostrictive behaviour was also of interest in the early years (Ginder *et al.*, 2002; Zhou and Jiang, 2003), but the results were rather contradictory (see Figure 2.2 and Gong *et al.* (2012)). Diguet *et al.* (2010) reported the maximum magnetostrictive stretch in MREs of about 10%. The effect was further investigated by Gong *et al.* (2012), who measured the full-field deformation of an MRE sample. Larger reported deformations (Stepanov *et al.* (2013a) reported 250% elongation) can be attributed to the material which are ferro-gels rather than MREs, and to the non-uniformity of the applied magnetic inductions.

From 2009 interest in the magnetic and electrical properties of MREs increased as the potential of MREs as sensing materials was recognised (Li *et al.*, 2009). Their resistance was found to increase with increasing magnetic field and increasing compressive force (Bica, 2009a; Wang *et al.*, 2009). Magnetisation curves of MREs were studied by Boczkowska and Awietjan (2012), who observed strong anisotropy in the magnetic properties in anisotropic MREs. The magnetic permeability of isotropic and anisotropic MREs was also investigated by both Kallio (2005) and Zeng *et al.* (2013). Fatigue behaviour of MREs was studied by Krolewicz *et al.* (2013) using simple shear tests (up to 12.5% strain), and also by Zhou *et al.* (2013a) using the bubble inflation method to induce equi-biaxial tension. More details are presented in Figure 2.2.

2.3 Manufacture and Microstructure of MREs

Most researchers manufacture MREs using silicone rubber with a low zero-field stiffness as the matrix component. The silicone rubber is often blended with silicone oil to decrease the rubber's final moduli. Various other matrix materials have also been used, such as natural rubber, thermoplastic elastomers, and polyurethane (see Figure 2.2). Carbonyl Iron Powder (CIP) is the most commonly used magnetic particle component. CIP are spherical particles with an average size of about $5\ \mu\text{m}$. Nano-sized particles such as magnetite, and irregularly shaped particles of about $200\ \mu\text{m}$ diameter have also been used. Iron is said to be the best choice due to the high magnetic permeability, high saturation magnetisation, and a very low remnant magnetisation (Zhang, 2005). Recently, tests on MREs with nickel or cobalt particles have been performed, though iron-based MREs were found to generate the highest MR effect (Padalka *et al.*, 2010; Song *et al.*, 2009). Nevertheless, nickel particles seem to result in better sensing capabilities compared to iron-based MREs (Bossis *et al.*, 2012). Graphite particles were also added to enhance the sensing properties of MREs (Bica, 2012; Li *et al.*, 2009).

The microstructure of MREs has been observed by optical microscopy (Farshad and Benine, 2004), scanning electron microscopy (SEM) (Chen *et al.*, 2007b), and also with x-ray micro-computed tomography ($X\mu\text{CT}$) (Borbath *et al.*, 2012; Günther *et al.*, 2012). Many researchers have recorded images that demonstrate both the random distribution of the particles in isotropic MREs, and the particle alignment in anisotropic MREs (Farshad and Benine, 2004). Various investigations aim to understand the relationship between magnetic flux intensity during the curing process and final microstructure (*e.g.* Chen *et al.*, 2007b). The chains of the aligned particles were found to be thicker and more widely separated when higher magnetic flux densities were applied during the curing process (Chen *et al.*, 2007b). Günther *et al.* (2012) and Borbath *et al.* (2012) performed very interesting studies using μCT . They found that gravity has a large influence on the microstructure, and that magnetic inductions larger than $200\ \text{mT}$ are required to stop the particles from settling during the curing process.

2.4 Applications

MRE research is still at an early stage and the material is not yet actively used in industrial applications. However, quite a few applications have been designed and prototyped. This section provides an overview of the applications employing MREs.

Most of the developed and patented applications are adaptively tuned vibration absorbers and variable stiffness devices. MREs are usually used in a shear mode under small deformations, although applications using the MRE in a compression mode or compression-shear mode were proposed. The first known application of MREs is a suspension bushing developed

by Watson (1997) and Ginder (2004) and illustrated in Figure 2.3. The MRE between the shaft and the outer cylinder works in a shear mode. The properties of the prototype bushing

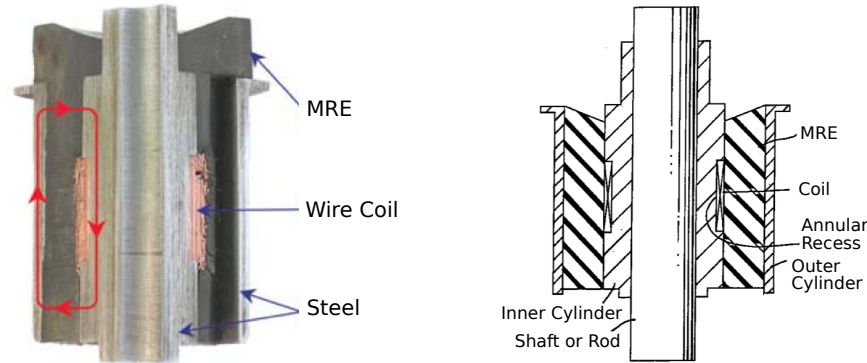


Figure 2.3: Automotive suspension bushing developed by the *Ford Motor Company*
left) Photograph of the bushing, flux path is shown in red (Ginder, 2004), right) Scheme of the bushing (Elie *et al.*, 1997)

were examined by Ginder *et al.* (2000) and the spring rate magnitude and the damping rate can be increased in axial direction about 25% and 40%, respectively, by applying a current of 5 A. Further, the response time of the bushing is less than 10 ms. Ginder *et al.* (2001) also constructed a Tuned Vibration Absorber (TVA). The TVA is a one degree-of-freedom (DOF) system where the reaction mass is dynamically excited and the MRE is sheared. The TVA is able to shift its natural frequency from 500 to 610 Hz by the application of 560 mT magnetic flux. An Adaptive Tunable Vibration Absorber (ATVA) was later developed by Deng *et al.* (2006). The storage modulus of the ATVA could be increased by 130% and the frequency could be shifted by about 45% when a 900 mT flux was applied. Hitchcock *et al.* (2006) patented a tunable isolation device, composed of an MRE sandwich structure with two magnetic activation layers. The device was designed as either a curved or flat beam or in form of a plate. The magnetic activation layer could hold either electromagnets or permanent magnets. In the curved beam configuration the MRE works in a compression-shear mode, shown in Figure 2.4. The device is supposed to work in the small-strain regime, but the

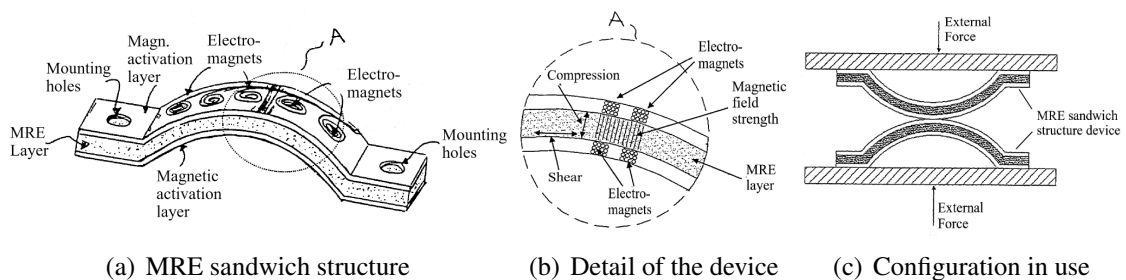


Figure 2.4: Tunable vibration isolation device developed by Hitchcock *et al.* (2006).

performance of the device was not investigated (Hitchcock *et al.*, 2006). Albanese Lerner

(2005) invented an adaptive vibration absorber (AVA) with the MRE working in the compression mode (Albanese and Cunefare, 2003; Albanese Lerner and Cunefare, 2006, 2008); see Figure 2.5a. The natural frequency of this device could be shifted from 57 to 347 Hz , a relative increase of 510% (Albanese Lerner, 2005). Opie developed a tunable vibration isolator using permanent magnets (Opie and Yim, 2007). An ATVA working in a torsional mode was developed by Zhang *et al.* (2008a). This ATVA was designed for powertrain vibration reduction. The multi-degree-of-freedom (MDOF) system represented a novel development for vibration absorbers. A schematic of the ATVA is shown in Figure 2.5b. The application was reported to work well for a wide frequency range and could handle multi-harmonic excitations (Zhang *et al.*, 2008a). In 2008 Keinanen *et al.* developed a prototype of an adaptive

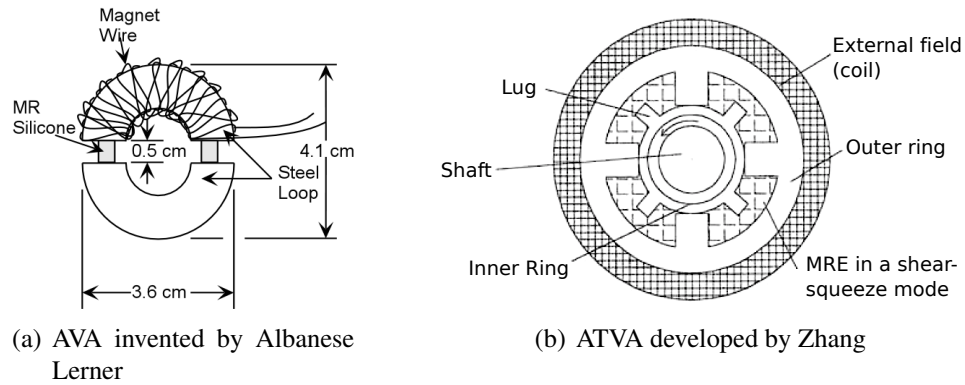


Figure 2.5: (a) Scheme of the adaptive vibration absorbers (AVA) invented by Albanese Lerner and Cunefare (2006). (b) Scheme of the adaptive tuned vibration absorber (ATVA) developed by Zhang *et al.* (2008a).

tuned mass damper (ATMD). The functionality of MREs and temperature-sensitive elastic epoxy was combined to achieve operations across a wider frequency range. An alternative ATVA was designed by Ni *et al.* (2009) to work in combination with a piezoelectric device. This device used the MRE in a shear mode but the piezoelectric component could change the compression strain of the MRE in the direction of the particle alignment to enhance the MR effect. Choi (2009) worked on large-scale structures such as ships, and developed a vibration absorber to act on a propeller shaft. The MRE worked in a rotational mode similar to the ATVA developed by Zhang *et al.* (2008a). In the first eigenstate of the propeller shaft the natural frequency could be changed from 426 to 491 Hz by applying 500 mT magnetic flux. Xu *et al.* (2010) found that due to the high damping ratio of MREs the performance of ATVAs could be unsatisfactory and developed an active-damping-compensated ATVA to overcome this problem. The damping of this ATVA could be actively reduced with a voice coil motor. This ATVA was able to shift its natural frequency from 29 to 45 Hz , which is a relative change of 55%. Sinko *et al.* (2012) designed an ATVA employing a special hybrid electromagnetic design, here both permanent and electromagnets are used to decrease the required current input. A vehicle suspension with the MRE working in the compression mode

was developed by Marur (2013).

Thus far, MRE applications have been designed for use under large strain in only three applications: Crist (2009) patented an active vibration damper, with the MRE working up to 20% strain. A schematic of the device is shown in Figure 2.6. An increase in shear modulus

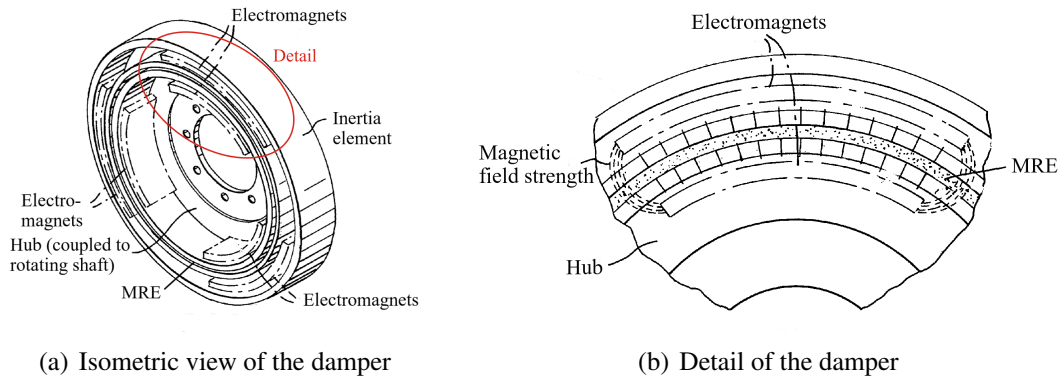


Figure 2.6: Scheme of the active vibrational damper invented by Crist (2009)

of 7.4% at 20% strain with 200 mT were achieved (Crist, 2009). A prototype of an isolator for seat vibration control with considerable loads were developed by Du *et al.* (2011) and Li *et al.* (2012b). Here the MRE works in a combined compression-shear mode. Gudmundsson (2011) and Össur *et al.* (2013) developed a prototype of an MRE spring for a prosthetic foot shown in Figure 2.7. The MRE in this application were used in large compressive strains.

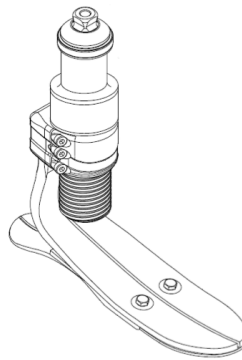


Figure 2.7: Design of the prosthetic foot having an MRE element on the vertical axis (Gudmundsson, 2011; Össur *et al.*, 2013).

More recently the magnetostriction effect of MREs was used in various applications. For example, MREs have been used to change the flow of a fluid or a gas (Böse *et al.*, 2011; Heier and Schubert, 2010) and to activate piezo-electric devices (Du and Chen, 2012). Heier and Schubert (2010) invented an actuator, in which the MRE changed its shape by application of a magnetic field. In the active state the MRE squeezed a tube which increased fluid flow. The inactive and active state of the actuator are illustrated in Figure 2.8. The patent (Heier and Schubert, 2010) gives neither magnitudes of the magnetostriction effect nor

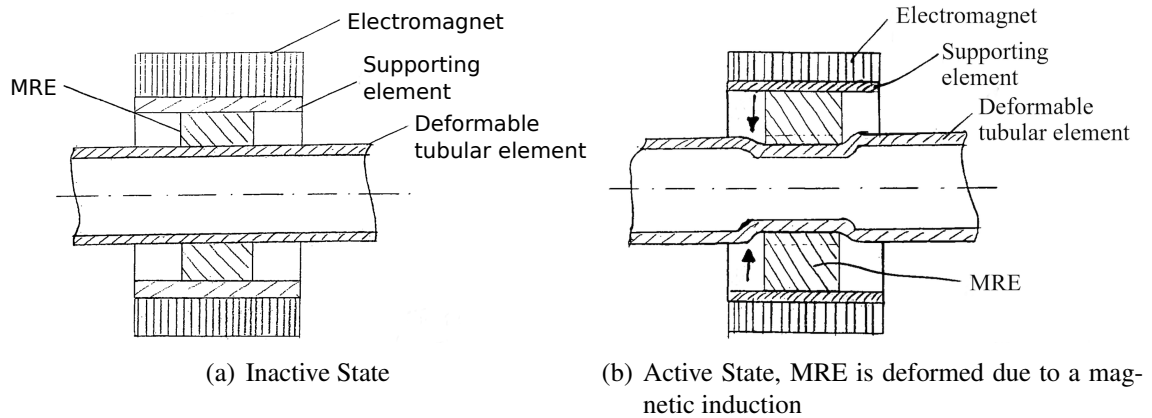


Figure 2.8: Scheme of the actuator which employs the magnetostriction property of MREs invented by Heier and Schubert (2010)

details concerning the material used for the MRE. Böse *et al.* (2011) developed a valve to control the air or fluid flow, in which a ring-shaped MRE expands radially due to an applied magnetic field. Another valve to control flow was also designed by Stepanov *et al.* (2013a). A micro-electro-mechanical magnetometer was developed by Du and Chen (2012); here the magnetostriction effect of an MRE activated a piezoresistive pressure sensor. An epoxy resin mixed with 55w% carbonyl nickel particles with a size of $2.73 \mu\text{m}$ was used for the MRE. Du and Chen (2012) planned to improve the performance of the magnetometer using a better material.

Li *et al.* (2009) used the sensing properties of MREs to develop the first force sensor employing MREs and found that an MRE with 55w% CIP and 25w% graphite particles provided the best sensing properties: the resistance changed by about 85% when the normal force is increased from 5 N to 15 N.

Most of the published and patented applications concerning MREs are relevant to the small strain region. MREs are used to reduce vibrations by shifting the natural frequency, and are used to change the elastic stiffness. Consequently, the small-strain behaviour of MREs is the best explored of their properties. Only three applications have been proposed with MREs working up to large strains, all of which were developed after 2009. It is likely that MREs can be effectively used under large strain, though because the large-strain behaviour of MREs has not been well explored so far, only a very few applications have been proposed that exploit the use of MREs under such conditions. To advance the development of large-strain applications, both experimental data and accurate constitutive models to describe the MREs under finite strains are required. This will permit design and manufacture of novel devices using the advantages offered by the latest computational engineering tools.

2.5 Large-Strain Experiments on MREs

The historical overview in Section 2.2 and especially Figure 2.2 show that experiments to study the large-strain properties of MREs are relatively few. In this section previous investigations involving large strain experiments with the application of magnetic flux densities are described and compared. The reviewed experiments will be sorted by deformation modes: uniaxial tension, uniaxial compression, and simple shear. The used materials, the maximum strain level, the applied magnetic field strength, and the resulting MR effects are presented in Tables 2.1 to 2.5 to allow comparison with the results of large-strain experiments presented in this study. The text highlights important achievements, draws out trends, and compares the results achieved. The absolute MR effect $E_M - E_0$ is the difference between the no-field modulus E_0 and the modulus E_M achieved with the application of a magnetic induction during the test. The relative MR effect is defined as the increase in moduli with $(E_M/E_0 - 1) \times 100$. Some researchers worked with a change in stress or with a change in hysteresis of the stress-strain curves rather than with the tangent moduli to obtain MR effects.

Uniaxial Tension Tests The first large strain tensile tests were performed by Bellan and Bossis (2002). The stress difference was considered rather than the differences in moduli to characterise the behaviour with and without applied magnetic flux, but no MR effect could be ascertained from the stress-strain data provided. The increase in stress due to the applied field could only be observed in the small-strain region up to 5%. Stepanov *et al.* (2007) conducted tensile tests on MREs with iron particles of two different sizes, and achieved higher MR effects with particles having a broad size distribution from 2 to 70 μm . The stress-strain curves and the tangent modulus versus strain are shown in Figure 2.9. Stepanov *et al.* (2007)

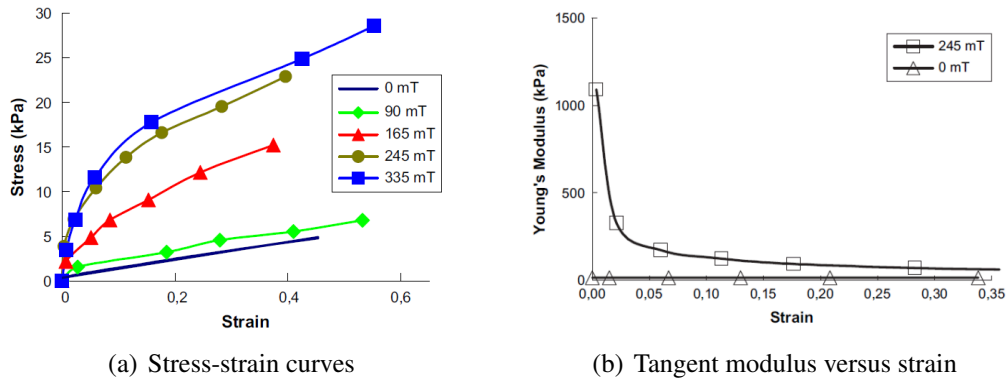


Figure 2.9: Results of the uniaxial tension tests performed by Stepanov *et al.* (2007).

reported an absolute MR effect of about 1000 kPa in the small-strain region. However, in the author's point of view the moduli and MR effects calculated at very small strain may not

be reliable, as experimental errors can easily occur, *i.e.* the tension sample might be slightly stretched or bulged as result of clamping them into the setup. The data are also sensitive to the method of analysis, since the raw data of the test machine have to be cut and shifted in a certain way, which may also induce errors. For a deeper discussion on the method of analysis see Section 5.1.2. Much more reliable data for the MR effect are obtained from 2% strain. The data in this range still suggest a very large MR effect of 400 *kPa* absolute, and 3000% relative increase as seen in Figure 2.9. The high MR effect is due to the low no-field modulus of the MRE material. The MRE materials used and the magnetic inductions applied in the described uniaxial tension tests are summarised in Table 2.1.

		Bellan2002	Stepanov2007
MRE Material	Matrix	Silicone Rubber and Oil	Vinyl Rubber
	Particles	CIP, 2 μm	Iron, 2 to 70 μm
	VPC	15%	37%
	Magnetic Flux	250 <i>mT</i>	Isotropic
	Modulus E_0	530 <i>kPa</i>	13 <i>kPa</i>
Test	Strain Level	10%	60%
	Magnetic Flux	155 <i>mT</i>	335 <i>mT</i>
	Direction	\parallel loading \parallel alignment	\perp loading
MR	absolute	not provided	400 <i>kPa</i>
	relative	not provided	3000%

Table 2.1: Uniaxial tension tests performed by Bellan and Bossis (2002) and Stepanov *et al.* (2007) are summarised. The MRE material (matrix, particles, VPC, magnetic flux during curing, and no-field moduli E_0), the strain level and applied flux during the experiment, and the resulting MR effects are listed.

Uniaxial Compression Tests Farshad and Le Roux (2005) performed compression tests in which permanent magnets were attached to one side of the test setup. However, placing magnets on just one side of the setup most likely led to a non-uniform magnetic field. The stress-strain results of Farshad's experiments are illustrated in Figure 2.10. The stress-strain curves up to 5% strain are identical regardless of the applied magnetic induction. Once again, this indicates that the data in the small-strain region are not reliable due to experimental error and the method of analysis as discussed above. The moduli show an increase above 5% strain, and the results are listed in Table 2.2. Compression tests performed earlier by Farshad and Benine (2004) used permanent magnets attached to both sides of the test setup, which moved towards each other while the test proceeded. This was not a suitable test setup as the magnetic attraction force between the magnets increased as the distance between them became smaller, which clearly influenced the results. Compression tests with up to 1 *T* magnetic induction created with a ring-shaped solenoid around the tested specimen were performed by Kallio (2005). The solenoid ensured a uniform magnetic flux

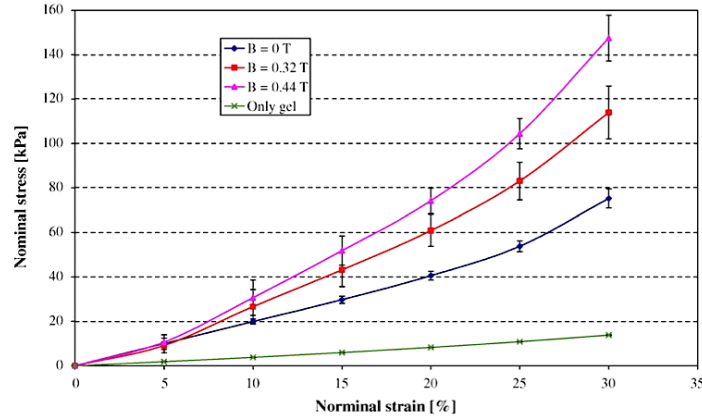


Figure 2.10: Results of the uniaxial compression tests performed by Farshad and Le Roux (2005).

distribution, but it blocked visual access to the experiment. The resulting stress-strain curves and the linear moduli calculated from stress-strain data up to 2% strain are illustrated in Figure 2.11. Saturation occurs in the MRE material above 700 mT applied induction, so

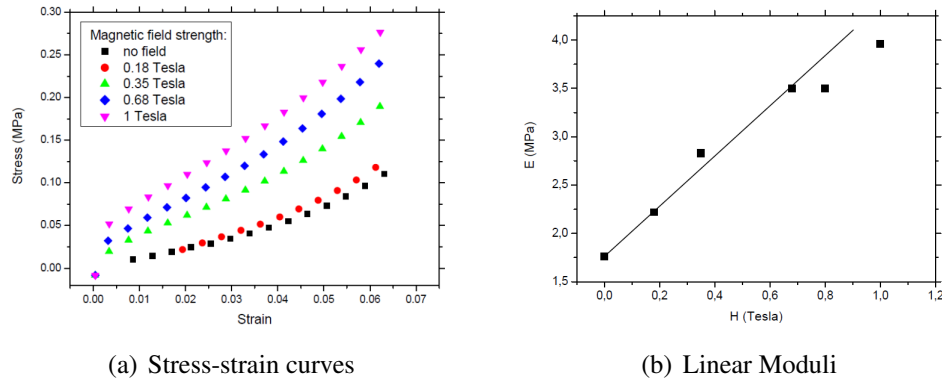


Figure 2.11: Results of the uniaxial compression tests performed by Kallio (2005).

that effectively the highest relative effect of 100% was achieved when 700 mT flux was applied. Varga *et al.* (2005a, 2006) conducted compression tests with magnetic inductions in all possible directions. Experimental data were fitted using the *Neo-Hookean Model* to obtain the moduli illustrated in Figure 2.12. The direction of the applied magnetic flux is indicated in the figure. The highest MR effect (58% increase in G) was found for the anisotropic MRE with particle alignment parallel to the applied magnetic flux and parallel to the loading direction. Note that the iron content was only 30wt% (5.45 vol%) and the magnetic induction was low at only 100 mT . Note also that in the case of anisotropic MREs, and even when magnetic fields are applied to isotropic MREs, calculation of the shear modulus G using the *Neo-Hookean Model* is questionable, since the model is formulated to describe the behaviour of isotropic rubber-like materials, not anisotropic materials. Abramchuk *et al.* (2006) performed compression tests to study the loading-unloading behaviour of MREs. A remnant deformation was observed which “stayed unchanged as long as the magnetic field

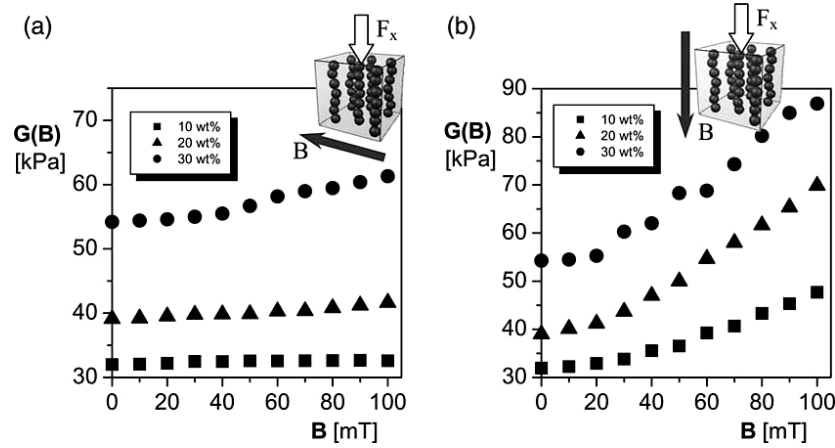


Figure 2.12: Results of the uniaxial compression tests performed by Varga *et al.* (2006). The *Neo-Hookean Model* is used to calculate the modulus G .

was switched on” (Abramchuk *et al.*, 2006), which is a similar behaviour as seen in Shape Memory Polymers but with a different external stimuli. Boczkowska *et al.* (2007) performed compression tests, but the achieved MR effects are very low compared to other experiments performed. The reason for this is not known. Uniaxial compression tests were performed by Gudmundsson (2011) on anisotropic silicone-based and PU-based MREs. The highest MR effects were achieved with the silicone rubber matrix material. Gudmundsson’s results of the moduli and the MR effects versus the engineering strain are shown in Figure 2.13. Gordaninejad *et al.* (2012) studied MREs not only under compression up to 20% strain, but

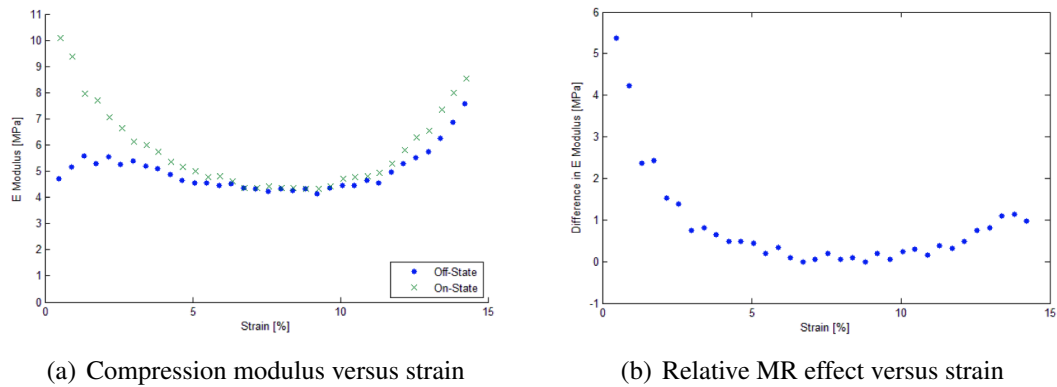


Figure 2.13: Results of the uniaxial compression tests performed by Gudmundsson (2011).

also under simple shear up to 15% strain. The moduli versus the compressive and shear strains are shown in Figure 2.14. In both tests the moduli decreased at larger strain values. Also indicated by the plots is that magnetic saturation of the MRE material occurred above a magnetic induction of 700 mT, as earlier reported by Kallio (2005). Gordaninejad *et al.* (2012) found additionally that the thickness of MRE samples had no influence on the MR effect. The material used, the magnetic flux, and the resulting MR effects of the discussed compression experiments are compared in Tables 2.2 and 2.3.

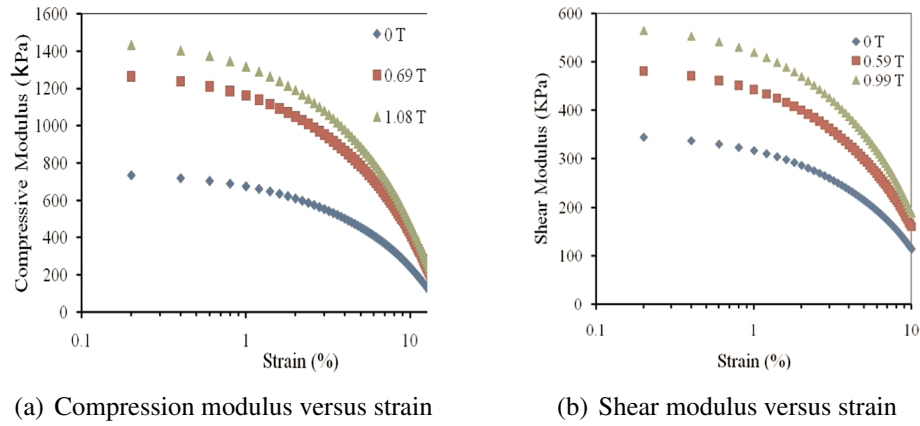


Figure 2.14: Results of the uniaxial compression and simple shear tests performed by Gordaninejad *et al.* (2012).

		Farshad2005	Kallio2005	Varga2006	Abramchuk2006
MRE Material	Matrix	Silicone Gel	Silicone Rubber	Silicone Rubber	Silicone Rubber
	Particles	CIP, $3.8 \mu m$	CIP, $5 \mu m$	CIP, $2.5 \mu m$	Iron, 2 to $3 \mu m$
	VPC	35%	30%	5.45%	9.2%
	Magnetic Flux	Isotropic	1 T	400 mT	Isotropic
Modulus E_0		200 kPa	1.75 MPa	55 kPa	17.4 kPa
Test	Strain Level	30%	6.5%	40%	30%
	Magnetic Flux	440 mT	700 mT	100 mT	230 mT
	Direction	loading	loading alignment	loading alignment	⊥ loading
MR	absolute	280 kPa	1.75 MPa	32 kPa	38.9 kPa
	relative	140%	100%	58%	223%

Table 2.2: Uniaxial compression tests performed by Farshad and Le Roux (2005), Kallio (2005), Varga *et al.* (2006), and Abramchuk *et al.* (2006) are summarised. The MRE material (matrix, particles, VPC, magnetic flux during curing, and no-field moduli E_0), the strain level and applied flux during the experiment, and the resulting MR effects are listed.

		Boczkowska	Gudmundsson	Gordaninejad
MRE Material	Matrix	Polyurethane Gel	Silicone Rubber	Silicone Rubber
	Particles	CIP, 6 to $9 \mu m$	CIP, 7 to $9.5 \mu m$	CIP, 2 to $8 \mu m$
	VPC	33%	27%	23.9%
	Magnetic Flux	100 mT	not provided	1 T
Modulus E_0		1.79 MPa	4.5 MPa	750 kPa
Test	Strain Level	30%	15%	20%
	Magnetic Flux	300 mT	700 mT	700 mT
	Direction	not provided	loading alignment	loading alignment
MR	absolute	80 kPa	5.5 MPa	550 kPa
	relative	4.5%	120%	73%

Table 2.3: Uniaxial compression tests performed by Boczkowska *et al.* (2007), Gudmundsson (2011), and Gordaninejad *et al.* (2012) are summarised. The MRE material (matrix, particles, VPC, magnetic flux during curing, and no-field moduli E_0), the strain level and applied flux during the experiment, and the resulting MR effects are listed.

Simple Shear Tests Shen *et al.* (2004) performed quasi-static simple shear tests on a Natural Rubber (NR) based MRE with 20.1 vol% CIP up to 80% shear strain, and on a Poly-Urethane (PU) based MRE with 25 vol% CIP up to 12% strain. Larger MR effects were found for the PU-based MREs as listed in Table 2.4. The stress-strain results achieved by Shen *et al.* (2004) are shown in Figure 2.15. Stepanov *et al.* (2007) performed simple

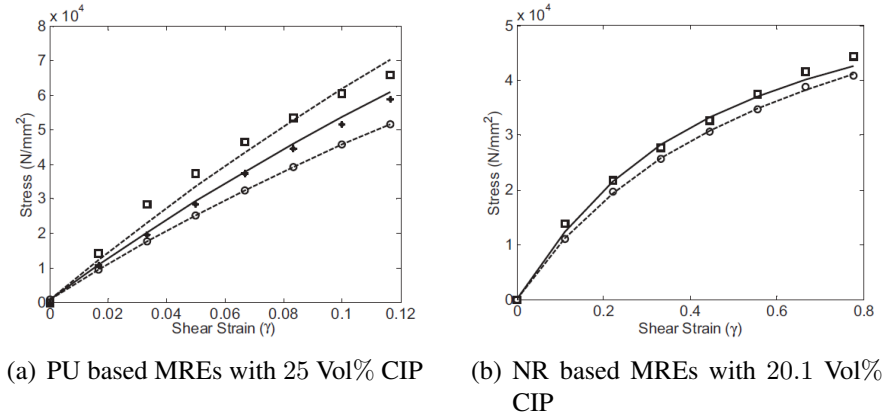


Figure 2.15: Results of the simple shear tests performed by Shen *et al.* (2004). Stress-strain curves achieved with 0 mT (\circ), 300 mT (\star) and 395 mT (\square) applied magnetic induction. Solid and dashed lines are results of a data fitting to a modified Ogden Model.

shear tests on the same MRE material used for the compression tests presented earlier. The stress-strain results and the tangent modulus versus the strain are illustrated in Figure 2.16. A relative MR effect of about 750% at small strains, and still a 160% increase at 10% strain

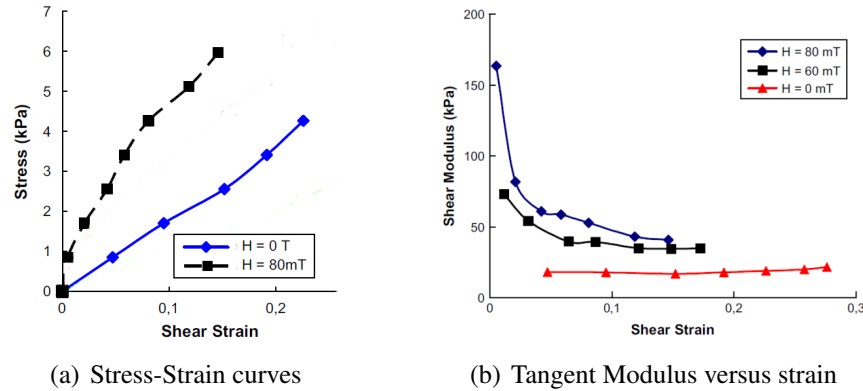
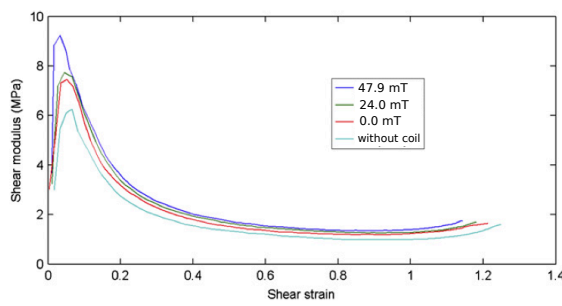


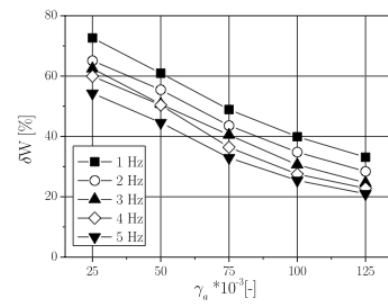
Figure 2.16: Results of the simple shear tests performed by Stepanov *et al.* (2007).

were achieved. Stepanov *et al.* (2007) also studied the loading-unloading behaviour under different levels of magnetic induction. The “stress-strain curves showed a very pronounced hysteresis behaviour” (Stepanov *et al.*, 2007). As was previously observed by Abramchuk *et al.* (2006) for an MRE under compression, a distinct remnant deformation was observed as long as the magnetic field remained switched on. Stepanov *et al.* (2007) called this phenomenon “pseudo-plasticity induced by a magnetic field”. Choi (2009) and Opie and Yim

(2007) performed dynamic shear tests up to 10% and 20% strain, respectively. Both found that the MR effects decreased at larger strains. However, Opie and Yim (2007) stated that “the change in storage modulus is still reasonably high for the 20% strain amplitude”. These tests are not further detailed here. Yu and Wang (2010) designed a sample in which the copper coil that produced the magnetic field was inside the MRE itself. The stress-strain results and the shear modulus are illustrated in Figure 2.17a. A 77% MR increase in the small strain region was reported, but only 25% increase is observable from the plot provided. However, the MR effect is still reasonably high with 15% in the large strain region. The copper coil inside the MRE sample stiffens the specimen leading to a no-field modulus of 7 MPa. Lower relative MR effects are usually achieved when the no-field moduli are large. Zajac *et al.*



(a) Shear tests performed by Yu and Wang (2010)



(b) Shear tests performed by Zajac *et al.* (2010)

Figure 2.17: Results of the shear tests performed by (a) Yu and Wang (2010) and (b) Zajac *et al.* (2010). Yu and Wang designed a new MRE setup with the copper coil inside the MRE sample itself: the legend in the Figure referring to ‘without coil’ means a simple MRE sample.

(2010) characterised the MR effect as a change of the area enclosing the stress-strain hysteresis curve, and as a change of stress amplitude (Kaleta *et al.*, 2011; Krolewicz *et al.*, 2012; Zajac *et al.*, 2010). The relative change of hysteresis area versus the strain amplitude for various frequencies is illustrated in Figure 2.17b. Hu *et al.* (2011) performed dynamic shear experiments, and the storage and loss moduli are shown in Figure 2.18. Details of the MRE materials used, the magnetic inductions applied and the resulting MR effect of the discussed simple shear experiments are summarised in Tables 2.4 and 2.5.

Equi-Biaxial Tests Thus far, no biaxial tests with an applied magnetic field have been performed on MREs. Recently, Zhou *et al.* (2013b) performed the first equi-biaxial tests on MREs made of silicone rubber and 20 vol% CIP using the bubble inflation method, in the absence of a magnetic field. Zhou *et al.* (2013a) studied the fatigue behaviour of isotropic and anisotropic MREs with 1000 cycles up to 200% strain.

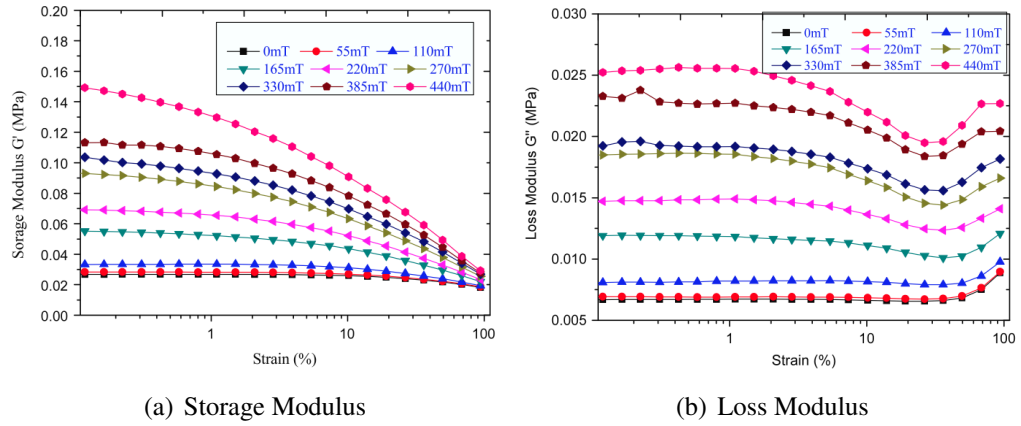


Figure 2.18: Results of the dynamic shear tests performed by Hu *et al.* (2011).

		Gordaninejad	Shen	Stepanov
MRE Material	Matrix	Silicone Rubber	Poly-Urethane	Vinyl Rubber
	Particles	CIP, 2 to 8 μm	CIP	Iron, 2 to 70 μm
	VPC	23.9%	25%	23.9%
	Magnetic Flux	1 T	400 mT	400 mT
	Modulus E_0	350 kPa	513 kPa	20 kPa
Test	Strain Level	15%	12%	20%
	Magnetic Flux	700 mT	395 mT	80 mT
	Direction	\perp loading \parallel alignment	\perp loading \parallel alignment	\perp loading
MR	absolute	130 kPa	327 kPa	150 kPa
	relative	37%	64%	750%

Table 2.4: Simple shear tests performed by Gordaninejad *et al.* (2012), Shen *et al.* (2004), and Stepanov *et al.* (2007) are summarised. The MRE material (matrix, particles, VPC, magnetic flux during curing, and no-field moduli E_0), the strain level and applied flux during the experiment, and the resulting MR effects are listed.

		Yu	Zajac	Hu
MRE Material	Matrix	Silicone Rubber	Thermoplastic	Silicone Rubber and Oil
	Particles	CIP, 2 to 5 μm	Iron, 60 μm	CIP, 4.5 to 5.2 μm
	VPC	33%	35%	23.9%
	Magnetic Flux	not provided	Isotropic	Isotropic
	Modulus E_0	7 MPa	not provided	30 kPa
Test	Strain Level	120%	12.5%	100%
	Magnetic Flux	47.9 mT	163 mT	400 mT
	Direction	not provided \parallel alignment	\perp loading	not provided
MR	absolute	1.75 MPa	not provided	125 kPa
	relative	25%	70%	500%

Table 2.5: Simple shear tests performed by Yu and Wang (2010), Zajac *et al.* (2010), and Hu *et al.* (2011) are summarised. The MRE material (matrix, particles, VPC, magnetic flux during curing, and no-field moduli E_0), the strain level and applied flux during the experiment, and the resulting MR effects are listed.

Summary To summarise in the literature, MREs have been tested under uniaxial compression with a maximum strain level of 40% (Varga *et al.*, 2006). The MRE materials differed in each investigation, with the no-field moduli of the MREs ranging from as low as 17.4 *kPa* up to 4.5 *MPa*, and the volume particle concentrations from 5.5% to 35%. The applied magnetic inductions ranged from only 100 *mT* up to 1 *T*. Relative MR effects from as low as 4.5% up to 223% were reported. Given the large differences in the compression tests, direct comparison is difficult. MREs have also been characterised using simple shear tests. The maximum strain was as large as 120%, the smallest strain level only 12.5%. The no-field moduli of the tested MREs ranged from 20 *kPa* up to 7.2 *MPa*, and the applied inductions from 80 *mT* up to 1 *T*. The achieved relative MR effects varied from 64% up to 750%. Once again, a direct comparison of the results is difficult, though certain trends emerge. Only the uniaxial tension tests performed by Stepanov *et al.* (2007) achieved an MR effect. MREs have yet to be studied under pure shear deformation and under multi-axial deformations.

It is not only that the chosen MRE materials differ in each investigation that makes comparison difficult: The investigators often failed to provide information about the preconditioning of the samples, it is not stated whether the MR effects were obtained from the first loading cycle, or whether the material experienced several loading-unloading cycles prior to the recording of data. As MREs are highly sensitive to the stress-softening known as the *Mullins Effect* (Mullins, 1969) this would be very important to know. The different maximum strain levels in each investigation is another fact that cannot be ignored as MREs are softer when stretched up to a higher level (*Mullins Effect*). Also, the volume iron concentration and the structure of the MREs (isotropic or anisotropic) must be known as they play an important role in the achieved MR effects. All these considerations are important for meaningful comparison of the results of such investigations.

To compare all large-strain experiments found in the literature the absolute and relative MR effects related to 100 *mT* applied induction are illustrated in Figures 2.19 and 2.20. The no-field moduli, the iron content, the structure of the MREs, and the level of strain applied during the experiment influence the resulting MR effects as discussed above. This information is provided in the figures, and is also listed in Tables 2.1 to 2.5.

Stepanov *et al.* (2007) achieved the highest relative MR effects of about 3000% in tension with 335 *mT* induction, and of about 750% in simple shear with only 80 *mT*. These results are remarkably high, but when compared to the absolute MR effect they are well within the range of other reported results. The large relative MR effects are due to the very low no-field moduli of 13 *kPa* and 20 *kPa* in tension and shear, respectively. On the other hand, Gudmundsson (2011) achieved a very large absolute MR effect of 5.5 *MPa* with an applied flux of 700 *mT*. Despite this, the relative effects are well within the range of others findings. This is due to the very high no-field modulus of about 4.5 *MPa*. Thus, both the absolute

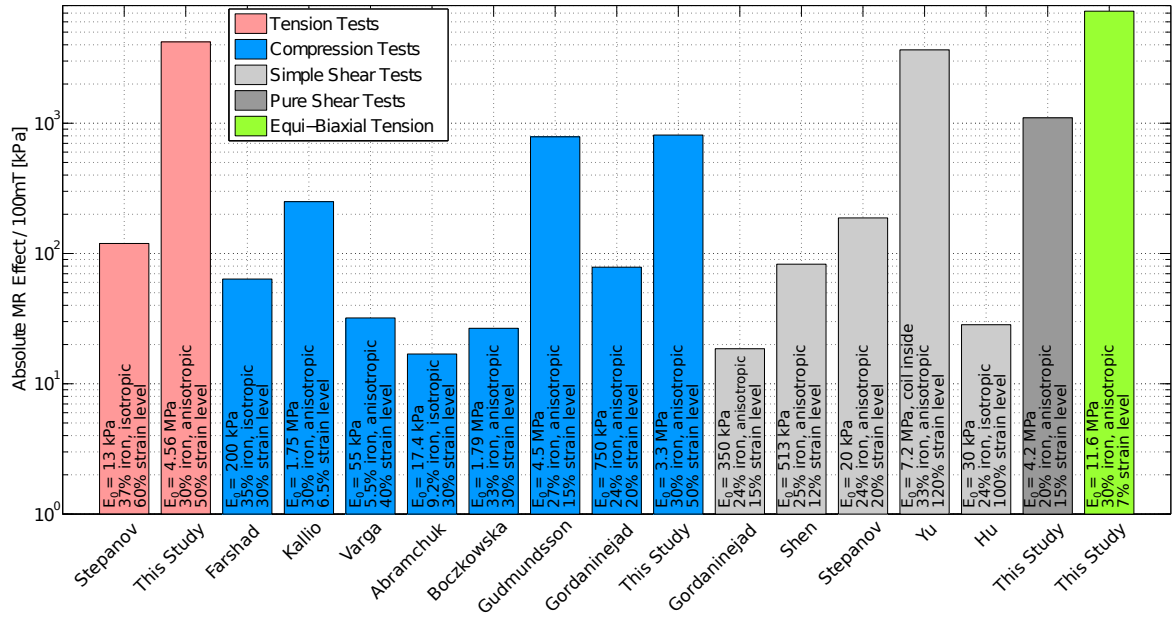


Figure 2.19: The absolute MR effects related to 100 mT applied magnetic induction are compared for each of the performed large-strain experiments published in the literature. The no-field modulus E_0 , the VPC, and the structure of the MRE used, and the level of strain are provided. The MR effects achieved in this study are also included.

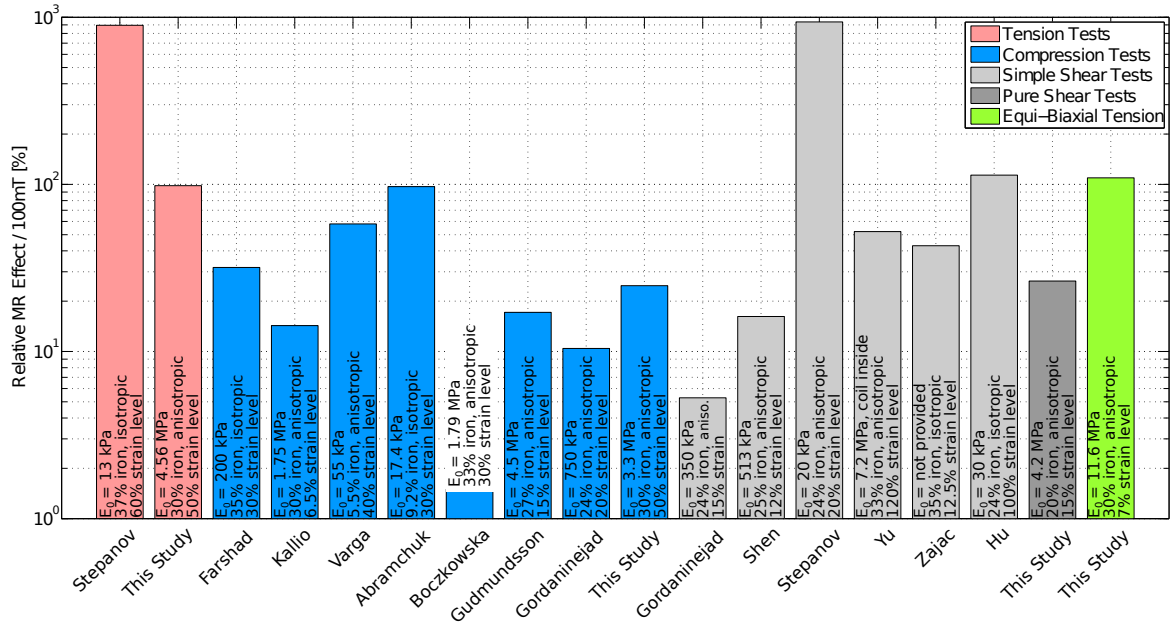


Figure 2.20: The relative MR effects related to 100 mT applied magnetic induction are compared for each of the performed large-strain experiments published in the literature. The no-field modulus E_0 , the VPC, and the structure of the MRE used, and the level of strain are provided. The MR effects achieved in this study are also included.

and relative MR effects should be considered when interpreting the results.

The following trends were observed in the reported large strain experiments:

- Low no-field moduli of the MRE material lead to higher relative MR effects, but not inevitably to large absolute MR effects.
- The MR effect increases with increasing iron content.
- Anisotropic MREs perform better than isotropic MREs. The highest effect were achieved when the magnetic flux density was applied in the loading direction and parallel to the particle alignment (Varga *et al.*, 2006).
- The MRE material saturates above 700 *mT* magnetic induction and the MR effects do not increase further when higher levels of magnetic flux are applied (Gordaninejad *et al.*, 2012; Kallio, 2005).
- Uniaxial compression tests revealed lower MR effects than other deformation modes.
- No conclusions can be drawn regarding the applied strain level.

To develop constitutive models, combinations of several deformation modes performed on the same type of material, and ideally up to the same extent of strain, are essential (Miller, 1999). The large differences in materials and strain amplitudes applied in the research published thus far, make it impossible to use such data to develop accurate constitutive models. In the present study, the MRE behaviour is examined in uniaxial compression and tension, in pure shear, and in equi-biaxial tension deformation modes. The same type of material was used in all the experiments. This study presents a consistent set of experimental data obtained from different deformation modes. The experimental data are suitable for the development of constitutive models using the phenomenological approach. The maximum absolute and relative MR effects achieved in this investigation are included in the comparison shown in Figures 2.19 and 2.20. Despite the fact that the no-field moduli of the MREs used in this study are relatively large compared to many previous studies, the relative MR effects are within the range published in the literature. Very high absolute MR effects were measured during the large strain experiments performed in this investigation.

3 Manufacture of MREs

MREs consist of a non-magnetic elastomeric matrix material in which magnetic particles are dispersed. The magnetic particles are locked into position after the elastomeric material has been cured, as such anisotropic materials can be produced by placing the MRE mixture in a magnetic field during the curing process. This forces the magnetic particles to align in chains. A silicone rubber mixed with silicone fluid, resulting in a matrix material with low viscosity and small zero-field modulus, was used as the matrix material. Carbonyl Iron Powder (CIP), with an average particle size of approximately $4\ \mu\text{m}$, was employed as the magnetic particles. Details and properties of the chosen materials are discussed in Sections 3.1 and 3.2. Isotropic and anisotropic MREs with up to 40 vol% iron particle content were produced with a reliable and repeatable manufacturing process as described in Section 3.3. Details about the designed moulds, and the use of the electromagnet are provided. The microstructure of the MREs is presented in Section 3.4.

3.1 Elastomeric Matrix

The matrix material is an Room Temperature Vulcanising (*RTV*) two-component silicone elastomer. Silicone rubber exhibits excellent high and low temperature performance, it can handle temperatures ranging from -40°C to 200°C . It shows excellent ozone and chemical resistance and very good UV resistance, it is also very easy to use. Silicone rubber seems to be the best choice of matrix material for MRE materials due to the good properties. It has been used previously by many researchers to test the performance of MREs (see Section 2.3). In this investigation, silicone rubber from the company *ACC Silicones* has been used (product code: *MM 240 TV*). The system consists of the rubber component (A) and the hardener component (B): these both are mixed together with the ratio $A : B = 10 : 1$. The system can be cured at ambient temperatures within 24 hours, but the rate of cure can be accelerated by heating. Flexible heaters (*Watlow Silicone Rubber Heaters*, see Appendix A.5) were used in this investigation to cure the material at 100°C , this reduced the curing time to 1.5 hours. Mechanical properties of the neat silicone rubber are listed in Table 3.1 (the data sheet can be found in Appendix A.1). The viscosity of the silicone rubber is relatively high, making it difficult to mix in significant quantities of CI particles. The high viscosity also creates difficulties in aligning the particles using a magnetic field. Finally, the Young's modulus (see Table 3.1) is quite high for use in an MRE, and a high no-field modulus leads to lower relative MR effects (see Section 2.5). To reduce the viscosity of the uncured product and also to reduce the modulus of the final cured elastomer, silicone fluid was added to the silicone rubber. In this investigation, silicone oil from the company *ACC Silicones* was used

Property	<i>MM 240 TV</i>	
Viscosity	96000	$mPa \cdot s$
Tensile Strength	5.4	MPa
Elongation at break	330	%
Young's Modulus	1.88	MPa
Hardness	40	$^{\circ}ShoreA$

Table 3.1: Properties of silicone rubber *MM 240 TV* (provided by *ACC Silicones*)

(product code *ACC 34*). The latter is a low-viscosity silicone diluent that can be employed as a viscosity modifier. It is a clear, colourless liquid with a viscosity of $5 mPa \cdot s$ (see data sheet in Appendix A.2). *ACC Silicones* recommends adding of 30% by weight to silicone rubber *MM 240 TV*.

3.2 Magnetic Particles

Carbonyl Iron Powder (CIP) was chosen as the magnetic particles (Type *SQ*) purchased from the company *BASF*, see Appendix A.4). This mechanically soft powder has a diameter of $d_{50} = 3.7 - 4.7 \mu m$, meaning that 50% of the particle volume has a diameter lower than that. This powder is a grey, fine powder comprised of spherical particles. CIP is characterised by its high purity, it contains 99.5% iron (see Table 3.2). CI powder is obtained from a thermal decomposition of iron pentacarbonyl; the name CIP results from the manufacture process. Iron particles are often considered to be the best choice for manufacturing MREs because of their “high permeability, low remnant magnetisation and high saturation magnetisation” (Lokander, 2002). These properties lead to a good inter-particle attraction, and consequently to high MR effects (Carlson and Jolly, 2000). Many researchers have used CIP as magnetic particles (see Section 2.3). The properties of *CIP-SQ* are listed in Table 3.2. In order to

Property	<i>CIP-SQ</i>	
Particle Size d_{50}	3.7 – 4.7	μm
Iron content	> 99.5	%
Carbon content	< 0.05	%
Nitrogen content	< 0.01	%
Oxygen content	< 0.3	%
SiO_2 content	< 0.1	%

Table 3.2: Properties and composition of the carbonyl iron powder *CIP - SQ* provided by *BASF*

characterise the particle size distribution a *Coulter Laser Machine LS230* was employed. To this end, a few grams of the iron powder were mixed with 25 *ml* water and 10 *ml* of Calgon (Sodiumhexametaphosphate SHMP) to prevent agglomeration. The mixture was put into the laser machine and the laser diffraction was measured to infer particle size distribution. The

cumulative distribution curves are shown in Figure 3.1, and the d_{50} can be read with $4\ \mu\text{m}$: this is in agreement with the values provided by the company (see Table 3.2). A Scanning

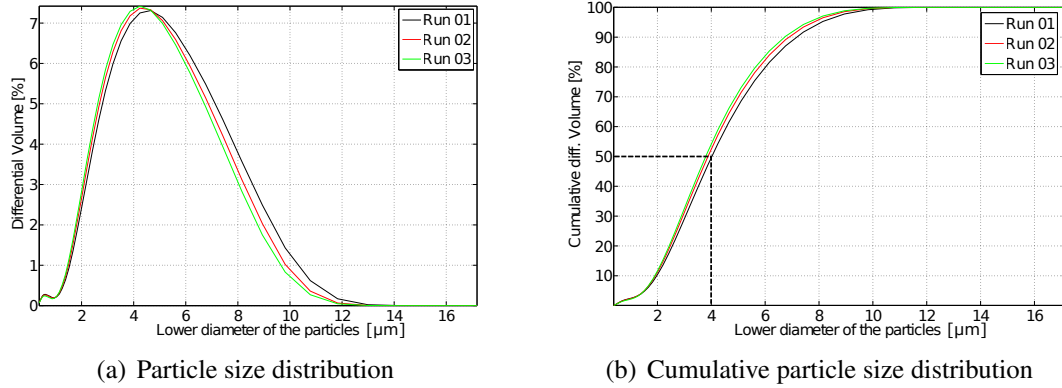


Figure 3.1: Laser diffraction analysis of carbonyl iron powder (CIP) of type *SQ* from the company *BASF* done with a *Coulter Laser Machine LS230*, $d_{50} = 4\ \mu\text{m}$ is marked.

Electron Microscope (SEM) image of CIP is shown in Figure 3.2.

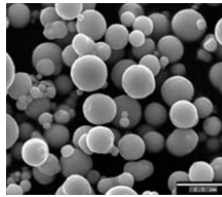
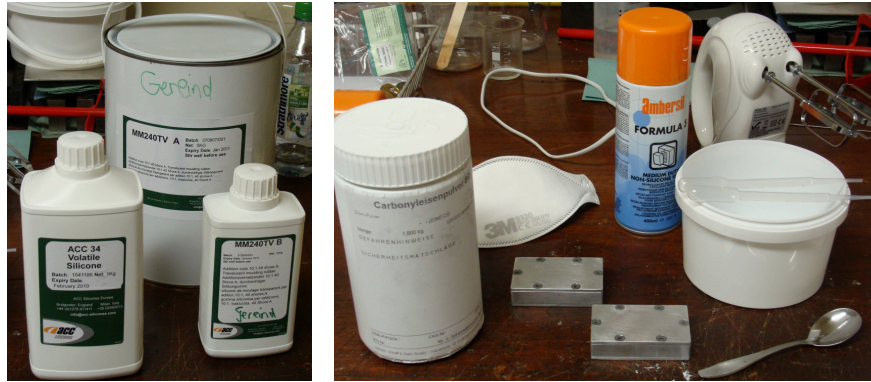


Figure 3.2: SEM image of carbonyl iron powder (CIP) (courtesy of *BASF*)

3.3 Manufacture Process

A manufacture process was developed to prepare the MRE test samples. This involved mixing the two components of the silicone rubber (*MM 240 TV*), at a ratio of 10:1, 30 *w%* of the thinner (*ACC 34*) and the desired amount of magnetic particles (*CIP-SQ*), for 3 *min* using a standard kitchen hand mixer. The hardener (component B of the silicone rubber) was added as the last component; the pot life of the silicone rubber (*MM 240 TV*) is one hour (see Appendix A.1). The pot life starts as soon as the hardener is added to the rubber component, and is the time until the curing process starts. Volume particle concentrations from 0 to 30% were added to produce MREs: these volume concentrations are related to the final volume of the MRE product. The mixture was prepared in disposable buckets of one litre volume, and disposable pipettes were used to accurately measure the correct amount of each component. The components and consumables are shown in Figure 3.3.

After mixing, the bucket was placed into a vacuum apparatus for 10 *min* to degas the uncured fluid mixture. All parts of the moulds were sprayed with a silicone release agent to ensure

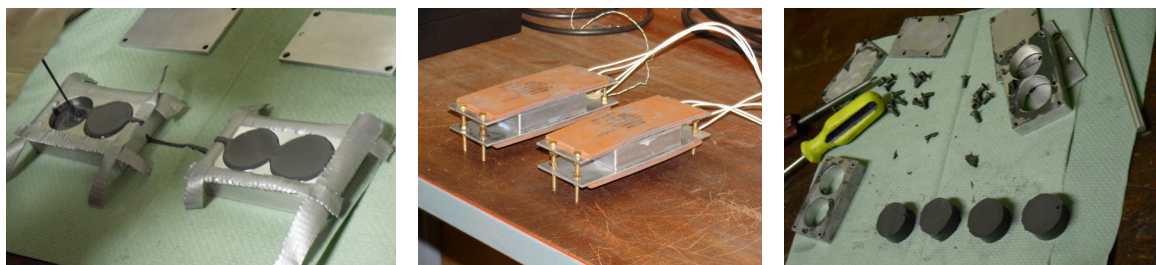


(a) *MM 240 TV* and *ACC 34* (b) *CIP-SQ*, silicone release agent, hand mixer, consumables, compression moulds

Figure 3.3: Silicone rubber components of *MM 240 TV*, the silicone fluid *ACC 34*, the carbonyl iron powder *CIP-SQ* and the used consumables to manufacture MRE material

release of the cured product from the mould after curing. The MRE mixture was poured into the moulds immediately after the degassing process. The moulds were made of aluminium, a non-magnetic material. The moulds were properly closed using brass screws, and were placed between flexible heaters (silicone rubber heaters provided by *Watlow*, see Appendix A.5). After 1.5 hours curing time at $100\text{ }^{\circ}\text{C}$ the final product was demoulded.

Different moulds were used according to the desired specimen shape. Samples for compression tests were cylindrical with a diameter of 29 mm and a height of 13 mm . The sample dimensions are in accordance with the *British Standard* (BS ISO 7743, 2008). Two samples were prepared in each mould. An image of the compression moulds is shown in Figure 3.4, technical drawings can be found in Appendix B.1.



(a) MRE mixtures is poured into compression moulds (b) Moulds between flexible heater plates (c) Demoulded MRE samples and moulds after usage

Figure 3.4: Aluminium moulds for preparing compression samples.

The tension samples were dog-bone shaped with a narrow part of $16 \times 4\text{ mm}$ and a thickness of 2 mm , the overall length was 50 mm . The sample dimensions are in accordance with *British Standard* (BS ISO 37, 2005). The moulds were built with a reservoir at the top through which the mixture was poured; this is because the mixture needed time to flow into the mould. The moulds can be opened completely for demoulding. Pictures of the tension

moulds are shown in Figure 3.5, technical drawings can be found in the Appendices B.2 and B.3. The tension moulds were put in the vacuum apparatus for another 10 *min* after the

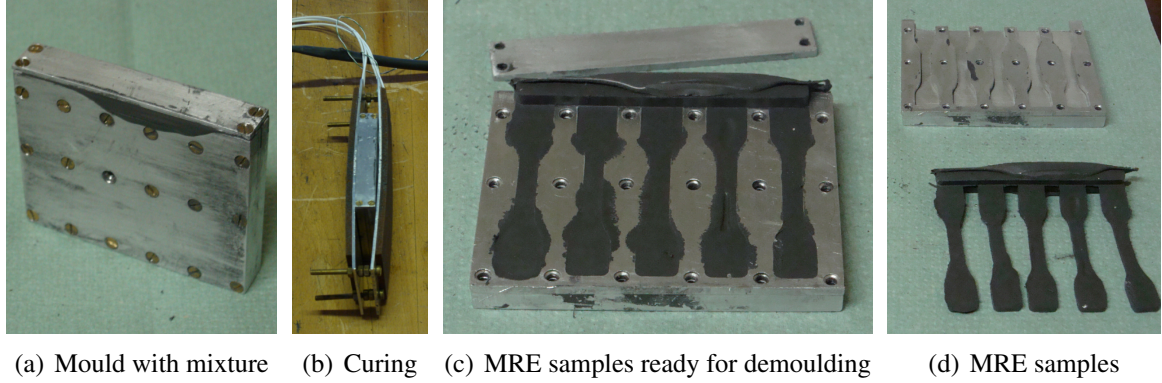


Figure 3.5: Aluminium moulds for preparing tension samples. Please note that one of the MRE samples shows an imperfection and can not be used.

mixture was poured in, to reduce imperfections as seen in Figure 3.5.

Samples for equi-biaxial tension tests and pure shear tests were thin sheets of MRE material. The moulds to prepare these samples were identical except for the sample dimensions. The samples for equi-biaxial tests were square sheets with a side length of 50 *mm* and a thickness of 2 *mm*. Samples for pure shear tests were 1 *mm* thick and rectangular with a length of 50 *mm* and a height of 30 *mm*. Similar to the tension moulds, there was a reservoir at the top through which the MRE mixture was poured. Again, moulds could be opened completely for demoulding. Four samples were prepared in each mould, as shown in Figure 3.6. Technical drawings of the moulds used for the pure shear and the biaxial samples can be found in Appendices B.4 and B.5. After the mixture was poured into the moulds they were placed

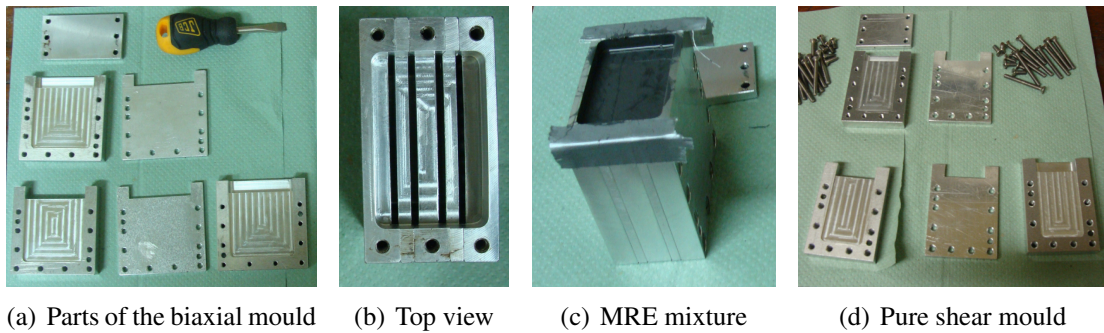
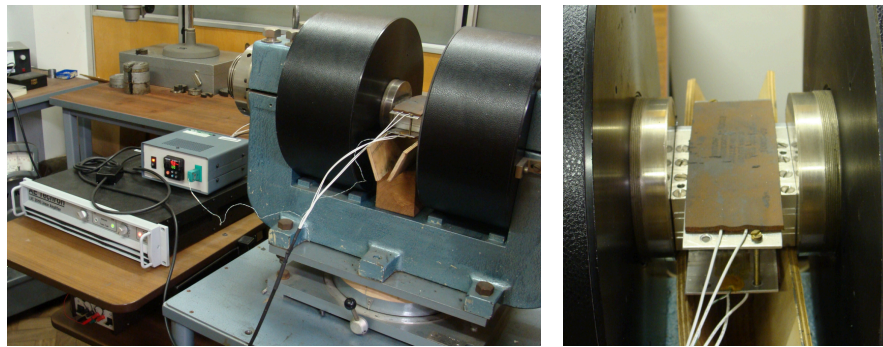


Figure 3.6: Aluminium moulds for preparing pure shear and biaxial tension samples.

in a vacuum apparatus for another 10 *min* to eliminate air bubbles. To fast-cure the MRE samples these moulds were also placed between heater plates. The amounts of silicone rubber, silicone fluid and CIP used for each of the sample types are provided in Appendix C. To prepare anisotropic MREs, the moulds were placed between the magnetic poles of an electromagnet during the curing process. The electromagnet was driven by a DC power sup-

ply and a DC amplifier (*AE Techron LVC 623*, see Appendix A.7). High magnetic inductions of up to 2 T could be produced, depending on the distance between the poles and the current input. To achieve the same magnetic field strength for all moulds in all directions a magnetic field strength of 400 mT was chosen to align the particles. The magnetic field was measured with a Gaussmeter (*FW Bell 5180*, see Appendix A.9). The electromagnet shown with the biaxial mould positioned between the magnetic poles, together with the DC supply and amplifier are shown in Figure 3.7a. A close-up of the mould and heater plates (the latter driven by a temperature controller) are shown in Figure 3.7b.



(a) Electromagnet with DC supply and amplifier, heater plates with temperature controller (b) Biaxial mould is in between magnetic poles

Figure 3.7: Manufacturing of anisotropic MRE samples with an electromagnet; a magnetic induction of 400 mT is used to align the particles

The longest sample dimension was restricted to 5 cm , partly due to maximum pole-to-pole distance of the electromagnet, due to the length of the flexible heaters (5.1 cm wide and 12.7 cm long), and also due to the distance between the permanent magnets that were used during the mechanical characterisation experiments (see Chapter 5). The latter distance has to be short enough to produce magnetic fields of a certain required strength. The larger the distance between the magnets the less magnetic field strength is produced.

3.4 Microscopic Analysis of MREs

Both isotropic and anisotropic MREs were analysed under an optical microscope using *Nor-marsky* optics to check whether: (i) the distribution of the particles in MRE samples cured in the absence of a magnetic field (isotropic MRE) were random and uniform, and (ii) the particles in MRE samples cured under a magnetic field (anisotropic MREs) were aligned into oriented parallel chains. Isotropic MREs were also observed with confocal microscopy using a *Zeiss LSM 510 META*. The microstructure of an isotropic sample containing 10 vol\% iron particles, observed using the optical microscope is shown in Figure 3.8a. The confocal microscope can focus on a very narrow depth of field, effectively imaging one very thin slice

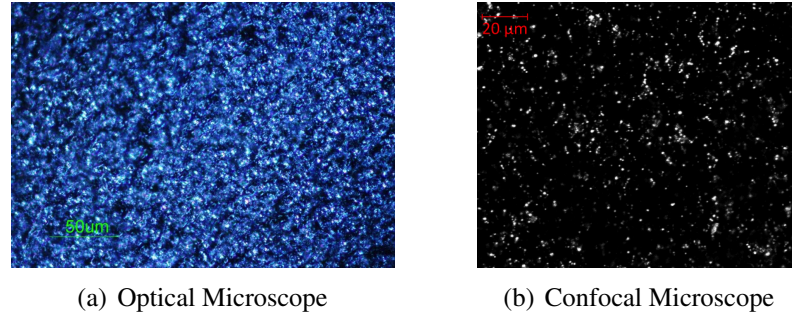


Figure 3.8: Microscopic images of isotropic MREs containing 10 Vol% CIP. An optical and a confocal microscope were used. The magnification scale is shown on the images.

of the MRE sample as shown in Figure 3.8b. In contrast, images from the optical microscope show a large depth of field, consequently the image shows many more particles. The distribution of the particles within the observed sample show no obvious directionality (see Figure 3.8). Particles within anisotropic MREs, prepared using 400 *mT* magnetic induction, show strongly aligned chains of particles. A sample containing 10 vol% iron particles is illustrated under different magnifications in Figure 3.9. Thus it was concluded that a 400 *mT* magnetic

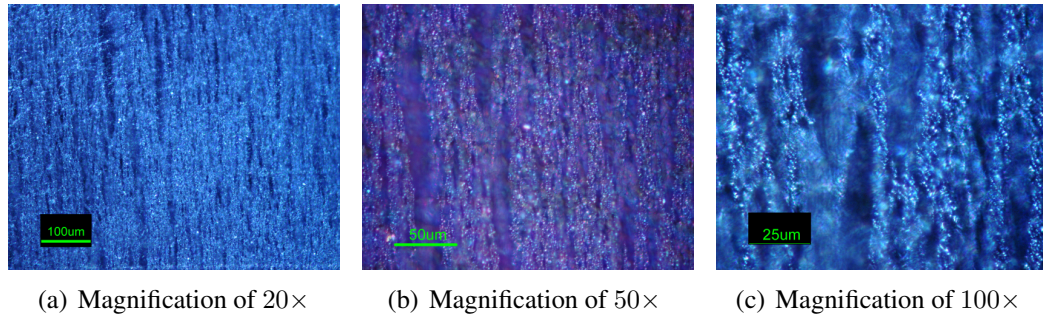


Figure 3.9: Microscopic images of anisotropic MREs containing 10 Vol% CIP. An optical microscope were used, and the MRE is shown in different magnifications.

induction applied during the curing process is enough to align the particles strongly within the elastomeric matrix material.

4 Magnetic Permeability of MREs

The magnetic flux density, B , has been measured in close proximity to the MRE specimens in order to identify the relative permeability, μ_r , of both the isotropic and anisotropic MREs. The magnetic permeability of MRE materials must be clarified in order to simulate the strength and distribution of the magnetic flux density within experimental setups used to characterise the MRE behaviour (see Chapter 5). To understand and interpret MR effects, and to develop constitutive models that correctly characterise the MRE behaviour under the influence of a magnetic field, the magnetic properties of MREs must be known. A short theoretical overview on the electromagnetic theory is provided in Section 4.1. The magnetic permeability of CIP, and measurements and calculations of the effective permeability of composite structures found in the literature are presented in Section 4.2. The performed experimental measurements of both the magnetic induction and magnetic attractive force are reported in Section 4.3. Simulations using the commercial multi-physics finite element software *Comsol* were performed in order to identify the magnetic permeability of MRE samples using an inverse modelling approach; this is detailed in Section 4.4.

4.1 Theoretical Overview

The relation between the magnetic induction, B , and the magnetic field, H in vacuum, in air, or any other non-magnetic environment is constant and defined as

$$B = \mu_0 \cdot H \quad (4.1)$$

where μ_0 is the constant of permeability and has a value of $4\pi \cdot 10^{-7} \text{ Vs/Am}$ or $1.256 \cdot 10^{-6} \text{ Vs/Am}$. The units of H are *ampere per meter*, and those of the magnetic induction, B are *Teslas* (*SI* system of units). In magnetic environments B is no longer constant, and is defined with

$$B = \mu_0 \mu_r H \quad (4.2)$$

with the relative permeability $\mu_r = \mu/\mu_0$. The value of μ_r is 1 for vacuum but can reach values above 1000 for soft magnetic materials such as iron. The magnetic susceptibility, χ , is closely related to the relative permeability and is defined as

$$\mu_r = 1 + \chi. \quad (4.3)$$

Using the susceptibility, the magnetic induction, B , can also be defined as

$$B = \mu_0(1 + \chi)H = \mu_0(H + \chi H) = \mu_0(H + M) \quad (4.4)$$

where the magnetisation, M , contributes to the magnetic material.

For ferromagnetic materials, which are non-linear, the specific permeability of the material, μ , is a function of H , and the magnetisation curve, $B(H)$, is characterised by the initial permeability, μ_{in} , and by the saturation magnetisation, B_S . The initial permeability, μ_{in} , is defined as

$$\mu_{in} = \left(\frac{dB}{dH} \right)_{B=0, H=0} = \left(\frac{B}{H} \right)_{B \rightarrow 0, H \rightarrow 0}. \quad (4.5)$$

Every magnetic material saturates at a certain level of magnetic induction defined as B_S , at which point the slope of the magnetisation curve, $B(H)$, is then the relative permeability of a vacuum. The permeability of composites such as MREs is best described by an effective permeability, μ_e , because composites are a mixture of magnetic and non-magnetic materials. For a more detailed description of electromagnetic theory, see Jiles (1998).

4.2 Magnetic Permeability of CIP and MREs

To enable the comparison with the identified permeabilities in this investigation, the literature was reviewed for models and experimental investigations determining the magnetic properties of composites. In this section, the non-linear magnetic properties of CIP as a ferromagnetic material are discussed with the main goal to clarify whether or not the magnetic non-linearity of the CIP material have to be acknowledged in order to calculate the effective permeability of composites. The models and experiments giving the magnetic permeability of composites such as MREs are also reviewed in this section.

4.2.1 Magnetic Permeability of Carbonyl Iron Powder (CIP)

CI powder is the most common type of magnetic particles used in MREs. CIP is a soft ferromagnetic material with a non-linear magnetisation curve. For more information about the classification of magnetic materials see Sibley (1996). The magnetic permeability is dependant on the strength of the magnetic field H . The initial permeability is provided in technical data sheets of CIP manufactured by *BASF*, *i.e.* the type *CIP-SQ* has an initial permeability of $\mu_{in} = 37 - 38$. Williams (2006) stated the initial permeability of CIP as $\mu_{in} = 35$ of a similar type of CIP. Jiles (1998) provides a value for the saturation flux density of $B_S = 2.15 \text{ T}$ (the same as iron).

There are several options to estimate the magnetisation curve $B(H)$ using the parameters μ_{in} and B_S . A bilinear approach can be used with the initial permeability, μ_{in} , taken to be the initial slope and the permeability of vacuum $\mu_r = 1$ to be the final slope of $B(H)$. The intersection point between the two linear functions is the saturation induction, B_S . The magnetisation curve, $B(H)$, and the permeability, μ_r , calculated with the bilinear approach are illustrated in Figure 4.1.

Integrated Engineering Software (2013) provides a tool to estimate the relationship between the magnetic induction, B , and the magnetic field, H , more exactly. “Reasonable transition data” are provided between the initial linear part of the $B(H)$ curve, where $B = \mu_{in}\mu_0 H$ and the final linear function, where $B = B_S + \mu_0 H$ (Integrated Engineering Software, 2013). The result of this approach is plotted in Figure 4.1.

Since the analytical function used by Integrated Engineering Software (2013) is not provided, a function describing the transition curves between the two linear functions, similar to the one provided by Integrated Engineering Software (2013), can be derived. The initial and the saturated regime can be well described using linear functions defined as:

$$B_{lin1}(H) = \mu_{in}\mu_0 H \quad (4.6)$$

$$B_{lin2}(H) = \mu_0 \cdot H + B_S (1 - 1/\mu_{in}) \quad (4.7)$$

Judging from the curve shape, a root function is suitable for the transition. In order to determine the exact form and parameters of the function, the starting point of the transition curve was set to $B_1 = 0.9 \text{ T}$ with a slope of $B'(H) = \mu_{in}\mu_0$ to match the initial linear function. The end point of the transition curve was defined with $B_2 = 2.35 \text{ T}$ with a slope at this point of $B'(H) = \mu_0$. The positions of start and end points together with the slopes at these points lead to four constraints. A root function with a linear part having four unknown parameters is suggested:

$$B_{trans}(H) = p_1 \cdot H^{p_2} + p_3 \cdot H + p_4 \quad (4.8)$$

The system of non-linear equations is then solved using the *Matlab* function *fsolve* (Matlab, 2013). The resulting matrix of parameters, p for the initial permeability $\mu_{in} = 37$, and the saturation induction $B_S = 2.15 \text{ T}$, are:

$$p = \begin{pmatrix} -3.5417 \cdot 10^1 \\ -2.1147 \cdot 10^{-1} \\ -1.4875 \cdot 10^{-6} \\ 5.3208 \cdot 10^0 \end{pmatrix} \quad (4.9)$$

The resulting magnetisation curve $B(H)$ and also its first derivative $B'(H) = \mu(H)$ are illustrated in Figure 4.1. The magnetisation curve is similar to the one provided by Integrated Engineering Software (2013) but with a clearly defined analytical function. Using this function, the parameter μ_{in} can be changed as required. The analytical function is summarised

with the following equation:

$$B(H) = \left\{ \begin{array}{ll} \mu_0 \mu_{in} H & : 0 < H < \frac{B_1}{\mu_{in} \mu_0} \\ p_1 \cdot H^{p_2} + p_3 \cdot H + p_4 & : \frac{B_1}{\mu_{in} \mu_0} < H < \frac{1}{\mu_0} [B_2 - B_S (1 - 1/\mu_{in})] \\ \mu_0 \cdot H + B_S (1 - 1/\mu_{in}) & : H > \frac{1}{\mu_0} [B_2 - B_S (1 - 1/\mu_{in})] \end{array} \right\} \quad (4.10)$$

for which the parameters p_1 to p_4 have to be determined for each special case of μ_{in} and B_S . An empirical relationship between the magnetisation M , and the magnetic field H , is the *Fröhlich and Kennelly Model* given in Zhang *et al.* (2007) as

$$\mu(H) = \frac{H \cdot (\mu_{in} - 1) + \mu_{in} M_S}{H \cdot (\mu_{in} - 1) + M_S} \quad (4.11)$$

where M_S is the saturation magnetisation given by $B_S/\mu_0 = 1.71e6$ A/m. The magnetisation curves, $B(H)$, and the relative permeability, μ_r , versus the magnetic field H produced using each of these approaches are compared in Figure 4.1.

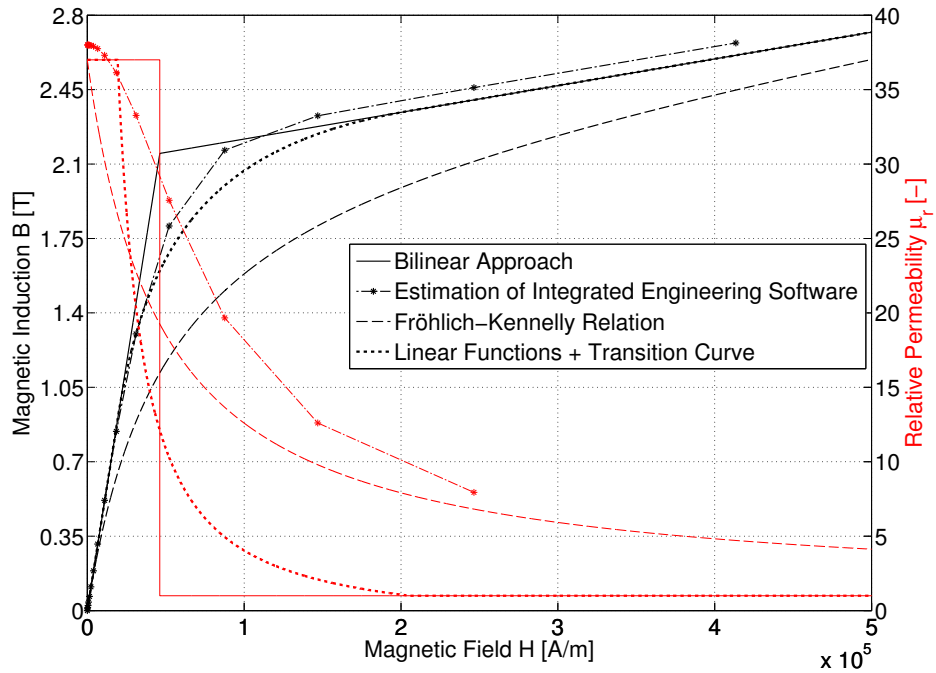


Figure 4.1: Estimation of the magnetisation curve $B(H)$ (black lines) and the related relative permeability μ_r (red lines) of carbonyl iron powder (CIP). The bilinear approach, the estimation of Integrated Engineering, the *Fröhlich-Kennelly* relation, and the root function (Equation 4.10) are compared. Parameters are $\mu_{in} = 37$ and $B_S = 2.15$ T.

Now considering the permeability of composites such as MREs, Martin *et al.* (2006) stated that “the susceptibility of a single particle is much more a function of shape and orientation of the particle than the material of which it is composed”. The susceptibility, χ , of a spherical

particle is defined as

$$\chi_p = 3(\mu_p - 1)/(\mu_p + 2) \quad (4.12)$$

where μ_p is the relative permeability of the material of which the particle is composed. This equation predicts that the susceptibility and thus the relative permeability of the particle is very small compared to the permeability of the material itself. For materials such as iron with a high permeability of $\mu_p = 1000$, Equation 4.12 predicts the susceptibility $\chi_p \simeq 3$. When taking the initial permeability of CIP $\mu_p = 37$ the susceptibility is $\chi_p = 2.77$. It can therefore be concluded that the permeability of MREs is much smaller than that of iron due to the particulate nature of the iron within the composite.

Returning to Equation 4.10 and changing the initial permeability μ_{in} in a range from 1 to 37, Figure 4.2 shows that up to a high magnetic field of $H = 5 \cdot 10^5 \text{ A/m}$ the magnetisation curve, $B(H)$ can be considered to be linear for initial permeabilities of $\mu_{in} \leq 5$. The maximum

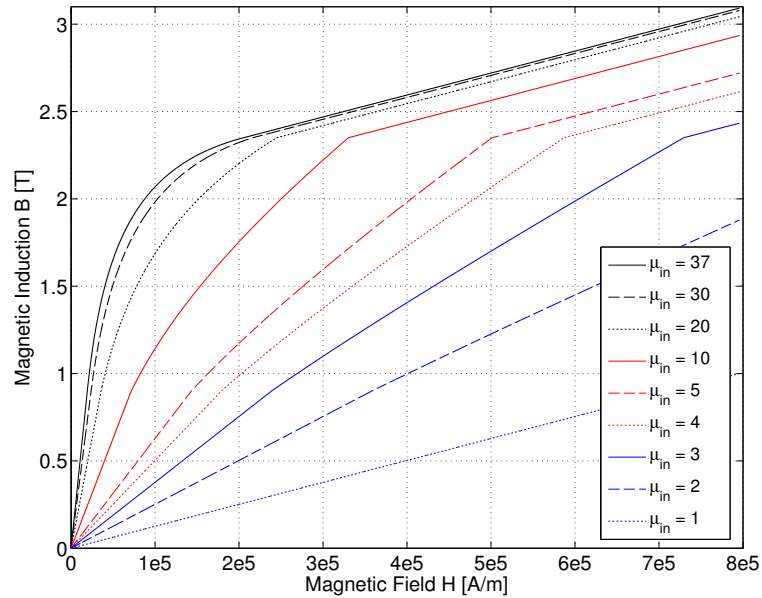


Figure 4.2: Estimation of the magnetisation curve $B(H)$ using the analytical root function (Equation 4.10). The initial permeability μ_{in} ranges from 1 to 37, while the saturation flux density is kept constant with $B_S = 2.15 \text{ T}$.

permeability of MREs reported in the literature is $\mu_e = 6.68$ (Zeng *et al.*, 2013). Therefore it is sufficient to assume the CIP material to be magnetically linear with a constant relative permeability, μ_r , rather than being dependant on the magnetic field, H . This simplifies all further considerations about the magnetic permeability of composites.

4.2.2 Permeability of Composite Structures

To calculate the effective permeability μ_e of composites it is sufficient to work with a constant relative permeability of the particles μ_p as discussed in the previous section. The initial permeability of CIP is used as the permeability of the magnetic particles $\mu_p = 37$, although

other researchers use $\mu_p = 1000$ (Chen *et al.*, 2007b; Martin *et al.*, 2006). The matrix material is non-magnetic with a permeability of $\mu_m = 1$. Different theoretical approaches and experimental investigations to find the permeability of composites are reviewed and compared in this section, although most are not specific to MREs.

The *Maxwell-Garnett* mixing rule is the best known for predicting the permittivity ϵ of isotropic structures. Since the permittivity and the permeability are both material properties for electrical and magnetic behaviour, respectively, and both are connected through the speed of light c only, the *Maxwell-Garnett* mixing rule can equally be used for calculating magnetic permeability. The *Maxwell-Garnett* mixing rule as a three-dimensional mixing model for spherical inclusions is given by Sihvola and Lindell (1997) as

$$\mu_{iso} = \mu_m + \frac{3\Phi\mu_m(\mu_p - \mu_m)}{\mu_p + 2\mu_m - \Phi(\mu_p - \mu_m)} \quad (4.13)$$

where Φ is the volume particle concentration. The permeabilities of isotropic MREs are calculated with the *Maxwell-Garnett* mixing rule, the results of which are shown in Figure 4.4. Karkkainen *et al.* (2000) provided a two-dimensional version of this mixing rule, but this is not discussed here as it underestimates the effective permeability of three-dimensional microstructures. Bruggeman (1935) suggested a model to estimate the effective permeability for unstructured composites. This model belongs to the effective medium theory and considers the particles to be embedded in the effective medium, rather than in the matrix material itself (as assumed for the *Maxwell-Garnett* mixing rule). A full discussion of effective medium theory is beyond the scope of this work and can be studied elsewhere (Giordano, 2003, and references therein). The *Bruggeman* model given by Ramprasad *et al.* (2004) is written as:

$$\Phi_m \frac{\mu_m - \mu_{iso}}{\mu_m + 2\mu_{iso}} + \Phi_p \frac{\mu_p - \mu_{iso}}{\mu_p + 2\mu_{iso}} = 0 \quad (4.14)$$

where the volume concentration of the matrix material $\Phi_m = 1 - \Phi_p$. The results for μ_{iso} using the *Bruggeman* model are illustrated in Figure 4.4. Vicente *et al.* (2002) conducted measurements on CIP in silicone oil-elastomer suspensions on both unstructured and structured composites. The structured composite was cured under a magnetic field of 63 kA/m . The sample was suspended at the end of a long non-magnetic rod. A magnetic field was applied and the force on the sample was measured using a magneto-optic device. The permeability was proportional to the measured force. The results of Vicente's measurements are illustrated in Figure 4.3, and maximal values are shown in Figure 4.4. Chen *et al.* (2007b) worked on MREs made of natural rubber with 11 vol% CIPs. The effective permeability of isotropic and anisotropic samples was calculated. Chen used the two-dimensional version of the *Maxwell Garnett* mixing rule to calculate the permeability of an isotropic structure (ignoring the three-dimensional nature of the actual samples). *Wiener bounds* were used to predict the effective permeability of anisotropic composites. Chen divided the MREs into

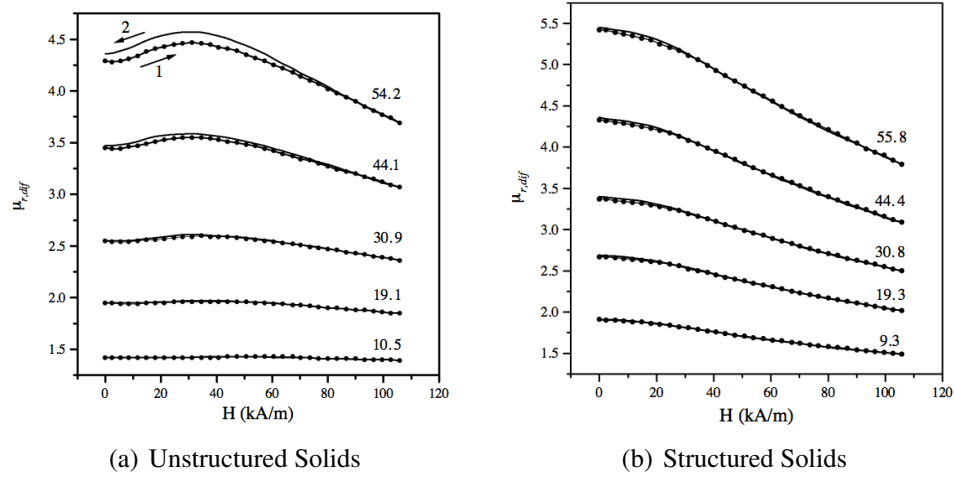


Figure 4.3: Permeability measurements on CIP in silicone oil-elastomer suspensions performed by Vicente *et al.* (2002). The differential relative permeability $\mu_{r,dif}$ versus the applied magnetic field H of (a) unstructured and (b) structured solids cured under 63 kA/m for different particle volume fractions

several parts connected either in series or parallel (see Chen *et al.*, 2007b, Fig.5). The permeability reached a maximum when the parts of the composite were placed in parallel and reached a minimum when placed in series. The minimum and maximum permeability are gives as:

$$\begin{aligned}\mu_{max} &= \Phi\mu_{\alpha} + (1 - \Phi)\mu_{\beta} \\ \mu_{min} &= \frac{\mu_{\alpha}\mu_{\beta}}{\Phi\mu_{\beta} + (1 - \Phi)\mu_{\alpha}}\end{aligned}\quad (4.15)$$

Chen *et al.* subsequently calculated the permeability both parallel μ_{\parallel} and perpendicular μ_{\perp} to the direction of particle alignment (see Chen *et al.*, 2007b, Eq.8-12). Different magnetic field strengths were applied during the curing process of anisotropic MREs. It was found that particle lines become stronger and thicker with higher applied fields, resulting in larger permeability along the alignment direction. Using Chen's formulas the permeability can be calculated when a magnetic induction of 400 mT is applied during the curing process. The permeability parallel to the particle alignment is shown in Figure 4.4. Predictions by Chen *et al.* underestimate the permeabilities when comparing the results against other models and experimental investigations. Martin *et al.* (2006) performed measurements of magnetostriction on an MRE made of silicone rubber and CIPs. The magnetostriction effect was found to be strongly related to the permeability of the composite. Martin *et al.* (2006) produced a formula for the effective permeability as part of the self-consistent point-dipole theory

$$\mu_e = \frac{1 + 2\beta(\Phi + \Psi_2)}{1 - \beta(\Phi - 2\Psi_2)} \quad (4.16)$$

where $\beta = (\mu_p - 1)/(\mu_p + 2)$ is the so-called ‘contrast factor’, Ψ_2 is a structural parameter, and Φ is the volume particle concentration. An equation for the structural parameter, Ψ_2 was provided by Martin *et al.* (2006), who performed finite element simulations with 10,000 particles to determine values for Ψ_2 for anisotropic structures: a list of these values is provided in Martin and Anderson (1999). With these values the effective permeability for anisotropic composites can be calculated and is shown in Figure 4.4. For isotropic structures the structural parameter $\Psi_2 = 0$, and Martin’s formula is identical to the *Maxwell-Garnett* mixing rule (Equation 4.13). Göktürk *et al.* (1993) conducted permeability measurements on isotropic MREs composed of thermoplastic polymer and iron particles. The inductance and resistance of the samples were measured to identify the magnetic permeability and magnetic loss factor. The relevant results are illustrated in Figure 4.4. Göktürk *et al.* provided a theoretical approach for calculating the permeability of composites with a particle volume fraction $\Phi < 0.2$. Below this particle content the “particles act like isolated particles” (Göktürk *et al.*, 1993), which means that each particle experiences only the external field B_0 without being influenced by neighbouring particles. The effective permeability for composites with small particle contents is given as:

$$\mu_e = \mu_0(1 + 3\Phi) \quad (4.17)$$

Results calculated with the *Göktürk* theory are shown in Figure 4.4. Recently, Zeng *et al.* (2013) measured the permeability of MREs prepared from silicone rubber and oil with 70 wt% (24 vol%) CIP. The relative permeability of this MRE material was determined with $\mu_e = 6.68$.

4.2.3 Comparison and Summary

Comparison of these prior theoretical and experimental investigations is presented in Figure 4.4. Permeabilities determined from the present work are also illustrated. The measurements performed by Vicente *et al.* (2002) are quite close to the *Maxwell Garnett Mixing Rule*. However, as stated by Zeng *et al.* (2013), the *Maxwell Garnett Mixing Rule* does not take the “interaction between the particles into account”, which means that permeabilities may well be underestimated. Chen *et al.* (2007b) employed the two-dimensional *Maxell Garnett* mixing rule, and their results are clearly below the results of other experiments and theories. The theoretical approach of Bruggeman (1935) considers the interaction of the particles, showing higher permeabilities especially for larger volume particle concentrations. Measurements on isotropic structures performed by Göktürk *et al.* (1993) show the same tendency as the *Bruggeman* model, although larger permeabilities were measured in the case of low particle concentrations and smaller permeabilities were measured for high particle concentrations. Permeabilities determined from the present work are also illustrated in Figure 4.4 and agree very well with the *Bruggeman* model. The identification of the permeabilities for

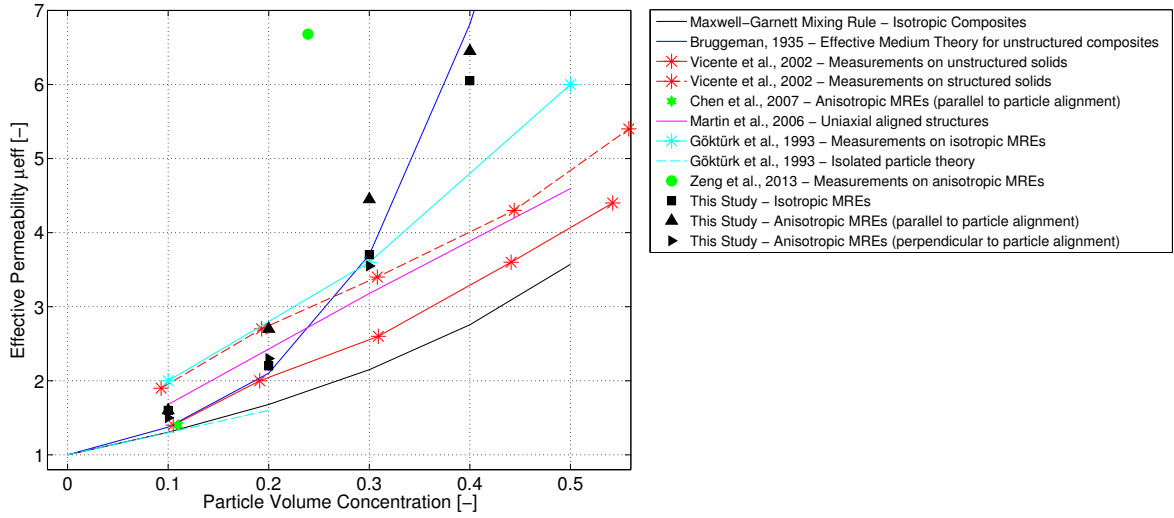


Figure 4.4: Effective permeability μ_e versus the volume particle concentration. Theoretical and experimental investigations to determine the permeability of isotropic and anisotropic composites are compared. The identified permeabilities of this study are illustrated as well.

the several types of MREs is described in Sections 4.3 and 4.4.

4.3 Measurement of Magnetic Flux Density and Attractive Force

In order to identify the permeability of MRE samples the magnetic flux density at various positions around the specimen, and the magnetic attractive force existent between the permanent magnets, was measured. The test setup was attached to the uniaxial test machine *Zwick Z250*, and strong permanent magnets (*Neodymium N52*, see Appendix A.12) were fixed to the setup, positioned on either side of the MRE sample with an inter-magnet distance of 33 mm. As the setup was designed to perform large strain uniaxial compression tests, further details about the setup are given in Section 5.2.2. Here, the test machine and the setup did not actually move to perform an experiments, rather they were used as a fixture to obtain reliable results of the magnetic flux density measurements. The load-cell of the test machine was used to measure the attractive force, created by the two permanent magnets facing each other. Cylindrical shaped compression samples, both isotropic and anisotropic with differing amounts of iron particles were sequentially placed on the cradle positioned between the magnets, and the magnetic flux was measured using a Gaussmeter (*Bell Type 5180*, see Appendices A.9 to A.11) at various positions around the specimen defined in Figure 4.6 and Table 4.1. The test setup together with the Gaussmeter is shown in Figure 4.5a. To ensure a consistent Gaussmeter probe positioning, the latter was held by a clamp and the tip of the probe was taped onto the plates of the setup. For the *Top* and *Bottom* positions the

probe was taped on the top and bottom plate of the setup, respectively. To hold the probe in the *Mid-Height* positions a small aluminium spacer of 6.2 mm height was fixed on the bottom plate and the probe was taped onto this. The probe in the *Top01* position is illustrated in Figure 4.5b. The positions of the Gaussmeter probe were measured using a ruler and using

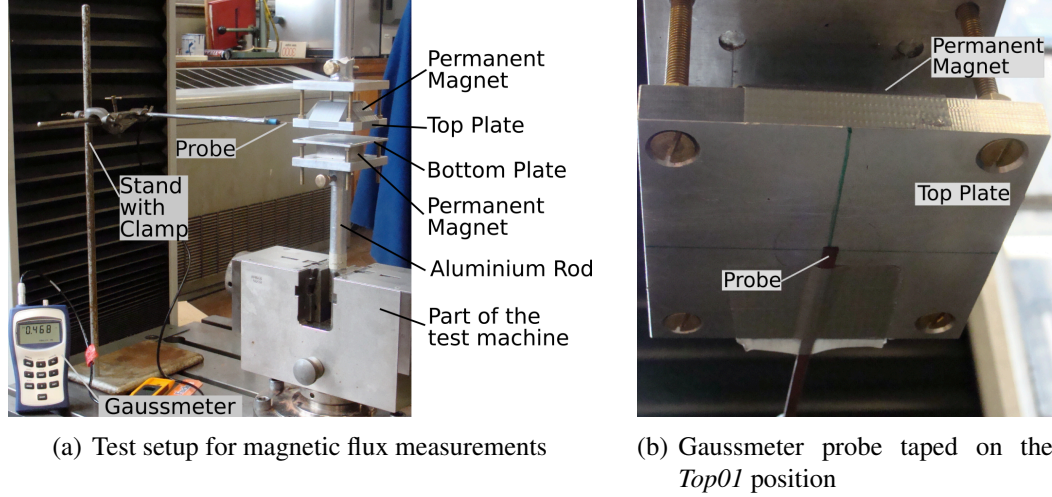


Figure 4.5: Setup for the magnetic flux density measurements to identify the permeability of isotropic and anisotropic MRE samples.

photographs. The positions above and at the side of the specimen, where the magnetic flux density was measured, are illustrated in the scheme in Figure 4.6, and the coordinates of the points are listed in Table 4.1. To ensure same positioning of the different MRE samples,

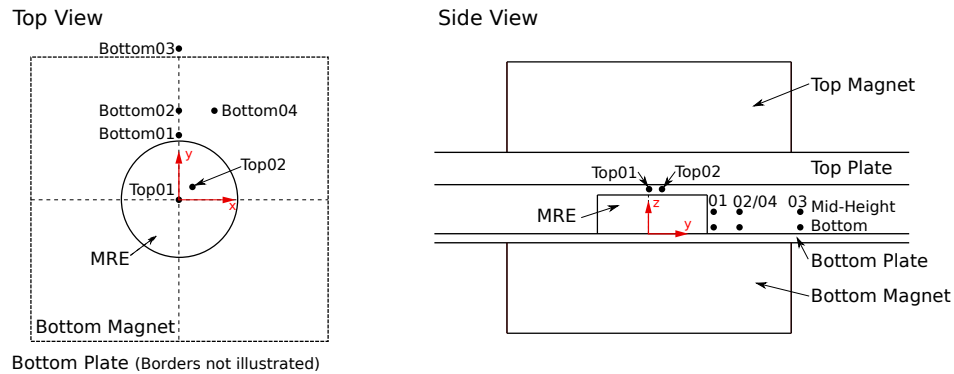


Figure 4.6: Scheme showing the positions where the magnetic flux density was measured experimentally using a Gaussmeter.

the position was marked on the bottom plate of the setup. The measurements were repeated on three samples of each MRE type: isotropic and anisotropic MRE with 10, 20, 30, and 40% volume iron concentration. For the anisotropic samples, measurements were taken with particle alignment in vertical and the two horizontal directions (samples were rotated). The direction of the particle alignment was marked while manufacturing the samples, in accordance to the direction of magnetic flux density applied during the curing process. Mean values

	x [mm]	y [mm]	z [mm]
Top01	0.5	2.7	17.6
Top02	4.0	4.0	17.6
Bottom01	1.2	19.4	0.6
Bottom02	2.4	21.7	0.6
Bottom03	1.1	26.0	0.6
Bottom04	12.6	22.5	0.6
Mid-Height01	0.4	19.0	6.8
Mid-Height02	1.1	21.0	6.8
Mid-Height03	0.8	28.0	6.8
Mid-Height04	9.1	21.0	6.8

Table 4.1: Coordinates of the positions where the magnetic flux density was measured experimentally using a Gaussmeter. The coordinate system is defined in Figure 4.6.

and standard deviations are presented in the Figures 4.7 and 4.8; the measured magnetic flux density is plotted versus the iron content of MRE samples. The magnetic flux measured

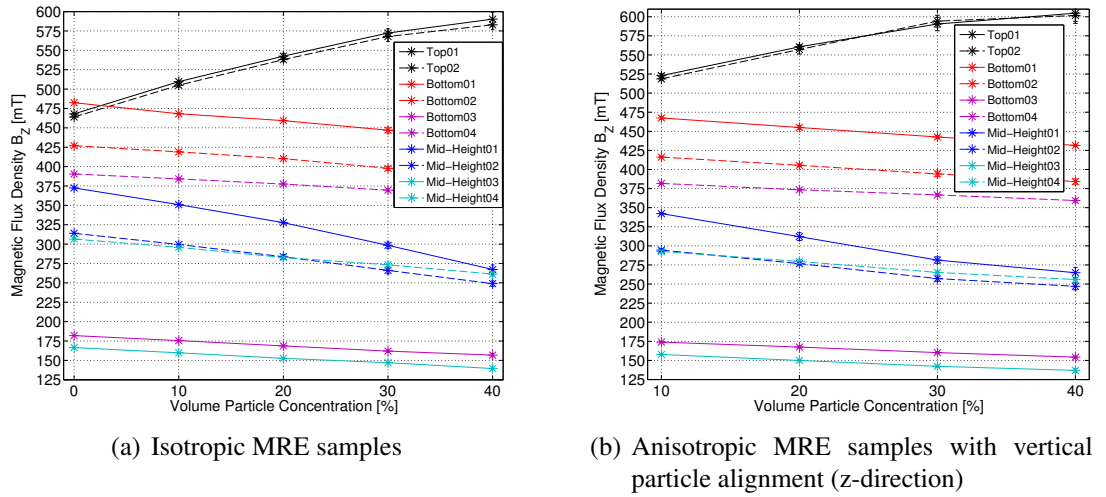


Figure 4.7: Results of the magnetic flux measurements with a Gaussmeter at various positions (defined in Figure 4.6 and Table 4.1). Mean values and standard deviations for isotropic and anisotropic MREs with particle alignment in the vertical direction are illustrated versus the volume particle concentration.

above the MRE samples (*Top* positions) increases with increasing iron content and decreases at the side of the samples (*Bottom* and *Mid-Height* positions). Higher iron contents within the MRE samples are observed to result in higher effective permeability (see Figure 4.4). This higher magnetic permeability concentrates the magnetic flux lines within the MRE samples, effectively reducing the flux density at the side of the sample. As observed from the experimental results shown in Figures 4.7b and 4.8, the particle alignment direction of anisotropic MREs plays an important role. The increase in magnetic flux density measured above, and the decrease in magnetic flux measured at the side of anisotropic MREs with vertical particle alignment are larger, compared to equivalent measurements on anisotropic MREs with ho-

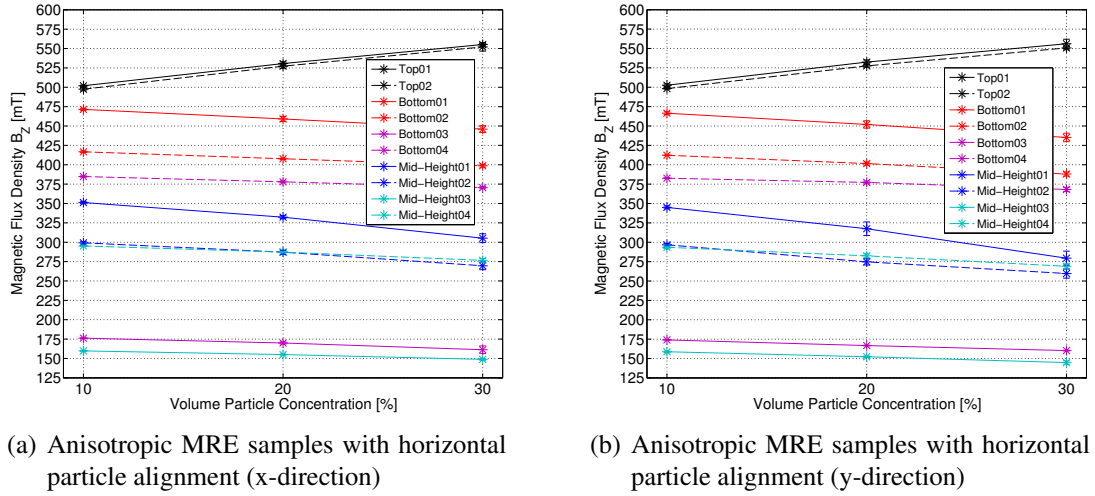


Figure 4.8: Results of the magnetic flux measurements with a Gaussmeter at various positions (defined in Figure 4.6 and Table 4.1). Mean values and standard deviations for anisotropic MREs with particle alignment in the two horizontal directions are illustrated versus the volume particle concentration.

horizontal particle alignment. From this it can be concluded that the magnetic permeability behaves anisotropically in the anisotropic MREs with the highest value in the particle alignment direction. The attractive force between the permanent magnets, both with and without the specimens placed between the magnets, was measured using the 1 kN load-cell of the uniaxial test machine. The measured forces are shown in Figure 4.9. The top magnet was

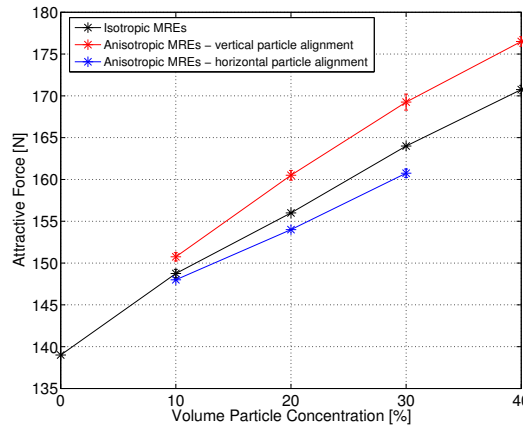


Figure 4.9: Results of the attractive force measurements. Mean values and standard deviations for isotropic and anisotropic MREs with particle alignment in vertical and horizontal directions are illustrated versus the volume particle concentration.

held by the upper rig structure of the setup attached to the test machine and load-cell. To zero the force, the machine cross-head was raised as far as possible to maximise the distance between the permanent magnets and minimise any influence of the magnetic field (measured flux was 0 mT). Once the force was zeroed, the cross-head was moved back to the original position with the permanent magnets positioned 33 mm apart. The attractive force is higher

for higher iron contents within the MRE sample. Anisotropic samples with vertical particle alignment show the steepest increase. The mean values of the magnetic flux density and the attractive force measurements are summarised in Tables 4.2 and 4.3.

MRE Sample	Iron [%]	Magnetic Field Strength $B[mT]$					
		Top 01	Top 02	Bottom01	Bottom02	Bottom03	Bottom04
Pure Rubber	0	468.00	464.00	482.50	427.00	182.00	390.50
Isotropic MREs	10	509.63	505.00	468.25	419.00	175.50	384.13
	20	542.50	538.00	459.33	410.33	168.67	377.50
	30	572.38	567.88	447.00	397.75	162.00	369.60
	40	590.25	583.00	433.50	386.75	156.75	362.00
Anisotropic MREs - vertical alignment	10	522.88	518.63	467.50	416.25	174.00	381.75
	20	560.63	557.13	455.00	405.50	167.50	373.38
	30	590.50	594.25	442.50	394.25	160.25	366.75
	40	604.63	601.63	431.50	384.20	154.25	359.40
Anisotropic MREs - horizontal alignment in x-dir.	10	502.00	497.50	471.50	416.75	176.25	384.80
	20	530.63	527.25	459.13	407.75	170.00	378.00
	30	555.25	552.13	446.00	398.75	161.25	370.43
Anisotropic MREs - horizontal alignment in y-dir.	10	502.63	498.25	466.50	412.25	174.00	382.60
	20	532.50	527.50	452.00	401.50	166.75	377.20
	30	556.13	550.75	435.25	388.00	160.25	368.14

Table 4.2: Average results of the magnetic flux density measurements at the *Top* and *Bottom* positions (Figure 4.6 and Table 4.1). These results were plotted versus the volume particle concentration in Figures 4.7 and 4.8.

MRE Sample	Iron [%]	Magnetic Field Strength $B[mT]$				Force [N]
		Mid-Height01	Mid-Height02	Mid-Height03	Mid-Height04	
Pure Rubber	0	372.50	314.00	166.50	306.50	139.00
Isotropic MREs	10	351.00	299.50	159.75	295.75	148.75
	20	327.67	283.67	152.67	282.67	156.00
	30	298.50	266.13	147.00	273.25	164.00
	40	267.25	249.00	139.50	261.38	170.75
Anisotropic MREs - vertical alignment	10	342.25	294.50	157.75	292.75	150.75
	20	312.11	276.75	150.00	279.63	160.50
	30	281.38	257.13	142.25	265.25	169.25
	40	264.89	247.00	137.00	255.88	176.50
Anisotropic MREs - horizontal alignment in x-dir.	10	351.25	299.25	159.75	295.25	148.00
	20	332.38	287.13	155.00	287.25	154.00
	30	305.25	269.63	148.80	276.63	160.75
Anisotropic MREs - horizontal alignment in y-dir.	10	345.00	296.75	158.75	293.50	148.00
	20	317.50	274.75	152.25	282.50	154.00
	30	279.50	259.63	144.80	269.00	160.75

Table 4.3: Average results of the magnetic flux density measurements at the *Mid-Height* positions (Figure 4.5 and Table 4.1), and of the attractive force measurements. These results were plotted versus the volume particle concentration in Figures 4.7, 4.8, and 4.9.

4.4 Simulation of the Magnetic Flux Density using Comsol

The aim of the work presented in this section is to determine the magnetic permeability of the various MRE specimens through an inverse analysis. To do this, the experimental measurements presented in the previous section are compared with results of a magnetic field simulation performed in the multi-physics software *Comsol* (Comsol, 2011). *Comsol* is a finite element code, and the *AC/DC* package is designed to simulate magnetic field distributions. The experimental setup was described in Section 4.3, but only the permanent magnets and the MRE sample were implemented into *Comsol* to simplify the model. The setup itself was built of non-magnetic aluminium and brass materials, so these parts had no influence on the magnetic flux simulation. The model geometry defined in *Comsol* is shown in Figure 4.10. A model of one quarter of the experimental setup was created using two

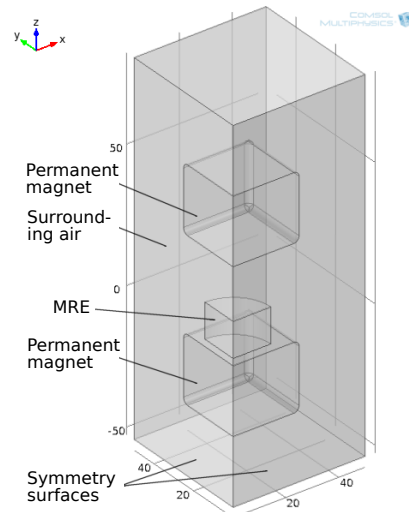


Figure 4.10: Geometry defined in *Comsol*. Only the permanent magnets and the MRE sample were implemented. Symmetry conditions were applied, and so only one quarter of the setup was modelled.

planes of symmetry. The two magnets were modelled as cubes with rounded corners using a fillet radius of 2 mm. To achieve that the magnets create a flux density of 550 mT at their surface (see data sheet in Appendix A.12) the relation between the magnetic induction, B , and the magnetic field, H , was set as defined in Equation 4.4 with a magnetisation M of 1155 kA/m. The dimensions of the MRE samples were measured and average values for both isotropic and anisotropic samples were used in the *Comsol* model, and are listed in Table 4.4. In the case of anisotropic samples with horizontal particle alignment, the shape is slightly ellipsoid with a larger diameter measured along the direction of particle alignment. The $B(H)$ relation is defined via the relative permeability (Equation 4.2), and μ_r of the MRE sample is defined as a parameter in *Comsol* which can be varied using parametric

	Diameter \varnothing [mm]	Height [mm]
Isotropic MREs	28.57	13.35
Anisotropic MREs - vertical alignment	28.62	13.76
Anisotropic MREs - horizontal alignment	30.04 / 27.86	12.98

Table 4.4: Averaged dimensions of MRE samples used for the *Comsol* model. Isotropic and anisotropic samples with vertical particle alignment have circular cross sections, anisotropic MREs with horizontal alignment have elliptical cross sections with a larger diameter in the direction of particle alignment.

sweeps. The permeability of a material can be either defined as isotropic, with the same value in all directions, or as anisotropic with different values in the three directions. The positions where the magnetic flux density was measured experimentally (defined in Figure 4.6 and Table 4.1) are defined as points in *Comsol* using the same coordinates. A large box of air around the magnets and the MRE sample is required in the *Comsol* model to simulate the reality as exactly as possible. If no medium would have been defined in between and around the magnets, magnetic flux lines would not exist. The permeability of the air is set to $\mu_r = 1$. The air box must be large enough to ensure that the boundary conditions are defined correctly. A parametric study was performed changing the size of the air box until convergence of the magnetic flux results was achieved. The size of the air box was determined with 300×600 mm. The size of the created finite element mesh was 3 mm in the magnets and the samples, and was as big as 60 mm at the borders of the large air box, with constantly increasing element sizes in between. The mesh size was defined as a parameter in *Comsol* and a parametric study was performed with smaller and larger finite elements. The results of the 3 mm mesh size achieved convergence.

To study the magnetic field distribution within the setup, and to enable comparison to the experimental magnetic flux measurements, the magnetic permeability of the materials within the model was adjusted using parametric sweeps. In this way, the magnetic flux density at the same positions at those used to monitor the flux density in the experiments could be changed, until a good agreement with the experimental data is obtained. This is done separately for isotropic and anisotropic MREs.

4.4.1 Permeability of Isotropic MREs

In the *Comsol* model the magnetic permeability of the MRE sample was defined as isotropic, implying that the MRE sample has the same permeability in all directions. A parametric sweep was used to alter the relative permeability, μ_r from 1 to 10 in increments of 0.1. The magnetic flux density at the various positions (Figure 4.6 and Table 4.1) and the attractive force generated at the top magnet were then calculated. Results for flux and force are plotted versus the relative permeability in Figures 4.11 and 4.12, respectively. Symmetry conditions

were applied in the model; as such the predicted force had to be multiplied by four to provide the actual total force generated between the two magnets. In order to identify the magnetic

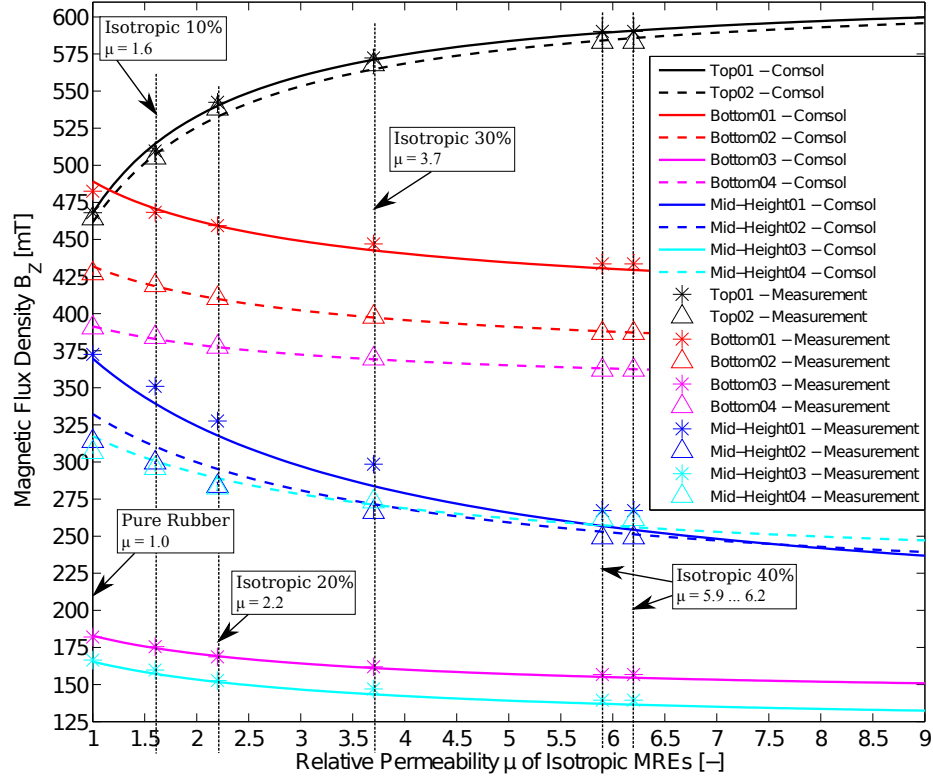


Figure 4.11: The magnetic flux density B_z at various positions (Figure 4.6 and Table 4.1) calculated with *Comsol* is illustrated versus the permeability of isotropic MRE samples. Average experimentally measured values (Tables 4.2 and 4.3) are plotted using the identified permeabilities (Table 4.6). For the case of isotropic MREs with 40 vol% iron content a range of magnetic permeabilities was identified: two markers have been used to indicate the lower and upper limit of this range. The text inside the figure lists the results for each isotropic MRE sample.

permeability of each isotropic MRE (with 10, 20, 30, and 40% volume iron concentration), the simulation results were compared with the experimental measurements.

The identification process was performed as follows: For each position and for the attractive force a range of possible permeabilities was identified by comparing the average experimental values together with their standard deviations with the simulation results. Then an intersection between those permeability ranges was calculated. The identified permeability range at the *Top01* position was used to start with the intersection process, and the other position and attractive force permeability ranges were used to narrow the range down to a final possible permeability. This was done in the order *Top02*, *Bottom01* to *Bottom04*, and *Mid-Height01* to *Mid-Height04* positions, and finally the permeability range found from the attractive force measurements were compared with the already narrowed permeability range, and either a single value of permeability or still a permeability range was identified for each type of MRE. Note that in some cases, certain experimental data had to be ignored in the

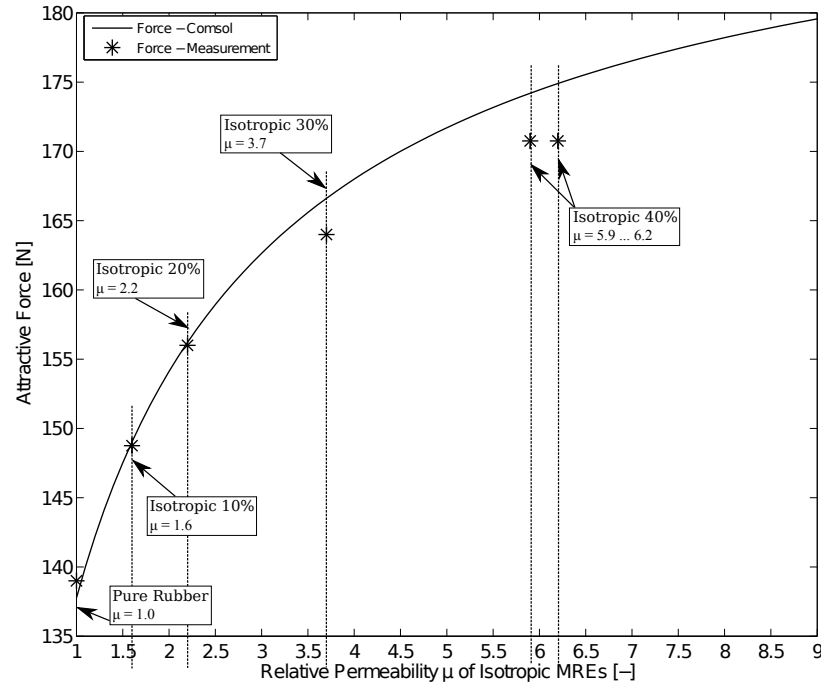


Figure 4.12: The attractive force between the permanent magnets calculated with *Comsol* is illustrated versus the permeability of isotropic MRE samples. Average experimentally measured values (Table 4.3) are plotted using the identified permeabilities (Table 4.6). For the case of isotropic MREs with 40 vol% iron content a range of magnetic permeabilities was identified: two markers have been used to indicate the lower and upper limit of this range. The text inside the Figure lists the results for each isotropic MRE sample.

intersection process as the permeability range found from the single positions or from the attractive force measurements did not match with the narrowed permeability range determined so far. An example to clarify the identification process is given in Table 4.5, the identified permeability range for each position, and the ranges narrowed with the intersection process are listed for the isotropic 30% MREs. The *Top01* position was chosen as a starting point for the intersection process as the measurements (Figure 4.7) and also the simulation results (Figure 4.11) showed that the magnetic flux at the *Top01* and *Top02* positions are close together. The magnetic flux density is uniformly distributed in the centre of the permanent magnets (where the *Top* positions are), whereas the distribution is less uniform closer to the borders of the magnets (where the *Mid-Height* and *Bottom* positions are). The experimental measurements of the *Top01* and *Top02* positions are judged to be the most reliable ones. The values of magnetic flux density beside the sample (*Bottom* and *Mid-Height* positions) are very sensitive to the position where they are measured or simulated, and due to this the *Mid-Height* positions were judged as secondary results that are better at the end of the intersection list. The attractive force between the two permanent magnets is a global value, independent of any measurement position, so only one value was determined for each tested MRE in contrast to the magnetic flux that was measured at 10 different positions. It has been

Position / Force	Range of permeability		Intersection Process	
	Min [-]	Max [-]	Min [-]	Max [-]
Top01	3.4	4.3	3.4	4.3
Top02	3.4	4.6	3.4	4.3
Bottom01	2.8	3.7	3.4	3.7
Bottom02	3.2	4.2	3.4	3.7
Bottom03	3.1	3.9	3.4	3.7
Bottom03	3.1	4.2	3.4	3.7
Mid-Height01	2.7	3.2	discard	
Mid-Height02	3.7	4.7	3.7	3.7
Mid-Height03	2.7	3.1	discard	
Mid-Height04	3.2	3.7	3.7	3.7
Attractive Force	3.2	3.3	discard	

Table 4.5: Permeability range identified for each single measurement position and for the attractive force results of an isotropic 30% MRE. An intersection process is performed to narrow the range of permeabilities and to identify the final permeability of $\mu_{iso} = 3.7$ for the isotropic 30% MREs. The identification process is done analogously for the other types of MREs, and the identified permeabilities are listed in Table 4.6.

decided that in the intersection process the attractive force results are the last ones in the order. Having the order in the intersection process as described above led to the best possible solution, whereas for all other orders more positions had to be discarded.

The permeabilities finally determined for isotropic MREs are listed in Table 4.6. In the case of isotropic MREs with 40% iron content a range of permeabilities were identified rather than a unique value. Experimental data measured from isotropic samples with different iron

	Permeability μ_e [-]
Isotropic 10% MREs	1.6
Isotropic 20% MREs	2.2
Isotropic 30% MREs	3.7
Isotropic 40% MREs	5.9 ... 6.2

Table 4.6: Identified permeability, μ_{iso} , of isotropic MRE samples. The permeabilities were identified with experimental magnetic flux and attractive force measurements in combination with the *Comsol* simulation.

contents are plotted in Figures 4.11 and 4.12 using the identified magnetic permeabilities listed in Table 4.6. The measurements of magnetic flux density are in very good agreement with the *Comsol* simulation results. Only the measurements at the *Mid-Height01* and *Mid-Height02* positions disagree slightly with the *Comsol* results, but this is acceptable as the magnetic flux density in the region beside the MRE specimen is sensitive to the position where it is measured or simulated, as discussed above. The attractive force measurements agree well with the simulation results for isotropic MREs with 10 and 20% iron content but the experimental values are lower than the force calculated by *Comsol* in the case of higher particle contents.

4.4.2 Permeability of Anisotropic MREs

Anisotropic MREs with vertical particle alignment. In order to simulate samples with vertical particle alignment, the magnetic permeability in the *Comsol* model was defined as anisotropic, using values of μ_Z in the vertical direction and μ_X in the two horizontal directions. An inner and outer parametric sweep was performed in *Comsol* to calculate the magnetic flux density and the attractive force for all possible combinations of μ_Z and μ_X . The sweep was performed using $\mu = 1$ to 15 in increments of 0.1 for both μ_Z and μ_X . In Figure 4.13 the magnetic flux density B_Z (calculated at the positions defined in Figure 4.6 and Table 4.1), and in Figure 4.14 the attractive force results are plotted versus the relative permeability, μ_Z . Solid lines represent the isotropic case where $\mu_Z = \mu_X$. The dotted lines represent the anisotropic case with $\mu_Z > \mu_X$, with μ_Z as the largest permeability in the direction of particle alignment ($\mu_Z < \mu_X$ would rotate the particle alignment direction); the dotted lines for different μ_X are plotted in steps of 1. Note that the change in μ_X does not significantly change the magnetic flux density B_Z calculated at the side of the specimen (the

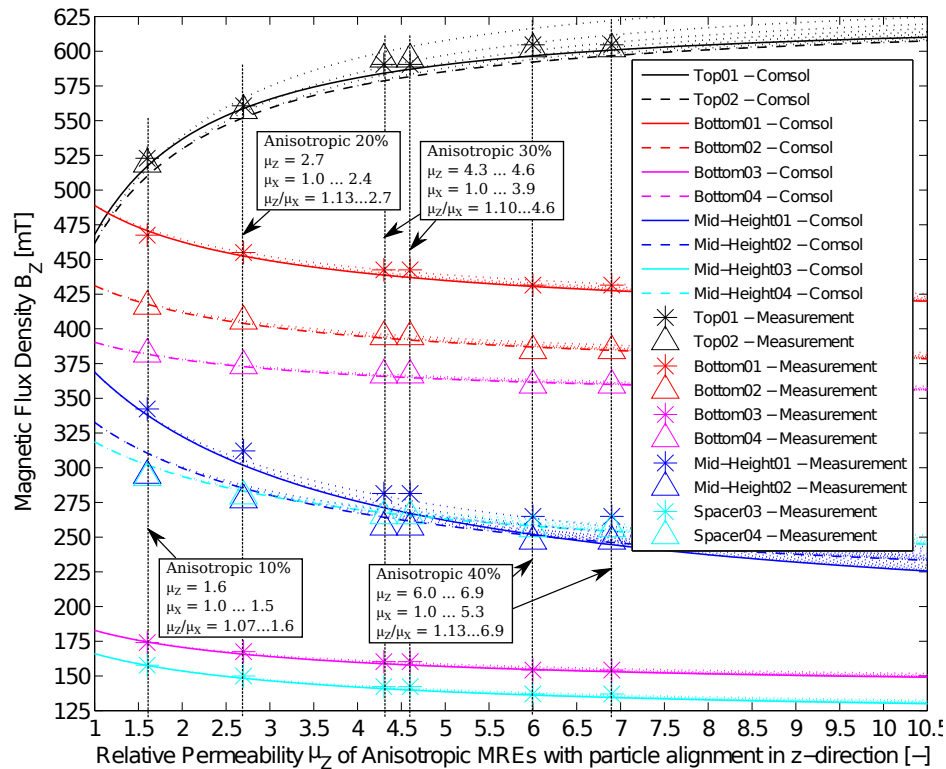


Figure 4.13: The magnetic flux density B_Z at various positions (Figure 4.6 and Table 4.1) calculated with *Comsol* is illustrated versus the permeability μ_Z of anisotropic MRE samples with particle alignment in z -direction: solid lines represent the isotropic case with $\mu_Z = \mu_X$ and dotted lines the anisotropic case with $\mu_Z > \mu_X$. Average experimentally measured values (Tables 4.2 and 4.3) are plotted using the identified permeabilities (Table 4.7). For the cases where a range of permeabilities was identified, two markers have been used to indicate the lower and upper limit of this range. The text inside the figure lists the results for each anisotropic MRE sample.

dotted lines for *Bottom* and *Mid-Height* positions are close to the isotropic case). A larger change in B_Z for different values of μ_X is noticed only for the positions *Top01* and *Top02*. Note also, that the change in μ_X does not change the attractive force results much, so the

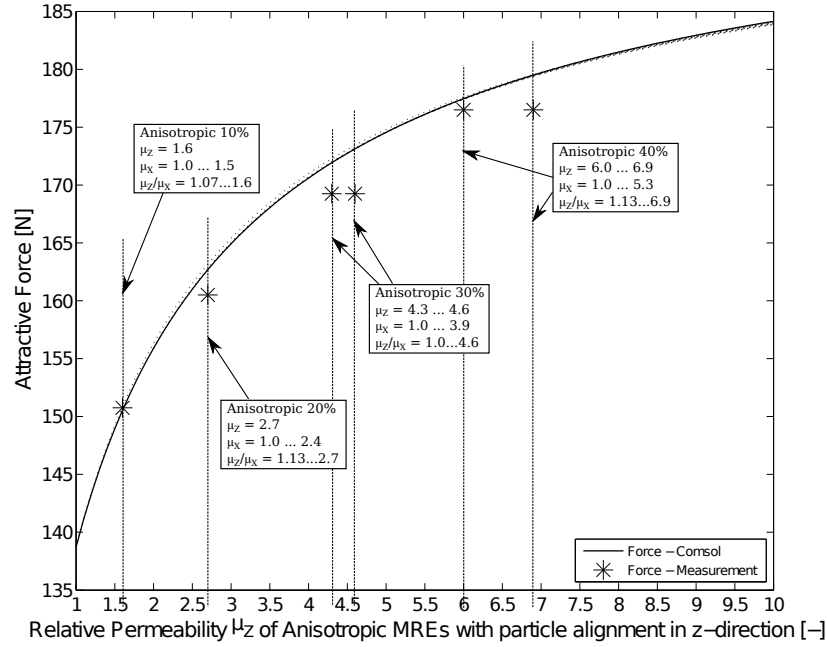


Figure 4.14: The attractive force between the permanent magnets calculated with *Comsol* is illustrated versus the permeability μ_Z of anisotropic MRE samples with particle alignment in z-direction: the solid line represents the isotropic case with $\mu_Z = \mu_X$ and dotted lines the anisotropic case with $\mu_Z > \mu_X$. Average experimentally measured values (Table 4.3) are plotted using the identified permeabilities (Table 4.7). For the cases where a range of permeabilities was identified, two markers have been used to indicate the lower and upper limit of this range. The text inside the Figure lists the results for each anisotropic MRE sample.

dotted lines in Figure 4.14 are hardly seen as the results are close to the isotropic case. The permeabilities of anisotropic MREs with vertical particle alignment were identified analogously to the identification process described above. But in contrast to the isotropic MREs, both the permeability in the vertical direction, μ_Z , and in the two horizontal directions, μ_X , have to be identified. For each position and for the attractive force a range of possible μ_Z and μ_X was identified by comparing the average experimental values together with their standard deviations with the simulation results. Then an intersection between the permeability ranges was built in the same way as it was done for the isotropic MREs, to narrow the range of permeabilities. Unlike the isotropic MRE samples, it was not possible to determine one specific permeability as a result, rather a range of possible permeabilities was found. The results are summarised in Table 4.7. The ratio μ_Z/μ_X is provided to demonstrate the strength of the particle alignment and the resulting magnetic anisotropy. The range of permeabilities μ_X is very large as the change in μ_X does not significantly change the magnetic flux B_Z especially at the *Mid-Height* and *Bottom* positions, and does not change the attractive force much. The average experimental values (listed in Tables 4.2 and 4.3) are plotted in the Figures 4.13 and

	Permeability μ_Z	Permeability μ_X	Ratio μ_Z/μ_X
Anisotropic 10% MREs	1.6	1.0 ... 1.5	1.07 ... 1.6
Anisotropic 20% MREs	2.7	1.0 ... 2.4	1.13 ... 2.7
Anisotropic 30% MREs	4.3 ... 4.6	1.0 ... 3.9	1.10 ... 4.6
Anisotropic 40% MREs	6.0 ... 6.9	1.0 ... 5.3	1.13 ... 6.9

Table 4.7: Identified permeabilities in vertical direction, μ_Z , and in the two horizontal directions, μ_X , of anisotropic MRE samples with particle alignment in z-direction. The permeabilities were identified with experimental magnetic flux and attractive force measurements in combination with the *Comsol* simulation. The ratio μ_Z/μ_X is provided to show the strength of particle alignment and the resulting magnetic anisotropy.

4.14 using the identified permeabilities μ_Z (Table 4.7) to compare with the *Comsol* simulation results. In the case of a determined range of permeabilities (MREs with 30 and 40% iron content) two markers were used to indicate the lower and upper limit of this range. The experimental measurements agree very well with the *Comsol* simulation results. Measured values and numerical predictions do not match exactly at *Mid-Height01* and *Mid-Height02* positions (Figure 4.13) for the same reason as discussed for isotropic MREs. However, the results at the other positions are excellent. The attractive force simulation results are in acceptable agreement with the experimental force measurements.

The anisotropic MREs with horizontal particle alignment are analysed in the next paragraph to narrow the identified range of permeabilities (Table 4.7) further. The final permeabilities of anisotropic MRE parallel ($\mu_{||}$) and perpendicular (μ_{\perp}) to the particle alignment direction are listed in Table 4.10.

Anisotropic MREs with horizontal particle alignment. In order to calculate the magnetic flux and attractive force when MREs with horizontal particle alignment are placed in between the magnets, two cases are considered: MREs with particle alignment in x - and y -direction. In *Comsol*, the permeability was defined as anisotropic, with μ_X as the largest permeability when particle chains were aligned in the x -direction, likewise with μ_Y as the largest permeability when particle chains were aligned in the y -direction. The two other directions were assigned equal permeabilities, both defined with μ_Z . The shape of the MRE samples was slightly ellipsoid: the dimensions used for the *Comsol* model are listed in Table 4.4. The magnetic flux density, B_Z calculated in *Comsol* can be plotted either versus the permeability in the particle alignment direction (μ_X or μ_Y), or versus the permeability perpendicular to the alignment direction μ_Z . Both are plotted in Figure 4.15 for the anisotropic samples with particle alignment in x -direction. The same can be done with the attractive force as illustrated in Figure 4.16. The magnetic flux density and the attractive force for MRE samples with particle alignment in the y -direction are not illustrated as the figures would be almost identical to Figure 4.15 and 4.16, respectively. The magnetic flux density B_Z does not change significantly with increasing permeability μ_X ; this results in

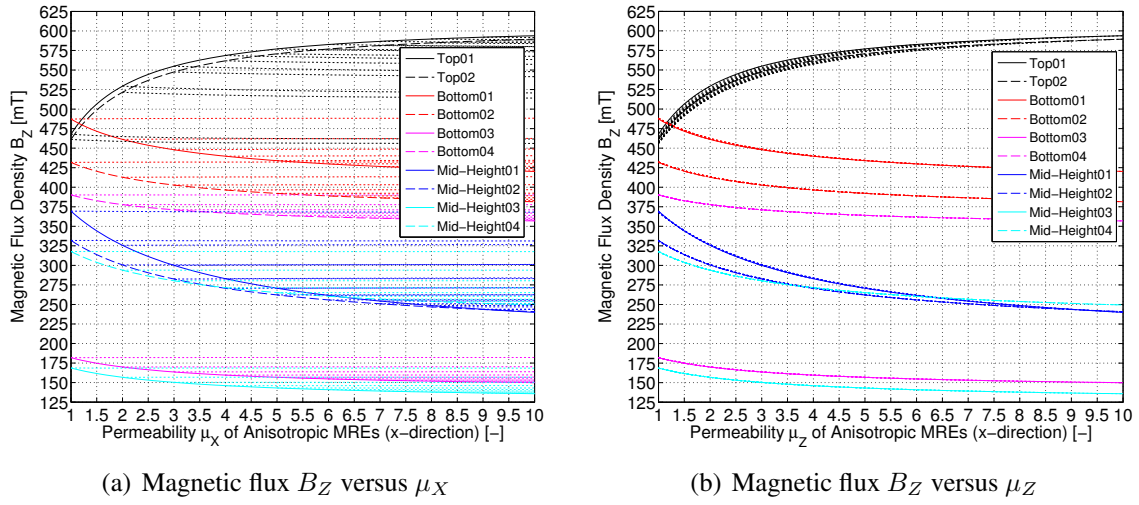


Figure 4.15: The magnetic flux density B_Z at various positions (Figure 4.6 and Table 4.1) calculated in *Comsol* is illustrated versus the permeability (a) in particle alignment direction μ_X and (b) perpendicular to the alignment direction μ_Z . Solid lines represent the isotropic case with $\mu_X = \mu_Z$ and dotted lines the anisotropic case with $\mu_X > \mu_Z$.

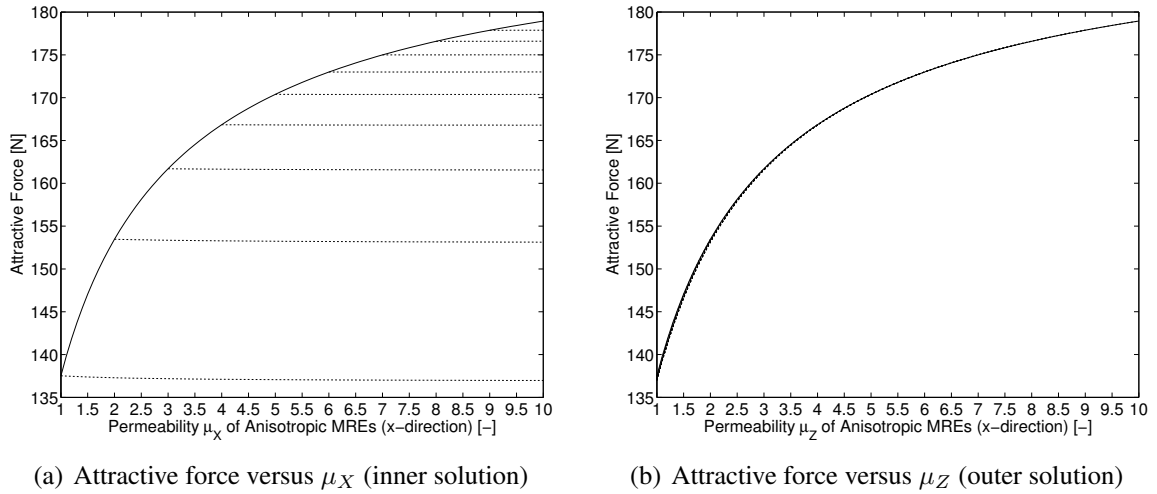


Figure 4.16: The attractive force between the permanent magnets calculated with *Comsol* is illustrated versus the permeability (a) in particle alignment direction μ_X and (b) perpendicular to the alignment direction μ_Z . Solid lines represent the isotropic case with $\mu_X = \mu_Z$ and dotted lines the anisotropic case with $\mu_X > \mu_Z$.

virtually horizontal lines when plotting the results versus μ_X (see Figure 4.15a) and produces nearly no variation of the dotted lines when plotting the results versus μ_Z (see Figure 4.15b). The same behaviour is observed for the attractive force as seen in Figure 4.16.

To identify the permeabilities the same procedure as that used for isotropic MREs and anisotropic MREs with vertical particle alignment was used. The identified permeabilities of MREs with particle alignment in x- and y-directions are listed in Tables 4.8 and 4.9, respectively. Note the large range of possible permeabilities in the particle alignment direction (μ_X or μ_Y); this is due to the small variation in B_Z when increasing this permeability. The upper

	Permeability μ_X	Permeability μ_Z
Anisotropic 10% MREs	2.0 ... 10.0	1.6
Anisotropic 20% MREs	2.6 ... 10.0	2.3
Anisotropic 30% MREs	3.7 ... 10.0	3.2 ... 3.5

Table 4.8: Identified permeabilities, in the direction of particle alignment, μ_X , and in the other horizontal and vertical direction, μ_Z , of the anisotropic MRE samples with particle alignment in x-direction. The permeabilities were identified with experimental magnetic flux and attractive force measurements in combination with the *Comsol* simulation.

	Permeability μ_Y	Permeability μ_Z
Anisotropic 10% MREs	2.0 ... 10.0	1.7
Anisotropic 20% MREs	2.8 ... 10.0	2.2
Anisotropic 30% MREs	4.3 ... 10.0	3.8

Table 4.9: Identified permeabilities, in the direction of particle alignment, μ_Y , and in the other horizontal and vertical direction, μ_Z , of the anisotropic MRE samples with particle alignment in y-direction. The permeabilities were identified with experimental magnetic flux and attractive force measurements in combination with the *Comsol* simulation.

limit 10 listed in Tables 4.8 and 4.9 is the maximum permeability used in the parametric sweep in *Comsol*. Unique values were only identified for permeabilities perpendicular to the alignment direction, μ_Z .

Summary - Permeability of Anisotropic MREs The lack of sensitivity of magnetic flux and force measurements to sample permeability in the horizontal directions means that experiments with particle alignment in both the vertical and horizontal directions have to be conducted in order to identify the permeabilities in both directions. The results of all experiments on anisotropic samples, involving both vertical and horizontal particle alignment, are therefore required in order to narrow the final range of possible permeabilities for anisotropic samples. Permeabilities parallel to the particle alignment are best determined with vertically aligned MRE samples: the results of μ_Z are listed in Table 4.7. The lower limits of μ_X (Table 4.8) and μ_Y (Table 4.9) do agree with the identified μ_Z of vertical aligned samples (Table 4.7). Only the results of anisotropic samples with 10% iron content are too high. Permeabilities perpendicular to the particle alignment are best determined with horizontally aligned MRE samples: the results are listed in Table 4.8 and 4.9. The upper limits of μ_X (Table 4.7) do agree with the identified μ_Z of horizontally aligned MREs (Tables 4.8 and 4.9). Only the samples with 10% iron are overestimated in the case of horizontally aligned MRE samples, and as μ_{\perp} must be smaller than μ_{\parallel} the upper limit of μ_X from vertically aligned samples (Table 4.7) have been chosen. The final permeabilities parallel and perpendicular to the particle alignment are summarised in Table 4.10. The ratio $\mu_{\parallel}/\mu_{\perp}$ is provided to show the strength of the particle alignment and the resulting magnetic anisotropy. Unfortunately,

	Permeability μ_{\parallel}	Permeability μ_{\perp}	Ratio $\mu_{\parallel}/\mu_{\perp}$
Anisotropic 10% MREs	1.6	1.5	1.07
Anisotropic 20% MREs	2.7	2.2 ... 2.4	1.13 ... 1.23
Anisotropic 30% MREs	4.3 ... 4.6	3.2 ... 3.9	1.10 ... 1.44
Anisotropic 40% MREs	6.0 ... 6.9	1.0 ... 5.3	1.13 ... 6.90

Table 4.10: Identified relative permeabilities in particle alignment direction, μ_{\parallel} , and perpendicular to the alignment direction, μ_{\perp} of anisotropic MRE samples. The minimum and maximum ratio $\mu_{\parallel}/\mu_{\perp}$ is provided to show the strength of particle alignment and resulting anisotropy.

horizontally aligned MRE samples with 40% iron content were not manufactured and therefore the range of permeabilities for such MREs cannot be narrowed. However, as seen from MREs with 10% to 30% the permeability perpendicular to the alignment direction μ_{\perp} is expected to be near the upper limit of μ_X provided in Table 4.10.

4.5 Conclusions of Chapter 4

The permeabilities of isotropic and anisotropic MREs were successfully identified by comparing experimental magnetic flux measurements at various positions around the MRE specimen, with calculations of the magnetic flux densities at the same positions simulated with the finite element software *Comsol*. The magnetic flux was calculated for various permeabilities of the isotropic and anisotropic MRE samples, and ranges of possible permeabilities were determined for each isotropic and anisotropic MRE with 10% to 40% iron content. Unique permeabilities were only determined for MREs with low iron contents. The attractive force between the magnets was also experimentally measured and simulated in *Comsol* to aid with the determination of the permeabilities of MREs. In this study the permeabilities of MREs are required to simulate the distribution of the magnetic flux density within the experimental setups used to characterise the MRE behaviour without and with applied magnetic inductions, the results of which are presented in Chapter 5. The level of magnetic induction, the uniformity of the magnetic flux distribution and direction of flux lines are studied. The level of magnetic induction is especially important in the case of equi-biaxial tension experiments as this is used for a required assumption in order to calculate stresses in the stretching directions, as detailed in Section 5.5.

In future, the knowledge about the permeability can help to characterise the MR effect more specifically (*i.e.* normalised to the magnetic flux distribution), and is also needed to develop constitutive material equations that describe the MRE behaviour under the influence of a magnetic flux. For all further considerations using the permeabilities of MREs identified here, mean values of the determined ranges (Tables 4.6 and 4.10) are used. The final results for all types of MREs are summarised in Table 4.11.

	$\mu_{iso} / \mu_{\parallel}$	μ_{\perp}
Isotropic 10% MREs	1.60	
Isotropic 20% MREs	2.20	
Isotropic 30% MREs	3.70	
Isotropic 40% MREs	6.05	
Anisotropic 10% MREs	1.60	1.50
Anisotropic 20% MREs	2.70	2.30
Anisotropic 30% MREs	4.45	3.55
Anisotropic 40% MREs	6.45	-

Table 4.11: Relative permeabilities for isotropic MREs, and for anisotropic MREs in particle alignment direction, μ_{\parallel} , and perpendicular to the alignment direction, μ_{\perp} . In the case where a range of permeabilities was identified rather than a unique permeability, the average values are listed.

A comparison of the results determined here with other results from both theoretical and experimental investigations found in the literature, was conducted previously in Section 4.2, and illustrated in Figure 4.4. The identified isotropic permeabilities agree very well with the *Bruggeman* model, and also with measurements performed by Göktürk *et al.* (1993). The permeabilities of anisotropic MREs with up to 20% iron content are within ranges of those calculated by both Martin *et al.* (2006) and Chen *et al.* (2007b), and are also in agreement with measurements performed by Vicente *et al.* (2002). Permeabilities of MREs with higher iron contents are greater than those found in almost all previous investigations. Only Zeng *et al.* (2013) measured higher permeabilities for anisotropic MREs, in that case with 24% volume iron content. The permeability of anisotropic MREs perpendicular to the particle alignment are below those in the alignment direction, and are very close to the permeabilities of isotropic MREs. This is a reasonable result.

The novel method used for the identification of magnetic permeabilities in this investigation did not require highly sophisticated equipment. A simple test setup involving two permanent magnets, a Gaussmeter, and a *Zwick Z250* test machine were all that was required. A multi-physics software (*Comsol*) was then used to analyse the measured data and to identify the permeabilities. This experiment therefore provides a simple and low-cost method of determining the permeabilities of MREs.

5 Large-Strain Experiments on MREs

Large-strain mechanical tests have been conducted to characterise the mechanical response of isotropic and anisotropic MRE samples under various deformation modes. The MRE behaviour has been characterised without and with the application of magnetic fields to study the increase in stiffness defined as the Magneto-Rheological (MR) effect. MREs show a complex mechanical behaviour: They are sensitive to stress softening known as the *Mullins* effect (Mullins and Tobin, 1965), isotropic and anisotropic MREs show considerably different stress-strain behaviours, and the application of external magnetic fields changes their mechanical properties significantly. Studies on the MRE behaviour under large-strain are relatively rare, and no consistent experimental data sets exist that characterise the same type of MRE material under different deformation modes (discussed in Section 2.5). Extensive experimental data derived from uniaxial and multiaxial experiments are required to develop accurate constitutive models (BS 903-5, 2004; Miller, 1999; Ogden, 2004) and are required to achieve the ultimate goal of virtual design with MREs in large-strain applications. The complexity of the mechanical behaviour of MREs means that a wide range of tests are required to fully characterise their response. This complexity is reflected in the large number of parameters required in constitutive models (see Chapter 6). To this end, uniaxial compression, uniaxial tension, pure shear, and equi-biaxial tension tests have been conducted.

This chapter is structured as follows: in Section 5.1 the general test method is described and the method of analysing the experimental data is clarified. Uniaxial compression tests are detailed in Section 5.2, uniaxial tension tests in Section 5.3, pure shear experiments in Section 5.4, and equi-biaxial tension tests in Section 5.5. Conclusions are given in Section 5.6, where the results of large-strain experiments are compared. In Sections 5.2 to 5.5, specific descriptions of the test procedure, the test setup, and the results of each type of experiment are provided.

5.1 Test and Analysis Method

5.1.1 General Test Method

Tests on both isotropic and anisotropic MREs with 0, 10, 20, and 30 *vol%* iron content have been conducted. For anisotropic MREs, these tests were carried out with particle alignment both parallel and perpendicular to the loading direction. All tests were performed both with and without the application of an external magnetic field in the loading direction. The experiments were carried out using a *Zwick Z250* uniaxial test machine equipped with a 250 *kN* load-cell in the case of compression tests, whereas a 1 *kN* load-cell was used for all other tests. Bespoke test rigs were designed for each of the experiments, enabling the

use of strong permanent magnets (*Neodymium N52*, see Appendix A.12), which were used to induce magnetic fields during the tests. The dimensions of the permanent magnets were $50 \times 50 \times 25 \text{ mm}$. Test setups were designed so that the top magnet remained stationary, while the crosshead of the test machine was moving; consequently the distance between the two magnets remained fixed throughout the test. By maintaining position, the magnetic flux density remained relatively constant throughout the mechanical tests (small changes are inevitable due to the changing shape of the test specimens), reducing the influence of a changing magnetic attractive force during the tests. All test rigs were built using non-magnetic materials including aluminium, brass, and PTFE (Teflon). To ensure a fixed minimum distance from the magnets used in the test rig to the steel components and the load-cell of the test machine, relatively long aluminium rods (200 mm) were attached to the test rigs. All tests were displacement controlled. Where possible, strains were measured optically using a *Digital Image Correlation* (DIC) system and also verified using manual image analysis. The *Limess* DIC system was loaned from the *Engineering and Physical Sciences Research Council* (EPSRC). This system consists of two high-resolution cameras ($4M$ pixels, which can record up to 15 frames per second), two lights and the software *VIC-3D*. The sample shapes and dimensions used for each test have been described in Section 3.3 and are also given in the technical drawings in Appendix B. Sample dimensions were measured three times before each test.

5.1.1.1 Influence of the Mullins Effect

The MRE materials are sensitive to stress softening, a well-known effect in rubber-like materials known as the *Mullins* effect. This effect was first discovered by Mullins and Tobin (1965), and a comprehensive review of this phenomenon is provided by Diani *et al.* (2009). As the stress softening effect has an influence on all the large-strain experiments discussed in this chapter, a few findings are discussed here in advance to make it easier for the reader to understand the slightly evolving test procedures used to characterise the MRE behaviour under different deformation modes.

The influence of the Mullins effect on stress-strain results are demonstrated in Figure 5.1. The first loading cycle shows the highest stresses and is very different compared to the second loading cycle, where the stresses are much lower. After the first cycle, the sample experiences a remnant deformation, which can be either permanent or temporary or a combination of both. Note that the strain level that the sample experiences in the first loading cycle is called the ‘preconditioning strain’ or ‘strain level’ throughout this investigation. The uniaxial tension and compression specimens experienced permanent deformations in each of the cycle tests performed, *i.e.* the permanent deformation increased with increasing number of tests. However, pure shear and equi-biaxial tension specimens experienced no permanent deformations, and the remnant deformation present after the first cycle was only tempor-

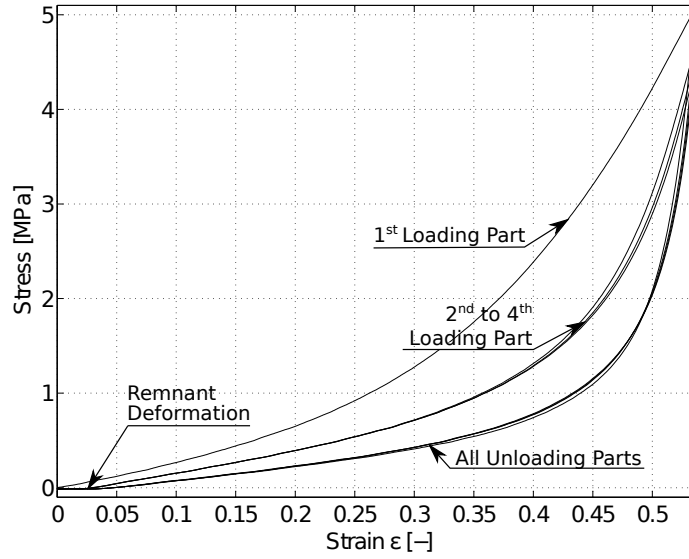


Figure 5.1: Stress-strain results of a four-cycle compression tests up to 6.25 mm equivalent to 50% strain of an isotropic MRE with 30% CIP. The number of loading cycles, and the remnant deformation is indicated.

ary. Note also that the *Mullins* effect is time-dependant, so when repeatedly testing the same MRE specimen after reasonable intervals of time (*e.g.* a few hours) the stress-softening effect again becomes apparent, although not usually as significant as in the first test sequence.

It should be noted that the preconditioning strain (the set strain of the first cycle) has been found to be of great importance in influencing the material's subsequent mechanical response. Preconditioning a sample up to a larger strain results in a softer material, and as soon as the material is tested up to a new larger level of strain its properties significantly change once again (Miller, 1999).

In order to mitigate the influence of the *Mullins* effect a four-cycle test procedure was performed. The third loading cycle was consistently used to characterise the material while the fourth cycle was performed merely to check that no further significant changes occurred after the third cycle (see Figure 5.1).

5.1.1.2 Test Procedure

The general test procedure evolved slightly throughout this investigation, as the importance of the *Mullins* effect was gradually better understood. To characterise the MRE material both in the absence and in the presence of magnetic fields, a minimum of three distinct test steps were conducted, each involving four loading cycles and re-use of the MRE samples in each subsequent step in the test series. Re-use of samples was the norm for most experiments with the exception of equi-biaxial tension tests. In general, the basic test series consisted of three test steps:

- (i) Initial tests in the absence of a magnetic field (*NoField01*)

- (ii) Tests with different levels of magnetic field strength
- (iii) Repetition of the no-field tests (*NoField02*)

However, in some experiments, additional test steps were introduced to examine issues such as stress-softening and damage. Measurements of sample dimensions were repeated before each testing step to detect any permanent deformation that may have occurred during the previous test. The no-field tests were repeated at the end of the three-step test series to identify any divergence between results of the *NoField01* and *NoField02* tests. Two reasons could potentially cause differences in these results: (i) The *Mullins* effect; this effect causes material properties to change significantly when the material experiences new larger strain levels. (ii) The magnetic field applied to the MREs between the no-field tests; this could have a permanent influence on the MREs when they were tested up to large strains, *i.e.* due to micro-structural changes. Although MREs are meant to change their properties reversibly and almost instantaneously under the influence of a magnetic field, this idea has only been tested under small-strain conditions (see literature review in Section 2).

In the uniaxial compression tests (Section 5.2), stress-strain curves resulting from the two no-field tests were found to diverge from a certain level of strain (see Section 5.2.3). At this early stage of the experimental investigation, the reason for the divergence was not clear. To investigate the reason for the divergence, additional test steps were introduced in the tension test investigation (Section 5.3). This involved:

- (i) Fatigue tests to investigate whether stress-softening depends on the strain level, *i.e.* to determine if a sample reaches a ‘stable’ state when testing above a certain strain level (see Section 5.3.3). During these fatigue tests a ‘stability strain limit’ was determined for each type of MRE. Samples that were stretched beyond this strain limit continued to experience a stress-softening even after 100 cycles. Samples subsequently examined in the main tension test series (and all other large strain experiments) were only stretched up to or below this stability strain limit.
- (ii) Samples were preconditioned in the main tension test series with an additional 50 cycles prior to the first no-field test to examine whether or not this improves the stability of the results, *i.e.* whether divergence between *NoField01* and *NoField02* stress-strain results still occurs.
- (iii) Each type of MRE was tested up to two different preconditioning levels to observe the differences in stress-softening.

At this stage of the project, the stress-softening was found to have a large influence, as MRE samples stretched up to larger strain levels were found to be softer than those preconditioned to lower levels (see Section 5.3.5). Despite the additional preconditioning step and despite

stretching the samples to less than the ‘stability strain limit’, the no-field tension tests were still found to diverge from a certain level of strain (see Section 5.3.5). At this stage of the test program, the reason was still not completely clear, but the Mullins effect did seem to be the most likely reason. In pure shear tests (Section 5.4), the test procedure was further enhanced by recording DIC images during the 50 preconditioning cycles, enabling detailed comparison between the strains and stresses of three sets of no-field tests: the preconditioning and *NoField01* tests conducted before any magnetic field was applied, and the *NoField02* tests conducted after the MRE specimens had experienced a magnetic field. This was done to exclude the magnetic field as a possible reason for the divergence. The stress-strain curves resulting from the three pure shear no-field tests did not diverge (see Section 5.4.4). The reason for the divergence present in compression and tension was therefore clarified and identified as being the permanent deformations present in uniaxial compression and tension samples, but not in the pure shear specimens. The permanent deformations in the samples effectively imposed new larger strain levels in each of the subsequent four-cycle tests in the test series, and due to the *Mullins* effect this changed the material properties significantly. Further details are given in the Sections 5.2, 5.3, and 5.4 describing each large-strain experiment performed during this investigation. In the equi-biaxial tension tests (Section 5.5) re-use of the MRE specimens was not possible due to the test setup (described in Section 5.5.2). Permanent deformations were not observed in equi-biaxial tension specimens, and therefore divergences between several stress-strain curves are not expected.

To eliminate the influence of the stress softening *Mullins* effect only stress-strain results measured over a strain range in which the no-field tests are in agreement (up to the points of divergence, as discussed in Sections 5.2.3 and 5.3.5), are used to characterise the MRE material behaviour in the absence and the presence of a magnetic field.

5.1.2 Analysis Method

The method of analysing the load-displacement test data, provided from the uniaxial test machine, is detailed in this section. Several methods of determining the moduli and the MR effects from the stress-strain data are defined. The latter is used to assess the performance of MREs under the influence of a magnetic field. MREs are very sensitive to the *Mullins* effect as discussed in the previous section, and it is therewith important to keep the method of analysis constant throughout all large-strain experiments performed in this investigation. As mentioned in Section 5.1.1, four-cycle tests were carried out and the third loading cycle was used for interpretation and comparison of the test results. To aid with the analysis of the experimental data, several *Matlab* functions were written, each one designed for a specific experiment. All of the *Matlab* functions are listed in Appendix D together with a brief description and saved on a DVD attached to this document.

The method of analysis involves first separating the four load-displacement cycles into four loading and unloading parts. In order to cut and shift the last three cycles horizontally to zero displacement, a shifting value (or cutting point) has to be chosen. This is the most difficult part of the analysis, and involves some degree of manual assessment, either by choosing the point where a distinctive change of slope occurs, or by specifying a displacement range; the method of determining the cutting point is discussed further in the next section. Using the cutting point, the load-displacement data were shifted to zero displacement. Stresses were calculated with the reference area (original dimensions), determined using three measurements taken on each sample. In the case of compression samples, strain values were calculated using the original height of the samples. In the case of tension, pure shear, and equi-biaxial tension experiments an optical strain measurement device (DIC system) was used and engineering strains were calculated. Strain analysis is discussed in Sections 5.3.4, 5.4.3, and 5.5.3 separately for each large-strain experiment. Once both stress and strain data were calculated, they were cut and shifted to the same extent as the load-displacement data. Mean values and standard deviations of three repeated tests were calculated, and are illustrated in all subsequent figures in this chapter.

5.1.2.1 Determination of the *Cutting Point* for Data Shifting

In order to explain the choice of cutting point, actual test data are used. The magnification of stress-strain data up to 10% strain of an isotropic MRE with 30% iron content tested under uniaxial compression (*NoField01*) is shown in Figure 5.2. The complete data were shown in Figure 5.1. The stress softening behaviour can be clearly seen; the loading cycles are numbered in the figure. In the case of compression test data, the cutting point is very obvious and easy to define. The red arrow in Figure 5.2 indicates the choice of the cutting

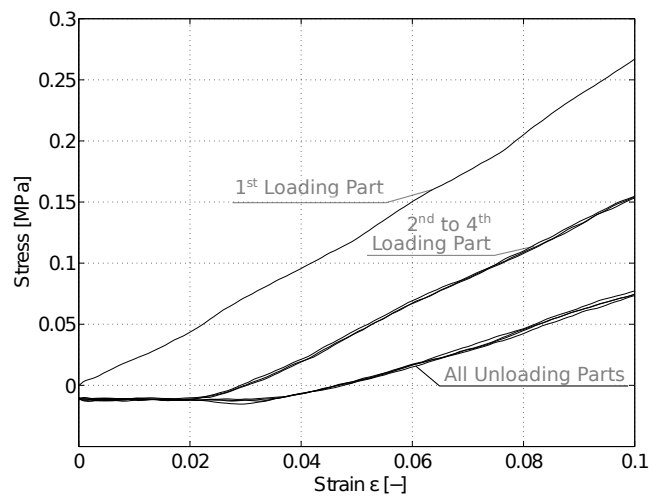


Figure 5.2: Magnification up to 10% strain of the of a four-cycle compression test (*NoField01*) of an isotropic MRE with 30% CIP, the complete four-cycle tests is shown in Figure 5.1. The red arrow indicates the choice of cutting point in this case.

point. The slope changes noticeably as soon as the sample loses contact with the test rig.

The choice of the cutting point is less obvious in the case of uniaxial tension, pure shear, and equi-biaxial tension tests. The tension samples were clamped into the test setup (described later in Section 5.3.2) with the aim of starting the test with a straight sample. When clamping the tension samples, slight buckling was induced when tightening the clamps. Thus, in order to start the test with a straight sample, the top clamp was first moved down beyond the saved start position, the clamps were tightened, and the top clamp was moved back up to the saved start position. The amount of movement was dependent on the type of MRE sample; pure rubber samples buckled far more than anisotropic samples, especially those with high iron content. The movement was chosen so that a zero (or a small positive tensile) force was achieved at the end of the adjustment. The method of clamping the samples is important when deciding on the best cutting point. In contrast to the compression data (Figure 5.2), the four-cycle uniaxial tension test data show negative forces at the start of the second, third, and fourth cycle. The first attempt is to eliminate all these negative forces, but these negative forces are not necessarily compressive forces. As the samples were straightened prior to testing, a small positive (tensile) load was induced; this load was automatically set to zero by the test machine at the start of the test. This potentially means that the measured force could apparently become negative at the end of the first unloading cycle despite the fact that the sample was still under tension.

To investigate this potential source of error, a few preliminary tests were performed in which the tension samples were cycled up to $+15\text{ mm}$ (stretching) and then down to -5 mm (compression) in relation to the zero position. Both straight samples (clamped using the method described above) and slightly buckled samples (clamped without subsequent adjustment of displacement) were tested. The results of this test, using isotropic MREs with 30 vol% iron content, are shown in Figure 5.3; the magnification of the load-displacement curve up to only 2.5 mm is illustrated in this figure. Negative forces occur when the samples were straightened (Figure 5.3a) and the forces remain positive when this ‘straightening-adjustment’ was not performed (Figure 5.3b). However, considering the start of the 2nd to 4th loading parts in Figure 5.3b, the slope is too small to represent stretching of the sample when the curves cross the y-axis, which indicates that the sample is still not straight at this point. On the other hand, the slope at the start of the 2nd to 4th loading part is much steeper at the zero displacement for the straightened samples of Figure 5.3a, this indicates a straight, non-buckled sample. A perfect starting point would be somewhere in between these two extremes, but experimentally this is not achievable. The change in slope at the beginning of each loading cycle is more important in deciding the choice of cutting point than the occurrence of negative or positive forces at zero displacement. Thus, the true start of the test is identified as being close to the point at which a distinct change in the slope of the data occurs. However, because the tension samples can support a slight amount of compressive

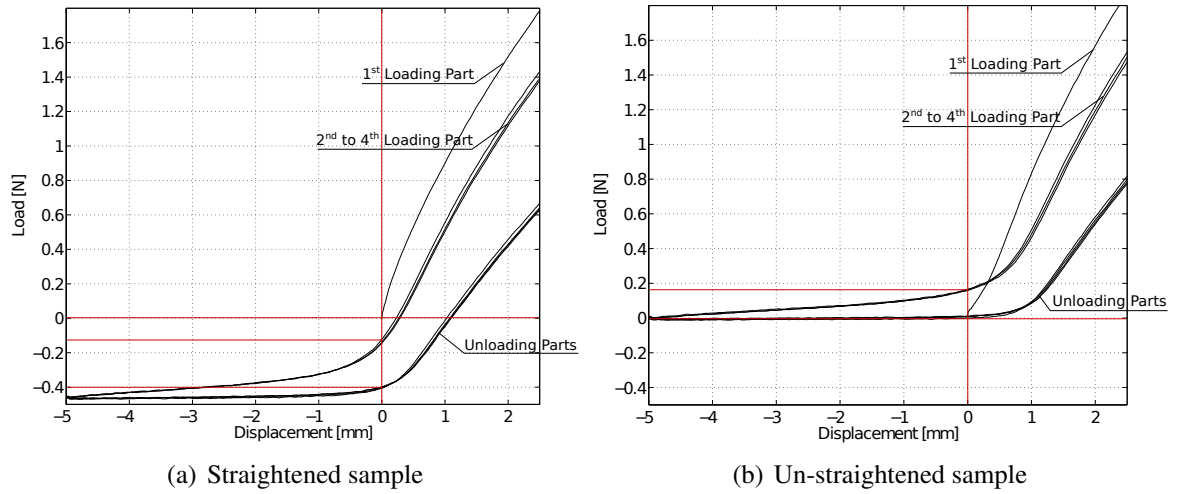


Figure 5.3: Detail of the load-displacement curve of a 4-cycle test up to 15 mm and down to -5 mm of an isotropic tension sample with 30% iron content. (Left) The sample were straightened before the 1st cycle and (right) the sample was not straightened, the screws were tightened in the saved start position and the test started with a slightly buckled sample.

stress, the change in slope is not abrupt (see Figure 5.3) and therefore defining the start point inevitably involves some degree of error.

In this investigation, the cutting point is determined either using a single distinct value for the displacement (used when the change in slope is obvious, as with the compression tests), or a range of displacement values is first provided and then the cutting point is determined as the point at which the slope is 20% less than the average slope in the specified range (used when the change in slope is not abrupt, as in the tension, pure shear, and equi-biaxial tests).

5.1.2.2 Definitions of Moduli and Magneto-Rheological Effect

To interpret the stress-strain results both secant and tangent moduli are used. The initial secant modulus E_{0-5} , is used as a first attempt to interpret and compare the data. The E_{0-5} is measured only in the small-strain region, and is calculated as the linear slope of stress-strain data from 0% to 5% strain, neglecting non-linearities in the stress-strain data. The tangent modulus, E_T , is used to interpret the non-linear behaviour, and is calculated as the linear slope of 1% strain increments. Use of this small increment makes this a reasonable approximation of the first derivative of the stress-strain curves. The tangent moduli are plotted versus engineering strain in the figures (smoothed using the moving average method involving a span of 10), and the value between 1% and 2% strain is provided in the tables in each section (this is where largest relative MR effects usually occur). The tangent moduli in the figures are illustrated from 1% strain, as experimental results at lower strains are not reliable due to experimental issues and the method of analysis (as discussed in Section 5.1.2.1). To aid with the calculation of different moduli from the stress-strain data, a *Matlab* code

modulus_linearfit.m was written (see Appendix D). MR effects are characterised by comparing the stress-strain curves resulting from tests conducted, both with and without magnetic fields. The absolute MR effect is defined as the difference between the moduli resulting from both tests

$$MR_{abs} = E_M - E_0 \quad (5.1)$$

where E_M and E_0 are the moduli resulting from tests with and without magnetic field, respectively. The relative MR effect is defined as the relative factor between the moduli:

$$MR_{rel} = E_M/E_0 \quad (5.2)$$

This can also be expressed as the increase in moduli $(E_M/E_0 - 1) \times 100$ defined here as a percentage value. The moduli used to calculate the MR effect can be either E_{0-5} (for small strains), or E_T (non-linear behaviour up to large strains). MR effects, calculated using E_T , are plotted versus large engineering strain in the figures (smoothed using the moving average method involving a span of 10), and the maximum MR effect is provided in the tables in each section. To aid with the calculation of the MR effect the *Matlab* code *MReffect.m* was written (see Appendix D).

5.2 Uniaxial Compression Tests

Uniaxial compression tests were conducted in the absence and in the presence of magnetic fields, in order to characterise the MRE behaviour; the results are presented in this section. The general test method, and the method of analysis was described in Section 5.1, and the specific procedure of the uniaxial compression tests is given in Section 5.2.1. The test setup together with calculations of the compliance of the test rig, and the magnetic flux distribution, are described in Section 5.2.2. The mechanical behaviour of MREs in the absence of a magnetic flux is detailed in Section 5.2.3. Finally, the tests with an applied magnetic induction and the resulting MR effects are presented in Section 5.2.4. The results of the compression tests are summarised in Section 5.2.5.

To aid with the analysis of the compression tests, the *Matlab* function *compression.m* was written, which includes the cut-and-shift process described previously in Section 5.1.2. For further details on the *Matlab* procedure and the employed sub-functions, the reader is referred to Appendix D. The *Matlab* codes are saved on a DVD attached to this document and can be consulted for more detailed information.

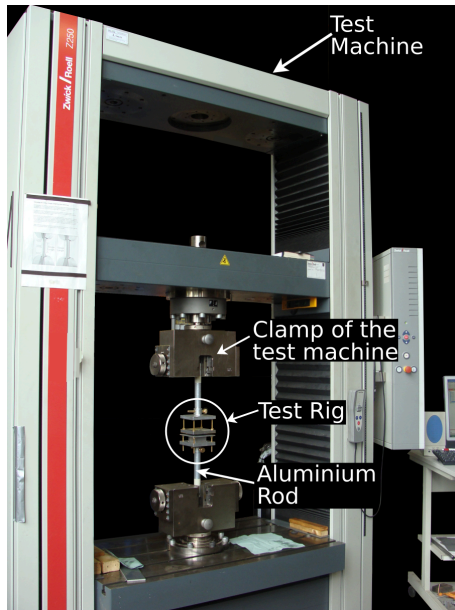
5.2.1 Procedure of the Compression Tests

Uniaxial compression tests were performed in accordance with the *British Standard* (BS ISO 7743, 2008). Tests were carried out using a test speed of 10 mm/min on circular MRE samples with up to 40% volume iron content. Samples were compressed up to 6.5 mm ; equivalent to 50% engineering strain. The polished aluminium plates of the setup were lubricated as described in *Method A* in the *British Standard*. Four repeat tests on each type of MRE (isotropic and anisotropic with different amounts of iron particles) were conducted re-using the samples, including tests: (i) without a magnetic flux (*NoField01*), (ii) with a magnetic flux of 450 mT created with an inter-magnet distance of 35 mm (*Magnet35*), (iii) with a magnetic flux of 210 mT created with 62 mm distance between the magnets (*Magnet62*), and (iv) without magnetic flux (*NoField02*); this last test was a repeat of (i) and conducted in order to verify the results (as discussed already in Section 5.1.1 and explained in more detail in Section 5.2.3).

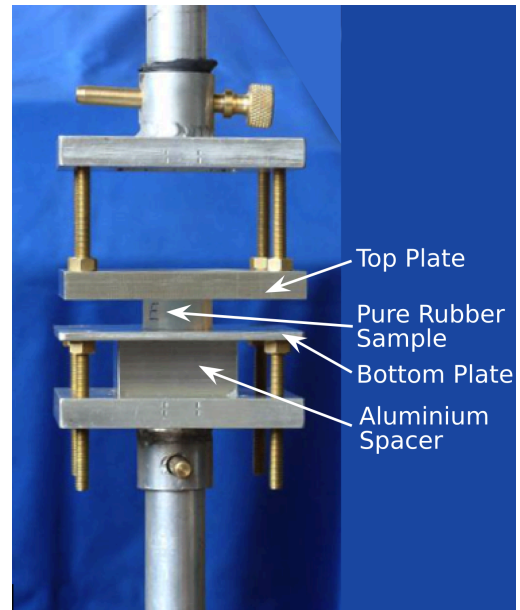
5.2.2 Compression Test Setup

Within this section the test rig used to carry out the uniaxial compression tests is described. The compliance of the test rig is studied, and the distribution of the magnetic flux density is simulated, both using finite element calculations.

The test rig was specifically designed with the goal to employ permanent magnets, holding their positions fixed while running the test. An open setup had to be designed, with enough space for the permanent magnets. Movement of the machine crosshead during the test had to be permitted. It was necessary to remove the magnets easily in order to perform experiments both with and without a magnetic flux. It was also desirable to create high magnetic flux densities, which meant the distance between the magnets had to be as small as possible. Therefore plates within the setup were chosen to be relatively thin. The material used to manufacture the rig had to be non-magnetic: thus aluminium and brass were used. The designed test setup with and without the use of permanent magnets is shown in Figures 5.4 and 5.5. When using the setup without permanent magnets an aluminium spacer, of the same size as the permanent magnets, was placed into the bottom half of the rig structure (Figure 5.4b). This mitigated deformation of the bottom plate during the tests. Two different magnetic field strengths were possible using this setup. A magnetic induction of 450 mT was created using a distance of 35 mm (Figure 5.5a) between the magnets. Also, a lower magnetic induction of 210 mT was created using a distance of 62 mm (Figure 5.5b) between the magnets. In this case, the aluminium spacer was used to increase the distance between the magnets. The magnetic flux density was measured in the centre of the volume usually occupied by the MRE sample but measured in the absence of a sample ($\mu_r = 1$). Dimensions of the test rig are given in the technical drawings in the Appendices B.7 to B.9.

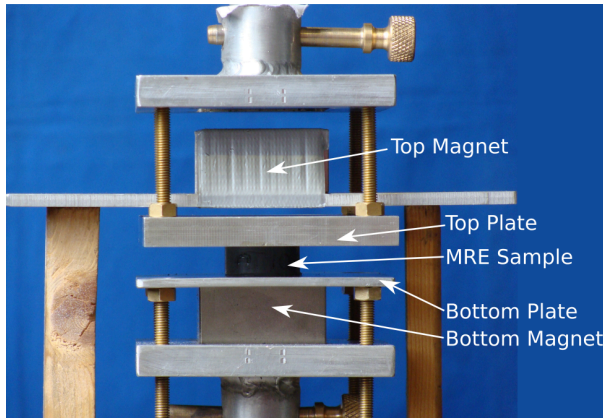


(a) Universal test machine (Zwick Z250)

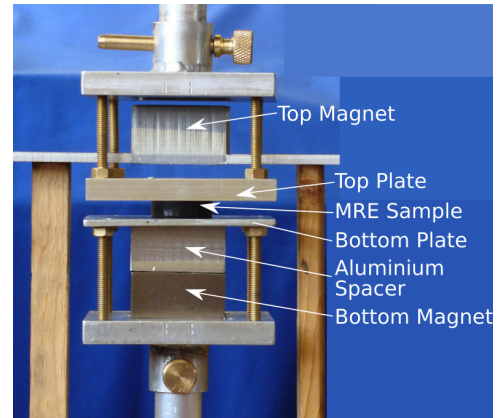


(b) Setup with pure rubber sample

Figure 5.4: Test setup for compression tests designed so that permanent magnets can remain in a fixed position during tests. The rig material is non-magnetic. An aluminium spacer under the bottom plate was used to avoid deformation of the setup.



(a) Setup with 450 mT induction



(b) Setup with 210 mT induction

Figure 5.5: Test setup for compression tests with permanent magnets. 35 mm and 62 mm distance between the magnets led to 450 mT and 210 mT magnetic field strength, respectively. The magnets remained in a fixed position during the tests.

5.2.2.1 Compliance of the Test Rig

The compliance of the test rig is studied using finite-element simulations in *Abaqus* (Abaqus, 2010). In the case of compression tests, the use of a strain gauge or the DIC system to determine exact engineering strain values was not possible. Since a deformable test rig could introduce significant errors into the strain values, at least the deformation of the test rig should be simulated. Due to the design requirements as discussed above, thin plates and

relatively soft materials had to be used for the rig, so it is even more important to verify the compliance of the test rig. To evaluate the numerical simulations, experiments on a rigid test setup with the same type of MREs were carried out, and stress-strain results are compared with results achieved using the test rig from this investigation.

The top and bottom of the rig structure were considered separately. In both cases the geometry was kept as simple as possible; the geometries used in *Abaqus* are illustrated in Figure 5.6. The aluminium rod was clamped into the test machine. The boundary conditions pre-

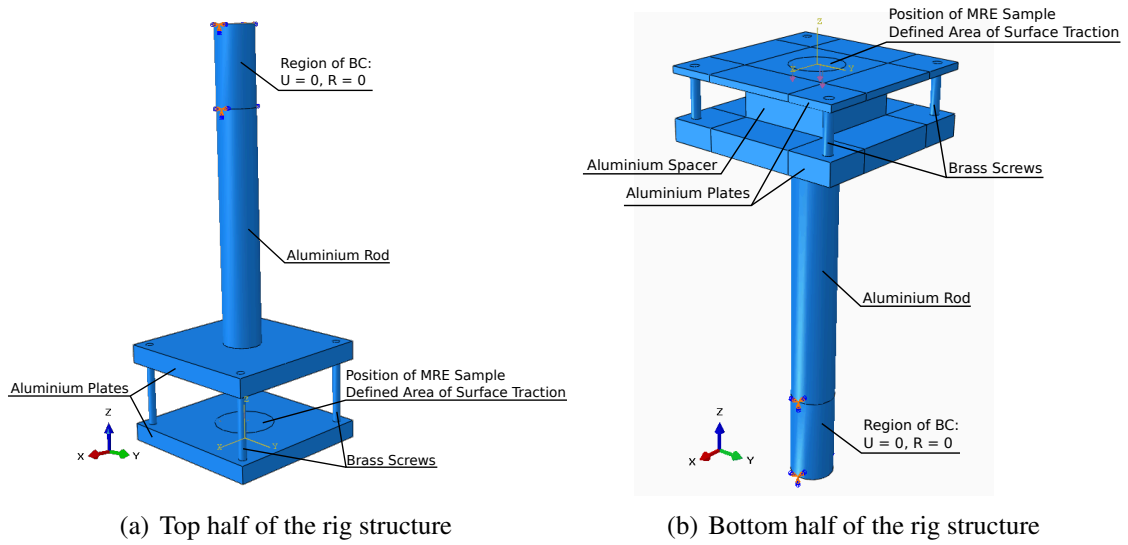


Figure 5.6: Geometry of top and bottom rig structure modelled using *Abaqus* (Abaqus, 2010).

vented any deformation or rotation of the aluminium rod over a length of 5 cm in keeping with the experimental setup. A pressure was applied to the surface over the region where the MRE sample was positioned during the experiments. Anisotropic MRE samples with 40% CIP volume fraction were exposed to 6 MPa during compression tests, these were the stiffest samples tested throughout this investigation. This pressure was used in the *Abaqus* model to examine the maximum compliance of the test rig. The mesh was created automatically by *Abaqus* using ‘swept mesh’ algorithm. An approximate element length of 5 mm was used to generate the mesh. For more information on meshing techniques see Abaqus (2010). A mesh sensitivity study was performed by comparing results of finer and coarser meshes; the results achieved with the 5 mm mesh size were found to provide good convergence. The material properties used for aluminium and brass are listed in Table 5.1 (from (MatWeb, 2013a) and (MatWeb, 2013b)). The main result of interest is the vertical displacement in the centre of the plates. The deformed geometries of the top and bottom halves of the test rig together with the values of the vertical displacement are illustrated in Figure 5.7. The plate in the bottom half of the rig structure can be considered as almost rigid due to the aluminium spacer used between the plates; here the maximum vertical displacement is just 0.02 mm. More critical is the compliance of the plate in the top half of the rig, which was found to bend

Property	Unit	Aluminium	Brass
Elastic Modulus	<i>GPa</i>	68.9	97
Poisson's Ratio	—	0.33	0.31
Tensile Strength, ultimate	<i>MPa</i>	310	403
Tensile Strength, yield	<i>MPa</i>	276	217

Table 5.1: Material properties of aluminium (MatWeb, 2013a) and brass (MatWeb, 2013b) used for the *Abaqus* model. In the case of brass mean values are listed.

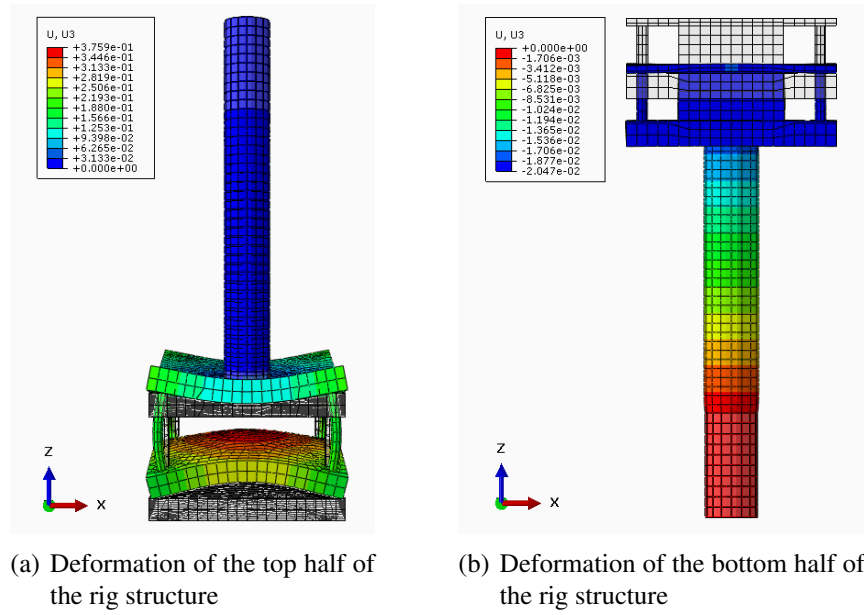


Figure 5.7: Deformed geometry of the top and bottom halves of the test rig with values of displacement in vertical direction, U_3 , given in *mm*. The maximum deformation of the top and bottom clamp are 0.376 *mm* and 0.02 *mm* respectively when 6 *MPa* pressure are applied to the surface. Scale factors of (a) 2.5 and (b) 30 are used for the illustrations.

upwards by about 0.376 *mm* in the vertical direction when the 6 *MPa* pressure was applied. The MRE samples were displaced by 6.5 *mm* to achieve 50% strain, producing an overall deformation of the test rig of about 0.4 *mm*; this reduces to 46.9% strain, an error in strain of about 3.1%, *i.e.* thus, if the displacement of the test machine crosshead is used to calculate the compressive strain (rather than using a strain gauge) then in the worst case, the compliance of the test rig might be expected to lead to an underestimate of the sample stiffness of about 3%. Note that this error is at a maximum for the case of anisotropic MREs with high iron contents of 40% CIP at maximum compression strain; given that the deformation of the rig is small and the material behaviour of the rig linear, the error might reasonably be expected to decrease linearly with the stress applied to the sample. All other MRE samples experience considerably lower stresses: an anisotropic MRE with 30% vertically aligned particles exhibits 2.5 *MPa*, and a pure rubber sample only 0.74 *MPa* at 45% strain (see Figure 5.12). This would lead to 0.17 *mm* and 0.05 *mm* deformation of the test rig assuming linearity as

discussed above, and results in a strain error of about 1.3% and 0.38% for anisotropic 30% MREs and pure rubber, respectively.

The maximum stresses are not an issue as they are well below the tensile strengths and also reasonably below the yield strengths given in Table 5.1. The brass screws used in the top clamp experience the highest stress of 155.7 MPa (*von Mises* criteria) when applying 6 MPa pressure. The deformation of the entire setup is in the elastic regime which means that there will not be any permanent deformation in the test rig.

In addition to finite element simulations, the compliance of the test setup was checked by comparing the stress-strain results of specimens measured using the setup described above with that measured using a very rigid steel setup; this is illustrated in Figure 5.8. Both pure rubber and isotropic and anisotropic MREs containing 30% volume particle concentration were used for the comparison. The tests with the rigid setup were carried out using the 1 kN load-cell in the test machine, rather than the 250 kN load-cell used for the compression test series. Very little difference between the stress-strain curves of either the pure rubber

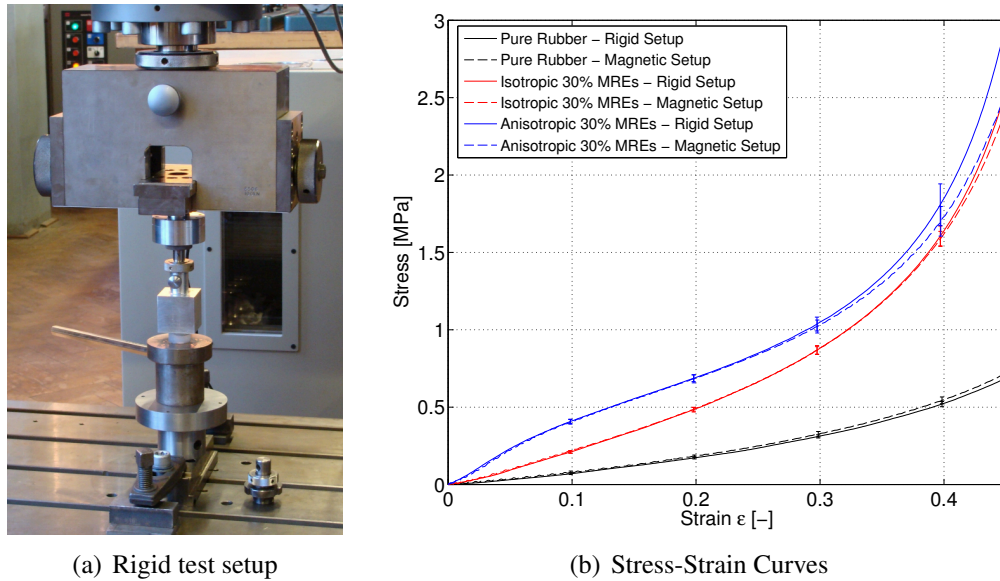


Figure 5.8: Comparison of stress-strain results achieved with the setup specifically designed for the use of permanent magnets and a very rigid setup. Stress-strain data of the third loading cycles are compared to check compliance of test setup. The rigid setup is shown with a photograph (a).

specimen or the isotropic 30% MREs is discernible. The stress-strain curves of anisotropic 30% MREs do separate from approximately 30% strain. However, given that the variation of the results indicated by the standard deviation is of a similar order as this underestimate, the reason for the underestimate cannot be reliably attributed to the lower compliance of the magnetic test rig. A *Matlab* code *divergence.m* (see Appendix D) was written to check whether curves diverge and determines from which strain point the divergence of the two curves starts. Here, a significant divergence occurs when the absolute difference between

two curves is larger than the sum of the associated standard deviations of both curves. Using this criterion, the stress-strain curves of the anisotropic 30% MREs from both tests do not diverge. The error in strain is about 1.36% (see Figure 5.8b), as 2.5 MPa stress is achieved at 43.6% strain with the rigid setup, and at 45% strain with the magnetic setup. As the strains were calculated from the crosshead displacement, the strains of samples in the magnetic setup are overestimated. The error in strain seen here is in agreement with the calculations performed in *Abaqus* (1.3% error in strain was estimated for an anisotropic 30% MRE). The 1 kN load-cell was used in the tests with the rigid setup, and as the error in strain of experiment and simulation are in agreement, the influence of the 250 kN load-cell is considered to be negligible. The compliance of the test machine parts is not verified with the finite element calculation, nor with the experiment performed, but the influence is considered to be small compared to the compliance of the test rig.

5.2.2.2 Distribution of the Magnetic Flux Density

Simulations using the finite element software *Comsol* were performed to calculate the distribution of the magnetic flux density within the test rig used in the compression setup. The finite element model used for the calculation is illustrated in Figure 4.10; the model was used earlier to identify the permeabilities of MREs. The geometry, the material and physical settings, and the finite element mesh size of the *Comsol* model were described earlier in Section 4.4. Ideally, the magnetic flux density would be uniformly distributed within the region occupied by the MRE sample. To investigate this, both setups with distances between the permanent magnets of 35 mm and 62 mm were studied in the absence of an MRE sample ($\mu_r = 1$). Slice plots of the magnetic flux distribution within the MRE sample and line plots representing the vertical distribution are illustrated in Figure 5.9 and 5.10. The position of the MRE sample, the lower magnet, and the upper magnet are all indicated in Figures 5.9b and 5.10b. In both setups there is a variation in the magnetic flux density throughout the volume occupied by the MRE sample. The minimum and maximum magnetic flux densities within, and the average value taken over the volume occupied by the MRE sample calculated by *Comsol*, together with the percentage variation are listed in Table 5.2. The *Comsol* sim-

	Experimental	<i>Comsol</i> Simulations			
	B [mT]	B_{min} [mT]	B_{max} [mT]	B_{mean} [mT]	$\frac{B_{max}-B_{min}}{B_{mean}}$ [%]
<i>Magnet35</i>	450	374.9	544.7	460.8	36.85
<i>Magnet62</i>	210	187.2	249.1	209.9	29.49

Table 5.2: Magnetic flux densities measured with a Gaussmeter in the centre of the volume usually occupied by the MRE samples, and determined with a finite element simulation in *Comsol*. Minimum, maximum, average, and variation of the magnetic flux distribution B_z within the volume occupied by the sample ($\mu_r = 1$).

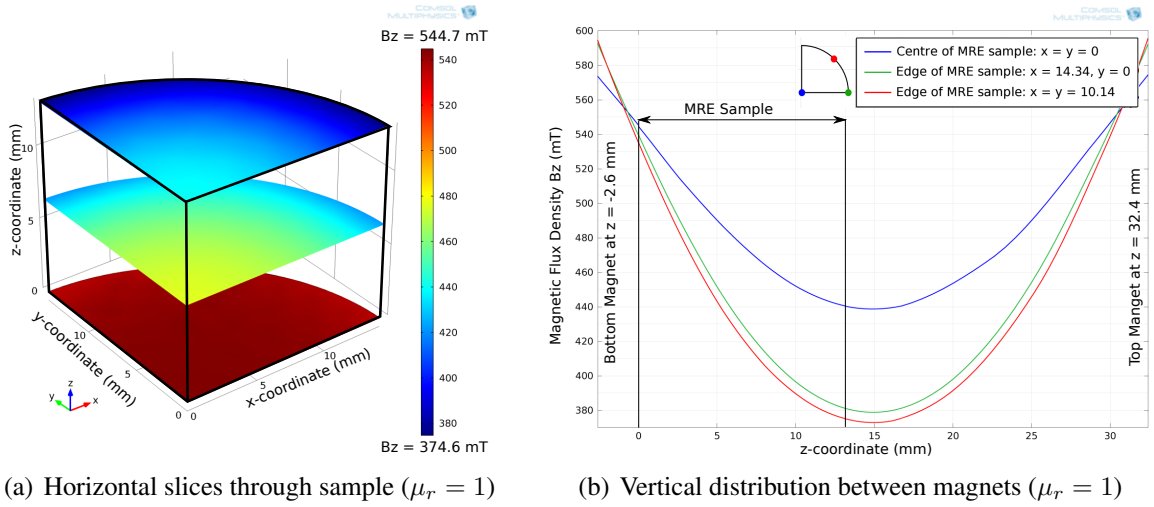


Figure 5.9: Distribution of the magnetic flux density B_Z in the setup using an inter-magnet distance of 35 mm. The slice plots in (a) illustrate the distribution of B_Z field across selected horizontal planes within the volume occupied by the MRE sample. The line plots in (b) show B_Z versus the vertical distance between the two magnets at three selected positions in the x-y plane (see legend). The relative permeability of the MRE sample is set to $\mu_r = 1$.

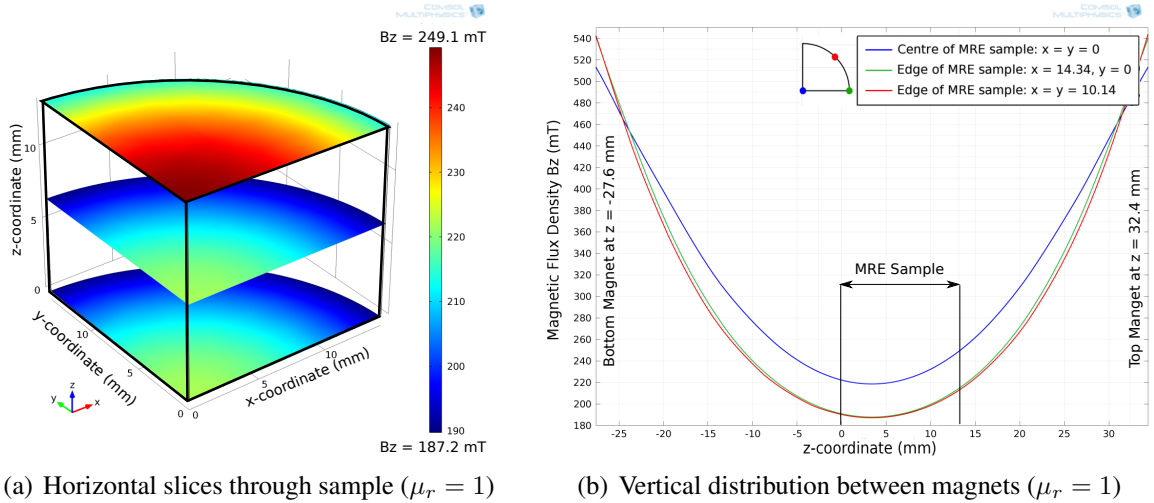


Figure 5.10: Distribution of the magnetic flux density B_Z in the setup using an inter-magnet distance of 62 mm. The slice plots in (a) illustrate the distribution of B_Z field across selected horizontal planes within the volume occupied by the MRE sample. The line plots in (b) show B_Z versus the vertical distance between the two magnets at three selected positions in the x-y plane (see legend). The relative permeability of the MRE sample is set to $\mu_r = 1$.

ulation results are in very good agreement with the magnetic flux measured in the centre of the volume usually occupied by the MRE sample (see Table 5.2).

To study the influence of the MRE samples on the magnetic flux distribution, the magnetic induction was calculated for permeabilities with $\mu_r > 1$. The relative permeabilities identified in Chapter 4, and summarised in Table 4.11 for isotropic and anisotropic MRE samples,

are used in the *Comsol* model. The average values of the magnetic induction, B_Z , together with the percentage variation of the latter are summarised in Table 5.3 for both setups. As

MRE Sample	Iron [%]	<i>Magnet35</i>		<i>Magnet62</i>	
		B_{mean}	$\frac{B_{max}-B_{min}}{B_{mean}}$	B_{mean}	$\frac{B_{max}-B_{min}}{B_{mean}}$
Pure Rubber	0	460.8	36.9	209.9	29.5
Isotropic MREs	10	572.5	44.4	260.3	22.0
	20	648.9	57.3	294.8	34.0
	30	768.4	83.4	348.5	62.0
	40	867.7	109.7	393.1	90.4
Anisotropic MREs - vertical alignment	10	572.5	44.5	260.4	21.9
	20	697.9	67.6	316.9	44.1
	30	810.5	94.9	367.4	72.5
	40	906.0	115.9	410.1	93.6
Anisotropic MREs - horizontal alignment	10	556.9	42.0	253.3	22.5
	20	659.0	58.5	299.4	36.3
	30	757.2	79.9	343.5	59.7

Table 5.3: Differences in the magnetic flux distribution of B_Z within the volume occupied by isotropic and anisotropic MRE sample ($\mu_r > 1$). The permeability of isotropic MREs and anisotropic MREs (Table 4.11) were used to calculate B_Z . B_{mean} is given in mT and the variation in %.

expected the strength of the magnetic field increases with increasing iron content in the MRE samples. Anisotropic MREs produce the highest magnetic flux densities. Perhaps surprisingly, the distribution of the flux is less uniform for samples with higher permeabilities; as the strength of the magnetic field increases, the difference between minimum and maximum values also increases as does the relative variation in flux density across the sample volume.

5.2.3 Tests in the Absence of a Magnetic Field

Compression tests conducted in the absence of a magnetic field were performed using the setup shown in Figure 5.4. The general test method was explained in detail in Section 5.1.1, and the specific test procedure of the uniaxial compression tests was given in Section 5.2.1. In this section, the stress-strain results of the two no-field tests are compared to verify the results. The behaviour of isotropic and anisotropic MREs is characterised using the *NoField02* results. The stress-strain data and moduli are analysed as described in Section 5.1.2.

5.2.3.1 Comparison of NoField01 and NoField02 Tests

Stress-strain results from the third loading cycle of the first and second sets of tests conducted in the absence of an applied magnetic field (*NoField01* and *NoField02*) are compared in Figure 5.11. The stress-strain curves diverge after a certain level of strain. The *NoField02* tests

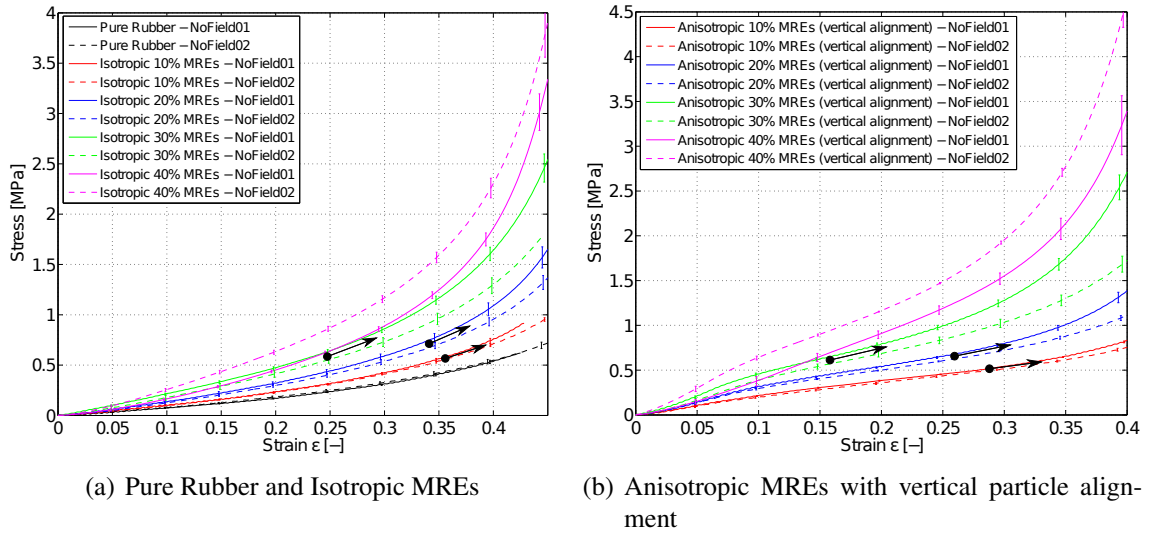


Figure 5.11: Stress-strain curves from *NoField01* and *NoField02* compression tests. Isotropic and anisotropic MREs with 10% to 40% CIP content are compared. The arrows indicate the divergence point.

resulted in lower stresses in most of the cases, indicating increased stress-softening compared to the *NoField01* tests. The divergence of the curves was studied with the *Matlab* code *divergence.m* (see Appendix D). Divergence points, defined as the strain values where the absolute difference between the two mean curves become larger than the associated standard deviations, are indicated with arrows in Figure 5.11. These points are listed in Table 5.4, together with the relative differences in stress observed between the two sets of curves at 40% strain. Divergence is seen to start earlier for MREs with higher iron content. The relative differences in stress are large with up to 37%. At this early stage of the investigation, it is difficult to explain the discrepancies between *NoField01* and *NoField02* results, but two possible reasons were discussed in Section 5.1.1: (i) Compression specimens experienced permanent deformations after each cyclic test in the test series (the samples height decreased and area increased). Given that the cross-head displacement during all compression tests was constant at 6.5 mm, the reduced height of the samples imposed a new higher maximum strain level in each subsequent test. In combination with the *Mullins* effect this could cause the divergences observed. (ii) The magnetic field, which was applied to the MREs between the *NoField01* and the *NoField02* tests could have a permanent influence on the microstructure of MREs when testing them up to large strain. The phenomenon of divergence of the stress-strain curves requires further study if reliable conclusions are to be drawn, this is done in Sections 5.3.5 and 5.4.4, respectively.

For the 40% MREs, the divergence between *NoField01* and *NoField02* stress-strain curves begins immediately at 0% strain and surprisingly, the samples are stiffer in the *NoField02* tests. This might be explained by a densification of the material due to the high iron content. When considering a cube full of mono-disperse spherical particles of 4 μm diameter, a

MRE Sample	Iron [%]	Divergence Point [—]	Relative Difference at 40% strain [%]
Pure Rubber	0	no separation	2.02
Isotropic MREs	10	0.36	6.05
	20	0.34	12.36
	30	0.25	20.73
	40	0.00	23.78
Anisotropic MREs - vertical alignment	10	0.28	9.41
	20	0.26	19.96
	30	0.16	34.94
	40	0.00	37.61
Anisotropic MREs - horizontal alignment	10	no separation	2.72
	20	0.35	7.30
	30	0.27	13.83

Table 5.4: Comparison between *NoField01* and *NoField02* compression tests. The divergence point is defined as the strain value where the absolute difference between the two stress-strain curves is larger than the associated standard deviations. The relative differences in stress at 40% strain are related to the *NoField01* data and are decreases in the case of samples with 10% to 30% iron content, but are increases in the case of 40% MREs.

theoretical maximum particle volume concentration of 52.2% (calculated with $10 \times 10 \times 10$ touching particles in a cube with a side length of 0.04 mm) is possible. Theoretically, 40% iron volume fraction allows a very thin film of elastomer around the particles of just 0.19 μm thickness. It is possible that such a high iron particle content could lead to problems during mixing MRE samples, *i.e.* there may be agglomerations of particles containing no elastomer. This would provide a plausible densification mechanism for the 40% MREs when exposed to compressive load and may be a reason for the higher stresses in the *NoField02* tests. Unfortunately, the microscopic structure of an 40% MRE before and after testing was not investigated. Due to the large divergence present in the 40% MRE data, these samples cannot be further analysed.

In all further studies, the results of the *NoField02* tests will be used. When calculating the MR effect in Section 5.2.4, the stress-strain results are interpreted just up to the point where *NoField01* and *NoField02* curves start to diverge: the divergence points are listed in Table 5.4. In this way, the influence of stress-softening is eliminated when determining the MR effect. The use of MRE samples up to strains above the divergence points is questionable.

5.2.3.2 Comparison of MRE Samples

The *NoField02* tests are considered to compare the different types of MRE samples. Both the increase in stiffness and stress due to higher particle concentration in the elastomer and due to particle alignment are studied. The stress-strain curves of all the MREs tested under compression in the absence of a magnetic flux are illustrated up to 45% compressive strain in Figure 5.12. Clearly, the anisotropic samples with vertical particle alignment exhibit the

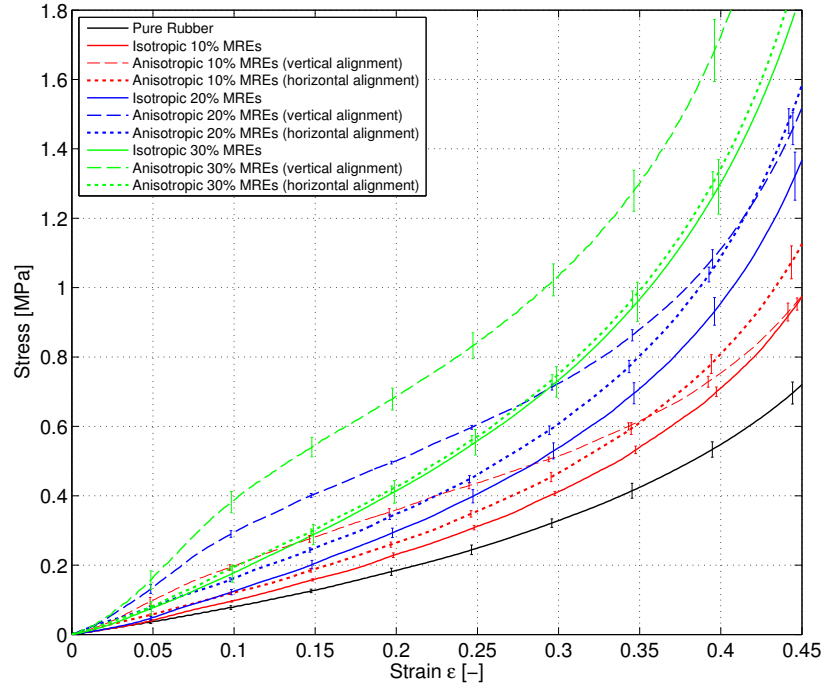


Figure 5.12: Stress-strain results of *NoField02* tests of pure rubber, isotropic, and anisotropic MREs with 10% to 30% iron content.

highest stresses. Results start with a steep slope that flattens from approximately 10% strain and increases again above 30% strain; this trend is independent of particle content. Isotropic and anisotropic MREs with horizontal particle alignment show a very similar stress-strain curve shape with constantly increasing slope, although the isotropic MREs exhibit slightly lower stresses. Higher volume particle concentrations lead to higher stresses; which is valid for all types of MRE samples. To study the slope in the region from 0% to 10% strain a magnification of the stress-strain curves is illustrated separately in Figure 5.13 for isotropic and anisotropic MREs. Even in the small strain regime non-linear behaviour can be observed, and is more evident in case of anisotropic MREs but is also present in the isotropic MREs with larger iron content. To characterise the behaviour in the small strain regime the initial secant moduli, E_{0-5} , are listed in Table 5.5. To study the non-linear behaviour the tangent moduli, E_T , are illustrated in Figure 5.14. As previously observed in the stress-strain curves shown in Figure 5.12, the anisotropic MREs with vertical particle alignment have a large tangent modulus in the small-strain regime, which decreases in the mid-strain regime, then rapidly increases once again in the large-strain regime. Isotropic and anisotropic MREs with horizontal particle alignment show a very similar curve shapes with constantly increasing tangent moduli. The tangent moduli in the region from 1% to 2% strain are listed in Table 5.5. The relative increases of isotropic MREs compared to the pure rubber samples, and the increases of anisotropic samples compared to isotropic MREs with the same amount of iron particles are listed in the same table. The moduli, E_{0-5} and E_T (Table 5.5), are plotted versus the iron volume fraction in Figure 5.15. The moduli increase with increasing iron content.

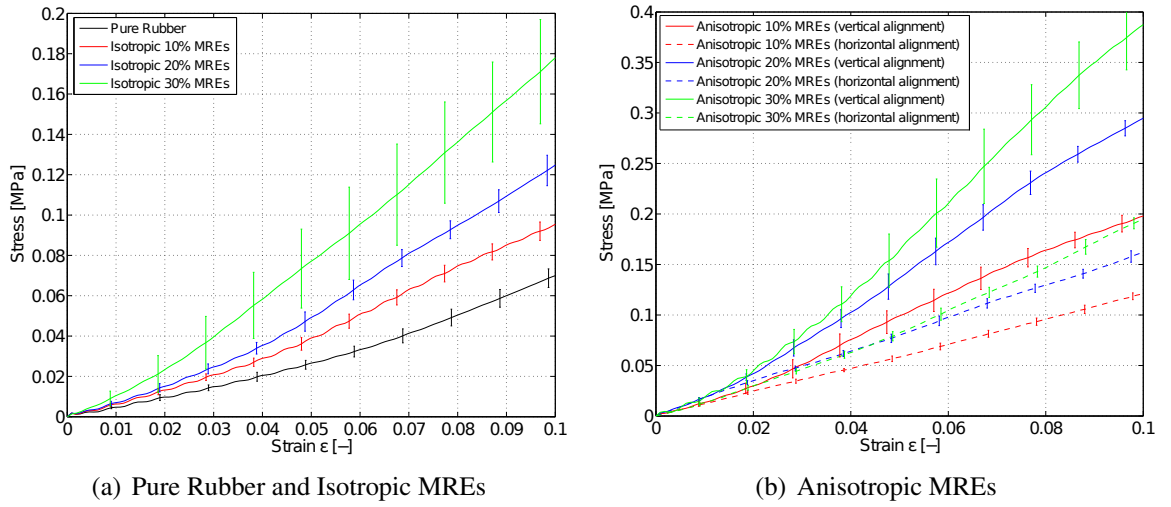


Figure 5.13: Stress-strain results of *NoField02* tests of pure rubber, isotropic, and anisotropic MREs with 10% to 30% iron content. Magnification of stress-strain data up to 10% strain (complete data shown in Figure 5.12).

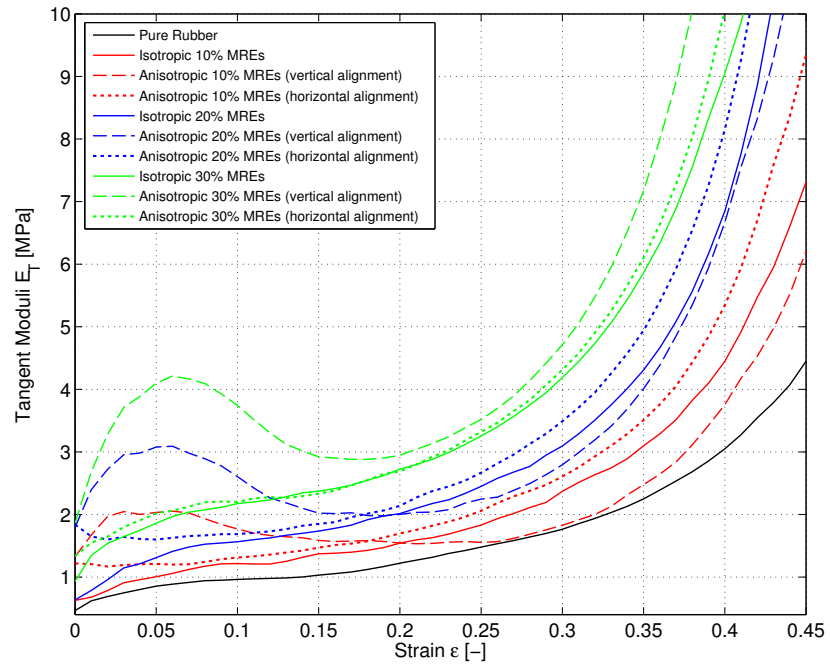


Figure 5.14: Tangent Moduli E_T versus strain of pure rubber, isotropic, and anisotropic MREs with 10% to 30% CIP content. The tangent moduli are the linear slopes taken over 1% strain increments.

MRE Sample	Iron [%]	E_{0-5} [MPa]	E_T [MPa]	Increase compared to ... [%]	
Pure Rubber	0	0.69	0.62		
Isotropic MREs	10	0.78	0.68	Pure	13.0
	20	0.96	0.79		39.1
	30	1.54	1.35		123.2
Anisotropic MREs - vertical alignment	10	1.97	1.67	Isotropic	152.6
	20	2.72	2.40		183.3
	30	3.28	2.68		113.0
Anisotropic MREs - horizontal alignment	10	1.17	1.21	Isotropic	50.0
	20	1.60	1.65		66.7
	30	1.64	1.55		6.5

Table 5.5: Initial secant moduli, E_{0-5} , and tangent moduli, E_T , obtained from stress-strain curves of pure rubber, isotropic, and anisotropic MREs with 10% to 30% CIP content (*NoField02*) are listed. The relative increase of isotropic MREs compared to pure rubber and the relative increase of anisotropic MREs compared to isotropic MREs with the same CIP content, calculated with E_{0-5} , are provided.

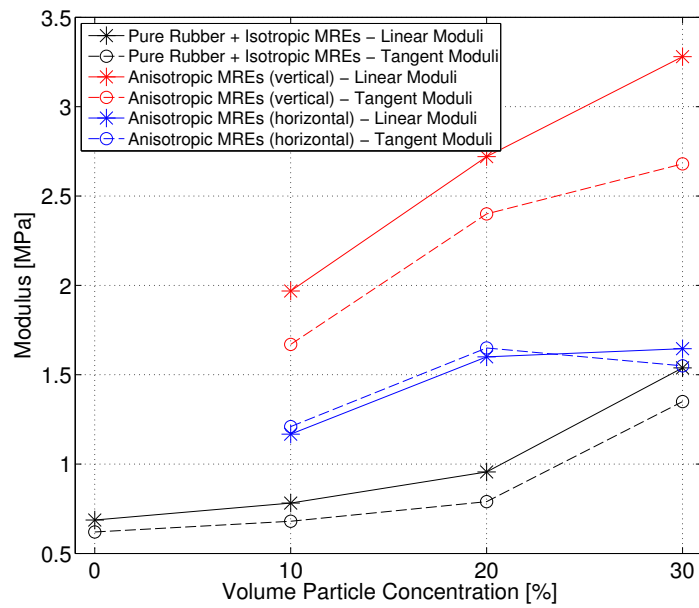


Figure 5.15: Moduli E_{0-5} and E_T as listed in Table 5.5 versus volume particle concentration of pure rubber, isotropic, and anisotropic MREs with 10% to 30% CIP content.

5.2.4 Characterisation of the Magneto-Rheological Effect

Compression tests with two different magnetic field strengths, 450 mT and 210 mT, were performed to determine the increase in stiffness due to exposure to a magnetic flux. The setups illustrated in Figure 5.5 were used to carry out these tests. In most samples an increase in stress is observed due to an applied magnetic flux. To study the influence of the magnetic field both the absolute and relative MR effects (Equations 5.1 and 5.2) are plotted versus engineering strain in Figure 5.16 for the *Magnet35* tests, and in Figure 5.17 for the *Magnet62* tests. The bold lines used in Figures 5.16 and 5.17 represent the MR effects up to the

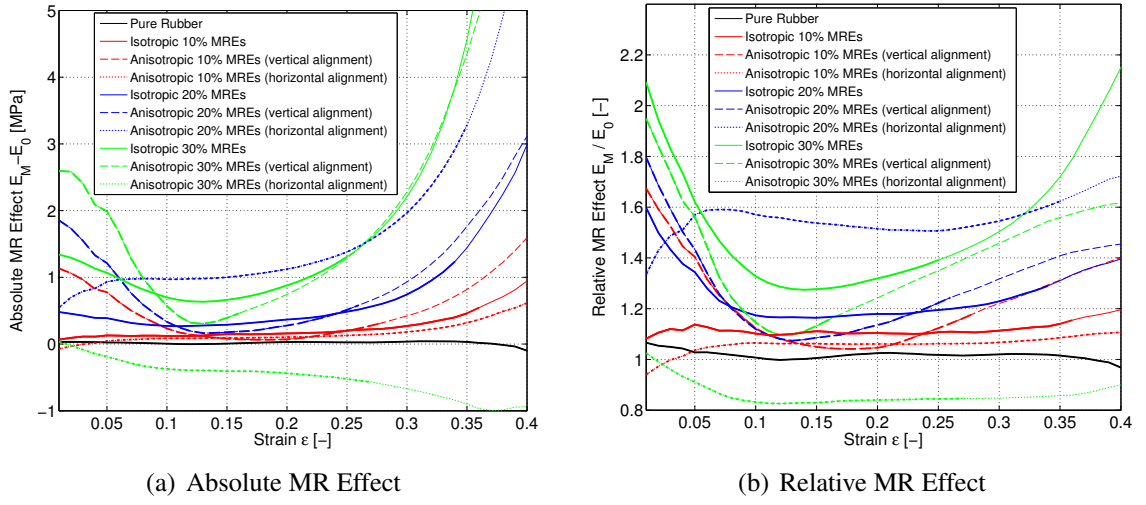


Figure 5.16: Absolute and relative MR effects, calculated with E_T , of all types of MREs achieved in the *Magnet35* tests are illustrated versus compressive strain. Bold lines are used up to the divergence points (see Table 5.4).

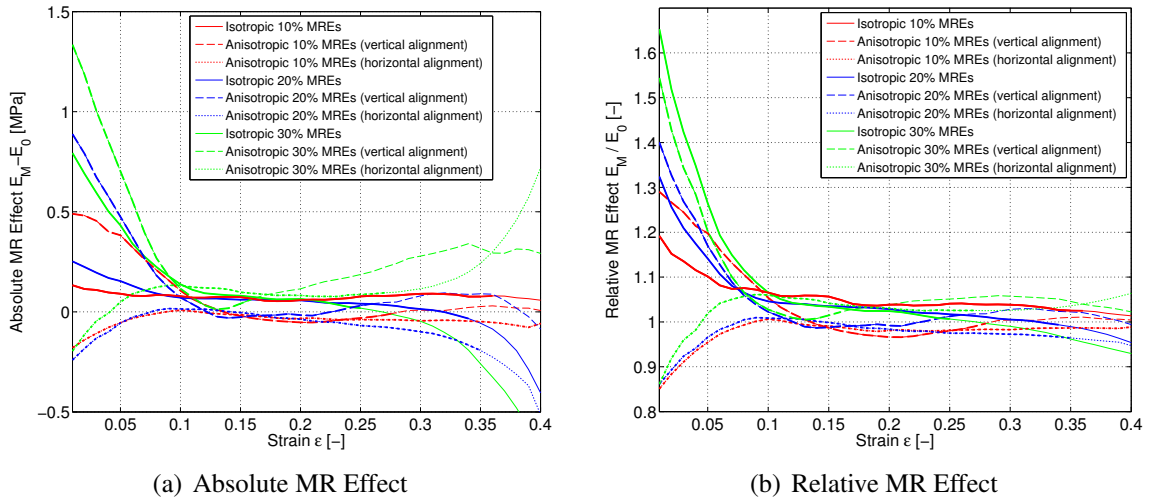


Figure 5.17: Absolute and relative MR effects, calculated with E_T , of all types of MREs achieved in the *Magnet62* tests are illustrated versus compressive strain. Bold lines are used up to the divergence points (see Table 5.4).

divergence points discussed in Section 5.2.3. The full set of results including stresses, tangent moduli, and relative MR effects for all types of MRE samples, and for both magnetic setups, are presented in Appendix E.1. The MR effects increase with increasing iron content, with the vertically aligned anisotropic samples achieving the highest relative MR effects. Most of the MR effect curves in Figures 5.16 and 5.17 start with high effects in the small-strain region that decrease to nearly zero effect in the mid-strain region, but in the case of the *Magnet35* tests the effect increases again at larger strains. The maximal values of the MR effect calculated using E_T are determined for the region from 1% to 15% strain ($E_{T,1-15}$), and are determined in the large strain region above 15% strain ($E_{T,>15}$). These values are

summarised for all types of MREs in Table 5.6. The MR effects calculated with the initial secant moduli E_{0-5} are listed in the same table. Note that $E_{T,1-15}$ and E_{0-5} represent the moduli in the small strain region, where the differences are due to the non-linear stress-strain behaviour, already present at small strain levels. The maximum values of relative MR effects

MRE Sample	Iron [%]	Magnet Test	Absolute MR Effect		Relative MR Effect		
			E_{0-5}	$E_{T,1-15}$	E_{0-5}	$E_{T,1-15}$	$E_{T,>15}$
Pure Rubber	0	35	0.0272	0.0337	1.0396	1.0660	1.0260
Isotropic MREs	10	35	0.1873	0.1292	1.2396	1.1376	1.1402
		62	0.1288	0.1328	1.1648	1.1917	1.0565
	20	35	0.5705	0.4803	1.5967	1.5977	1.2897
		62	0.2551	0.2522	1.2668	1.3241	1.0349
	30	35	1.4110	1.3419	1.9172	2.0914	1.3913
		62	0.6788	0.7934	1.4413	1.6530	1.0339
Anisotropic MREs - vertical alignment	10	35	1.2853	1.1344	1.6530	1.6735	1.1824
		62	0.5784	0.4896	1.2938	1.2902	0.9967
	20	35	2.1992	1.8543	1.8084	1.7957	1.2438
		62	0.8636	0.8879	1.3175	1.4002	1.0161
	30	35	3.6529	2.5969	2.1137	1.9490	1.1563
		62	1.3323	1.3346	1.4062	1.5441	1.0223
Anisotropic MREs - horizontal alignment	10	35	0.0116	0.0848	1.0099	1.0650	1.1465
		62	-0.1187	0.0078	0.8983	1.0062	1.0002
	20	35	0.8648	0.9754	1.5406	1.5905	1.6233
		62	-0.1099	0.0163	0.9313	1.0095	0.9986
	30	35	0.0308	0.0375	1.0187	1.0248	0.8462
		62	-0.0308	0.1328	0.9813	1.0610	1.0416

Table 5.6: Absolute and relative MR effects achieved with 450 mT and 210 mT applied magnetic flux, and calculated with E_{0-5} and with E_T (Figures 5.16 and 5.17) are listed. Maximum values of the relative MR effects calculated using $E_{T,1-15}$ (small strain), and $E_{T,>15}$ (large strain) are presented. The maximum relative MR effects in the small-strain region (E_{0-5} or $E_{T,1-15}$) are shaded grey. The MR effects in the large-strain region are coloured in blue when they exceed the MR effect in the small-strain region.

calculated with either E_{0-5} or with $E_{T,1-15}$ are shaded in grey in Table 5.6.

As expected, pure rubber samples exhibit no MR effect, and effectively serve to verify that the experimental setup is reliable. The relative MR effect of 1.066 at 2% strain, measured for the pure rubber indicates that an experimental error of about 6.6% is present in the results. The anisotropic MREs with 30% vertically aligned particles exhibit the highest MR effects, with an absolute increase in modulus of 3.65 MPa, which is over twice as stiff in the presence of a magnetic field as without. Interestingly, the anisotropic MREs with horizontal particle alignment exhibit nearly no MR effect and start with a decreased stiffness in the small-strain region. Only the anisotropic MREs with horizontal particle alignment containing 20% CIP exhibit a considerably large relative MR effect of 59%, but the curve shape of the MR effect versus strain is different compared to other curves, and this effect occurs

at 7% strain. The different behaviours of anisotropic MREs with horizontal particle alignment cannot be explained at this point, but the same samples will be studied under uniaxial tension, pure shear, and equi-biaxial tension in order to verify this unexpected response. Examining the influence of the strength of the applied magnetic field, the MR effects are approximately half when applying 210 mT magnetic flux in comparison to 450 mT flux. This may indicate an approximately linear increase of the MR effect with increasing magnetic field strength, although application of only two different field strengths in this investigation means that definitive assertions in this regard are not possible. The relative MR effects are studied versus the magnetic induction, and also versus the volume particle concentration in Figure 5.18. To summarise, the MR effect increases with increasing volume particle concen-

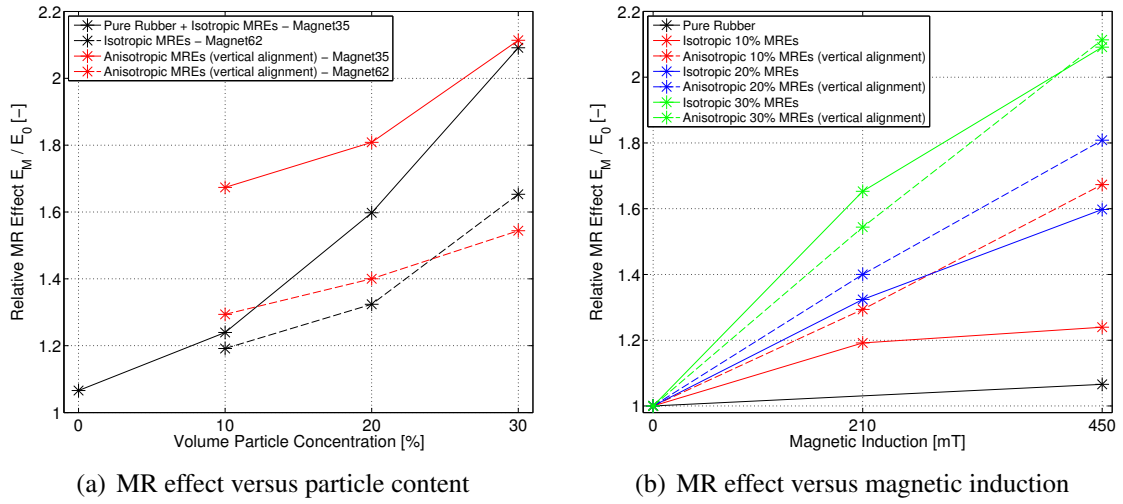


Figure 5.18: MR effects of pure rubber, isotropic, and anisotropic MREs with vertical particle alignment are illustrated (a) versus the volume particle concentration and (b) versus the applied magnetic field strength. Maximum MR effects as indicated in Table 5.6 are used.

tration, the MR effect of anisotropic MREs is higher than that of isotropic MREs, and the MR effect increases approximately linearly with increasing applied magnetic field strength.

5.2.5 Summary of Compression Tests

Comparison between *NoField01* and *NoField02* tests revealed large discrepancies. The reason for this might be the *Mullins Effect*, but this was not completely clarified and will be studied in greater detail for the tension and pure shear experiments in Sections 5.3 and 5.4. The different types of MREs were compared. Anisotropic MREs with particle alignment in the loading direction revealed the highest stresses and moduli. Isotropic and anisotropic MREs with horizontal particle alignment showed similar stress-strain curves and moduli, where the stresses of isotropic MREs were lower than those of anisotropic MREs. The moduli increase with increasing iron content. A possible densification of the MREs containing

40% CIP was postulated, as these samples were found to be much stiffer in the *NoField02* tests than they were in the *NoField01* tests. The magnetic field distribution was studied using finite element simulations conducted with *Comsol*. The latter showed that the magnetic flux density was not completely uniform, but a variation of 37% in the volume occupied by the samples is reasonable. The stresses, the tangent moduli, and the absolute and relative MR effects were studied versus engineering strain by comparing tests both without and with magnetic fields. MR effects were highest in the small strain region, decreased rapidly to nearly no effect in the mid-strain region, but in the case of 450 mT applied induction, the MR effect increased again for strains larger than 15%. The effects in the large-strain region did not exceed the effects in the small-strain region. MR effects of anisotropic MREs with horizontal particle alignment were negligible: this unexpected result will be further studied in the other large strain experiments. The MR effect increases with increasing particle volume fraction, and appears to increase approximately linearly with increasing magnetic field strength.

5.3 Uniaxial Tension Tests

Uniaxial tension tests were performed in order to characterise the MRE behaviour in the absence and in the presence of a magnetic field. The general test method and the method of analysis was described in Section 5.1, and Section 5.3.1 gives the specific procedure of the uniaxial tension experiments. Description of the test setup and calculations of the magnetic field distribution within the test rig are provided in Section 5.3.2. As mentioned earlier in Section 5.1.1, fatigue tests were conducted in advance of the main tension test series to determine a stability strain limit as detailed in Section 5.3.3. The DIC strain analysis is described in Section 5.3.4. The stress-strain behaviour of MREs in the absence of a magnetic field, and the MR effects in the presence of a magnetic field, are discussed in Section 5.3.5 and 5.3.6, respectively. The tension tests are summarised in Section 5.3.7.

To aid with the analysis of the uniaxial tension tests, the *Matlab* functions *tension_DIC.m* and *tension_pixel.m* were written, which includes the cut-and-shift process described previously in Section 5.1.2 and the analysis of the optically measured strains (see Section 5.3.4). For further details on the *Matlab* procedure and the employed sub-functions, the reader is referred to Appendix D. The *Matlab* codes are saved on a DVD attached to this document and can be consulted for even more in-depth information.

5.3.1 Procedure of the Tension Tests

Tests were performed on MREs with up to 30% iron volume fraction at a speed of 50mm/min, and up to a maximum of 100% engineering strain. The dog-bone shaped samples are in accordance to the *British Standard* (BS ISO 37, 2005). The stresses were calculated us-

ing the reference area of the gauge section of the samples. A *Digital Image Correlation* (DIC) system was used to measure strains. Overall, a series of six different tests were performed, including: (i) the preconditioning of the samples, (ii) tests without a magnetic field (*NoField01*), (iii) tests with an average applied magnetic induction of 220.6 mT using an inter-magnet distance of 89 mm (*Magnet89*) were conducted up to a maximum of 100% strain, (iv) tests with an average magnetic induction of 251.2 mT with an inter-magnet distance of 73 mm (*Magnet73*); in this test the displacement was restricted to 15 mm , equivalent to 50% strain, (v) tests with an average applied magnetic induction of 289.2 mT with an inter-magnet distance of 63 mm (*Magnet63*); here the displacement was restricted to 5 mm , equivalent to 15% strain, and (vi) tests without magnetic field were repeated (*NoField02*). The given average magnetic inductions taken over the volume occupied by the MRE samples were calculated in the absence of an MRE sample ($\mu_r = 1$) using finite element simulations (see Section 5.3.5). The maximum strain was restricted as higher magnetic inductions required lower distances between the permanent magnets and consequently, due to the nature of the test setup, lower tensile strains were possible. To investigate further the *Mullins* effect present in MRE samples, and to find reasons for the divergence observed between *NoField01* and *NoField02* compression tests (discussed in Section 5.2.3) three additional procedures were introduced to the test method: (i) Fatigue tests were used to determine how far the different types of MRE samples could be stretched before damage occurred, these tests were carried out prior to the main tension test series described above. (ii) A preconditioning step was introduced into the main testing procedure to condition the MRE samples. Fifty loading and unloading cycles with a test speed of 50 mm/min were employed to precondition the samples. (iii) Each type of MRE was tested up to two different strain levels to observe the differences in stress softening. A list of the displacement levels to which the different types of MREs were stretched is given in Table 5.7. The set strain levels are below the stability

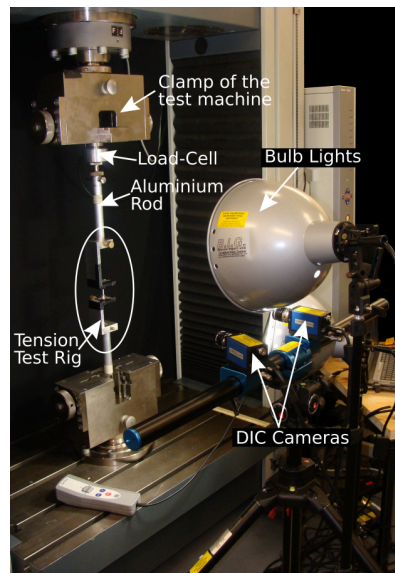
MRE Sample	Iron [%]	Displacement [mm] (Strain [%])			
Pure Rubber	0	15.0	(50)	30.0	(100)
Isotropic MREs	10	15.0	(50)	30.0	(100)
	20	15.0	(50)	22.5	(75)
	30	5.0	(15)	15.0	(50)
Anisotropic MREs - vertical alignment	10	15.0	(50)	22.5	(75)
	20	5.0	(15)	15.0	(50)
	30	5.0	(15)	15.0	(50)
Anisotropic MREs - horizontal alignment	10	15.0	(50)	22.5	(75)
	20	5.0	(15)	15.0	(50)
	30	5.0	(15)	15.0	(50)

Table 5.7: Types of MRE samples tested under uniaxial tension. The samples were stretched up to the given displacements, where 5 mm , 15 mm , 22.5 mm , and 30 mm are equivalent to 15%, 50%, 75%, and 100% strain, respectively. All samples are tested up to 15 mm to enable comparison between the different types of MREs.

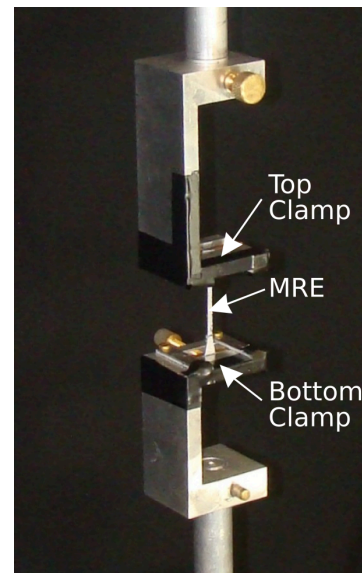
strain limit determined with fatigue tests (see Section 5.3.3). All MREs are tested up to 15 mm to enable comparison between the different types.

5.3.2 Tension Test Setup

The tensile test setup (Figures 5.19 and 5.20) was specifically designed for the use of permanent magnets. An ‘open’ setup was manufactured to enable movement of the top part of the test rig, while the position of the magnets remained fixed during the tests. The dimensions of the setup were determined largely by the dimensions of the permanent magnets; samples were positioned directly below the centre of these magnets. The cameras and lights of the *Digital Image Correlation* (DIC) system are shown in Figure 5.19a. Dimensions of



(a) Uniaxial test machine Zwick Z250 with tension test rig, DIC cameras and lights



(b) Clamps to hold tensile sample, designed for the use of magnets

Figure 5.19: Test Setup for uniaxial tension tests with the DIC system are shown. Parts of the setup are covered in black tape to avoid reflection.

the top and bottom parts of the test rig structure, and the final mounted setup, including the distances between the permanent magnets, are given in the technical drawings in Appendices B.10 to B.13. A photograph of the setup with permanent magnets in place is shown in Figure 5.20. A wooden structure was used to hold the top magnet. Both the magnets and parts of the rig structure were covered in black tape to avoid reflections, which could cause problems when using the DIC system. The relative position of the top magnet was changed in order to alter the strength of the magnetic field. The position of the bottom magnet remained fixed. To maximise the magnetic field strength, the bottom magnet was positioned as close to the MRE samples as possible, although this meant that the samples were not centred vertically in between the magnets.

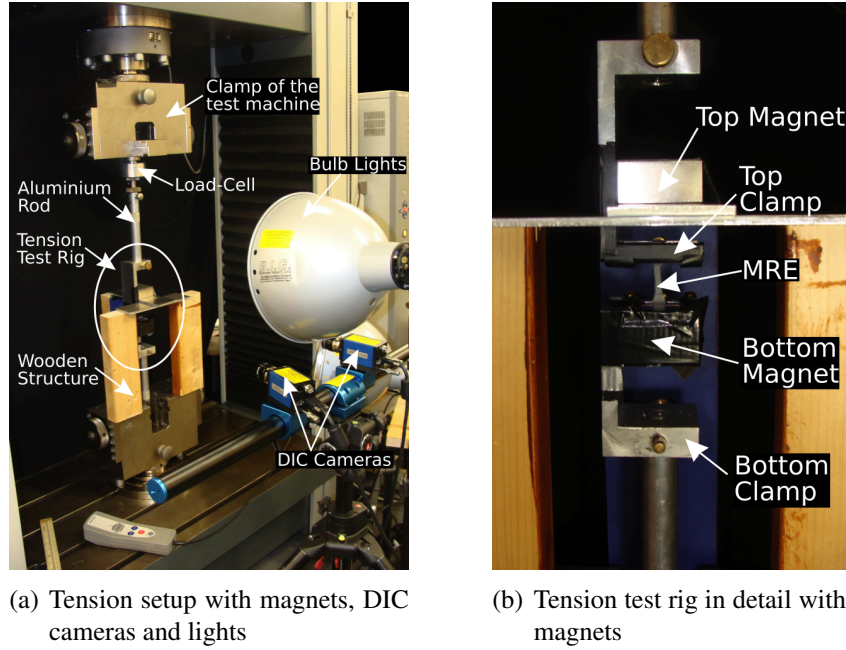


Figure 5.20: Test Setup (*Magnet73*) for uniaxial tension tests with the permanent magnets are shown. A wooden construction is used to hold the top magnet and to enable the view of the MRE sample for recording DIC data. Parts of the setup are covered in black tape to avoid reflection.

The compliance of the tension test rig is not studied (as done with the compression test rig, see Section 5.2.2), as issues related to compliance can be overcome by the optical strain measurement performed (see Section 5.3.4).

5.3.2.1 Distribution of the Magnetic Flux Density

The multi-physics finite element software *Comsol* was used to simulate the magnetic flux distribution within the tension test setup. Symmetry conditions were applied and only one quarter of the setup is modelled. The model geometry with the permanent magnets positioned 63 mm apart is shown in Figure 5.21a. Further details on the *Comsol* model are given in Section 4.4: the settings used here are the same as those used to identify the magnetic permeabilities of MRE samples (Chapter 4). First, all three magnetic setups were studied in the absence of an MRE sample, so the relative permeability of the sample is set to $\mu_r = 1$. The vertical distribution of the magnetic flux density, B_z , between the magnets is shown with line plots of all three setups in Figure 5.21b. The position of the MRE sample is marked in the plot. The top and bottom end of the free length of the MRE samples are the positions where the magnetic flux was measured experimentally with a Gaussmeter. The minimum, maximum, and average magnetic flux densities, B_z , together with the percentage variation within the MRE sample calculated by *Comsol* are listed in Table 5.8 for each magnetic setup. The values at the bottom and top end of the free length of the MRE sample are compared

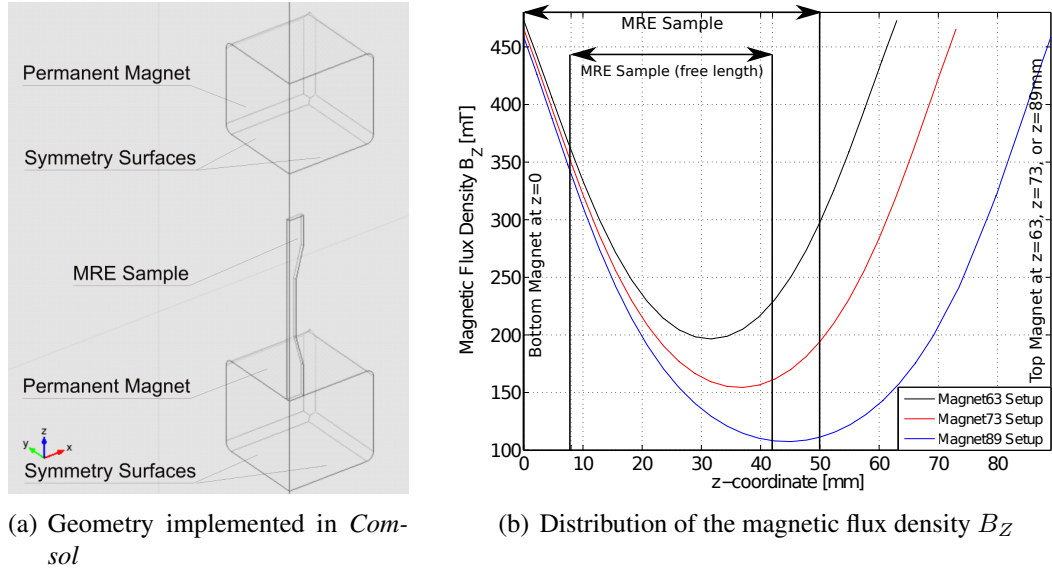


Figure 5.21: Geometry implemented in *Comsol* (*Magnet63* setup) and resulting vertical distribution of the magnetic flux density B_z between the permanent magnets (for all setups). The position of the MRE sample (free length) is marked in the line plots.

		B_{bottom}	B_{top}	B_{max}	B_{min}	B_{mean}	$\frac{B_{max}-B_{min}}{B_{mean}}$
<i>Magnet63</i>	<i>Comsol</i>	360.0	228.7	475.3	196.3	289.2	96.5
	Experimental	360	215				
<i>Magnet73</i>	<i>Comsol</i>	349.6	160.9	467.9	153.7	251.2	125.1
	Experimental	345	190				
<i>Magnet89</i>	<i>Comsol</i>	339.8	108.3	460.8	106.3	220.6	160.7
	Experimental	335	115				

Table 5.8: Magnetic flux densities at the bottom (B_{bottom}) and top (B_{top}) end of the free length of the MRE sample, measured with a Gaussmeter and determined with *Comsol*, are listed. Minimum, maximum, average, and variation of the magnetic flux distribution, B_z , within the volume occupied by the sample ($\mu_r = 1$) are given. The magnetic inductions, B , are given in *mT* and the variation in percent.

with the experimentally measured values in the same table, and are in good agreement. The distances between the magnets are large, and consequently the differences within the volume occupied by the MRE samples are very large, ranging from 96.5% up to 160.7%. To illustrate the distributions of magnetic flux density, volume plots are shown in Figure 5.22.

Now, the distribution of the magnetic induction with the MRE samples in place ($\mu_r > 1$) is discussed. The magnetic permeabilities identified in Section 4.4 were used in the *Comsol* simulations. These are either isotropic or anisotropic depending on the MRE sample in question (Table 4.11). The mean values of the magnetic flux density, B_z , together with the variation of the magnetic flux density within the volume occupied by the MRE samples are listed in the Tables 5.9 for all three test setups. As expected, the strength of the magnetic field increases with increasing iron content. It is interesting to note that the differences in the

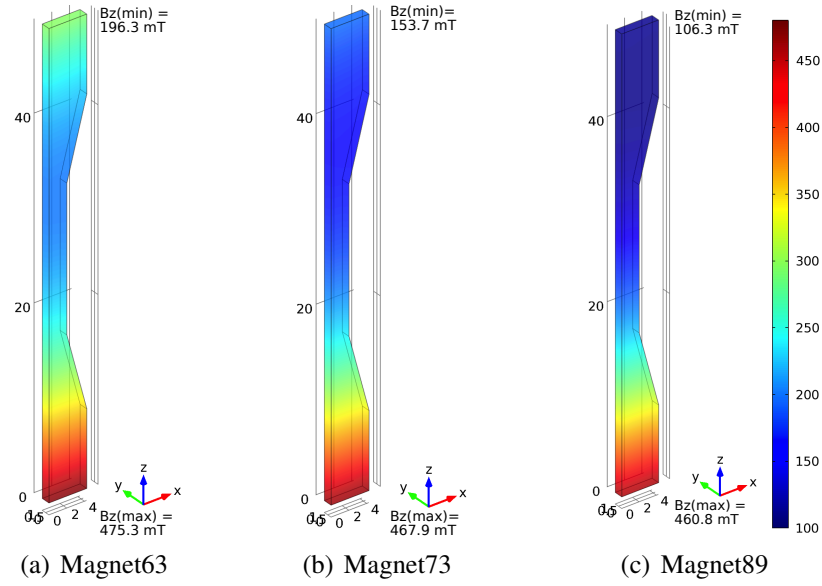


Figure 5.22: Distribution of the magnetic flux density B_Z within the MRE sample ($\mu_r = 1$). Simulation results of *Magnet63*, *Magnet73*, and *Magnet89* setups are illustrated as volume plots.

MRE Sample	Iron [%]	<i>Magnet63</i>		<i>Magnet73</i>		<i>Magnet89</i>	
		B_{mean}	$\frac{B_{max}-B_{min}}{B_{mean}}$	B_{mean}	$\frac{B_{max}-B_{min}}{B_{mean}}$	B_{mean}	$\frac{B_{max}-B_{min}}{B_{mean}}$
Pure Rubber	0	289.2	96.5	251.2	125.1	220.6	160.7
Isotropic MREs	10	443.7	86.8	385.6	116.6	338.7	159.7
	20	590.1	84.1	513.0	121.4	450.7	161.2
	30	931.0	94.9	809.6	126.7	711.7	161.2
Vertical Anisotropic MREs	10	443.7	86.9	385.5	116.8	338.7	159.8
	20	707.1	89.5	614.7	124.6	540.3	162.3
	30	1090.1	98.9	948.0	129.2	833.5	162.0
Horizontal Anisotropic MREs	10	418.6	87.8	363.7	117.2	319.5	159.1
	20	613.9	85.1	533.6	121.6	468.9	161.0
	30	897.8	93.8	780.7	125.7	686.2	160.6

Table 5.9: Differences in the magnetic flux distribution of B_Z within the volume occupied by isotropic and anisotropic MREs ($\mu_r > 1$) in all three magnetic setups. The permeability of isotropic and anisotropic MREs (Table 4.11) were used to calculate B_Z . The mean magnetic flux, B_{mean} , is given in *mT* and the variation in percent.

magnetic flux density remain quite constant irrespective of MRE sample type.

5.3.3 Fatigue Tests

Prior to the main tension test series, fatigue tests were performed to determine whether or not testing to a pre-set level of tensile strain resulted in a ‘stable’ MRE sample. These stand-alone tests were carried out in advance using dog-bone shaped MRE samples other than those used in the main tension test series. The samples were stretched up to a set displacement at

50 mm/min for up to 100 cycles. The load in each cycle at the maximum displacement was related to the load in the first cycle, and the stress softening is plotted as the relative load ratio versus the number of cycles in Figure 5.23. In this investigation, a sample is considered

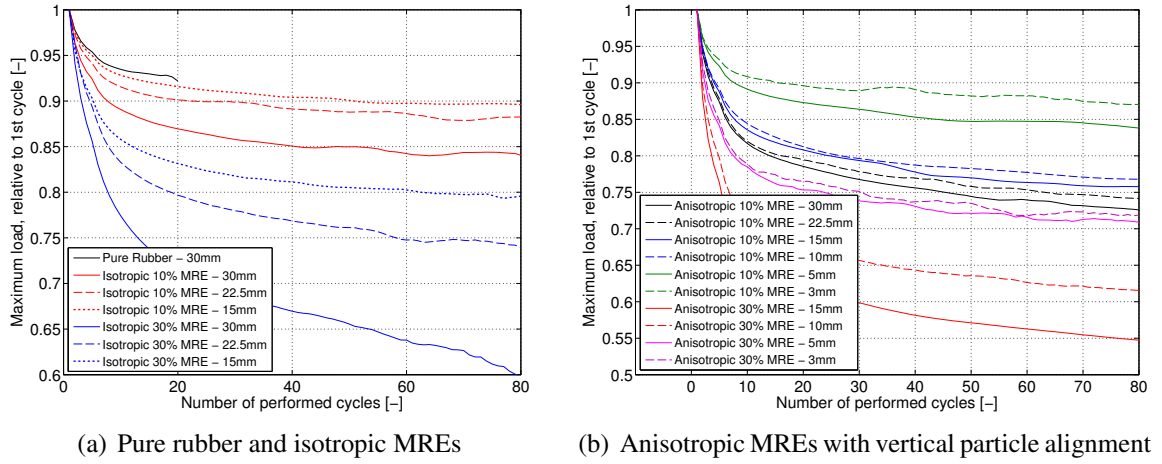


Figure 5.23: Maximum load versus the number of cycles, of pure rubber, isotropic and anisotropic MREs with 10% and 30% iron content. The maximum load is a relative value referring to the load of the first cycle.

as stable when the relative tensile load no longer decreases during continued loading cycles. Over certain strain levels, it was noted that some MRE samples failed to reach a stable state within 80 cycles, this so-called ‘*stability strain limit*’ was found to depend on the type of MRE. A relative load change of less than 0.1% between consecutive cycles was used as a stability criterion. The results, whether or not the samples become stable, and if so, at which cycle number stability occurs, are given in Table 5.10. Only the pure rubber samples and isotropic MREs with 10% iron content could be stretched by up to 30 mm (or 100% strain) and still reach a stable state within the 100 loading cycles. Anisotropic MREs with 10% iron only reached a stable state when stretched by less than 22.5 mm (or 75% strain). MRE samples with 30% iron volume fraction only reached a stable state when stretched by less than 15 mm (or 50% strain). Care was taken not to test MREs over these predetermined stability strain limits during the main tensile test series, and in all subsequent large-strain experiments.

5.3.4 Strain Measurement - Digital Image Correlation

A *Digital image correlation* (DIC) system was used to measure strains, the use of which is described in the manual (VIC-3D Testing Guide, 2010). Test samples were sprayed with a white random speckle pattern. A series of images was recorded during the cyclic test. The DIC software *VIC-3D* performs the correlation analysis by comparing the defined Area of Interest (AoI) in each image. The software divides the pattern into smaller areas and follows

MRE Sample	tested up to ...		Cycle Number
	[mm]	[%]	
Pure Rubber	30.0	100.0	11
Isotropic 10% MREs	30.0	100.0	60
	22.5	75.0	65
	15.0	50.0	15
Isotropic 30% MREs	30.0	100.0	not stable
	22.5	75.0	not stable
	15.0	50.0	52
Anisotropic 10% MREs	30.0	100.0	not stable
	22.5	75.0	64
	15.0	50.0	42
	10.0	33.3	33
	5.0	16.7	39
	3.0	10.0	44
Anisotropic 30% MREs	15.0	50.0	45
	10.0	33.3	65
	5.0	16.7	67
	3.0	10.0	63

Table 5.10: Results of the fatigue tests: cycle number from which the specific type of MRE sample can be considered as ‘stable’ when stretched up to the given displacement (or equivalent strain). In this investigation, if the relative load continues to decrease after the 80th cycle, the MRE sample is not considered to be stable.

the same areas of the pattern in each image. During the test, the patterns in each subsequent image are stretched and displaced. Using this information, the software calculates the displacements and the resulting strains of the tested sample. The output of the DIC software *VIC-3D* are matrices containing values of displacements and strains in the vertical and horizontal directions of each point in the AoI, which in this case is the gauge section of the dog-bone test specimens. As an example, the calculated displacement across an isotropic MRE with 30% iron volume fraction, tested up to 15 mm, is shown in Figure 5.24. Also observable in the figure are the two lines drawn onto the sample to enable a manual verification of the strain values using *ImageJ* (a freely available image processing software (ImageJ, 2014)). The maximum displacement calculated by the DIC software is 13.5 mm, which is a reasonable result as this value was not determined at the very top of the sample. The calculated strain within the narrow part of the sample is uniformly distributed.

The DIC data has been post-processed using the function *strainDICLimess_tension.m* (written in *Matlab*, see Appendix D). This code loads several *Matlab* files (provided by the DIC software) from the file containing the data of the reference image data to the file containing the information of the last deformed image. The *Matlab* files contain the matrices for horizontal and vertical displacements and the engineering strain values, they also contain a matrix with confidence values (*sigma*). The confidence interval describes the matching at any given point (measured in pixels): if the value is -1 the point in the DIC field cannot

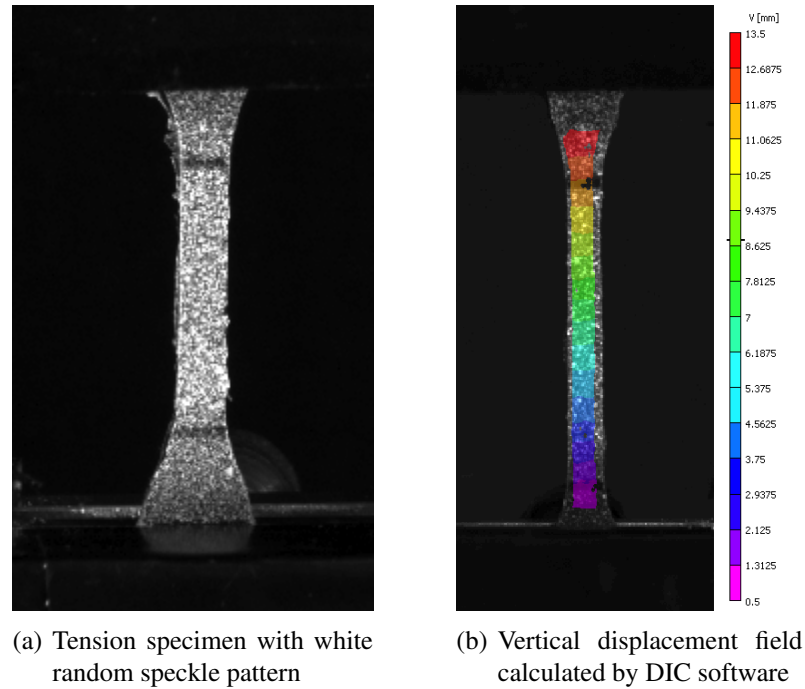


Figure 5.24: Digital Image Correlation (DIC) system (*Limes*) used for the tension tests: pattern sprayed on sample used to calculate the vertical displacement and strain field with the software *VIC-3D 2010*. The two lines seen on the sample are used for manual verification of the DIC results.

be used at all. The provided strain values ϵ_{xx} and ϵ_{yy} are engineering strains. After loading the files, the confidence interval is used to reduce the size of the AoI, such that any point with $\sigma = -1$ is eliminated. Mean values and standard deviations of the strain values are calculated from the remaining AoI. The code also loads the time when each image was recorded from a *csv*-file, provided by the DIC system. The mean strain values together with their standard deviations are plotted versus time in Figure 5.25. The strain results determined by the DIC system are reasonable: the isotropic 30% MRE was tested up to 15 mm, equivalent to approximately 50% strain, as confirmed by the DIC system. The maximum strain in the horizontal direction was 15%. The standard deviation increased in each subsequent cycle and was largest in the fourth cycle. This is understandable as the error in the image analysis is cumulative in time. Despite this, the mean values of all four cycles are in very good agreement. The strain-time data are then split into the loading and unloading parts and handed over to the main tension analysis function *tension_DIC.m* (see Appendix D). Here, the load versus displacement data recorded by test machine is connected to the strain-time data of the DIC analysis via the time recorded by the test machine. By matching the time of the DIC system with the time of the test machine (using linear interpolation between the several indices), a relation between displacement and strain is found. For details of the exact analysis the reader is referred to the *Matlab* algorithms listed in Appendix D and saved on a DVD attached to this document.

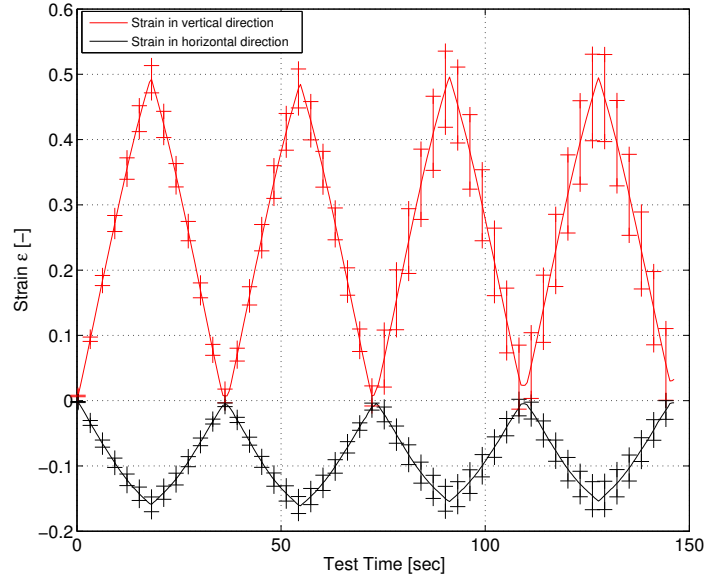


Figure 5.25: Mean and standard deviation of the strain in the vertical and horizontal directions calculated by the DIC software *VIC-3D* and post-processed by the *Matlab* function *strainDICLimess_tension.m*. The strain is plotted versus the time when images were taken, provided by the DIC software. Results of an isotropic MRE with 30% iron content tested up to 15 mm which is equivalent to 50% strain are shown.

To enable the manual calculation of the strain values, two lines were drawn onto the samples. *ImageJ* was used to measure pixels at various positions. The vertical positions of both the bottom and top tension clamps, and the bottom and top end of the two lines were measured in each image. A *Matlab* code *strainpixel_tension.m* was written to aid with the analysis (see Appendix D). The initial distance between the clamps in the reference state was 32 mm allowing a conversion from *pixel* to *mm* in the image. Figure 5.26 shows the reference image and the image of the stretched state of a sample. Measured positions and calculated distances are illustrated. To calculate the strain, the mean value of the inner and outer distance between the two lines is taken. The engineering strain is calculated as:

$$\varepsilon_y = \frac{l_1 - l_0}{l_0} \quad (5.3)$$

where ε_y is the vertical strain and l_0 and l_1 are the distances between the lines in the reference and stretched states, respectively. The distance between the clamps measured in each image is used to connect to the crosshead displacement of the test machine. The pixel measurement process is very time-consuming, so to reduce the time of analysis, usually only the reference image and images of the third loading cycle were analysed. As the relation between strain and displacement is almost linear, it was sufficient to analyse only six images of the loading cycle. A linear fit of the strain-displacement relation is performed and the coefficients of the linear function are handed over to the main tension analysis function *tension_pixel.m*, and used to connect the displacement provided by the test machine to the strain calculated from

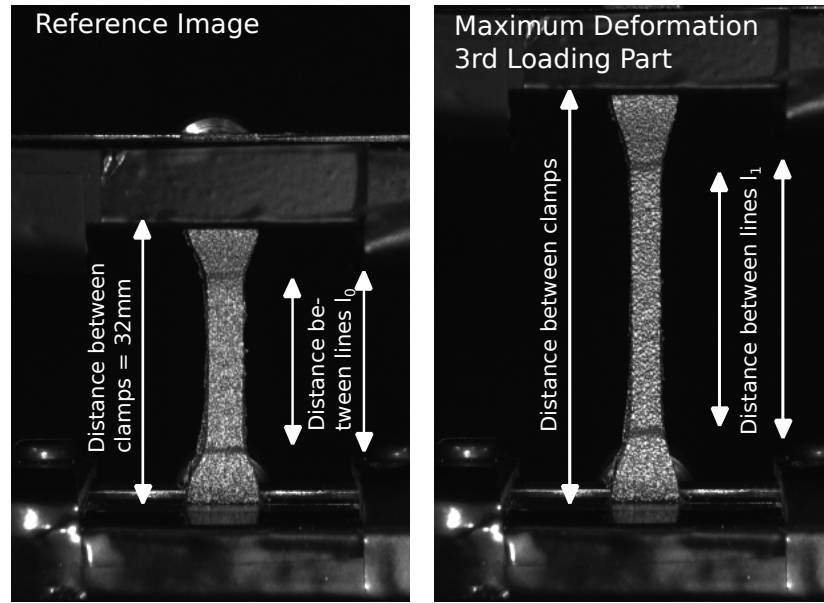
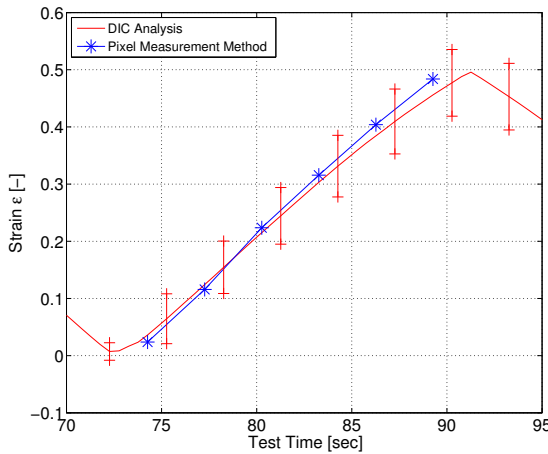


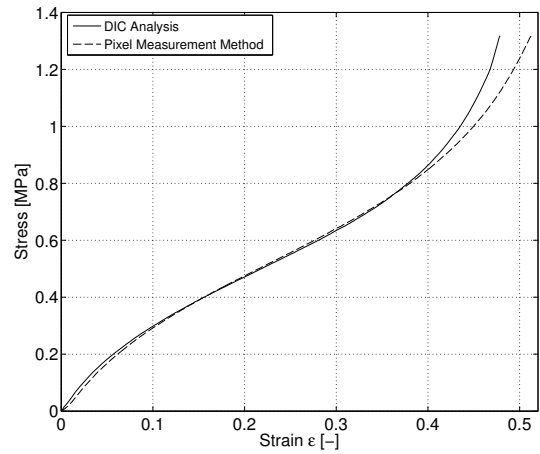
Figure 5.26: Reference image and image of the stretched state of a MRE sample. Distances between the clamps and inner and outer distance between the lines are marked.

measured pixels.

The DIC analysis and the pixel measurement method are compared in Figure 5.27; the strain versus time, and the resulting stress-strain curves of the third loading cycle are illustrated for both. An isotropic MRE with 30% iron content is chosen as a representative example. There are discrepancies in the strain results especially at the end of the loading part when the



(a) Strain-Time Plot



(b) Stress-Strain Data of the 3rd loading part

Figure 5.27: Comparison of strains obtained from the DIC analysis and from the pixel measurement method. Strain-time and stress-strain data of the third loading part of an isotropic MRE with 30% iron content are shown as a representative example.

strains are large. In both methods errors are possible. As seen in Figure 5.25 the standard deviation of the strain obtained from the DIC system increased in each subsequent cycle due to lost pieces of patterns. The larger the tested strains and the larger the number of the cycles,

the more difficulties the DIC system has to calculate the strains. In the pixel measurement method, systematic errors are likely due to the changing perspective in the images when strains are increasing, since the top clamp together with the sample changes its position in each image.

An error analysis was performed to gain knowledge about the possible differences in strain comparing the DIC analysis with the pixel measurement method. All samples tested in the *NoField02* tests (those stretched up to 15 mm) were analysed using both methods. Mean stress-strain data obtained either with the DIC analysis or with the pixel measurement method were calculated. The absolute differences in strain comparing average stress-strain data are determined, and the maximum differences are listed in Table 5.11. The anisotropic 30%

MRE Sample	Iron [%]	Stress Level [MPa]	Difference in strain [%]
Pure Rubber	0	0.30	2.76
Isotropic MREs	10	0.40	1.14
	20	0.53	0.97
	30	0.63	1.64
Anisotropic MREs - vertical alignment	10	0.48	0.98
	20	0.97	0.96
	30	0.73	3.83
Anisotropic MREs - horizontal alignment	10	0.47	2.24
	20	0.54	2.73
	30	0.58	0.84

Table 5.11: Maximum absolute difference in strain between average stress-strain curves obtained with the DIC analysis and the pixel measurement method. The stress level where this maximum difference in strain occurred is provided.

MREs exhibit the largest error: about 3.83% at a stress level of 0.73 MPa. The strain value resulting from the pixel measurement at this point is 45.9% while that from the DIC analysis is 49.7%. There are some significant errors in strain but these occur only in the large strain regime. It is not possible to state which method is more accurate, since there are clearly errors involved in both methods. The pixel measurement method is very time consuming and can only be performed easily in simple tests like the uniaxial tension tests.

5.3.5 Tests in the Absence of a Magnetic Field

Uniaxial tension tests conducted in the absence of an applied magnetic field were performed using the setup illustrated in Figure 5.19. The general test method was clarified in Section 5.1.1, and the specific test procedure of the uniaxial tension tests was given in Section 5.3.1. In this section, the stress-strain results of the two no-field tests are compared, in order to identify any discrepancies between them. Further, the behaviour of isotropic and anisotropic MREs is characterised using the *NoField02* stress-strain results. Each type of MRE sample

was stretched up to two different strain levels (Table 5.7) and the stress-strain behaviour dependant on the strain level is examined. The stress-strain data and moduli are analysed as described in Section 5.1.2.

5.3.5.1 Comparison of NoField01 and NoField02 Tests

Prior to the *NoField01* tests all samples were preconditioned using 50 cycles up to the displacements listed in Table 5.7. DIC images were not recorded during the preconditioning cycles. In uniaxial compression tests, discrepancies between the *NoField01* and *NoField02* tests were observed (Section 5.2.3). This, together with the results of tension fatigue tests (Section 5.3.3) provided the motivation to precondition the MRE samples prior to conducting the main tension test series. Comparisons of the stress-strain results of *NoField01* and *NoField02* tension tests of samples stretched up to 15 mm (50% strain) are illustrated in Figure 5.28, and the comparison of all MREs is given in Appendix E.2. In the figures, arrows indicate the point of divergence. The latter is determined when the standard deviations

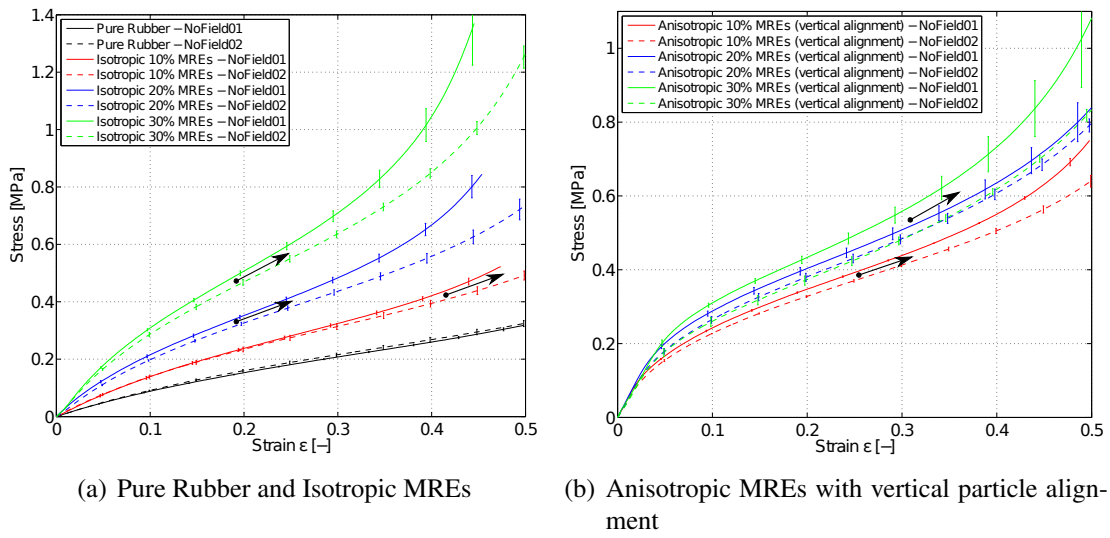


Figure 5.28: Stress-strain curves from *NoField01* and *NoField02* tension tests. Isotropic and anisotropic MREs with 10% to 30% CIP content that were stretched up to 15 mm (50% strain) are compared. The arrows indicate the divergence points.

of both curves are less than the absolute errors between the mean stress-strain curves. The Matlab function *divergence.m* aids with the calculation of this point; results are listed in Table 5.12 for all MREs tested. Discrepancies between the two tests are evident despite preconditioning of the samples. Divergence between the two tests is particularly strong for the MRE samples with higher iron contents. Samples were tested up to two different levels of strain; usually the stress-strain curves of samples tested to smaller maximum strain diverged earlier than those tested to higher maximum strains. Staying within the maximum strain limits (determined with the fatigue tests presented in Section 5.3.3) did not improve the stability between the no-field stress-strain results.

MRE Sample	Iron [%]	up to ... [mm]	Divergence Point [–]
Pure Rubber	0	15.0 30.0	no separation no separation
Isotropic MREs	10	15.0	0.42
		30.0	no separation
	20	15.0	0.19
		22.5	0.55
		5.0	0.13
Anisotropic MREs - vertical alignment	10	15.0	0.19
		30.0	
	20	15.0	0.26
		22.5	0.60
		5.0	0.09
Anisotropic MREs - horizontal alignment	10	15.0	no separation
		30.0	
	20	15.0	0.13
		22.5	0.31
		5.0	
Anisotropic MREs - horizontal alignment	10	15.0	0.35
		30.0	no separation
	20	15.0	0.05
		22.5	0.29
		5.0	0.11
Anisotropic MREs - horizontal alignment	10	15.0	0.06
		30.0	
	20	15.0	
		22.5	
		5.0	

Table 5.12: Comparison between *NoField01* and *NoField02* tension tests. The divergence point is defined as the strain value where the absolute difference between the two mean stress-strain curves is larger than the associated standard deviations.

To study this phenomenon further, the gauge section of the test samples was studied. Measurements of the dimensions were repeated before each test. Mean values for each type of MRE were determined; results are plotted versus the specific tests in Figure 5.29. A clear tendency towards a reduction of area is observed as the test series proceeds. If incompressible behaviour is assumed, a decreasing area implies that the remaining permanent stretch of the samples increases after each step of test series. Note that in the test procedure the initial distance between the clamps holding the MRE samples and the final displacement during the tests were kept constant (see Table 5.7). Keeping the same free length of the ‘pre-extended’ samples and testing them to the same displacement, effectively imposed a higher maximum strain in each successive testing step.

Potentially, the magnetic induction tests performed between the no-field tests could also have contributed to changes in the stress-strain results, *i.e.* due to permanent changes in the microstructure. Though, the presence of the *Mullins* effect seems to be the more likely reason for the divergences found. This phenomenon is studied further in the subsequent pure shear tests before drawing firm conclusions. For now, as with the compression tests (see Section 5.2.3) the MR effects measured in Section 5.3.6 can only be calculated in the regions where *NoField01* and *NoField02* tests are in agreement. MR effects are calculated by comparing the magnetic field tests with the *NoField02* tests. Bold lines are used in the figures to represent

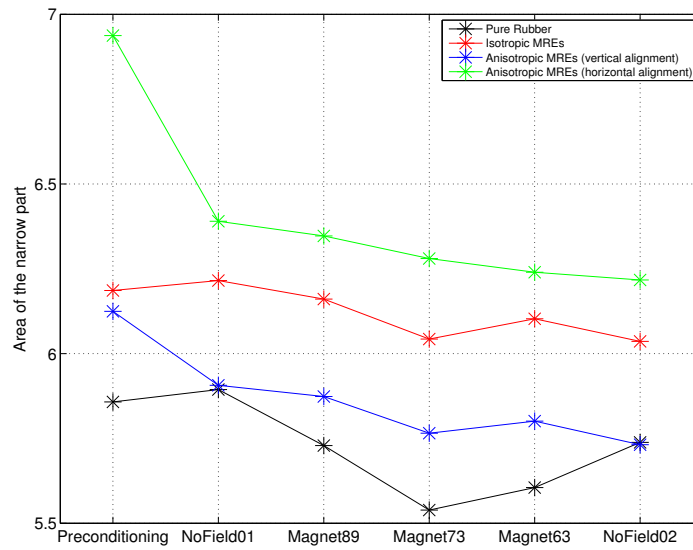


Figure 5.29: Mean values of the sample areas for each type of MRE versus the performed tests *Preconditioning*, *NoField01*, *Magnet89*, *Magnet73*, *Magnet63*, and *NoField02*. The cross-sectional areas of the gauge section were measured prior to each test.

the sections of the curves that are measured prior to the divergence points (see Table 5.12).

5.3.5.2 Comparison of MRE Samples

The third cycle of the *NoField02* tests is used to investigate the differences in stress-strain curves measured using the same type of MRE tested up to two different strain levels (see Table 5.7). The results are shown in Figure 5.30. MRE samples preconditioned and tested up to higher strains are apparently softer than the same type of MRE tested to lower strain levels. This is attributed to the *Mullins Effect* (Mullins and Tobin, 1965) and the effect is more significant in anisotropic MRE samples. The differences in anisotropic samples with 20% and 30% iron content tested up to 5 mm and 15 mm are large; not even the moduli in the small strain regime are the same. The effect is less obvious but can be seen at larger strains in both the pure rubber and isotropic MREs. To compare the different types of MRE samples, a separate plot of the samples tested up to 15 mm is provided in Figure 5.31. All types of MREs exhibit a non-linear stress-strain behaviour that is apparent even in the small strain region (up to 10% strain). The non-linear behaviour is most evident in the anisotropic samples with vertical particle alignment and increases with higher iron content. The isotropic and anisotropic samples with horizontal particle alignment have similar curve shapes and stress levels. An exception are the MREs with 30% iron content, here the isotropic samples clearly exhibit larger stresses in the large-strain region than either of the anisotropic MREs, the latter show similar curve shapes and stress levels. As with the compression tests (see Section 5.2.3), the anisotropic MREs with vertically aligned particles are stiffest with the steepest slope in the small-strain regime and, in the case of 10% and 20% MREs, with the highest stresses in the large strain regime. The slope and stresses increase with increasing

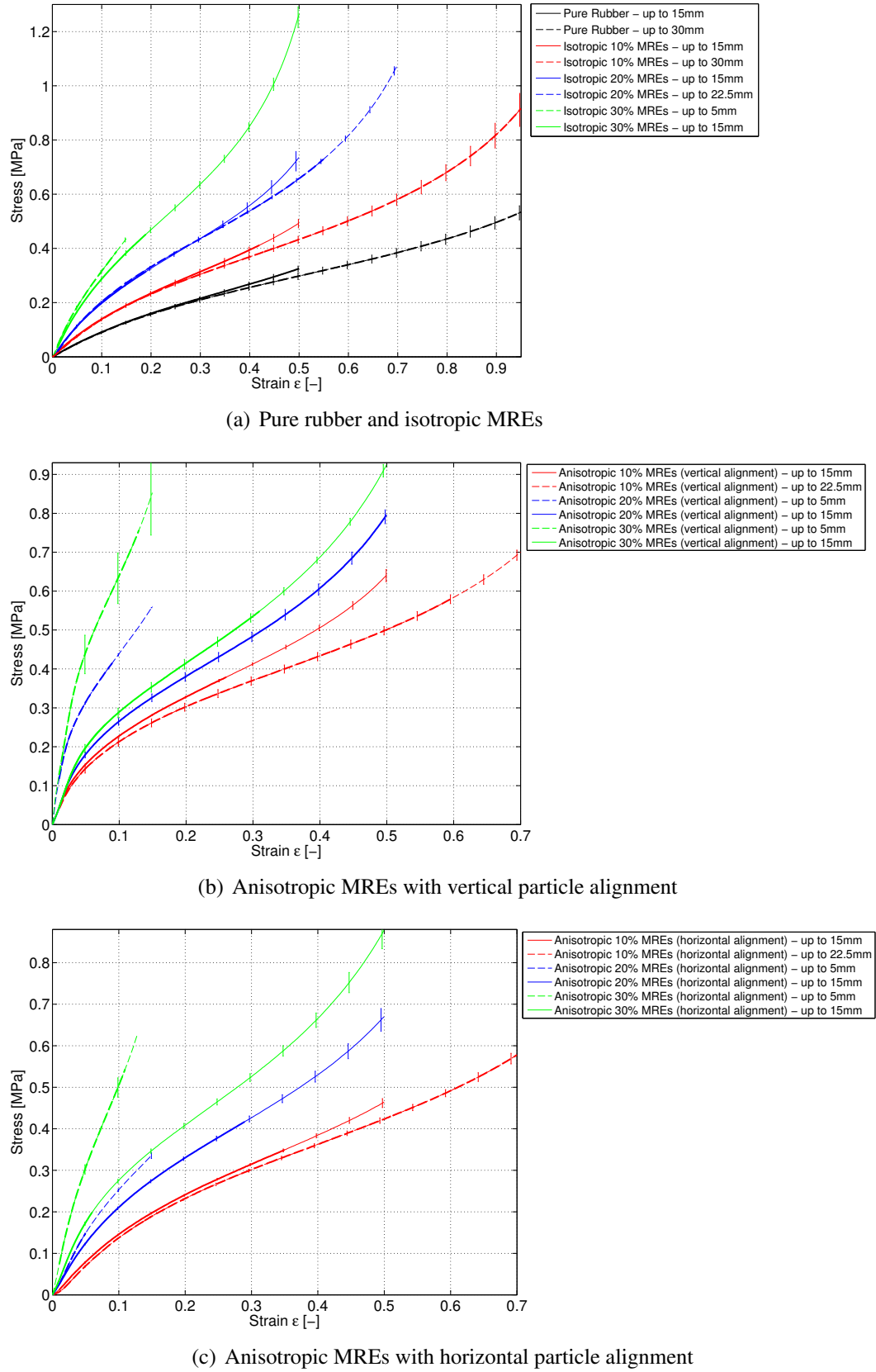


Figure 5.30: Stress-strain curves of the *NoField02* tests comparing different types of MRE samples: (a) pure rubber and isotropic MREs, (b) anisotropic MREs with vertical particle alignment, and (c) anisotropic MREs with horizontal particle alignment. Samples were tested to two different maximum strains, as listed in Table 5.7. Bold lines represent the parts of the stress-strain data where *NoField01* and *NoField02* test results are in good agreement.

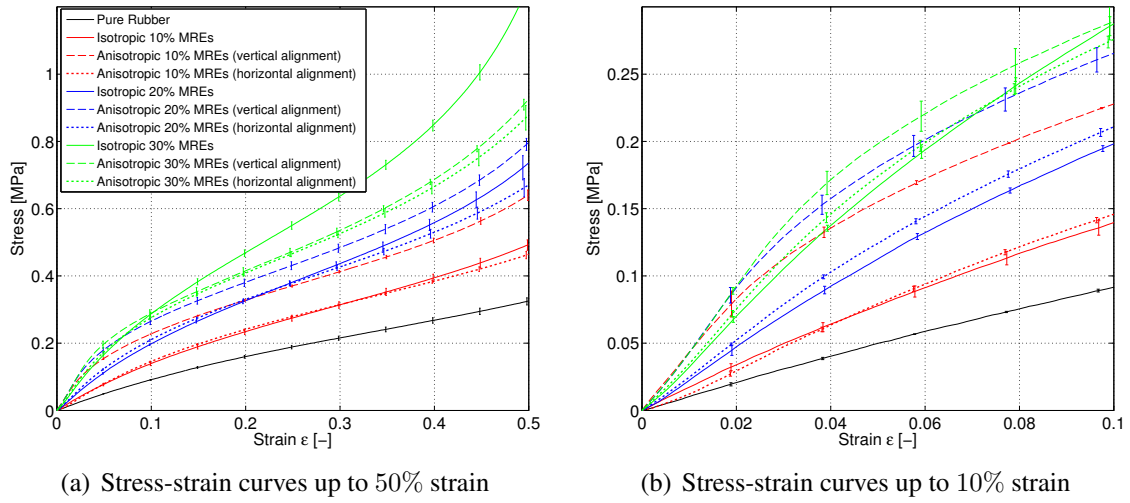


Figure 5.31: Stress-Strain results of the *NoField02* tests of pure rubber, isotropic and anisotropic MREs with 10% to 30% iron content tested up to 15 mm. Figure (b) shows a magnification of the stress-strain results up to 10% strain.

iron content for all types of MREs. To interpret the non-linear stress-strain curves the tangent moduli, E_T , are plotted versus engineering strain in Figure 5.32 for all samples tested up to 15 mm (the full set of results is presented in Appendix E.2). As expected, the tangent moduli

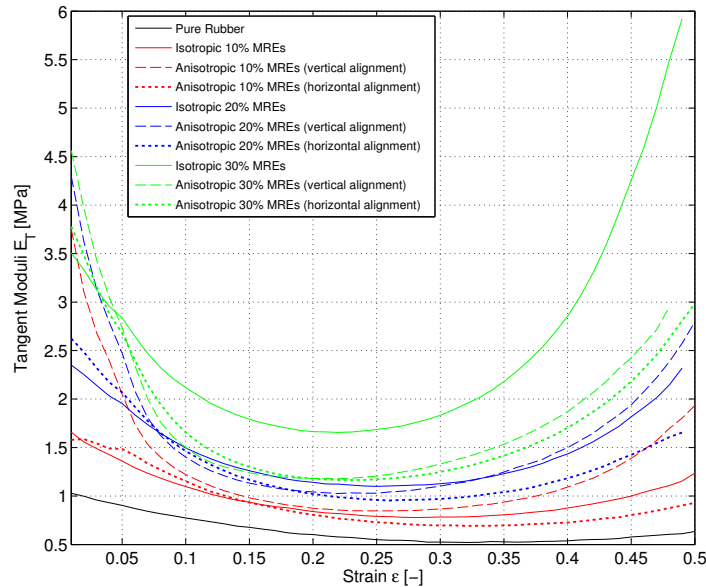


Figure 5.32: Tangent Moduli E_T versus strain of pure rubber, isotropic, and anisotropic MREs with vertical and horizontal particle alignment with 10% to 30% CIP content. Only samples tested up to 15 mm are presented as the others are not comparable due to the stress softening phenomenon. The tangent moduli of all tested MREs are presented in the Appendix E.2.

are largest for the anisotropic samples with vertical particle alignment. Note however that for all samples the stiffness decreases in the mid-strain regime and eventually increases again at strains greater than 30%. The tangent moduli E_T between 1% and 2% strain, and the

linear moduli E_{0-5} are listed in Table 5.13 and plotted in Figure 5.33. A comparison of the moduli of isotropic MREs and the pure rubber samples, and of isotropic and anisotropic MREs with the same iron content, is also provided in the Table 5.13. The increase of the

MRE Sample	Iron [%]	up to ... [mm]	E_{0-5} [MPa]	E_T [MPa]	Increase compared to ... [%]
Pure Rubber	0	15.0 30.0	1.00 0.97	1.03 0.98	
Isotropic MREs	10	15.0	1.56	1.66	56.0
		30.0	1.50	1.68	50.0
	20	15.0	2.25	2.35	125.0
		22.5	2.27	2.30	-
	30	5.0	3.67	3.95	-
		15.0	3.33	3.51	233.0
Anisotropic MREs - vertical alignment	10	15.0	3.10	3.75	98.7
		22.5	2.89	3.46	-
	20	5.0	6.30	8.19	-
		15.0	3.62	4.30	60.9
	30	5.0	8.87	10.78	141.7
		15.0	3.96	4.56	18.9
Anisotropic MREs - horizontal alignment	10	15.0	1.59	1.58	1.9
		22.5	1.39	1.23	-
	20	5.0	2.97	3.04	-
		15.0	2.48	2.63	10.2
	30	5.0	6.12	6.89	66.8
		15.0	3.48	3.78	4.5

Table 5.13: Initial secant moduli, E_{0-5} , and tangent moduli, E_T (between 1% and 2% strain), obtained from stress-strain curves of pure rubber, isotropic, and anisotropic MREs with 10% to 30% CIP content (*NoField02*) are listed. The relative increase of isotropic MREs compared to pure rubber and the relative increase of anisotropic MREs compared to isotropic MREs with same CIP content, calculated with E_{0-5} , are provided. This is only done for samples tested up to the same displacement.

moduli of anisotropic samples compared to the isotropic MREs decreases with increasing iron content, indicating that the anisotropy effect diminishes when more iron particles are present. Interestingly, the moduli of samples with horizontal alignment are nearly identical to those of isotropic MREs. This comparison can only be provided for samples that were stretched to the same extent, and are calculated using E_{0-5} . The moduli (Table 5.13) of MREs tested up to 15 mm are also plotted versus the volume particle concentration in Figure 5.33. The moduli increase almost linearly with increasing iron content, although the moduli increase more slowly in the case of anisotropic MREs with vertical particle alignment than in the two other cases (Figure 5.33).

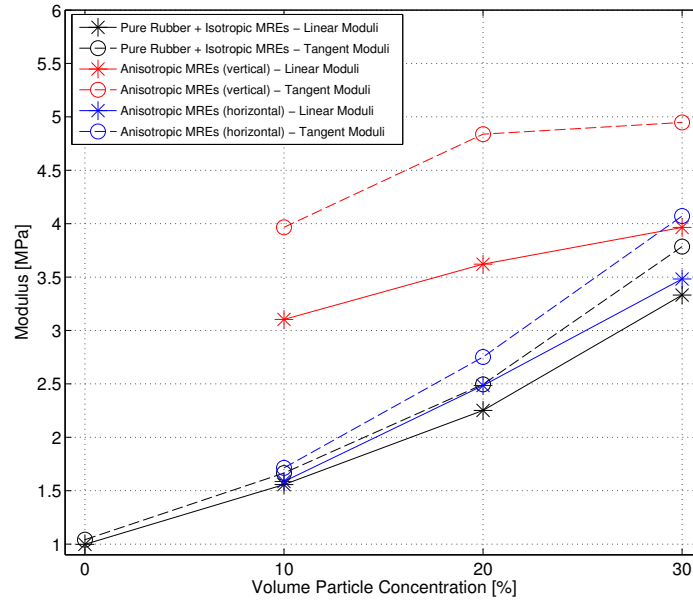


Figure 5.33: Moduli E_{0-5} and E_T as listed in Table 5.13 versus the volume particle concentration of pure rubber, isotropic, and anisotropic MREs with 10% to 30% CIP content. Only samples tested up to 15 mm are presented as the others are not comparable due to the stress softening phenomenon.

5.3.6 Characterisation of the Magneto-Rheological Effect

Three different magnetic field strengths, on average 289.2 mT, 251.2 mT, and 220.6 mT (in the absence of the test specimen), were applied to determine the response of the MRE materials. The specific test procedure of uniaxial tension tests was described in Section 5.3.1. The maximum strain level in the magnetic tests was restricted due to the fixed inter-magnet distance. The setup illustrated in Figure 5.20 was used to carry out these tests. Absolute and relative MR effects (Equations 5.1 and 5.2) are used to characterise the MRE behaviour in the presence of a magnetic field. A full comparison of stress-strain data, the resulting tangent moduli, and the relative MR effects calculated using E_T , are provided in Appendix E.2.

5.3.6.1 Magnet63 Tests

First, the MR effect resulting from the *Magnet63* tests are studied in detail. In Figure 5.34 the absolute and relative MR effects of MREs, previously preconditioned up to 15 mm, are compared. Bold lines in Figure 5.34 represent the results where *NoField01* and *NoField02* results are in agreement. The divergence points have been investigated in Section 5.3.5 and are listed in Table 5.12. The anisotropic samples with vertical particle alignment exhibit the

highest MR effects, followed by the anisotropic MREs with horizontal particle alignment; whereas isotropic MREs show the lowest MR effects. The results achieved with the pure rubber samples indicate an experimental error of about 7.6%. All MR effects are largest in the small strain regime and decrease rapidly to nearly 1 in the mid-strain regime, but the relative

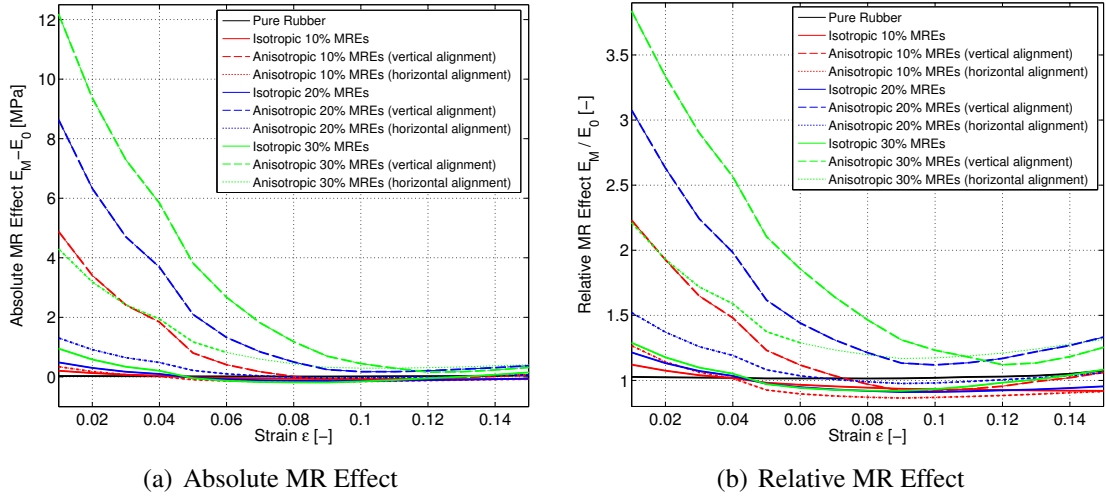


Figure 5.34: Absolute and relative MR effects, calculated with E_T , of all types of MREs preconditioned to 15 mm, achieved with an average magnetic induction of 289.2 mT (*Magnet63*) are illustrated versus tensile strain. Bold lines are used up to the divergence point (see Table 5.12).

effects tend to increase again for strains above 10%. As the samples are only stretched up to 15% strain in the *Magnet63* tests, the large-strain behaviour cannot be studied here, and will be discussed when presenting the results of the *Magnet73* and *Magnet89* tests. The modulus of an anisotropic MRE with 30% vertical aligned particles increases about 12.17 MPa in absolute terms, equivalent to a relative increase of about 284% (almost three times stiffer) in the small strain regime. Table 5.14 lists the MR effects calculated with E_{0-5} and the maximum MR effects calculated with E_T for all MREs tested in this investigation. The maximum MR effect resulting either from E_{0-5} or E_T are grey-shaded in the table. In the case of the *Magnet63* tests, the highest MR effects always result from the tangent modulus calculation, and are observed in the very small-strain region. The values in Table 5.14 clearly show a higher MR effect when the samples were preconditioned to a larger strain level. The maximum relative MR effects (as indicated in Table 5.14) versus the volume particle concentration and also versus the different preconditioning levels are plotted in Figure 5.35. The increase of the MR effect with increasing iron content is most evident in the case of the anisotropic samples. When studying the MR effect versus the preconditioning level (Figure 5.35b) higher MR effects are achieved with samples preconditioned up to larger strain levels. This effect is more pronounced in the case of anisotropic MREs with vertical particle alignment. This observation leads to the conclusion that preconditioning samples to the highest possible strain level enhances MR effects. However, there are restrictions on the preconditioning level associated with stress softening effects and stability of the MREs, as discussed in Section 5.3.3.

MRE Sample	Iron [%]	up to ... [mm]	Absolute MR Effect		Relative MR Effect	
			E_{0-5}	E_T	E_{0-5}	E_T
Pure Rubber	0	15.0	0.0076	0.0513	1.0076	1.0756
Isotropic MREs	10	15.0	0.0580	0.2046	1.0373	1.1208
		30.0	0.0306	0.2920	1.0204	1.2080
	20	15.0	0.1422	0.4845	1.0632	1.2145
		22.5	0.1174	0.5987	1.0516	1.3073
	30	5.0	0.0177	0.3446	1.0048	1.1393
		15.0	0.2246	0.9480	1.0674	1.2891
Anisotropic MREs - vertical alignment	10	15.0	1.9987	4.8782	1.6441	2.2293
		22.5	2.1069	4.6481	1.7286	2.2800
	20	5.0	2.4525	5.0352	1.3896	1.5430
		15.0	4.4690	8.6320	2.2341	3.0754
	30	5.0	4.0505	6.8014	1.4566	1.6053
		15.0	7.8057	12.1761	2.9689	3.8373
Anisotropic MREs - horizontal alignment	10	15.0	0.0249	0.3413	1.0157	1.2665
		22.5	0.1726	0.6671	1.1239	1.7973
	20	5.0	0.0734	0.8835	1.0247	1.3367
		15.0	0.5717	1.3059	1.2301	1.5208
	30	5.0	1.1592	2.8500	1.1893	1.4112
		15.0	2.2754	4.2915	1.6535	2.2103

Table 5.14: Absolute and relative MR effects achieved in the *Magnet63* setup (289.2 mT average magnetic induction), and calculated with E_{0-5} and with E_T (Figure 5.34) are listed. Maximum values of the relative MR effects calculated with E_T are presented. The maximum relative MR effects (E_{0-5} or E_T) are shaded in grey.

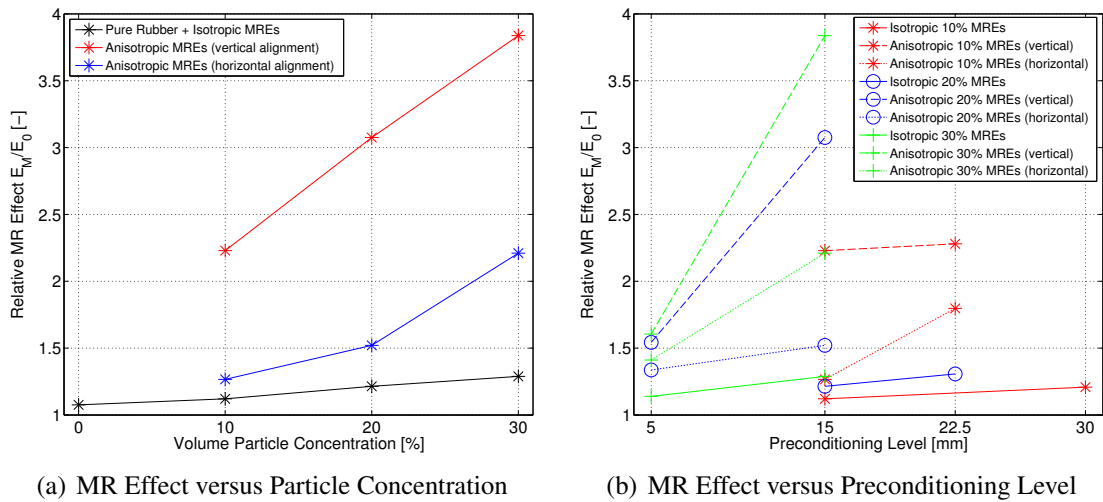


Figure 5.35: Relative MR effect of pure rubber, isotropic, and anisotropic MREs achieved with an average magnetic induction of 289.2 mT (*Magnet63*) are illustrated (a) versus the volume particle concentration (MREs preconditioned up to 15 mm) and (b) versus the displacement level to which the samples were preconditioned. Maximum MR effects as indicated in Table 5.14 are used.

5.3.6.2 Magnet73 and Magnet89 Tests

This section reports the results of tests conducted with lower magnetic field strengths but with samples tested to higher strain levels. The absolute and relative MR effects obtained calculated using E_T and plotted versus engineering strain are shown in Figures 5.36 and 5.37. Only samples preconditioned to 15 mm are presented as they allow direct comparison between the different types of MREs. As expected, the MR effects in these tests are lower

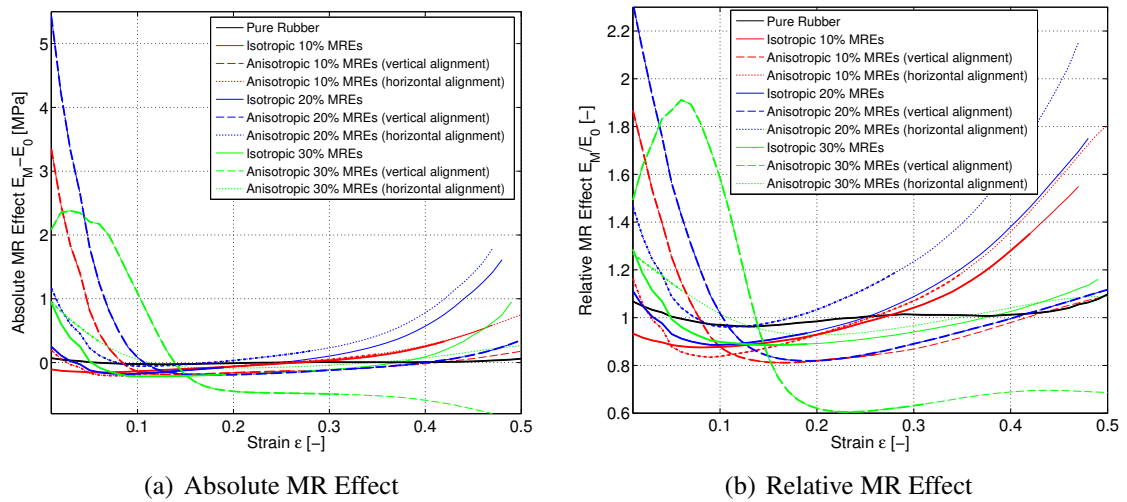


Figure 5.36: Absolute and relative MR effects, calculated with E_T , of all types of MREs preconditioned to 15 mm, achieved with an average magnetic induction of 251.2 mT (*Magnet73*) are illustrated versus strain. Bold lines are used up to the divergence points (see Table 5.12).

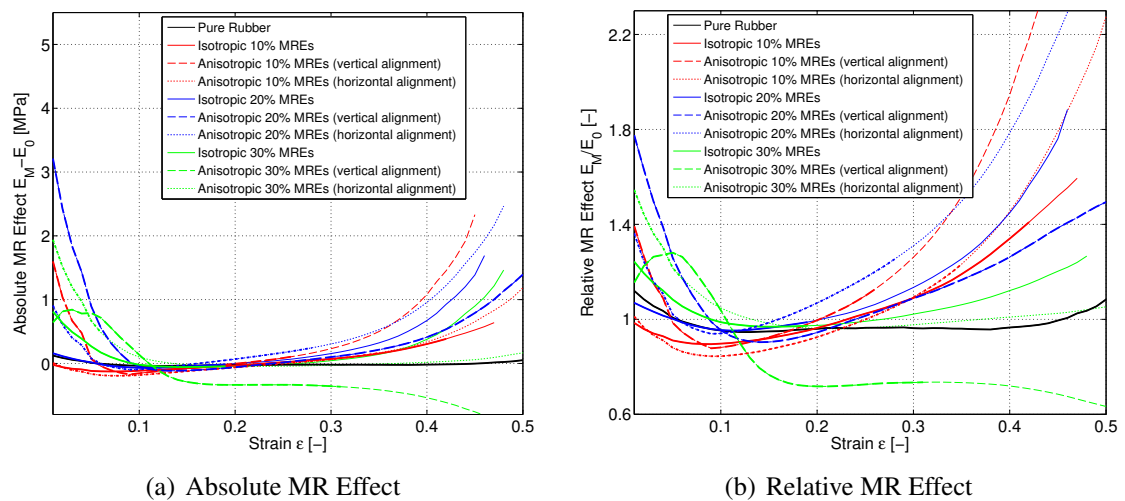


Figure 5.37: Absolute and relative MR effects, calculated with E_T , of all types of MREs preconditioned to 15 mm, achieved with an average magnetic induction of 220.6 mT (*Magnet89*) are illustrated versus strain. Bold lines are used up to the divergence points (see Table 5.12).

than those obtained in the *Magnet63* tests due to the lower magnetic field strength. The

MR effect of pure rubber indicates an experimental error of 10%. In the main, the shape of the MR effect versus strain curves looks similar to those measured in the *Magnet63* tests, with higher MR effects in the small strain region, rapidly decreasing to 1 or less in the mid-strain region but increasing again above 15% strain. Curiously, the anisotropic MREs with 30% vertically aligned particles are an exception; here the MR effect appears to have a maximum at approximately 5% strain, which is lower than that achieved with a vertically aligned anisotropic MRE with 20% iron content. Isotropic MREs with 10% iron volume fraction do not show an MR effect in the small strain region. Not all samples were analysed at strains larger than 15% due to the discrepancies found between *NoField01* and *NoField02* tests for certain types of MRE (see Section 5.3.5). Nevertheless, the MR effect was once again observed to increase in the large-strain region, and some of the observed effects at large strain are even higher than the effects seen in the small strain region. Tables 5.15 and 5.16 list the absolute and relative MR effects calculated with E_{0-5} , the maximum MR effects obtained using E_T in the region from 1% to 15% strain ($E_{T,1-15}$), and in the large-strain region ($> 15\%$ strain) up to the point of divergence ($E_{T,>15}$). The MR effects obtained

MRE Sample	Iron [%]	up to ... [mm]	Absolute MR Effect		Relative MR Effect		
			E_{0-5}	$E_{T,1-15}$	E_{0-5}	$E_{T,1-15}$	$E_{T,>15}$
Pure Rubber	0	15.0	0.0362	0.0694	1.0363	1.0677	1.0977
Isotropic MREs	10	15.0	-0.1425	-0.1074	0.9085	0.9338	1.3523
		30.0	-0.1009	0.0474	0.9327	1.0369	0.9996
	20	15.0	-0.0178	0.2508	0.9921	1.1116	0.9355
		22.5	-0.0408	0.4063	0.9821	1.2151	1.1191
	30	5.0	-0.1325	0.5596	0.9639	1.2266	-
		15.0	0.3026	0.9382	1.0908	1.2853	0.8897
Anisotropic MREs - vertical alignment	10	15.0	1.8914	3.3528	1.6095	1.8686	0.8452
		22.5	1.7002	3.2258	1.5879	1.8999	1.0582
	20	5.0	2.3329	2.0143	1.3706	1.3028	-
		15.0	3.6603	5.4300	2.0108	2.3177	1.1173
	30	5.0	4.3990	5.7747	1.4958	1.5305	-
		15.0	2.0812	2.1739	1.5249	1.9121	0.8321
Anisotropic MREs - horizontal alignment	10	15.0	-0.0887	0.1955	0.9441	1.1632	1.1874
		22.5	0.2097	0.7586	1.1505	1.9100	1.1548
	20	5.0	-0.1279	0.3845	0.9570	1.1497	-
		15.0	0.5745	1.1700	1.2312	1.4660	1.2103
	30	5.0	1.0945	1.6628	1.1787	1.2441	-
		15.0	0.7924	0.9560	1.2276	1.2678	-

Table 5.15: Absolute and relative MR effects achieved in the *Magnet73* setup (251.2 mT average magnetic induction), and calculated using E_{0-5} and E_T (Figure 5.36) are listed. Maximum values of the relative MR effects calculated using $E_{T,1-15}$ (small-strain) and $E_{T,>15}$ (large-strain) are presented. The maximum relative MR effects in the small-strain region (E_{0-5} or $E_{T,1-15}$) are shaded in grey. The MR effects in the large-strain region are coloured in blue when they exceed the MR effects in the small-strain region.

MRE Sample	Iron [%]	up to ... [mm]	Absolute MR Effect		Relative MR Effect		
			E_{0-5}	$E_{T,1-15}$	E_{0-5}	$E_{T,1-15}$	$E_{T,>15}$
Pure Rubber	0	15.0	0.0554	0.1233	1.0555	1.1203	1.0839
Isotropic MREs	10	15.0	-0.0875	-0.0221	0.9438	0.9849	1.4092
		30.0	0.0700	0.1657	1.0467	1.1154	1.8526
	20	15.0	0.1186	0.1594	1.0527	1.0697	0.9884
		22.5	0.4520	0.6918	1.1988	1.3342	1.3200
	30	5.0	0.2783	0.8474	1.0758	1.3468	-
		15.0	0.5571	0.8103	1.1672	1.2431	0.9728
Anisotropic MREs - vertical alignment	10	15.0	0.4147	1.5983	1.1336	1.3927	1.1266
		22.5	0.9997	1.8765	1.3457	1.5218	1.8682
	20	5.0	-0.3124	1.1137	0.9504	1.4361	-
		15.0	1.9448	3.2101	1.5371	1.7758	1.4939
	30	5.0	0.8183	1.8326	1.0922	1.3564	-
		15.0	1.1925	0.7886	1.3008	1.2806	0.7659
Anisotropic MREs - horizontal alignment	10	15.0	-0.1043	0.0053	0.9342	1.0121	1.2326
		22.5	0.2116	0.6699	1.1519	1.7913	2.1076
	20	5.0	-0.1612	0.2516	0.9458	1.0989	-
		15.0	0.3319	0.9066	1.1336	1.3620	1.2805
	30	5.0	0.2817	0.5594	1.0460	1.0814	-
		15.0	1.2361	1.9372	1.3550	1.5451	-

Table 5.16: Absolute and relative MR effects achieved in the *Magnet89* setup (220.6 mT average magnetic induction), and calculated using E_{0-5} and E_T (Figure 5.37 are listed. Maximum values of the relative MR effects calculated using $E_{T,1-15}$ (small-strain) and $E_{T,>15}$ (large-strain) are presented. The maximum relative MR effects in the small-strain region (E_{0-5} or $E_{T,1-15}$) are shaded in grey. The MR effects in the large-strain region are coloured in blue when they exceed the MR effects in the small-strain region.

using $E_{T,1-15}$ are comparable to the *Magnet63* results. To allow a fair comparison between the different types of MRE samples, it is also important to distinguish MR effects occurring in the smaller strain region and MR effects in the large-strain region (above 15% strain). The maximum MR effects resulting from either E_{0-5} or $E_{T,1-15}$ are shaded in grey in Tables 5.15 and 5.16. For those cases where MR effects measured using $E_{T,>15}$ are larger than those measured using $E_{T,1-15}$, the values are coloured in blue. Preconditioning levels play an important role: as in the *Magnet63* tests, samples preconditioned to higher levels exhibit higher MR effects; while this is true for all types of MRE samples, it is more apparent for anisotropic MREs. Also, aside from vertically-aligned anisotropic MREs with 30% iron volume fraction, MR effects are found to increase with increasing iron content (see Figures 5.36 and 5.37).

5.3.6.3 MR Effect versus Magnetic Field Strength

In this section, MR effects resulting from different applied magnetic field strengths are compared; the results of samples (preconditioned up to 15 mm) are plotted versus the average

magnetic flux density in Figure 5.38. Maximum values of the relative MR effects, occurring in the small-strain region (see Tables 5.14, 5.15, and 5.16) are used for the plot. The magnetic flux densities were calculated with *Comsol* in the absence of an MRE samples, and the average is taken over the volume of the samples (see Section 5.3.2). The relative MR effect

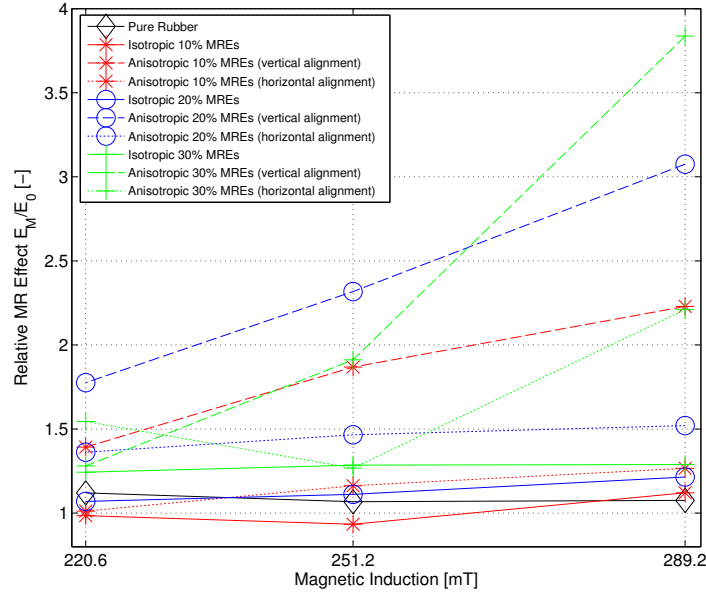


Figure 5.38: Relative MR effect of pure rubber, isotropic, and anisotropic MREs (preconditioned to 15 mm) are plotted versus the average magnetic flux density (calculated in the absence of an MRE sample, see Section 5.3.2). The maximum relative MR effects listed in Tables 5.14, 5.15, and 5.16 are used.

is linear when plotted versus the applied magnetic induction for most of the MRE samples. Anisotropic MREs with 30% iron content are an exception: in this case the MR effects are not as high as expected when subjected to lower magnetic flux densities. Also, isotropic MREs with 10% particles do not behave as expected, again especially when subjected to lower magnetic field strengths; here MR effects are negligible. These findings are all subject to about 10% error, as determined from experiments on pure rubber samples.

5.3.7 Summary of Tension Tests

Fatigue tests revealed a ‘maximum stability limit’ that differed according to the type of elastomeric material under consideration (see Section 5.3.3). MRE samples used in the main tension test series were just stretched up to strain levels below the maximum stability limit. Comparisons between *NoField01* and *NoField02* tests revealed large discrepancies most likely due to: (i) permanent deformation of the samples and (ii) the *Mullins* effect (see Section 5.3.5). In order to eliminate the influence of these factors and to isolate the MR effect, only those test results obtained up to a divergence point (Table 5.12) were used. MREs were tested up to two maximum strain levels; these tests showed that larger strains resulted in a softer stress-strain behaviour. A direct comparison of different types of MREs were only

possible for samples preconditioned and tested up to 15 mm (50% strain). Anisotropic MREs with particle alignment in the loading direction were the stiffest samples reaching the highest stresses. Isotropic and anisotropic MREs with horizontal particle alignment showed similar stress-strain curves and moduli. The magnetic field distribution within the testing space was studied using finite element simulations (*Comsol*). Due to the large distances between the magnets (63 to 89 mm), large variations in magnetic flux density across the volume of the MRE test specimens were found. The stresses, tangent moduli, and absolute and relative MR effects were studied versus engineering strain by comparing tests both without and with magnetic fields. The MR effects were found to be large in the small strain region ($< 10\%$ strain), almost negligible in the mid-strain region (10 to 15% strain), but become significant again for strains larger than 15%. MREs with 10% CIP exhibit larger MR effects in the large-strain region than in the small-strain region. This is an interesting result in so far as MREs were previously reported to perform best in the small-strain region (see Chapter 2). MR effects in the strain region below 15% generally increase approximately linearly with increasing iron volume fraction and magnetic field strength. Larger preconditioning levels led to larger MR effects, presumably due to softening effects (a softer matrix tends to produce a greater MR effect, see Section 2.5).

5.4 Pure Shear Tests

Pure shear experiments were never before conducted on MREs up to large strain levels (see literature review in Section 2.5), but are essential as they provide different deformation kinematics with which to evaluate constitutive material models (as discussed in Chapter 6). MREs are characterised under pure shear deformation in the absence and the presence of a magnetic field. The pure shear experiment is basically a “very wide tensile test” (Miller, 1999), but due to the incompressibility of the MRE material “a state of pure shear exists at a 45 degree angle to the stretching direction” (Miller, 1999).

The general test method and the method of analysis were described in Section 5.1. The structure of this section is as follows: Section 5.4.1 gives the specific procedure of the pure shear tests. In Section 5.4.2 the test setup used for the pure shear tests is described, including the magnetic flux distribution within the volume occupied by the sample. The analysis of the DIC strain data is presented in Section 5.4.3. The MRE behaviour in the absence of a magnetic field, and the MR effect resulting from tests with an applied magnetic field are detailed in Sections 5.4.4 and 5.4.5, respectively. The pure shear experiments are summarised in Section 5.4.6. To aid with the analysis of the pure shear tests, the *Matlab* functions *pureshear_DIC.m* and *pureshear_pixel.m* were written, which include the cut-and-shift process described previously in Section 5.1.2, and the analysis of the optically measured strains (see Section 5.4.3). For further details on the *Matlab* procedure and the employed sub-functions,

the reader is referred to Appendix D. The *Matlab* codes are saved on a DVD attached to this document and can be consulted for even more in-depth information.

5.4.1 Procedure of the Pure Shear Tests

Pure shear, also called planar shear experiments, were performed on MREs with up to 30% iron content. The tests were performed in accordance with the *British Standard* (BS 903-5, 2004). To achieve the state of pure shear, a thin strip of rubber is required; “the height of the strip in the straining direction should be no more than one-fifth of its longest dimension” (BS 903-5, 2004). The sample width was restricted to 50 mm due to both the manufacturing process (see Chapter 3) and the size of the permanent magnets (see Section 5.1.1). The thickness of the sample was set at 1 mm; since thinner samples were difficult to manufacture. The height was set at 30 mm, leading to a free height between the testing clamps of about 12 mm. The final ratio between height and width of the sample was 1/4, slightly less than the recommended ratio in the *British Standard*, but still acceptable as experimental strains measured in the horizontal direction were small (ideally these should be zero).

Cyclic tests up to a maximum of 70% strain were performed using a test speed of 50 mm/min. The strains were measured optically with the DIC system, and a grid of lines was drawn onto the samples to enable manual verification of the strain values. Overall four repeat tests on each type of MRE were conducted re-using the samples, including tests: (i) to precondition the samples over 50 cycles at a test speed of 200 mm/min, (ii) without a magnetic flux (*NoField01*), (iii) with an magnetic flux density of 290 mT using a distance between the magnets of 53 mm (*Magnet53*), and (iv) without a magnetic flux (*NoField02*). To investigate further the *Mullins* effect present in the MRE samples; (i) the samples were preconditioned and in contrast to the tension tests, DIC images were recorded to determine the strain values. This meant that a direct comparison between the *Preconditioning*, *NoField01*, and *NoField02* stress-strain results became possible, and (ii) as with the tension tests, each type of MRE was tested up to two different displacement levels to observe the differences in stress softening. A list of the displacement (or equivalent strain) levels to which the different types of MREs were stretched, is given in Table 5.17. All MRE samples are tested up to 6 mm to enable comparison between the different types of MRE samples. In the case of pure shear tests identical displacement levels failed to produce identical levels of strains (Table 5.17), because the dimensions of the initial MRE samples differed slightly, in that they were longer in the direction of particle alignment. Average dimensions for each type of MRE are listed in Table 5.18. Due to the slightly different dimensions, it was necessary to adjust the initial distance between clamps for each type of MRE sample to ensure proper clamping. The set displacement levels were not adjusted to compensate for the different initial lengths of the specimen leading to slightly different strains.

MRE Sample	Iron [%]	Displacement [mm] (Strain [%])			
Pure Rubber	0	6.0	(47)	9.0	(70)
Isotropic MREs	10	6.0	(45)	9.0	(67)
	20	3.0	(23)	6.0	(45)
	30	3.0	(23)	6.0	(45)
Anisotropic MREs - vertical alignment	10	3.0	(22)	6.0	(43)
	20	3.0	(22)	6.0	(43)
	30	3.0	(22)	6.0	(43)
Anisotropic MREs - horizontal alignment	10	3.0	(25)	6.0	(49)
	20	3.0	(25)	6.0	(49)
	30	3.0	(25)	6.0	(49)

Table 5.17: Types of MRE samples tested under pure shear. The samples were stretched to the given displacements. All samples were tested up to 6 mm to allow comparison.

	$w[mm]$	$h[mm]$	$t[mm]$
Pure Rubber	45.4	27.4	0.93
Isotropic MREs	45.7	28.3	0.95
Anisotropic MREs - vertical alignment	45.2	29.6	0.94
Anisotropic MREs - horizontal alignment	49.4	27.5	0.93

Table 5.18: Averaged dimensions of pure shear samples.

Note that a separation distance between the magnets of 53 mm allowed displacements up to 6 mm (equivalent to approximately 45% strain). The samples were only tested with this single magnetic field strength; decreasing the distance between the magnets was not possible as space was required to clamp the samples into the setup. Tests using smaller magnetic fields would have been possible but were not conducted due to time constraints. Given that uniaxial compression and tension tests had already confirmed an approximately linear relationship between the MR effect and applied magnetic field strength (see Section 5.2.4 and 5.3.6), the importance of these tests was deemed less crucial at this stage.

Note that pure shear MRE samples experience large remnant deformations during each cycle test, so the stress-strain data of the third loading cycle used for the characterisation of the MRE behaviour (analysed as described in Section 5.1.2) show large variations in maximum strain. The remnant deformation was dependant on the type of MRE; this issue will be discussed further in Section 5.4.4 when characterising the MRE behaviour in the absence of a magnetic field. However, for these pure shear experiments this remnant deformation was found to be temporary: samples recovered completely to their original dimensions between the four testing steps of the main test series (unlike the compression and tension test samples).

5.4.2 Pure Shear Test Setup

The same test rig as that used for uniaxial tension tests was used for the pure shear experiments. The test setup for the uniaxial tension tests was described in Section 5.3.2; the dimensions of the test rig are provided in Appendices B.10 and B.11, and a technical drawing of the pure shear setup involving permanent magnets is provided in Appendix B.14. Figure 5.39 shows a pure shear sample clamped into the test rig. The sample is sprayed with white paint to create a random speckle pattern for DIC analysis. Grid lines on the sample are visible, enabling the manual calculation of strain to verify the DIC measurements. The DIC

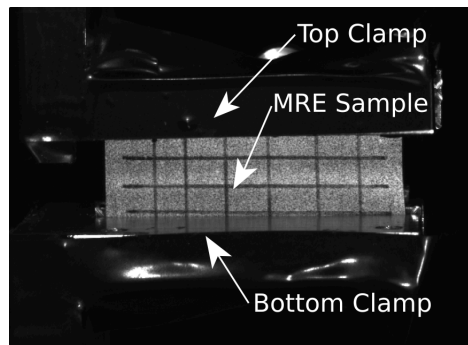
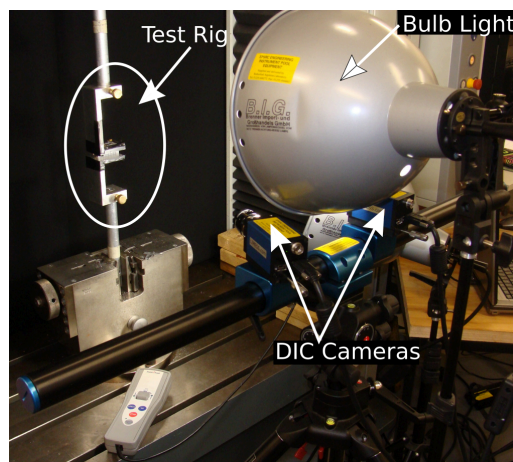
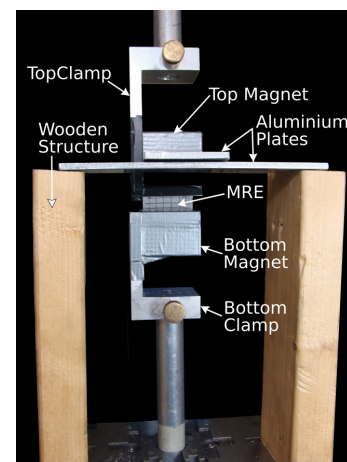


Figure 5.39: Pure shear sample clamped in the tension test rig. Parts of the setup are covered in black tape to eliminate reflections in the DIC images. The sample is sprayed with a white paint to enable DIC calculation, and the grid of lines is drawn on the sample to enable manual verification of strains.

system comprised of cameras and lights is shown in Figure 5.40a. Figure 5.40b shows the test setup with the two permanent magnets in place. The top magnet was held by a wooden structure.



(a) DIC cameras and light



(b) Permanent magnets in place

Figure 5.40: Test Setup for pure shear tests without and with magnets in place. The cameras and bulb lights of the DIC system are shown. Permanent magnets are held by a wooden structure, and the distance between them is 53 mm.

5.4.2.1 Distribution of the Magnetic Flux Density

As previously seen in the uniaxial tension tests (Section 5.3.2) the magnetic field distribution is not expected to be uniform as the distance of 53 mm between the permanent magnets is relatively large. The flux density was calculated using the finite element simulations (*Comsol*), the model geometry of which is shown in Figure 5.41. Application of symmetry conditions meant that only one quarter of the setup had to be modelled. Note that only the permanent magnets and the MRE sample is modelled; the test setup is built of non-magnetic material and has no influence on the magnetic flux simulation. Further details about the *Comsol*

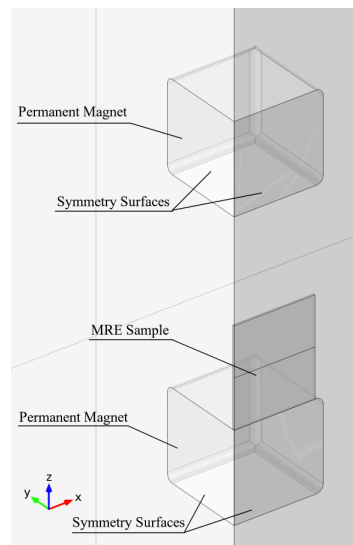


Figure 5.41: Model geometry used to calculate the magnetic flux distribution within the pure shear test setup. The distance between the magnets is 53 mm . Symmetry conditions are applied, so only one quarter of the setup is modelled.

model are given in Section 4.4; the settings used here are the same as those used to identify permeabilities (Chapter 4). Contrary to the uniaxial tension tests, the magnetic flux density in the vertical and horizontal directions must be considered as the pure shear samples are much wider. In the area occupied by the narrow uniaxial tension test samples, the direction of the magnetic flux was practically uniform, directed in vertical direction only (see Section 5.3.2). Nearer to the borders of the permanent magnets, the magnetic flux is also directed horizontally and therefore, in the case of pure shear samples, the direction of the magnetic flux cannot be considered to be uniform. The importance of a uniform level and direction of the magnetic flux was emphasised by Gorman *et al.* (2012). The use of permanent magnets with such a large distance between them is not perfect, but note that it is very difficult to achieve uniform magnetic levels in large strain experiments and some compromise is required. An open view to the experiments is required to enable the DIC measurements and also access to the setup is essential for changing samples. Thus even when using an electromagnetic setup where the magnetic field can simply be switched on and off (the main advantage of using electromagnets compared to using permanent magnets), it is still very difficult to achieve

uniformity of the magnetic field. By simulating the distribution of the magnetic flux the degree of non-uniformity can be understood, and this knowledge can potentially be used in modelling the material behaviour at some later stage (*i.e.* during evaluation of constitutive models). The distributions of the vertical and horizontal flux in the area occupied by the MRE samples (calculated in the absence of a sample with $\mu_r = 1$) are illustrated in Figure 5.42. The bottom end of the MRE sample touches the bottom magnet, resulting in the largest

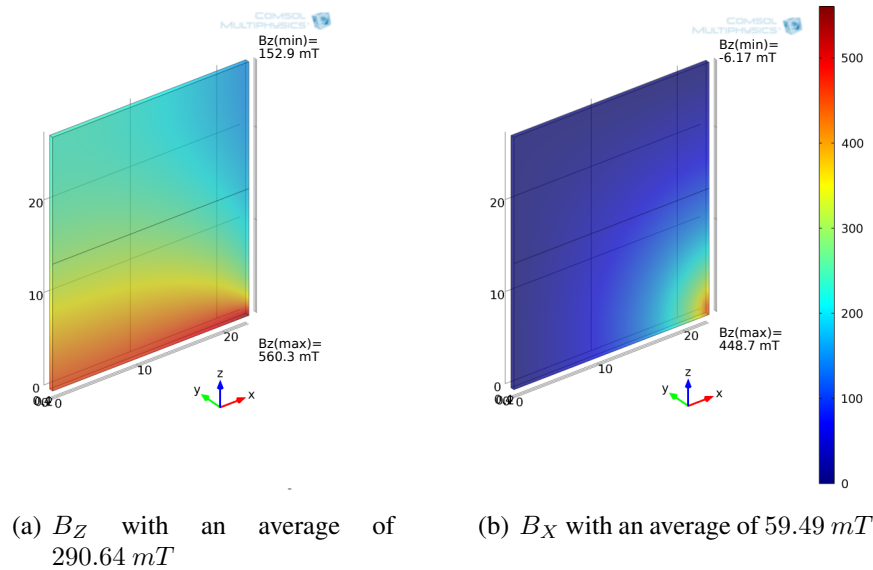


Figure 5.42: Distribution of the magnetic flux density B_Z and B_X within the region occupied by the MRE sample but calculated in the absence of a sample ($\mu_r = 1$). Symmetry conditions are applied at the y-z and the x-z plane, so only one fourth of the sample is modelled.

magnetic flux density at the bottom end of the sample. A minimum and maximum flux of $B_Z = 152.86 \text{ mT}$ and 560.25 mT was calculated, and the vertical flux differs within the volume usually occupied by the MRE sample up to 140%. The local horizontal magnetic flux in the corner of the sample is very large with $B_X = 448.7 \text{ mT}$, but is nearly zero in the remaining volume of the MRE sample, resulting in a 743.9% relative variation of B_X across the volume of the sample.

The magnetic field distribution is also studied when MRE samples are present ($\mu_r > 1$). The identified permeabilities in Chapter 4, listed in Table 4.11, are used to calculate the magnetic flux densities within the pure shear setup for the different types of MREs. Parametric sweeps are used in *Comsol* to calculate the flux for the different permeabilities. Average dimensions of the pure shear samples, which are slightly different depending on the type of MRE (see Table 5.18), are used in *Comsol* to perform the simulations. The mean values of B_Z and B_X together with the variation within the area occupied by the MRE sample for each type of MRE are listed in Table 5.19. The level of magnetic induction increases with increasing iron content, and in most cases the differences within the volume occupied by the MRE sample

MRE Sample	Iron [%]	Flux in Z -direction		Flux in X -direction	
		B_{mean} [mT]	$\frac{B_{max}-B_{min}}{B_{mean}}$ [%]	B_{mean} [mT]	$\frac{B_{max}-B_{min}}{B_{mean}}$ [%]
Pure Rubber	0	290.64	140.2	59.49	743.9
Isotropic MREs	10	447.06	123.0	92.85	643.1
	20	596.52	112.3	122.46	580.9
	30	941.34	108.0	189.29	505.5
Anisotropic MREs - vertical alignment	10	442.40	120.2	80.74	635.8
	20	710.48	110.9	117.11	555.8
	30	1096.72	110.3	168.35	502.2
Anisotropic MREs - horizontal alignment	10	411.53	176.6	112.56	1050.1
	20	605.48	180.1	178.0	973.5
	30	884.09	180.4	269.98	880.3

Table 5.19: Mean values and differences of the magnetic flux density, B_Z and B_X , in the *Magnet53* setup within the volume occupied by isotropic and anisotropic MRE samples ($\mu_r > 1$). The permeability of isotropic and anisotropic MREs (Table 4.11) were used to calculate B_Z and B_X . Values for B_X are calculated with absolute values.

decreases with higher iron content. In general, the mean vertical flux is much higher than the horizontal flux, although the latter is nevertheless significant.

5.4.3 Strain Measurement - Digital Image Correlation

The strain values were measured optically, as previously described for the uniaxial tension tests (Section 5.3.4). The DIC system was described in Section 5.1.1, and its use is described in the manual (VIC-3D Testing Guide, 2010). To facilitate the DIC analysis samples were sprayed with a white random speckle pattern (see Figure 5.43a). Grid lines were drawn onto the sample to enable manual calculation of the strains using ImageJ (2014)). Figure 5.43b shows the vertical displacement field across the AoI (calculated by the DIC software) of an isotropic MRE with 20% iron content, tested here up to 6 mm displacement. The displacements within the AoI range from 1.32 mm to 4.02 mm, which is reasonable since the AoI is not defined from the bottom to the top clamp to exclude boundary effects. The DIC software also calculates engineering strain values ε_{yy} and ε_{xx} . These strains, at maximum displacement, are illustrated in Figure 5.44. These original results from the DIC software are presented without any post-processing. The strains in the vertical direction range from 0.23 to 0.34. The localised strains in the horizontal direction are relatively large at the vertical edges of the samples (-0.121) but are much smaller in the centre of the specimen, away from the edges (-0.009). A *Matlab* code *strainDICLimess_pure.m* was written by the author to post-process the data provided by the DIC software. The code loads all *Matlab* files that contain matrices of engineering strains and confidence values. A confidence check is performed using the *sigma* values (which describe the match at a given point, see Section 5.3.4). The small horizontal strains (occurring in the centre of the sample) remain after the confidence check, but most of the values near the edges of the sample are eliminated due

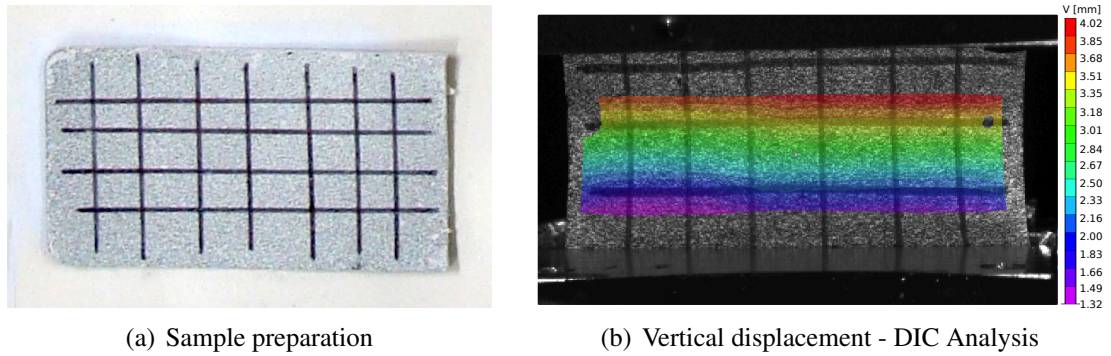


Figure 5.43: (a) Pure shear sample prepared for optical strain measurement. A white random speckle pattern and grid lines are both visible. (b) Displacement field, calculated by the DIC system at maximum vertical displacement (6 mm) of an isotropic 20% MRE, is shown. The vertical displacement ranges from 1.32 mm to 4.02 mm.

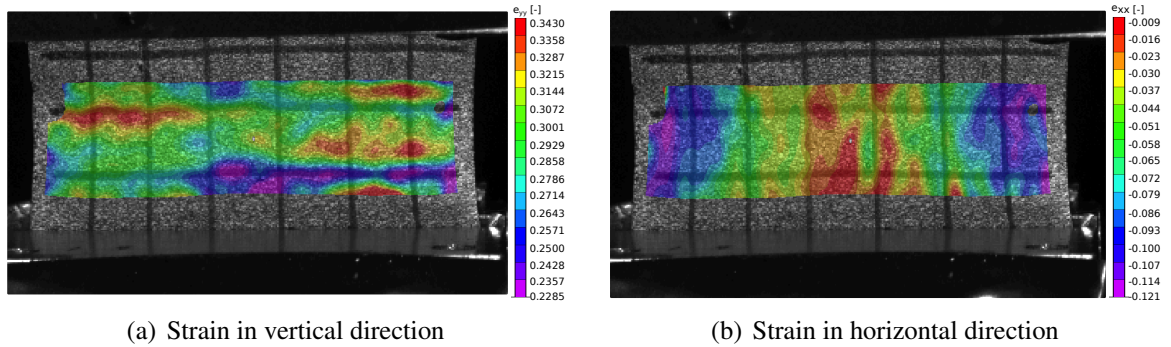


Figure 5.44: Vertical and horizontal strains calculated by the DIC system. An isotropic 20% MRE is shown at a displacement of 6 mm. The vertical strain ranges from 0.23 to 0.34 and the horizontal strain ranges from -0.009 to -0.121 ; smaller horizontal strains occur in the centre of the MRE sample, away from the edges of the sample.

to $\sigma = -1$. Larger values of strain remain just in a 5% region from the left and right edges of the sample, which are likely to be caused by boundary effects. The horizontal strain field after the confidence check is shown in Figure 5.45. The size of the AoI is reduced by cutting off this 5% from the left and the right ends. The mean values and standard deviations of both strains are calculated from the remaining AoI, and are plotted versus test time in Figure 5.46. The DIC results are good, as all subsequent cycles are similar and standard deviations are small. After the samples were stretched, a permanent deformation occurred, leading to buckling of the sample when the test machine crosshead moved back to the initial zero-displacement position. Pure shear samples buckled out of plane to a greater extent than uniaxial tension test samples (see Sections 5.1.2 and 5.3.4). The DIC software was unable to determine the strains near zero-displacement correctly, leading to oscillations in the strain versus time data near zero strain (see Figure 5.46). As the strain-time relationship is generally linear (except for the problems at the end of each unloading part), linear functions were fitted to each section of the loading and unloading cycles, and were used to relate the DIC data to

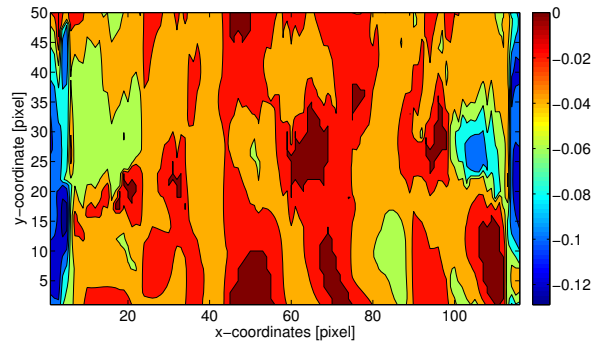


Figure 5.45: Horizontal strains calculated by the DIC system after unreliable values with $\sigma = -1$ were eliminated. The original horizontal strain field is shown in Figure 5.44b.

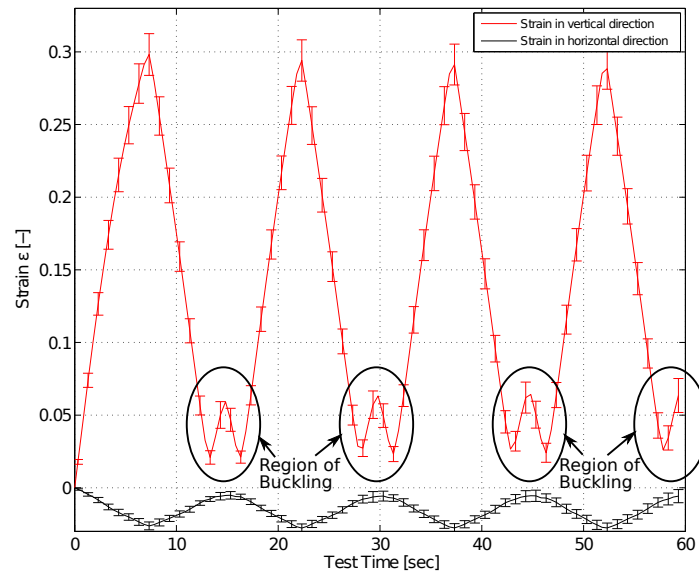


Figure 5.46: Mean and standard deviation of the strain in vertical and horizontal directions calculated by the DIC software and post-processed by the *Matlab* function *strainDIC-Limess_pure.m*. Both strains are plotted versus time. The regions where the DIC software is unable to determine the strains correctly are indicated. In this example, results were obtained from an anisotropic MRE with 20% horizontally aligned iron particles tested up to 6 mm.

the load-displacement data provided by the test machine. The coefficients were passed to a *Matlab* function *pureshear_DIC.m* to perform the rest of the analysis, *i.e.* the extraction of the third loading part and cutting and shifting (see Section 5.1.2).

DIC strains were verified using the gridlines and manual image analysis. A *Matlab* code *strainpixel_pure.m* was written to aid with the analysis of the measured pixel-positions. The distance between clamps in the reference state was used to convert from *pixel* to *mm*. The calculated distances in the reference image and in an image of a stretched state are marked in Figure 5.47. The vertical strain is determined using

$$\varepsilon_y = \frac{l_{v,1} - l_{v,0}}{l_{v,0}} \quad (5.4)$$

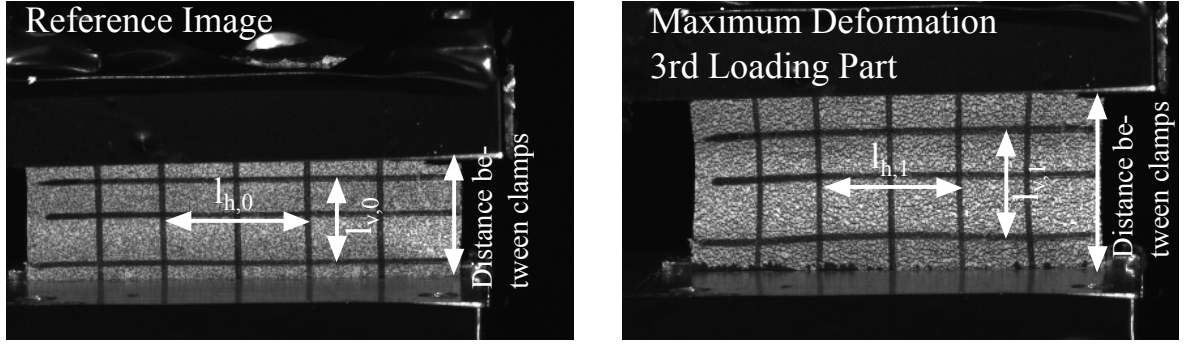


Figure 5.47: Reference image and image of the stretched state of an MRE sample. Distances between the clamps and vertical distances l_v and horizontal distances l_h between the lines in the reference image ($l_{v,0}$ and $l_{h,0}$) and in all subsequent images ($l_{v,1}$ and $l_{h,1}$) are defined.

where $l_{v,0}$ and $l_{v,1}$ are the mean values of the vertical distances between horizontal lines measured at all crossing points. The distances between the two inner vertical lines were taken to calculate the strains in the horizontal direction (to eliminate boundary effects as seen in the DIC analysis). Mean values from all crossing points are taken to calculate $l_{h,0}$ and $l_{h,1}$, respectively. The horizontal strain is calculated with:

$$\varepsilon_x = \frac{l_{h,1} - l_{h,0}}{l_{h,0}} \quad (5.5)$$

To link the results of the manual image analysis method to the load-displacement data of the test machine, the displacement of the top clamp was measured and a linear fit of the strain versus displacement data was performed. The coefficients of this linear functions were passed to a *Matlab* function *pureshear_pixel.m* to perform the rest of the data analysis. The manual image analysis method is time consuming and so only the pixel positions of the reference image and of six images of the third loading part were measured, which is sufficient to determine the linear relation between strain values and the displacement of the clamps.

To compare the DIC analysis with the manual image analysis method, the strain-time data and the stress-strain data of the third loading cycle are both shown in Figure 5.48. An anisotropic MRE with 20% horizontally aligned particles was used in this example. The manual method is found to capture the negative vertical strains which occur at the end of each unloading phase due to remnant deformation in the sample. The strains in the horizontal direction calculated with the manual image analysis method result in a zigzagging curve. The horizontal displacements are small; thus, considering the size of the measured crossing points, the manual method is probably not accurate enough to capture such small changes. Since in both methods data fitting to a linear function was used to relate force and strain, these problems are considered to be of minor importance. Figure 5.48b shows almost perfect agreement when plotting the final stress versus strain results produced by both methods.

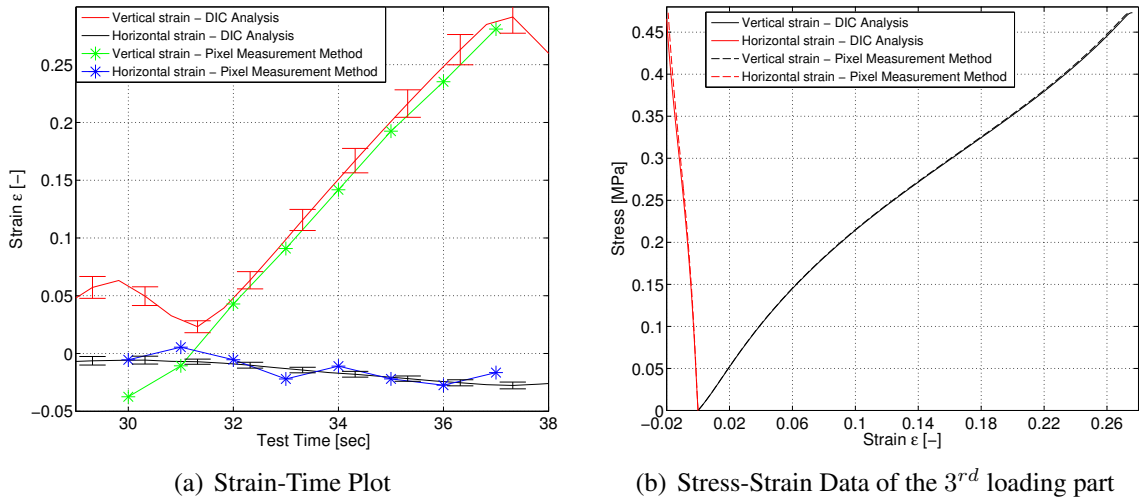


Figure 5.48: Comparison of strains obtained from the DIC analysis and from the pixel measurement method. Strain-time and stress-strain data of the third loading part of an anisotropic MRE with 20% horizontal aligned iron particles are shown as an example.

5.4.4 Tests in the Absence of a Magnetic Field

Pure shear tests conducted in the absence of a magnetic field were performed using the setup illustrated in Figure 5.40b. The general test method was explained in Section 5.1.1, and the specific procedure of the pure shear tests was given in Section 5.4.1. In this section, the stress-strain results of the preconditioning tests and the two no-field tests are compared. The behaviour of isotropic and anisotropic MREs is characterised using the *NoField02* stress-strain results, analysed as described in Section 5.1.2.

5.4.4.1 Comparison of Preconditioning, NoField01, and NoField02 Tests

In both the uniaxial compression (Section 5.2.3) and tension tests (Section 5.3.5), stress-strain results obtained from *NoField01* and *NoField02* test were found to diverge from a certain level of strain (see Tables 5.4 and 5.12). To study this issue further, here, the stress-strain data of the *Preconditioning*, the *NoField01*, and the *NoField02* tests are compared. The results of isotropic and anisotropic MREs that were tested up to 6 mm are illustrated in Figure 5.49. The full set of data for all types of MREs is provided in Appendix E.3. Surprisingly, in the case of pure shear experiments, the stress-strain results do not diverge. This is perhaps because the pure shear samples were found to recover to their original dimensions between each cycle test performed in the test series. The fact that no divergence between the *NoField01* and *NoField02* pure shear tests occurred leads to the conclusion that the magnetic field applied before the *NoField02* tests is not the reason for the divergence seen in uniaxial tension and compression tests (see Sections 5.2.3 and 5.3.5), and therefore points to the *Mullins* effect as a more likely cause of the divergence. It can be concluded that the strategy (used in both tension and compression tests) of directly comparing only the data

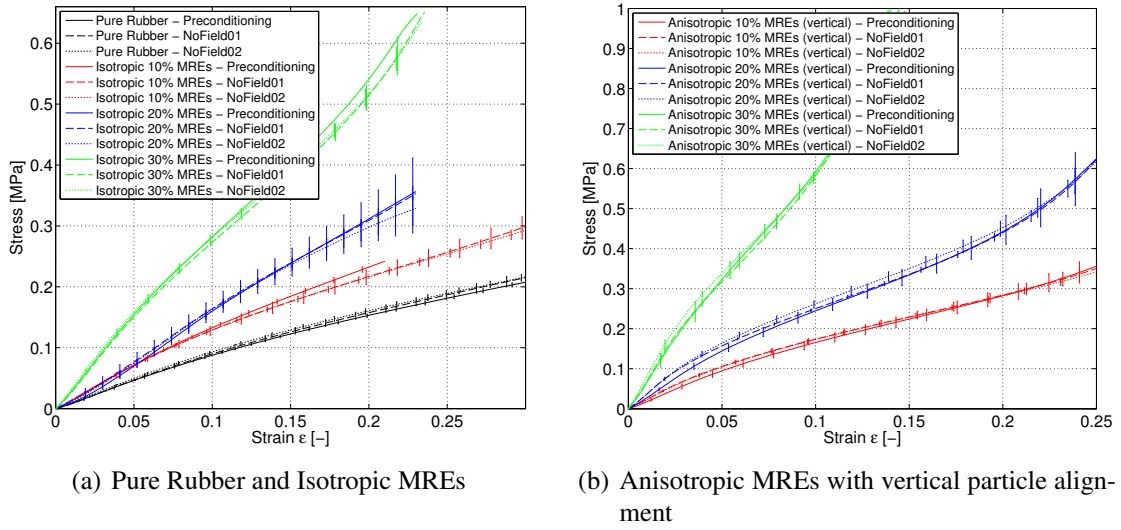


Figure 5.49: Stress-strain curves from *NoField01* and *NoField02* pure shear tests. Isotropic and anisotropic MREs with 10% to 30% CIP content, that were stretched up to 6 mm ($\approx 45\%$ strain), are compared.

that remain in agreement up to the point where the *NoField01* and *NoField02* tests diverge, is the best way to eliminate the influence of the *Mullins* effect when investigating the MR effect in MREs.

5.4.4.2 Comparison of MRE Samples

The stress-strain curves of the different types of MREs are compared in Figure 5.50 when tested up to two different strain levels (see Table 5.17). Note that large temporary remnant deformations within *NoField02* cycle tests were present in pure shear tests (this was the same

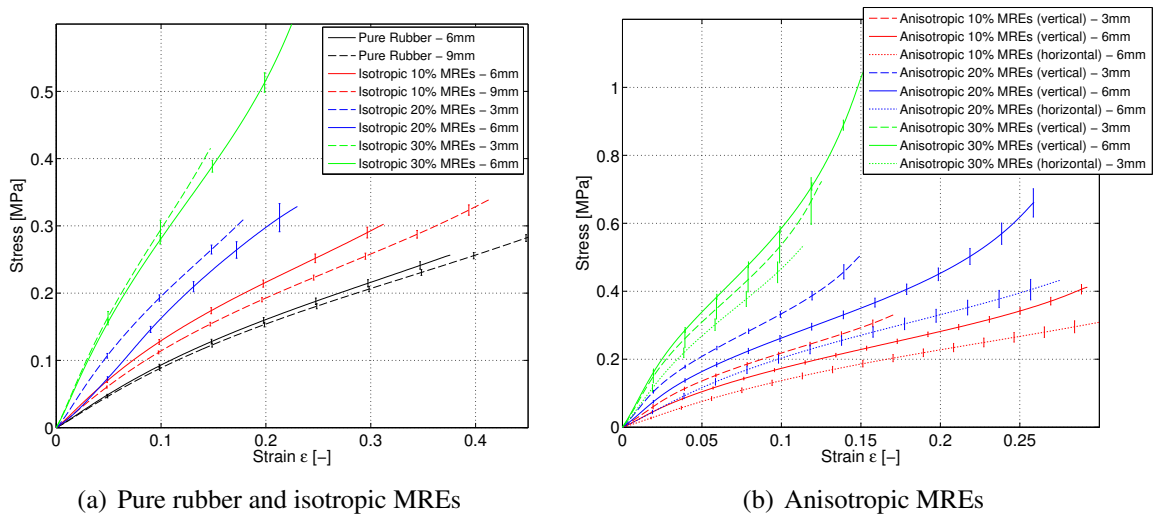


Figure 5.50: Stress-strain curves comparing different types of MRE samples: (a) pure rubber and isotropic MREs and (b) anisotropic MREs with vertical and horizontal particle alignment. Samples were tested up to different strain levels as listed in Table 5.17.

in each of the four tests performed in the test series, as the pure shear samples recovered to the original state between each test). This temporary remnant deformation was far larger for anisotropic MREs with high iron content compared to isotropic MREs with low iron content, resulting in the different strain levels observed in Figure 5.50 and all subsequent figures. Nevertheless, the samples were preconditioned to the strain levels listed in Table 5.17; this was the strain in the first cycle.

As expected, higher iron contents lead to higher stresses. Anisotropic MREs with vertical particle alignment exhibit higher stresses than the isotropic MREs with the same amount of iron, while the anisotropic MREs with horizontal particle alignment are quite similar to the isotropic MREs. Samples that were tested to larger strain levels result in softer stress-strain curves. Comparison of results from samples tested up to the same displacement is shown in Figure 5.51. To interpret the non-linear stress-strain behaviour, the tangent moduli, E_T ,

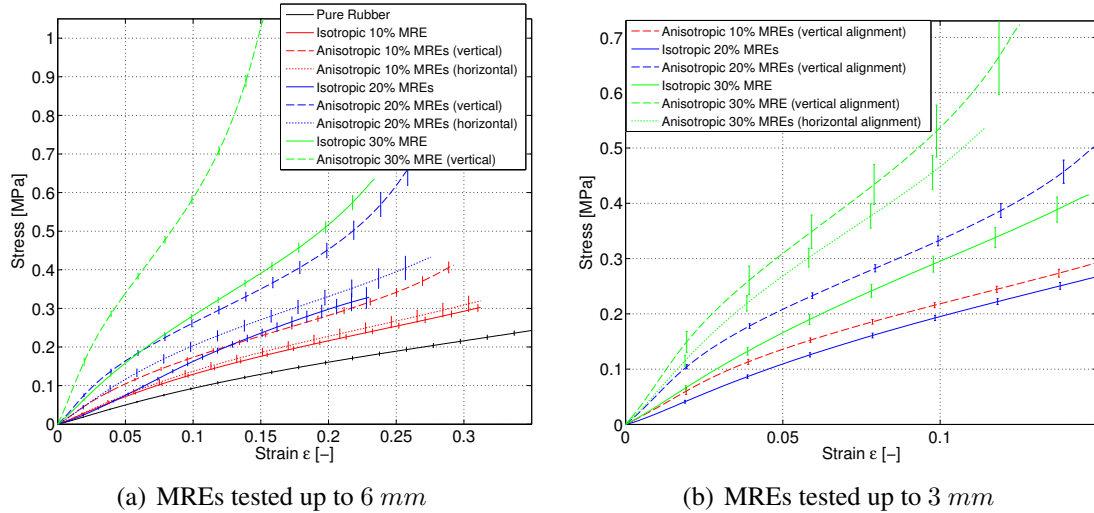


Figure 5.51: Stress-strain results comparing different types of MRE samples (a) tested up to 6 mm and (b) tested up to 3 mm.

are plotted versus the engineering strain in Figure 5.52 for MRE samples tested up to 6 mm and 3 mm. The MREs exhibit large moduli in the small-strain regime which decrease to a minimum at approximately 10% strain, but increase again at higher strains. An exception are the isotropic MREs with 20% iron volume fraction; here the curve shape is different. Anisotropic samples exhibit larger tangent moduli than isotropic MREs. Usually, the MRE samples tested up to 3 mm exhibit larger moduli compared to the same type of MRE tested up to 6 mm. This is explained by the stress-softening *Mullins* effect. The tangent moduli, E_T , between 1% and 2% strain and the initial secant moduli, E_{0-5} , are listed in Table 5.20. The stiffness increase of the isotropic MREs compared to the pure rubber samples and the stiffness increase of the anisotropic MREs compared to isotropic MREs (with the same iron content) calculated with E_{0-5} are provided in the same table for those samples tested up to the same displacement. The moduli and also the increases in moduli (listed in Table

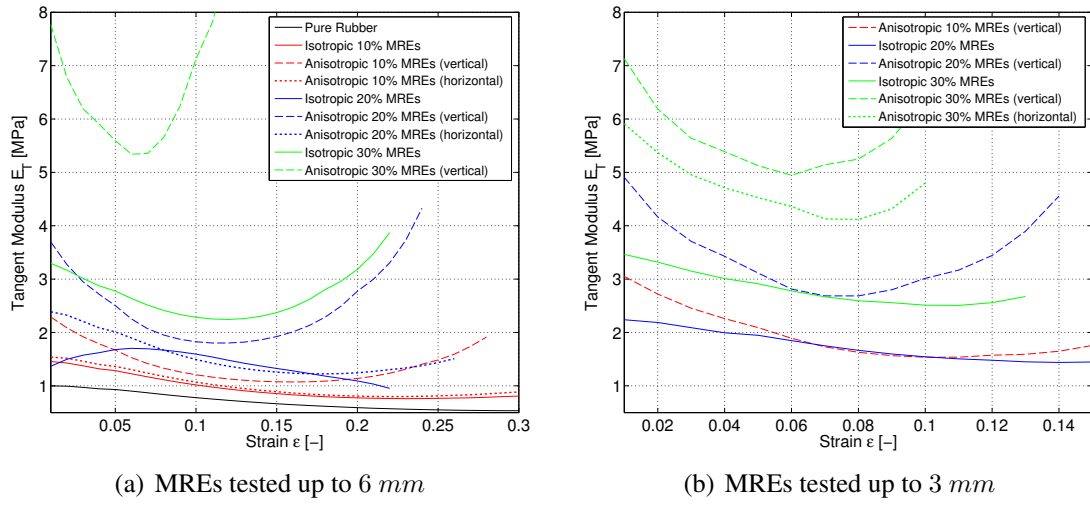


Figure 5.52: Tangent moduli versus strain comparing different types of MRE samples (a) tested up to 6 mm and (b) tested up to 3 mm. The tangent moduli are calculated with linear fits of 1% strain increments of the stress-strain data, and are illustrated from 1% strain.

MRE Sample	Iron [%]	up to ... [mm]	E_{0-5} MPa	E_T MPa	Increase compared to ... [%]
Pure Rubber	0	6.0 9.0	1.00 0.94	1.00 0.94	
Isotropic MREs	10	6.0	1.43	1.46	43.0
		9.0	1.25	1.26	33.0
	20	3.0	2.19	2.24	-
		6.0	1.50	1.37	50.0
	30	3.0	3.32	3.46	-
		6.0	3.17	3.30	217.0
Anisotropic MREs - vertical alignment	10	3.0	2.72	3.05	-
		6.0	2.09	2.29	46.2
	20	3.0	4.16	4.91	90.0
		6.0	3.27	3.70	118.0
	30	3.0	6.19	7.13	86.4
		6.0	6.78	7.77	113.9
Anisotropic MREs - horizontal alignment	10	6.0	1.52	1.54	6.3
	20	6.0	2.33	2.39	55.3
	30	3.0	5.37	5.91	61.7

Table 5.20: Initial secant moduli, E_{0-5} , and tangent moduli, E_T , obtained from stress-strain curves of pure rubber, isotropic, and anisotropic MREs with 10% to 30% CIP content (*NoField02*) are listed. The relative increase of isotropic MREs compared to pure rubber and the relative increases of anisotropic MREs compared to isotropic MREs with same iron content, calculated with E_{0-5} , are provided (only for samples tested up to the same displacement).

5.20) are similar to the results of uniaxial tension tests (compare to Table 5.13). The initial secant and tangent moduli (Table 5.20) are plotted versus the iron volume fraction (samples preconditioned to 6 mm) in Figure 5.53a and versus the preconditioning level in Figure 5.53b. The moduli increase with increasing iron content in the MREs. However, in contrast

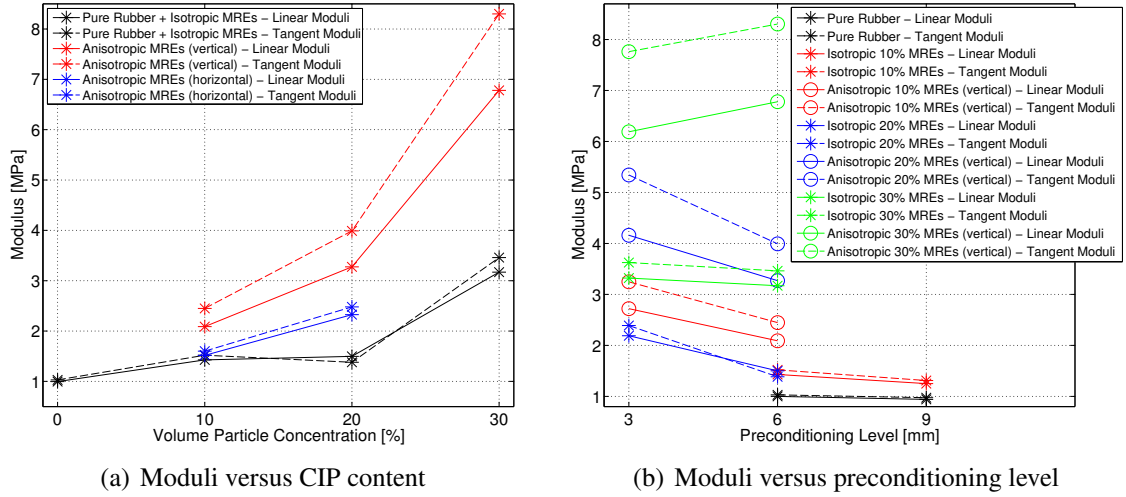


Figure 5.53: Moduli E_{0-5} and E_T as listed in Table 5.20 versus (a) the volume particle concentration (MREs preconditioned up to 6 mm) and (b) the preconditioning level.

to the results found in tension tests (see Figure 5.33) the relationship between the moduli and the iron content is not linear. In agreement with the tension tests, the moduli are smaller when the samples are stretched to a higher strain level. An exception are the anisotropic MREs with 30% iron content, where the samples are stiffer when tested up to 6 mm.

5.4.4.3 Strain in the Horizontal Direction

For the case of pure shear, ideally the strain in the horizontal direction should be zero, since the theory of pure shear assumes only through-thickness contraction of the sample. Experimentally this was not perfectly achieved as discussed in Section 5.4.3. The strains in the horizontal versus vertical directions for all types of MRE samples tested up to 6 mm are shown in Figure 5.54. The maximum observed horizontal strain observed in the AoI is 3%, and occurs in isotropic MREs with 30% iron content stretched to 24% vertical strain (in the third loading cycle). Usually, the vertically-aligned anisotropic MREs exhibit larger horizontal strains than isotropic MREs with the same iron content, while horizontally-aligned anisotropic MREs tend to exhibit lower horizontal strains compared to equivalent isotropic samples.

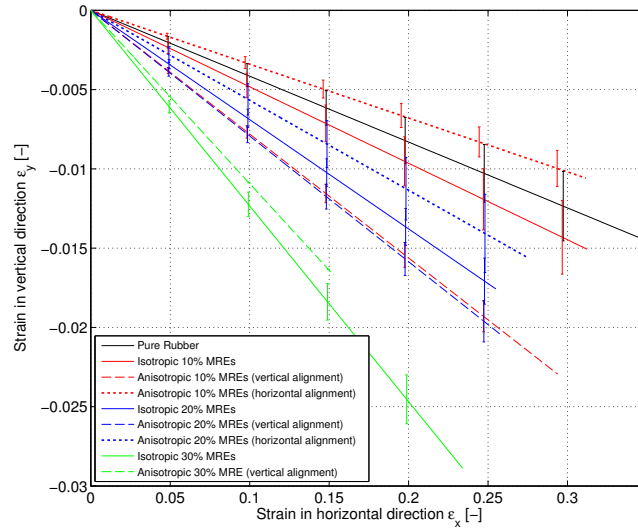


Figure 5.54: Strain in the horizontal versus vertical direction of all MRE samples tested up to 6 mm. Mean values and standard deviations of the third loading cycle are shown.

5.4.5 Characterisation of the Magneto-Rheological Effect

In the pure shear test series, only one magnetic field strength was applied to study the MR effect. The average applied magnetic flux was 290.6 mT in the vertical direction within the volume occupied by the MRE sample ($\mu_r = 1$). Due to the large width of the pure shear specimens, a magnetic field strength in the horizontal direction was present, with an average strength of 59.5 mT. The magnetic field was non-uniform in terms of both strength and direction of the flux lines (see Section 5.4.4). This adds to the complexity of the test environment in the pure shear test setup. Nevertheless, MR effects were found. The absolute and relative MR effects (Equations 5.1 and 5.2) are compared in Figure 5.55 and 5.56 for samples tested up to 6 mm and 3 mm, respectively. The full set of test results for stress, tangent moduli, and relative MR effect versus engineering strain, for both the *NoField02* and the *Magnet53* tests are given in Appendix E.3. In contrast to the results of uniaxial tension tests (Section 5.3.6), the MR effects are usually larger in MRE samples preconditioned to a lower displacement level. The largest relative increases in stiffness of about 75% were achieved with anisotropic vertically-aligned MREs with 10% and 20% iron volume fraction tested up to 3 mm (approximately 23% strain). MREs with 30% iron content do not show high MR effects at all and also the anisotropic MREs with horizontal particle alignment do not perform well (seen earlier in compression, Section 5.2.4). The MR effect of pure rubber in the small strain regime indicates an experimental error of about 20%, which is large compared to the errors found in compression and tension tests. The relatively small MR effects and the large experimental error might be due to non-uniformity of the magnetic flux density in pure shear experiments. MR effects calculated using E_{0-5} and the maximum MR effects calculated using E_T are listed in Table 5.21 for all types of MREs. The maximum

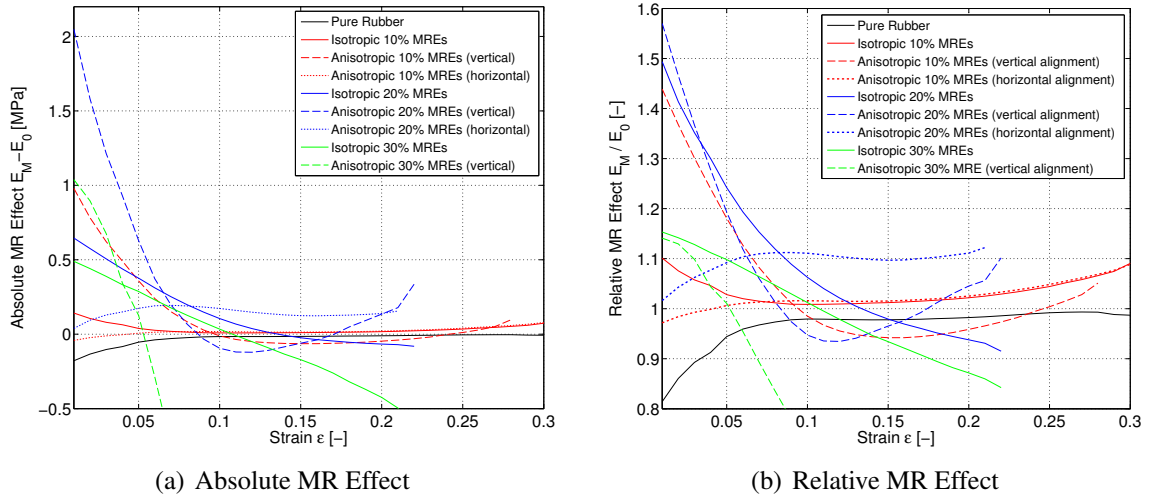


Figure 5.55: Absolute and relative MR effects, calculated with E_T , of MRE samples tested up to 6 mm achieved with a magnetic induction of 290 mT are illustrated versus strain.

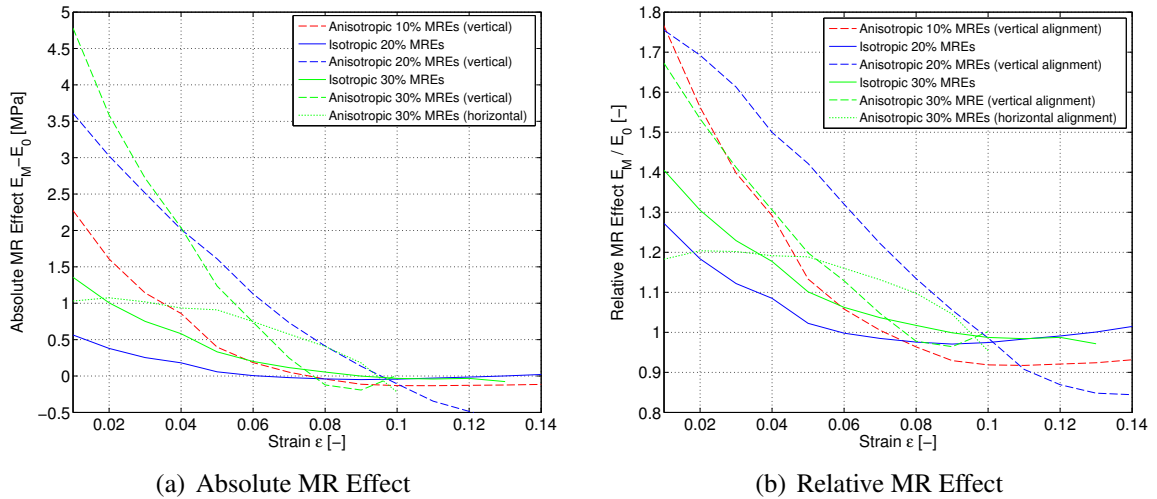


Figure 5.56: Absolute and relative MR effects, calculated with E_T of MRE samples tested up to 3 mm achieved with a magnetic induction of 290 mT are illustrated versus strain.

of the two values is shaded in grey in the table and used to study the relationship between the MR effect and the volume particle concentration in Figure 5.57a and also between the MR effect and the preconditioning level in Figure 5.57b.

In contrast to the compression and tension tests, where the relative MR effect increased linearly with increasing iron content, the MREs with 20% iron content show relatively high MR effects while MREs with 30% iron volume fraction exhibit very low increases in stiffness. The no-field moduli found for MREs with 30% iron volume fraction were found to be very high (see Figure 5.53) compared to MREs with lower iron content. A very large no-field modulus results in a lower relative MR effect. Consequently, a probable reason for the low MR effects in the 30% MREs might lie in the material's micro-structure; the pure shear samples are just 1 mm thick and the particles may have struggled to distribute uniformly

MRE Sample	Iron [%]	up to ... [mm]	Absolute MR Effect		Relative MR Effect	
			E_{0-5}	E_T	E_{0-5}	E_T
Pure Rubber	0	6.0	-0.0974	-0.0037	0.9021	0.9933
		9.0	-0.0782	0.0122	0.9170	1.0157
Isotropic MREs	10	6.0	0.0763	0.1418	1.0534	1.1012
		9.0	0.0589	0.1140	1.0473	1.0942
	20	3.0	0.2189	0.5635	1.1001	1.2721
		6.0	0.5859	0.6460	1.3914	1.4937
	30	3.0	0.7470	1.3567	1.2251	1.4050
		6.0	0.4709	0.4896	1.1486	1.1532
Anisotropic MREs - vertical alignment	10	3.0	1.0408	2.2728	1.3826	1.7655
		6.0	0.7398	0.9798	1.3542	1.4389
	20	3.0	3.1894	3.6096	1.7659	1.7547
		6.0	1.4276	2.0481	1.4359	1.5701
	30	3.0	2.8807	4.7781	1.4657	1.6722
		6.0	1.3208	1.0382	1.1948	1.1411
Anisotropic MREs - horizontal	10	6.0	-0.0100	0.0783	0.9934	1.0884
	20	6.0	0.1200	0.1552	1.0516	1.1222
	30	3.0	1.4374	1.0747	1.2677	1.2038

Table 5.21: Absolute and relative MR effects achieved with 290 mT average magnetic induction, and calculated using E_{0-5} and E_T (maximum values), see Figures 5.55 and 5.56). The maximum relative MR effects (E_{0-5} or E_T) are shaded grey.

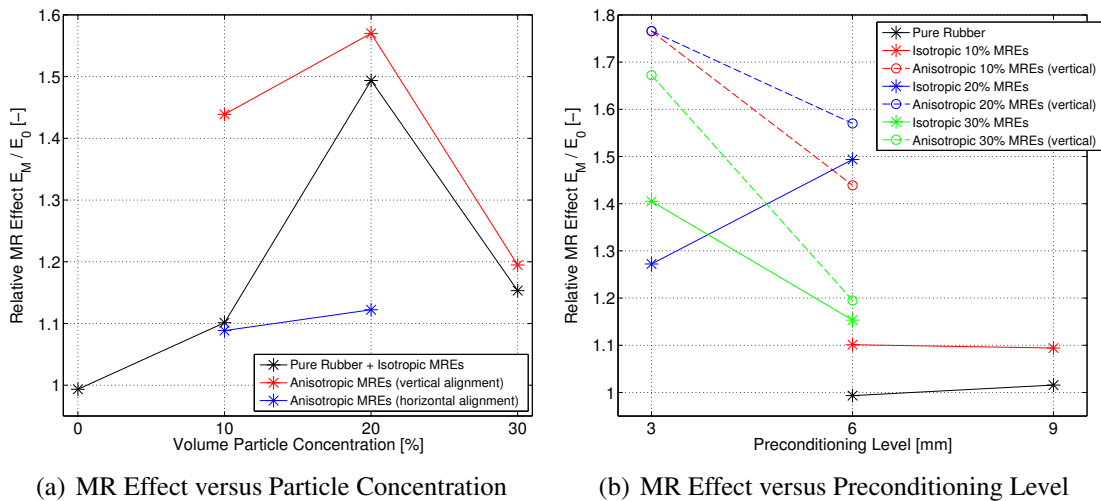


Figure 5.57: Relative MR effect of MRE samples achieved with a magnetic induction of 290 mT are illustrated versus (a) the volume particle concentration (MREs preconditioned up to 6 mm) and (b) the preconditioning level. Maximum MR effects as indicated in Table 5.21 are used.

in isotropic and to align properly in anisotropic MREs. Problems with the manufacture of MREs containing 30% iron volume fraction have been reported previously in the literature. Boczkowska *et al.* (2012) observed reduced micro-structural alignment of the particles in MREs containing 30% iron content, and also measured a drop in the magnetic anisotropy coefficient by performing magnetic field measurements (Boczkowska *et al.*, 2007).

5.4.6 Summary of Pure Shear Tests

Comparison between the no-magnetic field tests revealed no divergence between the results, in contrast to the compression and tension tests where stress-strain curves of *NoField01* and *NoField02* test diverged from a certain level of strain. Pure shear samples recovered quickly to their original dimensions between each of the tests performed in the test series due to their lower thickness. Both compression and tension samples experienced permanent deformations that led to a higher strain level in the subsequent test, and consequently due to the *Mullins* effect, to differences in the stress-strain results. Different types of MREs, tested up to both 6 mm and 3 mm displacement in pure shear tests, were compared. In agreement with the compression and tension test results, anisotropic MREs with particle alignment in the loading direction revealed the highest stresses and moduli, and isotropic and anisotropic MREs with horizontal particle alignment showed similar stress-strain curves and moduli. The moduli increased with increasing iron content. In the case of pure shear experiments, the magnetic flux density was non-uniform in terms of both the strength of the field and the direction of the flux lines. In the case of isotropic 20% MREs and vertically-aligned anisotropic MREs with 10% and 20% iron volume fraction, the MR effects were large in the small strain region, decreasing down to 1 or even lower in the mid-strain region, but increasing again for strains larger than 15%. The MR effects increased with increasing iron volume fraction. In contrast to the results achieved in uniaxial tension, a lower preconditioning level led to larger MR effects. In general, the MR effects achieved in the pure shear setup are lower than those achieved in uniaxial compression and tension.

The ideal state of pure shear, where the horizontal strains are zero, was experimentally not achieved, small strains up to 3% were measured. This, and the non-uniformity of the magnetic flux distribution must be taken into account when using these experimental data to develop constitutive models in future.

5.5 Equi-Biaxial Tension Tests

Experimental data from a multi-axial deformation mode are important to determine unique model parameters of constitutive material equations. To this end, equi-biaxial tension tests were performed to characterise the MRE behaviour in the absence and in the presence of a magnetic field. A bespoke test rig was designed to facilitate testing of MREs under equi-biaxial deformations using a standard uniaxial test machine.

The general test method and the method of analysis was described in Section 5.1. The structure of Section 5.5 is as follows: Section 5.5.1 gives the specific procedure of the equi-biaxial tension tests. A detailed description of the test rig is given in Section 5.5.2. The compliance of the setup and the magnetic field distribution within the volume occupied by

the MRE sample are also examined in this section. Strain measurement is discussed in Section 5.5.3. Equations for the stress calculations are given in Section 5.5.4. Results of the *NoField* tests are presented in Section 5.5.5 for both isotropic and anisotropic MREs, and the MR effects resulting from the applied magnetic flux density are discussed in Section 5.5.6. Suggestions for improvements of the test setup and procedure are given in Section 5.5.7. The investigations are summarised in Section 5.5.8.

To aid with the analysis of the equi-biaxial tension tests, the *Matlab* function *biaxial.m* was written, which includes the cut-and-shift process described previously in Section 5.1.2, the stress calculations specific to each type of MRE (detailed in Section 5.5.4), and the analysis of the optically measured strains (see Section 5.5.3). For further details on the *Matlab* procedure and the employed sub-functions, the reader is referred to Appendix D. The *Matlab* codes are saved on a DVD and can be consulted for even more in-depth information.

5.5.1 Procedure of the Equi-Biaxial Tests

Tests were performed on isotropic and anisotropic MREs with up to 30% iron content, conducted at a test speed of 10 *mm/min* with up to 10 *mm* vertical displacements, resulting in approximately 10% strain in the stretching directions. An exception are the anisotropic MREs with 30% iron particles (the strongest MREs tested), which were only stretched up to 7% strain. Due to the clamping system (described in Section 5.5.2) it was not possible to stretch these sample to a larger strain level. Also due to damage to the specimens following clamping, it was not possible to re-use the MRE samples in subsequent tests in a test series. This is a notable change in procedure compared to the previous tests discussed in Sections 5.2 to 5.4. Consequently, only two different testing steps were carried out: tests without an applied magnetic field (*NoField*), followed by tests with an average magnetic flux of 67.5 *mT* (*Magnet*). Note that both the *NoField* and the *Magnet* tests were 4-cycle tests and the third loading cycle was used for the analysis (see Section 5.1.2), as with the previous large-strain experiments. It is expected in the case of equi-biaxial tests that divergence between several test results would not occur, and that it is therefore acceptable to use the samples only once. The reasons for this are as follows: Stress-strain curves from repeated tests in the absence of a magnetic field were found to be in agreement in the case of pure shear tests. The divergence between no-field tests observed in compression and tension tests were found to be due to the *Mullins* effect (as permanent deformations led to higher strain levels in subsequent tests). Pure shear samples were found to recover to their original dimensions after each step in the test series; *i.e.* permanent deformations did not occur in pure shear samples and consequently no divergence between test results occurred (see Sections 5.2.3, 5.3.5 and 5.3.5). Both the pure shear and equi-biaxial tension specimens are thin sheets of material and measurements of the biaxial sample dimensions after testing confirmed that permanent deformations were

not present. A DIC system was used to measure engineering strains, and grid lines were drawn on the samples to enable a manual verification of the DIC strain. The equi-biaxial tension tests were conducted with the uniaxial *Zwick Z250* test machine, measuring the vertical force and displacement. A special test rig was designed to enable equi-biaxial testing on this uniaxial test machine (described in Section 5.5.2). However, in order to calculate the stresses in the two principal stretching directions, assumptions were required in the case of both anisotropic MREs and during the application of magnetic fields (see Section 5.5.4).

5.5.2 Equi-Biaxial Test Setup

A special test rig, designed in accordance with the *British Standard* (BS 903-5, 2004), was manufactured to perform equi-biaxial tension tests using a universal test machine (*Zwick Z250*), see Figure 5.58. The rig consists of upper and lower frames, both manufactured from PTFE (Teflon). The two frames do not contact each other, and are attached to the test machine. Test specimens are held in the rig using three sliding clamps on each side of the specimen; the clamps were free to move along the frame side length as the test proceeded, ensuring an almost uniform biaxial stretch of the MRE samples. To reduce friction and to avoid interactions between the test rig and the magnetic field, the rig and the sliding clamps were made of Teflon. The clamps for holding the rubber were made of aluminium and brass screws. The dimensions of the parts of the test rig and the assembled setup are given in the technical drawings in Appendices B.15 to B.18. A naming convention is used in this section when describing the different types of experiment (see Section 5.5.4). CASE 1: An isotropic MRE tested without permanent magnets is shown in Figure 5.58. The vertical load, P_V ,

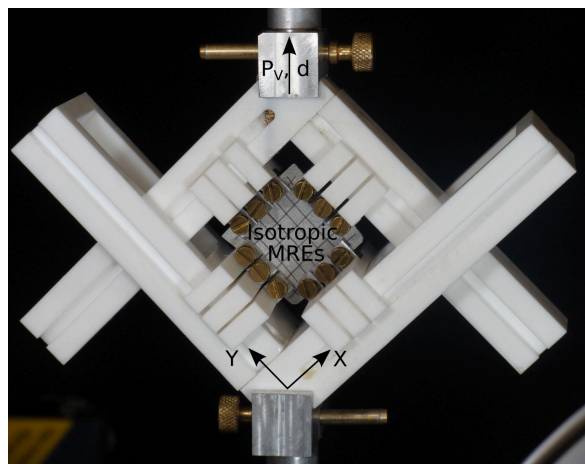


Figure 5.58: Biaxial test rig attached to the uniaxial *Zwick Z250* test machine. The rig consists of upper and lower frames that do not touch. The MRE sample is held by three sliding clamps on each side. The rig is made of Teflon and aluminium to reduce friction and to avoid magnetisation of the rig. An isotropic MRE is clamped into the rig (CASE1), and the vertical recorded load, P_V , and displacement, d , and the coordinate system are indicated.

and displacement, d , recorded by the test machine are indicated in the figure. The magnetic field was created using four permanent magnets, two placed on either side of the test rig with a separation distance of 140 mm. Permanent magnets and the direction of the particle alignment in anisotropic MREs are shown in Figure 5.59 (CASE2 to CASE5).

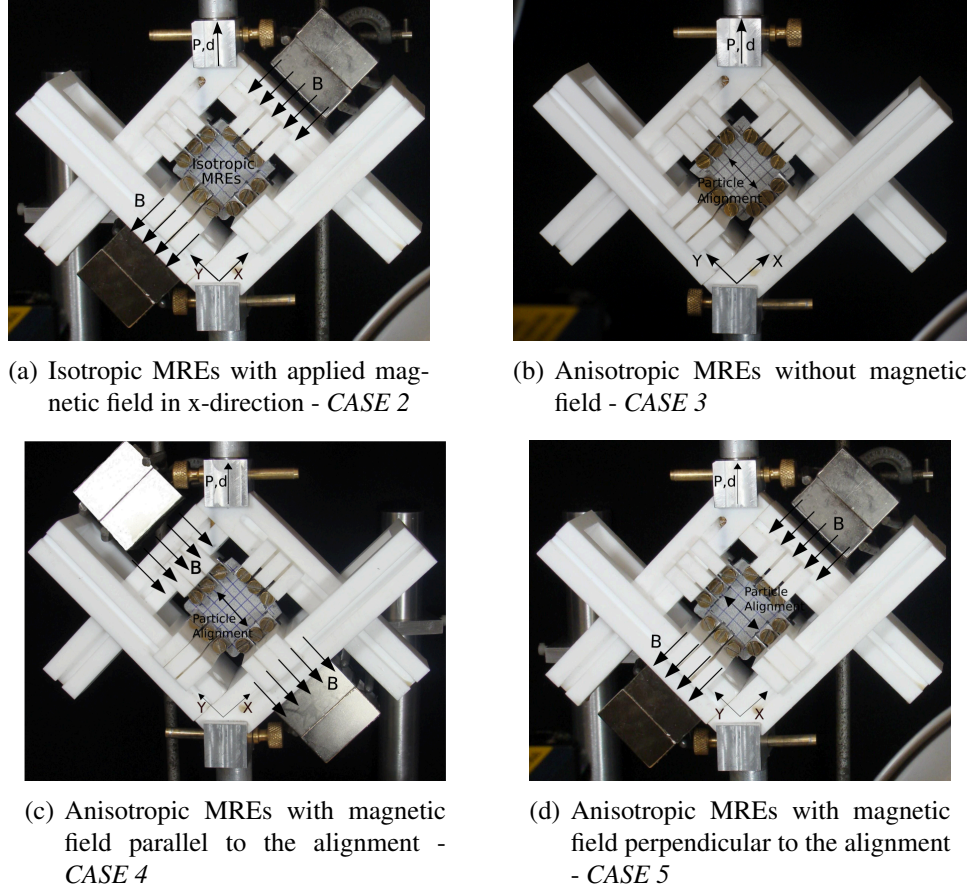


Figure 5.59: Biaxial test setup with (a) an isotropic MRE with applied magnetic induction in x-direction, (b) an anisotropic MREs with particle alignment in y-direction, without magnetic field, and with magnetic field (c) in y-direction parallel to the particle alignment, and (d) in x-direction perpendicular to the particle alignment. The definitions of CASE 2 to CASE 5 are used to derive the equations for the stress calculation in Section 5.5.4.

5.5.2.1 Compliance of the Test Rig

Manufacturing the test rig using Teflon created concerns regarding the stiffness of the test rig, so finite element simulations (using *Abaqus*, see Figure 5.60) were performed to investigate this issue, *i.e* the ability of the test rig to induce equi-biaxial deformation kinematics. To simplify the finite element model, only the stretched state of the test rig (to 10 mm in vertical direction in accordance to the experiment) was implemented, ignoring the motion of the sliding clamps. The forces generated by the stretched samples were used as boundary conditions in the simulation. Model dimensions are provided in Appendix B.18. Boundary

conditions defined in the model prevent deformation or rotation of the frame at the point of attachment with the aluminium rods, which are not modelled in the simulation. Loading is implemented as a surface traction over the $10 \times 8 \text{ mm}$ area of each clamp attached to the upper and lower frames of the test rig. The applied stress is estimated using the maximum vertical force of 80 N (recorded during experiments). The material properties used in the simulations are taken from (MatWeb, 2013c); a Teflon modulus of 0.496 GPa and Poisson's ratio of 0.46 are used. The properties of aluminium were given in Table 5.1, *i.e.* an elastic modulus of 68.9 GPa and a Poisson's ratio of 0.33 . The model of the biaxial test rig, together with the defined boundary conditions and surface tractions are illustrated in Figure 5.60a. The deformed geometry is shown with a scale factor of 15 in Figure 5.60b. The

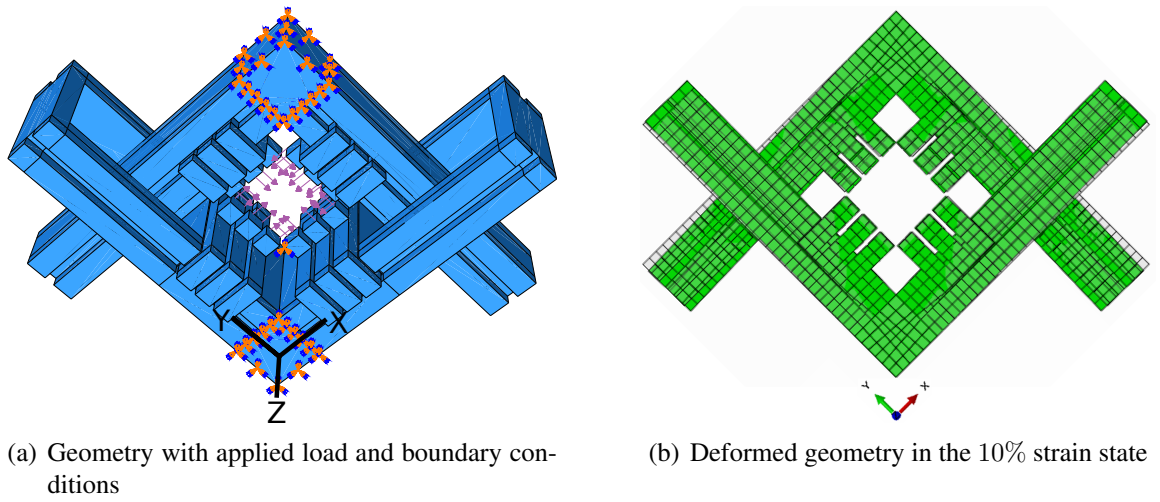


Figure 5.60: Geometry implemented into *Abaqus*. (a) Isometric view of the geometry together with the defined load and boundary conditions, and (b) the deformed geometry in the $x-y$ view in the 10% strain state, which is when the top frame is displaced by 10 mm in the vertical direction. The maximum deformation is 0.292 mm (magnitude value of U). The scale factor of 15 is used to illustrate the deformations.

magnitude of the deformation, U , is illustrated in the contour plot in Figure 5.61a, and also plotted versus the length along the inner sides of the frames in Figure 5.61b. The position of the MRE test specimen is indicated in the figure. The deformation of the frame results in a maximum displacement across the upper frame in the region of the MRE sample of about 0.125 mm . The equivalent displacement across the lower frame in the region of the MRE sample is about 0.06 mm . To examine the additional deformation of the clamps, distinct models of the clamps (not merged to the upper and lower frame structures of the test rig) were created in *Abaqus*. The undeformed and deformed geometry of the clamps, together with the values of vertical deformation U_2 are illustrated in Figure 5.62. The clamps are pin-joined to the biaxial frames. The boundary conditions are applied at the areas of size $6 \times 10 \text{ mm}$ that hang in the biaxial frames. The applied surface traction is consistent with that applied in the model of the complete biaxial rig. The deformation of the clamps must be

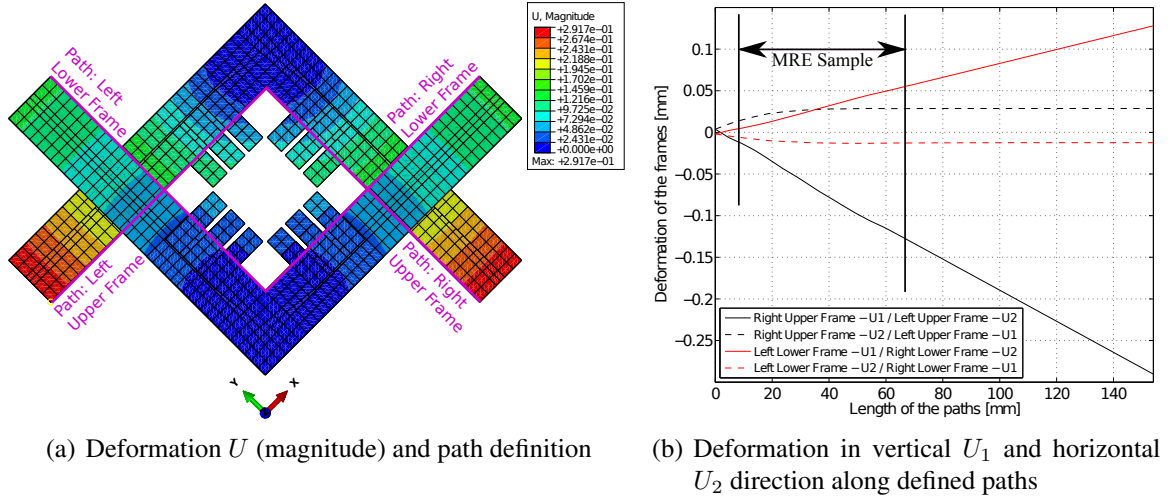


Figure 5.61: The deformation of the biaxial test rig. (a) Contour plot of the deformation U (magnitude): the maximum deformation is 0.292 mm . The defined paths *Left Upper Frame*, *Right Upper Frame*, *Left Lower Frame*, and *Right Lower Frame* are illustrated. (b) Line plots of vertical and horizontal deformation U_1 and U_2 , respectively, along the defined paths. The position of the MRE sample in the 10% strain state is indicated.

added to the deformation of the frames in order to determine the total rig deformation at the borders of the MRE sample. The maximum overall deformation of the upper frame structure is $0.125 + 0.057 = 0.18 \text{ mm}$ at one end of the sample, and 0.08 mm at the other end. The maximum overall deformation of the lower frame structure is $0.06 + 0.402 = 0.46 \text{ mm}$ at one end of the sample, and 0.41 mm at the other. The deformation of the lower frame structure results mainly from the deformation of the clamps. The deformation of the biaxial rig leads to a reduction in strain compared to a perfectly rigid rig of 0.76% . As the differences in strain are less than 1% , this is an acceptable deformation validating the test rig as a rig that can stretch the MRE samples equally in both directions. Note, however, that the deformation of the test rig becomes larger when stretching the MRE samples beyond 10% strain, poten-

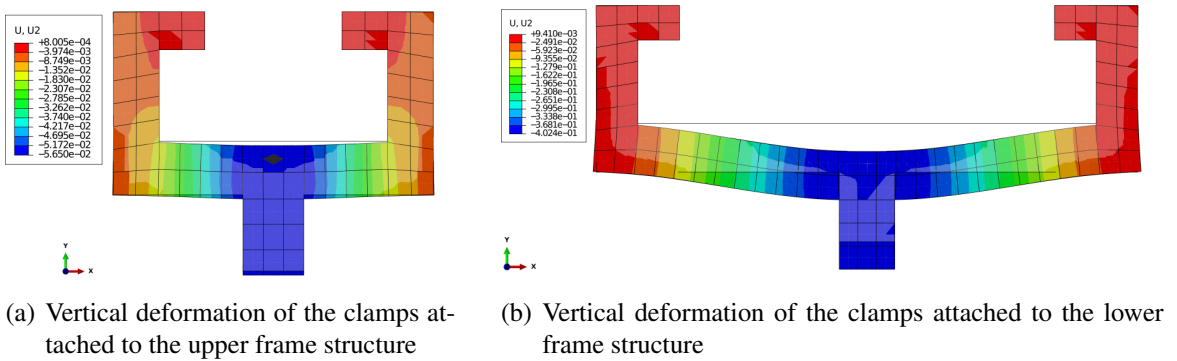


Figure 5.62: Contour plot of the vertical deformation of the clamps attached to the (a) upper frame structure and (b) lower frame structure of the test rig, is shown on the deformed geometry (scale factor 10).

tially inducing kinematics significantly different to the equi-biaxial kinematics aimed for in these tests.

The strains are measured optically rather than calculated from the cross-head displacement in order to eliminate errors due to the compliance of the test machine and test rig. The stresses are well below the ultimate tensile strength of 34.5 MPa (MatWeb, 2013c) with 9.93 MPa occurring in the clamp attached to the lower frame structure in the region where the aluminium clamps are connected to the Teflon sliding clamps.

5.5.2.2 Distribution of the Magnetic Flux Density

The magnetic field distributions within the volume of space occupied by the MRE sample is investigated; to this end a finite element model of the biaxial setup is created using *Comsol*. The settings in *Comsol* are the same as for the model described in Section 4.4 to identify the permeabilities of MRE samples. The geometry for the biaxial setup is shown in Figure 5.63. Symmetry conditions meant that only one quarter of the setup was modelled. The test rig itself is made of non-magnetic material, and has no influence on the magnetic flux calculations. As with the pure shear tests (Section 5.4.2) the magnetic flux density in x- and

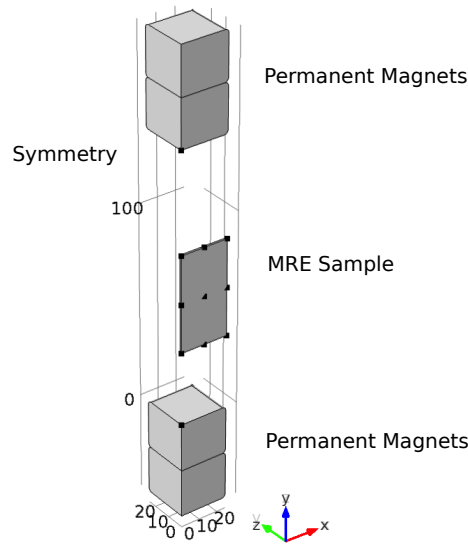


Figure 5.63: Geometry implemented in *Comsol* to calculate the magnetic flux distribution within the biaxial test setup. Two magnets are placed on either side of the test rig with an inter-magnet distance of 140 mm . Symmetry conditions are applied, so only one quarter of the setup is modelled.

y-directions have to be considered. Since the biaxial test samples are square, a significant component of the magnetic flux exists perpendicular to the main magnetic flux direction. Knowledge of B_Y and B_X is even more important in the case of the biaxial tests as deformation is induced in both these directions. The distribution of the magnetic flux density, B_Y and B_X , within the volume usually occupied by an MRE sample (but calculated in the absence of a sample with $\mu_r = 1$) is shown as a contour plot in Figure 5.64. The average value

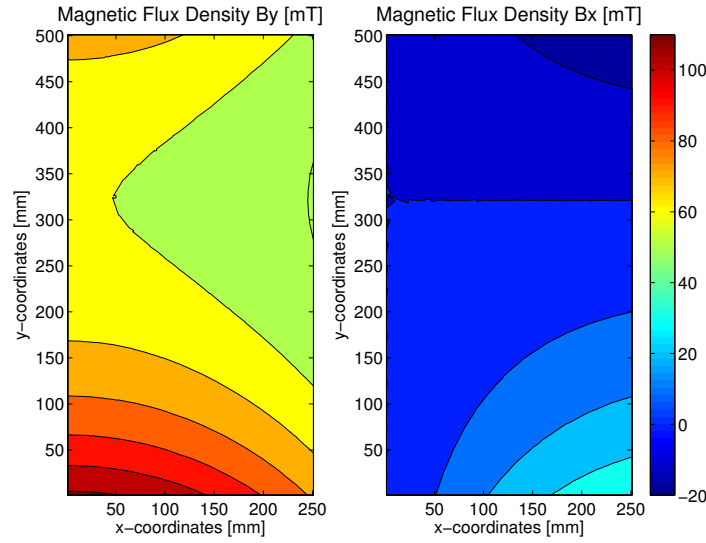
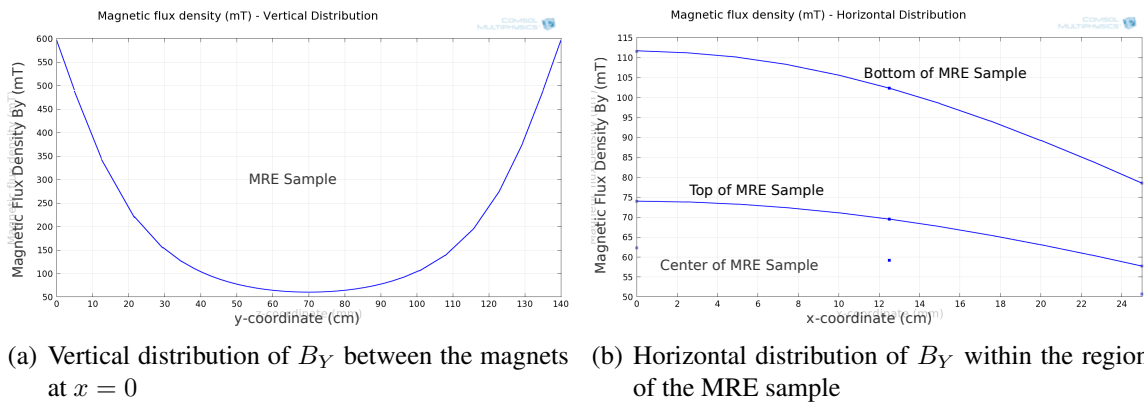


Figure 5.64: Magnetic flux density B_Y in the vertical direction (main magnetic flux direction) and B_X in the horizontal direction within the area of the MRE sample in $[mT]$ (calculated in the absence of a sample with $\mu_r = 1$) with $B_{Y,mean} = 67.5 \text{ mT}$ and $B_{X,mean} = 7.1 \text{ mT}$.

of B_Y taken over the volume of the MRE sample is 67.5 mT , and the flux density differs across this volume by about 90.4%. In contrast, the average value of B_X is only 7.1 mT , but with great variation in the field strength of around 357.2%. The differences in the horizontal flux density are far larger than that of the vertical flux density, as the samples are wide and the magnetic flux in the horizontal direction occurs mainly at the borders of the MREs; the horizontal field strength in the middle of the samples is nearly 0 mT .

The magnetic field strength in the experimental setup was measured with a Gaussmeter at various positions. The vertical and horizontal distribution of B_Y are shown in Figure 5.65 and are compared with the experimental results. The *Comsol* predictions match very well



(a) Vertical distribution of B_Y between the magnets at $x = 0$ (b) Horizontal distribution of B_Y within the region of the MRE sample

Figure 5.65: Magnetic induction B_Y calculated by *Comsol* are compared with the experimental measurements (red crosses). (a) The vertical distribution between the permanent magnets and (b) the horizontal distribution in the region of the MRE sample are shown. Both the calculation and experimental measurements were performed in the absence of an MRE sample, and are in good agreement.

with the experimental measurements. The vertical distribution of the magnetic flux density in Figure 5.65a confirms that the MRE samples are placed almost at the centre between the permanent magnets, and while this results in low magnetic field strength it also produces quite low variation in the magnetic flux density within the sample volume compared to that experienced in the pure shear setup (Section 5.4.2).

The magnetic induction within the volume occupied by the MRE sample was also calculated in the presence of the samples ($\mu_r > 1$). Averaged dimensions of all MRE test specimens were used in the finite element model. The permeabilities identified in Chapter 4 (see Table 4.11) are used to calculate the magnetic field strengths for each type of MRE. The levels of magnetic flux density in both directions are needed to calculate the stresses in the directions of principal stretch induced by the biaxial rig. The ratio of $B_{Y,mean}$ to $B_{X,mean}$ is used to account for the MR effect in the two different stretching directions (explained in Section 5.5.4). The results of the finite element calculations for each type of MRE sample are summarised in Table 5.22. The level of magnetic flux in the y-direction is largest and the flux in x-direction

MRE Sample	Iron [%]	Flux in Y-direction		Flux in X-direction		Ratio $B_{ }/B_{\perp}$
		B_{mean}	$\frac{B_{max}-B_{min}}{B_{mean}}$	B_{mean}	$\frac{B_{max}-B_{min}}{B_{mean}}$	
Pure Rubber	0	67.53	90.4	7.09	357.2	9.52
Isotropic MREs	10	103.95	80.3	10.47	328.4	9.93
	20	138.45	82.1	13.27	324.8	10.43
	30	217.74	85.3	18.61	352.1	11.69
Anisotropic MREs - vertical alignment	10	104.53	77.2	9.9	289.3	10.58
	20	167.20	80.6	13.35	296.6	12.52
	30	257.03	83.6	17.16	306.1	14.98
Anisotropic MREs - horizontal alignment	10	97.62	83.0	11.16	329.0	8.75
	20	143.10	85.7	16.66	338.6	8.59
	30	208.12	87.9	23.20	358.7	8.97

Table 5.22: Mean values, B_{mean} in mT , and differences $B_{max}-B_{min}/B_{mean}$ in percent, of the magnetic flux distribution, B_Y and B_X , within the volume occupied by isotropic and anisotropic MRE samples ($\mu_r > 1$). The ratio $B_Y/B_X = B_{||}/B_{\perp}$ is calculated with the average values of the magnetic flux. Values for B_X are calculated with absolute values. The permeability of isotropic MREs and anisotropic MREs (Table 4.11) were used to calculate B_Y and B_X .

is lowest in the case of anisotropic samples with particle alignment in the y-direction (main magnetic flux direction), whereas the opposite was observed in the case of anisotropic MREs with particle alignment in the x-direction (perpendicular to the main magnetic flux direction). The factor $B_Y/B_X = B_{||}/B_{\perp}$ is largest at 14.98 for y-aligned anisotropic MREs with 30% iron content, and smallest at 8.59 for x-aligned anisotropic MREs with 20% iron content.

5.5.3 Strain Measurement - Digital Image Correlation

The strains were measured optically as previously described in the case of uniaxial tension (Section 5.3.4) and pure shear tests (Section 5.4.3). Sample preparation and the use of the DIC system was described in detail in those sections. An image of a sample sprayed with a white random speckle pattern, and also the grid lines drawn onto the sample, is shown in Figure 5.58. The Area of Interest (AoI) was defined on the MRE sample as a square area inside the boundaries of the free length of the sample. The resulting engineering strains in the x-direction of a pure rubber sample are shown in Figure 5.66a. To avoid the influence of the boundary area, the AoI is cropped, and also rotated for better handling in the *Matlab* code *strainDICLimess_biaxial.m* (see Appendix D). In the second processing step, unreliable values are eliminated using the confidence interval, *sigma*. The post-processed strain field is also shown in Figure 5.66b. The strains in the x-direction in the post-processed AoI are

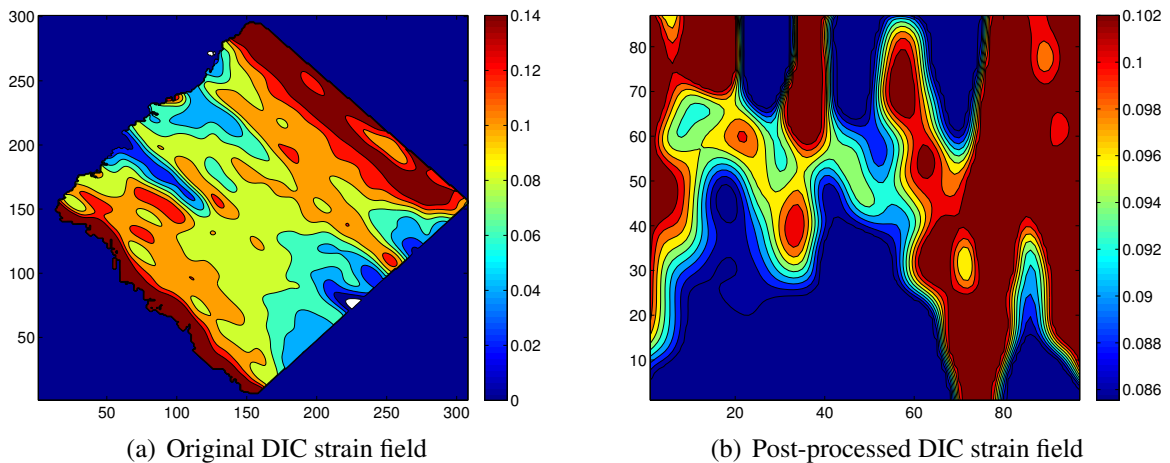


Figure 5.66: Maximum strain in the x-direction in the third loading part of a pure rubber sample calculated by the DIC software. (a) The original strain field as calculated by the DIC software and (b) the strain matrix was rotated, unreliable values eliminated, and borders cut.

relatively uniform, differing from 8.6% to 10.2%. Mean values of the post-processed strain field are calculated and plotted versus time in Figure 5.67, where the strain in both the local x- and y-directions are shown to be in excellent agreement. Mean values of the original AoI and of the cropped strain field were compared and do agree; however the standard deviations in strains resulting from the original AoI (see Figure 5.66a) are larger than those shown in the cropped and processed AoI (see Figure 5.66b). As the strain in the local x- and y-directions are nearly identical these results confirm the conclusion from the finite element analysis on the frame compliance (see Section 5.5.2), *i.e.* the frame structure is rigid enough to impose equi-biaxial deformation kinematics. This was also found to be the case for MREs with higher iron contents. This assumption is required to determine the stress values, using the analysis presented in Section 5.5.4. A linear fit to the strain-time relation (shown in Figure

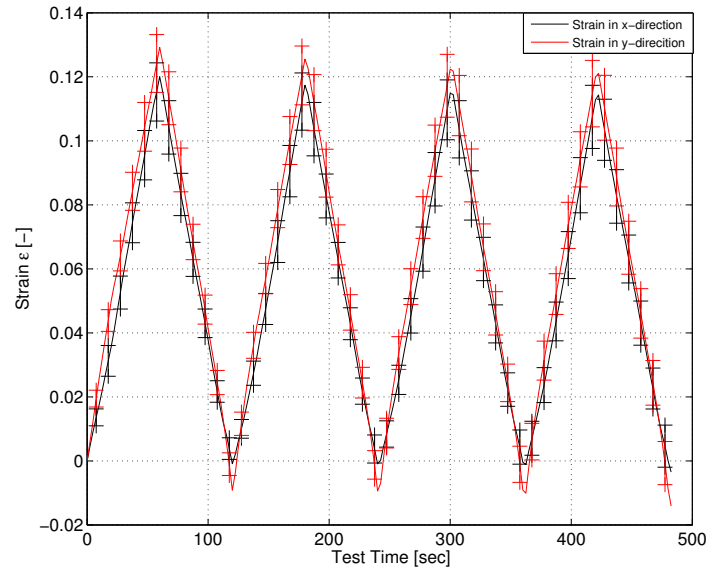


Figure 5.67: Engineering strain of a pure rubber sample in both stretching directions versus time is shown. Mean values and standard deviation of the cropped DIC field from the complete four-cycle test are illustrated.

5.67) is performed separately for each loading and unloading cycle. The coefficients of these linear functions are passed to the main *Matlab* analysis function *biaxial.m* (see Appendix D) in order to relate test machine data with DIC data.

To verify the DIC strain values, strains can also be determined manually by measuring the positions of the clamps and of the crossing points between the lines drawn onto the samples in the image processing software, ImageJ (2014). A *Matlab* function *strainpixel_biaxial.m* was written to post-process the measured positions, and to find the strains across the sample. The conversion from *pixels* to *mm* is made using a calibration distance (the distance between the clamps), and the connection to the load-displacement data measured by the test machine is done via time. Results of the pixel measurement method and results of the DIC system are in good agreement, which was shown earlier in case of uniaxial tension and pure shear tests; the comparison is not repeated here.

5.5.4 Stress Calculation and Assumptions

Only the vertical force, P_V , was recorded by the uniaxial test machine. To calculate stresses in the two stretching directions, the structural system of the biaxial test rig has to be analysed, and for the case of anisotropic MREs and when magnetic fields are applied, several assumptions have to be made to interpret the results. The biaxial rig is assumed to be a rigid body moving 10 *mm* in the vertical direction. This movement of the rig causes stresses within the MRE specimens. To simplify the structural system the stresses were assumed to be uniformly distributed over the length where the MRE specimens were clamped. The structural system is illustrated in Figure 5.68. The rigid body assumption of the biaxial frame is sup-

ported by the compliance studies of the test rig discussed in Section 5.5.2, and by the optical strain measurements that confirm equal strains in both stretching directions, as detailed in Section 5.5.3. The biaxial frame was held by the test machine allowing neither movement

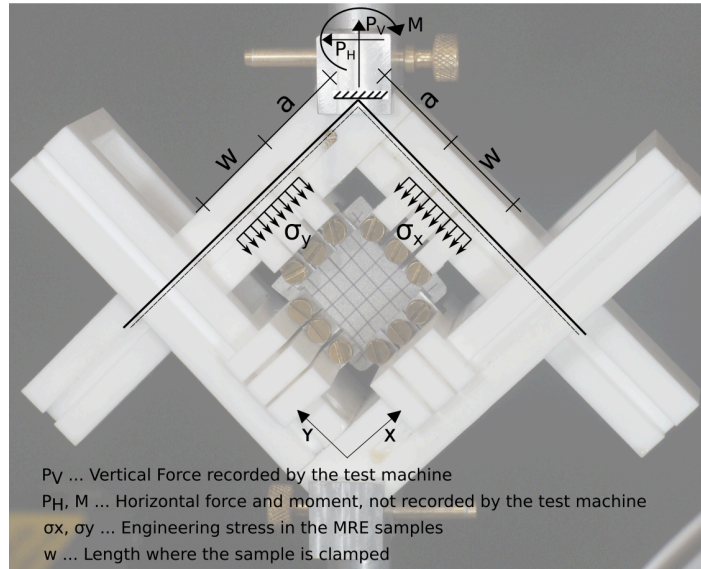


Figure 5.68: Structural system of the biaxial test setup used to calculate stresses within the MRE sample. The vertical force P_V was recorded by the test machine, where w is the length over the three clamps holding the samples, and σ_x and σ_y are the stresses occurring in the MRE sample.

nor rotation of the rig. The forces, P_V and P_H , and the moment, M , all act at the fixed support but only the vertical force, P_V , can be recorded by the load-cell of the test machine. The distance, a , is measured along the frame structure, between the fixed support and the sliding clamps. The stresses are calculated in the reference system, with original dimensions of the MRE specimens, and with the sliding clamps in their original positions.

Five cases are distinguished, as illustrated in Figures 5.58 and 5.59. *CASE 1* (isotropic MREs without magnetic field) is the simplest to analyse and no assumptions are required to interpret the results. In *CASE 2* isotropic MREs tested with magnetic field applied in the x-direction are analysed. Results of *CASE 1*, together with the factor $B_{||}/B_{\perp}$ (listed in Table 5.22) are used to address the increase in the force (due to the magnetic field) to each stretching direction. In *CASE 3* anisotropic MREs tested in the absence of a magnetic field are considered. Anisotropic MREs are stronger in the direction of particle alignment and therefore the stresses in this direction are expected to be higher. Results of the anisotropic MREs with particle alignment in loading direction and perpendicular to it, tested under uniaxial tension (Section 5.3), are used to calculate stresses acting in the two stretching directions. In *CASE 4* and *CASE 5* anisotropic MREs with the magnetic field applied both parallel and perpendicular to the direction of particle alignment, are analysed. Here, assumptions regarding both the mechanical anisotropy due to particle alignment, and the change in stiffness due to magnetic field, are required to interpret results. The formulas for all five cases are derived in the

following sections, and the assumptions are explained in detail.

Note that the assumptions used here are improved compared to the earlier conference paper based on this work (Schubert *et al.*, 2013).

5.5.4.1 CASE 1 - Isotropic MREs in the Absence of a Magnetic Field

Isotropic MREs are supposed to have equal properties in all directions, which implies that under equi-biaxial strains the in-plane stresses, σ_x and σ_y , are identical. Figure 5.58 shows the setup of *CASE 1*. From the equilibrium of stresses in the local x- and y-directions the stresses can be related to the force measured by the test machine as:

$$\sigma_x = \sigma_y = \frac{P_V}{\sqrt{2} \cdot t \cdot w} \quad (5.6)$$

If the force, P_V , is provided in *Newtons* and the thickness of the sample, t , and the width of the clamps, w , are provided in *mm*, the resulting stresses, σ_x and σ_y , are provided in *MPa*. In this case, the horizontal force, P_H , and the moment, M , at the fixed support are zero.

5.5.4.2 CASE 2 - Isotropic MREs with Magnetic Flux in the x-direction

The horizontal force, P_H , and the moment, M , in this case (or any of the subsequent cases) are not zero. These quantities would provide further information to evaluate the material response, although the current test-setup is unable to measure them. For this reason various assumptions are required to interpret the test results. The magnetic field is assumed to change the properties in the local x- and y-directions by the same factor as the ratio between the components of the magnetic flux density in these directions $B_{||}/B_{\perp}$ (acting within the volume occupied by the biaxial MRE sample). When a magnetic field is applied to the isotropic MRE specimens, the force measured, P_V , increases compared to the no-field case, $P_{V,CASE1}$. The increase, $P_{increase} = P_V - P_{V,CASE1}$ can be attributed to the increased stresses acting in the two principle stretching directions. The relation between the increased stresses, $\sigma_{x,increase}$ and $\sigma_{y,increase}$, is determined using the factor $B_{||}/B_{\perp}$ (listed in Table 5.22). As the main magnetic flux direction is oriented in the x-direction, the stresses in this direction are expected to be larger, *i.e.* $\sigma_x > \sigma_y$.

$$\frac{B_{||}}{B_{\perp}} = \frac{\sigma_{x,increase}}{\sigma_{y,increase}} \quad (5.7)$$

The setup of *CASE 2* is shown in Figure 5.59a. Using Equation 5.7 and the vertical equilibrium of forces, the stress definitions can be derived as follows:

$$\sigma_x = \sigma_{x,CASE1} + \sigma_{x,increase} = \frac{P_{V,CASE1}}{\sqrt{2} \cdot t \cdot w} + \frac{\sqrt{2}(P_V - P_{V,CASE1})}{\left(\frac{B_{\perp}}{B_{||}} + 1\right) \cdot t \cdot w} \quad (5.8)$$

$$\sigma_y = \sigma_{y,CASE1} + \sigma_{y,increase} = \frac{P_{V,CASE1}}{\sqrt{2} \cdot t \cdot w} + \frac{\sqrt{2}(P_V - P_{V,CASE1})}{\left(\frac{B_{\parallel}}{B_{\perp}} + 1\right) \cdot t \cdot w} \quad (5.9)$$

The value $P_{V,CASE1}$ is the mean value of forces measured on isotropic MREs (with the same iron volume fraction), tested without an applied magnetic field.

5.5.4.3 CASE 3 - Anisotropic MREs in the Absence of a Magnetic Field

The direction of particle alignment in anisotropic MREs is oriented in the local y-direction for all biaxial tests conducted in this investigation. The setup of *CASE 3* is illustrated in Figure 5.59b. Anisotropic MREs are much stiffer in the direction of particle alignment, $\sigma_y > \sigma_x$. As only the vertical forces, P_V , were measured by the test machine, an assumption is required to attribute the fraction of this force to the stresses acting in the two principle stretching directions. The ratio of these stresses, or relative stress factor, can be determined from the results of the uniaxial tension tests (Section 5.3.5); thus the ratio of the stresses produced when anisotropic samples were tested with their direction of particle alignment oriented in the loading direction, σ_A , to that produced when their direction of alignment was oriented perpendicular to the loading direction, σ_{AW} , can be used to evaluate the relationship between σ_x and σ_y in the biaxial tension tests. The relative stress factor can be defined as:

$$f(\varepsilon) = \frac{\sigma_A(\varepsilon)}{\sigma_{AW}(\varepsilon)} = \frac{\sigma_y}{\sigma_x} \quad (5.10)$$

Mean results from at least three repeated uniaxial tension tests are taken to calculate the relative stress factors, plotted versus uniaxial strain in Figure 5.69. Using the stress factor

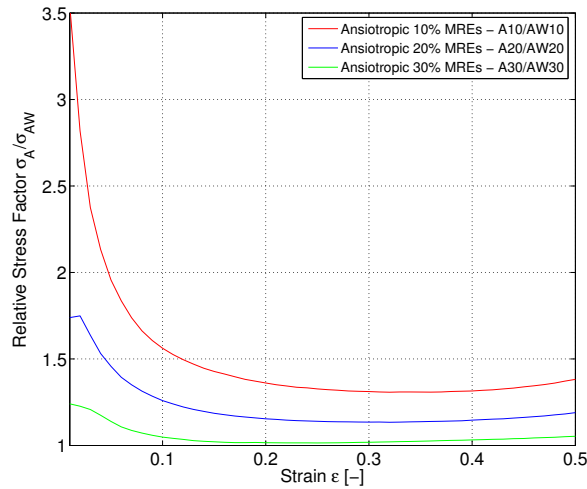


Figure 5.69: Relative stress factor $f(\varepsilon)$ between anisotropic MREs with alignment parallel (A) and perpendicular (AW) to the loading direction (tested under uniaxial tension) are shown. The stress factor is plotted versus the engineering strain in the uniaxial stretching direction. Note that the stress factor tends to infinity for small strains, so values below 2% strain are unreliable.

defined in Equation 5.10, and assuming equilibrium conditions, the stresses in both stretching directions can be calculated as:

$$\sigma_x = \frac{\sqrt{2} \cdot P_V}{(f(\varepsilon) + 1) \cdot t \cdot w} \quad (5.11)$$

$$\sigma_y = \frac{\sqrt{2} \cdot P_V \cdot f(\varepsilon)}{(f(\varepsilon) + 1) \cdot t \cdot w} \quad (5.12)$$

This method of using the relative stress factor obtained from uniaxial tension tests provides a means to perform first approximate analysis of the biaxial test data. It might be possible in the future to improve the analysis method by using constitutive models (Chapter 6).

5.5.4.4 CASE 4 - Anisotropic MREs with Magnetic Flux in the y-direction

Anisotropic MREs were tested with the main strength of the magnetic field in the y-direction (thus the direction of the particle alignment was parallel to the direction of the magnetic field). The setup is shown in Figure 5.59c. Two assumptions have to be made in *CASE 4* to account for both the inherent mechanical anisotropy of the samples in the absence of a magnetic field and the change in stiffness of the sample due to the magnetic field applied. The force measured at the test machine where no magnetic field was applied is that measured in *CASE 3*, i.e. $P_{V,CASE3}$, although with the application of a magnetic field the measured force will change to $P_V = P_{V,CASE3} + P_{V,increase}$. The stresses resulting from $P_{V,CASE3}$ are known and were defined in Equations 5.11 and 5.12, so the P_V in these equations must be replaced by $P_{V,CASE3}$ which is the mean value of forces measured in the no-magnetic field case. The increase in force $P_{V,increase}$ due to the MR effect, attributed to the stresses acting in the two principle stretching directions, is defined *CASE 2* (see Equations 5.8 and 5.9). The only difference here is that the magnetic field is now applied in the local y-direction rather than in the local x-direction. The relation between the magnetic factor, $B_{||}/B_{\perp}$, and the stresses, σ_x and σ_y , of the biaxial tests can thus defined as:

$$\frac{B_{||}}{B_{\perp}} = \frac{\sigma_{y,increase}}{\sigma_{x,increase}} \quad (5.13)$$

The final stresses, σ_x and σ_y , can be defined using Equation 5.13. As both the particle alignment and the applied magnetic field are in the local y-direction, the stresses in this direction are expected to be much higher than the stresses in the x-direction, i.e. $\sigma_y \gg \sigma_x$.

$$\sigma_x = \sigma_{x,CASE3} + \sigma_{x,increase} = \frac{\sqrt{2} \cdot P_{V,CASE3}}{(f(\varepsilon) + 1) \cdot t \cdot w} + \frac{\sqrt{2} (P_V - P_{V,CASE3})}{\left(\frac{B_{||}}{B_{\perp}} + 1\right) \cdot t \cdot w} \quad (5.14)$$

$$\sigma_y = \sigma_{y,CASE3} + \sigma_{y,increase} = \frac{\sqrt{2} \cdot P_{V,CASE3} \cdot f(\varepsilon)}{(f(\varepsilon) + 1) \cdot t \cdot w} + \frac{\sqrt{2} (P_V - P_{V,CASE3})}{\left(\frac{B_{\perp}}{B_{||}} + 1\right) \cdot t \cdot w} \quad (5.15)$$

Two assumptions had to be used to calculate the stresses in the two principal stretching directions. Given that these assumptions use experimental data measured from uniaxial tensile tests, any errors in these prior results are added to those errors inherent in the current biaxial test method. Consequently, the error accumulates in proportion to the number of assumptions used to analyse the data. Due to the increasing reliance of assumptions in analysing this case, care has to be taken when interpreting the test results in Section 5.5.6.

5.5.4.5 CASE 5 - Anisotropic MREs with Magnetic Flux in the x-direction

CASE 5 is very similar to CASE 4, the only difference being that the main strength of the magnetic field is applied in the local x-direction rather than in the local y-direction. The assumptions and the derived equation are analogous to those explained in CASE 4. The equations for the final stresses, σ_x and σ_y , are derived as:

$$\sigma_x = \sigma_{x,CASE3} + \sigma_{x,increase} = \frac{\sqrt{2} \cdot P_{V,CASE3}}{(f(\varepsilon) + 1) \cdot t \cdot w} + \frac{\sqrt{2} (P_V - P_{V,CASE3})}{\left(\frac{B_{\perp}}{B_{\parallel}} + 1\right) \cdot t \cdot w} \quad (5.16)$$

$$\sigma_y = \sigma_{y,CASE3} + \sigma_{y,increase} = \frac{\sqrt{2} \cdot P_{V,CASE3} \cdot f(\varepsilon)}{(f(\varepsilon) + 1) \cdot t \cdot w} + \frac{\sqrt{2} (P_V - P_{V,CASE3})}{\left(\frac{B_{\parallel}}{B_{\perp}} + 1\right) \cdot t \cdot w} \quad (5.17)$$

The experimental results of isotropic and anisotropic MREs of tests performed without magnetic field (CASE 1 and CASE 3) are presented in Section 5.5.5, and those of tests with an applied magnetic induction (CASE 2, CASE 4 and CASE 5) in Section 5.5.6.

5.5.5 Tests in the Absence of Magnetic Field (CASE1 and CASE3)

Equi-biaxial tension tests in the absence of a magnetic field were performed using the setup illustrated in Figures 5.58 and 5.59b. The general test method was clarified in Section 5.1.1, and the specific test procedure of the equi-biaxial tension tests was described in Section 5.5.1. In this section the behaviour of isotropic and anisotropic MREs under equi-biaxial tension in the absence of a magnetic field is examined. As with the other large-strain experiments the third loading cycle of the 4-cycle tests was extracted (see Section 5.1.2) and used to characterise the MRE behaviour. The stresses are calculated as discussed in Section 5.5.4, with Equation 5.6 for isotropic MREs, and Equations 5.11 and 5.12 for anisotropic MREs. The vertical load versus displacement data for all types of MREs tested in the absence of a magnetic field are shown in Figure 5.70a. The load-displacement data are directly recorded by the test machine and thus do not involve any assumptions. The stress-strain curves are shown in Figure 5.70b, and involve an assumption in the case of anisotropic MREs (see Section 5.5.4). The measured force increases with increasing iron content. Also, forces are

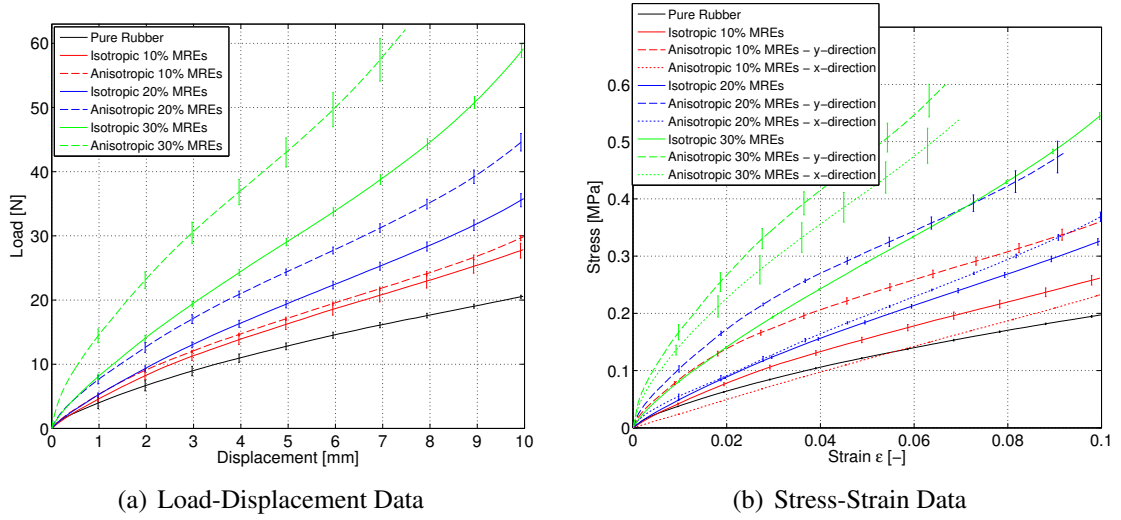


Figure 5.70: *NoField* test results: Vertical load-displacement curve and the stress-strain curves comparing all different types of MRE samples. Stresses of the isotropic MREs are compared with the stresses parallel (y-direction) and perpendicular (x-direction) to the particle alignment of anisotropic MREs.

larger in anisotropic MREs compared to the equivalent isotropic MREs. The difference in force between isotropic and anisotropic MREs increases with increasing iron particle concentration. Note that the anisotropic MREs with 30% particles are tested up to only 7% strain, which does not allow comparison to the other MREs tested up to 10% strain. Samples tested to larger strain levels are known to result in softer material properties due to the *Mullins Effect* (Mullins, 1969). The stresses of anisotropic MREs mirror the behaviour of the MREs tested under uniaxial tension as the relative stress factor (Equation 5.10) obtained from the tensile tests was used to determine the stresses in the two principal stretching directions of the biaxial tests. To interpret the non-linear behaviour the tangent moduli, E_T , are plotted versus engineering strain in Figure 5.71. All MREs exhibit larger moduli in the small-strain region, which tend to decrease continuously with increasing strain. Biaxial samples were stretched up to only 10% strain, thus, the increase in moduli at larger strains found in previous tests cannot be observed here. Anisotropic MREs exhibit the highest moduli in the direction of the particle alignment. The tangent moduli, E_T (between 1% and 2% strain), and the low secant moduli, E_{0-5} , are listed in Table 5.23. The relative increase in moduli of the isotropic MREs compared to the pure rubber samples, and of the anisotropic MREs compared to the isotropic MREs with the same iron content (calculated with E_{0-5}), are also provided in Table 5.23. The moduli are approximately 1.5 times higher compared to those resulting from compression, tension, and pure shear experiments (compare Tables 5.5, 5.13, and 5.20). Several reasons are conceivable to explain this increase: (i) equi-biaxial specimens were only stretched up to 10% while in the other experiments larger strain levels were applied (stress softening *Mullins effect*), (ii) the two-dimensional shape of the biaxial

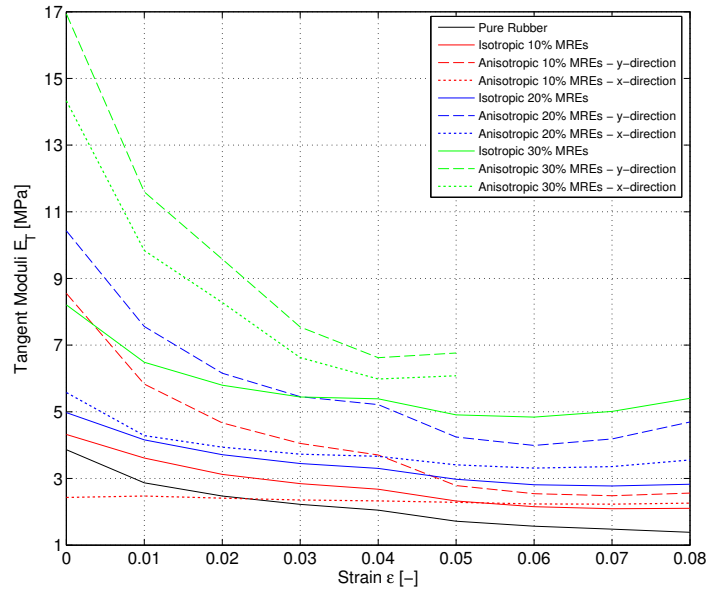


Figure 5.71: The tangent moduli versus engineering strain of isotropic MREs and anisotropic MREs in the particle alignment direction (y-direction) and perpendicular to it (x-direction) are shown.

samples adds some strengthening, and (iii) the contribution of friction between the sliding clamps and the frames of the biaxial rig. The moduli, E_{0-5} and E_T , as listed in Table 5.23 are plotted versus the iron volume fraction in Figure 5.72. The moduli increase linearly

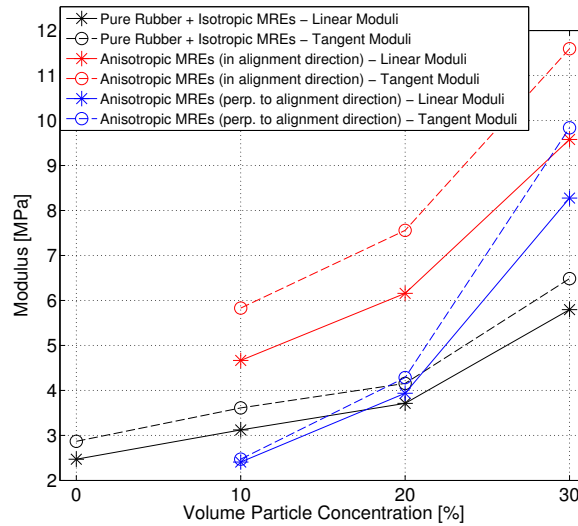


Figure 5.72: Moduli E_{0-5} and E_T (see Table 5.23) versus the iron volume fraction of isotropic MREs and anisotropic MREs parallel (y-direction) and perpendicular (x-direction) to the particle alignment direction.

with increasing iron content in the case of pure rubber and isotropic MREs. The anisotropic MREs with 30% iron particles exhibit higher moduli due to the smaller strain level applied; these samples were only stretched up to 7% instead of 10% strain.

MRE Sample	Iron [%]	E_{0-5} [MPa]	E_T [MPa]	Increase compared to ... [%]	
Pure Rubber	0	2.47	2.87	Pure	26.3
Isotropic MREs	10	3.12	3.61	Isotropic	50.0
	20	3.71	4.16		134.8
	30	5.80	6.49		
Anisotropic MREs - in particle alignment direction	10	4.67	5.83	Isotropic	49.7
	20	6.16	7.56		66.0
	30	9.58	11.60		65.2
Anisotropic MREs - perpendicular to the alignment direction	10	2.41	2.47	Isotropic	-22.8
	20	3.94	4.29		6.2
	30	8.28	9.84		42.8

Table 5.23: Initial secant moduli, E_{0-5} , and tangent moduli, E_T , obtained from stress-strain curves of pure rubber, isotropic, and anisotropic MREs with 10% to 30% CIP content are listed. Anisotropic MREs have their particle alignment in the y-direction. The relative increase of isotropic MREs compared to pure rubber and the relative increases of anisotropic MREs compared to isotropic MREs with same CIP content, calculated with E_{0-5} , are provided.

5.5.6 Characterisation of the Magneto-Rheological Effect

Only one magnetic field strength was applied to study the increase in stiffness of the MRE material in the equi-biaxial tension test series. The average magnetic flux density within the region occupied by the MRE sample (calculated in the absence of a sample) was 67.5 mT in the main magnetic field direction and 7.1 mT in the perpendicular direction (see Section 5.5.2). The magnetic flux lines were not unidirectional; when interpreting experimental data, this issue is taken into account using the analysis method described in Section 5.5.4.

5.5.6.1 Pure Rubber and Isotropic MREs (CASE2)

The vertical force and displacement data of isotropic MREs both with and without applied magnetic flux are shown in Figure 5.73. The load-displacement data were recorded directly by the test machine, and do not involve any assumptions. An increase in force is apparent when samples are subjected to a magnetic flux density, but only the isotropic MREs with 20% iron content show a significant increase in force. The stresses in both directions are calculated using Equation 5.6 (when no magnetic induction was applied) and using Equations 5.8 and 5.9 (when subjected to a magnetic flux). The full set of results for stresses, the tangent moduli, and relative MR effects are plotted versus engineering strain in Appendix E.27. There is nearly no increase in stresses acting in the y-direction (perpendicular to the magnetic field). Stresses acting in the local x-direction (main magnetic field direction) increase in the same manner as the load-displacement curves (Figure 5.73).

The absolute and relative MR effects (Equations 5.1 and 5.2) of pure rubber and isotropic MREs calculated using E_T are plotted versus engineering strain in Figure 5.74. The highest relative MR effect is 25% (1.09 MPa absolute), achieved with an isotropic 20% MRE. The

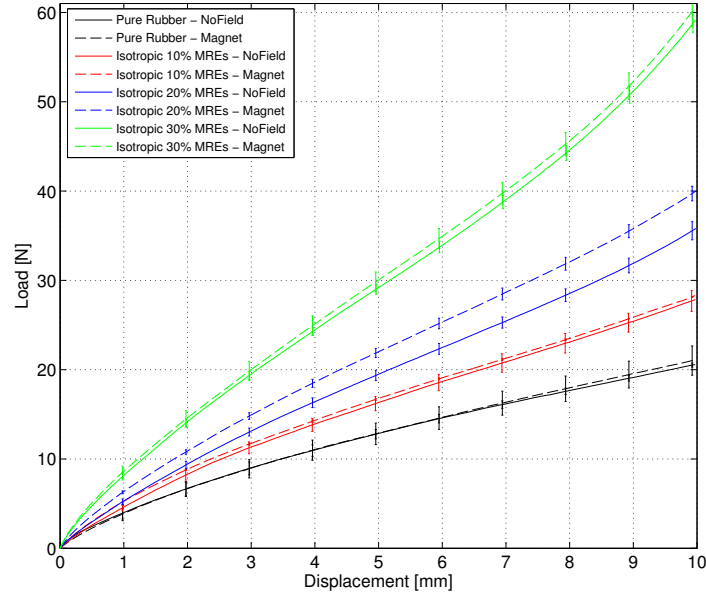


Figure 5.73: Vertical load-displacement curve of pure rubber and isotropic MRE samples with 10% to 30% iron content comparing the *NoField* with the *Magnet* tests. The magnetic flux density was applied in the x-direction.

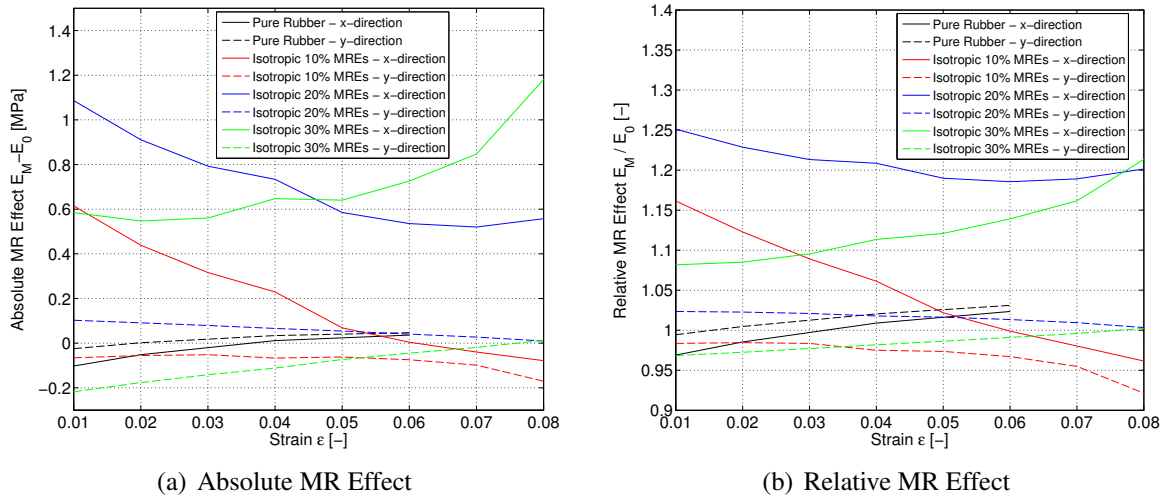


Figure 5.74: Absolute and relative MR effects, calculated with E_T , of pure rubber and isotropic MREs with 10%, 20%, and 30% iron content measured with an average magnetic induction of 67.5 mT applied in the x-direction, are plotted versus strain.

isotropic 30% MREs exhibit lower relative increases of about 21%. As expected the MR effects in the direction perpendicular to the applied induction are all close to 1. Results from pure rubber samples indicate an experimental and analytical error of about 3%. The MR effects obtained using both E_{0-5} and E_T are listed in Table 5.24.

5.5.6.2 Anisotropic MREs (CASE4 and CASE5)

The load-displacement curves of anisotropic MREs with magnetic field applied parallel to the direction of particle alignment are compared with those of the *NoField* tests in Figure 5.75. All of the samples show an increase in force, which is again largest for the MREs with

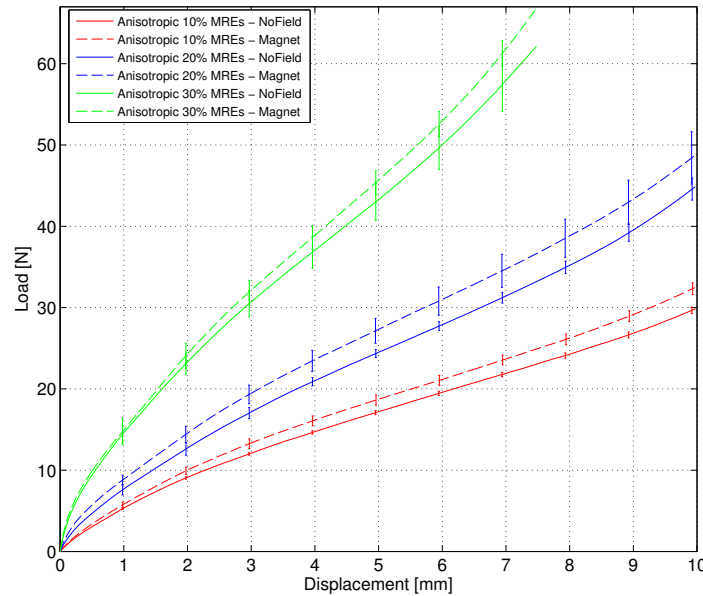


Figure 5.75: Vertical load-displacement curve of anisotropic MRE samples with 10% to 30% iron content comparing the *NoField* with the *Magnet* tests are illustrated. Both the particle alignment and the applied magnetic induction were in the y-direction.

20% iron volume fraction. Stresses are calculated using Equations 5.14 and 5.15. The full set of results for stresses, tangent moduli, and relative MR effects are plotted versus engineering strain in Appendix E.28. The magnetic field was applied in the local y-direction and the stresses in this direction clearly increase, whereas those in the x-direction show very little increase. This is expected based on the assumptions. The absolute and relative MR effects, calculated using E_T , are plotted versus strain values in Figure 5.76. In contrast to previously achieved MR effects in compression, tension, and pure shear tests, the MR effects are not significantly larger in the small-strain region and tend to increase with increasing strain. The highest MR effect of about 74% was measured for the anisotropic MREs with 30% iron content, but in the small-strain region the relative effect was just 27.9%. Again, the relative MR effects in the direction perpendicular to the magnetic field are close to 1.

The anisotropic MREs were also tested with a magnetic field applied perpendicular to the direction of particle alignment. The vertical load-displacement data are shown in Figure 5.77. Increase in the forces are small for MREs with 10% and 30% iron content and are relatively large in case of the anisotropic 20% MREs. The stresses in the two principal stretching directions are found using Equations 5.16 and 5.17. The full set of results for stresses, tangent moduli, and relative MR effects are plotted versus the engineering strain in

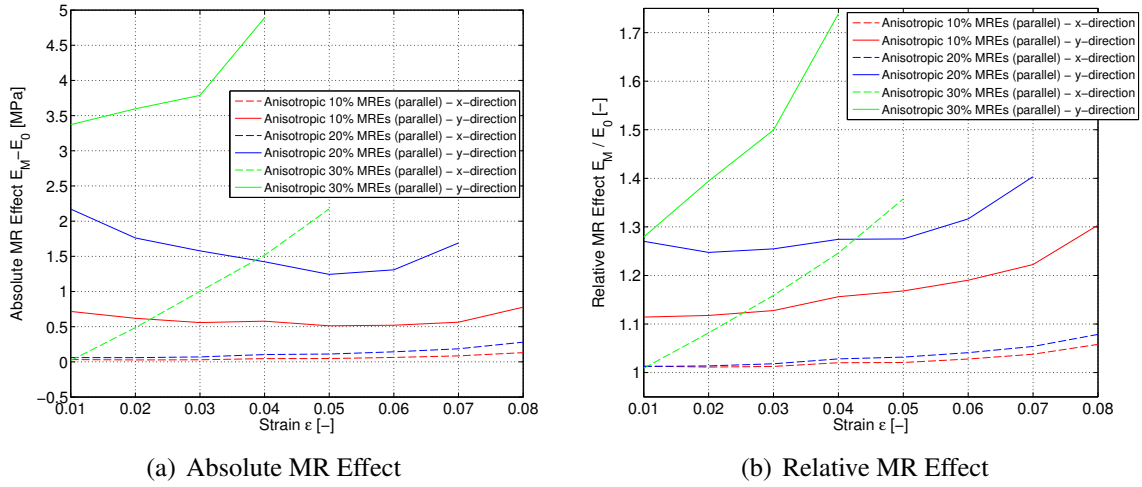


Figure 5.76: Absolute and relative MR effects, calculated using E_T , for anisotropic MREs with 10%, 20%, and 30% iron content measured with an average magnetic induction of 67.5 mT applied in the y-direction (parallel to the direction of particle alignment), are plotted versus strain.

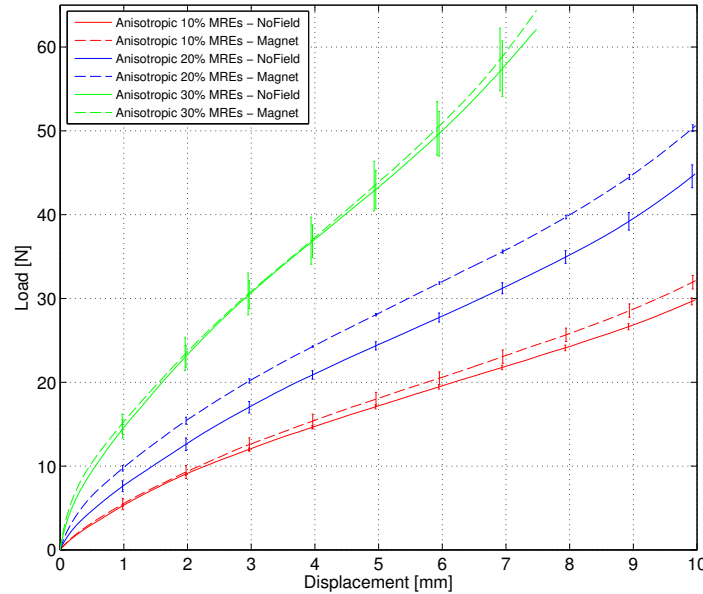


Figure 5.77: Vertical load-displacement curve of anisotropic MRE samples with 10% to 30% iron content comparing the *NoField* with the *Magnet* tests are illustrated. The particles in the MREs were aligned in the y-direction while the magnetic induction was applied in the x-direction.

Appendix E.29. MREs with 10% and 20% iron content show large MR effects in the local x-direction where the magnetic field was applied, and show nearly no effect in the y-direction perpendicular to the direction of applied induction. The absolute and relative MR effects are plotted versus strain in Figure 5.78. The highest relative MR effect of 46% (2.24 MPa absolute) was achieved with the anisotropic MREs with 20% iron content. The MR effects of anisotropic MREs with 10% and 20% iron content exceed the MR effects found when the magnetic flux was applied parallel to the direction of particle alignment. This contrasts with

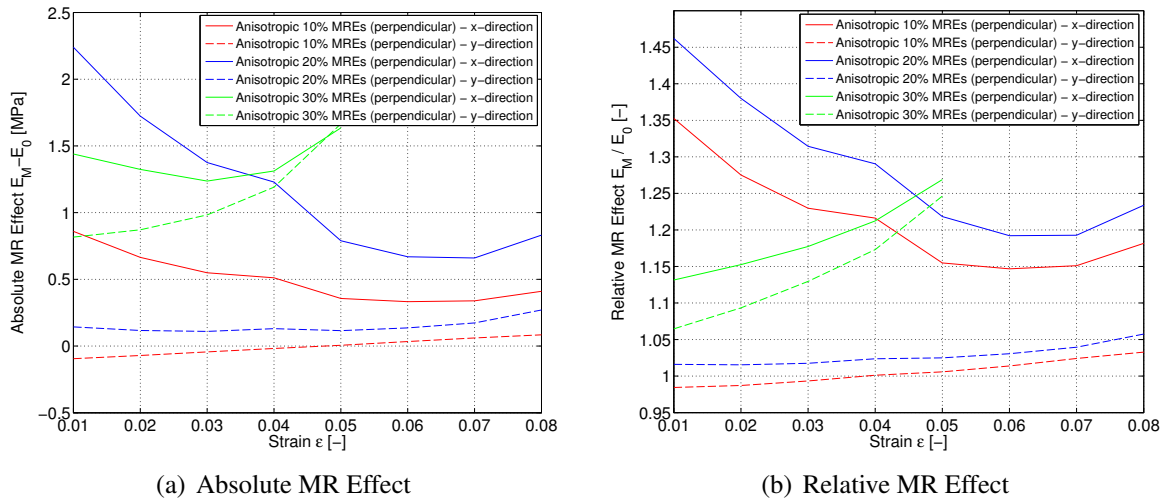


Figure 5.78: Absolute and relative MR effects, calculated with E_T , of anisotropic MREs with 10%, 20%, and 30% iron content, measured with an average magnetic induction of 67.5 mT applied in the x-direction (perpendicular to the direction of the particle alignment), are plotted versus strain.

the results found in uniaxial tension tests (compare Figure 5.34). The results achieved in equi-biaxial tension are influenced by the assumptions which were required to analyse the data, and could be improved with the use of constitutive modelling in future investigations. To compare all the anisotropic MREs with the magnetic flux density applied both parallel and perpendicular to the direction of particle alignment, the MR effects calculated with the low strain secant moduli, E_{0-5} , and the maximum MR effect calculated with the tangent moduli, E_T , are listed in Table 5.24. Maximum values of the MR effects (obtained from either E_{0-5} or $E_{T,max}$) are shaded in grey. The highest increase in modulus of 4.89 MPa absolute, equivalent to a 74% relative MR effect was achieved with an anisotropic MRE with 30% iron volume fraction with magnetic field applied parallel to the direction of particle alignment. To study the influence of the iron content, the maximum MR effects (see Table 5.24) are plotted versus volume particle concentration in Figure 5.79. Only the MR effects in the main magnetic field direction are presented. MR effects increase with increasing iron content.

5.5.7 Future Improvements of the Setup and Test Procedure

The test setup for the equi-biaxial tension tests clearly had disadvantages. It was only possible to stretch the samples up to 10% strain (7% in the case of anisotropic 30% MREs). The clamps required the use of brass screws, which was not ideal as they damaged the samples slightly, resulting in slight tearing after testing to 10% strain, meaning that the samples could only be used once. The clamping system of the test rig could be improved for future work. The compliance calculation described in Section 5.5.2 showed that the frame itself was quite

MRE Sample	Direction or \perp to magnetic field	Iron [%]	Absolute MR Effects		Relative MR Effects	
			E_{0-5}	E_T	E_{0-5}	E_T
Pure Rubber		0	-0.0310	0.0362	0.9875	1.0235
	\perp	0	0.0024	0.0469	1.0010	1.0311
Isotropic MREs Magnetic Induction in the x-direction		10	0.2598	0.6147	1.0858	1.1614
		20	0.7526	1.0866	1.2057	1.2511
		30	0.4125	1.1815	1.0709	1.2133
	\perp	10	-0.0291	-0.0556	0.9910	0.9845
		20	0.0943	0.1025	1.0250	1.0235
		30	-0.1607	0.0124	0.9722	1.0023
Anisotropic MREs - Magnetic induction and particle alignment in the y-direction		10	0.5304	0.7776	1.1136	1.3037
		20	1.6609	1.6892	1.2697	1.4035
		30	3.4892	4.8911	1.3643	1.7386
	\perp	10	0.0075	0.1312	1.0031	1.0580
		20	0.0303	0.2797	1.0077	1.0786
		30	0.4358	2.1748	1.0527	1.3577
Anisotropic MREs - Magnetic induction in x- and particle alignment in y-direction		10	0.4703	0.8592	1.1953	1.3526
		20	1.1813	2.2390	1.3000	1.4620
		30	1.1156	1.6349	1.1348	1.2689
	\perp	10	-0.0801	0.0841	0.9828	1.0328
		20	0.0623	0.2702	1.0101	1.0576
		30	0.7041	1.6657	1.0735	1.2462

Table 5.24: Absolute and relative MR effects measured with 67.5 mT average magnetic induction, and calculated using E_{0-5} and E_T (maximum values) are listed. The maximum relative MR effects (E_{0-5} or E_T) are shaded in grey.

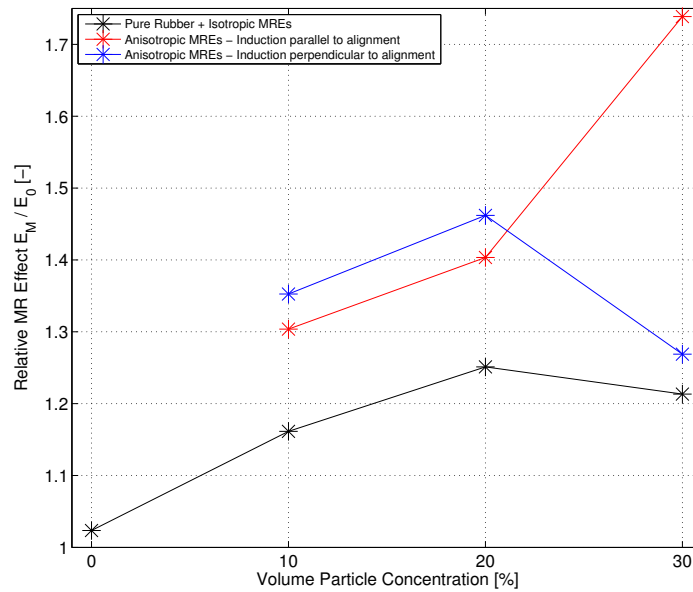


Figure 5.79: Relative MR effects in the direction of the applied magnetic induction of all types of MREs versus the volume particle concentration are illustrated. The maximum MR effects as indicated in Table 5.24 are used.

rigid, whereas the sliding clamps deformed considerably. The design of the Teflon clamps could be improved to eliminate this problem. The total rig deformation was acceptable when the samples were stretched up to 10% but application of larger strains would probably cause significant errors in terms of the kinematics applied to the samples.

Perhaps the most important point to improve is in measuring either the horizontal force or the moment at the test machine (in addition to the measured vertical force). This would make all the assumptions described in Section 5.5.4 redundant, and any errors associated with these assumptions would then be eliminated. Redesigning the rig to include biaxial or torque load-cells would significantly improve the quality of the results obtained from the equi-biaxial tension tests.

5.5.8 Summary of the Equi-Biaxial Tension Tests

Once again, the moduli of the MREs were found to increase with increasing iron content and anisotropic MREs loaded in the direction of particle alignment were stiffest. Due to the use of the assumptions discussed in Section 5.5.4, the stresses of the anisotropic MREs mirrored the material behaviour found in the uniaxial tension tests. The tangent moduli were largest in the small-strain region, and constantly decreased with increasing strain. Due to both the large distances between the magnets in the biaxial setup and the width of the biaxial samples, the direction of the magnetic flux lines was not uniform. In contrast to previous large-strain compression, tension and pure shear experiments, the MR effects were not always largest in the small-strain region in biaxial tests, and tended to increase with increasing level of strain. The MR effects increase with increasing iron contents. Considering the low magnetic fields applied during the biaxial tests, the MR effects measured during the tests are large.

5.6 Conclusions of Chapter 5

This experimental investigation was designed to characterise the mechanical behaviour of MREs both in the absence and in the presence of magnetic fields, under various deformation modes. The large-strain behaviour of MREs was investigated under uniaxial compression up to 50% strain, under uniaxial tension up to a maximum of 100% strain, under pure shear up to a maximum of 70% strain, and under equi-biaxial tension up to 10% strain.

Experimental data presented in this chapter can be used to develop constitutive models describing the behaviour of MREs without and with the application of external magnetic fields. Several deformation modes and multi-axial deformations are required to describe complex materials such as MREs sufficiently, to achieve the goal of determining unique model parameters of constitutive material models. The experimental data are saved on a DVD attached to this document and can be used for further investigations.

5.6.1 Stress-Softening Behaviour

During the course of this investigation, it became apparent that the behaviour of MREs was more complicated than initially anticipated. In particular, significant stress-softening behaviour was observed, which influenced the results in the absence and in the presence of magnetic fields. A distinctive test procedure and method of analysing the data were used (see Section 5.1) to account for the *Mullins* effect.

- Four-cycle tests were performed, and the third loading cycle (conditioned cycle) was used to characterise the MRE material. The method of analysing the experimental data was kept constant throughout this investigation (Section 5.1.2).
- In compression, tension, and pure shear tests, samples were re-used in a test series comprised of several tests in the absence and in the presence of magnetic fields (see Section 5.1.1). The results of two no-field tests were compared, and in case of compression and tension divergences between the *NoField01* and *NoField02* tests were observed. This was presented to be caused by permanent deformations present in compression and tension specimens after their first use, which induced new larger strain levels in subsequent tests. Due to the *Mullins* effect this significantly changed the properties of the MREs (see Sections 5.2.3 and 5.3.5). To eliminate this effect and to analyse reliable experimental data, the MREs were characterised using stress-strain data only up to the point of divergence. This was not an issue in pure shear and equi-biaxial tension tests, as no permanent deformation occurred in the specimens (see Section 5.4.4 and 5.5.5). Note that in future applications, MREs will also be ‘re-used’ and permanent deformations can occur. It is therefore recommended that MRE samples are preconditioned up to strain levels higher than those planned during working operation of the MRE application.
- Tensile fatigue tests were performed to determine a ‘stability strain limit’ for each type of MRE. It was found that when stretching samples beyond this strain limit, stress-softening was still present after 100 loading and unloading cycles; *i.e.* the samples did not reach a ‘stable’ state (see Section 5.3.3). Note that MRE samples cannot be used beyond these ‘stability strain limits’ in future applications.

Preconditioning and testing the MRE sample up to larger strain levels resulted in a softer material, with significantly lower stress-strain curves compared to MRE samples that were preconditioned to lower strain levels. In tension, larger preconditioning levels enhanced the MR effects achieved. The stress-softening is pronounced in anisotropic MREs and in MREs with high iron contents. Good practice in future might be to precondition the MRE samples as far as possible (obeying the maximum strain limit) to soften the material, and consequently to enhance the MR effects. Larger relative MR effects were reported to occur

when using softer matrix material (see literature review in Section 2); here it is shown that preconditioning the samples up to larger strain levels has the same effect.

5.6.2 Mechanical Response in the Absence of a Magnetic Field

Anisotropic MREs exhibited the highest stresses and moduli in the direction of the particle alignment in most of the tests performed, followed by the direction perpendicular to the alignment, and the isotropic MREs exhibited the lowest moduli. As the MRE material behaviour is strongly nonlinear, stresses and tangent moduli were studied versus engineering strain. Anisotropic MREs with vertical particle alignment exhibited very large moduli in the small strain region that decreased rapidly in the mid-strain region, but tended to increase again at larger strain, while both the isotropic and anisotropic MREs with horizontal particle alignment generally showed a similar curve shape with steadily increasing tangent moduli. The moduli were found to increase with increasing iron particle concentration, which was almost linear in the case of uniaxial tension tests, while in the other large-strain experiments the MREs containing 30% iron particles exhibited larger moduli exceeding the linear trend. In tension and pure shear tests, MREs were tested up to different strain levels, and the moduli were observed to be smaller when the samples were stretched up to higher levels of strain presumably due to the stress-softening behaviour.

The moduli present in the small strain region, are compared for all deformation modes and all types of MREs in Figure 5.80. The moduli represent results from 50% compressive strain, 50% tensile strain, 45% strain in pure shear, and 10% biaxial strain. Note that the MREs tested in compression, tension and pure shear are tested up to the same strain level. In equi-biaxial tests, higher strain levels were experimentally not achievable.

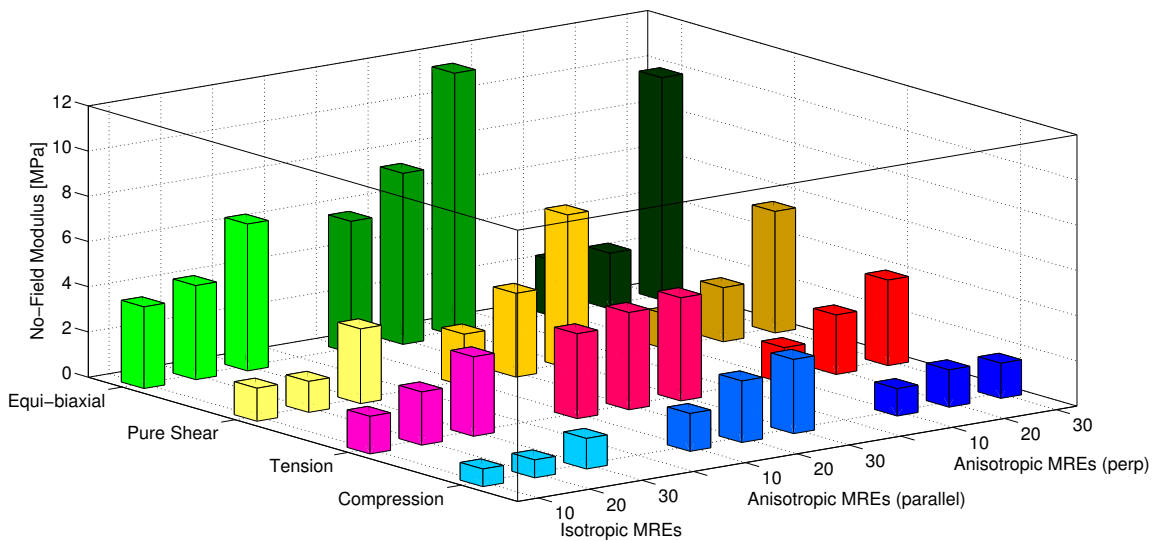


Figure 5.80: Comparison of the mechanical response for all deformation modes, and all types of MREs with particle concentrations from 10% to 30%. The no-field moduli as listed in Tables 5.5, 5.13, 5.20, and 5.23 are illustrated.

5.6.3 Mechanical Response when subject to a Magnetic Field

The MR effects, which are defined as the increase in moduli when MREs are subject to a magnetic field, were studied versus engineering strain to observe the non-linear behaviour. MR effects were usually largest in the small-strain region, which decreased rapidly to nearly no effect in the mid-strain region, but increased again at larger strains (larger than 15%), although exceptions to this trend were noted. Anisotropic MREs with their particle alignment direction oriented in the same direction as the magnetic field usually exhibited the largest MR effects, while isotropic MREs exhibited the lowest effects. The anisotropic MREs with their particle alignment perpendicular to the loading direction behaved somewhat unexpectedly, exhibiting almost no MR effect in both compression and pure shear experiments. MR effects were generally found to increase with increasing iron content, except during pure shear tests, where MREs with 20% iron content showed the highest MR effects, rather than the MREs with 30% iron content. A linear increase of MR effects with increasing magnetic field was found. The MR effects present in the small-strain region of all large-strain experiments, and in all types of MREs, are compared in Figure 5.81 and 5.82. Only the results obtained with the largest magnetic fields are summarised in the figure. The highest absolute

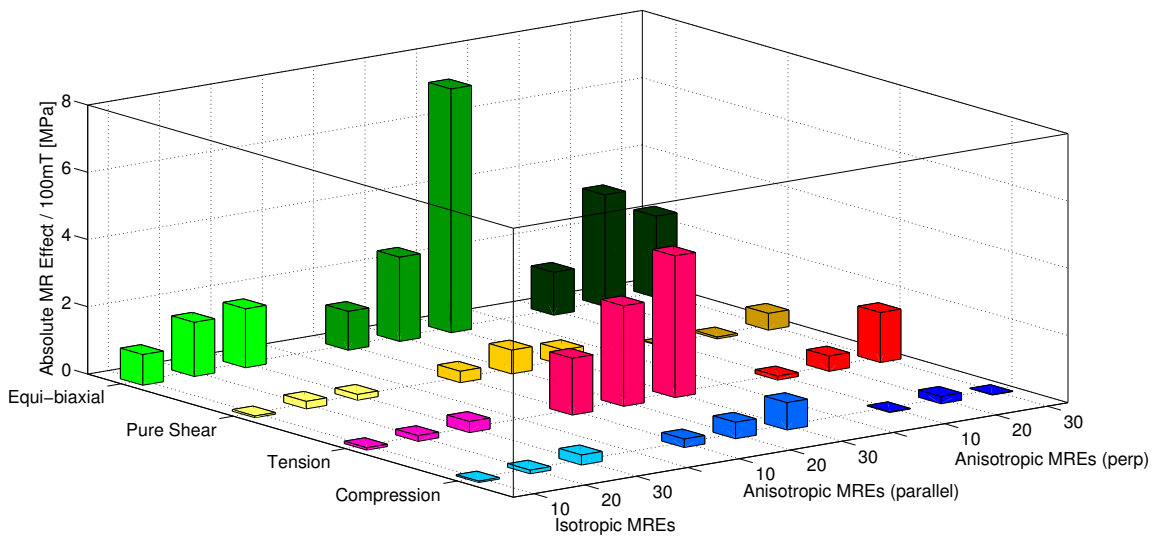


Figure 5.81: Comparison of the absolute Magneto-Rheological (MR) response for all deformation modes, and all types of MREs with particle concentrations from 10% to 30%. The absolute MR effects as listed in Tables 5.6, 5.14, 5.21, and 5.24 are related to 100 mT applied magnetic flux density.

and relative MR effects (per 100 mT applied flux) were achieved in the equi-biaxial tension tests, followed by the results of uniaxial tension tests. MR effects achieved with both the compression and the pure shear tests were comparatively low. Results of large-strain experiments published in the literature confirm both the large MR effects achieved in tension, and comparatively low effects observed in compression (see Figure 2.3). The low MR effects seen in the pure shear experiments might be due to the non-uniformity of both the strength

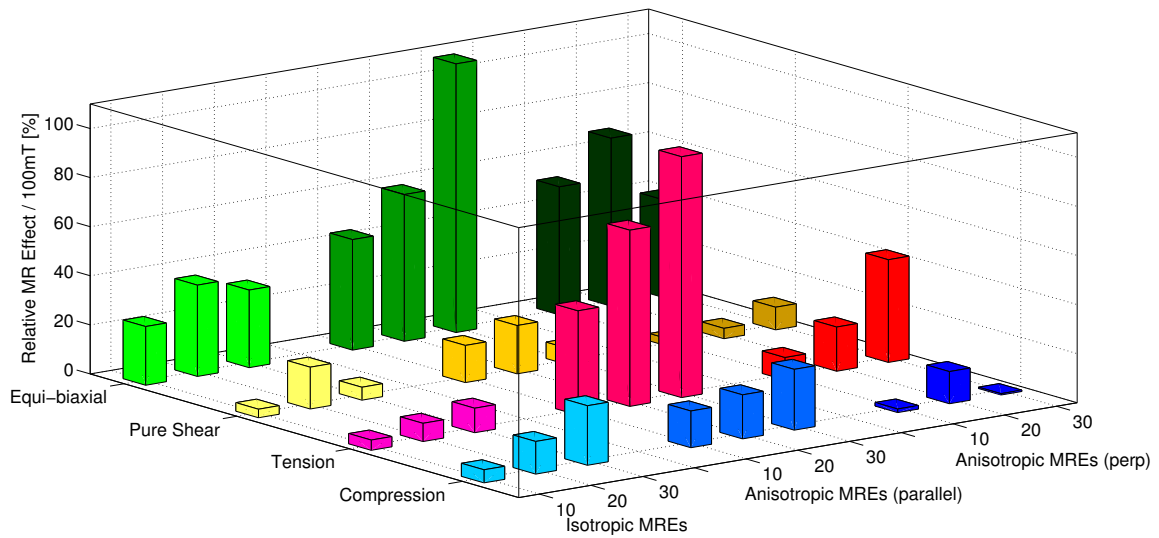


Figure 5.82: Comparison of relative Magneto-Rheological (MR) response for all deformation modes, and all types of MREs with particle concentrations from 10% to 30%. The relative MR effects as listed in Tables 5.6, 5.14, Table 5.21, and 5.24 are related to 100 mT applied magnetic flux density.

of the magnetic field and the direction of the flux lines. The performance of pure shear specimens with 30% iron content was considerably lower, which might be due to micro-structural characteristics in such samples. Note that pure shear samples were the thinnest (1 mm thickness) compared to the other specimens manufactured for this investigation. Results from the pure shear tests can not be compared to other experiments in the literature, as no other pure shear investigations on MREs have yet been published. Likewise, equi-biaxial tension tests on MREs have not been reported previously (see Section 2.5).

6 Constitutive Modelling of MREs

The purpose of this chapter is to test whether or not available constitutive models can accurately model the behaviour of MRE materials. The experimental data presented in Chapter 5 are used for a data fitting exercise, and the results are presented in this chapter. A limited choice of constitutive models describing isotropic and transversely isotropic materials, developed mainly by the group around Ogden (Dorfmann and Ogden, 2004a; Holzapfel, 2000; Ogden, 2004, *etc.*), have been considered. The list of models used here is certainly not exhaustive. More constitutive equations are available to model isotropic and anisotropic materials (for example Bergstroem and Boyce, 2000; Qi and Boyce, 2004; Varga, 1966), and also materials influenced by magnetic fields (Bustamante, 2010; Dorfmann and Ogden, 2005; Kankanala, 2007). The choice of models used in this investigation is motivated by the popularity of the *Ogden* model (Ogden, 1978) and its widespread use in commercial finite element software. Experimental data are saved on a DVD attached to this document and will be made openly available to facilitate study of other constitutive models not considered in this investigation.

This chapter is structured as follows: a brief introduction to the theory of continuum mechanics is given in Section 6.1. The optimisation method used to determine constitutive model parameters is described in Section 6.2. Section 6.3 is concerned with the modelling of isotropic MREs. The *Ogden* model for isotropic incompressible and rubber-like materials (Ogden, 1978) is presented and model parameters are determined by fitting to experimental data from isotropic MREs characterised in this investigation. The *Ogden-Roxburgh* model (Ogden and Roxburgh, 1999) is also presented to account for the stress-softening *Mullins* effect (Mullins, 1969). The importance of the availability of experimental data obtained from MREs tested up to the same strain level is emphasised. Finally, model parameters of the *Ogden* model are successfully determined when using experimental data obtained from different deformation modes up to the same strain level. Transversely isotropic constitutive models characterising material with one preferred direction are presented in Section 6.4. Model parameters are determined by fitting to experimental data from anisotropic MREs. Finally, in Section 6.5 a theoretical framework for constitutive modelling of magneto-elastic deformations is presented. Since this involves up to ten parameters and is in general very complicated, model parameters of such a constitutive model (Bustamante, 2010) are not determined here.

6.1 Introduction to Continuum Theory

A short overview of the theory of continuum mechanics is provided in this section; for further details, see, for example Holzapfel (2000). Mathematical notations used in this chapter are adopted from the latter. The basic definitions in continuum mechanics are given in Section 6.1.1 and the constitutive laws and their derivatives are presented in Section 6.1.2. The specific constitutive models, *i.e.* strain energy functions and derivation of the resulting stresses under the specific deformation kinematics imposed by each experiment are outlined in Section 6.3 for isotropic MREs and in Section 6.4 for anisotropic MREs.

The matrix material of MREs is usually a rubber-like material. Most polymeric elastomers are usually considered to be isotropic, incompressible, and hyperelastic (Holzapfel, 2000, Chapter 6). Therefore, theory presented in this section will focus on incompressible hyperelastic materials. For these materials the existence of a *Helmholtz* free-energy function Ψ , also called a ‘strain energy function’, is postulated (Holzapfel, 2000, page 206). The stress response of a hyperelastic material can be derived from a given strain energy function. Materials are incompressible when they maintain a constant volume during deformations (Holzapfel, 2000, page 222). The *Poisson’s* ratio of such materials is $\nu = 0.5$.

6.1.1 Basic Definitions in Continuum Mechanics

A fundamental definition in continuum mechanics is the deformation gradient \mathbf{F} , which provides the connection between reference and current configurations. It describes the deformation of a continuum body, and is defined as

$$\mathbf{F}(\mathbf{X}, t) = \frac{\partial \mathbf{x}}{\partial \mathbf{X}} = \frac{\partial \boldsymbol{\chi}(\mathbf{X}, t)}{\partial \mathbf{X}} \quad (6.1)$$

or in matrix form

$$\mathbf{F} = \begin{bmatrix} \frac{\partial x_1}{\partial X_1} & \frac{\partial x_1}{\partial X_2} & \frac{\partial x_1}{\partial X_3} \\ \frac{\partial x_2}{\partial X_1} & \frac{\partial x_2}{\partial X_2} & \frac{\partial x_2}{\partial X_3} \\ \frac{\partial x_3}{\partial X_1} & \frac{\partial x_3}{\partial X_2} & \frac{\partial x_3}{\partial X_3} \end{bmatrix} \quad (6.2)$$

where \mathbf{x} and \mathbf{X} are the material positions in the current and the reference configurations and 1, 2, and 3 represent the principal directions. A deformation is called homogeneous when \mathbf{F} is independent of \mathbf{X} . In large-strain theory the stretches, λ , are more commonly used than the strain values ε . Stretches are defined as follows:

$$\lambda = \varepsilon + 1 \quad (6.3)$$

In continuum mechanics several strain tensors can be defined. Material strain tensors expressed in the reference configuration include for example, the *right Cauchy-Green tensor*

\mathbf{C} , and spatial strain tensors in the current configuration include for example, the *left Cauchy-Green tensor* \mathbf{b} . Invariants of \mathbf{C} and \mathbf{b} are so-called strain invariants. In the case of isotropic materials, these strain invariants, I_a (with $a = 1, 2, 3$) are all independent and defined as:

$$I_1 = \lambda_1^2 + \lambda_2^2 + \lambda_3^2 \quad (6.4)$$

$$I_2 = \lambda_1^2 \cdot \lambda_2^2 + \lambda_1^2 \cdot \lambda_3^2 + \lambda_2^2 \cdot \lambda_3^2 \quad (6.5)$$

$$I_3 = \lambda_1^2 \cdot \lambda_2^2 \cdot \lambda_3^2 \quad (6.6)$$

The third strain invariant $I_3 = 1$ for incompressible materials.

The *Jacobian determinant*, J , is the change in volume moving from the reference to the current configurations,

$$J(\mathbf{X}, t) = \frac{dv}{dV} = \det \mathbf{F}(\mathbf{X}, t) \quad (6.7)$$

where dv and dV are infinitesimal volume elements in the current and reference configuration, respectively. The Jacobian determinant is always positive, and for an incompressible material $J = 1$.

To map from a surface element in the reference configuration, $d\mathbf{S}$, to the corresponding element in the current configuration, $d\mathbf{s}$, Nanson's formula is required,

$$d\mathbf{s} = J\mathbf{F}^{-T}d\mathbf{S} \quad (6.8)$$

$$\mathbf{n}d\mathbf{s} = J\mathbf{F}^{-T}\mathbf{N}d\mathbf{S} \quad (6.9)$$

where \mathbf{n} and \mathbf{N} are the unit vectors normal to the surface elements $d\mathbf{s}$ and $d\mathbf{S}$, respectively.

The main stress definitions in continuum mechanics are the *Cauchy* (or *True*) stress tensor, $\boldsymbol{\sigma}$, and the *first Piola-Kirchhoff* stress tensor, \mathbf{P} , defined in the current and reference configurations, respectively. They are related as

$$d\mathbf{f} = \boldsymbol{\sigma}(\mathbf{x}, t) \cdot \mathbf{n}d\mathbf{s} = \mathbf{P}(\mathbf{X}, t) \cdot \mathbf{N}d\mathbf{S} \quad (6.10)$$

where $d\mathbf{f}$ is the infinitesimal force acting on the surface element. Mapping from \mathbf{P} to $\boldsymbol{\sigma}$ can be performed using Equation 6.8.

$$\mathbf{P} = J\boldsymbol{\sigma}\mathbf{F}^{-T} \quad (6.11)$$

$$\boldsymbol{\sigma} = J^{-1}\mathbf{P}\mathbf{F}^T = \boldsymbol{\sigma}^T \quad (6.12)$$

Note that other stress definitions are available that refer to intermediate configurations. For example the *Kirchhoff* stress tensor, $\boldsymbol{\tau} = J\boldsymbol{\sigma}$ and the *second Piola-Kirchhoff* stress tensor, $\mathbf{S} = \mathbf{F}^{-1}\mathbf{P}$, but as they are not actively used here no further discussion is devoted to these stresses.

6.1.2 Constitutive equations

A constitutive law approximates the observed physical behaviour of a real material. It “determines the state of stress at any point, \mathbf{x} , of the continuum body at time t ” (Holzapfel, 2000, page 205), and relates the stress to state variables such as strain, temperature, and magnetic flux density. Data fitting performed in Sections 6.3 and 6.4 uses a phenomenological approach, *i.e.* model parameters are determined from experimental observations. Constitutive equations can be purely mathematically or can be based on empirical evidence. The general constitutive equation for a hyperelastic material is defined with:

$$\boldsymbol{\sigma}(\mathbf{x}, t) = \mathbf{g}(\mathbf{F}(\mathbf{X}, t), \mathbf{X}) \quad (6.13)$$

If the deformation is homogeneous the constitutive equation is independent of the material point \mathbf{X} , and so Equation 6.13 simplifies to:

$$\boldsymbol{\sigma}(\mathbf{x}, t) = \mathbf{g}(\mathbf{F}(\mathbf{X}, t)) \quad (6.14)$$

Using Equation 6.11, the *first Piola-Kirchhoff* stress can be defined as:

$$\mathbf{P}(\mathbf{x}, t) = J \boldsymbol{\sigma} \mathbf{F}^{-T} = \mathfrak{G}(\mathbf{F}) \quad (6.15)$$

The stress state of a hyperelastic material can be calculated from a strain-energy function Ψ . For **isotropic** and **homogeneous** materials the strain-energy function, Ψ , depends only on \mathbf{F} . The *first Piola-Kirchhoff* stress and the *Cauchy* stress can be derived from Ψ using:

$$\mathbf{P} = \frac{\partial \Psi(\mathbf{F})}{\partial \mathbf{F}} \quad (6.16)$$

$$\boldsymbol{\sigma} = J^{-1} \frac{\partial \Psi(\mathbf{F})}{\partial \mathbf{F}} \mathbf{F}^T = J^{-1} \mathbf{F} \left(\frac{\partial \Psi(\mathbf{F})}{\partial \mathbf{F}} \right)^T \quad (6.17)$$

For **isotropic** materials Ψ can be expressed as a function of the three independent strain invariants, I_a (Equation 6.4, 6.5, 6.6), or as a function of the three principal stretches, λ_a .

$$\Psi = \Psi(I_1, I_2, I_3) = \Psi(\lambda_1, \lambda_2, \lambda_3) \quad (6.18)$$

The principal *Piola-Kirchhoff* stresses, P_a , and the principal *Cauchy* stress, σ_a , can then be derived from Ψ as

$$P_a = \frac{\partial \Psi}{\partial \lambda_a} \quad (6.19)$$

$$\sigma_a = J^{-1} \lambda_a \frac{\partial \Psi}{\partial \lambda_a} \quad (6.20)$$

where $a = 1, 2, 3$ correspond to the three principal directions. Isotropic MREs are discussed in more detail in Section 6.3. The definitions for \mathbf{P} and $\boldsymbol{\sigma}$ in Equations 6.16 and 6.17 are still valid for more complex materials such as transversely isotropic materials, but the strain energy function $\Psi(\mathbf{F}, \mathbf{a})$ is no longer solely dependent on \mathbf{F} , rather it is also a function of the preferred direction, \mathbf{a} . Transversely isotropic materials are discussed in Section 6.4. Even more dependent variables have to be considered in formulating Ψ for more complex materials, *e.g.* for magneto-sensitive materials as discussed in Section 6.5. In Sections 6.4 and 6.5 pseudo-invariants are introduced, so Ψ can still be expressed as a function of the strain invariants or the principal stretches, and the derivations defined in Equations 6.19 and 6.20 are still valid.

For **incompressible** materials the following simplification can be applied,

$$J = \lambda_1 \lambda_2 \lambda_3 = 1 \quad (6.21)$$

and the strain energy function, Ψ , can be modified to the form

$$\Psi = \Psi(\mathbf{F}) - p(J - 1) \quad (6.22)$$

where the scalar, p , is a *Lagrange* multiplier which can be interpreted as an hydrostatic pressure. The value for p can be determined from equilibrium equations and boundary conditions, depending on the deformation state. The stress definitions change accordingly, thus

$$\mathbf{P} = -p\mathbf{F}^{-T} + \frac{\partial \Psi(\mathbf{F})}{\partial \mathbf{F}} \quad (6.23)$$

$$\boldsymbol{\sigma} = -p\mathbf{I} + \frac{\partial \Psi(\mathbf{F})}{\partial \mathbf{F}} \mathbf{F}^T = -p\mathbf{I} + \mathbf{F} \left(\frac{\partial \Psi(\mathbf{F})}{\partial \mathbf{F}} \right)^T \quad (6.24)$$

For **isotropic** and **incompressible** materials Ψ can be defined in terms of I_a or λ_a with:

$$\Psi = \Psi(I_1, I_2) - \frac{1}{2}p(I_3 - 1) = \Psi(\lambda_1, \lambda_2, \lambda_3) - p(J - 1) \quad (6.25)$$

The stresses can be expressed in terms of the principal stretches, λ_a , as:

$$P_a = -\frac{1}{\lambda_a}p + \frac{\partial \Psi}{\partial \lambda_a} \quad (6.26)$$

$$\sigma_a = -p + \lambda_a \frac{\partial \Psi}{\partial \lambda_a} \quad (6.27)$$

6.2 Optimisation Methods

The goal of this study is to test whether or not constitutive equations published in the literature can accurately model the behaviour of MREs. To determine constitutive model parameters, \mathbf{mp} , with the phenomenological approach, data fitting to experimental data is performed, the results of which are described in Sections 6.3 and 6.4. A least-square optimisation algorithm is used to determine the optimal parameters. The objective functions to be minimised when fitting to experimental data of single deformation, and of a combination of several deformation modes, are given. The implementation of this optimisation problem into *Matlab* is described.

Derivations of the specific strain energy functions are provided to enable direct comparison of the *Piola* stresses, \mathbf{P} , with experimentally measured stresses, both defined in the reference configuration. Recalling the definition in Equation 6.15, the constitutive law is also dependant on the model parameters \mathbf{mp} . In the case of isotropic materials the constitutive equation can be expressed in terms of $\boldsymbol{\lambda}$ rather than \mathbf{F} :

$$\mathbf{P} = \mathfrak{G}(\boldsymbol{\lambda}, \mathbf{mp}) \quad (6.28)$$

Following Ogden *et al.* (2004), this form for the constitutive model will be used throughout this section. To determine \mathbf{mp} , a minimisation problem needs to be solved using non-linear least-square techniques. The objective function to be minimised is the squared 2-Norm of the residuals between predictions of the constitutive equation and the experimental data for each deformation mode. If $\lambda_i = [\lambda_1, \lambda_2, \dots, \lambda_m]^T$ is the vector of stretches, and $\tau_i = [\tau_1, \tau_2, \dots, \tau_m]^T$ the corresponding experimental stresses, the equivalent stress predicted by the constitutive equation is $\mathfrak{G}(\boldsymbol{\lambda}, \mathbf{mp})$. The objective function to be minimised can be defined as:

$$\mathbf{S}_{\mathfrak{G}}(\mathbf{mp}) := \|\mathfrak{G}(\boldsymbol{\lambda}, \mathbf{mp}) - \boldsymbol{\tau}\|_2^2 = \sum_{i=1}^m [\mathfrak{G}(\lambda_i, \mathbf{mp}) - \tau_i]^2 \quad (6.29)$$

Thus the minimisation problem can be written as:

$$\min_p \mathbf{S}_{\mathfrak{G}}(\mathbf{mp}) \quad (6.30)$$

Solutions for this minimisation problem are not unique, and several sets of optimal model parameters can be identified depending on the chosen start parameters or the chosen numerical accuracy (Ogden *et al.*, 2004). To achieve unique solutions, additional experimental data sets measured under different deformation modes are required. The objective function to be minimised is then the sum of the squared 2-Norms from each experimental data set (Ogden *et al.*, 2004). In this study experimental data from uniaxial compression, tension, pure shear,

and equi-biaxial tension are reported and are finally combined to obtain a unique set of model parameters. The objective function is thus defined as,

$$\begin{aligned} \mathbf{S}_{\mathfrak{G}}(\mathbf{mp}) := & \|\mathfrak{G}_c(\boldsymbol{\lambda}_c, \mathbf{mp}) - \boldsymbol{\tau}_c\|_2^2 + \|\mathfrak{G}_t(\boldsymbol{\lambda}_t, \mathbf{mp}) - \boldsymbol{\tau}_t\|_2^2 + \\ & \|\mathfrak{G}_{ps}(\boldsymbol{\lambda}_{ps}, \mathbf{mp}) - \boldsymbol{\tau}_{ps}\|_2^2 + \|\mathfrak{G}_{eb}(\boldsymbol{\lambda}_{eb}, \mathbf{mp}) - \boldsymbol{\tau}_{eb}\|_2^2 \end{aligned} \quad (6.31)$$

where the subscript, c , defines the compression deformation mode, t , the uniaxial tension deformation mode, and ps and eb the pure shear and equi-biaxial tension deformation modes, respectively. Combination of the different deformation modes provides unique solutions for the model parameters at the expense of a reduction in the quality of the fit. To achieve unique solutions for the model parameters and still obtain a reasonably good fit when combining all of the deformation modes, weight factors can be introduced:

$$\begin{aligned} \mathbf{S}_{\mathfrak{G}}(\mathbf{mp}) := & \|w_c \cdot \mathfrak{G}_c(\boldsymbol{\lambda}_c, \mathbf{mp}) - \boldsymbol{\tau}_c\|_2^2 + \|\mathfrak{G}_t(\boldsymbol{\lambda}_t, \mathbf{mp}) - \boldsymbol{\tau}_t\|_2^2 + \\ & \|w_{ps} \cdot \mathfrak{G}_{ps}(\boldsymbol{\lambda}_{ps}, \mathbf{mp}) - \boldsymbol{\tau}_{ps}\|_2^2 + \|w_{eb} \cdot \mathfrak{G}_{eb}(\boldsymbol{\lambda}_{eb}, \mathbf{mp}) - \boldsymbol{\tau}_{eb}\|_2^2 \end{aligned} \quad (6.32)$$

The weight factors w_c , w_{ps} , and w_{eb} scale the constitutive equation separately for compression, pure shear, and equi-biaxial deformation modes. Basically this means that different model parameters are determined for each deformation mode, but also that they are all connected by a simple factor. The weight factors account for experimental issues that are present and of which the author is aware. The experimental setup and the test procedure of the uniaxial tension experiments were considered to be the most reliable. In the case of compression and equi-biaxial tension tests, friction might influence the experimental results (Sections 5.2 and 5.5). In pure shear tests the occurrence of small strains in the horizontal direction might cause the experimental data to differ from theoretical values (Section 5.4). The tension mode was chosen to have a constant weight scale of 1, as using a weight factor for all of the deformation modes leads to non-unique solutions of the model parameters. When using the weight factors, w , three additional model parameters are introduced in the minimisation problem when combining all four deformation modes.

A *Matlab* code was written to solve this minimisation problem, incorporating the available *Matlab* functions, *lsqcurvefit.m* (suitable when only one set of experimental data is provided) and *fmincon.m* (suitable when a combination of deformation modes is employed), *Matlab* (see 2013). The function *lsqcurvefit.m* solves non-linear curve-fitting problems in the least-squares sense. The constitutive equation (defined as a function handle in *Matlab*), the starting guess for the model parameters, \mathbf{mp} , lower and upper bounds for the parameters (taking care to meet any constraints), and the experimental data, are required inputs. *lsqcurvefit.m* automatically uses the squared 2-Norm as the objective function. When running this code, the default *Trust-Region Reflective Algorithm*, a large-scale optimisation method, was used.

The function *fminon.m* is a more general optimisation function which finds the minimum of a constrained nonlinear multivariable function. Here, the objective function is a required input and has to be defined by the user, so the squared 2-Norm must be calculated beforehand, and can easily be modified to perform the data fitting using a combination of deformation modes. Start parameters, lower and upper bounds, and the experimental data are also required inputs. The *Interior-Point Algorithm* (which will become the default in future releases of *Matlab*) was used. For both functions, the tolerance value of the function was set to $TolFun = 1e - 15$, the maximum number of function evaluations allowed was increased to 18000, and the maximum number of iterations was set to 3000, to ensure that a solution could be obtained.

To aid with the optimisation process, bespoke *Matlab* functions designed for each constitutive equations used in this investigation were written. The names of these functions and the algorithms used within the functions are detailed in Sections 6.3.2 and 6.4.3. These *Matlab* functions enable the input of either just one set of experimental data, or a combination of several sets of data, each measured under distinct deformation modes. Many sets of possible start parameters can be provided, and the *Matlab* functions perform the data fitting for each of these start parameter sets. The fitting algorithm run at least twice for each set of start parameters; newly determined model parameters are used as the new start values in the subsequent run. The fitting process is repeated as long as the 2-Norm decreases. The set of parameters with the smallest 2-Norm is used as the final solution for **mp**. Suitable start parameters were taken from the literature (Holzapfel, 2000), and from model parameters determined during this study. Several combinations of start values within a specified range were also used to ensure a wide range of initial start values.

Several error definitions are used to help interpret the results. The 2-Norm is defined as:

$$\|\mathfrak{G}(\boldsymbol{\lambda}, \mathbf{mp}) - \boldsymbol{\tau}\|_2 = \sqrt{\sum_{i=1}^m [\mathfrak{G}(\lambda_i, \mathbf{mp}) - \tau_i]^2} \quad (6.33)$$

The 2-Norm can be used to decide whether or not further fitting is required or to compare results obtained using different sets of start parameters. However, the 2-Norm is an absolute value and is therefore unsuitable for comparison of either (i) fitting results from different types of MREs, or (ii) fitting results obtained when using data sets employing different numbers of data points (a larger number of experimental data points automatically leads to a larger 2-Norm value as the latter is computed as a sum of residuals over all data points). The 2-Norm is a non-adjusted value that can only be used internally to control the performance of the fitting algorithm. In contrast, the coefficient of determination, R_2 , is suitable to compare different data sets, as this is a relative value. A value of R_2 of 1 indicates a perfect fit, whereas 0 indicates no correlation. R_2 is defined as the ratio between the squared

2-Norm of the residuals, and the total sum of squares using the average value of the stresses,

$$\bar{\tau} = \frac{1}{m} \sum_{i=1}^m \tau_i:$$

$$R_2 = 1 - \frac{\sum_{i=1}^m [\mathfrak{G}(\lambda_i, \mathbf{mp}) - \tau_i]^2}{\sum_{i=1}^m [\tau_i - \bar{\tau}]^2} \quad (6.34)$$

The coefficient of determination is preferred when comparing the data fitting results of different types of MREs, or results up to different strain levels as the use of the average stress $\bar{\tau}$ makes them comparable.

6.3 Modelling of Isotropic MREs

The *Ogden* model for isotropic incompressible rubber-like materials (Ogden, 1978) is described in this section, and model parameters are determined by fitting the model to experimental data of isotropic MREs presented in Chapter 5. The strain energy function of the *Ogden* model, and the derivations of stress functions for each deformation mode are presented in Section 6.3.1. The fitting procedure is described in Section 6.3.2. The parameters of the *Ogden* model are determined by data fitting to each deformation mode in turn, and then to a combination of several modes, the results of which are presented in Section 6.3.3. As emphasised in Chapter 5, MREs are very sensitive to the stress-softening *Mullins* effect, thus the preconditioning strain level is very important. The data fitting to a combination of deformation modes can only be successful when the data are obtained from tests up to the same strain level. The compression, tension, and pure shear experiments were performed up to approximately 50% strain, but in the equi-biaxial tension tests samples were only stretched up to 10% strain. The *Ogden-Roxburgh* model is employed to account for the stress-softening effect, and to adjust experimental data (using the determined model parameters of the *Ogden-Roxburgh* model) so that they represent data obtained from a lower strain level. This is a novel strategy used in this investigation as detailed in Section 6.3.4. The adjusted experimental data are then used to determine final parameters of the *Ogden* model using multiple data sets all obtained from tests up to the same strain level. The results of the *Ogden* model charactering MREs under general deformation when tested up to 50% and 10% strain are presented in Section 6.3.5.

6.3.1 Ogden Model, Tests Kinematics and Stress Definitions

The strain energy function of the *Ogden* model for incompressible isotropic elastomeric materials can be defined as a function of the principal stretches (Ogden, 1978) using,

$$\Psi = \Psi(\lambda_1, \lambda_2, \lambda_3) = \sum_{p=1}^N \frac{\mu_p}{\alpha_p} (\lambda_1^{\alpha_p} + \lambda_2^{\alpha_p} + \lambda_3^{\alpha_p} - 3) \quad (6.35)$$

where λ_a are the principal stretches, μ_p and α_p are the model parameters determined by fitting the *Ogden* model to experimental data, and N is an integer that determines the order of the *Ogden* model. The model parameters must fulfil a constraint when fitted to experimental data:

$$\mu_p \alpha_p > 0 \quad (6.36)$$

The modulus, μ , used in the well-known *Neo-Hookean* model can be calculated as follows:

$$\mu = \frac{1}{2} \sum_{p=1}^N \mu_p \alpha_p \quad (6.37)$$

Relating this to infinitesimal strain theory, the modulus, μ , is the shear modulus, G , in the case of uniaxial deformation. The relation between the shear modulus, G , and the Young's modulus, E , in linear theory is defined as

$$E = 2G(1 + \nu) \quad (6.38)$$

where ν is the Poisson's ratio (0.5 for incompressible materials). In general E can be calculated as the first derivative of the *Cauchy* stress function with respect to λ , and as the Young's modulus is defined in the small strain region the limit of this derivative with $\lambda \rightarrow 1$ is calculated as:

$$E = \left. \frac{\partial \sigma}{\partial \lambda} \right|_{\lambda=1} \quad (6.39)$$

Only the Young's modulus, E , can be compared with the moduli presented in Chapter 5 of this study. The stresses σ and P are derived using Equations 6.26, 6.27, and 6.35 as follows,

$$\sigma_a = -p + \sum_{p=1}^N \mu_p \cdot \lambda_a^{\alpha_p} \quad (6.40)$$

$$P_a = \frac{1}{\lambda_a} \left[-p + \sum_{p=1}^N \mu_p \cdot \lambda_a^{\alpha_p} \right] \quad (6.41)$$

where the *Lagrange* multiplier, p , still needs to be determined using the equilibrium equations and boundary conditions, which depend on the deformation mode.

Uniaxial deformation. The uniaxial deformation is a pure stretch deformation with the main stretch in the 1 direction; $\lambda_1 > 1$ in tension and $\lambda_1 < 1$ in compression. The stretches in the two other directions are equal and defined using the incompressibility constraint.

$$\lambda_1 = \lambda \quad (6.42)$$

$$\lambda_2 = \lambda_3 = \frac{1}{\sqrt{\lambda}} \quad (6.43)$$

The deformation gradient, \mathbf{F} , is therefore defined as:

$$\mathbf{F} = \begin{bmatrix} \lambda & 0 & 0 \\ 0 & \frac{1}{\sqrt{\lambda}} & 0 \\ 0 & 0 & \frac{1}{\sqrt{\lambda}} \end{bmatrix} \quad (6.44)$$

The strain energy function of the *Ogden* model (Equation 6.35) simplifies to:

$$\Psi(\lambda) = \sum_{p=1}^N \frac{\mu_p}{\alpha_p} (\lambda^{\alpha_p} + 2\lambda^{-\alpha_p/2} - 3) \quad (6.45)$$

To determine the *Lagrange* multiplier, p , in Equation 6.40, the boundary conditions and equilibrium equations are considered. Here the body is not constrained in the second and third direction which means the principal stresses in those directions are zero.

$$\sigma_1 \neq 0 \quad (6.46)$$

$$\sigma_2 = \sigma_3 = 0 \quad (6.47)$$

With this, the unknown scalar p can be calculated, and σ and P are completely determined as

$$\sigma_1 = \sum_{p=1}^N \mu_p (\lambda^{\alpha_p} - \lambda^{-\alpha_p/2}) \quad (6.48)$$

$$P_1 = \frac{1}{\lambda} \sum_{p=1}^N \mu_p (\lambda^{\alpha_p} - \lambda^{-\alpha_p/2}) \quad (6.49)$$

To connect to the linear theory the Young's modulus E_1 is defined as:

$$E_1 = \left. \frac{\partial \sigma_1}{\partial \lambda} \right|_{\lambda=1} = 3 \cdot \frac{1}{2} \sum_{p=1}^N \alpha_p \mu_p = 3 \cdot \mu \quad (6.50)$$

Pure Shear Deformation. When a very wide sheet of material is stretched a state of pure shear is achieved. According to BS 903-5 (2004), the width of the sample has to be

five times its height. This ensures that the contraction occurs predominantly in the through thickness direction. Ideally there is negligible stretch along the width of the samples. Due to the incompressibility of the material, a state of pure shear exists at an angle 45 degrees to the main stretching direction. Pure shear deformation is a pure stretch, thus no rotation is involved. The principal stretches are defined as follows:

$$\lambda_1 = \lambda \quad (6.51)$$

$$\lambda_2 = 1 \quad (6.52)$$

$$\lambda_3 = 1/\lambda \quad (6.53)$$

and the deformation gradient \mathbf{F} is given as:

$$\mathbf{F} = \begin{bmatrix} \lambda & 0 & 0 \\ 0 & 1 & 0 \\ 0 & 0 & \frac{1}{\lambda} \end{bmatrix} \quad (6.54)$$

Contrary to pure shear, simple shear involves rotation and for simple shear \mathbf{F} is defined as,

$$\mathbf{F} = \begin{bmatrix} 1 & \gamma & 0 \\ 0 & 1 & 0 \\ 0 & 0 & 1 \end{bmatrix} \quad (6.55)$$

where γ is the shear strain.

In the case of a pure shear deformation, the strain energy function, Ψ , of the *Ogden* model is defined as:

$$\Psi = \sum_{p=1}^N \frac{\mu_p}{\alpha_p} (\lambda^{\alpha_p} + \lambda^{-\alpha_p} - 2) \quad (6.56)$$

The thin sheet of material leads to a plane stress condition with zero stress in the through thickness direction. The boundary conditions are defined as:

$$\sigma_1 \neq 0 \quad (6.57)$$

$$\sigma_2 \neq 0 \quad (6.58)$$

$$\sigma_3 = 0 \quad (6.59)$$

The stresses in the reference and the current configuration are thus defined as:

$$\sigma_1 = \sum_{p=1}^N \mu_p [\lambda^{\alpha_p} - \lambda^{-\alpha_p}] \quad (6.60)$$

$$\sigma_2 = \sum_{p=1}^N -\mu_p \lambda^{-\alpha_p} \quad (6.61)$$

$$P_1 = \frac{1}{\lambda} \sum_{p=1}^N \mu_p [\lambda^{\alpha_p} - \lambda^{-\alpha_p}] \quad (6.62)$$

$$P_2 = \frac{1}{\lambda} \sum_{p=1}^N -\mu_p \lambda^{-\alpha_p} \quad (6.63)$$

The Young's modulus of the linear theory at small strains is defined as:

$$E_1 = \left. \frac{\partial \sigma_1}{\partial \lambda_1} \right|_{\lambda=1} = 4 \cdot \frac{1}{2} \sum_{p=1}^N \alpha_p \mu_p = 4 \cdot \mu \quad (6.64)$$

Biaxial Deformation. In the case of a biaxial deformation, the stretches, λ_1 and λ_2 , are the main stretches, and the stretch in the third direction is determined from the incompressibility constraint with:

$$\lambda_3 = \frac{1}{\lambda_1 \lambda_2} \quad (6.65)$$

In the case of equi-biaxial deformation the stretches in the two loading directions are equal and the kinematics are given as:

$$\lambda_1 = \lambda_2 = \lambda \quad (6.66)$$

$$\lambda_3 = \frac{1}{\lambda^2} \quad (6.67)$$

In this case the deformation gradient \mathbf{F} is determined as:

$$\mathbf{F} = \begin{bmatrix} \lambda & 0 & 0 \\ 0 & \lambda & 0 \\ 0 & 0 & \frac{1}{\lambda^2} \end{bmatrix} \quad (6.68)$$

In the case of equi-biaxial deformation, the strain energy function of the *Ogden* model (Equation 6.35), simplifies to:

$$\Psi(\lambda) = \sum_{p=1}^N \frac{\mu_p}{\alpha_p} (2\lambda^{\alpha_p} + \lambda^{-2\alpha_p} - 3) \quad (6.69)$$

To determine the *Lagrange* multiplier, p , the boundary conditions and equilibrium equations are considered. The equi-biaxial MRE samples are very thin sheets of material, which implies a plane stress condition with zero stress in the out of plane direction:

$$\sigma_1 = \sigma_2 \neq 0 \quad (6.70)$$

$$\sigma_3 = 0 \quad (6.71)$$

The stresses σ and P are completely defined with the determined scalar p as:

$$\sigma_1 = \sigma_2 = \sum_{p=1}^N \mu_p [\lambda^{\alpha_p} - \lambda^{-2\alpha_p}] \quad (6.72)$$

$$P_1 = P_2 = \frac{1}{\lambda} \sum_{p=1}^N \mu_p [\lambda^{\alpha_p} - \lambda^{-2\alpha_p}] \quad (6.73)$$

The Young's modulus of the linear theory at small strains is defined as

$$E_1 = E_2 = \left. \frac{\partial \sigma_1}{\partial \lambda} \right|_{\lambda=1} = 6 \cdot \frac{1}{2} \sum_{p=1}^N \alpha_p \mu_p = 6 \cdot \mu \quad (6.74)$$

6.3.2 Fitting Procedure

The general optimisation algorithm was described in Section 6.2, and here the specific optimisation procedure and the *Matlab* functions used for the experimental data fitting of the *Ogden* model are described. To aid with the determination of the *Ogden* model parameters, the *Matlab* function *constmodel_piola_incompiso.m* was written (see Appendix D). The *Ogden* model up to the model order $N = 5$ was implemented supporting the uniaxial, pure shear, and equi-biaxial deformation kinematics. Functions to calculate P (Equations 6.49, 6.62, and 6.73) are saved as 'function handles' in the function *ogden_modelfun_piola.m* (see Appendix D). Data fitting can be performed using data sets from each individual test condition, or using a combination of data sets measured under the different test kinematics. Optionally, each *Piola* stress function can be multiplied with a weight factor as discussed in Section 6.2 (see Equation 6.32). This introduces a maximum of three additional fitting parameters to be determined. Initial weighting factors are all set to $w = 1$ for the first fitting procedure. Start parameters for α_p and μ_p are required, and several sets of initial values can be used. The function *ogden_startparameters.m* stores previously determined model parameters from this study, and typical values found in Holzapfel (2000, page 236). It can also determine all possible combinations from a parameter range provided by the user. To fulfil the constraint of Equation 6.36, lower and upper bounds are defined with 0 and $\pm \inf$, respectively, and sign combinations of the initial parameters are defined. For example, in the case of a third order *Ogden* model, three start parameters for α_p and three for μ_p are required, and eight different combinations of \pm signs are possible. The fitting process runs separately for each of these sign combinations, and the combination that results in model parameters with the smallest 2-Norm are chosen either as a new set of initial values for a further run of the fitting process or as final solution for this set of start parameters. The fitting algorithm

runs at least twice and is repeated as long as the 2-Norm decreases. This procedure is performed separately for each set of start parameters, and the set resulting in model parameters, **mp**, with the smallest 2-Norm is the final solution. The fitting procedure is time-consuming: in the case of $N = 3$ and 10 sets of start parameters, the function *lsqcurvefit.m* or *fmincon.m* is called at least $2 \times 8 \times 10 = 160$ times, and six model parameters have to be determined on each call. When using weight factors (Equation 6.32) a maximum of nine parameters must be determined. The *Matlab* functions written for the data fitting process are listed in Appendix D and are saved on a DVD available with this thesis.

6.3.3 Experimental Data Fitting for the Ogden Model

In this section the results of the data fitting process to data obtained from both single deformation modes, and from a combination of compression, tension, pure shear, and equi-biaxial modes, without and with the use of weight factors, are presented. Figures comparing the experimental data with the *Piola* stress predictions of the fitted *Ogden* model of order $N = 3$ are provided. The modulus (Equation 6.37), the 2-Norm (Equation 6.33), and the coefficient of determination, R_2 (Equation 6.34) are also presented. The full sets of fitted model parameters can be found in Appendix F.1.

6.3.3.1 Fitting to Single Deformation Modes

When the model parameters are determined by a data fitting to experimental data of just one single deformation mode, the quality of the fits is very good with R_2 values of close to 1. However, the resulting model parameters, **mp**, are not valid under general deformations. For example, **mp** of the uniaxial compression mode cannot be used to interpret the behaviour of MREs under tension, pure shear, or equi-biaxial tension. In Figure 6.1, the predicted and experimental values for P are plotted versus the stretch for each deformation mode. Data fitting was performed using experimental data up to the maximum stretch imposed during the experiment, or up to the point of divergence between *NoField01* and *NoField02* compression and tension tests (see Sections 5.3.5 and 5.2.3). Tension samples (preconditioned to 15 mm, equivalent to 50% strain), and pure shear samples (preconditioned to 6 mm, equivalent to approximately 45% strain) are presented. The data fitting results for the uniaxial compression and tension tests are of very high quality. In the case of pure shear and equi-biaxial tension tests differences between the experimental data and the predicted *Piola* stress can be observed in the small-strain region (see Figure 6.1 c and d).

Different sets of model parameters are determined for each type of MRE and for each deformation mode. In Table 6.1, the results of the data fitting to stress-stretch data are summarised. The resulting moduli, μ , the Young's moduli, E , and the coefficients of determination, R_2 , are all provided. R_2 values confirm that the results of the compression and tension de-

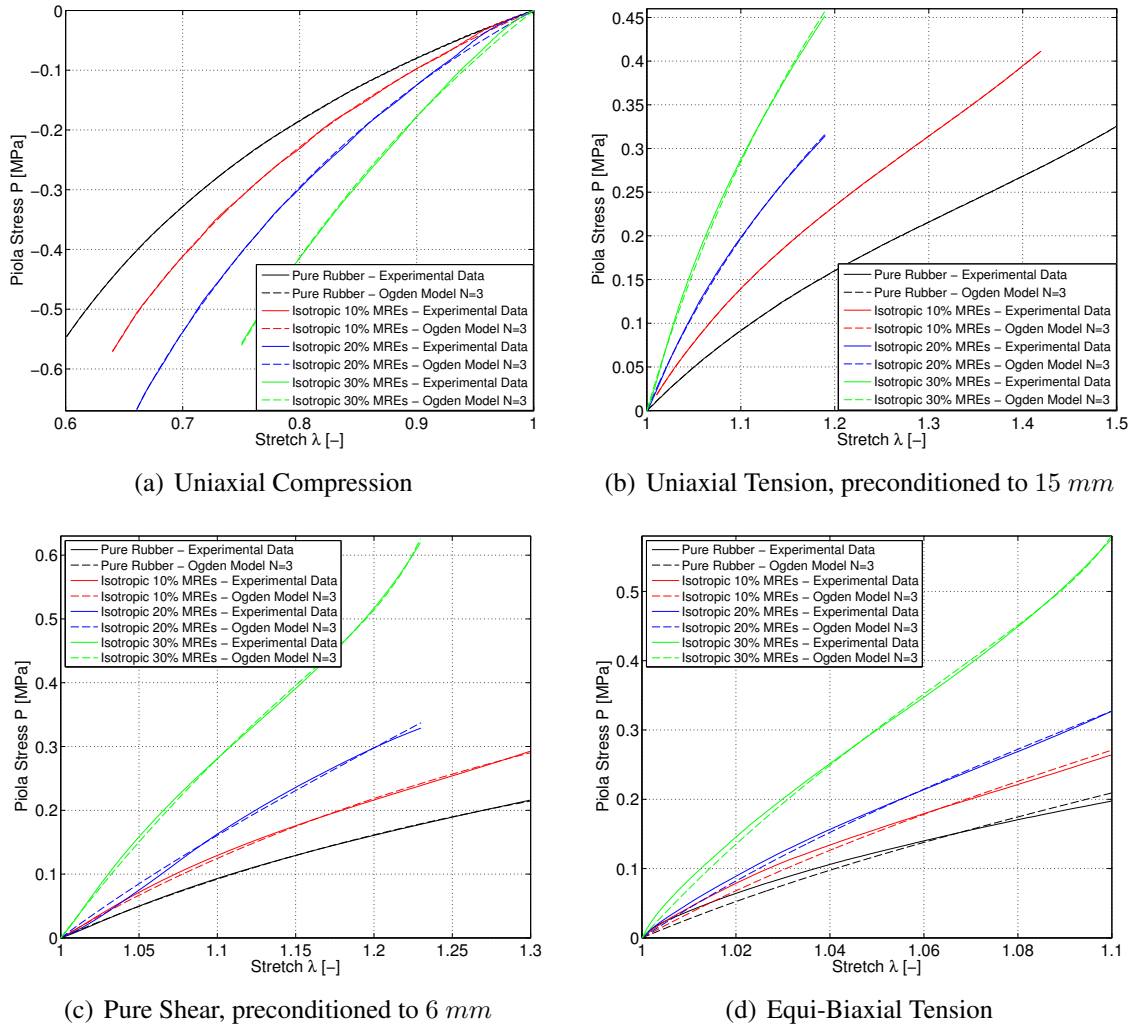


Figure 6.1: Predictions of the *Ogden* model fitted to single deformation modes are compared to the experimental data. Data of pure rubber and isotropic MREs, tested under uniaxial compression, uniaxial tension, pure shear, and equi-biaxial tension, are used for the data fitting.

formation modes are excellent, and that the fits to pure shear and equi-biaxial data are also very good. The fits are usually better in the case of pure rubber, whereas the quality decreases with increasing iron content.

Although the results of the fitting are very good, the problem is that the set of model parameters obtained during the fitting is not unique. Different sets of parameters can be identified for both different sets of initial values and set accuracy in the fitting algorithm, although the resulting moduli, μ , might be almost identical. In Appendix F.2 the different sets of start parameters and the resulting sets of model parameters are listed for pure rubber tested under uniaxial compression. Fitting to a combination of different deformation modes is required to achieve a unique solution. However, as shown in the next paragraph, the fit quality tends to decrease when using multiple deformation modes.

	MRE Type	μ [MPa]	E [MPa]	R_2
Uniaxial Compression	Pure Rubber	0.2359	0.7078	1.0000
	Isotropic 10% MREs	0.2817	0.8452	0.9999
	Isotropic 20% MREs	0.3566	1.0699	0.9996
	Isotropic 30% MREs	0.5189	1.5568	0.9994
Uniaxial Tension	Pure Rubber	0.3601	1.0803	1.0000
	Isotropic 10% MREs	0.5980	1.7941	1.0000
	Isotropic 20% MREs	0.8479	2.5438	0.9997
	Isotropic 30% MREs	1.2295	3.6885	0.9991
Pure Shear	Pure Rubber	0.2657	1.0629	0.9999
	Isotropic 10% MREs	0.3595	1.4378	0.9986
	Isotropic 20% MREs	0.4539	1.8157	0.9961
	Isotropic 30% MREs	0.8092	3.2367	0.9993
Equi-Biaxial Tension	Pure Rubber	0.4750	2.8498	0.9772
	Isotropic 10% MREs	0.6159	3.6952	0.9910
	Isotropic 20% MREs	0.7464	4.4784	0.9976
	Isotropic 30% MREs	1.2482	7.4891	0.9982

Table 6.1: The modulus, μ , the Young's modulus, E , and the coefficient of determination, R_2 , of the *Ogden* model fitted to the single deformation modes are listed. Data of pure rubber and isotropic MREs, tested under uniaxial compression, uniaxial tension, pure shear, and equi-biaxial tension, are used for the data fitting. The moduli, E , can be compared with the experimentally determined moduli (see Tables 5.5, 5.13, 5.20, and 5.23).

6.3.3.2 Fitting to a Combination of Deformation Modes

The importance of the preconditioning strain level was discussed in Chapter 5. As the MRE material is very sensitive to the *Mullins* effect, a different stress-strain behaviour is obtained when the same type of MRE specimen is tested up to a different strain level (see Section 5.1.1). When fitting the *Ogden* model to a combination of deformation modes, experimental data obtained from samples preconditioned to the same strain level are preferred. All available experimental data sets are also combined, but basically only to show that the results are not useful, and to emphasise the importance of using the same strain levels. Only with the use of weight factors (Equation 6.32) can good results be achieved when combining all deformation modes. Those weight factors account for the different strain levels that are present in the experimental data (equi-biaxial tests were only performed up to 10% strain), and also account for experimental issues like friction that might be present in compression tests (between test rig plate and sample) and equi-biaxial tension tests (sliding clamps), and the non-zero horizontal strains present in pure shear experiments. These experimental issues were discussed in Chapter 5, and the weight factors were introduced in Section 6.2.

Pure rubber and isotropic MRE specimens were tested under compression up to 50% strain, under tension up to 100%, 75%, 50%, or 15% strain (30, 22.5, 15, or 5 mm, see Table 5.7), under pure shear up to 67%, 45%, or 23% strain (9, 6, or 3 mm, see Table 5.17), and under equi-biaxial tension up to 10% strain (larger strains could not be achieved with the test apparatus used, see Section 5.5). Note that due to the analysis of experimental

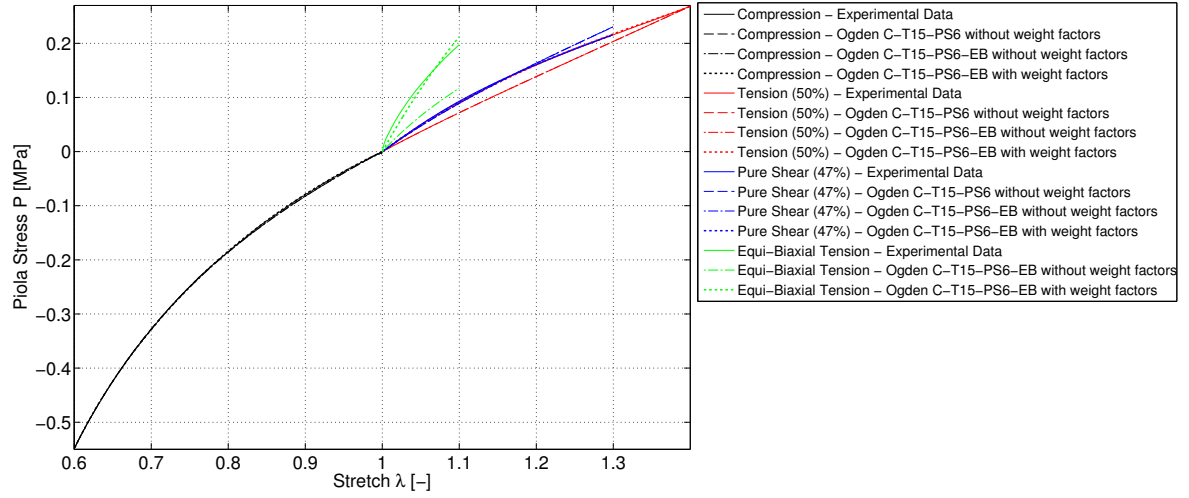
data (Section 5.1.2), and due to divergences between *NoField01* and *NoField02* compression and tension test data (see Sections 5.2.3 and 5.3.5) the strains in the third loading cycle, which is used for the data fitting, might be less than the strains in the first cycle (as seen in the subsequent figures in this section). All MRE samples were tested to a similar strain level of 50% ($\pm 5\%$) strain under compression, tension (15 mm), and pure shear (6 mm). These three deformation modes (C-T15-PS6) are combined to achieve results that describe the behaviour of pure rubber and isotropic MREs tested to approximately 50% strain under general deformation. For the isotropic MREs containing 30% volume iron fraction tests were performed up to 10% strain ($\pm 5\%$) in tension (5 mm) and equi-biaxial tension. These two deformation modes (T5-EB) are combined to characterise MREs with 30% iron that were tested up to 10% strain. All deformation modes are combined (C-T15-PS6-EB) first without and then with the use of weighting factors.

Predictions of the *Ogden* model are compared alongside the actual experimental data in Figures 6.2 and 6.3 for all isotropic MREs. In Table 6.2 the modulus, μ , calculated with the fitted model parameters of the *Ogden* model, and their corresponding R_2 values are summarised for all types of MREs. When weight factors are used, the resulting μ represent the tension mode, and the moduli for the other deformation modes are calculated with the weight factors, also provided in the table. R_2 values can be calculated for each deformation mode; listed in the table is the minimum value obtained. The full sets of model parameters for the several combinations are listed in Appendix F.3. Very good results are achieved with the

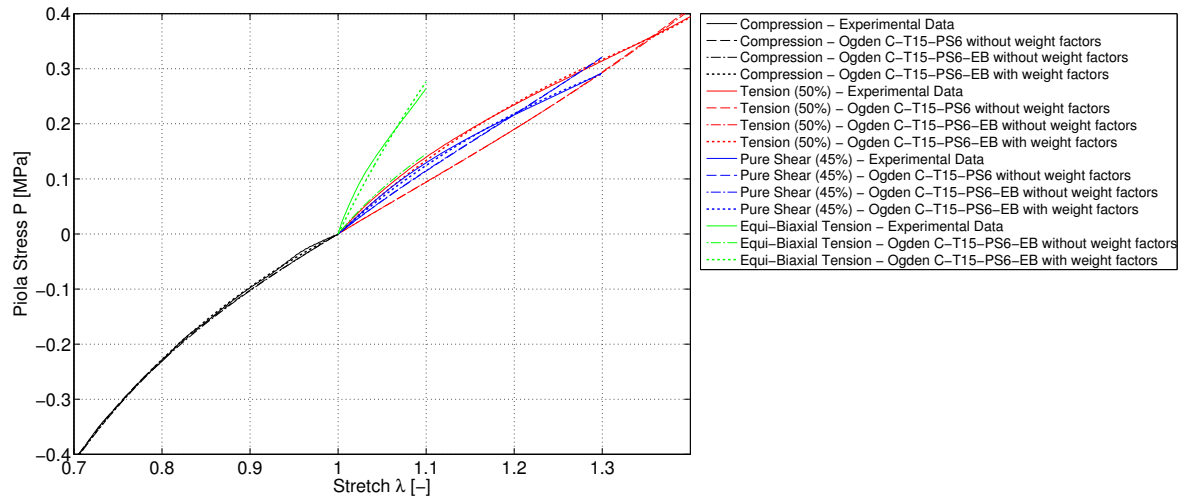
Combinations	Pure Rubber		Isotropic 10% MREs		Isotropic 20% MREs		Isotropic 30% MREs	
	μ	R_2	μ	R_2	μ	R_2	μ	R_2
C-T15-PS6	0.2529	0.9728	0.3197	0.9118	0.4163	0.5489	0.6299	0.7983
T5-EB							1.1491	0.9867
C-T15-PS6-EB	0.2539	0.1559	0.3225	0.1540	0.4282	0.1352	0.7676	0.3510
C-T15-PS6-EB	0.3368	0.9618	0.5096	0.9784	0.7357	0.9904	1.0499	0.9888
	μ	w	μ	w	μ	w	μ	w
Compression	0.2295	0.6814	0.2776	0.5448	0.3582	0.4868	0.5057	0.4817
Pure Shear	0.2641	0.7842	0.3590	0.7045	0.4798	0.6522	0.8142	0.7755
Equi-Biaxial	0.4241	1.2592	0.5401	1.0599	0.6486	0.8816	1.0904	1.0386

Table 6.2: The modulus, μ (provided in *MPa*), and the coefficient of determination, R_2 , of the *Ogden* model fitted to combined deformation modes of pure rubber and isotropic MREs with 10%, 20%, and 30% volume iron fraction are listed. C-T15-PS6 combines experimental data obtained from tests up to approximately 50% strain, and T5-EB combines data from tests up to approximately 10% strain. C-T15-PS6-EB combines all deformation modes without and with the use of weight factors. When weight factors are used the resulting μ represent the tension mode, and the resulting moduli for the other deformation modes are calculated.

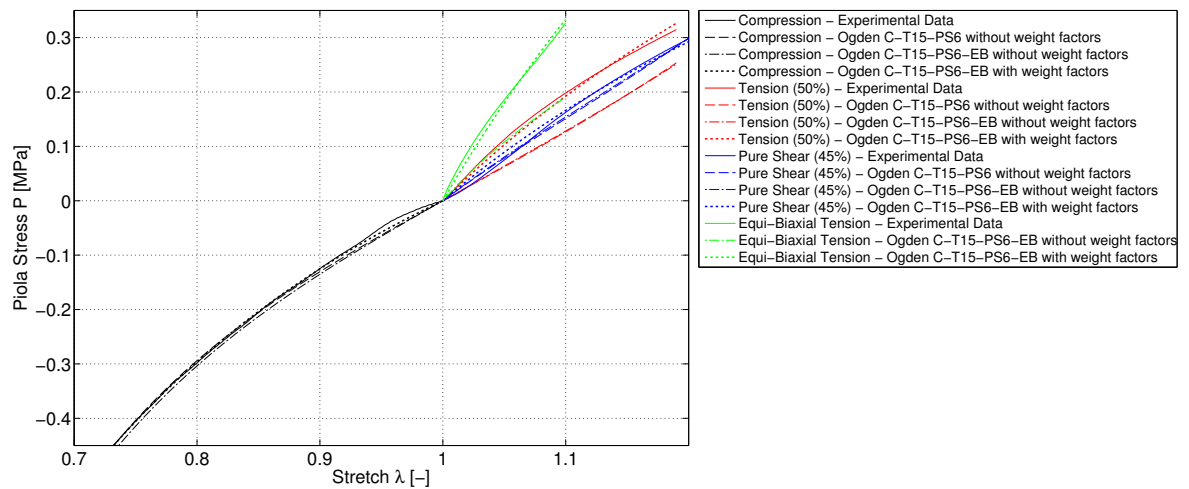
combination C-T15-PS6, which represents data to 50% strain, for pure rubber and isotropic MRE with 10% iron content. Only the experimental tension data are underestimated resulting in a value of $R_2 = 0.97$ for pure rubber and $R_2 = 0.91$ for isotropic 10% MREs. The



(a) Pure Rubber



(b) Isotropic 10% MREs



(c) Isotropic 20% MREs

Figure 6.2: Predictions of the *Ogden* model fitted to combined deformation modes for pure rubber and isotropic MREs with 10% and 20% volume iron fraction, are compared with the experimental data. C-T15-PS6 (without weight factors) combines experimental data obtained from tests up to approximately 50% strain). C-T15-PS6-EB combines all deformation modes without and with the use of weight factors.

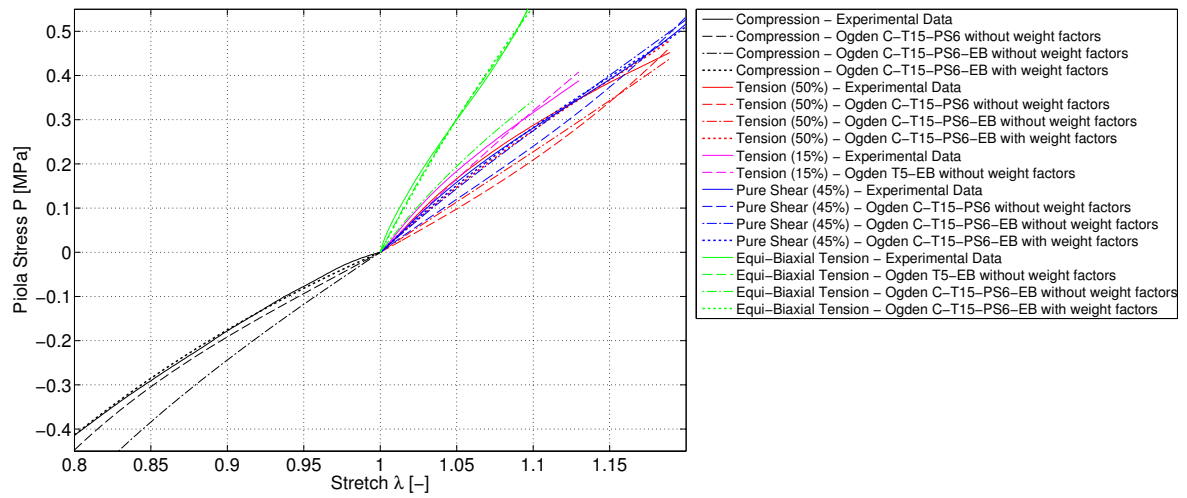


Figure 6.3: Predictions of the *Ogden* model fitted to combined deformation modes for isotropic 30% MREs are compared with the experimental data. C-T15-PS6 (without weight factors) combines experimental data obtained from tests up to approximately 50% strain, and T5-EB (without weight factors) combines data from tests up to approximately 10% strain. C-T15-PS6-EB combines all deformation modes without and with the use of weight factors.

results for isotropic MREs containing 20% and 30% iron particles are not of good quality, with a significant underestimation of the tension data. This might be due to other experimental issues as discussed above. The combination T5-EB, representing experimental data obtained from tests up to approximately 10% strain, leads to excellent *Ogden* stress predictions (isotropic 30% MREs). The predictions are of poor quality when combining all experimental data (C-T15-PS6-EB); the low values of R_2 listed in Table 6.2 result from the significant underestimation of the equi-biaxial tension data. Excellent results can only be obtained when weight factors are used. Now obviously the model parameters are different again for each deformation mode, but in contrast to data fitting of single deformation modes, the model parameters are related by a simple factor. The interpretation of the weight factors is difficult since there are many factors that influence them, as discussed in Section 6.2.

As confirmed by the data fitting results, it is very important to combine experimental data obtained from MRE specimens that were preconditioned and tested up to the same strain level. The experimental data presented in this study (Chapter 5) could not all be combined, as the equi-biaxial tension tests were only performed up to a 10% stretch. To overcome this problem a novel strategy is presented employing the *Ogden-Roxburgh* model.

6.3.4 Ogden-Roxburgh Model for the Mullins Effect

To study further the stress-softening behaviour of MREs the *Ogden-Roxburgh* model (Ogden and Roxburgh, 1999) is considered. The model parameters for compression and pure shear are determined, describing the ‘damage’ that occurs between the first loading cycle and a

conditioned loading cycle. The determined model parameters are then used for an adjustment of the experimental compression and pure shear data so that they represent a 10% strain level, to enable the comparison with the equi-biaxial tension test data. This is a novel approach that tries to enable the combination of experimental data that were not originally obtained from samples tested up to the same preconditioning level.

The *Ogden-Roxburgh* model is a pseudo-elastic model developed by Ogden and Roxburgh (1999). This model uses a dissipation or damage parameter to account for stress softening, which is dependant on the primary loading path and the maximum strain level that the sample experienced. Note that the remnant deformation observed in the experimental data (see Chapter 5) is not represented by the *Ogden-Roxburgh* model, rather the model extension developed by Dorfmann and Ogden (2004c) should be used. However, in this investigation, only the stress softening is modelled as this seems to be sufficiently accurate for the purposes of this fitting exercise. The *Ogden-Roxburgh* model can be understood as an extension to the *Ogden* model. The strain-energy function can be defined in terms of the principal stretches λ_a , but now a damage parameter η is introduced.

$$\Psi = \Psi(\lambda_1, \lambda_2, \lambda_3, \eta) \quad (6.75)$$

Using the incompressibility constraint, *i.e.* $\lambda_1 \lambda_2 \lambda_3 = 1$, λ_3 can be expressed by the stretches in the two other directions. The definitions for the stresses σ and P in terms of the principal stretches are still valid (see Equations 6.26 and 6.27).

The constitutive law proposed by Ogden and Roxburgh (1999) can be written as:

$$\Psi(\lambda_1, \lambda_2, \eta) = \eta \cdot \tilde{\Psi}(\lambda_1, \lambda_2) + \Phi(\eta) \quad (6.76)$$

The damage function $\Phi(\eta)$ is dependant on the damage parameter η , and the strain-energy function of the primary loading path (first loading cycle), $\tilde{\Psi}$, is best described using the strain-energy function of the *Ogden* model. Using this constitutive equation σ can be derived in the usual way. After elimination of the *Lagrange* multiplier, p , and for deformation modes with $\sigma_3 = 0$ the *Cauchy* stress is defined as

$$\sigma_a = \eta \cdot \lambda_a \cdot \frac{\partial \tilde{\Psi}}{\partial \lambda_a} = \eta \cdot \tilde{\sigma}_a \quad (6.77)$$

where $a = 1, 2$. Equivalently, this is defined for the *Piola* stress with $P_a = \eta \cdot \tilde{P}_a$. The damage parameter, η , in the original form proposed by Ogden and Roxburgh (1999) is defined as,

$$\eta = 1 - \frac{1}{r} \cdot \operatorname{erf} \left[\frac{1}{m} \cdot (\tilde{\Psi}_m - \tilde{\Psi}(\lambda_1, \lambda_2)) \right] \quad (6.78)$$

where r and m are positive material parameters, $\tilde{\Psi}(\lambda_1, \lambda_2)$ is the determined strain-energy

function describing the primary loading path, and $\tilde{\Psi}_m = \tilde{\Psi}(\lambda_{1m}, \lambda_{2m})$ is the value of the strain energy function at the maximum strain level of the primary loading path, just before the unloading cycle starts. The damage parameter η lies in between 0 and 1 with $\eta = 1$ indicating no damage so the *Ogden-Roxburgh* model is identical to the *Ogden* model. The function **erf** is the error function of the *Gaussian* distribution and is defined as:

$$\mathbf{erf}(x) = \frac{2}{\sqrt{\pi}} \int_0^x e^{-w^2} dw \quad (6.79)$$

In this investigation, the definition of the damage parameter η (Equation 6.78) has been modified slightly in accordance with Dorfmann and Ogden (2004c) so that the material parameter m is a dimensionless constant. The modulus, μ_{prim} , determined using the *Ogden* model, fitted to the path of the first loading cycle, is introduced into the definition

$$\eta = 1 - \frac{1}{r} \cdot \mathbf{erf} \left[\frac{1}{\mu_{prim} \cdot m} \cdot (\tilde{\Psi}_m - \tilde{\Psi}(\lambda_1, \lambda_2)) \right] \quad (6.80)$$

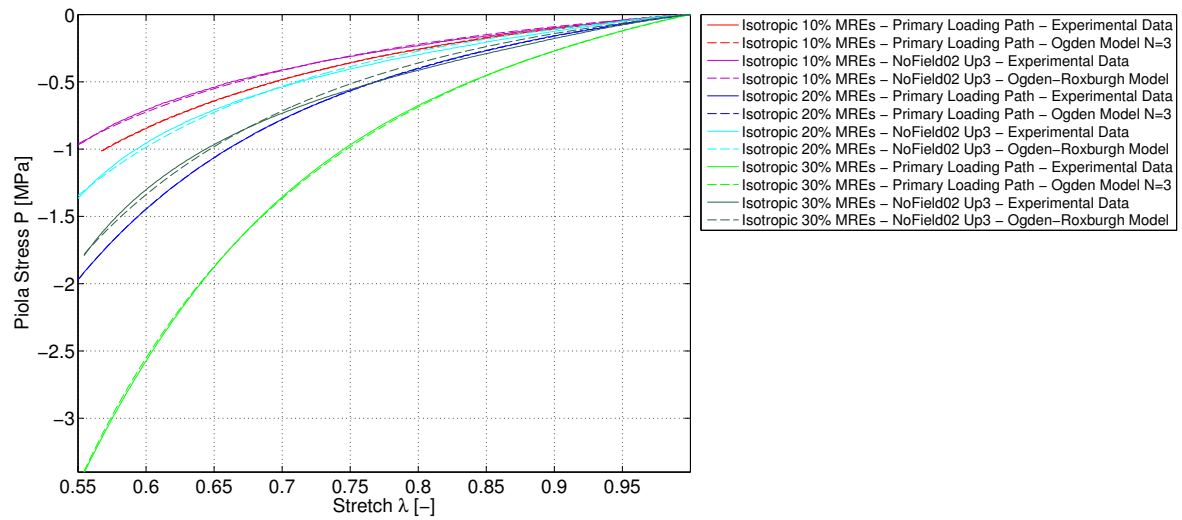
Once the *Ogden* model parameters of the primary loading path, **mp**, are determined, $\tilde{\Psi}$ and $\tilde{\Psi}_m$ are known and the material parameters, r and m , can be determined by a data fitting to one of the conditioned loading cycles. Here, the parameters are fitted using the third loading cycle from the *NoField02* tests (used throughout this investigation to present results). Data fitting of the *Ogden* model to the primary loading path is performed with the function *constmodel_piola_incompiso.m* as described in Section 6.3.2. To determine the parameters, r and m , the function $\eta \cdot \tilde{P}_a$ is fitted to the experimental *Piola* stress data, P_a of the conditioned loading cycle, using a least-square optimisation method (see Section 6.2). To aid with the analysis the function *constmodel_piola_incompiso_mullins.m* (see Appendix D) was written, which defines the start parameters as $r = 10$ and $m = 0.1$, the lower bounds of the parameters with $lb = [1, 0.01]$, and the upper bounds with $ub = [\infty, 1]$. The parameters are initially only constrained to only positive values (Ogden and Roxburgh, 1999), but as noted earlier for the *Ogden* model fitted to single deformation modes, the parameters are not unique and several sets of optimal parameters can be determined (see Section 6.3.3, so here the parameters were restricted to obtain parameters in a similar range for each type of MRE. The parameter $m > 0.01$ is defined to avoid discontinuities in the function shape of the damage parameter (see Ogden and Roxburgh, 1999). The function *constmodel_piola_incompiso_mullins.m* repeats the optimisation procedure as long as the 2-Norm decreases, as described in Section 6.2.

6.3.4.1 Experimental Data Fitting

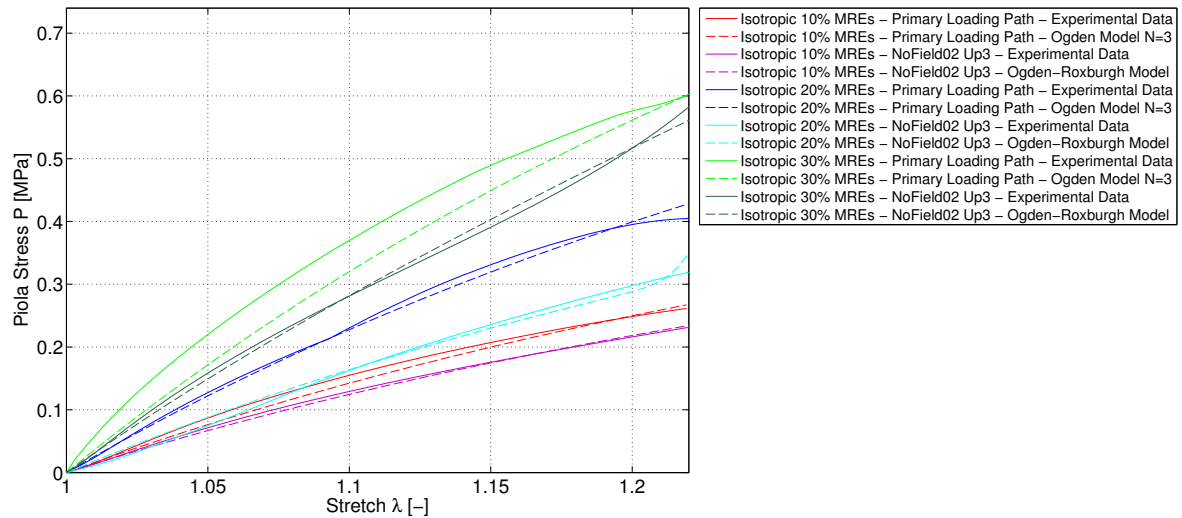
The *Ogden-Roxburgh* model was fitted to experimental data from compression and pure shear tests to evaluate the performance of this constitutive model. Stress-strain data of the

primary loading path are required to use the model. Such data are not available in the case of uniaxial tension tests as no DIC images were recorded during the preconditioning cycles, so strain values could not be calculated (see Chapter 5.3).

The experimental data measured during the first loading cycle (*NoField01* compression tests and *Preconditioning* pure shear tests, see Sections 5.2.1 and 5.4.1) and the third loading cycle of the *NoField02* tests are compared against the *Piola* stress predicted by both the *Ogden* model and the *Ogden-Roxburgh* model for compression tests in Figure 6.4a and for the pure shear tests in Figure 6.4b. The behaviour of pure rubber was not influenced by the *Mullins* effect, so nearly no stress softening occurred. The *Ogden-Roxburgh* model was fitted only to isotropic MREs with 10%, 20%, and 30% iron content. The moduli of the primary



(a) Compression Deformation Mode



(b) Pure Shear Deformation Mode

Figure 6.4: Predictions of the *Ogden* and the *Ogden-Roxburgh* model fitted to the compression and pure shear deformation mode are compared to the experimental primary loading (first loading cycle) and conditioned loading data (third loading cycle of *NoField02* tests).

loading path, μ and E , and the damage parameter, η , are listed in Table 6.3. The experimental

	MRE Type	Primary Loading Path			Conditioned Loading Path			
		$\mu[MPa]$	$E[MPa]$	R_2	r	m	η_{min}	R_2
Uniaxial Compression	Isotropic 10%	0.293	0.880	1.000	7.037	0.016	0.858	0.999
	Isotropic 20%	0.444	1.331	1.000	3.152	0.040	0.683	0.976
	Isotropic 30%	0.730	2.190	1.000	2.103	0.095	0.524	0.994
Pure Shear	Iso 10% - 6 mm	0.411	1.644	0.991	7.9591	0.025	0.874	0.999
	Iso 10% - 9 mm	0.367	1.468	0.953	7.4909	0.139	0.867	0.999
	Iso 20% - 3 mm	0.646	2.583	0.998	7.3206	0.010	0.863	0.962
	Iso 20% - 6 mm	0.657	2.628	0.985	3.5729	0.010	0.720	0.963
	Iso 30% - 6 mm	0.924	3.695	0.968	1.3249	1.000	0.865	0.995

Table 6.3: The moduli, μ and E , and the coefficient of determination, R_2 , of the *Ogden* model fitted to the primary loading path, and material parameters, r and m , the minimum value of the damage parameter, η , and R_2 of the *Ogden-Roxburgh* model fitted to the third loading part of the *NoField02* compression and pure shear tests are listed.

compression test data are very well described by the model, since the R_2 values are all greater than 0.976. The damage parameter, η_{min} , decreases with increasing iron content, meaning that the stress softening behaviour is more pronounced for MREs with higher iron content. For the pure shear mode, the fits of the *Ogden* model to the primary loading paths are not as good, but in contrast, the fits to the conditioned loading data are reasonably good (R_2 values are larger than those of the primary path fits), meaning that the damage parameters η are slightly underestimated. Using the *Ogden* model with the order $N = 4$ and $N = 5$ did not improve the primary loading fits.

The *Ogden-Roxburgh* model is useful for modelling the stress-softening behaviour of MREs. In the next section, a novel approach using the results of this model to estimate the response of MREs with arbitrary levels of preconditioning is presented.

6.3.4.2 Adjustment of Experimental Data to a Lower Strain Level

The determined damage parameter, η , of the *Ogden-Roxburgh* model is dependant on the model parameters, r and m , and on the maximum strain level of the primary loading path, *i.e.* the preconditioning level. When the model parameters r and m are assumed to be related only to the material behaviour (and not to the strain level), the damage parameter η (Equation 6.80), can be estimated for other preconditioning levels using the r and m values listed in Table 6.3. The strain energy function at the point of maximum stretch, $\tilde{\Psi}_m$, is recalculated and the energy function, $\tilde{\Psi}(\lambda_1, \lambda_2)$, is restricted to the new stretch level. This newly determined damage parameter is multiplied with the experimental data of the primary loading path to evaluate data of conditioned loading cycles up to different preconditioning levels. Note that the method of keeping r and m constant is based on an assumption (only dependant on the material behaviour), and should be further investigated in the future.

The $\text{erf}(x)$ function defined in Equation 6.79 tends to 1 for $x \gg 1$. This restricts the dependent variable x to values equal to or less than 1; otherwise the damage parameter cannot be determined correctly. Due to this purely mathematical issue, an extrapolation of the experimental data to larger preconditioning levels is not possible; thus experimental data can only be estimated for preconditioning levels smaller than those actually tested. The experimental data of compression and pure shear experiments are adjusted to a 10% preconditioning level using the method described above. By doing this, the adjusted data can be compared with the data of the equi-biaxial tension experiments which were restricted to 10% strain in the experiment. Unfortunately, primary loading paths of the uniaxial tension tests are not available, thus the tension data can not be scaled down to a 10% strain level. The primary loading paths (first loading cycle) and the estimated stress-stretch data (adjusted to 10% strain) of both the compression and pure shear tests are shown in Figure 6.5. From the theory of the *Mullins*

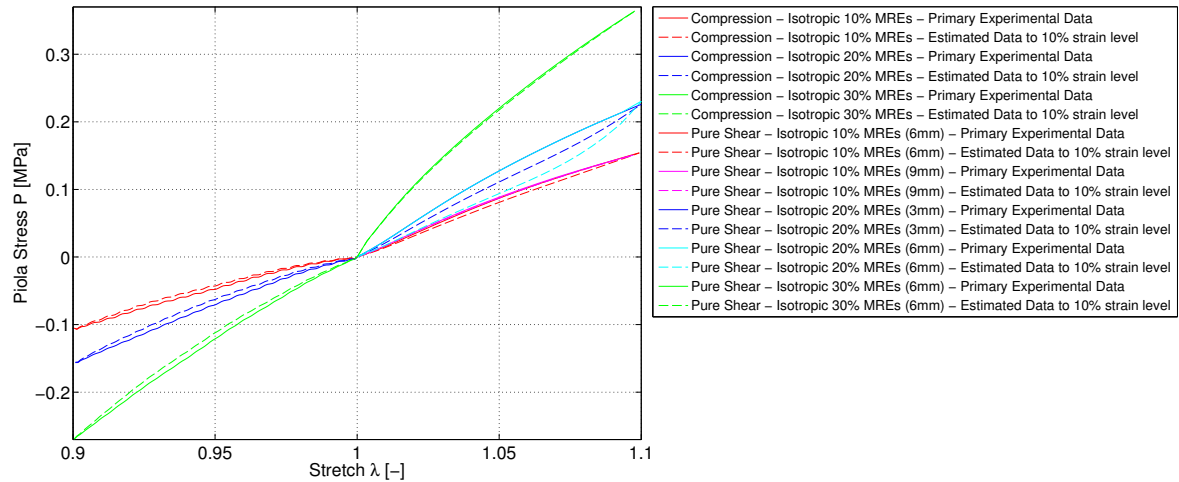


Figure 6.5: The experimental data of pure shear and compression tests are estimated for a 10% strain level. The primary loading paths and the estimated conditioned loading paths (conditioned to 10% strain) are compared for isotropic MREs with 10% to 30% volume iron content.

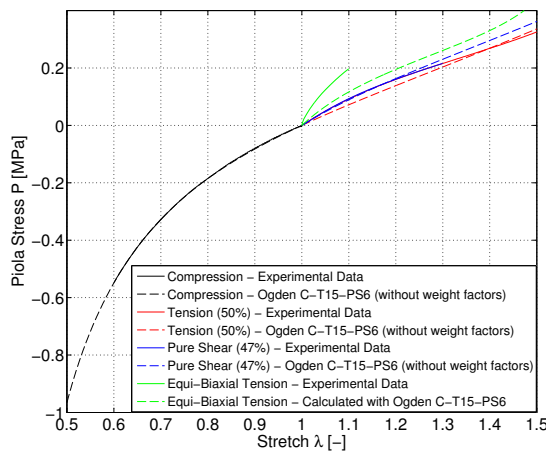
effect (Diani *et al.*, 2009) and from the experimental data analysis in Chapter 5 it is known that a larger stress-softening occurs when test specimens are tested up to larger strain levels. Since the compression and pure shear data were scaled to only 10% strain (not a very large strain), the estimated stress-softening is small, and consequently the modelled data of the conditioned loading parts are close to the primary loading paths (see Figure 6.5). The first loading cycles of isotropic 10% MREs tested to 6 and 9 *mm*, and of isotropic 20% MREs tested to 3 and 6 *mm* (pure shear) are identical (see Figure 6.5). This is expected since the first loading cycle is independent of the strain level, and the stress-softening occurs after the first loading cycle (see Diani *et al.*, 2009). The conditioned loading path (estimated data to 10% strain) of isotropic 20% MREs tested to 6 *mm* are underestimated, as they should be identical to the estimated path using the 3 *mm* pure shear data of the isotropic 20% MREs (dashed blue and cyan line in Figure 6.5).

The estimated experimental data of compression and pure shear are used in the next section to repeat the data fitting of the *Ogden* model to combined deformation modes, but now with experimental data representing samples tested up to the same preconditioning level.

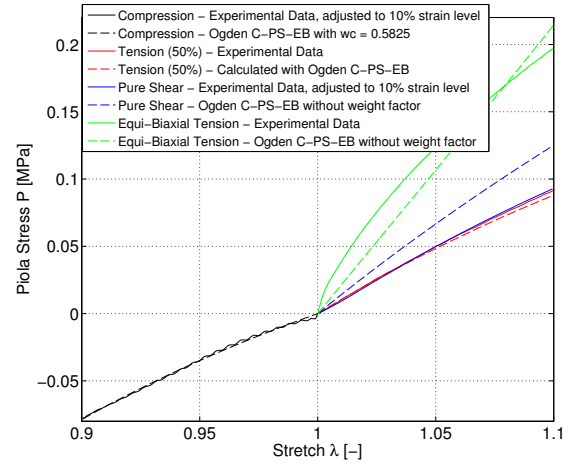
6.3.5 Fitting of the Ogden Model to Data of Same Strain Level

As shown in Section 6.3.3.2 the results of the *Ogden* model fitted to combined deformation modes are not satisfactory when different strain levels were applied in each of the deformation modes. In contrast, good fitting results were achieved with the C-T15-PS6 combination (in case of pure rubber and isotropic 10% MREs) of experimental data obtained from tests up to approximately 50% strain. In this section the *Ogden* model is fitted to experimental data obtained from tests under different deformation modes up to the same strain level. Final results of the *Ogden* model characterising MREs that are preconditioned to 10% and 50% strain under various deformation modes are presented. During this investigation it was found that with the use of a weight factor for the compression mode (w_c), reasonable good predictions of the *Ogden* model can be determined for all types of MREs under each deformation mode. It is noted in Miller (1999) that “pure states of strain are desired and this is especially difficult to achieve experimentally in compression” (Miller, 1999). Thus, it is reasonable to use a weight factor for compression.

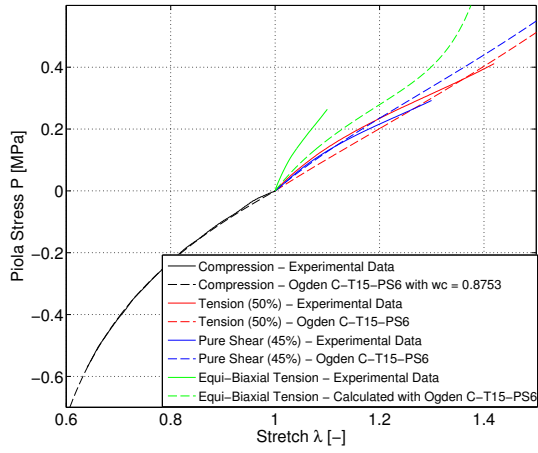
To obtain the model parameters for MREs preconditioned to 50% and 10% strain, the data fitting is performed to the combinations C-T15-PS6 (as presented in Section 6.3.3.2, but now with a weight factor for compression) and the combination of C-PS-EB (C-T5-PS-EB in case of the isotropic 30% MREs), respectively. For the 10% combination, estimated experimental compression and pure shear data (see Section 6.3.4) are used, and for isotropic 30% MREs tension data obtained from tests up to 15% are available and are used for the data fitting. The experimental data are compared with the *Ogden* model predictions in Figures 6.6 and 6.7. The deformation modes that were not used in the combinations to determine the *Ogden* model parameters are nevertheless illustrated in the figures, and the *Ogden* predictions are calculated with the determined model parameters. The moduli and the coefficients of determination R_2 are summarised in Table 6.4, and the full sets of parameters are listed in Appendix F.4. Considering the combinations representing a 50% strain level, the results are excellent in the case of pure rubber and isotropic 10% MREs as already shown in Section 6.3.3.2, but the quality of the fits is improved by using a weight factor for the compression mode. The quality of the predictions for the isotropic MREs containing 20% and 30% iron content is not as good (compared to pure rubber and isotropic 10% MREs), with an underestimation of the uniaxial tension data. Still, reasonable good predictions characterising the MRE under general deformation are achieved. The predicted *Piola* stress of the equi-biaxial tension mode (see Figures 6.6a and c, and 6.7a and c) suggests data that would have been



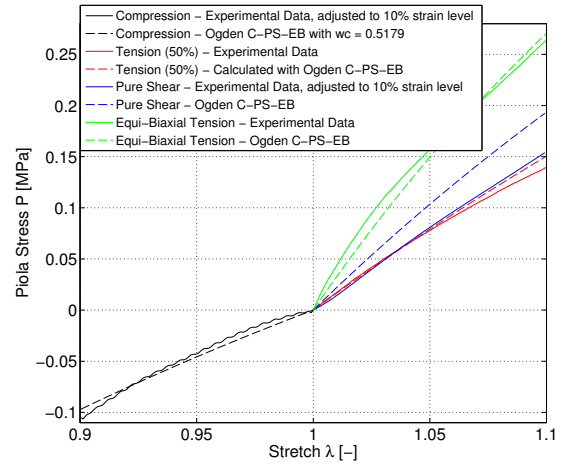
(a) Pure Rubber - 50% strain level



(b) Pure Rubber - 10% strain level



(c) Isotropic 10% MREs - 50% strain level



(d) Isotropic 10% MREs - 10% strain level

Figure 6.6: Predictions of the *Ogden* model fitted to combined experimental data for (a and b) pure rubber and (c and d) isotropic 10% MREs, representing a 50% and a 10% strain level (the experimental data were adjusted to this level using the *Ogden-Roxburgh* model).

	50% Strain Level		10% Strain Level	
	μ [MPa]	R_2	μ [MPa]	R_2
Pure Rubber $w_c = -/0.5825$	0.2529	0.9728	0.3575 0.2083	0.5255
Isotropic 10% MREs $w_c = 0.8753/0.5179$	0.3597 0.3148	0.9413	0.5564 0.2882	0.7172
Isotropic 20% MREs $w_c = 0.9094/0.6394$	0.4562 0.4149	0.6540	0.6712 0.4292	0.9630
Isotropic 30% MREs $w_c = 0.7215/0.6672$	0.7901 0.5701	0.8719	1.1639 0.7765	0.9736

Table 6.4: The modulus, μ , and the coefficient of determination, R_2 , of the *Ogden* model fitted to combined deformation modes, representing a 50% and a 10% preconditioning level, are listed. The results that characterise well the behaviour of MREs under general deformation are shaded in grey.

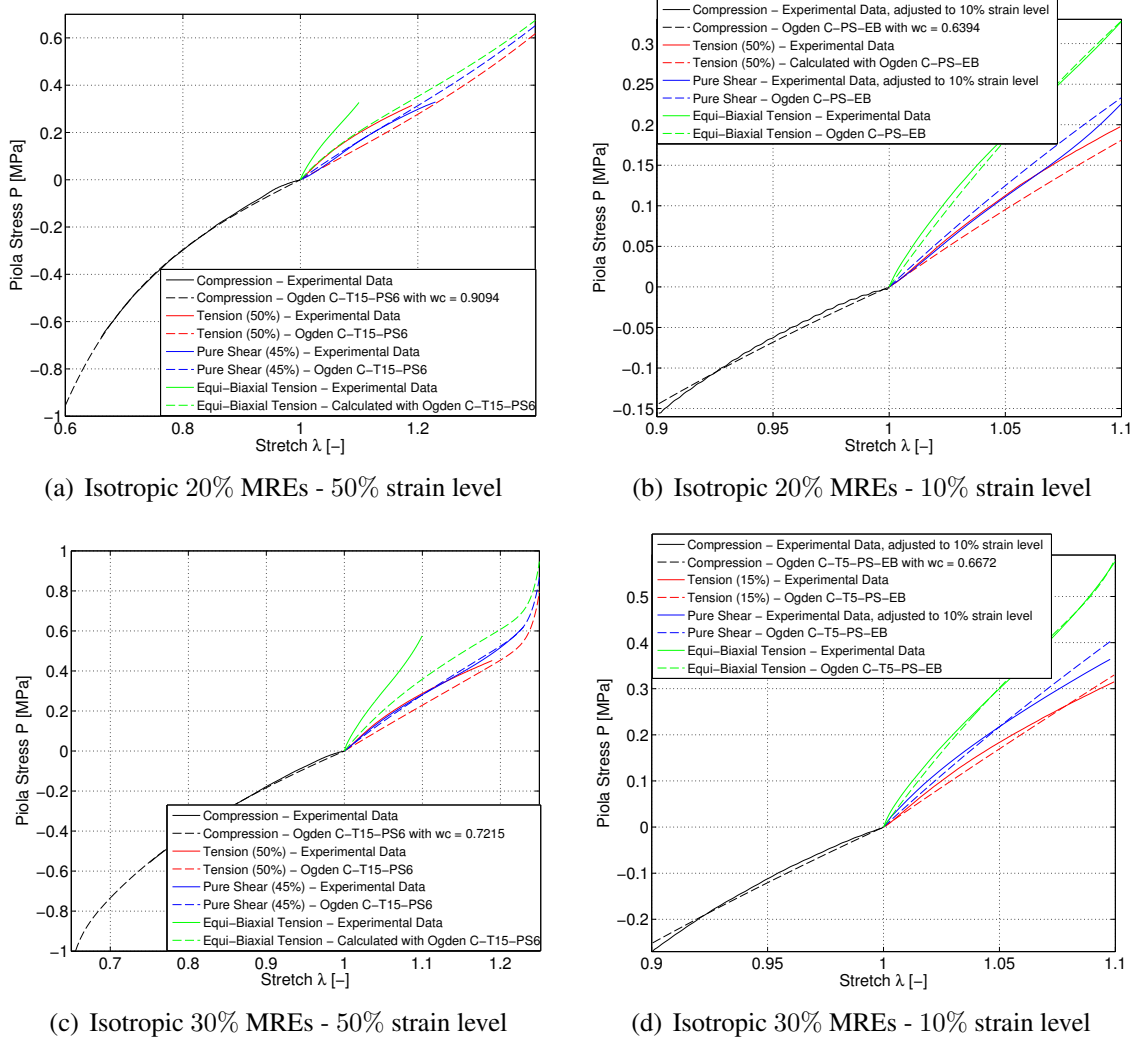


Figure 6.7: Predictions of the *Ogden* model fitted to combined experimental data for (a and b) isotropic 10% MREs and (c and d) isotropic 30% MREs, representing a 50% and a 10% strain level (the experimental data were adjusted to this level using the *Ogden-Roxburgh* model).

achieved when stretching the samples to 50% strain instead of the 10% strain actually used in the real experiments. Considering now the combinations representing a 10% strain level, excellent results are achieved for the isotropic MREs containing 20% and 30% iron content, which is especially evident for the isotropic 30% MREs where all four deformation modes were combined to perform the data fitting. The quality of the predictions for the pure rubber and isotropic 10% MREs is lower, with an overestimation of the experimental pure shear data. The prediction of the tension data (calculated with the determined model parameters) are too low as the shown experimental tension data are obtained from tests up to 50% strain (see Figure 6.6b and d).

6.3.6 Summary of the Modelling of Isotropic MREs

The *Ogden* model is able to represent the experimental data of single deformation modes very well. However, not only do the different types of MRE samples lead to different results of *Ogden* model parameters, but also the preconditioning levels up to which the samples were tested play an important role. Different sets of parameters are determined for each deformation mode, thus the identified model parameters are not valid under general deformations. Also, non-unique solutions are determined, meaning that more than one set of model parameters can be calculated resulting in the same quality of predicted *Ogden* stresses.

To obtain unique sets of identified model parameters, and also to characterise MREs under general deformations, experimental data obtained from different deformation modes have to be combined for the data fitting. The predictions of the *Ogden* model were of reasonable good quality when experimental data obtained from tests up to the same strain level were used for the combination. The fit quality was poor when data obtained from tests up to different strain levels were used. The importance of the preconditioning level was once again obvious. In this investigation, compression, tension, and pure shear experiments were performed up to 50% strain, while the equi-biaxial tension tests were only performed up to 10% strain. To enable the comparison of all four deformation modes, the *Ogden-Roxburgh* model was employed to estimate experimental data representing a 10% strain level; this scaling was performed with the compression and pure shear data. The estimated data were combined with the equi-biaxial data to determine *Ogden* model parameters representing MREs preconditioned to 10% strain. Weight factors were introduced into the objective function (Equation 6.32) to account for experimental issues (*i.e.* friction in compression tests). When combining experimental data representing different strain levels, the interpretation of the weight factors is difficult, as besides the experimental issues also the different strain levels contribute to them. When combining experimental data obtained from tests up to the same strain level, it was sufficient to use a weight factor for the compression mode only to achieve reasonable good results of the *Ogden* predictions.

Final *Ogden* model parameters were successfully determined describing MREs under general deformations. MREs that were preconditioned to 50% and 10% strain can be modelled under uniaxial compression and tension, pure shear, and equi-biaxial deformation modes.

6.4 Modelling of Anisotropic MREs

Transversely isotropic materials are a special class of anisotropic materials which are reinforced by only one family of fibres or aligned particles. Such materials have one preferred direction which is usually stiffer than in other directions. The material response in the directions perpendicular to the preferred direction is isotropic. Due to the particle alignment of

the iron particles within the MRE material achieved by applying a magnetic field during the curing process, the anisotropic MREs fall into the class of transversely isotropic materials. As an extension of Section 6.1, the theory, and some specific forms of strain energy functions are presented in Section 6.4.1. The *Qui-Pence* (Qiu and Pence, 1997), the *Merodio-Ogden* (Merodio and Ogden, 2005), the *Holzapfel-Gasser* (Holzapfel *et al.*, 2000), and the *Guo* (Guo *et al.*, 2007) models are discussed. The test kinematics and the derivations of the stress functions for each of the transversely isotropic models are provided in Section 6.4.2. The fitting procedure is described in Section 6.4.3. Finally, model parameters are determined by a data fitting to experimental data of anisotropic MREs. Results are compared and discussed in Section 6.4.4.

6.4.1 Theory and Forms of Strain Energy Functions

The stretch of the fibre, or in the case considered here the stretch of the aligned particle chains along their original orientation can be characterised as

$$\lambda_F \cdot \mathbf{a}(\mathbf{x}, t) = \mathbf{F}(\mathbf{X}, t) \cdot \mathbf{a}_0(\mathbf{X}) \quad (6.81)$$

$$\lambda_F^2 = \mathbf{a}_0 \cdot \mathbf{F}^T \mathbf{F} \mathbf{a}_0 = \mathbf{a}_0 \mathbf{C} \mathbf{a}_0 \quad (6.82)$$

where $\mathbf{a}_0(\mathbf{X})$ and $\mathbf{a}(\mathbf{x}, t)$ are unit vectors describing the direction of the aligned particle chains in the reference and current configuration, respectively. The strain energy function, Ψ , is not solely dependant on the deformation gradient, \mathbf{F} , but also on the direction of the aligned particles, \mathbf{a}_0 , and is defined as:

$$\Psi = \Psi(\mathbf{F}, \mathbf{a}_0)$$

To present Ψ in terms of strain invariants (analogous to isotropic materials), two pseudo-invariants, I_4 and I_5 , have to be introduced (Holzapfel, 2000; Spencer, 1984)):

$$\Psi = \Psi(I_1, I_2, I_3, I_4, I_5) \quad (6.83)$$

The invariants I_1 , I_2 , and I_3 were defined earlier in Equations 6.4, 6.5, and 6.6 for isotropic materials. I_4 and I_5 are required to describe the anisotropic material behaviour and are defined as,

$$I_4(\mathbf{C}, \mathbf{a}_0) = \mathbf{a}_0 \mathbf{C} \mathbf{a}_0 = \lambda_F^2 \quad (6.84)$$

$$I_5(\mathbf{C}, \mathbf{a}_0) = \mathbf{a}_0 \mathbf{C}^2 \mathbf{a}_0 \quad (6.85)$$

where \mathbf{C} is the *right Cauchy-Green* tensor. The two pseudo-invariants “describe the properties of the fibre family and its interaction with the other material constituents” (Holzapfel,

2000, page 268).

Two forms of **incompressible transversely isotropic** materials can be distinguished. When the fibres are extensible the invariant $I_3 = 1$ as with isotropic materials; Ψ is then a function of four invariants:

$$\Psi = \Psi(I_1, I_2, I_4, I_5) - \frac{1}{2}p(I_3 - 1) \quad (6.86)$$

When the fibres are inextensible then $I_4 = 1$ as well, which means that the stretch of the fibres $\lambda_F = 1$ and an additional *Lagrange* multiplier, q , has to be introduced, and Ψ is defined as follows:

$$\Psi = \Psi(I_1, I_2, I_5) - \frac{1}{2}p(I_3 - 1) - \frac{1}{2}q(I_4 - 1) \quad (6.87)$$

All of the transversely isotropic constitutive models mentioned above consist of an isotropic part and an anisotropic or reinforcing part; the strain energy functions can be separated:

$$\Psi(I_1, I_2, I_4, I_5) = \Psi_{iso}(I_1, I_2) + \Psi_{aniso}(I_4, I_5) \quad (6.88)$$

The original proposed models use the well-known *Neo-Hookean* model (Holzapfel, 2000; Ogden, 1978) to describe the isotropic part of the strain energy function. The models could be extended with the *Ogden* model to describe the isotropic part, but it was found by further studies of the author that the quality of the experimental data fits did not improve. In the case of isotropic MREs (see Section 6.3) the *Ogden* model delivered much better fits to the experimental data than the *Neo-Hookean* model, as the latter has only one fitting parameter and is therefore less flexible. However, for the anisotropic MREs it was found that the use of the *Ogden* model did not improve the quality, rather it complicated the equations enormously and often the model parameters of Ψ_{aniso} resulted in zero values as the *Ogden* model alone was able to represent the experimental data. In terms of characterising transversely isotropic material, the results were not useful as the directions parallel and perpendicular to the particle alignment direction cannot be distinguished. Here, only the original models involving the *Neo-Hookean* model are presented, although the equations can be extended to use the *Ogden* model and *Matlab* functions (written by the author to perform the data fitting) support the *Ogden*-based transversely isotropic models (see Appendix D).

The definitions of the *Piola* and *Cauchy* stresses were given in Equations 6.26 and 6.27; since the strain energy functions, Ψ , can be expressed in terms of the principal stretches these definitions are still valid. The particle alignment direction is assumed to be in the 1-direction for the derivation of the stress functions, *i.e.* $\lambda_F = \lambda_1$.

Standard Reinforcing Model The *Standard Reinforcing* model was developed by Qiu and Pence (1997); this is a reinforced *Neo-Hookean* material model. The strain-energy func-

tion for transversely isotropic materials is defined as

$$\Psi = \frac{1}{2}\mu [(\lambda_1^2 + \lambda_2^2 + \lambda_3^2 - 3) + \gamma(\lambda_F^2 - 1)^2] \quad (6.89)$$

where the first part of the equation is the *Neo-Hookean* model with the modulus, μ , and the quadratic term $(\lambda_F^2 - 1)^2/2$ is called the *standard reinforcing* term. The parameter $\gamma (> 0)$ is a dimensionless material parameter characterising the properties of the reinforcement. The *Cauchy* stresses are then:

$$\sigma_1 = \mu \cdot (\lambda_1^2 + 2\gamma\lambda_1^2(\lambda_1^2 - 1)) - p \quad (6.90)$$

$$\sigma_2 = \mu\lambda_2^2 - p \quad (6.91)$$

$$\sigma_3 = \mu\lambda_3^2 - p \quad (6.92)$$

Merodio-Ogden Model Merodio and Ogden (2005) developed a constitutive model with the reinforcing part dependant on the invariant I_5 rather than I_4 . I_5 is not solely dependant on the fibre stretch, λ_F , rather I_5 also registers an interaction between the fibre or aligned particles and the matrix material (Merodio and Ogden, 2005). The invariant is defined with $I_5 = \lambda_F^4$ in Merodio and Ogden (2005). The strain-energy function, Ψ , and the derived *Cauchy* stress in particle alignment direction, σ_1 , are then defined as,

$$\Psi = \frac{1}{2}\mu [(\lambda_1^2 + \lambda_2^2 + \lambda_3^2 - 3) + \gamma(\lambda_F^4 - 1)^2] \quad (6.93)$$

$$\sigma_1 = \mu \cdot \lambda_1^2 + 4\mu\gamma\lambda_1^4(\lambda_1^4 - 1) - p \quad (6.94)$$

where μ is the modulus of the *Neo-Hookean* model, and $\gamma (> 0)$ is a dimensionless material parameter. The stresses in the two other directions are only dependant on the isotropic *Neo-Hookean* part and are identical for all models (see Equations 6.91 and 6.92). As stated by Merodio and Ogden (2005) “there are no qualitative differences in the behaviour of the I_4 and I_5 model, although the results for shear deformation are different at some points”.

Holzapfel-Gasser Model The *Holzapfel-Gasser* model (Holzapfel *et al.*, 2000) was originally developed to model the different layers of an arterial wall. An arterial wall is treated as an anisotropic material with two families of fibres. Similar to the models proposed by Qiu and Pence (1997) and Merodio and Ogden (2005) this approach is a sum of the isotropic matrix material, treated as a *Neo-Hookean* material, and a function which describes the anisotropic behaviour. The fibre of an arterial wall is the collagen and due to its “strong stiffening effect” (Holzapfel *et al.*, 2000) an exponential function is used to describe the anisotropy. The original form of the strain-energy function, as given in Holzapfel *et al.* (2000)

is stated as:

$$\Psi(\mathbf{C}, \mathbf{a}_1, \mathbf{a}_2) = \Psi_{iso}(I_1) + \Psi_{aniso}(I_4, I_6) = \frac{1}{2}\mu(I_1 - 3) + \frac{k_1}{2k_2} \sum_{i=4,6} \left(e^{k_2(I_i-1)^2} - 1 \right) \quad (6.95)$$

As this work focusses on transversely isotropic materials (one family of fibres) the function simplifies to the following

$$\Psi(I_1, I_4) = \frac{1}{2}\mu(I_1 - 3) + \frac{k_1}{2k_2} \left(e^{k_2(I_4-1)^2} - 1 \right) \quad (6.96)$$

and can also be expressed in terms of the principal stretches

$$\Psi = \frac{1}{2}\mu(\lambda_1^2 + \lambda_2^2 + \lambda_3^2 - 3) + \frac{k_1}{2k_2} \left(e^{k_2(\lambda_F^2-1)^2} - 1 \right) \quad (6.97)$$

with μ the modulus of the *Neo-Hookean* model, k_1 (> 0) a stress-like parameter, and k_2 (> 0) a dimensionless material parameter. The *Cauchy* stress in the direction of particle alignment is defined as:

$$\sigma_1 = \mu \cdot \lambda_1^2 + 2k_1\lambda_1^2(\lambda_1^2 - 1)e^{k_2(\lambda_1^2-1)^2} - p \quad (6.98)$$

The stresses in the two other directions behave isotropically and are defined in Equations 6.91 and 6.92.

Guo Model Contrary to the models presented earlier, the model by Guo *et al.* (2007) considers both the matrix material and the particles as *Neo-Hookean* materials. The interaction between matrix and fibres is taken into account by using a multiplicative decomposition of the deformation gradient, \mathbf{F} . The final strain-energy function Ψ can be separated into an isotropic and an anisotropic part, and is again defined in terms of the principal stretches as,

$$\Psi = \frac{1}{2}\alpha [(\lambda_1^2 + \lambda_2^2 + \lambda_3^2 - 3) + \beta (\lambda_F^2 + 2\lambda_F^{-1} - 3)] \quad (6.99)$$

where α and β are material parameters and have a clear physical interpretation, given as,

$$\alpha = \mu_c = \frac{(1 + \Phi_p)\chi + (1 - \Phi_p)}{(1 - \Phi_p)\chi + (1 + \Phi_p)} \mu_m \quad (6.100)$$

$$\beta = \frac{(\chi - 1)^2 \Phi_p \Phi_m}{(1 + \Phi_p)\chi + (1 - \Phi_p)} \quad (6.101)$$

where Φ_m and Φ_f are the volume ratios of matrix and particles, and $\chi = \mu_p/\mu_m$ is the stiffness ratio between matrix and particles, calculated with the shear moduli μ_m and μ_p . The parameter α can be interpreted as the effective shear modulus of the composite, μ_c . The

parameter β is not only “the relative stiffness of the fibre to the matrix, the composite effect is included” (Guo *et al.*, 2007). So, the Guo model is not only a model to describe the large-strain behaviour of transversely isotropic materials, it also considers filler reinforcement effects. Here, $\alpha = \mu_c$ and β are model parameters to be determined during fitting to experimental data, and μ_c is the modulus of the *Neo-Hookean* model. The filler reinforcement interpretation of these parameters is ignored, as the performance of the model in describing experimental data of MREs is the main interest of this investigation. The stress in the fibre direction is derived as:

$$\sigma_1 = \mu_c \cdot \lambda_1^2 + \mu_c \beta (\lambda_1^2 - \lambda_1^{-1}) - p \quad (6.102)$$

The stresses in the two other directions are only dependant on the isotropic *Neo-Hookean* and are identical for all models (see Equation 6.91 and 6.92).

Connection to the linear theory. To connect to the linear theory and therewith calculate the Young’s moduli valid for small strains, the following equations are still valid:

$$E_1 = \left. \frac{\partial \sigma_1}{\partial \lambda_1} \right|_{\lambda_1=1} \quad (6.103)$$

$$E_2 = \left. \frac{\partial \sigma_2}{\partial \lambda_2} \right|_{\lambda_2=1} \quad (6.104)$$

The stress, P , and the Young’s moduli, E , will be derived for each of the deformation modes in the next section.

6.4.2 Kinematics and Stress Definitions

As transversely isotropic materials are reinforced in one direction the stretch definitions are somewhat different compared to isotropic materials. The incompressibility constraint $\lambda_1 \lambda_2 \lambda_3 = 1$ is still valid.

Uniaxial deformation in the fibre direction. When the load is applied in the fibre direction the derivations are quite straight forward and the stretch definitions are the same as those defined for isotropic materials,

$$\lambda_1 = \lambda_F \quad (6.105)$$

$$\lambda_2 = \lambda_3 = \frac{1}{\sqrt{\lambda_1}} \quad (6.106)$$

With the boundary conditions $\sigma_2 = \sigma_3 = 0$, the *Lagrange* multiplier, p , can be determined as $p = \mu \cdot \lambda_1^{-1}$. The isotropic part of the *Cauchy* stress equations is then determined as,

$$\sigma_{1,iso} = \mu \cdot (\lambda_1^2 - \lambda_1^{-1}) \quad (6.107)$$

and the anisotropic part remains as defined in Equations 6.90 for the *Qui-Pence* model, Equation 6.94 for the *Merodio-Ogden* model, Equation 6.98 for the *Holzappel-Gasser* model, and Equation 6.102 for the *Guo* model. The *Piola* stress is the stress definition used to perform the data fitting to experimental stress-strain values as both are defined in the reference configuration. The *Piola* stress equations for all models are summarised as follows:

$$\begin{aligned} P_1 &= \mu \cdot (\lambda_1 - \lambda_1^{-2}) + \dots \\ \text{Qui-Pence} &+ 2\mu\gamma\lambda_1(\lambda_1^2 - 1) \\ \text{Merodio-Ogden} &+ 4\mu\gamma\lambda_1^3(\lambda_1^4 - 1) \\ \text{Holzapfel-Gasser} &+ 2k_1\lambda_1(\lambda_1^2 - 1)e^{k_2(\lambda_1^2 - 1)^2} \\ \text{Guo} &+ \mu\beta(\lambda_1 - \lambda_1^{-2}) \end{aligned} \quad (6.108)$$

The Young's moduli, E_1 , are calculated with Equation 6.103 and are given as:

$$\begin{aligned} E_1 &= \\ \text{Qui-Pence} &\mu(3 + 4\gamma) \\ \text{Merodio-Ogden} &\mu(3 + 16\gamma) \\ \text{Holzapfel-Gasser} &3\mu + 4k_1 \\ \text{Guo} &3\mu(1 + \beta) \end{aligned} \quad (6.109)$$

Uniaxial deformation perpendicular to the fibre direction When the loading direction is perpendicular to the fibre direction, the derivations are more complicated. The particle alignment direction is still in the 1-direction, so that the equations defined in Section 6.4.1 are still valid. The loading direction is assumed to be in the 2-direction. The stretch $\lambda_1 = \lambda_F$ is in the fibre direction, the stretch λ_2 is in loading direction, and the third stretch is defined with the incompressibility constraint $\lambda_3 = 1/(\lambda_1\lambda_2)$. The stresses perpendicular to the loading direction $\sigma_1 = \sigma_3 = 0$ define the boundary conditions. The *Lagrange* multiplier, p , cannot be determined explicitly from the boundary conditions, rather a function for λ_2 in terms of λ_1 is derived for each of the models discussed. With this, functions for the stresses σ_2 and P_2 in the loading direction are derived in terms of the stretch in the fibre direction λ_1 . The model parameters of the transversely isotropic models are determined by fitting both $\lambda_2(\lambda_1)$ and $P_2(\lambda_1)$ simultaneously to experimental data. The functions $\lambda_2(\lambda_1)$, $\sigma_2(\lambda_1)$, and

$P_2(\lambda_1)$ are defined separately for each model. The following equations are derived for the *Qui-Pence* model:

$$\begin{aligned} p &= \mu [\lambda_1^2 (1 + 2\gamma(\lambda_1^2 - 1))] & \text{from } \sigma_1 &= 0 \\ p &= \mu / (\lambda_1^2 \lambda_2^2) & \text{from } \sigma_3 &= 0 \end{aligned} \quad (6.110)$$

$$\lambda_2 = [\lambda_1^4 (1 + 2\gamma(\lambda_1^2 - 1))]^{-1/2} \quad (6.111)$$

$$\begin{aligned} \sigma_2 &= \mu [\lambda_2^2 - \lambda_1^2 (1 + 2\gamma(\lambda_1^2 - 1))] \\ \sigma_2 &= \mu \left[(\lambda_1^4 (1 + 2\gamma(\lambda_1^2 - 1)))^{-1} - \lambda_1^2 (1 + 2\gamma(\lambda_1^2 - 1)) \right] \end{aligned} \quad (6.112)$$

$$\begin{aligned} P_2 &= \mu \left[(\lambda_1^4 (1 + 2\gamma(\lambda_1^2 - 1)))^{-1/2} - (\lambda_1^4 (1 + 2\gamma(\lambda_1^2 - 1)))^{1/2} \cdot \lambda_1^2 (1 + 2\gamma(\lambda_1^2 - 1)) \right] \\ P_2 &= \mu \left[\lambda_1^{-2} (1 + 2\gamma(\lambda_1^2 - 1))^{-1/2} - \lambda_1^4 (1 + 2\gamma(\lambda_1^2 - 1))^{3/2} \right] \end{aligned} \quad (6.113)$$

Similarly, the corresponding equations for the *Merodio-Ogden*, the *Holzappel-Gasser*, and the *Guo* models are:

$$\begin{aligned} \lambda_2 &= [\lambda_1^4 (1 + 4\gamma\lambda_1^2(\lambda_1^4 - 1))]^{-1/2} \\ \sigma_2 &= \mu \left[(\lambda_1^4 (1 + 4\gamma\lambda_1^2(\lambda_1^4 - 1)))^{-1} - \lambda_1^2 (1 + 4\gamma\lambda_1^2(\lambda_1^4 - 1)) \right] \\ P_2 &= \mu \left[\lambda_1^{-2} (1 + 4\gamma\lambda_1^2(\lambda_1^4 - 1))^{-1/2} - \lambda_1^4 (1 + 4\gamma\lambda_1^2(\lambda_1^4 - 1))^{3/2} \right] \end{aligned} \quad (6.114)$$

$$\begin{aligned} \lambda_2 &= \left[\lambda_1^4 \left(1 + 2k_1/\mu(\lambda_1^2 - 1)e^{k_2(\lambda_1^2 - 1)^2} \right) \right]^{-1/2} \\ \sigma_2 &= \mu \left[\left(\lambda_1^4 \left(1 + 2k_1/\mu(\lambda_1^2 - 1)e^{k_2(\lambda_1^2 - 1)^2} \right) \right)^{-1} - \lambda_1^2 \left(1 + 2k_1/\mu(\lambda_1^2 - 1)e^{k_2(\lambda_1^2 - 1)^2} \right) \right] \\ P_2 &= \mu \left[\lambda_1^{-2} \left(1 + 2k_1/\mu(\lambda_1^2 - 1)e^{k_2(\lambda_1^2 - 1)^2} \right)^{-1/2} - \lambda_1^4 \left(1 + 2k_1/\mu(\lambda_1^2 - 1)e^{k_2(\lambda_1^2 - 1)^2} \right)^{3/2} \right] \end{aligned} \quad (6.115)$$

$$\begin{aligned} \lambda_2 &= [(\beta + 1)\lambda_1^4 - \beta\lambda_1]^{-1/2} = [\lambda_1^2 ((\beta + 1)\lambda_1^2 - \beta\lambda_1^{-1})]^{-1/2} \\ \sigma_2 &= \mu_c \left[(\lambda_1^2 ((\beta + 1)\lambda_1^2 - \beta\lambda_1^{-1}))^{-1} - ((\beta + 1)\lambda_1^2 - \beta\lambda_1^{-1}) \right] \\ P_2 &= \mu_c \left[\left(\lambda_1^2 ((\beta + 1)\lambda_1^2 - \beta\lambda_1^{-1/2}) \right)^{-1} - \lambda_1 ((\beta + 1)\lambda_1^2 - \beta\lambda_1^{-1})^{3/2} \right] \end{aligned} \quad (6.116)$$

The strains in the particle alignment direction are required, but in the case of uniaxial com-

pression tests these strains were not measured experimentally, and in the case of uniaxial tension they were not very reliable. The DIC system was used to measure strains during the tension experiments, but as the narrow part of the tension samples was only 4 mm wide not many DIC points were available to analyse the strains. The importance of the horizontal strain measurement was realised too late, after performing the experiments. Here, the stretch in the fibre direction λ_1 is estimated using the function $\lambda_2(\lambda_1)$ (solved with the *Matlab* function *fsolve.m* (Matlab, 2013)). The initial values for λ_1 are calculated for the isotropic case $1/\sqrt{\lambda_2}$. An iterative process is performed involving two steps: (i) the stretch λ_1 is estimated, and (ii) the model parameters **mp** are calculated with an optimisation to both $\lambda_2(\lambda_1)$ and $P_2(\lambda_1)$ simultaneously (minimising the sum of the squared 2-Norms) using the *Matlab* function *fmincon.m*. This iterative process was repeated until the 2-Norm no longer decreased. For the calculation of the Young's modulus, E_2 , the Equation 6.104 is valid, but σ_2 is not defined in terms of λ_2 , but is rather a function of the stretch λ_1 in the fibre direction. Thus, a direct derivative cannot be calculated, instead the total derivative is calculated using:

$$\frac{\partial \sigma_2}{\partial \lambda_2} = \frac{\partial \sigma_2}{\partial \lambda_1} \cdot \frac{\partial \lambda_1}{\partial \lambda_2} \quad (6.117)$$

As only the function, $\lambda_2(\lambda_1)$ is available and a solution for λ_1 cannot be found analytically, the derivative must be solved using the implicit function $F(\lambda_2, \lambda_1) = 0$. The derivative can be solved as follows:

$$\frac{\partial \lambda_1}{\partial \lambda_2} = - \frac{\partial F}{\partial \lambda_2} \bigg/ \frac{\partial F}{\partial \lambda_1} \quad (6.118)$$

The Young's moduli, E_2 , in loading direction are derived for all models using:

$$E_2 = \begin{array}{ll} \text{Qui-Pence} & \mu \frac{3 + 4\gamma}{1 + \gamma} \\ \text{Merodio-Ogden} & \mu \frac{3 + 16\gamma}{1 + 4\gamma} \\ \text{Holzapfel-Gasser} & \mu \frac{3\mu + 4k_1}{\mu + k_1} \\ \text{Guo} & \frac{12\mu(1 + \beta)}{3\beta + 4} \end{array} \quad (6.119)$$

Pure shear with fibre direction in the loading direction. The kinematics for a pure shear deformation with loading direction in the particle alignment direction are identical to the isotropic case. The stretch $\lambda_1 = \lambda_F$ is in fibre direction, the stretch $\lambda_2 = 1$ as defined for the ideal case of pure shear, and the third direction is derived from the incompressibility constraint with $\lambda_3 = 1/\lambda_1$. With the boundary condition, $\sigma_3 = 0$, the *Lagrange* multiplier can

be determined as $p = \mu\lambda_1^{-2}$. The derivations of the *Piola* stress functions can be summarised as:

$$\begin{aligned}
 P_1 &= \mu \cdot (\lambda_1 - \lambda_1^{-3}) + \dots \\
 \text{Qui-Pence} &+ 2\mu\gamma\lambda_1(\lambda_1^2 - 1) \\
 \text{Merodio-Ogden} &+ 4\mu\gamma\lambda_1^3(\lambda_1^4 - 1) \\
 \text{Holzapfel-Gasser} &+ 2k_1\lambda_1(\lambda_1^2 - 1)e^{k_2(\lambda_1^2 - 1)^2} \\
 \text{Guo} &+ \mu\beta(\lambda_1 - \lambda_1^{-2})
 \end{aligned} \tag{6.120}$$

The Young's moduli, E_1 , are calculated using Equation 6.103 and are given as:

$$\begin{aligned}
 E_1 &= \\
 \text{Qui-Pence} &4\mu(1 + \gamma) \\
 \text{Merodio-Ogden} &4\mu(1 + 4\gamma) \\
 \text{Holzapfel-Gasser} &4(\mu + k_1) \\
 \text{Guo} &\mu(4 + 3\beta)
 \end{aligned} \tag{6.121}$$

Pure shear with fibre direction perpendicular to the loading direction. When the loading direction is perpendicular to the particle alignment direction in pure shear deformation the stretch $\lambda_1 = \lambda_F = 1$ due to the large width of the samples in this direction. The stretch λ_2 is in loading direction. The third direction is deforming with $\lambda_3 = 1/\lambda_2$ and the stress in this direction is $\sigma_3 = 0$. The *Lagrange* multiplier is determined as $p = \mu\lambda_2^{-2}$. The reinforcing part of the constitutive models neither contributes to the definition of σ_2 nor to the definition of p , so the stress in the loading direction is identical to the isotropic case and is independent of any transversely isotropic model. The *Piola* stresses are defined as:

$$P_2 = \mu(\lambda_2 - \lambda_2^{-3}) \tag{6.122}$$

The Young's modulus, E_2 , in the loading direction is calculated using Equation 6.104 and is identical to the isotropic case with

$$E_2 = 4\mu \tag{6.123}$$

The experimental data of pure shear with the particle alignment in the horizontal direction can thus not be used to determine the model parameters of transversely isotropic models, and only the parameter, μ , of the *Neo-Hookean* model can be determined.

Equi-biaxial deformation with in-plane fibre direction. In the case of equi-biaxial deformation, both the 1- and the 2-directions are loading directions, and the stretches are equal, *i.e.* $\lambda_1 = \lambda_2 = \lambda$. The fibre direction is still the 1-direction and the equations

in Section 6.4.1 are still valid. The stretch in the third direction is determined using the incompressibility constraint leading to $\lambda_3 = 1/\lambda^2$. The *Lagrange* multiplier p is determined with the boundary condition, $\sigma_3 = 0$, as $p = \mu\lambda^{-4}$. The derivations of the *Piola* stress functions are straight-forward and are given as follows (note that the stress P_2 is identical to the isotropic case):

$$\begin{aligned}
 P_1 &= \mu \cdot (\lambda - \lambda^{-5}) + \dots \\
 \text{Qui-Pence} &+ 2\mu\gamma\lambda(\lambda^2 - 1) \\
 \text{Merodio-Ogden} &+ 4\mu\gamma\lambda^3(\lambda^4 - 1) \\
 \text{Holzapfel-Gasser} &+ 2k_1\lambda(\lambda^2 - 1)e^{k_2(\lambda^2 - 1)^2} \\
 \text{Guo} &+ \mu\beta(\lambda - \lambda^{-2}) \\
 P_2 &= \mu \cdot (\lambda - \lambda^{-5})
 \end{aligned} \tag{6.124}$$

The Young's moduli, E_1 , in the fibre direction and, E_2 in the other loading direction are calculated using Equations 6.103 and 6.104 and are given as:

$$\begin{aligned}
 E_1 &= \\
 \text{Qui-Pence} &2\mu(3 + 2\gamma) \\
 \text{Merodio-Ogden} &2\mu(3 + 8\gamma) \\
 \text{Holzapfel-Gasser} &2(3\mu + 2k_1) \\
 \text{Guo} &3\mu(2 + \beta) \\
 E_2 &= 6\mu
 \end{aligned} \tag{6.125}$$

6.4.3 Fitting Procedure

The general optimisation algorithm was described in Section 6.2, and here the specific optimisation procedure and the *Matlab* functions used for the experimental data fitting of transversely isotropic models are described. To aid with the determination of the model parameters for the transversely isotropic models presented in Sections 6.4.1 and 6.4.2, a *Matlab* function *constmodel_piola_incompaniso.m* (see Appendix D) was written. The *Qui-Pence*, the *Merodio-Ogden*, *Holzapfel-Gasser*, and the *Guo* models with either a *Neo-Hookean*-based isotropic part or an *Ogden*-based isotropic part (up to the order $N = 3$) are supported in the code. All the deformation modes discussed in Section 6.4.2 are supported. Experimental data from either single-mode or multi-mode deformations can be used to determine the model parameters. Further, the model parameters can be determined by two different methods: (i) by constraining the model parameters such that the parameters in the isotropic part of the model (\mathbf{mp}_{iso}) are equal to those determined for corresponding isotropic MREs

in Section 6.3.3 and only the parameters in the reinforcing part (\mathbf{mp}_{aniso}) are determined by an experimental data fitting, and (ii) by fitting all parameters of the transversely isotropic models (\mathbf{mp}_{iso} and \mathbf{mp}_{aniso}) without constraint. When considering multi-mode deformations for the data fitting, weight factors (Equation 6.32) can be used as discussed in Section 6.2. Once again, the minimisation problems defined in Equations 6.29 and 6.31 are solved with the *Matlab* functions *lsqcurvefit.m* or *fmincon.m*.

Start parameters for the fitting parameters of the strain energy function are provided, and several sets of parameters are used to cover a broad range of possible solutions (*Matlab* function *aniso_startparameters.m*, see Appendix D). The parameter, μ , of the *Neo-Hookean* model and the parameters, γ , β , or k_1 and k_2 of the reinforcing parts of the models must be greater than 0, which is fulfilled by setting a lower bound in *lsqcurvefit.m* or *fmincon.m*. The fitting procedure is repeated as long as the 2-Norm decreases and is performed separately for each set of start parameters (described in Section 6.2). The *Matlab* functions written for the data fitting process are listed in Appendix D and are saved on a DVD available with this thesis. Not all the features implemented in the code are actually used here, as only a small choice of data fitting results is presented in the next section.

6.4.4 Experimental Data Fitting for Transversely Isotropic Models

In this investigation, only the data fitting results to single deformations are presented. As such, the model parameters are determined by a data fitting to experimental data of compression, tension, pure shear, and equi-biaxial tension test, and for all these deformations both data are used simultaneously, with the loading parallel and perpendicular to the particle alignment direction. Further studies by the author showed that experimental data fitting to a combination of different deformation modes resulted in poor predictions. The transversely isotropic models usually consist of an isotropic and a reinforcing part (Equation 6.88). The use of \mathbf{mp}_{iso} , determined from a data fitting to isotropic MREs (Section 6.3.3), was investigated to determine whether or not the transversely isotropic models can be understood as an extension to the isotropic models. This would connect the isotropic and anisotropic MRE behaviour, and thus would really model the anisotropy effect (which could then be studied in dependence of the applied magnetic field during the curing process, for example). Unfortunately, this is not possible with the transversely isotropic models used in this investigation, and the results were rather confusing. As even the predictions obtained from one specific deformation are not satisfying in most cases, only the results of the *Qui-Pence* model are presented and discussed in the main text. The results of the *Merodio-Ogden*, *Holzappel-Gasser*, and *Guo* models are provided in Appendix F.2.

The predictions of the *Qui-Pence* model fitted to experimental data obtained from compres-

sion, tension, pure shear, and equi-biaxial tension tests are illustrated in Figures 6.8 to 6.11. Experimental data are compared with the predictions of the *Qui-Pence* model in both the directions with loading parallel and perpendicular to the direction of particle chains. The *Qui-*

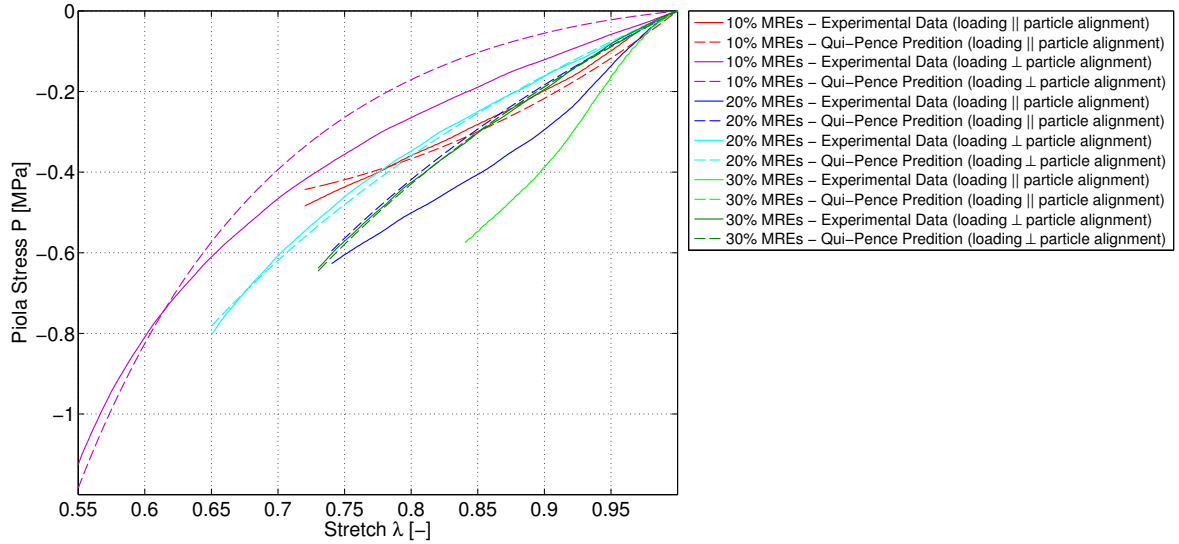


Figure 6.8: Predictions of the *Qui-Pence* model fitted to uniaxial compression data with both loading parallel and perpendicular to the direction of particle alignment are compared to experimental data from anisotropic MREs with 10%, 20%, and 30% CIP content.

Pence model is not able to capture the non-linear stress-strain behaviour of MRE materials. Only the compression data of anisotropic MREs with 10% iron content are fitted with an acceptable quality, but the large stiffness of anisotropic MREs with 20% and 30% when loaded in the direction of particle alignment are not well predicted (see Figure 6.8). The same is true

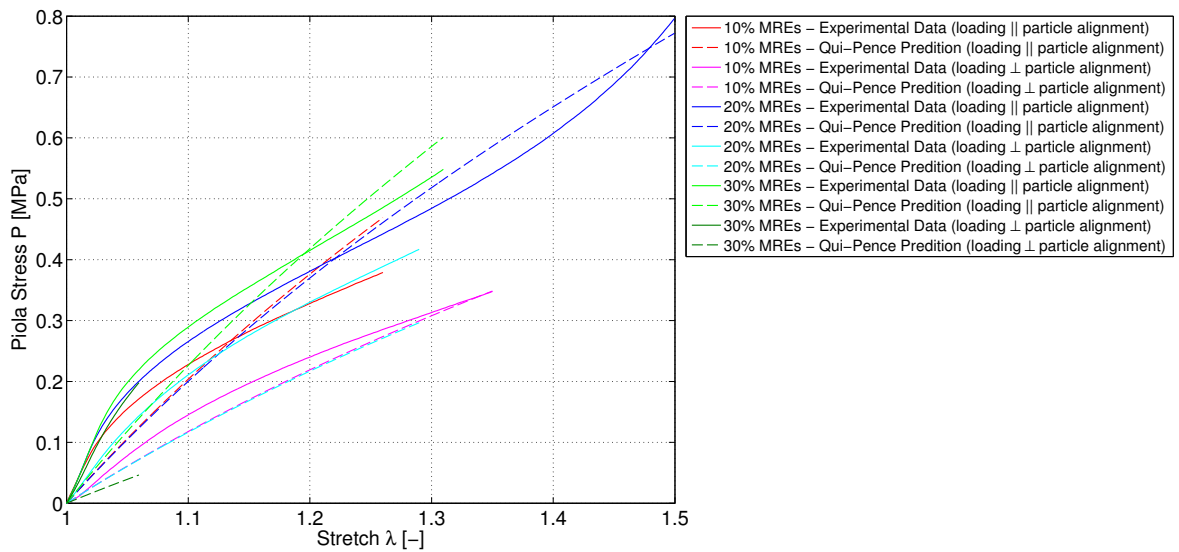


Figure 6.9: Predictions of the *Qui-Pence* model fitted to uniaxial tension data with both loading parallel and perpendicular to the direction of particle alignment are compared to experimental data from anisotropic MREs with 10%, 20%, and 30% CIP content.

for the tension deformation mode, where the quality of the results is very poor for all MREs

(see Figure 6.9). The fitting results for the pure shear deformation are surprisingly good,

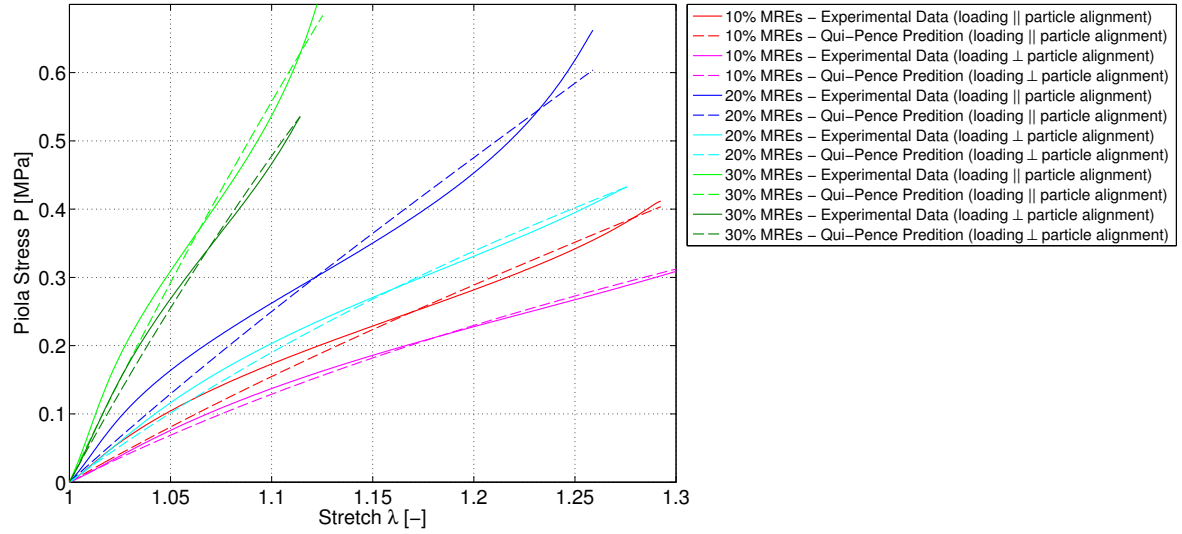


Figure 6.10: Predictions of the *Qui-Pence* model fitted to pure shear data with both loading parallel and perpendicular to the direction of particle alignment are compared to experimental data from anisotropic MREs with 10%, 20%, and 30% CIP content.

but still the non-linear behaviour of the stress-strain curves is not interpreted well, rather the predicted stresses behave linearly (see Figure 6.10). Fitting to the equi-biaxial tension mode

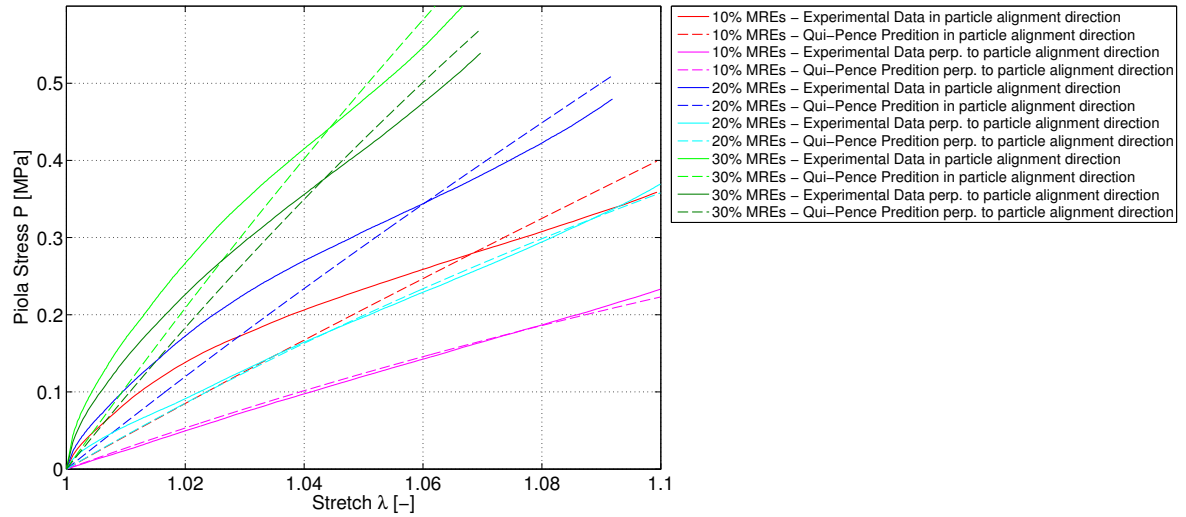


Figure 6.11: Predictions of the *Qui-Pence* model fitted to equi-biaxial tension data are compared to experimental data from anisotropic MREs with 10%, 20%, and 30% CIP content. Predictions and experimental data are illustrated for both directions, parallel and perpendicular to the direction of particle alignment.

provides reasonable good predictions perpendicular to the particle alignment, but once again the steep slope in the small-strain region, and the non-linear stress-strain behaviour is not well predicted in the direction of particle alignment (see Figure 6.11).

The parameters, μ and γ , of the *Qui-Pence* model, the Young's moduli, E_1 in the particle alignment direction, and E_2 perpendicular to the alignment direction, and the coefficient of

determination, R_2 , are summarised in Table 6.5 for all deformation modes. In the table,

	MRE	$\mu [MPa]$	$\gamma [-]$	$E_1 [MPa]$	$E_2 [MPa]$	R_2
Compression	Anisotropic 10% MREs	0.7444	2.7051e-16	2.2331	2.2331	0.7868
	Anisotropic 20% MREs	0.7316	1.1846e-16	2.1949	2.1949	0.2707
	Anisotropic 30% MREs	0.8272	4.9866e-16	2.4817	2.4817	0.8814
Tension	Anisotropic 10% MREs	0.0062	1.0119e+2	2.5321	0.0248	0.9718
	Anisotropic 20% MREs	0.5488	4.7074e-17	1.6463	1.6463	0.7933
	Anisotropic 30% MREs	0.5633	7.8495e-17	1.6900	1.6900	0.1773
Pure Shear	Anisotropic 10% MREs	0.3695	1.5164e-1	1.7023	1.4782	0.9840
	Anisotropic 20% MREs	0.5447	2.3816e-1	2.6977	2.1788	0.9817
	Anisotropic 30% MREs	1.3704	1.2577e-1	6.1712	5.4818	0.9877
Equi-Biaxial Tension	Anisotropic 10% MREs	0.4658	8.2898e-1	4.3391	2.7947	0.8583
	Anisotropic 20% MREs	0.7473	5.5943e-1	6.1562	4.4839	0.9192
	Anisotropic 30% MREs	1.6028	1.9303e-1	10.8542	9.6166	0.9185

Table 6.5: The parameters, μ and γ , of the *Qui-Pence* model fitted to data of each deformation mode (fit to tests with both the loading parallel and perpendicular to the particle alignment direction), are listed. The Young's moduli, E_1 parallel and E_2 perpendicular to the direction of particle direction can be compared with the experimentally determined moduli (Tables 5.5, 5.13, 5.20, and 5.23).

it is obvious that for the compression mode the reinforcing part of the *Qui-Pence* model is determined with 0, thus only the *Neo-Hookean* model is used to predict the stresses. The same is true for anisotropic MREs with 20% and 30% iron content when tested under tension. The reasonably good results of the pure shear and equi-biaxial tension modes is indicated by the R_2 values listed in Table 6.5. In both cases the reinforcing part exists, and the stresses in both directions can be distinguished (see Figures 6.10 and 6.11).

The problem of all transversely isotropic models considered in this investigation is that the reinforcing components of the models predict a small reinforcing stiffness in the small-strain region, and much higher stiffness at larger strains; indeed they follow the shape of an exponential function. A root function would produce a more suitable fit to characterise the anisotropic MREs, producing a relatively large reinforcing stiffness in the small strain region. However, no such model was found in the literature. The quality of the data fits in general is much lower than that achieved with a data fitting to isotropic MREs using the *Ogden* model. None of the transversely isotropic models is able to model the steep slopes present in the small-strain regions in the experimental data of anisotropic MREs and the moduli determined experimentally were usually underestimated.

6.5 Models to describe the MR effect

Data fitting of constitutive equations to describe MRE behaviour under the influence of a magnetic field is not performed in this study. The previous section showed that several transversely isotropic models failed to represent the experimental data of anisotropic MREs well,

so it would not be meaningful to perform data fitting to experimental results of tests with an applied magnetic field. A constitutive model that describes the behaviour of magneto-elastic materials is proposed by Bustamante (2010), it is very complicated and involves ten invariants to be determined by a data fitting.

The theoretical framework of magneto-elastic constitutive modelling is presented briefly in this section. Once again, the theory concentrates on the equations developed by Ogden; for further details on magneto-elastic theory the author refers to Dorfmann and Ogden (2003, 2004a,b, 2005), Bustamante *et al.* (2006, 2008), and Bustamante (2010). A brief theoretical overview of the electromagnetic theory was provided in Section 4.1, a deeper discussion can be found in the listed references.

From the theoretically point of view, isotropic magneto-elastic materials under the influence of a magnetic field can be modelled in a similar way to mechanically transversely isotropic materials, though here the fibre direction, \mathbf{a}_0 , is replaced by the magnetic induction vector \mathbf{B}_0 . The pseudo-invariants, I_4 , I_5 , and I_6 can be defined analogously to Equations 6.84 and 6.85, *i.e.*

$$I_4 = |\mathbf{B}_0|^2 \quad (6.126)$$

$$I_5 = \mathbf{B}_0 \mathbf{C} \mathbf{B}_0 \quad (6.127)$$

$$I_6 = \mathbf{B}_0 \mathbf{C}^2 \mathbf{B}_0 \quad (6.128)$$

The invariant, I_4 , is not required in modelling transversely isotropic materials (Equations 6.84 and 6.85) as there the vector, \mathbf{a}_0 , was simply a unit vector and thus I_4 was omitted. The strain energy function for isotropic materials that are under the influence of a magnetic induction, \mathbf{B}_0 , is a function of the six invariants (the invariants I_1 , I_2 , and I_3 were defined in Equations 6.4, 6.5, and 6.6)

$$\Psi = \Psi(I_1, I_2, I_3, I_4, I_5, I_6) \quad (6.129)$$

For incompressible materials the invariant $I_3 = 1$ and so the strain energy function becomes a function of just five invariants (a *Lagrange* multiplier is needed).

The situation is more complex for transversely isotropic magneto-elastic materials subject to a magnetic field; in this case both the fibre direction, \mathbf{a}_0 , and the magnetic induction vector, \mathbf{B}_0 , must be considered. Bustamante (2010) states that seven additional invariants (beside the three already defined for isotropic materials) are required. The pseudo-invariants I_4 , I_5 , and I_6 are the same as in the isotropic case with an applied magnetic field (Equations 6.126, 6.127, and 6.128), the other invariants are defined as follows:

$$I_7 = \mathbf{a}_0 \mathbf{C} \mathbf{a}_0 \quad (6.130)$$

$$I_8 = \mathbf{a}_0 \mathbf{C}^2 \mathbf{a}_0 \quad (6.131)$$

$$I_9 = \mathbf{a}_0 \mathbf{B}_0$$

$$I_{10} = \mathbf{a}_0 \mathbf{C} \mathbf{B}_0 \quad (6.132)$$

with I_7 and I_8 characterising the fibre direction of the transversely isotropic material, and I_9 and I_{10} coupling both the fibre direction and the magnetic induction vector. The strain energy function is now a function of 10 invariants:

$$\Psi = \Psi(I_1, I_2, I_3, I_4, I_5, I_6, I_7, I_8, I_9, I_{10}) \quad (6.133)$$

As noted earlier, specific strain energy functions are not presented, and a data fitting is not performed in this study. The experimental data presented in Chapter 5 are saved on a DVD available with this thesis, and can be used to develop constitutive equations that describe MREs under the influence of a magnetic field in future.

6.6 Conclusions of Chapter 6

Several strain energy functions have been discussed and experimental data presented in Chapter 5 were used to determine the constitutive model parameters using the phenomenological approach. The *Ogden* model was found to be suitable to model isotropic MREs. Experimental data measured under different deformation modes were combined to determine unique solutions, and to obtain model parameters that describe the MREs under general deformation. However, the importance of correct preconditioning of experimental data to account for the stress-softening *Mullins* effect was emphasised. The *Ogden-Roxburgh* model was employed to account for the latter and experimental data were adjusted to effectively represent the likely form of data following the same preconditioning level. Weight factors were introduced into the fitting procedure when combining different deformation modes to account for experimental issues as for example the friction between compression specimen and test rig plate. It is emphasised by Miller (1999) that pure states of strain are desired for the determination of correct constitutive model parameters. As this is not always achievable in experiments weight factors can be used to scale the experimental data by a simple factor. It was found that only one weight factor for the compression data was needed to achieve good results when combining experimental data presenting the same preconditioning strain level. Final fitted parameters of the *Ogden* model were found accurately to describe the MRE behaviour under different deformation modes up to both 10% and 50% preconditioning strain (a weight factor for compression was used).

Various transversely isotropic models were fitted to experimental data of anisotropic MREs, but none of the constitutive models represented the material behaviour of anisotropic MREs

well. It is suggested that an alternative formulation for the reinforcing part of the transversely isotropic models would be useful in capturing the characteristic shape of test data from anisotropic MREs. Furthermore, it would be nice to understand the transversely isotropic models as an extension to the constitutive models for isotropic materials, so that the model parameters determined earlier for isotropic MREs could be used and only the anisotropy effect would be needed to be added to the result.

The constitutive modelling performed in this study presents only a small choice of available constitutive equations and data fitting options. The unsuccessful fitting of anisotropic MREs showed that MREs are very complex materials even in the absence of magnetic fields. Constitutive models that describe anisotropic MREs, and MREs under the influence of a magnetic field must be developed to enable the virtual design of large-strain applications employing MREs. Thus far this has not been achieved, and large-strain applications using MREs are very rare and are still in the prototype stage. The mean values of all experimental data together with the *Matlab* functions used to perform the data fitting are saved on a DVD available with this thesis. The author hopes that this advances the development of constitutive models for MREs.

7 Conclusions and Future Work

This chapter summarises the work presented in this thesis, draws conclusions and gives recommendations for future work.

The literature review revealed that MREs are promising materials with a wide range of possible applications. This investigation concentrated on the large-strain mechanical behaviour of MREs and on the increase in stiffness when magnetic fields were applied. Reviewing the literature in this area showed that there is a lack of experimental data using the same material tested under different deformation modes. Experimental data published in the literature thus far are insufficient for accurate development of constitutive models. This investigation aims to address this lack of a comprehensive data set measured using the same type of MRE material. To this end, silicone rubber based isotropic and anisotropic MREs with up to 40% carbonyl iron particles were manufactured using a reliable and repeatable manufacturing process. Different shapes of MRE specimens were moulded according to the needs of each large-strain experiment. Isotropic and anisotropic MREs were tested under compression, tension, pure shear and equi-biaxial tension up to a maximum of 100% strain. Tests in the absence and in the presence of magnetic fields were conducted. The *Mullins* effect has been found to be of great importance. MREs are very sensitive to this stress-softening effect. To account for the *Mullins* effect a novel test procedure was developed. MRE test samples were repeatedly used in a test series comprised of four-cycle test steps, conducted both in the absence and in the presence of magnetic fields. The third loading cycle of each test step was used to characterise the MRE behaviour and the method of analysis was the same for all experimental data. Tests in the absence of magnetic fields were repeated as part of the test series to verify the stress-strain results. Divergences between the repeated ‘no-field’ tests were attributed to the *Mullins* effect. To eliminate the influence of the *Mullins* effect when interpreting results, stress-strain data measured only up to the ‘divergence strain’ were used for the characterisation of MREs and to calculate Magneto-Rheological effects. To create experimental data useful for the evaluation of constitutive models, tests up to 50% strain were conducted under compression, tension, and pure shear. In the equi-biaxial tension tests strains were limited to just 10% due to practical considerations. The following conclusions can be drawn from the experimental investigation:

- MREs show a strong non-linear stress-strain behaviour under large-strain.
- Anisotropic MREs with their particle alignment in the loading direction are stiffest, with large moduli in the small-strain region that rapidly decrease at larger strains. Isotropic and anisotropic MREs with their particle alignment perpendicular to the loading direction exhibit steadily increasing tangent moduli, where the isotropic MREs are slightly softer.

- The moduli usually increase with increasing iron content.
- The highest MR effects are achieved with anisotropic MRE containing 30% iron volume fraction, and with particle chains aligned in the direction of both the magnetic field and loading. The highest relative effect of 109.5% was achieved in the equi-biaxial tension tests, followed by 98.1% relative increase in tension tests, both related to 100 mT applied magnetic flux.
- MR effects are largest in the small-strain region, decrease rapidly to nearly no effect in the mid-strain region, but increase again at larger strain ($> 15\%$).
- MR effects increase with increasing iron content and increase linearly with increasing magnetic field.
- MREs are very sensitive to the *Mullins* effect: The moduli in the absence of a magnetic field are smaller and the MR effects can be enhanced when MREs are tested to a larger level of strains.
- MREs with high iron contents can only be used up to a maximum level of 50% strain. Fatigue tests revealed that when stretching MREs beyond this stability strain limit, the stress-softening is still apparent even after 100 loading and unloading cycles.

When characterising MREs experimentally, and when designing application employing MREs in future, several recommendations can be given:

- In applications, MRE specimens should be preconditioned to a higher level of strain than planned for the working operation of MREs. As the *Mullins* effect is time-dependant, a ‘warming-up’ phase should be performed prior to each use of the application. Consider, preconditioning of MREs up to quite large strains to enhance the MR effects.
- In experiments, it might be useful to precondition the MRE specimens up to a larger level of strain than used in the cyclic tests to characterise the material.
- The permanent deformation that can occur in MRE specimens have to be carefully examined and the test machine settings should be adjusted in each subsequent test carried out on the same sample to ensure that the same strain is applied to the sample in subsequent tests.
- Consider cutting the MRE specimens to the same size prior testing.
- Experiments up to more different strain levels should be conducted, as this has been found to be of great importance for the final stress-strain properties.

- The novel test procedure used in this investigation can be recommended for the experimental characterisation of MREs. Cyclic testing must be performed in order to characterise the MREs under correct conditions. The repetition of tests in the absence of magnetic field is highly recommended to ensure that the stress-softening *Mullins* effect is eliminated when interpreting the final results.

Data fitting to pre-established hyperelastic constitutive models were conducted to evaluate constitutive models in their ability to characterise MRE materials and to demonstrate the utility of the experimental data set generated in this investigation for the development of such models. The *Ogden* model has been shown to accurately describe the response of isotropic MREs in the absence of a magnetic field under general deformations. The main findings are listed:

- *Ogden* model parameters can only be successfully determined when combining experimental data obtained from tests up to the same strain level. Once again the preconditioning level and therefore the *Mullins* effect is of high importance.
- The *Ogden-Roxburgh* model was used to successfully interpolate experimental data to lower strain levels, than the strain originally applied in the experiment. This is useful when combining experimental data from different tests not originally conducted up to the same strain level.
- Weight factors were introduced as a method to account for experimental issues (*i.e.* friction and non-ideal deformation kinematics). To obtain good results using the *Ogden* model in describing the behaviour of isotropic MREs, only a weight factor for compression test results was needed. As noted by Miller (1999), it is especially difficult to achieve pure states of strain in compression experiments.
- Data fitting to several transversely isotropic models was not successful. The models failed to predict the non-linear stress-strain behaviour of transversely isotropic MREs. In particular, the steep slope present in the small-strain region was not correctly represented. A root function incorporated in the reinforcing component of the models would perhaps provide a better representation.

To summarise, this work presents a thorough characterisation of MREs under large strain. The experimental data, together with the *Matlab* codes developed during this investigation are saved on a DVD attached to this document. The author hopes that this will help to advance the development of constitutive models designed to represent MREs both in the absence and in the presence of magnetic fields.

Bibliography

- Abaqus. Abaqus 6.10 Documentation. ©Dassault Systemes Simulia, 2010. URL <http://www.sharcnet.ca/Software/Abaqus610/Documentation/docs/v6.10/>. Retrieved 08/2013.
- S. Abramchuk, D.A. Grishin, E.Yu. Kramarenko, G.V. Stepanov, and A.R. Khokhlov. Effect of a homogeneous magnetic field on the mechanical behavior of soft magnetic elastomers under compression. *Polymer Science Series A*, 48(2):138–145, Feb 2006.
- S. Abramchuk, E. Kramarenko, G. Stepanov, L.V. Nikitin, G. Filipcsei, A.R. Khokhlov, and M. Zrinyi. Novel highly elastic magnetic materials for dampers and seals: Part I. Preparation and characterization of the elastic materials. *Polymers for advanced Technologies*, 18(11):883–890, 2007.
- Z. Aga and L. Faidley. Characterisation of the magnetostrictive of magnetorheological elastomers. In *SMASIS 2008: Proceedings of the ASME Conference on smart materials, adaptive structures and intelligent systems*, volume 1, pages 447–452, 2008.
- Z. Aga, D. Feimster, and L. Faidley. Magnetorheological elastomers with increased structural integrity for multifunction applications. In *Proceedings of IMECE, ASME International Mechanical Engineering Congress and Exposition*, 2007.
- A.M. Albanese and K.A. Cunefare. Properties of a magnetorheological semiactive vibration absorber. In *Smart Structures and Materials*, 2003.
- A. Albanese Lerner and K.A. Cunefare. Adaptable vibration absorbers employing a magnetorheological elastomer with variable gap length and methods and systems thereof, 2006.
- A. Albanese Lerner and K.A. Cunefare. Performance of MRE-based vibration absorbers. *Journal of Intelligent Material Systems and Structures*, 19:551–563, 2008.
- A.M. Albanese Lerner. The Design and Implementation of a Magnetorheological Silicone Composite State-Switched Absorber. Master’s thesis, School of Mechanical Engineering Georgia Institute of Technology, 2005.
- C. Bellan and G. Bossis. Field dependence of viscoelastic properties of MR elastomers. *International Journal of modern Physics B*, 16:2447–2453, 2002. 8th International Conference on Electro-Rheological Fluids and Magneto-Rheological Suspensions, Nice, France.
- J.S. Bergstroem and M.C. Boyce. Large Strain Time-Dependent Behavior of Filled Elastomers. *Mechanics and Materials*, 32:627–644, 2000.

- I. Bica. Compressibility modulus and principal deformations in magneto-rheological elastomer: The effect of the magnetic field. *Journal of Industrial and Engineering Chemistry*, 15:773–776, 2009a.
- I. Bica. Quadrupolar magnetoresistor based on electroconductive magnetorheological elastomer. *Journal of Industrial and Engineering Chemistry*, 15:769–772, 2009b.
- I. Bica. Influence of the transverse magnetic field intensity upon the electric resistance of the magnetorheological elastomer containing graphite microparticles. *Materials Letters*, 63: 2230–2232, 2009c.
- I. Bica. Magnetoresistor sensor with magnetorheological elastomers. *Journal of Industrial and Engineering Chemistry*, 17(1):83 – 89, 2011.
- I. Bica. The influence of the magnetic field on the elastic properties of anisotropic magnetorheological elastomers. *Journal of Industrial and Engineering Chemistry*, 18:1666–1669, 2012.
- A. Boczkowska and S. Awietjan. Smart composites of urethane elastomers with carbonyl iron. *Journal of Materials Science*, 44:4104–4111, 2009.
- A. Boczkowska and S. Awietjan. Microstructure and Properties of Magnetorheological Elastomers, 2012.
- A. Boczkowska, S.F. Awietjan, and R. Wroblewski. Microstructure - property relationships of urethane magnetorheological elastomers. *Smart Materials and Structures*, 16:1924–1930, 2007.
- A. Boczkowska, S.F. Awietjan, T. Wejrzanowski, and K.J. Kurzydowski. Image analysis of the microstructure of magnetorheological elastomers. *Journal of Materials Science*, 44: 3135–3140, 2009.
- A. Boczkowska, S.F. Awietjan, S. Pietrzko, and K.J. Kurzydowski. Mechanical properties of magnetorheological elastomers under shear deformation. *Composites Part B: Engineering*, 43(2):636 – 640, 2012.
- T. Borbath, S. Günther, D.Y. Borin, T. Gundermann, and S. Odenbach. XmicroCT analysis of magnetic field-induced phase transitions in magnetorheological elastomers. *Smart Materials and Structures*, 21(10), 2012.
- D. Borin, D. Günther, C. Hintze, G. Heinrich, and S. Odenbach. The level of cross-linking and the structure of anisotropic magnetorheological elastomers. *Journal of Magnetism and Magnetic Materials*, 324(21):3452 – 3454, 2012.

- H. Böse. Viscoelastic Properties of Silicone-Based Magnetorheological Elastomers. *International Journal of Modern Physics B*, 21:4790–4797, 2007.
- H. Böse and R. Röder. *Magnetorheological Elastomer Composites and use thereof*. Patent US 20090039309, 2009.
- H. Böse, R. Rabindranath, and J. Ehrlich. Soft magnetorheological elastomers as new actuators for valves. *Journal of Intelligent Material Systems and Structures*, 23, 2011.
- G. Bossis, N. Kchit, P. Lancon, A. Meunier, O. Volkova, and A. Zubarev. Mechanical and electrical properties of magnetorheological elastomers in relation with percolating microstructures. In *International Summer School and Workshop: Complex and Magnetic Soft Matter*, 2012.
- D. Bruggeman. Berechnung verschiedener physikalischer Konstanten von heterogenen Substanzen. *Dielektrizitätskonstanten und Leitfähigkeiten der Mischkörper aus isotropen Substanzen: Annalen der Physik*, 416:636–664, 1935.
- BS 903-5. Physical testing of rubber - Part 5: Guide to the application of rubber testing to finite element analysis, 2004.
- BS ISO 37. Rubber, vulcanized or thermoplastic - Determination of tensile stress-strain properties, 2005.
- BS ISO 7743. Rubber, vulcanized or thermoplastic - Determination of compression stress-strain properties, 2008.
- R. Bustamante. Transversely isotropic nonlinear magneto-active elastomers. *Acta Mechanica*, 210:183–214, 2010.
- R. Bustamante, A. Dorfmann, and R. W. Ogden. Universal relations in isotropic nonlinear magnetoelasticity. *Quarterly Journal of Mechanics and Applied Mathematics*, 59, 2006.
- R. Bustamante, A. Dorfmann, and R. W. Ogden. On Variational Formulations in Nonlinear Magnetoelastostatics. *Mathematics and Mechanics of Solids*, 13:725–745, 2008.
- J.D. Carlson and M.R. Jolly. MR fluid, foam and elastomer devices. *Mechatronics*, 10:555 – 569, 2000.
- L. Chen, X.L. Gong, W.Q. Jiang, J.J. Yao, H.X. Deng, and W.H. Li. Investigation on magnetorheological elastomers based on natural rubber. *Journal of Materials Science*, 42: 5483–5489, 2007a.
- L. Chen, X.L. Gong, and W.H. Li. Microstructures and viscoelastic properties of anisotropic magnetorheological elastomers. *Smart Materials and Structures*, 16:2645–2650, 2007b.

- L. Chen, X.L. Gong, and W.H. Li. Effect of carbon black on the mechanical performances of magnetorheological elastomers. *Polymer Testing*, 27:340 – 345, 2008.
- W.J. Choi. *Dynamic analysis of magnetorheological elastomer configured sandwich structures*. Phd thesis, University of Southampton, School of Engineering Sciences, 2009.
- W.J. Choi, Y.P. Xiong, and R.A. Shenoi. Characterisation of magnetorheological elastomer materials for the core of smart sandwich structures. In *Proceedings of the 8th International Conference on Sandwich Structures (ICSS8)*, 2008.
- Comsol. Comsol Multiphysics 4.2 Documentation. ©1998-2011 COMSOL, 2011. URL <http://www.comsol.com/comsol-multiphysics>. Retrieved 06/2014.
- Correlated Solutions. *VIC-3D Testing Guide*, 2010.
- R.J. Crist. *Active vibrational damper*. Patent 7584685, September 2009.
- K. Danas, S.V. Kankanala, and N. Triantafyllidis. Experiments and modeling of iron-particle-filled magnetorheological elastomers. *Journal of the Mechanics and Physics of Solids*, 60:120–138, 2012.
- H.X. Deng, X.L. Gong, and L.H. Wang. Development of an adaptive tuned vibration absorber with magnetorheological elastomer. *Smart Materials and Structures*, 15, 2006.
- J. Diani, B. Fayolle, and P. Gilormini. A review on the Mullins effect. *European Polymer Journal*, 45:601–612, 2009.
- G. Diguët, E. Beaunon, and J.Y. Cavaille. From dipolar interactions of a random distribution of ferromagnetic particles to magnetostriction. *Journal of Magnetism and Magnetic Materials*, 321:396–401, 2009.
- G. Diguët, E. Beaunon, and J.Y. Cavaille. Shape effect in the magnetostriction of ferromagnetic composite. *Journal of Magnetism and Magnetic Materials*, 322:3337–3341, 2010.
- X.F. Dong, N. Ma, M. Qi, J. Li, R. Chen, and J. Ou. The pressure-dependent MR effect of magnetorheological elastomers. *Smart Materials and Structures*, 21, 2012.
- X.M. Dong, M. Yu, C.R. Liao, and W.M. Chen. A new variable stiffness absorber based on magneto-rheological elastomer. *Trans. Nonferrous Metal Society China*, 19, 2009.
- A. Dorfmann and R.W. Ogden. Magnetoelastic modelling of elastomers. *European Journal of Mechanics A - Solids*, 22(4):497–507, 2003.
- A. Dorfmann and R.W. Ogden. Nonlinear magnetoelastic deformations. *Quarterly Journal of Mechanics and Applied Mathematics*, 57(4):599–622, 2004a.

- A. Dorfmann and R.W. Ogden. Nonlinear magnetoelastic deformations of elastomers. *Acta Mechanica*, 167(1-2):13–28, 2004b.
- A. Dorfmann and R.W. Ogden. A constitutive model for the mullins effect with permanent set in particle-reinforced rubber. *International Journal of Solids and Structures*, 41(7): 1855 – 1878, 2004c.
- A. Dorfmann and R.W. Ogden. Some problems in nonlinear magnetoelasticity. *Zeitschrift Für Angewandte Mathematik Und Physik*, 56(4):718–745, 2005.
- G. Du and X.D. Chen. MEMS magnetometer based on magnetorheological elastomer. *Measurement*, 45:54–58, 2012.
- H. Du, W. Li, and N. Zhang. Semi-active variable stiffness vibration control of vehicle seat suspension using an MR elastomer isolator. *Smart Materials and Structures*, 20, 2011.
- L.D. Elie, J.M. Ginder, W.M. Stewart, and M.E. Nichols. *Variable stiffness bushing using magnetorheological elastomers*. Patent EP 0784163 (A1), 1997.
- L. Faidley, D. Macias, and E. Harrington. Cyclic Actuator Behavior of Ferrogels. In *Proceedings of the ASME Conference on Smart Materials, Adaptive Structures and Intelligent Systems*, 2008.
- L. Faidley, Y. Han, K. Tucker, S. Timmons, and W. Hong. Axial strain of ferrogels under cyclic magnetic fields. *Smart Materials and Structures*, 19, 2010.
- M. Farshad and A. Benine. Magnetoactive elastomer composites. *Polymer Testing*, 23: 347–353, 2004.
- M. Farshad and M. Le Roux. Compression properties of magnetostrictive polymer composite gels. *Polymer Testing*, 24:163–168, 2005.
- G. Filipcsei, I. Csetneki, A. Szilagy, and M. Zrinyi. Magnetic field-responsive smart polymer composites. *Oligomers Polymer Composites Molecular Imprinting*, 206, 2007.
- E. Forster, M. Mayer, R. Rabindranath, H. Böse, G. Schlunck, G. J. Monkman, and M. Shamonin. Patterning of ultrasoft, agglutinative magnetorheological elastomers. *Journal of Applied Polymer Science*, 2012.
- J. Fu, M. Yu, X.M. Dong, and L.X. Zhu. Magnetorheological elastomer and its application on impact buffer. *Journal of Physics: Conference Series*, 412, 2013.
- A. Fuchs, F. Gordaninejad, G.H. Hitchcock, J. Elkins, and Q. Zhang. *Tunable magnetorheological elastomers and processes for their manufacture*. Patent US Patent 7261834, 2007.

- A. Fuchs, J. Sutrisno, F. Gordaninejad, M.B. Caglar, and L. Yanming. Surface polymerization of iron particles for magnetorheological elastomers. *Journal of Applied Polymer Science*, 117:934–942, 2010.
- L. Ge, X.L. Gong, Y. Fan, and S. Xuan. Preparation and mechanical properties of the magnetorheological elastomer based on natural rubber/rosin glycerin hybrid matrix. *Smart Materials and Structures*, 22, 2013.
- N. Ghafoorianfar, X. Wang, and F. Gordaninejad. On the sensing of magnetorheological elastomers. *Proc. SPIE*, 8692, 2013.
- J.M. Ginder. Magnetorheological Materials. *Physics and Technology Forefronts*, 13, 2004.
- J.M. Ginder, M.E. Nichols, L.D. Elie, and J.L. Tardiff. Magnetorheological elastomers: properties and applications. In *Smart Structures and Materials*, 1999.
- J.M. Ginder, M.E. Nichols, L.D. Elie, and S.M. Clark. Controllable-stiffness components based on magnetorheological elastomers. In *Smart Structures and Materials*, 2000.
- J.M. Ginder, W.F. Schlotter, and M.E. Nichols. Magnetorheological Elastomers in Tunable Vibration Absorbers. In *Smart Structures and Materials*, 2001.
- J.M. Ginder, S.M. Clark, W.F. Schlotter, and M.E. Nichols. Magnetostrictive phenomena in magnetorheological elastomers. *International Journal of modern Physics B*, 16:2412–2418, 2002. 8th International Conference on Electro-Rheological Fluids and Magnetorheological Suspensions, Nice, France.
- S. Giordano. Effective medium theory for dispersions of dielectric ellipsoids. *Journal of Electrostatics*, 58:59–76, 2003.
- H.S. Göktürk, T.J. Fiske, and D.M. Kalyon. Electric and magnetic properties of a thermoplastic elastomer incorporated with ferromagnetic powders. *IEEE Transactions on Magnetics*, 29:4170–4176, 1993.
- X.L. Gong, X.Z. Zhang, and P.Q. Zhang. Fabrication and characterization of isotropic magnetorheological elastomers. *Polymer Testing*, 24:669–676, 2005.
- X.L. Gong, L. Chen, and J.F. Li. Study of utilizable magnetorheological elastomers. *International journal of modern physics B*, 21:4875–4882, 2007. 10th International Conference on Electrorheological fluids and Magnetorheological Suspensions.
- X.L. Gong, G. Liao, and S. Xuan. Full-field deformation of magnetorheological elastomer under uniform magnetic field. *Applied Physics Letters*, 100, 2012.

- F. Gordaninejad, X. Wang, and P. Mysore. Behavior of thick magnetorheological elastomers. *Journal of Intelligent Material Systems and Structures*, 23:1033–1039, 2012.
- D. Gorman, S. Jerrams, R. Ekins, and N. Murphy. Creating a uniform magnetic field for the equi-biaxial physical testing of magnetorheological elastomers: electromagnet design, development and testing. *Constitutive Models for Rubber VII*, pages 403–407, 2012.
- X. Guan, X. Dong, and J. Ou. Magnetostrictive effect of magnetorheological elastomer. *Journal of Magnetism and Magnetic Materials*, 320:158–163, 2008.
- I. Gudmundsson. A Feasibility Study of Magnetorheological Elastomers for a Potential Application in Prosthetic Devices. Master’s thesis, Faculty of Industrial Engineering, Mechanical Engineering and Computer Science, School of Engineering and Natural Sciences, University of Iceland, 2011.
- D. Günther, D.Y. Borin, S. Günther, and S. Odenbach. X-ray micro-tomographic characterization of field-structured magnetorheological elastomers. *Smart Materials and Structures*, 21(1), 2012.
- Z.Y. Guo, X.Q. Peng, and B. Moran. Mechanical response of neo-hookean fiber reinforced incompressible nonlinearly elastic solids. *International Journal of Solids and Structures*, 44:1949–1969, 2007.
- T. Heier and C. Schubert. *Actuator having a magnetorheological elastomer element*. Patent WO2010 / 054775 A1, 2010.
- C. Hintze and G. Heinrich. Curing Studies of Magnetorheological Elastomers. In *Presented at the Fall 180th Technical Meeting of the Rubber Division of the American Chemical Society, Inc.*, 2011.
- G.H. Hitchcock, F. Gordaninejad, and A. Fuchs. *Controllable magneto-rheological elastomer vibration isolator*. Patent 7086507, August 2006.
- N. Hoang, N. Zhang, and H. Du. A dynamic absorber with a soft magnetorheological elastomer for powertrain vibration suppression. *Smart Materials and Structures*, 18:10, 2009.
- N. Hoang, N. Zhang, and H. Du. An adaptive tunable vibration absorber using a new magnetorheological elastomer for vehicular powertrain transient vibration reduction. *Smart Materials and Structures*, 20, 2011.
- G.A. Holzapfel. *Nonlinear solid mechanics: A Continuum Approach for Engineering*. Wiley, Chichester; New York, 2000.

- G.A. Holzapfel, T.C. Gasser, and R.W. Ogden. A new constitutive framework for arterial wall mechanics and a comparative study of material models. *Journal of Elasticity*, 61: 1–48, 2000.
- G. Hu, M. Guo, W.H. Li, H. Du, and G. Alici. Experimental investigation of the vibration characteristics of a magnetorheological elastomer sandwich beam under non-homogeneous small magnetic fields. *Smart Materials and Structures*, 20, 2011.
- Y. Hu, Y.L. Wang, X.L. Gong, X.Q. Gong, X.Z. Zhang, W.Q. Jiang, P.Q. Zhang, and Z.Y. Chen. New magnetorheological elastomers based on polyurethane/Si-rubber hybrid. *Polymer Testing*, 24:324–329, 2005.
- ImageJ. Image Processing Analysis in Java, 2014. URL <http://imagej.nih.gov/ij/docs/index.html>. Retrieved 06/2014.
- Integrated Engineering Software. Integrated's Quick Engineering Tools - Magnetisation Curve Generator, 2013. URL <http://www.integratedsoft.com/Tools/Magnetization-Curve>. Retrieved 07/2013.
- D. Jiles. *Introduction to Magnetism and Magnetic Materials*. Chapman & Hall - London, 1998.
- M.R. Jolly, J.D. Carlson, and B.C. Munoz. A model of the behaviour of magnetorheological materials. *Smart Materials and Structures*, 5:607, 1996a.
- M.R. Jolly, J.D. Carlson, B.C. Munoz, and T.A. Bullions. The Magnetoviscoelastic Response of Elastomer Composites Consisting of Ferrous Particles Embedded in a Polymer Matrix. *Journal of Intelligent Material Systems and Structures*, 7:613–622, 1996b.
- M.R. Jolly, J.W. Bender, and J.D. Carlson. Properties and applications of commercial magnetorheological fluids. *Journal of Intelligent Material Systems and Structures*, 10:5–13, 1999.
- B.X. Ju, M. Yu, J. Fu, X. Zheng, and Q. Yang. Study on the properties of porous magnetorheological elastomers under shock effect. *Journal of Physics: Conference Series*, 412, 2013.
- H.J. Jung, S.J. Lee, D.D. Jang, I.H. Kim, J.H. Koo, and F. Khan. Dynamic Characterization of Magneto-Rheological Elastomers in Shear Mode. *Magnetics, IEEE Transactions*, 45: 3930–3933, 2009.
- J. Kaleta, M. Krolewicz, and D. Lewandowski. Magnetomechanical properties of anisotropic and isotropic magnetorheological composites with thermoplastic elastomer matrices. *Smart Materials and Structures*, 20, 2011.

- M. Kallio. *The elastic and damping properties of magnetorheological elastomers*. PhD thesis, VTT Technical Research Centre of Finland, 2005.
- M. Kallio, S. Aalto, T. Lindroos, E. Jarvinen, T. Karna, and T. Meinander. Preliminary test on a MRE device. In *AMAS Workshop on Smart Materials and Structures*, 2003.
- M. Kallio, T. Lindroos, S. Aalto, E. Jaervinen, T. Kaernae, and T. Meinander. Dynamic compression testing of a tunable spring element consisting of a magnetorheological elastomer. *Smart Materials and Structures*, 16:506, 2007.
- S.V. Kankanala. *On Finitely Strained Magnetoelastic Solids*. PhD thesis, University of Michigan, 2007.
- K.K. Karkkainen, A.H. Sihvola, and K.I. Nikoskinen. Effective permittivity of mixtures: numerical validation by the FDTD method. *Geoscience and Remote Sensing, IEEE Transactions on*, 38:1303–1308, 2000.
- N. Kchit and G. Bossis. Electrical resistivity mechanism in magnetorheological elastomer. *Journal of Physics D: Applied Physics*, 42, 2009.
- N. Kchit, P. Lancon, and G. Bossis. Thermoresistance and giant magnetoresistance of magnetorheological elastomers. *Journal of Physics D - Applied Physics*, 42:5, 2009.
- J. Keinanen, T. Lindroos, T. Lienes, I. Vessonen, and P. Klinge. Adaptive Tuned Mass Damper Concept - Magnetorheologic and Elastic Elastomers. In *Actuator 08, Conference Proceedings*, 2008. 11th International Conference on New Actuators / 5th International Exhibition on Smart Actuators and Drive Systems.
- Y.K. Kim, J.H. Koo, K. Kim, and S. Kim. Vibration isolation strategies using magnetorheological elastomer for a miniature cryogenic cooler in space application. In *Advanced Intelligent Mechatronics (AIM)*, 2010.
- D.J. Klingenberg. Magnetorheology: Applications and challenges. *AIChE Journal*, 47(2): 246–249, 2001.
- J.H. Koo, F. Khan, D.D. Jang, and H.J. Jung. Dynamic characterization and modeling of magneto-rheological elastomers under compressive loadings. *Smart Materials and Structures*, 19, 2010.
- J.H. Koo, A. Dawson, and H.J. Jung. Characterization of actuation properties of magnetorheological elastomers with embedded hard magnetic particles. *Journal of Intelligent Material Systems and Structures*, 23:1049–1054, 2012.

- M. Krolewicz, D. Lewandowski, M. Przybylski, and J. Kaleta. Manufacture and Testing of Anisotropic Magnetorheologic Elastomers. In *IMEKO TC15 - Experimental Mechanics: Proceedings of the 11th Youth Symposium on Experimental Solid Mechanics*, 2012.
- M. Krolewicz, J. Kaleta, D. Lewandowski, and M. Przybylski. Cyclic tests of thermoplastic magnetorheological elastomers. In *6th Conference on Smart Structures and Materials*, 2013.
- J.F. Li and X.L. Gong. Influence of curing time on the anisotropic microstructure of magnetorheological elastomer. In *International Conference on Heterogeneous Material Mechanics (ICHMM)*, 2008.
- J.F. Li, X.L. Gong, Z. Xu, and W.Q. Jiang. The effect of pre-structure process on magnetorheological elastomer performance. *IJMR*, 99:1358–1364, 2008.
- W. Li, K. Kostidis, X. Zhang, and Y. Zhou. Development of a Force Sensor Working with MR Elastomers. In *IEEE/ASME International Conference on Advanced Intelligent Mechatronics, AIM, IEEE*, 2009.
- W.H. Li and X.Z. Zhang. A study of the magnetorheological effect of bimodal particle based magnetorheological elastomers. *Smart Materials and Structures*, 19, 2010.
- W.H. Li, T.F. Tian, and H. Du. Sensing and Rheological Capabilities of MR Elastomers. In *Smart Actuation and Sensing Systems - Recent Advances and Future Challenges*. InTech, 2012a.
- W.H. Li, X. Zhang, and H. Du. Development and simulation evaluation of a magnetorheological elastomer isolator for seat vibration control. *Journal of Intelligent Material Systems and Structures*, 23:1041–1048, 2012b.
- W.H. Li, X.Z. Zhang, and H. Du. Magnetorheological Elastomers and Their Applications. In *Advances in Elastomers I*. Springer Berlin Heidelberg, 2013.
- G. Liao, X.L. Gong, S. Xuan, C. Guo, and L. Zong. Magnetic-Field-Induced Normal Force of Magnetorheological Elastomer under Compression Status. *Industrial and Engineering Chemistry Research*, 51:3322–3328, 2012a.
- G.J. Liao, X.L. Gong, C.J. Kang, and S.H. Xuan. The design of an active adaptive tuned vibration absorber based on magnetorheological elastomer and its vibration attenuation performance. *Smart Materials and Structures*, 20, 2011.
- G.J. Liao, X.L. Gong, S.H. Xuan, C.J. Kang, and L.H. Zong. Development of a real-time tunable stiffness and damping vibration isolator based on magnetorheological elastomer. *Journal of Intelligent Material Systems and Structures*, 23:25–33, 2012b.

- P. Lockette, S.E. Lofland, J. Biggs, J. Roche, J. Mineroff, and M. Babcock. Investigating New Symmetry Classes in Magnetorheological Elastomers: Cantilever Bending Behavior. *Smart Materials and Structures*, 20, 2011.
- P.R. Lockette, J. Kadlowec, and J.H. Koo. Particle mixtures in magnetorheological elastomers (MREs). In *Proc. SPIE: Smart Structures and Materials*, 2006.
- P.R. Lockette, S.E. Lofland, J.H. Koo, J. Kadlowec, and M. Dermond. Dynamic characterization of bimodal particle mixtures in silicone rubber magnetorheological materials. *Polymer Testing*, 27:931–935, 2008.
- M. Lokander. Performance of Isotropic Magnetorheological Rubber Materials. Masterthesis, Royal Institute of Technology Stockholm, 2002.
- M. Lokander. *Performance of Magnetorheological Rubber Materials*. Doctoral thesis, comprehensive summary, Department of Fibre and Polymer Technology Royal Institute of Technology Stockholm, 2004.
- M. Lokander and B. Stenberg. Improving the magnetorheological effect in isotropic magnetorheological rubber materials. *Polymer Testing*, 22:677–680, 2003.
- X. Lu, X. Qiao, H. Watanabe, X.L. Gong, T. Yang, W. Li, K. Sun, M. Li, K. Yang, H. Xie, Q. Yin, D. Wang, and X.D. Chen. Mechanical and structural investigation of isotropic and anisotropic thermoplastic magnetorheological elastomer composites based on poly(styrene-*b*-ethylene-co-butylene-*b*-styrene) (SEBS). *Rheologica Acta*, 51, 2012.
- J.E. Martin and R.A. Anderson. Electrostriction in field-structured composites: Basis for a fast artificial muscle? *Journal of Chemical Physics*, 111:4273–4280, 1999.
- J.E. Martin, R.A. Anderson, D. Read, and G. Gulley. Magnetostriction of field-structured magnetoelastomers. *Phys. Rev. E*, 74, 2006.
- P.R. Marur. *Magneto-rheological elastomer-based vehicle suspension*. US20130087985 A1, 2013. US Patent App. 13/253,147.
- Matlab. Optimisation Toolbox - User's Guide. ©1994-2013 The MathWorks, Inc, 2013. URL <http://www.mathworks.de/de/help/optim/index.html>. Retrieved 08/2013.
- MatWeb. Material Property Data - Aluminum 6061-T6. ©1996-2013 by MatWeb, LLC, 2013a. URL <http://www.matweb.com/search/DataSheet.aspx?MatGUID=1b8c06d0ca7c456694c7777d9e10be5b>. Retrieved 08/2013.

- MatWeb. Material Property Data - Free-Cutting Brass, UNS C36000. ©1996-2013 by MatWeb, LLC, 2013b. URL <http://www.matweb.com/search/DataSheet.aspx?MatGUID=bae961d2d6ed497a9096986641162def>. Retrieved 08/2013.
- MatWeb. Material Property Data - Teflon PTFE 7A. ©1996-2013 by MatWeb, LLC, 2013c. URL <http://www.matweb.com/search/DataSheet.aspx?MatGUID=5c4883a40a5b4868bc7e736d00d97422&ckck=1>. Retrieved 12/2013.
- M. Mayer, R. Rabindranath, J. Börner, E. Hörner, and A. Bentz. Ultra-Soft PDMS-Based Magnetoactive Elastomers as Dynamic Cell Culture Substrata. *PLoS ONE*, 8:10, 2013.
- J. Merodio and R.W. Ogden. Mechanical response of fiber-reinforced incompressible nonlinearly elastic solids. *International Journal of Non-Linear Mechanics*, 40:213–227, 2005.
- K. Miller. Testing and Analysis - Testing Elastomers for Hyperelastic Material Models in Finite Element Analysis. *Rubber Technology International*, page 88, 1999. URL <http://www.axelproducts.com/pages/downloads.html#p1>. Retrieved 09/2013.
- L. Mullins. Softening of rubber by deformation. *Rubber Chemistry and Technology*, 42: 339–362, 1969.
- L. Mullins and N.R. Tobin. Stress softening in rubber vulcanizates. Part 1. Use of a strain amplification factor to describe the elastic behavior of filler-reinforced vulcanized rubber. *Journal of Applied Polymer Science*, 9:2993–3009, 1965.
- Z.C. Ni, X.L. Gong, J.F. Li, and L. Chen. Study on a Dynamic Stiffness-tuning Absorber with Squeeze-strain Enhanced Magnetorheological Elastomer. *Journal of Intelligent Material Systems and Structures*, 20:1195–1202, 2009.
- R.W. Ogden. Nearly isochoric elastic deformations: Application to rubberlike solids. *Journal of the Mechanics and Physics of Solids*, 26(1):37 – 57, 1978.
- R.W. Ogden. Mechanics of Rubberlike Solids. *Mechanics of the 21st Century*, pages 263–274, 2004.
- R.W. Ogden and D.G. Roxburgh. A pseudo-elastic model for the Mullins effect in filled rubber. *Proceedings of the Royal Society of London Series A - Mathematical Physical and Engineering Sciences*, 455:2861–2877, 1999.
- R.W. Ogden, G. Saccomandi, and I. Sgura. Fitting hyperelastic models to experimental data. *Computational Mechanics*, 34(6):484–502, 2004.

- S. Opie and W. Yim. A tunable vibration isolator using a magnetorheological elastomer with a field induced modulus bias. In *Proceedings of the ASME International Mechanical Engineering Congress and Exposition - Mechanics of solids and structures*, 2007.
- H.F. Össur, I. Gudmundsson, F. Thorsteinsson, and C. Leomte. Prosthetic and Orthotic Devices Having Magnetorheological Elastomer Spring with Controllable Stiffness, 2013.
- O. Padalka, H.J. Song, N.M. Wereley, J.A. Filer, and R.C. Bell. Stiffness and Damping in Fe,Co and Ni Nanowire-Based Magnetorheological ElastomericComposites. *IEEE Transactions on Magnetics*, 46:2275–2277, 2010.
- G. Park, E.J. McLaurin, and L. Faidley. Characterization of the actuator behavior of blended-system ferrogels. *Proc. SPIE*, 6929:–, 2008.
- K.M. Popp, P.B. Kosasih, X.Z. Zhang, and W.H Li. Fabrication and Characterization of MR Elastomers with high MR Effect. In *15th International Congress on Sound and Vibration*, 2008.
- K.M. Popp, M. Kröger, W. Li, X. Zhang, and P.B. Kosasih. MRE Properties under Shear and Squeeze Modes and Applications. *Journal of Intelligent Material Systems and Structures*, 21:1471–1477, 2010.
- H.J. Qi and M.C. Boyce. Constitutive model for stretch-induced softening of the stress-stretch behavior of elastomeric materials. *Journal of the Mechanics and Physics of Solids*, 2004.
- X. Qiao, X. Lu, W.H. Li, J. Chen, X.L. Gong, T. Yang, W. Li, K. Sun, and X. Chen. Microstructure and magnetorheological properties of the thermoplastic magnetorheological elastomer composites containing modified carbonyl iron particles and poly(styrene-*b* -ethylene-ethylenepropylene- *b* -styrene) matrix. *Smart Materials and Structures*, 21: 115028, 2012.
- G.Y. Qiu and T.J. Pence. Remarks on the behavior of simple directionally reinforced incompressible nonlinearly elastic solids. *Journal of Elasticity*, 49:1–30, 1997.
- J. Rabinow. The magnetic fluid clutch. *American Institute of Electrical Engineers, Transactions of the*, 67:1308–1315, 1948.
- R. Ramprasad, P. Zurcher, M. Petras, and M. Miller. Magnetic properties of metallic ferromagnetic nanoparticle composites. *Journal of Applied Physics*, 96:519–529, 2004.
- Z. Rigbi and L. Jilken. The response of an elastomer filled with soft ferrite to mechanical and magnetic influences. *Journal of Magnetism and Magnetic Materials*, 37:267 – 276, 1983.

- A. Ritter. *Smart Materials in architecture, interior architecture and design*. Birkhaeuser - Publishers for Architecture, 2007.
- G. Schubert, P. Harrison, and Z. Guo. The Behaviour of Magneto-Rheological Elastomers under Equi-Biaxial Tension. In *The 19th International Conference on Composite Materials, Montreal*, 2013.
- Y. Shen, M.F. Golnaraghi, and G.R. Heppler. Experimental Research and Modeling of Magnetorheological Elastomers. *Journal of Intelligent Material Systems and Structures*, 15: 27–35, 2004.
- T. Shiga, A. Okada, and T. Kurauchi. Magnetorheological behavior of composite gels. *Journal of Applied Polymer Science*, 58:787–792, 1995.
- M. Sibley. *Introduction to Electromagnetism*. Arnold, London, 1 edition, 1996.
- A. Sihvola and I.V. Lindell. Homogenisation problems of mixtures involving non-isotropic constituent materials. Technical report, Electromagnetics Laboratory, Helsinki University of Technology, 1997.
- R. Sinko, M. Karnes, J.H. Koo, Y.K. Kim, and K.S. Kim. Design and test of an adaptive vibration absorber based on magnetorheological elastomers and a hybrid electromagnet. *Journal of Intelligent Material Systems and Structures*, 2012.
- H. Song, O. Padalka, N. Wereley, and R. Bell. Impact of Nanowire Versus Spherical Microparticles in Magnetorheological Elastomer Composites. In *Structures, Structural Dynamics, and Materials*. American Institute of Aeronautics and Astronautics, 2009.
- A.J.M. Spencer. *Continuum theory of the mechanics of fibre-reinforced composites*. Springer-Verlag, 1984.
- G.V. Stepanov, S.S. Abramchuk, D.A. Grishin, L.V. Nikitin, E.Yu. Kramarenko, and A.R. Khokhlov. Effect of a homogeneous magnetic field on the viscoelastic behavior of magnetic elastomers. *Polymer*, 48:488 – 495, 2007.
- G.V. Stepanov, D.Y. Borin, Y.L. Raikher, P.V. Melenev, and N.S. Perov. Motion of ferro-particles inside the polymeric matrix in magnetoactive elastomers. *Journal of Physics: Condensed Matter*, 20, 2008.
- G.V. Stepanov, E.Y. Kramarenko, and D.A. Semerenko. Magnetodeformational effect of the magnetoactive elastomer and its possible applications. *Journal of Physics: Conference Series*, 412, 2013a.

- G.V. Stepanov, D.A. Semerenko, A.V. Bakhtiiarov, and P.A. Storozhenko. Magnetoresistive Effect in Magnetoactive Elastomers. *Journal of Superconductivity and Novel Magnetism*, 26:1055–1059, 2013b.
- W.M. Stewart, J.M. Ginder, L.D. Elie, and M.E. Nichols. *Method and apparatus for reducing brake shudder*. Patent US 5816587 (A), 1998.
- T.L. Sun, X.L. Gong, W.Q. Jiang, J.F. Li, Z.B. Xu, and W.H. Li. Study on the damping properties of magnetorheological elastomers based on cis-polybutadiene rubber. *Polymer Testing*, 27:520–526, 2008.
- T.F. Tian, W.H. Li, G. Alici, H. Du, and Y.M. Deng. Microstructure and magnetorheology of graphite-based MR elastomers. *Rheologica Acta*, 50:825–836, 2011a.
- T.F. Tian, W.H. Li, and Y.M. Deng. Sensing capabilities of graphite based MR elastomers. *Smart Materials and Structures*, 20, 2011b.
- O.H. Varga. *Stress-strain behavior of elastic materials*. Interscience, New York, 1966, 1966.
- Z. Varga, G. Filipcsei, A. Szilagyi, and M. Zrinyi. Electric and Magnetic Field-Structured Smart Composites. *Macromolecular Symposia*, 227:123–134, 2005a.
- Z. Varga, G. Filipcsei, and M. Zrinyi. Smart composites with controlled anisotropy. *Polymer*, 46:7779–7787, 2005b.
- Z. Varga, G. Filipcsei, and M. Zrinyi. Magnetic field sensitive functional elastomers with tuneable elastic modulus. *Polymer*, 47:227–233, 2006.
- J. de Vicente, G. Bossis, S. Lacis, and M. Guyot. Permeability measurements in cobalt ferrite and carbonyl iron powders and suspensions. *Journal of Magnetism and Magnetic Particles*, 251:100–108, 2002.
- X. Wang and F. Gordaninejad. A new magnetorheological fluid-elastomer mount: phenomenological modeling and experimental study. *Smart Materials and Structures*, 18, 2009.
- X. Wang, F. Gordaninejad, M. Calgar, Y. Liu, J. Sutrisno, and A. Fuchs. Sensing behavior of Magnetorheological Elastomers. *Journal of Mechanical Design*, 131, 2009.
- Y.L. Wang, Y.A. Hu, L. Chen, X.L. Gong, W.Q. Jiang, P.Q. Zhang, and Z.Y. Chen. Effects of rubber/magnetic particle interactions on the performance of magnetorheological elastomers. *Polymer Testing*, 25:262–267, 2006.
- J.R. Watson. *Method and apparatus for varying the stiffness of a suspension bushing*. Patent US 19960585069, 1997.

- B. Wei, X.L. Gong, and W. Jiang. Influence of polyurethane properties on mechanical performances of magnetorheological elastomers. *Journal of Applied Polymer Science*, 116: 771–778, 2010.
- B. Williams. *Power Electronics: Devices, Drivers, Applications, and Passive Components*. Williams, B., 2006. URL <http://project.eee.strath.ac.uk/textbook/website/main.php>. Retrieved 08/2013.
- B.K. Woods, N. Wereley, R. Hoffmaster, and N. Nersessian. Manufacture of Bulk Magnetorheologic Elastomers using Vacuum Assisted Resin Transfer Molding. *International Journal of Modern Physics B*, 21:5010–5017, 2007.
- J. Wu, X. Gong, L. Chen, H. Xia, and Z. Hu. Preparation and characterization of isotropic polyurethane magnetorheological elastomer through in situ polymerization. *J. Appl. Polym. Sci.*, 114:901–910, 2009.
- J. Wu, X. Gong, Y. Fan, and H. Xia. Anisotropic polyurethane magnetorheological elastomer prepared through in situ polycondensation under a magnetic field. *Smart Materials and Structures*, 19, 2010.
- Z. Xu, X.L. Gong, G. Liao, and X. Chen. An Active-damping-compensated Magnetorheological Elastomer Adaptive Tuned Vibration Absorber. *Journal of Intelligent Material Systems and Structures*, 21:1039–1047, 2010.
- M. Yu and S. Wang. The composite MRE embedded with a copper coil. *Smart Materials and Structures*, 19, 2010.
- P. Zajac, J. Kaleta, D. Lewandowski, and A. Gasperowicz. Isotropic magnetorheological elastomers with thermoplastic matrices: structure, damping properties and testing. *Smart Materials and Structures*, 19, 2010.
- J. Zeng, Y.G. Guo, Y. Li, J. Zhu, and J.C. Li. Two-dimensional magnetic property measurement for magneto-rheological elastomer. *Journal of Applied Physics*, 113, 2013.
- N. Zhang, N. Hoang, and H. Du. A novel dynamic absorber using enhanced magnetorheological elastomers for powertrain vibration control. In *Multi-functional materials and structures*, pages 117–120, 2008a.
- Q. Zhang. *Development and Characterization of Magnetorheological Elastomers*. PhD thesis, University of Nevada, Reno Chemical engineering, 2005.
- W. Zhang, X.L. Gong, W.Q. Jiang, and Y.C. Fan. Investigation of the durability of anisotropic magnetorheological elastomers based on mixed rubber. *Smart Materials and Structures*, 19, 2010.

- W. Zhang, X.L. Gong, S. Xuan, and W. Jiang. Temperature-Dependent Mechanical Properties and Model of Magnetorheological Elastomers. *I & EC Research, ASC Publications*, 2011.
- X. Zhang, W. Li, and X.L. Gong. An effective permeability model to predict field-dependent modulus of magnetorheological elastomers. *Communications in Nonlinear Science and Numerical Simulation*, 13:1910–1916, 2007.
- X. Zhang, S. Peng, W. Wen, and W. Li. Analysis and fabrication of patterned magnetorheological elastomers. *Smart Materials and Structures*, 17:5, 2008b.
- G.Y. Zhou. Shear properties of a magnetorheological elastomer. *Smart Materials and Structures*, 12:139, 2003.
- G.Y. Zhou and Z.Y. Jiang. Dynamic deformation in MR elastomer driven by magnetic field. *Smart Structures and Materials*, 5053:603–611, 2003.
- G.Y. Zhou and Z.Y. Jiang. Deformation in magnetorheological elastomer and elastomer-ferromagnet composite driven by a magnetic field. *Smart Materials and Structures*, 13, 2004.
- Y. Zhou, S. Jerrams, A. Betts, and L. Chen. The Effect of Microstructure on the Dynamic Equi-Biaxial Fatigue Behaviour of Magnetorheological Elastomers. In *8th European Conference on Constitutive Models for Rubbers (ECCMR VIII)*, 2013a.
- Y. Zhou, S. Jerrams, and L. Chen. Multi-Axial Fatigue in Magnetorheological Elastomers using Bubble Inflation. *Journal of Materials and Design*, 50, 2013b.
- M. Zrinyi, L. Barsi, and A. Büki. Deformation of ferrogels induced by nonuniform magnetic fields. *J. Chem. Phys.*, 104, 1996.
- M. Zrinyi, L. Barsi, and A. Büki. Ferrogel: a new magneto-controlled elastic medium. *Polymer Gels and Networks*, 5:415 – 427, 1997.
- M. Zrinyi, D. Szab, and H.G. Kilian. Kinetics of the shape change of magnetic field sensitive polymer gels. *Polymer Gels and Networks*, 6:441–454, 1998.

Appendix A

Technical Data Sheets

The materials used to manufacture MRE materials, and the company that provided them are listed in Table A.1. The manufacturing process of MREs was described in Chapter 3.

Material	Type	Company
Silicone Rubber	<i>MM 240 TV</i>	<i>ACC Silicones</i>
Silicone Fluid	<i>ACC 34</i>	<i>ACC Silicones</i>
Carbonyl Iron Powder	<i>CIP-SQ</i>	<i>BASF</i>

Table A.1: List of materials used to manufacture MRE materials

The required equipment used to manufacture isotropic and anisotropic MREs (Chapter 3), together with the company that provided them are listed in Table A.2. Equipment needed for the magnetic field measurements (Chapter 4), and for the experimental characterisation of MREs (Chapter 5) are also listed. The technical data sheets of all materials and the

Equipment	Type	Company
Flexible Heaters	Silicone Rubber Heaters	<i>Watlow</i>
Linear Amplifier	<i>LVC 623</i>	<i>AE Techtron</i>
Gaussmeter	<i>Model 5180</i>	<i>F.W. Bell</i>
Transverse Probe	<i>STD18 0404</i>	<i>F.W. Bell</i>
Permanent Magnets	<i>F4335-N52 Neodymium</i>	<i>First4Magnets</i>

Table A.2: List of equipment used to manufacture MRE materials, to measure magnetic flux densities, and to perform experiments with magnetic fields.

equipment are provided in this Appendix.

Technical Data Sheet



MM240TV () 2 part addition cure moulding rubber

Introduction

MM240TV is a pourable 2-part addition cure silicone elastomer system. After mixing parts 'A' and 'B' in the correct proportions, the system will cure at ambient temperatures within 24 hours, but the rate of cure can be accelerated by heat. The cured rubber exhibits excellent physical and electrical properties.

Key Features

- High dimensional stability
- Curing accelerated by heat
- High chemical resistance (PU)
- Very low shrinkage

Food Approvals

MM240TV No

Use and Cure Information

How to Use

IMPORTANT: **MM240TV** contains the platinum catalyst, great care should be taken when using automatic dispensing equipment. Please ensure that it is not contaminated by residual hydride containing rubber in the dispensing equipment, as curing will result. If in doubt, it's advised to thoroughly purge the equipment with a suitable hydrocarbon solvent or silicone fluid.

Mix both the A and B parts gently to ensure homogeneity. Place the required amount of A and B parts by weight at the ration of **10 to 1** (A to B) in a clean plastic or metal container of approximately 3 times their volume, and mix until the colour of the mixture is uniform. Degas by intermittent evacuation, the larger volume of the mixing vessel helps prevent overflow during this operation. In case of automatic dispensing with static mixing head, the two components should be degassed before processing. Recommended vacuum conditions are 30-50 mbar intermittently over 5-10 minutes. Cast the mixture either by gravity or pressure injection.

Curing Conditions

The following table offers a guide to the rate of cure of **MM240TV** at various temperatures, mixing of the components between 15 and 25°C is recommended to ensure adequate pot life for degassing and handling. The pot life can be extended to several hours by chilling the components.

Temperature, °C	Max Cure Time	De-mould Time
25	24 hrs	12
100	1 hrs	
150		

Inhibition of Cure

Great care must be taken when handling and mixing all addition cured silicone elastomer systems, that all the mixing tools (vessels and spatulas) are clean and constructed in materials which do not interfere with the curing mechanism. The cure of the rubber can be inhibited by the presence of compounds of nitrogen, sulphur, phosphorus and arsenic; organotin catalysts and PVC stabilizers; epoxy resin catalysts and even contact with materials containing certain of these substances e.g. moulding clays, sulphur vulcanised rubbers, condensation cure silicone rubbers, onion and garlic.

Property Test Method Value

Uncured Product

Colour A Part:		Translucent
Colour B Part		Translucent
Colour Mixed		Translucent
Appearance:		Translucent
liquid		
Viscosity:	Brookfield	96000 mPa.s
Catalysed viscosity	Brookfield	45000mPa.s
Pot Life:		60 minutes *
De-mould time		12 hours *
* measured at 23+/-2°C and 65% relative humidity using standard catalyst.		
Approved for use with food		No

Cured Elastomer

(after 7 days cure at 23+/-2°C and 65% relative humidity)

Tensile Strength:	BS903 Part A2	5.4 MPa
Elongation at Break:	BS903 Part A2	330 %
Youngs Modulus:		1.88MPa
Modulus at 100% Strain:	BS903 Part A2	1.07MPa
Tear Strength:	BS903 Part A3	22 kN/m
Hardness:	ASTM D 2240-95	40° Shore A
Specific Gravity:	BS 903 Part A1	1.08
Linear Shrinkage:		0.08 %
Coefficient of Thermal Expansion:		
Volumetric		837 ppm / °C
Linear		279 ppm / °C
Min. Service Temperature:		-50°C
Max. Service Temperature:	AFS 1540B	200 °C

All values are typical and should not be accepted as a specification

FDA compliance

If approved for food use all components present in the fully cured product are listed in CFR 21, 175.300, "Resinous and polymeric coatings" and CFR 21, 177.2600, "Rubber articles intended for repeated use". The fully cured rubber satisfies the requirements of CFR21, 175.300 and 177.2600, sub paragraphs (e) and (f) for applications involving both aqueous and fatty foods

Health and Safety - Material Safety Data Sheets available on request.

Packages – **MM240TV** is supplied in 1.1kg, 5.5 kg and 20 kg bu containers.

Storage and Shelf Life – Expected to be 12 months in original unopened containers below 30°C.

Revision Date: 02/05/2007

The information and recommendations in this publication are to the best of our knowledge reliable. However nothing herein is to be construed as a warranty or representation. Users should make their own tests to determine the applicability of such information or the suitability of any products for their own particular purposes. Statements concerning the use of the products described herein are not to be construed as recommending the infringement of any patent and no liability for infringement arising out of any such use is to be assumed.

ACC Silicones Ltd, Amber House,
Showground Road, Bridgwater, Somerset, UK
Tel. +44(0)1278 411400 Fax. +44(0)1278 411444

Treco S.R.L., Via Romagna N.8,
20098 Sesto Uteriano (MI), Italia.
Tel. 39/02/9880913 Fax. +39/02/98280413

Figure A.1: Technical information of the silicone rubber *MM 240 TV* provided by the company *ACC Silicones*.

Technical Data Sheet



ACC34 Thinner

Introduction

ACC34 Thinner is a low viscosity silicone diluent that can be employed as viscosity modifier for many 1-Part RTV sealants, and conformal coatings. It is specially recommended for use with ACC14UV conformal coating (please see separate Technical Data Sheet for ACC14UV). ACC34 Thinner is volatile. It will be lost slowly at room temperature from a thin section of cured silicone rubber or coating, but is readily removed at temperatures from 80°C to 150°C. In the case of 1-Part RTV's or conformal coatings this heating cycle is best carried out after about 24 hours cure.

ACC34 Thinner has not been classified as a Volatile Organic Compound (VOC) and no legislation to this effect is expected. It is a cosmetically approved ingredient and is a much safer choice than conventional organic solvents for many reasons, a few of which are:-

- wide liquid temperature range
- odourless
- not regarded as an environmental hazard
- extremely low toxicity (Oral LD₅₀ = 35,000 mg/kg)
- compatible with virtually all silicones
- very low surface tension (<18 N/m) which enhances spreading of films.
- good rate of evaporation considering its high boiling point (205°C), due to unusually low heat of vaporisation.
- high Flash Point (not classified as Flammable)

General Characteristics

Appearance	:	Clear, colourless liquid
Odour	:	Virtually odourless
Boiling Point	:	205°C
Melting Point	:	< - 50°C
Latent Heat of Vaporisation	:	113 KJ/kg
Surface Tension	:	18 N/m (dynes/cm)
Viscosity at 25°C	:	5 mm ² s ⁻¹ (centistokes)
Autoignition Temperature	:	> 400°C
Flash Point	:	77°C
Evaporation Rate at 22°C	:	12 (Butyl Acetate = 100)
(White spirit has an evaporation rate of 14 on same scale)		

How to Use ACC34 Thinner

1. For 1-Part RTV Sealant Adhesives

There are applications, particularly in the art world of special effects, where a paint-able or spray-able form of the 1-Part Silicone RTV Sealant/Adhesive is required. Most 1-Part Silicone RTV's can be dispersed readily in ACC34 Thinner for immediate use as paint-able or spray-able dispersions.

Formulations depend on the nature of the RTV employed i.e. flow-able or non-slump. A Typical formulation for a spray-able, translucent silicone sealant is:-

ACC Silicone Sealant*	30 to 50 parts
ACC34 Thinner	70 to 50 parts

* ACC AS1521, AS1602 or ACC Silcoset 153

Unless special anhydrous mixing facilities and special packaging are available, customers are advised to make up small quantities as required.

After painting or spraying the substrate with the diluted RTV, the product should be allowed to cure at ambient temperature. With thin coatings, ACC34 Thinner will evaporate from the surface in approximately 24 hours, and will be down to less than 10% in this time at 20 to 25°C. If further removal is necessary, this can be achieved by heating the fully cured coated article to 50°C for about 2-3 hours to 120°C for 5 to 10 minutes. The exact times and temperatures will depend on the substrate and coating thickness.

2. Use with ACC14UV Conformal Coating

SPRAYING

ACC14 UV needs to be thinned with thinners before spraying. For manual air guns (e.g. Devilbliss etc) use ACC34 Thinner - typically 1 part coating to 1 part ACC34 thinner for a 100 mPa.s viscosity. The nozzle of the spray gun needs to be selected to give an even spray to suit the selected viscosity of the coating material. The normal spray gun pressure required is 27.6 – 34.5 x 10 exp 6-kN/m exp2 (40-50 psi).

For airless spraying equipment (Nordson, PVA, DIMA, Speedline etc) a viscosity of 50-100 mPa.s is preferred. This may be achieved with the ACC34 Thinner at 1 part ACC14UV coating to 1 - 1.5 parts ACC34 Thinner. The board should be left to cure at 16 to 45°C with a relative humidity of >40%.

IMPORTANT: Allow 48 hours at 16 to 45°C for evaporation of the ACC34 Thinner in coatings between 100 to 1000 microns thickness.

The information and recommendations in this publication are to the best of our knowledge reliable. However nothing herein is to be construed as a warranty or representation. Users should make their own tests to determine the applicability of such information or the suitability of any products for their own particular purposes. Statements concerning the use of the products described herein are not to be construed as recommending the infringement of any patent and no liability for infringement arising out of any such use is to be assumed.

ACC Silicones Ltd, Amber House,
Showground Road, Bridgwater, Somerset, UK
Tel. +44(0)1278 411400 Fax. +44(0)1278 411444

Treco S.R.L., Via Romagna N.8,
20098 Sesto Uteriano (MI), Italia.
Tel. 39/02/9880913 Fax. +39/02/98280413

Figure A.2: Technical information of the silicone fluid ACC 34 provided by the company ACC Silicones (Page 1).

BRUSHING

Ensure the coating has been shaken or mixed thoroughly (refit the cap after mixing) and stood for 2 hours to allow bubbles to separate. The coating should be used at room temperature (above 16°C) using a good quality brush apply the product gently such as to achieve a good coating and not to disturb wiring. The board should be left to cure at 16 to 45°C with a relative humidity of >40%.

CURING TIMES / CONDITIONS

For brushing and manual spraying the film will be touch dry after 40 minutes at 23°C / 60% humidity). Using the ACC34 Thinner, this may be 5-10 minutes – depending on conditions.

The full properties of the coating will be obtained after 24 hours at room temperature (48 hours if using ACC34 Thinner) –curing can be accelerated by using a humidity oven at 45°C and 100% humidity.

Storage

ACC34 Thinner should be stored in closed containers to prevent contamination. In its original closed containers the shelf life is expected to be >5 years.

1 kg ; 5 kg ; 25kg and 200 kg

Health and Safety

Detailed information in CHIP format is given in the individual product Material Safety Data Sheet.

Revision date 01-2008


The information and recommendations in this publication are to the best of our knowledge reliable. However nothing herein is to be construed as a warranty or representation. Users should make their own tests to determine the applicability of such information or the suitability of any products for their own particular purposes. Statements concerning the use of the products described herein are not to be construed as recommending the infringement of any patent and no liability for infringement arising out of any such use is to be assumed.

ACC Silicones Ltd, Amber House,
Showground Road, Bridgwater, Somerset, UK
Tel. +44(0)1278 411400 Fax. +44(0)1278 411444

Treco S.R.L., Via Romagna N.8,
20098 Sesto Uteriano (MI), Italia.
Tel. 39/02/9880913 Fax. +39/02/98280413

...

Figure A.3: Technical information of the silicone fluid ACC 34 provided by the company ACC Silicones (Page 2).

Product specification		Inorganic Specialities	 BASF The Chemical Company
CAS-CEPSQ-E Revision 5	2008-02-01 Page 1 of 1		
supersedes: CAS-CEPSQ-E, Rev. 4 dated 2005-02-18			

CARBONYL IRON POWDER SQ

PRD-No.: 30042268

1. General

This product is produced and marketed by BASF SE, Ludwigshafen, Germany. The units producing and marketing this product are certified according to ISO 9001:2000.

Appearance:	grey, fine grained powder; mechanically soft, spherical particles, mit SiO ₂ -coating
Chemical name:	Iron, Fe
CAS no.:	7439-89-6
EINECS no.:	231-096-4

2. Specifications

Parameter	Unit	Specification	Test method
Fe	g/100 g	min. 99.5	calculated
C	g/100 g	max. 0.05	IRS (RCA/Q-C-296)
Permeability (μ _i) *	%	98 – 110	RCA/Q – C 302
Q-Value * at 100 KHz	%	95 – 120	RCA/Q – C 302
Particle size distribution:			
D ₅₀	μm	3.7 – 4.7	Microtrac X 100

* Values are based on BASF's SQ standard

The aforementioned data shall constitute the agreed contractual quality of the product at the time of passing of risk. The data are controlled at regular intervals as part of our quality assurance program. Neither these data nor the properties of product specimens shall imply any legally binding guarantee of certain properties or of fitness for a specific purpose. No liability of ours can be derived therefrom.

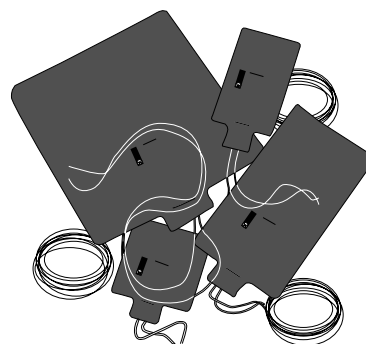
more information? Please visit us at www.carbonylironpowder.com

Figure A.4: Technical information of the carbonyl iron powder *CIP-SQ* provided by the company *BASF*.

The silicone rubber heaters are manufactured by the company *Watlow*. The ordered heaters have the product code *F020050C8-Y001B*, which gives a 51×127 mm silicone rubber heater with *Pressure Sensitive Adhesive Surface (PSAS)* on the one side and $1/8$ " insulating sponge on the other side. It comes with a standard 12" Teflon lead and operates with 240 Volt and 100 Watt.

SILICONE RUBBER HEATERS

Rugged, Thin, Lightweight and Flexible...Limited Only By Your Imagination



Rugged, yet thin, lightweight, and flexible ... the use of Watlow silicone rubber heaters is limited only by your imagination. With these heaters, you can put the heat where it's needed and, in the process, improve heat transfer, speed warm-ups and decrease wattage requirements.

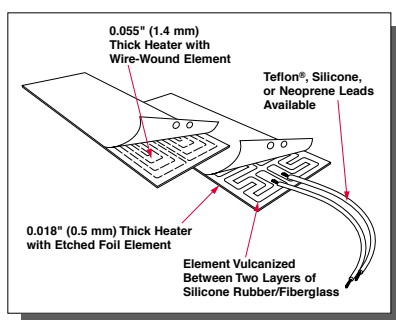
Fiberglass-reinforced silicone rubber gives your heater dimensional stability without sacrificing flexibility. Because very little material separates the element from the part, heat transfer is rapid and efficient.

Performance Capabilities

- Operating temperatures to 500°F (260°C)
- Watt densities to 80 W/in² (12.5 W/cm²) dependent upon application
- 0.055 inch (1.4 mm) thick with a wire-wound element; only 0.018 inch (0.5 mm) with an etched foil element

Applications

- Freeze protection and condensation prevention for many types of instrumentation and equipment
- Medical equipment such as blood analyzers, test tube heaters, etc.
- Computer peripherals such as laser printers
- Curing of plastic laminates
- Photo processing equipment



© 2001 Watlow Electric Manufacturing Company

Features and Benefits

Designed in the exact shape and size you need

- Conforms to your equipment

More than 80 designs available immediately from stock

- Reduces down time

UR®, cUR®, and VDE recognitions

- Available on many designs

Moisture and chemical-resistant silicone rubber material

- Provides longer heater life

Vulcanizing adhesives or fasteners available

- Heaters bond easily to your part



2101 Pennsylvania Dr.
Columbia, Missouri 65202 USA
Phone: 573-474-9402
Fax: 573-474-5859
Internet: www.watlow.com
e-mail: www.watlow.com

UR® and cUR® are registered trademarks of Underwriter's Laboratories, Inc.
Teflon® is a registered trademark of E.I. duPont de Nemours & Company.

FAX-1701-1100

Figure A.5: Technical information of the silicone rubber heaters manufactured by the company *Watlow* (Page 1).

S I L I C O N E R U B B E R H E A T E R S

Standard Silicone Rubber Specifications

Maximum width x maximum length:

- Wire-wound: 36 x 120 inches (915 mm x 3050 mm)
- Etched foil: 20 x 30 inches (510 mm x 760 mm)

Thickness (standard):

- Wire-wound: 0.055 inch (1.4 mm)
- Etched foil: 0.018 inch (0.5 mm)

Weight (standard):

- Wire-wound: 8 oz./ft² (0.24 g/cm²)
- Etched foil: 3 oz./ft² (0.09 g/cm²)

Maximum operating temperature:

- 500°F (260°C)

Maximum temperature for UL® Recognition:

- 428°F (220°C)

Minimum ambient temperature:

- -80°F (-62°C)

Maximum voltage:

- 600V~(ac)

Maximum wattage:

- Consult watt density graph on page 170 of the Watlow Heater's catalog.

Lead size:

- Sized to load

Lead length:

- 12 + 1½ - ½ inches (305 mm + 40 mm - 15 mm)

Wattage tolerance:

- Wire: ± 5 percent
- Foil: + 5 percent -10 percent

Dimensional tolerances:

- 0 to 6 inches (0 to 150 mm): ± ¼ inch (1.6 mm)
- 6 to 18 inches (150 to 455 mm): ± ⅝ inch (3.2 mm)
- 18 to 36 inches (455 mm to 915 mm): ± ¾ inch (4.8 mm)
- Over 36 inches (915 mm): ± 1 percent

How to Order

To order stock silicone rubber heaters, specify the Watlow code number (from the Watlow Heater's catalog) and the quantity. To order a heater with options, specify the code number, quantity and options desired (see page 165 in the Watlow Heater's catalog). Consult Watlow before combining options.

Made-to-Order: Consult factory

For made-to-order units, Watlow will need the following application information from you:

- Size (dimensions)
- Voltage
- Wattage/watt density
- Operating temperature
- Options (leads, thermostats, attachment techniques, etc.)
- Will heater be subject to flexing?
- Element type, if you have a preference
- Agency approvals
- Quantity

Availability

- Stock: Same day shipment of orders received by 11:00 a.m. CST.
- Stock with Options: Shipment in five working days or less. Not all options are available with stock heaters.

Figure A.6: Technical information of the silicone rubber heaters manufactured by the company Watlow (Page 2).



LVC623 Amplifier Specifications



APPLICATION

The LVC 623 is a general purpose, medium voltage, high continuous current, linear power amplifier. It works best when driving loads of 1 - 4ohms. The LVC 623 works well with continuous test signals. The LVC 623 has two (2) separate channels that can be operated independently or combined for greater maximum voltage or current. In bridge-mono mode the available output voltage doubles. In parallel-mono mode the amplifier operates with double the output current.

FEATURES

- > Output of 8.0 amperes rms, or 16 volts rms, per channel into a 2 ohm load.
- > Frequency bandwidth of DC to 20 kHz at full power, DC to 100kHz at reduced power.
- > Controlled Voltage or Controlled Current operation
- > User-adjustable voltage or current limiting.
- > Remote force to standby mode by contact closure.
- > External buffered monitoring of voltage and current output.
- > Protection provided against, input overloads, improper output connection (including shorts and improper loads), excessive temperature, voltage or current, and under voltage conditions.
- > Shipped ready to operate using single-phase, 120-volt, 20Amp or 230V, 10Amp AC mains.
- > Installs easily into a standard 19 inch rack, or stands alone for bench top operations.

OPTIONS - User Configurable

- > Variable voltage and current limiting
- > DC Coupled (DC Enabled) or AC Coupled (DC Blocked)
- > Controlled Voltage or Controlled Current Operation
- > In Voltage mode - Fixed gain (20, 44.5, 79.5) or Variable (0 - 20, 0 - 44.5, 0 - 79.5)
- > In Current mode - Fixed Trans-conductance (20) or Variable (0 - 20)
- > Channel configuration - two independent channels, two channels paralleled to Mono, two channels bridged to Mono



INDICATORS AND CONTROLS

- > Front panel LEDs indicate signal presence and output overload.
- > A pushbutton power "On/Off" located on the front panel.
- > Two gain controls on the front panel for controlled voltage applications.
- > Two circuit breaker resets on the back panel.
- > A back panel slide switch to choose between 2 channel, bridge mono and parallel mono operation.

PERFORMANCE (One hour continuous ratings)

Frequency Response

. +/- 0.1 dB from DC to 20 kHz at 1 watt.

Phase Response

OUTPUT POWER

Measurements taken at 1 kHz at .05% THD with amplifiers operating in controlled voltage mode.

One Channel Driven

Figure A.7: Technical information of the DC amplifier *AE Techron LVC 623* (Page 1).

- . +/- 10 Degrees (10 Hz to 20 kHz at 1 watt.
- Signal-to-Noise Ratio**
- . At Voltage gain of 20, better than 105 dB (A-weighted) below full output.
- THD**
- . Less than 0.05% from 20 Hz to 1 kHz increasing
- . linearly to 0.1% at 20 kHz at full output.
- I.M. Distortion**
- . <0.05% from 410 milliwatts to full output with a voltage gain of 20dB into an 8 ohm load.
- Slew Rate**
- . >13V per microsecond.
- Load Impedance**
- . Rated for 16, 8, 4, 2 and 1 ohm use. Safe with all load types, including
- . reactive loads.
- Input Impedance**
- . Greater than 10K ohms, balanced, and 5K ohms unbalanced.
- Output Impedance**
- . Less than 10 milliohms in series with less than 2 microhenries.

Ohms	40mSec Burst			1 Hour Continuous		
	Watts	Volts	Amps	Watts	Volts	Amps
2	364	27	13	144	17	8
4	240	31	8	240	31	8
8	148	34	4	145	34	4
16	89	38	2	89	37.78	2

Two Channel Bridged to Mono

Ohms	40mSec Burst			1 Hour Continuous		
	Watts	Volts	Amps	Watts	Volts	Amps
4	538	46.4	12	256	32	8
8	431	58.7	7	431	58.7	7
16	290	68	4	290	68	4

Two Channel Paralleled to Mono

Ohms	40mSec Burst			1 Hour Continuous		
	Watts	Volts	Amps	Watts	Volts	Amps
1	520	22.8	23	256	16	16
2	430	29	14	418	28.9	14
4	289	34	9	289	34	9
8	166	36	5	165	36	5



PHYSICAL CHARACTERISTICS

- Chassis:** The amplifier is designed for stand alone, or rack mounted, operation. The Chassis is black steel with a silver finished aluminum front panel. The unit occupies two EIA 19-inch-wide units.
- Weight:** 52 lbs. (23.5 kg), Shipping 66 lbs. (30 kg)
- AC Power:** Single phase, 120 volts, 60 Hz, 20 amperes AC service.
- Cooling:** Forced air cooling from the front, through removable filters, to side panels.
- Dimensions:** 19 in. x 16 in. x 3.5 in (48.3 cm x 40.3.0 cm x 8.9 cm)

SUPPORT

- When you purchase an AE Techtron amplifier, a full complement of technical and factory support personnel join your team. AE Techtron provides:
- > Applications engineering for your technical questions and customized product needs.
 - > A one year limited warranty to protect your equipment investment.
 - > A fully equipped service center to keep your amplifier operating at original performance requirements.

Copyright AE Techtron, Inc. 2007 Report site problems to the [webmaster](#).

Figure A.8: Technical information of the DC amplifier AE Techtron LVC 623 (Page 2).

5100 Series

Hall Effect Gauss / Tesla Meters



Description

The 5100 Series Hall effect portable gaussmeters represent the most recent design from the world leader in magnetic measuring equipment. This new design incorporates the use of digital signal processing technology making it the world's first hand-held gaussmeter to have a digital signal processor (DSP) on board. F.W. Bell's exclusive Dynamic Probe Correction allows measurements from 0 to 30 kG with a basic accuracy of 1%.

Key features include Auto Zero, Min./Max./Peak Hold, Auto Range and Relative Mode. Both models allow the user to select Gauss, Tesla or Ampere/Meter readings. The 5180 features a corrected analog output ($\pm 3V$ FS) and a USB communication port.

The 5100 Series Hand-Held Gaussmeter's built-in software eliminates the need for complex calibration procedures. User prompts on the custom formatted LCD allow fast, simple push button operation. All models come equipped with a detachable transverse probe, zero gauss chamber, instruction manual, hard carrying case, and four AA batteries. Axial, ultra thin transverse and low-field probes are available as options.

Applications for the 5100 Series range from the most sensitive laboratory environment to the most rugged industrial setting. All instruments are CE compliant.

Features

	Model 5170	Model 5180
Probe Included	X	X
Auto Zero	X	X
Min/Max Hold	X	X
True RMS	X	X
Auto Range	X	X
True Peak Hold		X
Relative Mode		X
Outputs (analog)		X
USB Communication Port		X

Figure A.9: Technical information of the Gaussmeter FW Bell 5180 (Page 1).

5100 Series Specifications

Model	5170	5180
Basic DC Accuracy	2%	1.1%
Frequency Bandwidth	DC-20 kHz	DC-25 kHz
Update Rates		
Display	4 readings/sec	4 readings/sec
Analog Output	None	100K samples/sec
Ranges		
Ultra Low Range (low-field probe only)	1 G	1 G
Low Range	200 G	300 G
Mid Range	2 kG	3 kG
High Range	20 kG	30 kG
Resolution		
Ultra Low Range (low-field probe only)	1 mG	1 mG
Low Range	0.1 G	0.1 G
Mid Range	1.0 G	1.0 G
High Range	10 G	10 G
Display	LCD	LCD
Digits	3 1/2	3 2/3
Readings	Gauss, Tesla, Amps/Meter	Gauss, Tesla, Amps/Meter
Analog Output	None	±3V FS
Communication Port	None	USB (1 samples/sec)

General Information

	All Models
Temperature	
Operating	0°C to 50°C
Storage	-25°C to 70°C
Power	4 AA batteries
Size	6.9 in x 3.9 in x 1.44 in.

Probes and Accessories

Model Number	Description
Model 5180 Probes	
HTD18-0604	4" Transverse Probe
STD18-0404	4" Transverse Probe (incl. w/5180)
STD18-0402	2" Transverse Probe
SAD18-1904	4" Axial Probe
SAD18-1902	2" Axial Probe

Model 5170 Probes

HTH17-0604	4" Transverse Probe
STH17-0404	4" Transverse Probe (incl. w/5170)
STH17-0402	2" Transverse Probe
SAH17-1904	4" Axial Probe
SAH17-1902	2" Axial Probe

Models 5170/5180 Gaussmeter Probes

STB1X-0201	Ultra Thin Transverse Probe (0.020" thick)
MOS51-3204	Low Field Probe

Models 5170/5180 Gaussmeter Accessories

YA-111	Zero Gauss Chamber (for axial, transverse and low-field probes)
PSRD-5	AC Adapter, +5VDC Regulated Output, 110VAC Input, Domestic
PSRI-5	AC Adapter, +5VDC Regulated Output, 220VAC Input, Switching, International

Note: Due to continuous process improvement, specifications are subject to change without notice.



SYPRIS
TEST & MEASUREMENT

6120 Hanging Moss Road • Orlando, Florida 32807 • www.fwbell.com
Phone (407) 678-6900 • Fax (407) 677-5765 • Toll Free (800) 778-6117

Shipping Weight

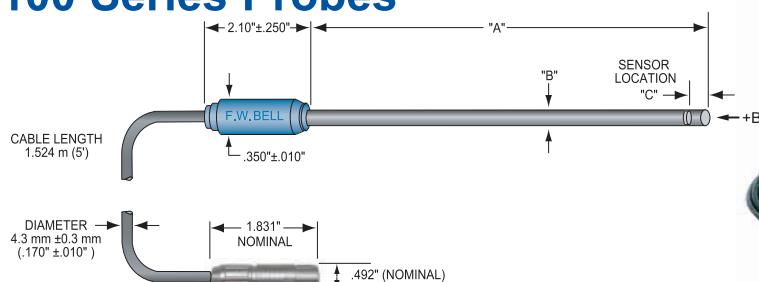
Domestic 3.5 lbs 1.59 kgs
International 4 lbs 1.82 kgs



Rev. date 07/2008

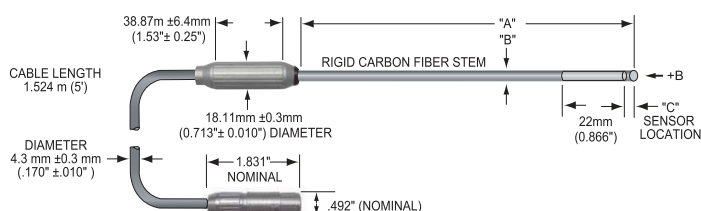
Figure A.10: Technical information of the Gaussmeter *FW Bell 5180* (Page 2).

5100 Series Probes



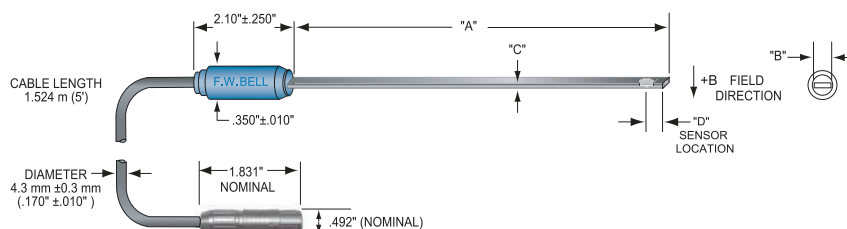
Axial Probes

Model	A ±.063"	B	C	Stem Material	Corrected Linearity	Sensitivity	Active area	Operating temp. range	Temp. stability (typical)		Frequency Response
									Zero	Calibrate	
SAD18-1902	2"	0.187" ±.003"	0.010" (NOMINAL)	RIGID PHENOLIC	0.5%/30kG	1X	0.015" DIA. (NOM)	0°C to +75°C	±0.300 Gauss / °C	-0.05% % / °C	DC to 20kHz
SAD18-1904	4"				1.0%/20kG						DC to 10kHz
SAH17-1902	2"										
SAH17-1904	4"										



Low Field Axial Probes

Model	A ±.063"	B	C	Stem Material	Corrected Linearity	Sensitivity	Active area	Operating temp. range	Temp. stability (typical)		Frequency Response
									Zero	Calibrate	
MOS51-3204	4"	0.285" ± 0.006"	0.050" (NOMINAL)	RIGID PHENOLIC	0.75%/1G	1X	0.866" (NOM)	0°C to +75°C	±0.02 mG / °C	-0.001 % / °C	DC to 700Hz (-3dB)



Transverse Probes

Model	A ±.063"	B	C	D	Material	Corrected Linearity	Sensitivity	Active area	Operating temp. range	Temp. stability (typical)		Frequency Response
										Zero	Calibrate	
STD18-0402	2"	0.158" ±.004"	0.045" ±.004"	0.0335" (NOMINAL)	Polypropylene	0.5%/30kG	1X	0.015" DIA. (NOM)	0°C to +75°C	±0.300 Gauss / °C (typical)	-0.05% % / °C (typical)	DC to 20kHz
STD18-0404	4"					1.0%/20kG						DC to 10kHz
STH17-0402	2"				ALUMINUM 3003 3/4 FH	1.0%/20kG						DC to 10kHz
STH17-0404	4"					0.5%/30kG						DC to 20kHz
HTH17-0604	4"	0.180" ±.004"	0.060" +.000" -.004"	0.030" (NOMINAL)		1.0%/10kG		0.025" DIA (NOM.)		±0.200 Gauss / °C	-0.1 % / °C	DC only
HTD18-0604	4"					0.5%/30kG						
STB1X-0201	1"	.050" ±.005"	.020" MAX	(NOMINAL)	KAPTON	1.0%/10kG						

Note: Due to continuous process improvement, specifications subject to change without notice.

****** Prior to late 2006 Transverse Probe Stems were rigid glass epoxy, .150 x .040".

Figure A.11: Technical information of the transverse probe *STD18-0404* used with the Gaussmeter *FW Bell 5180*.

**F4335-N52 Ultra High Performance -
50mm x 50mm x 25mm thick N52
Neodymium Magnet (Pack 1)**

This magnet is very effective at wiping Hard Drive Data.

Pack size

A pack of 1 magnet

Geometry

50mm x 50mm x 25mm thick neodymium magnet.
The NORTH pole is on one square face and the SOUTH is
on the opposite face.
The NORTH and SOUTH poles are 25mm apart.

Plating

These magnets are plated with 3 layers of protective
coatings - Nickel + Copper + Nickel (Ni-Cu-Ni)

Performance

These magnets will have approximately 5,500Gauss on
each face.
Each magnet can support a steel weight of up to 118 kgs

Extreme Power Warning!!

**These magnets are dangerous! If your fingers are
trapped between two of these magnets, they will be
crushed!**

**These magnets should only be handled and used after
a thorough risk assessment has been undertaken.**

Maximum Operating temperature

90 degrees C

Fixing

They can be bonded using 2 part adhesives such as
'Araldite'

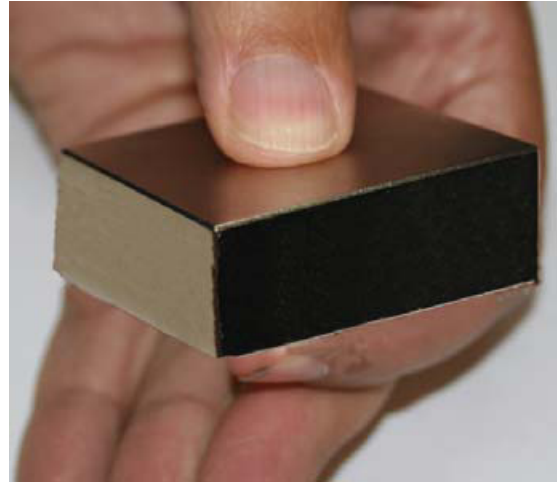


Figure A.12: Technical information of the permanent magnets *Neodymium N52*.

Appendix B

Technical Drawings

The technical drawings of the moulds used to manufacture MRE materials (Chapter 3) and the drawings of the setups used for uniaxial compression (Section 5.2.2), uniaxial tension (Section 5.3.2), pure shear (Section 5.4.2), and equi-biaxial tension (Section 5.5.2) tests are presented in this Appendix. All setups are presented without and with the use of permanent magnets to clarify the position of the magnets.

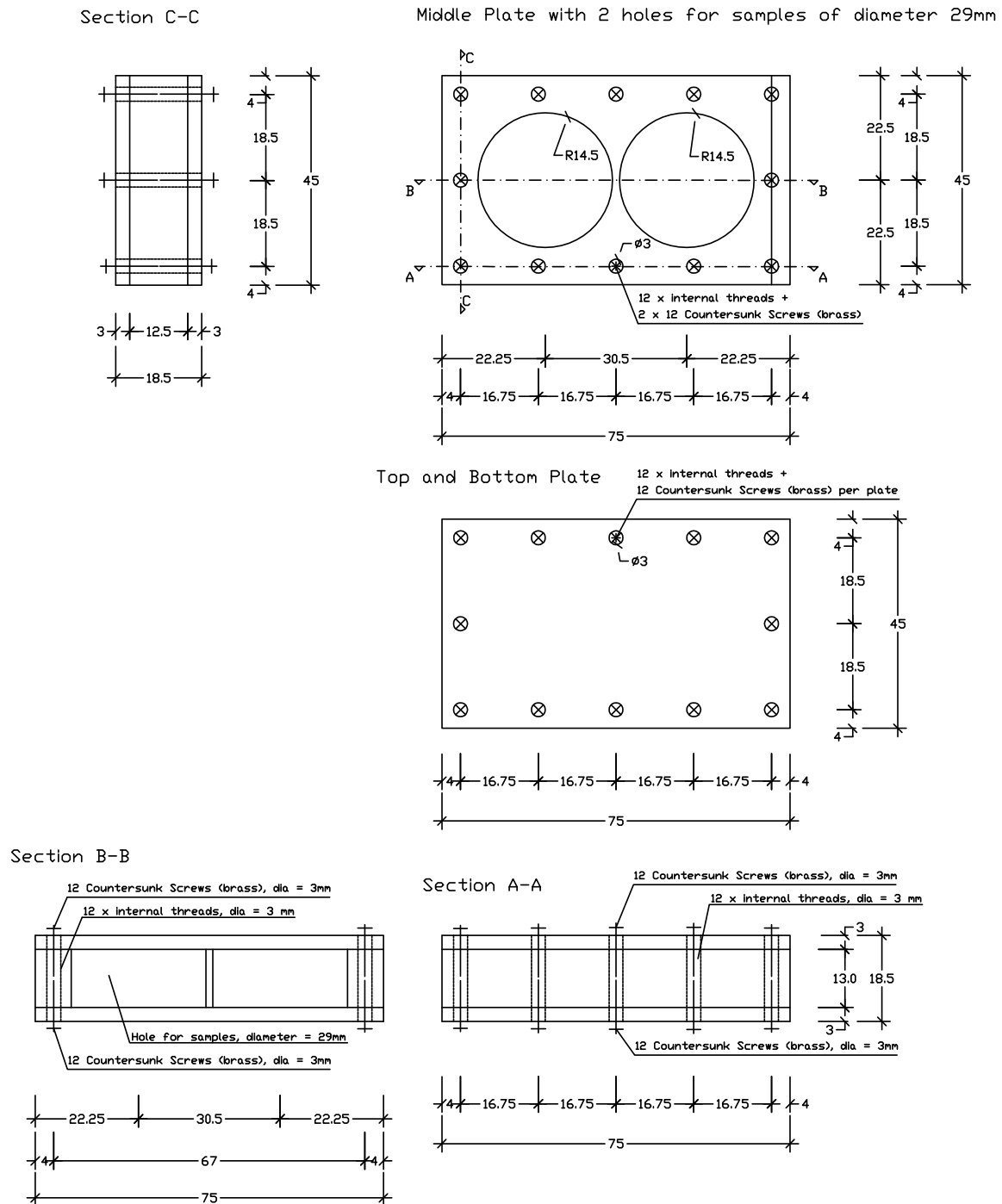


Figure B.1: Technical drawing of the moulds used for preparing two cylindrical compression samples ($\varnothing = 29\text{ mm}$, $h = 13\text{ mm}$).

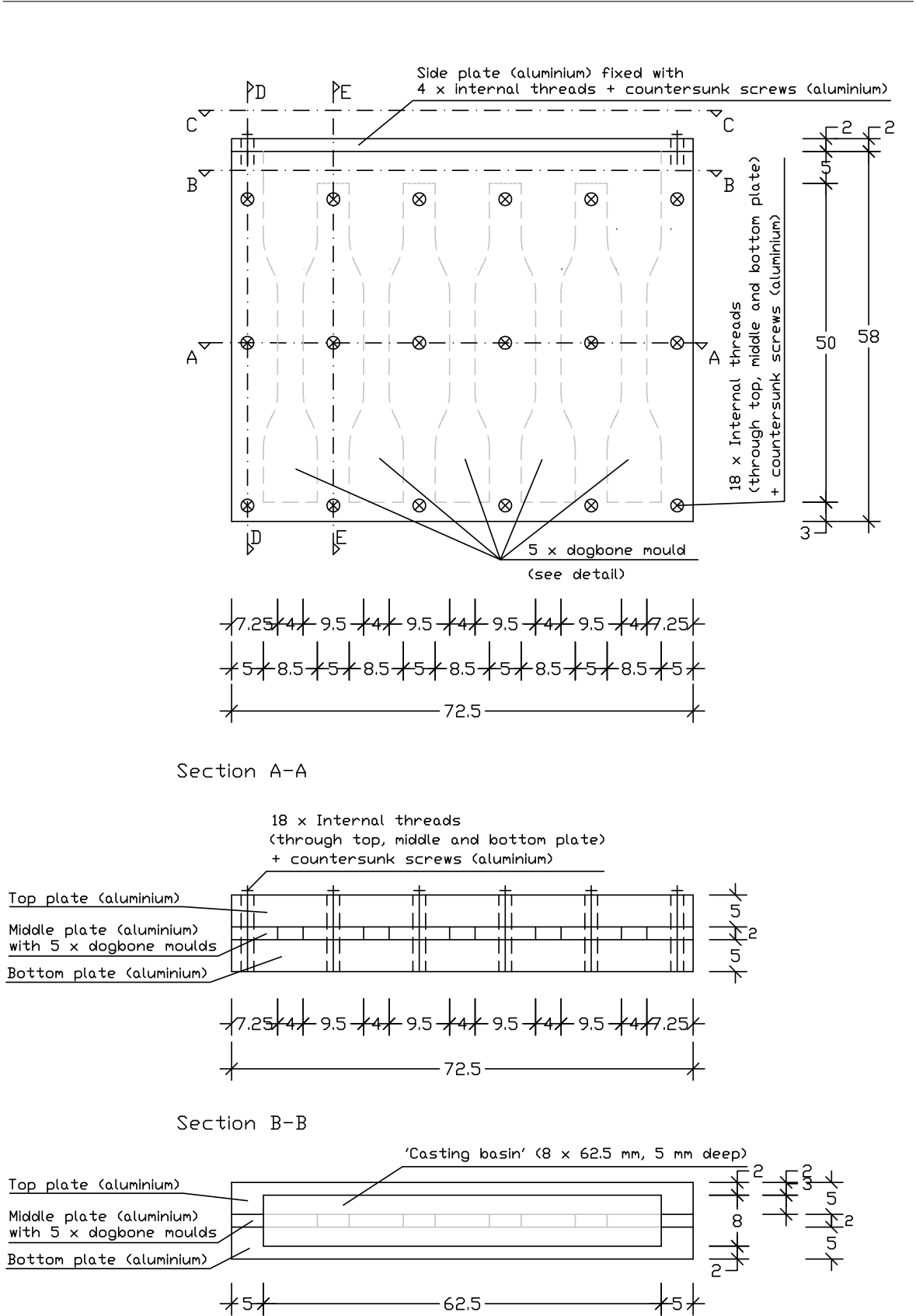
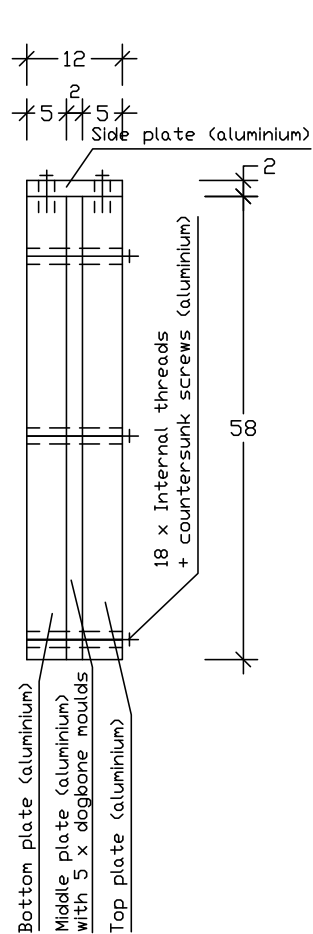
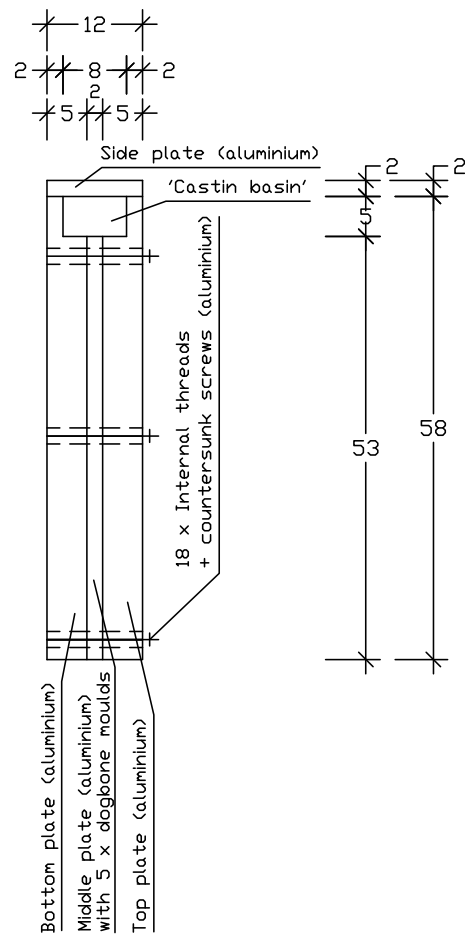


Figure B.2: Technical drawing of the moulds used for preparing five dog-bone shaped tension samples (narrow part $16 \times 4 \text{ mm}$) (Page 01).

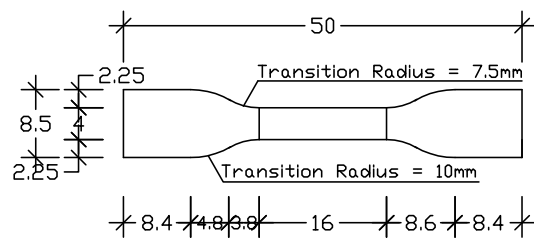
Section D-D



Section E-E



Detail of the dogbone mould



View C-C

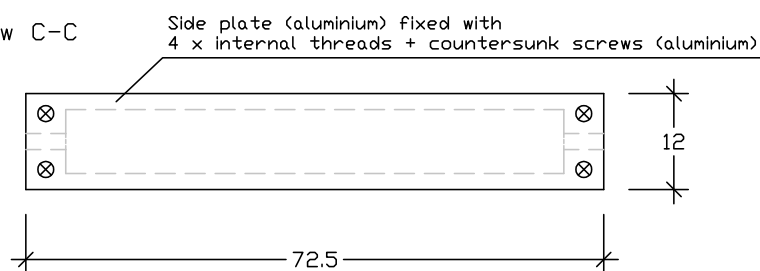


Figure B.3: Technical drawing of the moulds used for preparing five dog-bone shaped tension samples (narrow part $16 \times 4 \text{ mm}$) (Page 02).

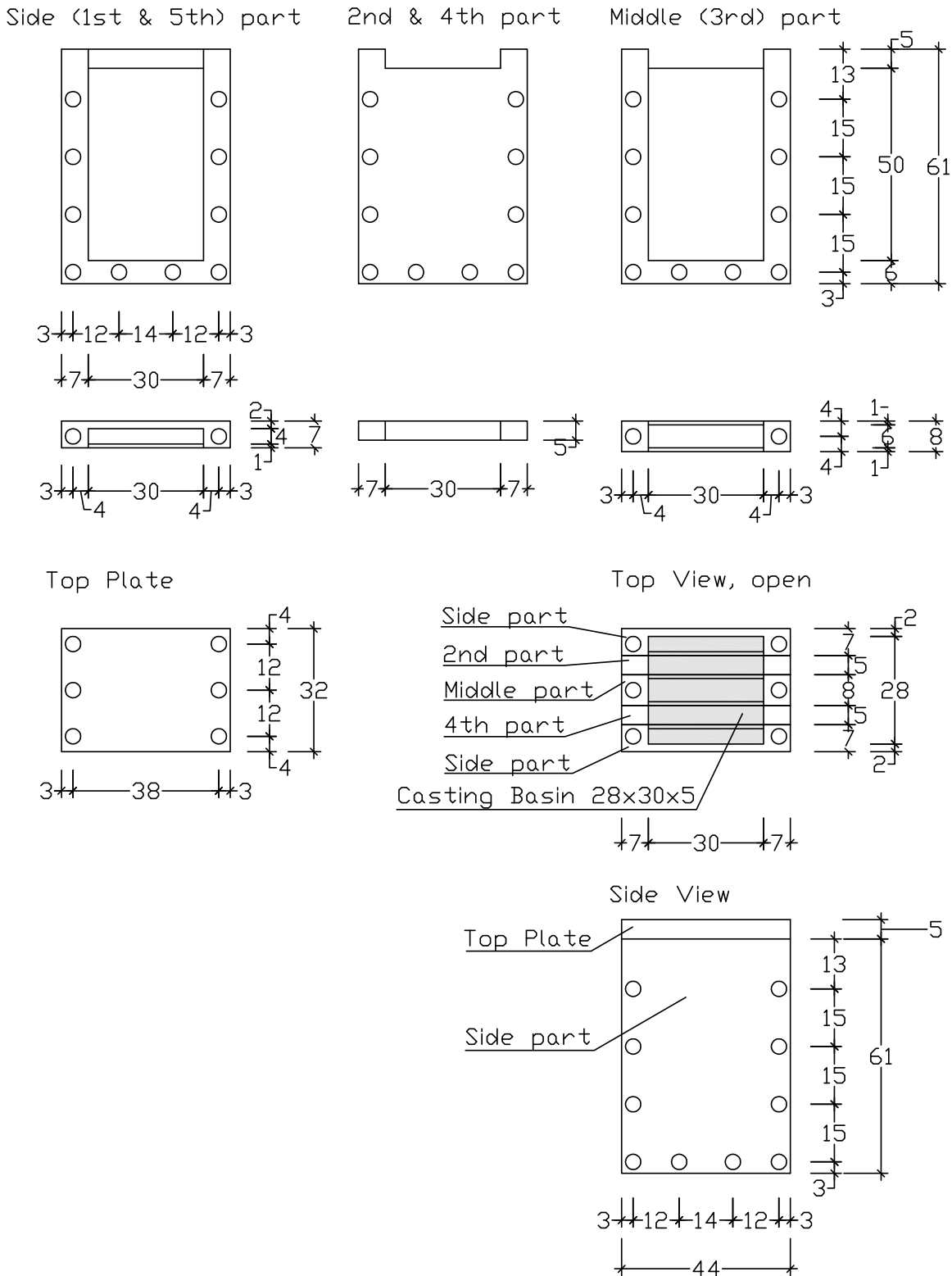


Figure B.4: Technical drawing of the moulds used for preparing four pure shear samples ($b = 50\text{ mm}$, $w = 30\text{ mm}$, and $t = 1\text{ mm}$).

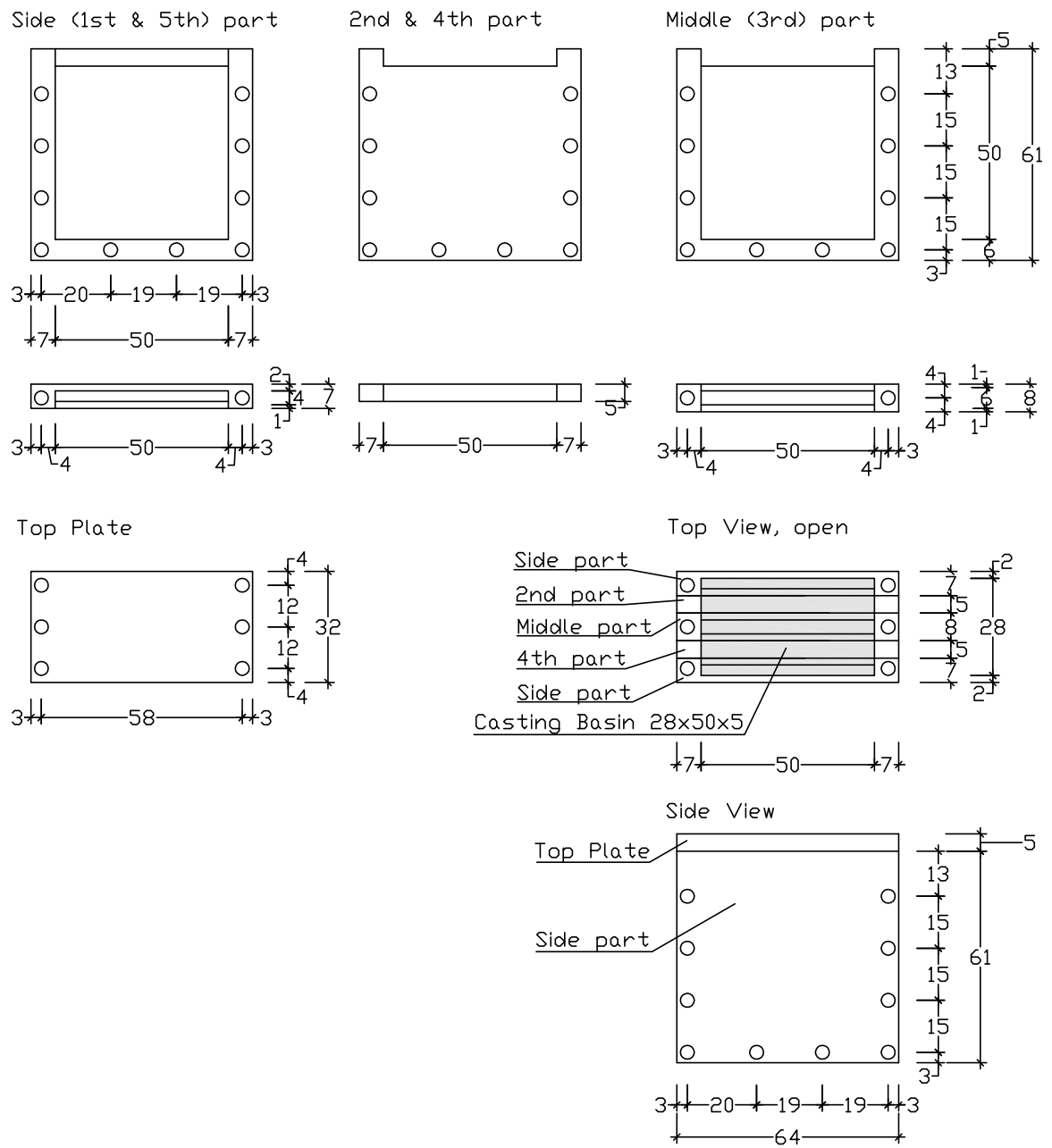


Figure B.5: Technical drawing of the moulds used for preparing four biaxial samples ($b = 50 \text{ mm}$, $w = 50 \text{ mm}$, and $t = 2 \text{ mm}$).

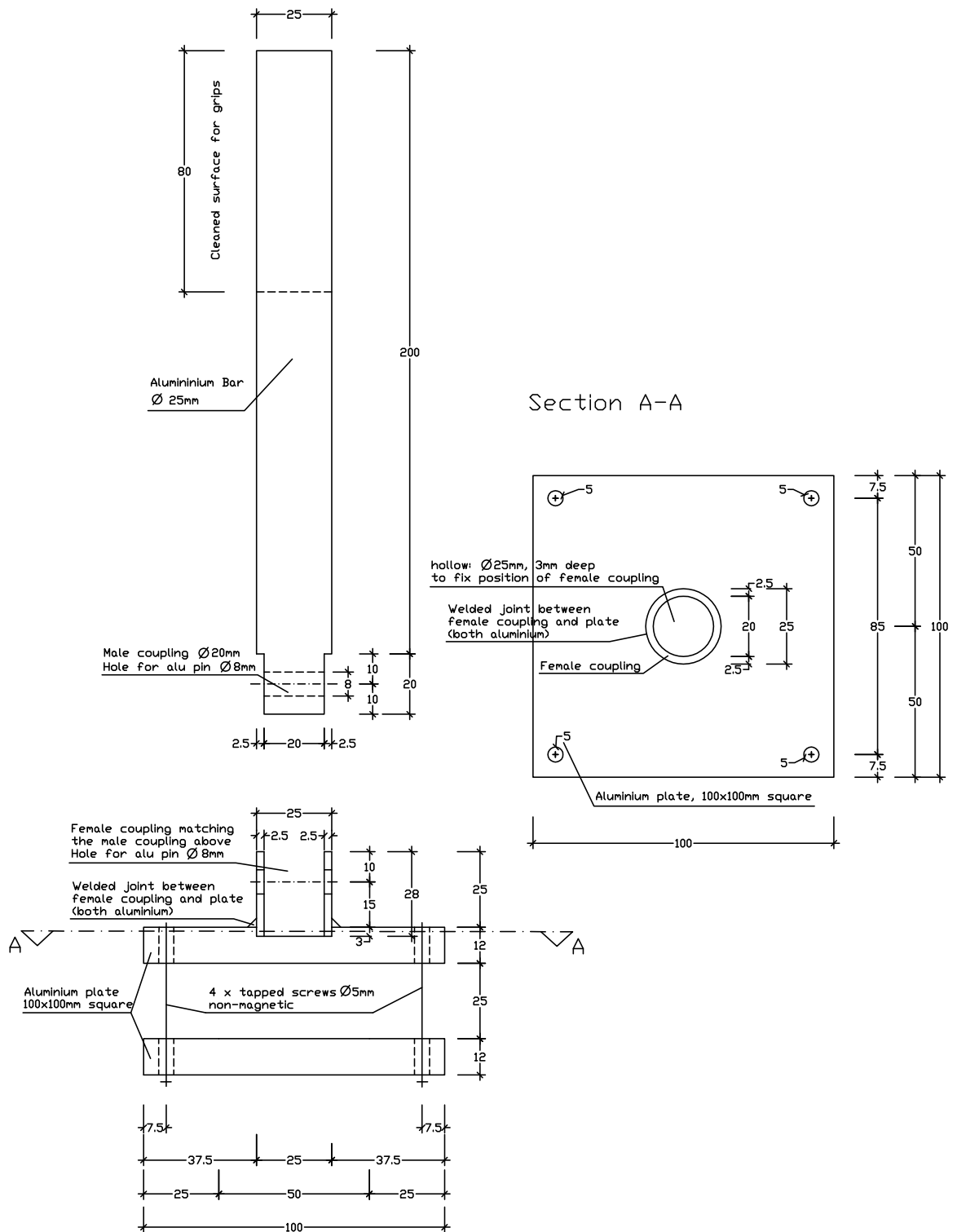


Figure B.6: Technical drawing of the top part of the test rig structure used for compression tests.

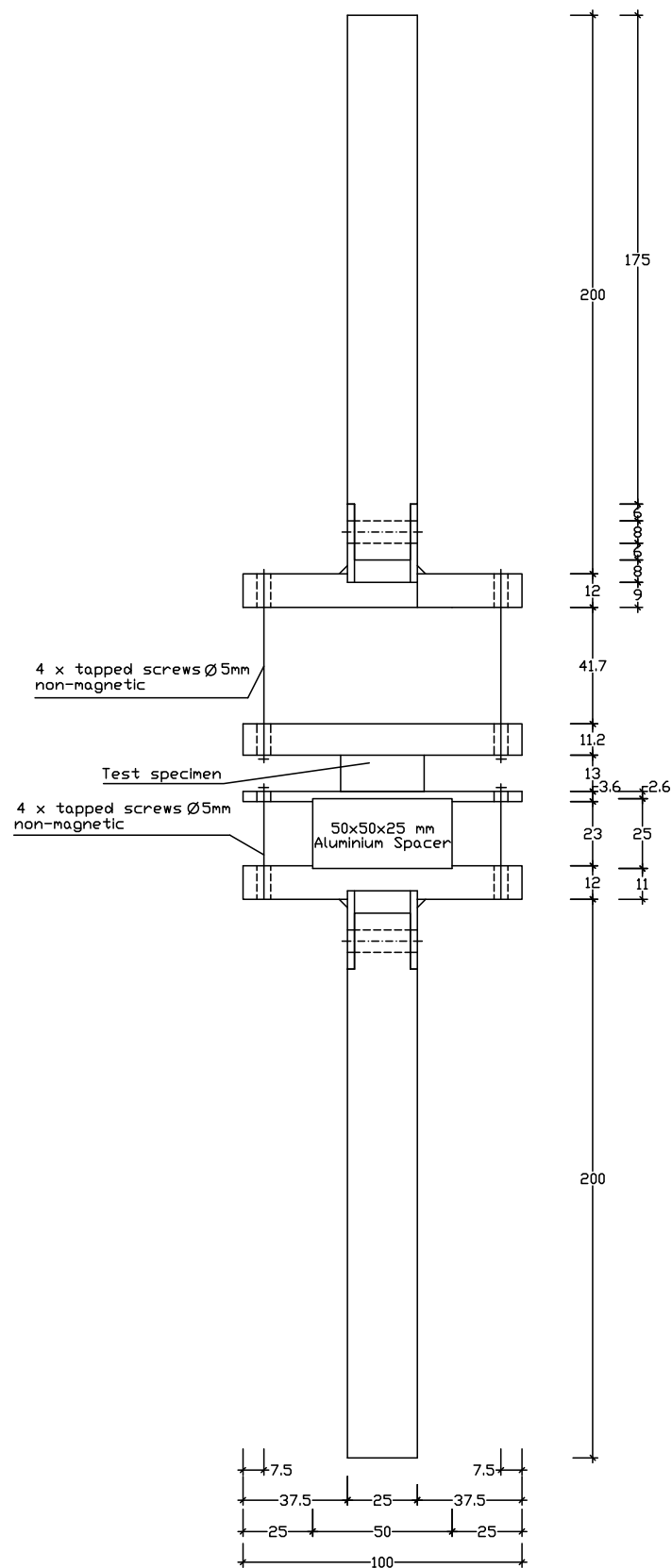


Figure B.7: Technical drawing of the compression setup without magnetic induction.

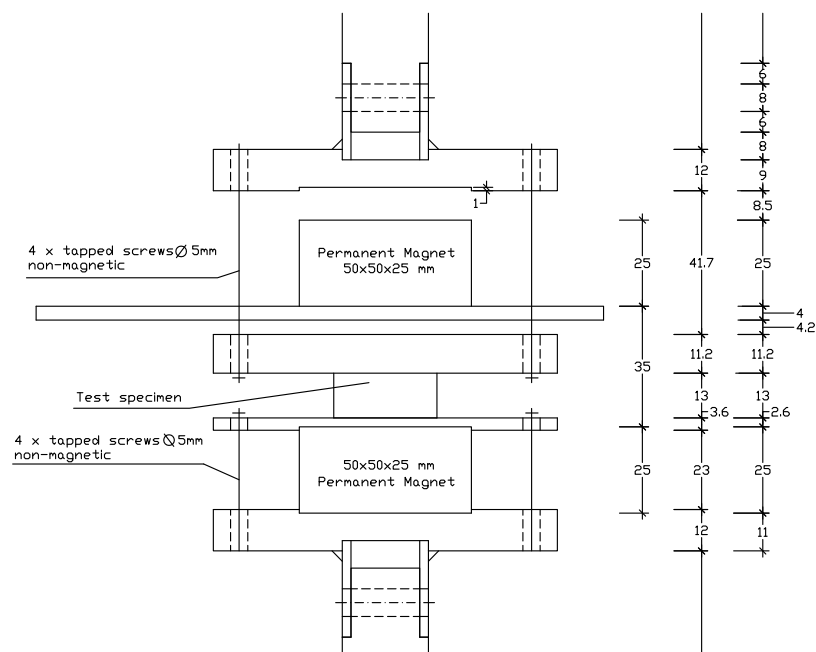


Figure B.8: Technical drawing of the compression test setup with permanent magnets 35 *mm* apart creating 450 *mT* magnetic induction.

[
Technical drawing of the compression *Magnet62* test

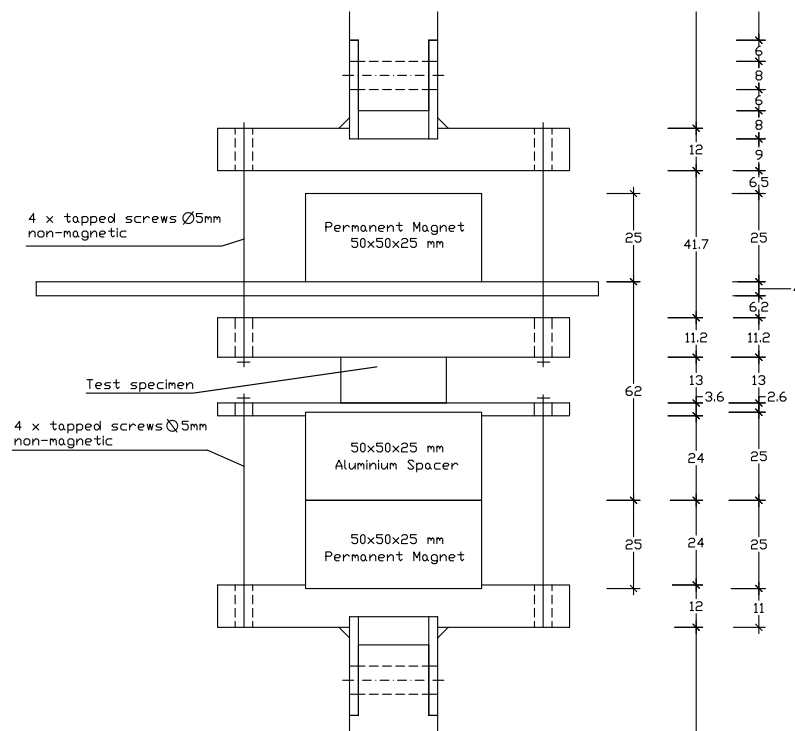


Figure B.9: Technical drawing of the compression test setup with permanent magnets 62 *mm* apart creating 210 *mT* magnetic induction.

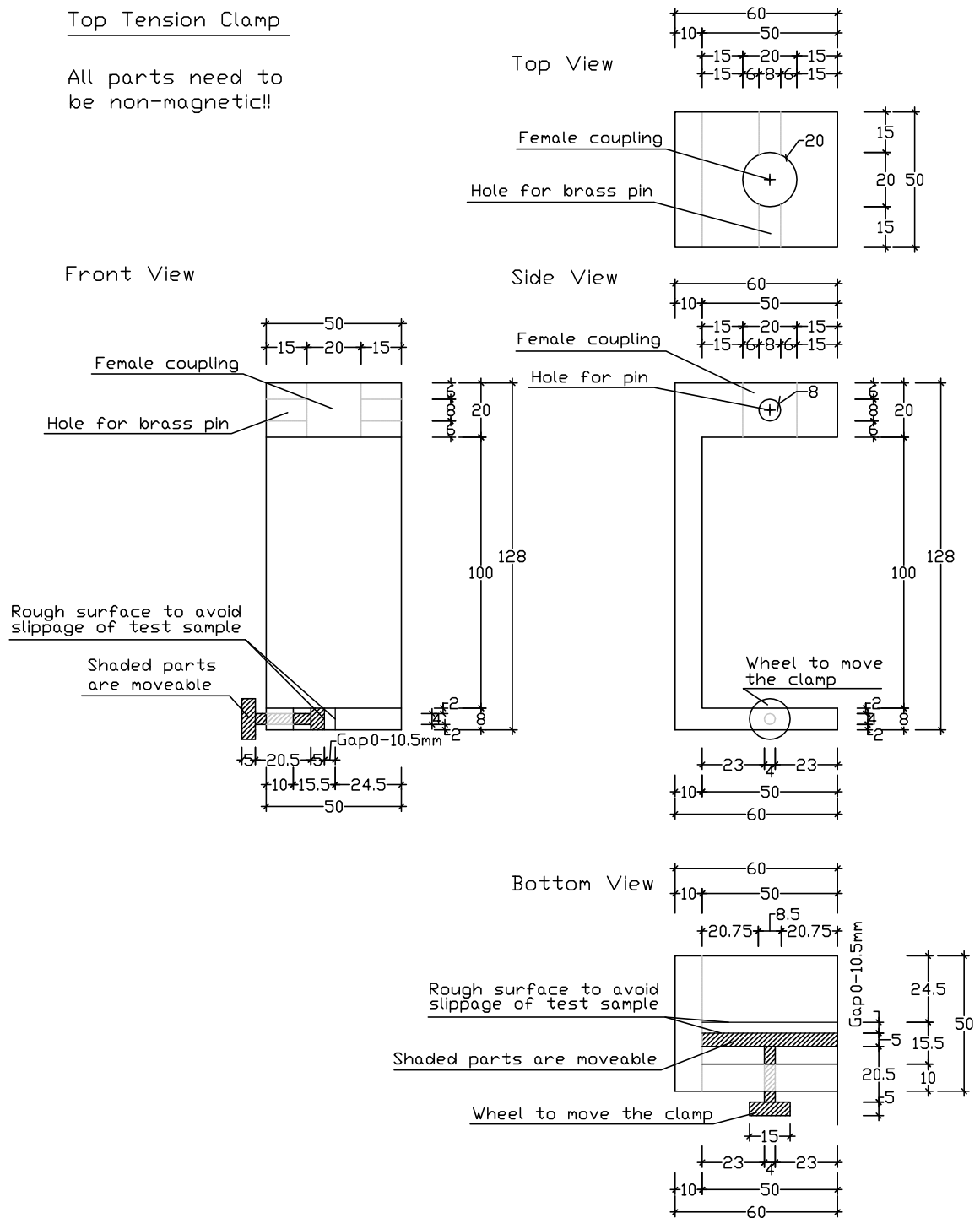


Figure B.10: Technical drawing of the top part of the test rig structure used for tension and pure shear tests.

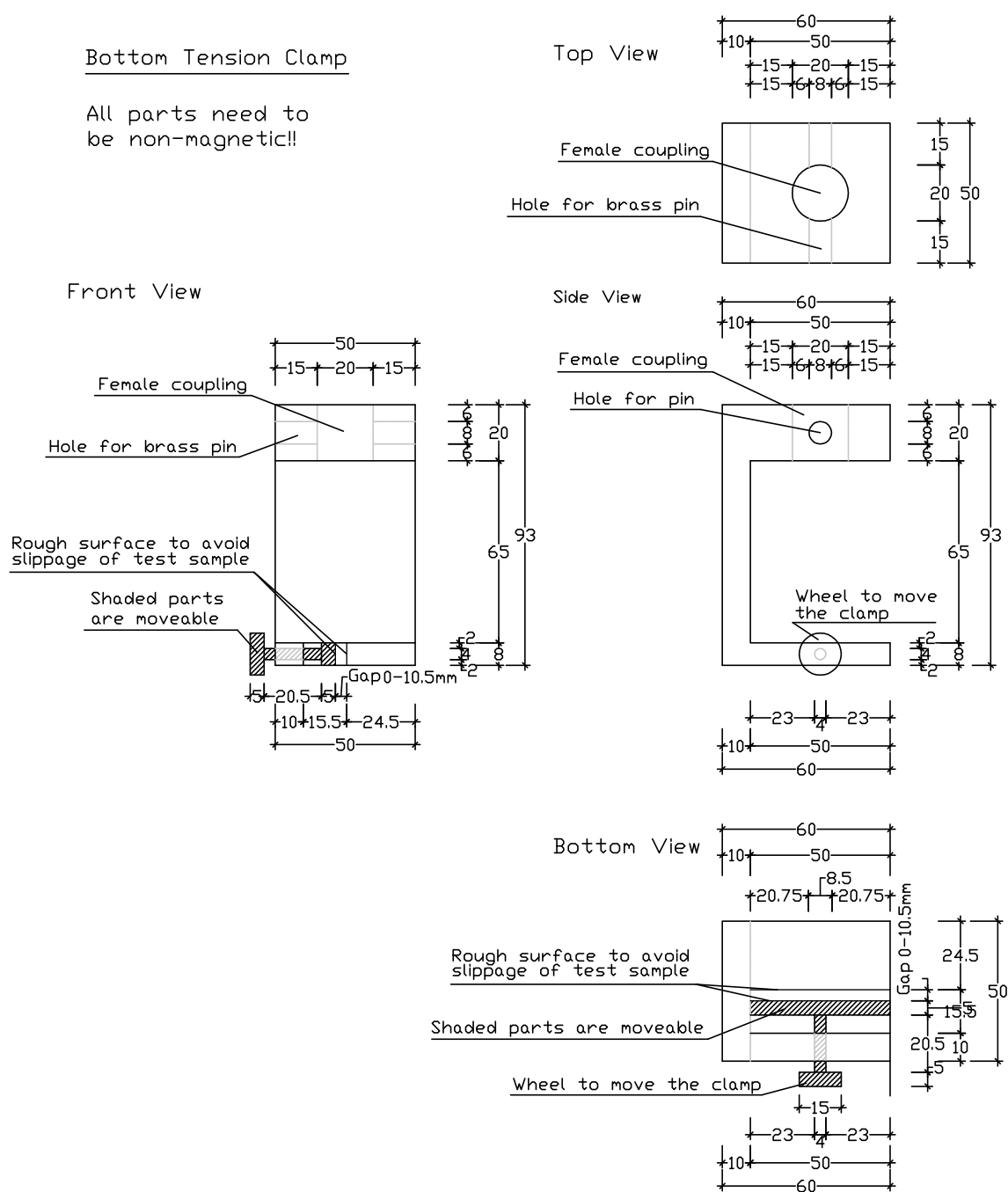
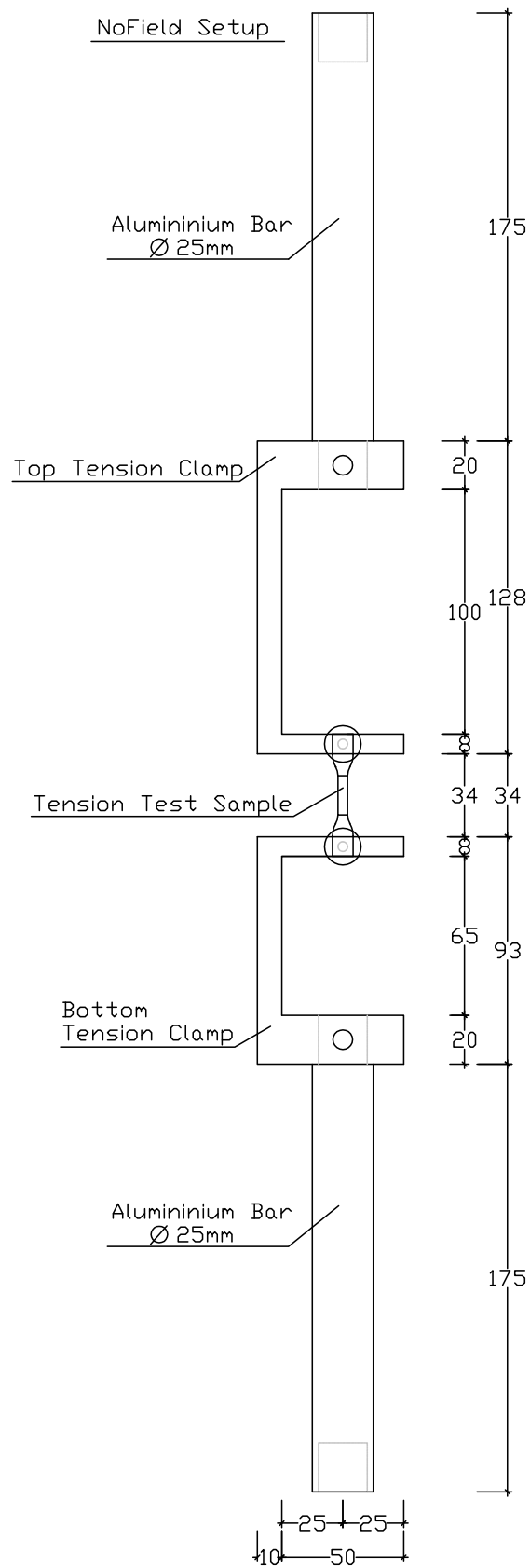


Figure B.11: Technical drawing of the bottom part of the rig structure used for tension and pure shear tests.

**Figure B.12:** Technical drawing of the tension test setup without magnetic induction.

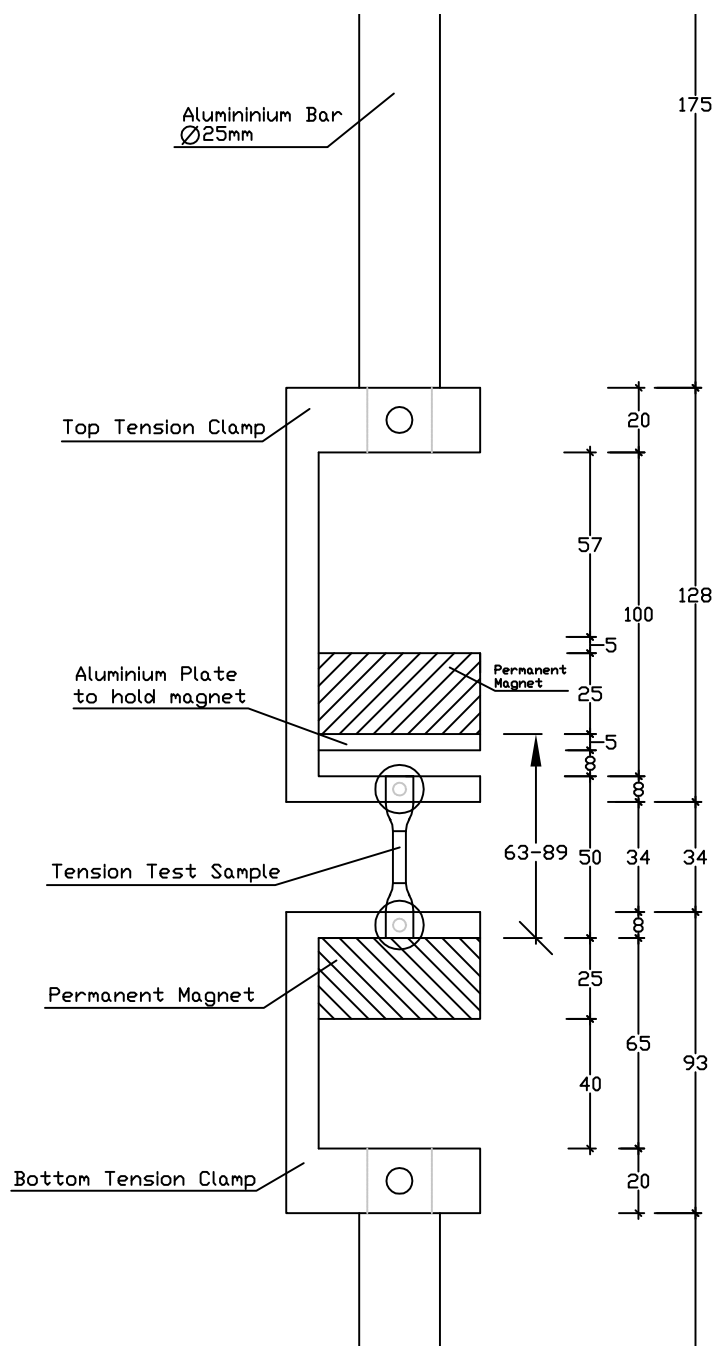


Figure B.13: Technical drawing of the tension test setup with permanent magnets in place. To decrease the magnetic induction the top magnet was moved upwards. The distance between the magnets was 63 mm in the *Magnet63* tests with 289.2 mT magnetic induction, 73 mm in the *Magnet73* tests with 251.2 mT, and 89 mm in the *Magnet89* tests with 220.6 mT.

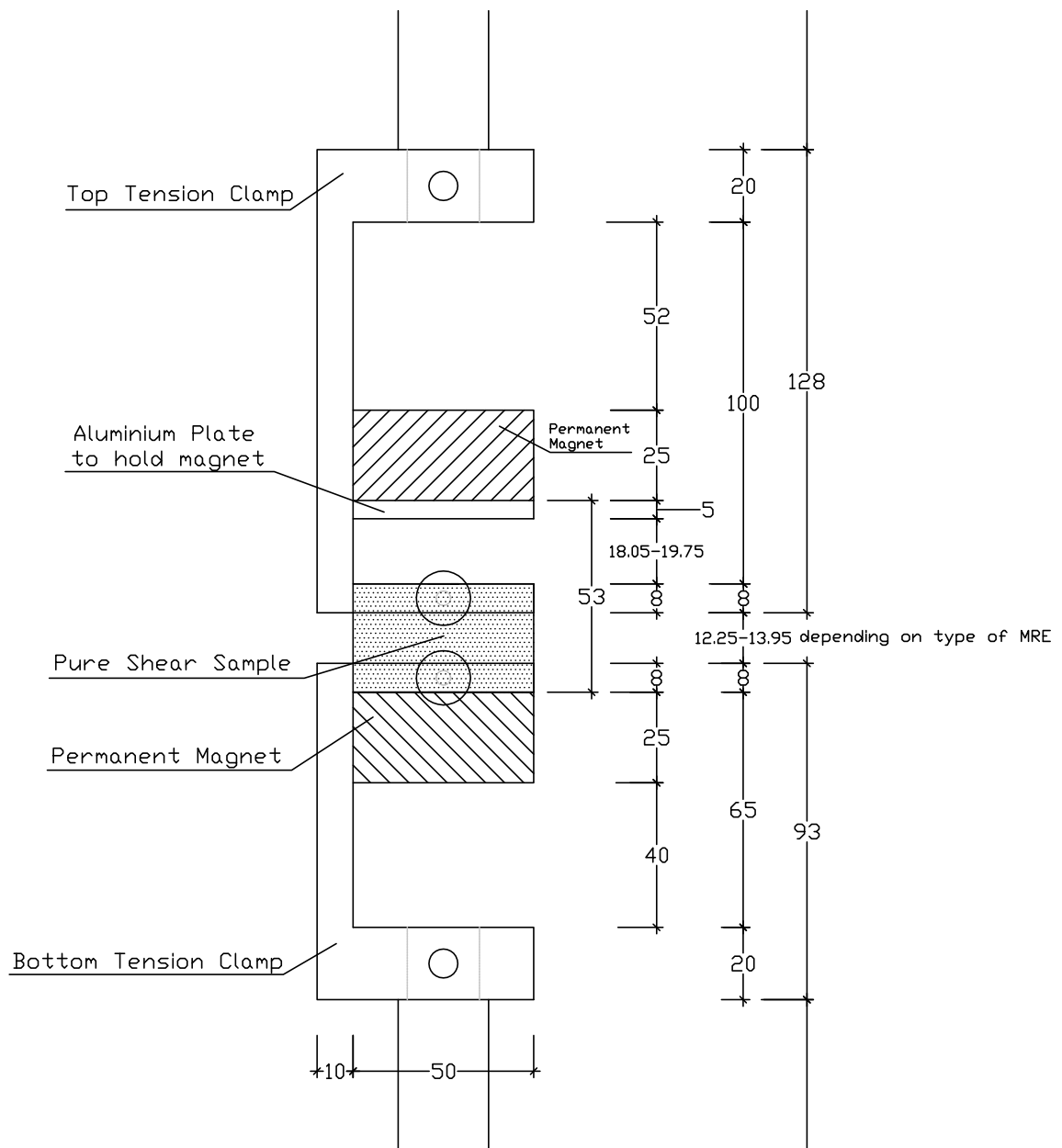
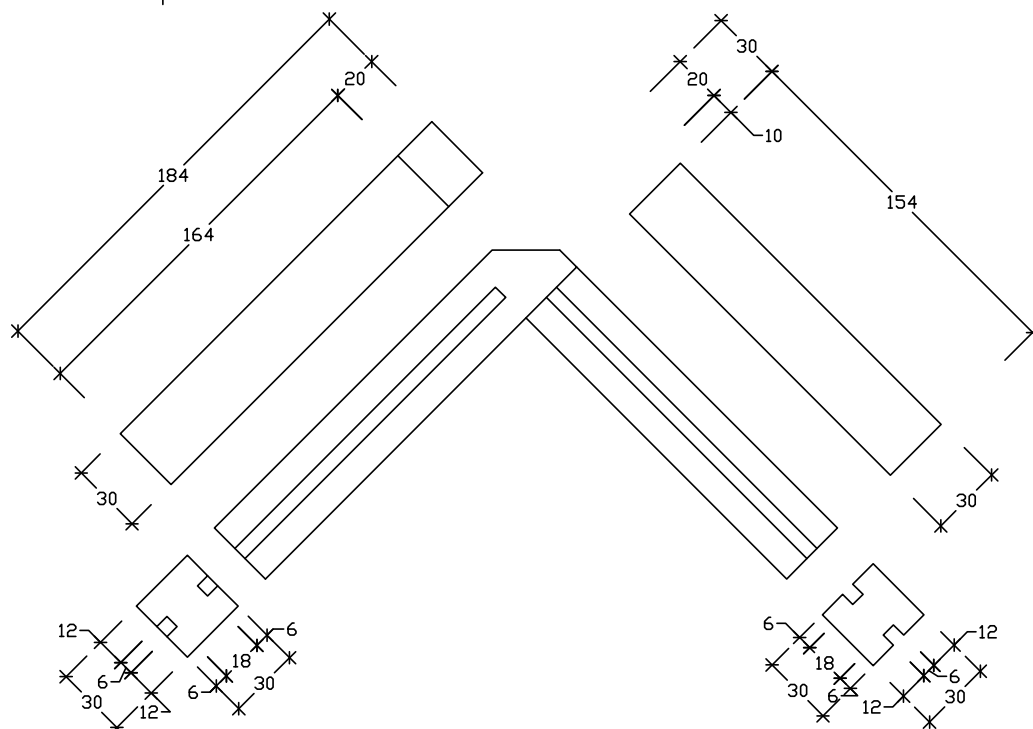


Figure B.14: Technical drawing of the pure shear test setup with permanent magnets 53 mm apart creating 290 mT magnetic induction.

Part A - Top Part of the biaxial frame



Part B - Bottom Part of the biaxial frame

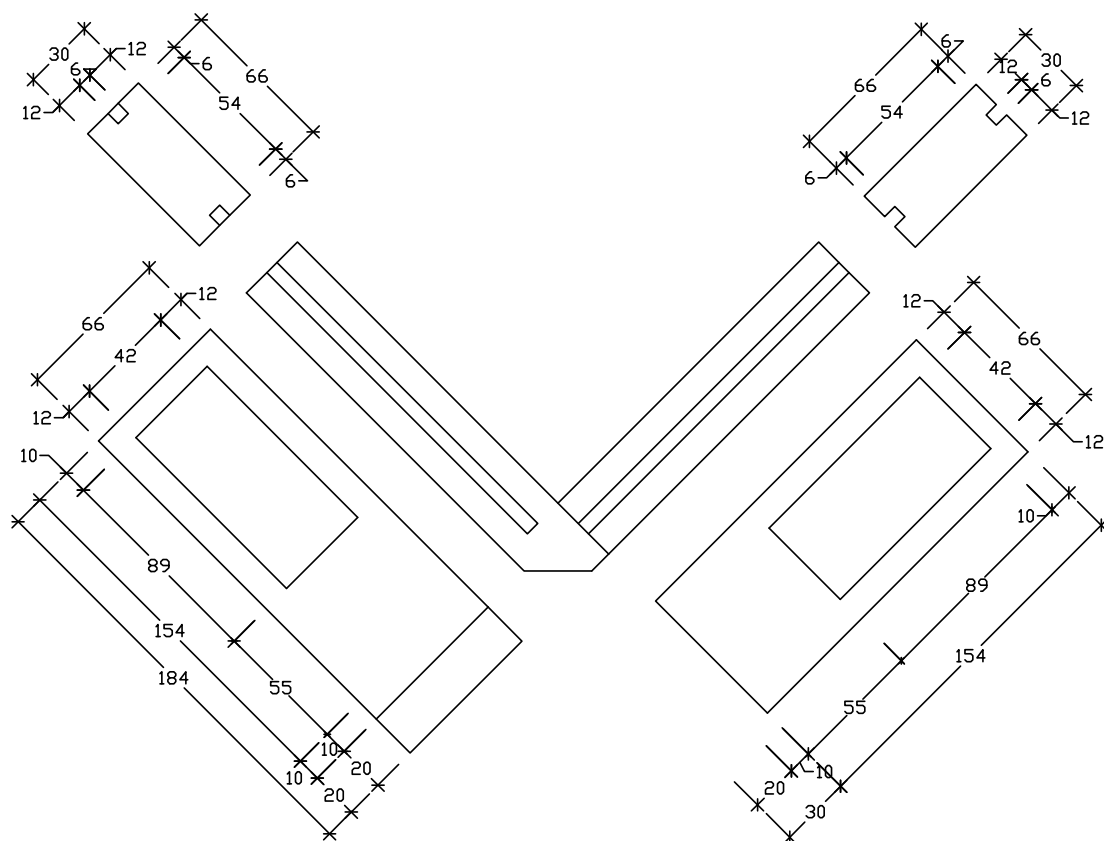


Figure B.15: Technical drawing of the biaxial test rig. Top and bottom part of the test rig structure are made of Teflon.

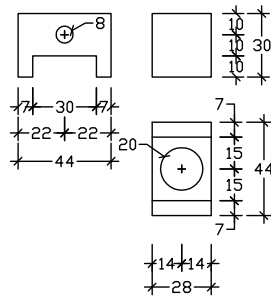
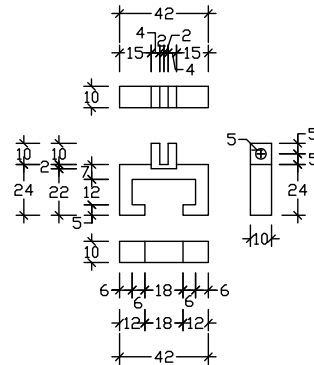
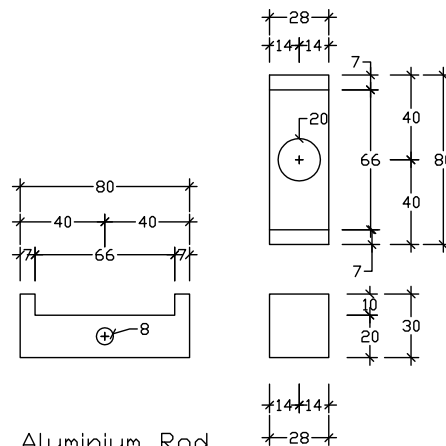
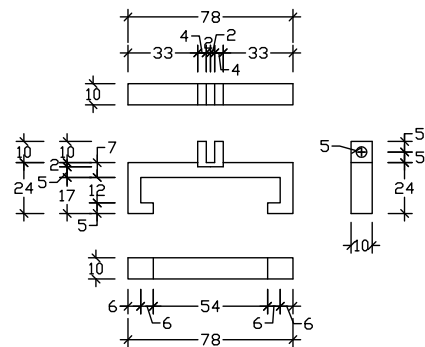
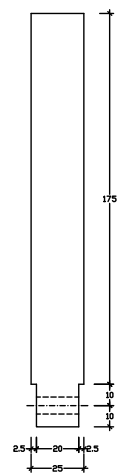
Connector to Aluminium Rod
for Part ASliding clamp for Part A
with grub screw connectorConnector to Aluminium Rod
for Part BSliding clamp for Part B
with grub screw connectorAluminium Rod
Diameter = 25mm

Figure B.16: Technical drawing of the biaxial test rig. Connectors to aluminium rods (already used for the other experimental setups) and sliding clamps are both made of Teflon.

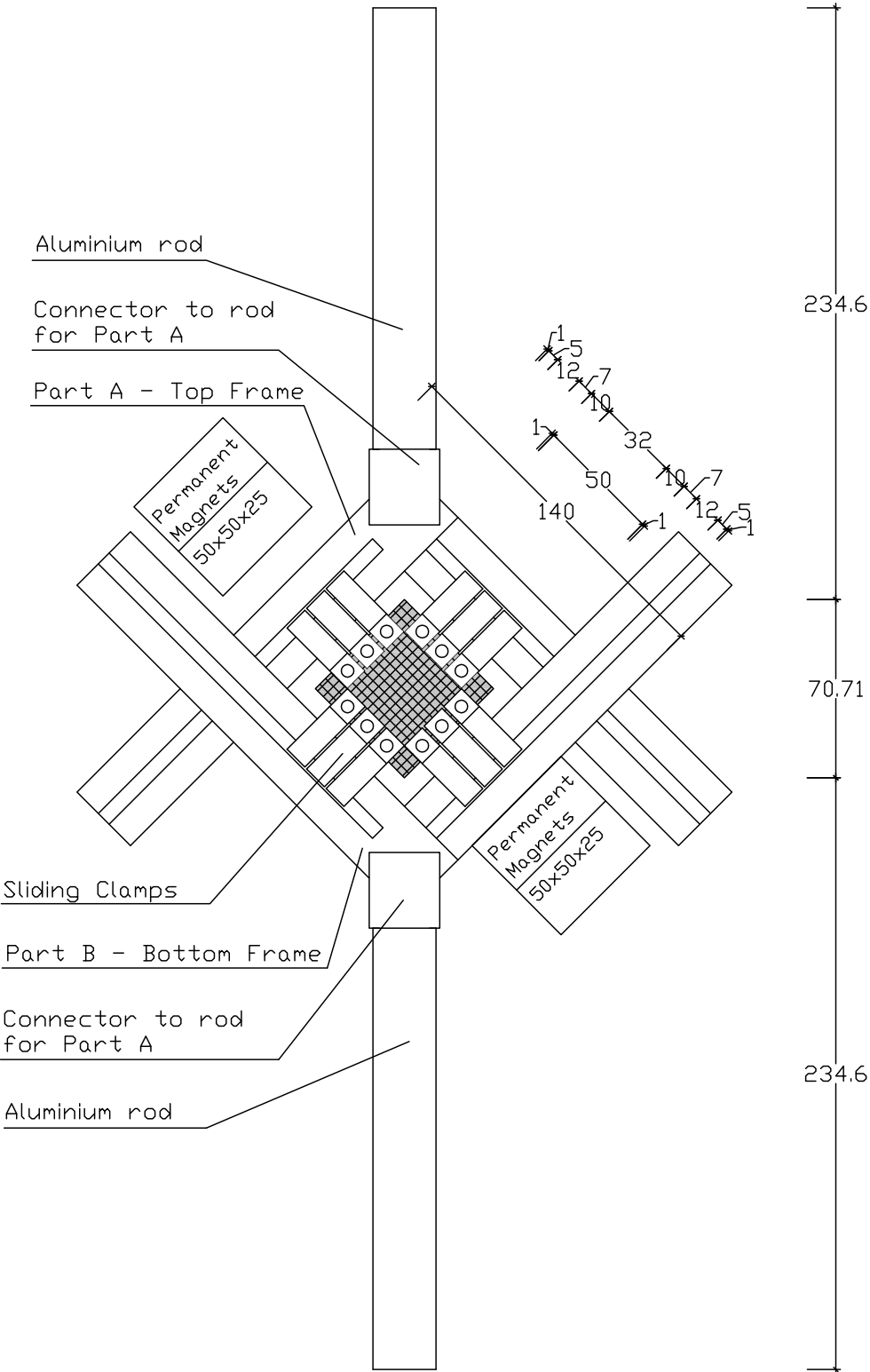


Figure B.17: Technical drawing of the equi-biaxial test setup in the reference configuration. Two permanent magnets on either side of the test rig with a distance of 140 mm between them are directed in x-direction.

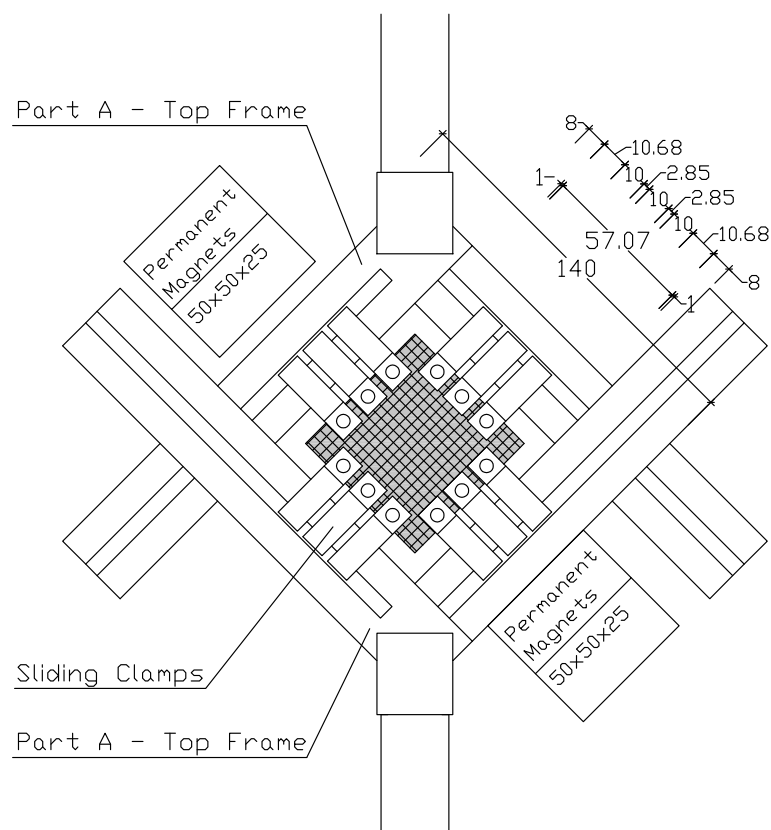


Figure B.18: Technical drawing of the equi-biaxial test setup in the deformed configuration. The top part of the rig structure is displaced by 10 mm upwards in vertical direction; the MRE sample is stretched and the sliding clamps are moved accordingly. Two permanent magnets on either side of the test rig with a distance of 140 mm between them are directed in x-direction.

Appendix C

Amounts of components used to manufacture MREs

To manufacture MRE samples, moulds were designed specific for each sample shape according to the needs of each large-strain experiment. Two moulds of each type were built in order to produce one set of isotropic and one set of anisotropic MREs from one batch of mixture. With the compression mould two samples, with the tension mould five samples, and with the pure shear and equi-biaxial mould 4 samples could be prepared. The amount of rubber mixture was roughly calculated with the dimensions of the moulds given in the technical drawings in Appendix B. The density of the silicone rubber is given with 1.08 g/cm^3 . The chosen amounts of the rubber component A are listed in Table C.1. Components A and B of the silicone rubber have to be in the ratio 10 : 1, and 30w % of the silicone fluid are added to the whole amount of silicone rubber. The iron content is given as volume percentages related to the final volume of the MRE mixture; in this study 10% to 30%, and in case of the compression samples up to 40% CIP were added. The density of the silicone fluid is not provided by the company, and is assumed to be 1.0 g/cm^3 . The density of the silicone rubber-oil blend can be calculated as $1.08 \times 0.7 + 1.0 \times 0.3 = 1.06 \text{ g/cm}^3$. The density of CIP is the one of iron given with 7.874 g/cm^3 . The amounts of CIP are calculated for a compression sample with 10 vol% CIP with the following equation:

$$10 \text{ vol\%} : \frac{x}{7.874} \bigg/ \left(\frac{71.5}{1.06} + \frac{x}{7.874} \right) = 0.1 \quad x = 59.0137 \text{ g}$$

Other CIP amounts, and amounts for the other sample shapes are calculated analogous. The amounts used to manufacture compression, tension, pure shear, and equi-biaxial tension specimens in this study are summarised in Table C.1.

Component	Amount [g]			
	Compression	Tension	Pure Shear	Equi-Biaxial
MM 240 TV Component A	50.00	30.00	40.00	80.00
MM 240 TV Component B	5.00	3.00	4.00	8.00
ACC 34	16.50	9.90	13.20	26.40
10Vol% CIP	59.01	35.41	47.21	94.42
20Vol% CIP	132.78	79.67	106.22	212.44
30Vol% CIP	227.62	136.57	182.10	364.20
40Vol% CIP	354.08			

Table C.1: Amounts of the components used to manufacture compression, tension, pure shear, and equi-biaxial tension specimens.

Appendix D

Matlab Codes

The software package *Matlab* was used to analyse experimental data, to plot figures, and also to perform data fitting to constitutive equations. To this end, several algorithms were written, so a short description of them is given in the following list. All *Matlab* codes, with a detailed description on how to use them, are saved on a DVD available with this thesis.

aniso_modelfun_piola.m This function defines the *Piola-Kirchhoff* stress functions of the *Qui-Pence*, the *Merodio-Ogden*, the *Holzapfel-Gasser*, and the *Guo* models as function handles for model orders up to $N = 3$ for each deformation mode, with and without the use of weight factors. The function handles are needed for the optimisation process in *constmodel_piola_incompaniso.m*.

aniso_startparameters.m Initial values for the model parameters are required in *constmodel_piola_incompaniso.m*. This function combines parameters required for the isotropic and anisotropic part of the constitutive equations, and a range for the parameters can be provided which is combined to several sets of start parameters.

biaxial.m This function analyses the data of cyclic equi-biaxial tension tests where the DIC system or the pixel measurement method is used to evaluate strain values. The functions *strainDICLimess_biaxial.m* or *strainpixel_biaxial.m* must run prior to this function. The original P-d data are split into several loading and unloading parts (*divide_cycles.m*). Each part is cut (*cut_parts.m*) and then shifted to the origin (*shift_cycles.m*). The stresses are calculated differently for the five cases: isotropic MREs without and with magnetic field, and anisotropic MREs without and with field parallel and perpendicular to the particle alignment. In Section 5.5.4 detailed information and equations are provided. The stresses are calculated with the original width and thickness of the samples.

compression.m This function analyses the data of cyclic compression tests. The original P-d data are split into several loading and unloading parts (*divide_cycles.m*). Each part is cut (*cut_parts.m*) and then shifted to the origin (*shift_cycles.m*). The stress-strain data of each loading and unloading part are calculated using the original height and area of the samples.

constmodel_aniso_lineartheory.m Subfunction of *constmodel_piola_incompaniso.m* to connect the model parameters to the linear theory in small strains. The Young's moduli are calculated depending on the constitutive model and deformation mode.

constmodel_piola_incompaniso.m Determination of transversely isotropic model parameters with a data fitting to experimental stretch-stress data. The *Qui-Pence*, the *Merodio-*

Ogden, the *Holzapfel-Gasser*, and the *Guo* models with a *Neo-Hookean* or *Ogden* based isotropic part are supported. Uniaxial, pure shear, and equi-biaxial deformation modes are supported and can be combined to determine unique solutions of model parameters. Several sets of start parameters can be provided, and the one resulting in the smallest 2-Norm is the final solution. The optimisation problem is solved with the *Matlab* functions *lsqcurvefit.m* or *fmincon.m*. Subfunctions of this function are *aniso_modelfun_piola.m*, *aniso_startparameters.m*, *ogden_sp_combinations.m*, and *constmodel_aniso_lineartheory.m*.

constmodel_piola_incompiso.m Determination of the *Neo-Hookean* and the *Ogden* model parameters with a data fitting to experimental stretch-stress data. The *Ogden* model up to a order of $N = 5$ is supported. Uniaxial, pure shear, and equi-biaxial deformation modes are supported and can be combined to determine unique solutions of model parameters. Several sets of start parameters can be provided, and the one resulting in the smallest 2-Norm is the final solution. The optimisation problem is solved with the *Matlab* functions *lsqcurvefit.m* or *fmincon.m*. Subfunctions of this function are *ogden_modelfun_piola.m*, *ogden_startparameters.m*, and *ogden_sp_combinations.m*.

constmodel_piola_incompiso_mullins.m Determination of the *Ogden-Roxburgh* model parameters to interpret the stress softening behaviour known as the *Mullins Effect*. The function *constmodel_piola_incompiso.m* is used to determine the parameters of the primary loading path.

cut_parts.m This function cuts loading and unloading cycles. A cut is required when the slope of the experimental data is zero at the start. The method of analysis was explained in Section 5.1.2.

datafit_lsqnonneg.m This function performs a data fitting to x-y-data with the *Matlab* function *lsqnonneg.m* to a polynomial function of any order.

DICLimess_load.m This function loads the *mat*-files provided by the DIC system and saves them in 3D-matrices. A confidence check of the loaded matrices can be performed.

DICLimess_load_biaxial.m This function loads the *mat*-files provided by the DIC system with *DICLimess_load.m*. The matrices are rotated for better handling, and a confidence check is performed. The DIC data are saved in 3D-matrices. When not provided by the DIC system directly, the data can be converted from the horizontal-vertical coordinate system to the 45° rotated coordinate system.

differences.m This function calculates absolute and relative differences between curves at various positions. The user decides whether the differences are related to one of the curves or to the mean value of the provided data.

divergence.m This function is a specialised function of *differences.m*. Two average curves and associated standard deviations are compared. The divergence points (x-data) are cal-

culated, determined when the absolute difference between the average curves becomes larger than the associated standard deviations.

divide_cycles.m This function divides the data of cyclic tests into loading and unloading parts.

load_imagetime.m This function loads the time when the DIC images were taken. This is provided by the DIC system in a *csv*-file.

loaddata.m This function provides a wide range of loading possibilities and is a subfunction in many other *Matlab* functions, *i.e.* the code *differences.m*, *mean_std.m*, and *plotxy.m*. Variables from several *mat*-files can be loaded.

mean_std.m Mean values and standard deviations from several loaded experimental data sets are calculated.

modulus_linearfit.m This function calculates the moduli of stress-strain increments with a data fit to a linear function. The slopes of these linear functions are the moduli. The user chooses the size of the increment. The modulus-strain curve can be smoothed with the moving average method.

MReffect.m This function calculates absolute and relative MR effects from provided stress-strain data. The moduli are calculated with the code *modulus_linearfit.m* and MR effects are calculated with these moduli. Two sets of data must be loaded, first the data of tests without magnetic field, and second the data of tests with magnetic field. The resulting MR effect versus strain curves can be smoothed with the moving average method.

mullins_adjustment.m This function adjusts the preconditioning (strain) level of experimental data using the damage parameter determined with the *Ogden-Roxburgh* model. The function *constmodel_piola_incompiso_mullins.m* must run prior to this function.

ogden_modelfun_energy.m This function defines the strain energy functions of the *Ogden* model as function handles up to the model order $N = 5$ and for each deformation mode. This is a subfunction in *constmodel_piola_incompiso_mullins.m*.

ogden_modelfun_piola.m This function defines the Piola-Kirchhoff stress functions of the *Neo-Hookean* and *Ogden* model as function handles for all model orders and for each deformation mode, and without and with the use of weight factors. The function handles are needed for the optimisation process in *constmodel_piola_incompiso.m*.

ogden_sp_combinations.m subfunction of *constmodel_piola_incompiso.m* to define the required sign combination of the start parameters, and lower and upper bounds required for the fitting process to fulfil the constraint of the *Ogden* model.

ogden_startparameters.m Initial values for the model parameters are required in *constmodel_piola_incompiso.m*. This function stores results previously determined, gives typ-

ical values (Holzapfel2000), and a range for the parameters can be provided which is combined to several sets of start parameters.

plotxy.m This is a quite generous function to plot x-y data. The user can choose colour and line styles, labels, title, and legend entries. The resulting figures are of the same size. A wide range of loading possibilities is provided with the function *loaddata.m*.

plotxy_meanstd.m This function is a specialised function of *plotxy.m*, so that average curves and associated standard deviations can be plotted. Increments of the standard deviation limits are plotted (user choice).

pureshear_DIC.m This function analyses the data of cyclic pure shear tests where the strain values are obtained from the DIC system. The original P-d data are split into several loading and unloading parts (*divide_cycles.m*). Each part is cut (*cut_parts.m*) and then shifted to the origin (*shift_cycles.m*). The stresses are calculated with the original width and thickness of the samples. Strains are obtained from the DIC system and analysed in the subfunction *strainDICLiness_pure.m*.

pureshear_pixel.m This function works the same way as *pureshear_DIC.m* but the strains are obtained from a pixel measurement method where the crossing points of grid lines, drawn on the samples, were measured manually with *ImageJ*. The subfunction *strain_pixel_pure.m* is used to analyse the measured pixels.

rsq.m This function calculates the coefficient of determination R_2 . This value is between 0 and 1 depending on the quality of the fit; 1 would mean the fit is exact.

shift_completecycletest.m This function cuts and shifts the first loading part of a cycle test to zero, and all of the subsequent loading and unloading parts will be shifted to the same extent, with all parts still connected.

shift_cycles.m This function shifts the separated loading and unloading parts that were cut with *cut_parts.m* to zero stress-strain.

strainDICLiness_biaxial.m This function must be used prior to the function *biaxial.m* when strain values are obtained with the DIC system. The function loads the *mat*-files with *DICLiness_load_biaxial.m*, calculates mean values and standard deviations of the DIC strain field, and splits the strain-time data into loading and unloading parts. Linear functions of the strain-time relations are determined, and the coefficients are input variables of the function *biaxial.m*.

strainDICLiness_pure.m This is a subfunction of *pureshear_DIC.m*. It loads the *mat*-files with *DICLiness_load.m*, performs a confidence check of the provided values, calculates mean values and standard deviations of the DIC strain field, and splits the strain-time data into loading and unloading parts. A linear function of the strain-time relation is determined, and the coefficients are passed to the main function.

strainDICLiness_tension.m This is a subfunction of *tension_DIC.m*. It loads the *mat*-files with *DICLiness_load.m*, calculates mean values and standard deviations of the DIC strain field, and splits the strain-time data into loading and unloading parts. A linear function of the strain-time relation is determined, and the coefficients are passed to the main function.

strainpixel_biaxial.m This function must be used prior to the function *biaxial.m* when strain values are obtained with the pixel measurement method. It calculates the strains in the two stretching directions from crossing points of grid lines drawn on the samples from manually measured *pixels*. The time when the images were taken is loaded with *load_image_time.m*. A linear fit to the strain-time relation is performed and the coefficients are passed to the main function.

strainpixel_pure.m This is a subfunction of *pureshear_pixel.m*. It calculates the strains in vertical and horizontal directions from crossing points of grid lines drawn on the samples, and the displacement of the top part of the test rig from manually measured *pixels*. A linear fit to the strain-displacement data is performed and the coefficients are passed to the main function.

strainpixel_tension.m This is a subfunction of *tension_pixel.m*. It calculates the strains between two lines drawn on the samples, and the displacement of the top part of the test rig from manually measured *pixels*. A linear fit to the strain-displacement data is performed and the coefficients are passed to the main function.

tension_DIC.m This function analyses the data of cyclic tension tests where the strain values are obtained from the DIC system. The original P-d data are split into several loading and unloading parts (*divide_cycles.m*). Each part is cut (*cut_parts.m*) and then shifted to the origin (*shift_cycles.m*). The stresses are calculated with the original area of the narrow part of the dog bone-shaped samples. Strains are obtained from the DIC system and analysed in the subfunction *strainDICLiness_tension.m*.

tension_pixel.m This function works the same way as *tension_DIC.m* but the strains are obtained from a pixel measurement method where the *pixels* of two lines drawn on the samples were measured manually with *ImageJ*. The subfunction *strainpixel_tension.m* is used to analyse the measured *pixels*.

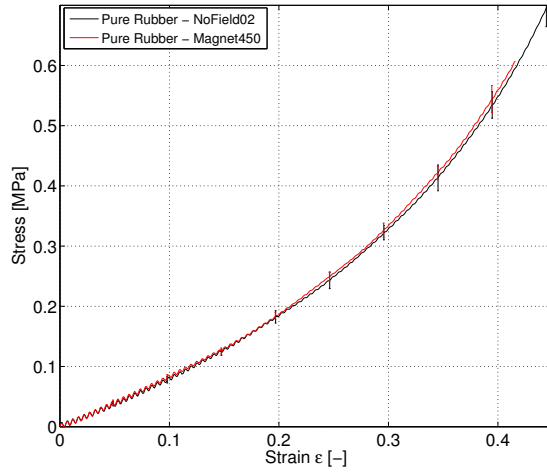
Appendix E

Experimental Results

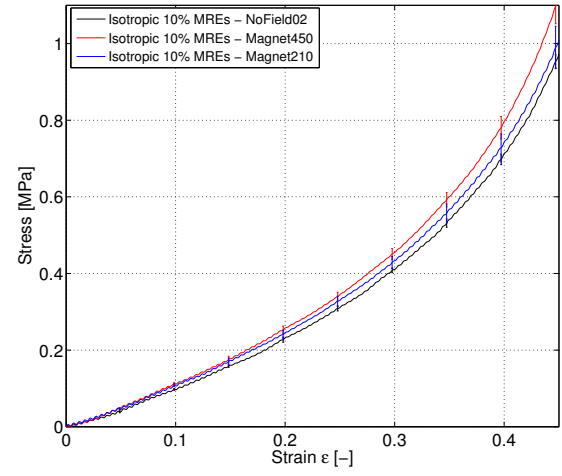
E.1 Uniaxial compression tests

The uniaxial compression tests were presented in Section 5.2. Pure rubber, isotropic, and anisotropic MREs with vertical and horizontal particle alignment containing 10% to 40% volume particle concentration were compressed with up to 50% strain. Three samples of each type were tested, and mean values and standard deviations of the third loading cycle are shown. The tests without an applied magnetic induction were discussed in Section 5.2.3. The tangent moduli, E_T , were used to describe the non-linear behaviour and the different types of MREs were compared.

The MR effects were analysed in Section 5.2.4. Two magnetic tests were performed with 450 mT and 210 mT applied magnetic induction. The stress-strain curves and the tangent moduli comparing the *NoField02* with the magnetic tests of all types of MREs are illustrated in this Appendix. The relative MR effects, calculated with the tangent moduli, E_T , of 1% stress-strain increments, are presented for each types of MRE.



(a) Stress-Strain curves



(b) Stress-Strain curves

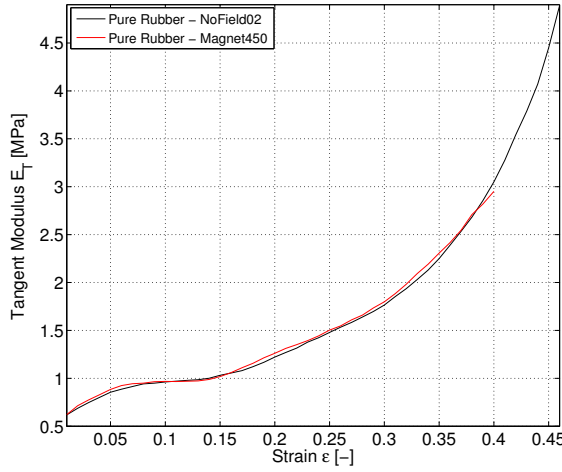
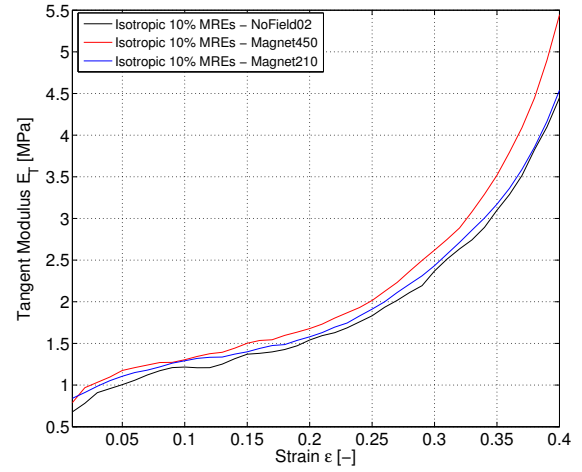
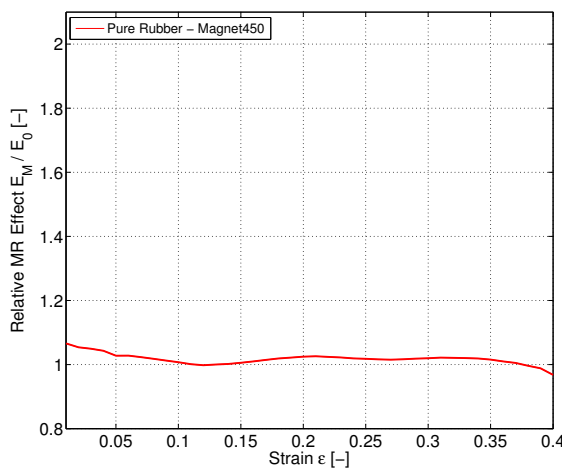
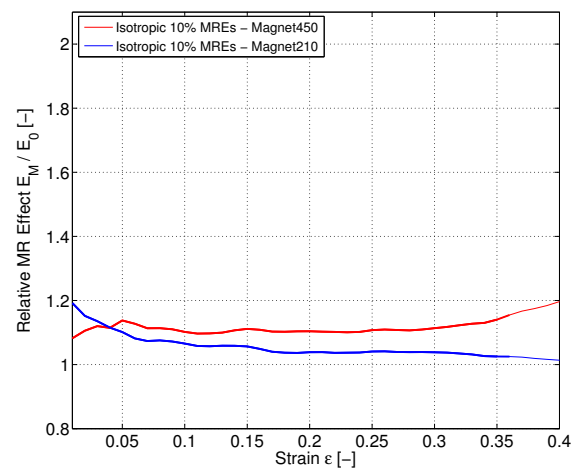
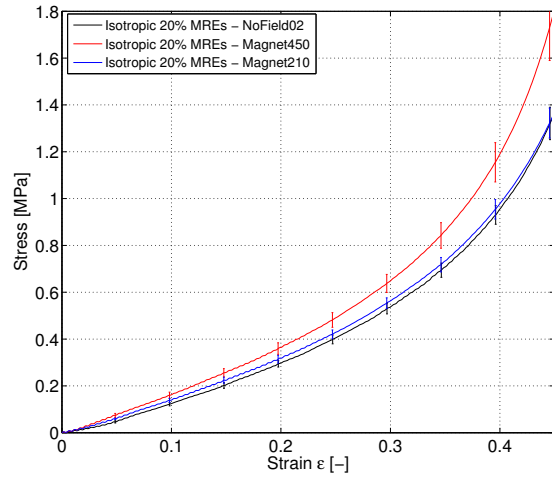
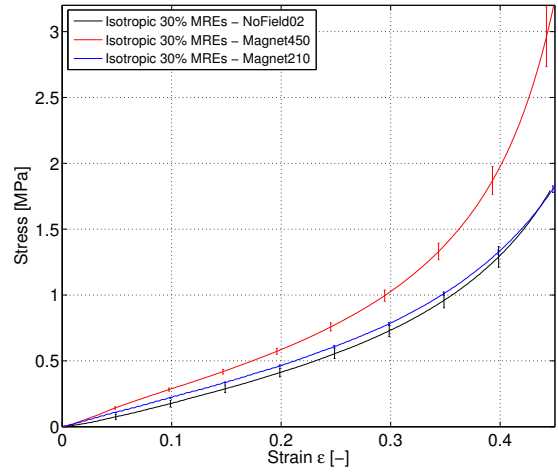
(c) Tangent Moduli E_T (d) Tangent Modulus E_T (e) Relative MR Effect E_M/E_0 (f) Relative MR Effect E_M/E_0

Figure E.1: Experimental results of (left) pure rubber, and (right) isotropic 10% MREs tested in uniaxial compression. Stress-strain curves, the tangent moduli, and the relative MR effects are presented.



(a) Stress-Strain curves



(b) Stress-Strain curves

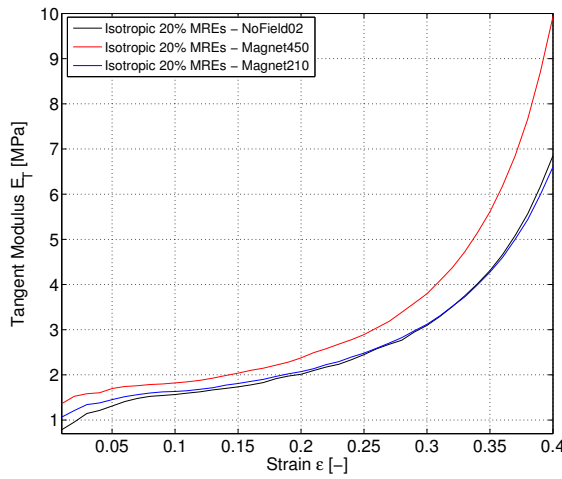
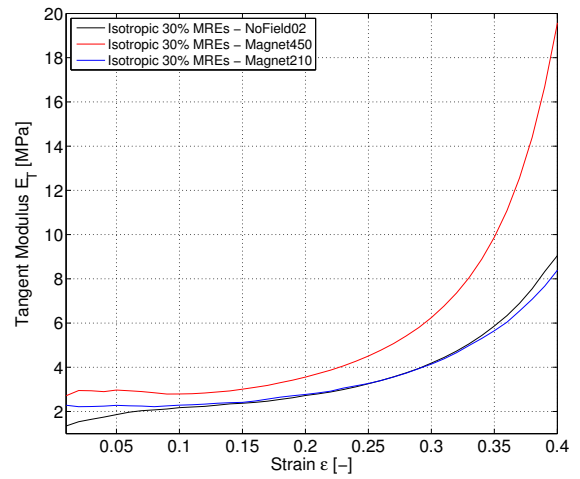
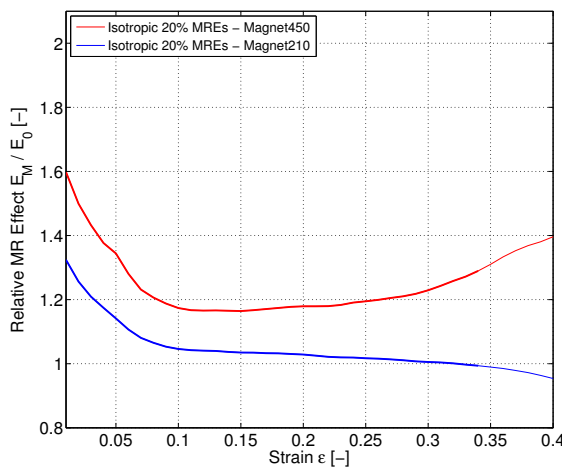
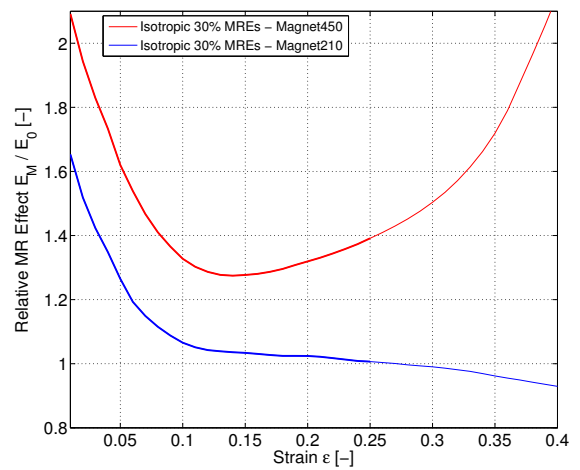
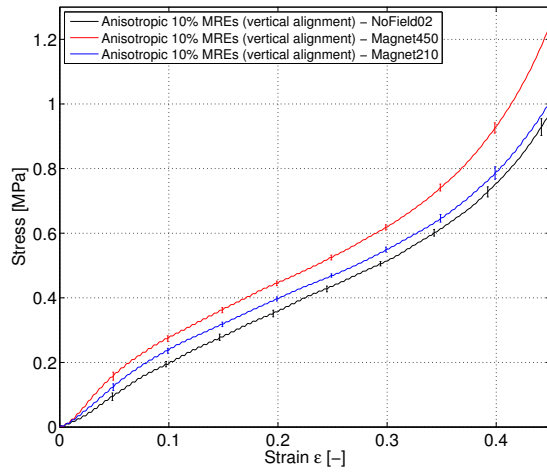
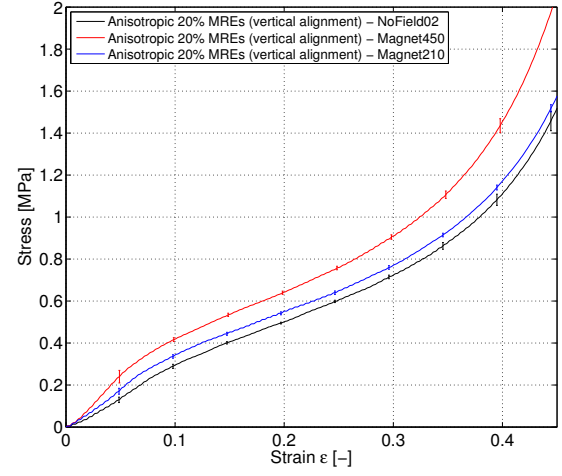
(c) Tangent Moduli E_T (d) Tangent Modulus E_T (e) Relative MR Effect E_M/E_0 (f) Relative MR Effect E_M/E_0

Figure E.2: Experimental results of (left) isotropic 20% MREs, and (right) isotropic 30% MREs tested in uniaxial compression. Stress-strain curves, the tangent moduli, and the relative MR effects are presented.



(a) Stress-Strain curves



(b) Stress-Strain curves

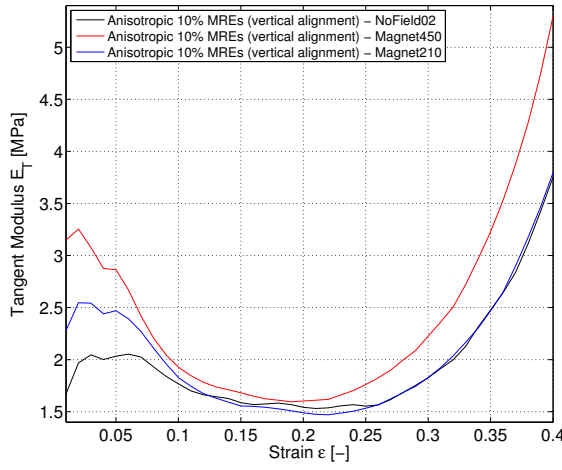
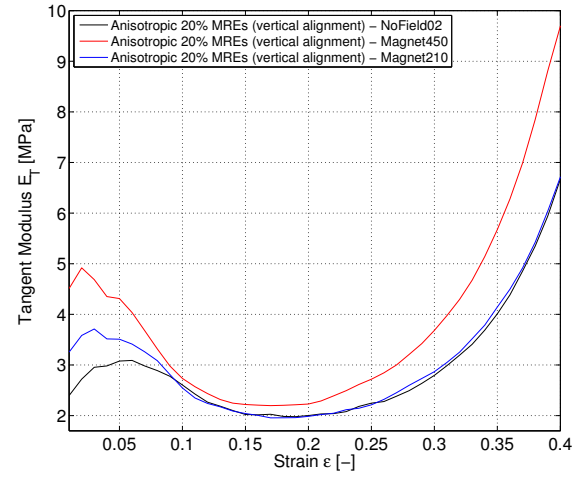
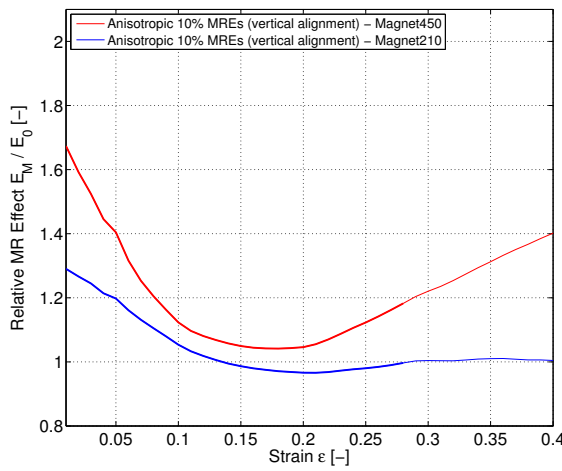
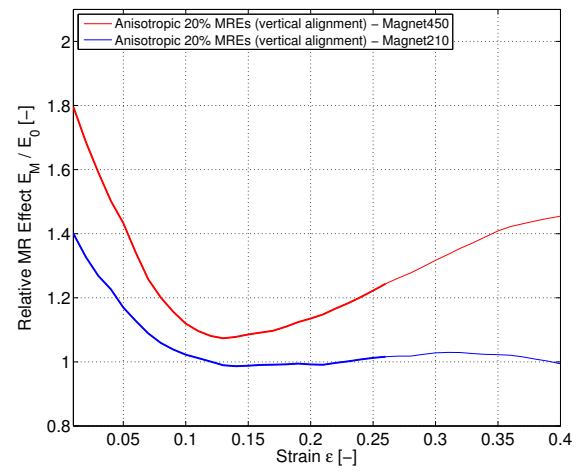
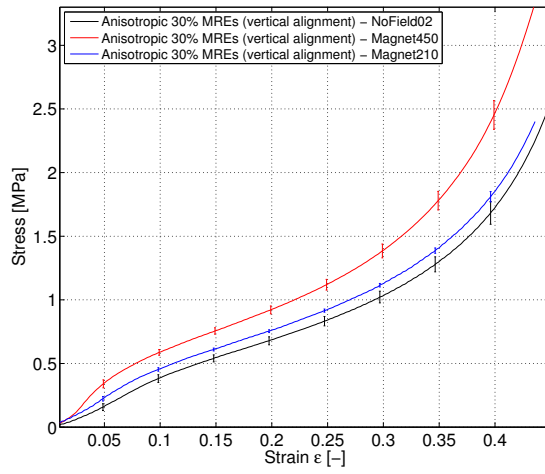
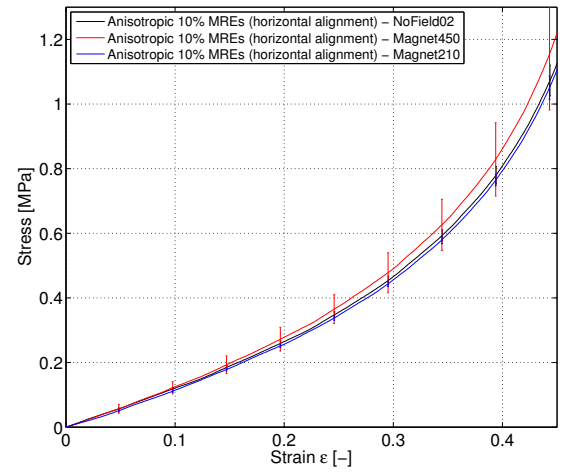
(c) Tangent Moduli E_T (d) Tangent Modulus E_T (e) Relative MR Effect E_M/E_0 (f) Relative MR Effect E_M/E_0

Figure E.3: Experimental results of (left) anisotropic 10% MREs, and (right) anisotropic 20% MREs, both with vertical particle alignment tested in uniaxial compression. Stress-strain curves, the tangent moduli, and the relative MR effects are presented.



(a) Stress-Strain curves



(b) Stress-Strain curves

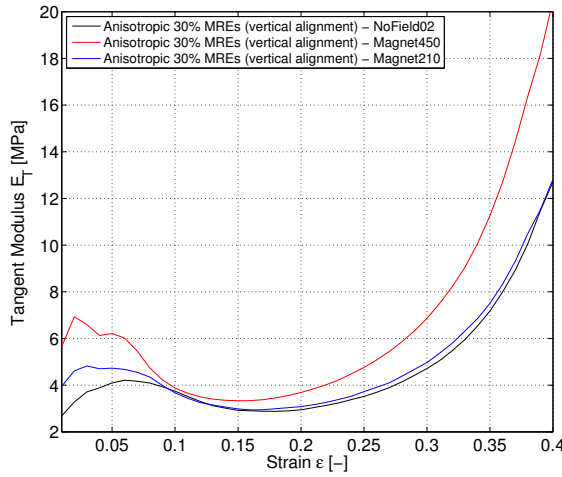
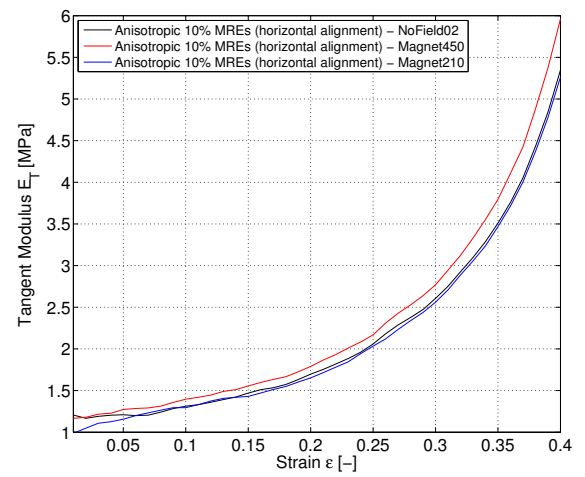
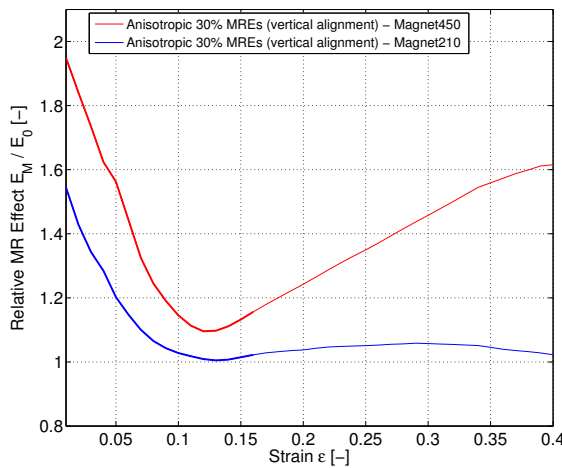
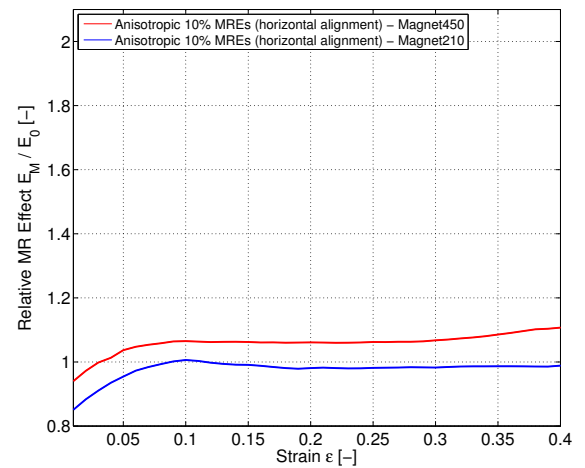
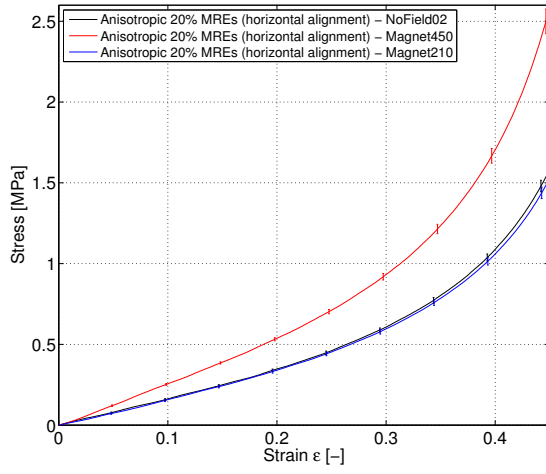
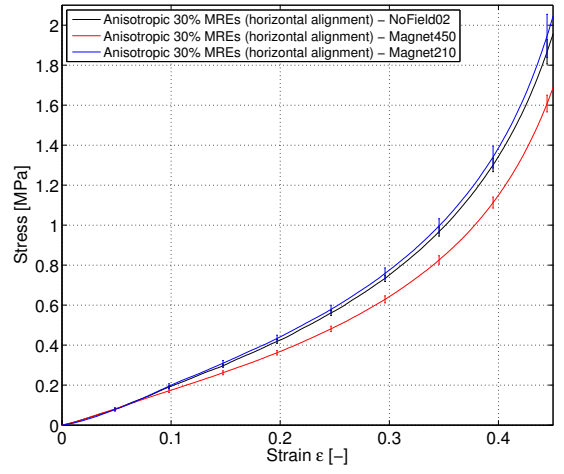
(c) Tangent Moduli E_T (d) Tangent Modulus E_T (e) Relative MR Effect E_M/E_0 (f) Relative MR Effect E_M/E_0

Figure E.4: Experimental results of (left) anisotropic 30% MREs with vertical particle alignment, and (right) anisotropic 10% MREs with horizontal particle alignment tested in uniaxial compression. Stress-strain curves, the tangent moduli, and the relative MR effects are presented.



(a) Stress-Strain curves



(b) Stress-Strain curves

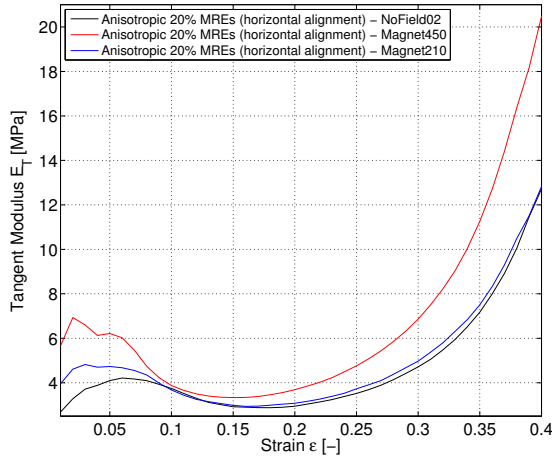
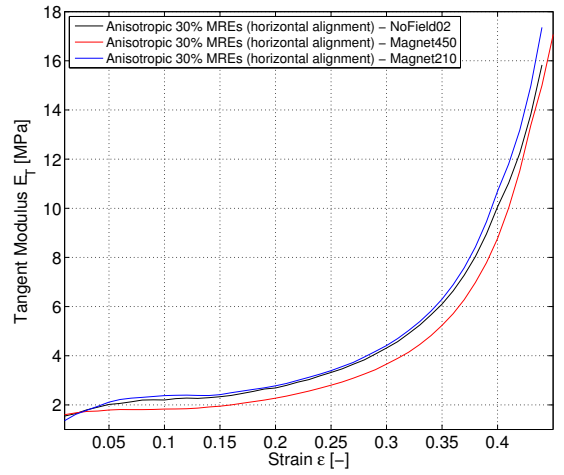
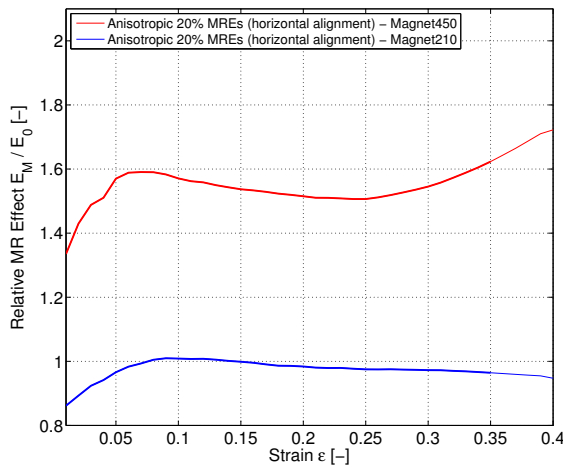
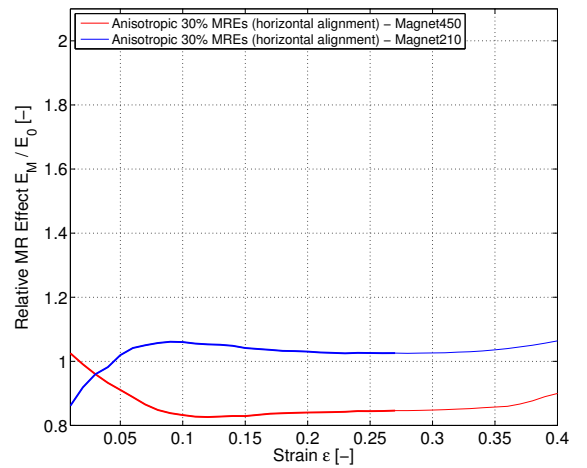
(c) Tangent Moduli E_T (d) Tangent Modulus E_T (e) Relative MR Effect E_M/E_0 (f) Relative MR Effect E_M/E_0

Figure E.5: Experimental results of (left) anisotropic 20% MREs, and (right) anisotropic 30% MREs, both with horizontal particle alignment tested in uniaxial compression. Stress-strain curves, the tangent moduli, and the relative MR effects are presented.

E.2 Uniaxial tension tests

The uniaxial tension tests were described in Section 5.3. Tests without and with applied magnetic inductions of 289.2 mT (*Magnet63*), 251.2 mT (*Magnet73*), and 220.6 mT (*Magnet89*) were performed. Pure rubber, isotropic, and anisotropic MREs with vertically and horizontally aligned particles, containing 10% to 30% volume particle concentration, were stretched up to two different displacements (Table 5.7). Three samples of each type, and up to each preconditioning level were tested. Mean values and standard deviations of the third loading cycle are shown. Tests without an applied magnetic induction were discussed in Section 5.3.5. The comparison between *NoField01* and *NoField02* stress-strain curves is illustrated in this Appendix. The tangent moduli were used to describe the non-linear behaviour and the different types of MREs were compared. The MR effects were discussed in Section 5.3.6. The stress-strain curves and the tangent moduli comparing the *NoField02* with the magnetic tests of all types of MREs tested up to two different displacement are illustrated in this Appendix. The relative MR effects, calculated with the tangent moduli of 1% stress-strain increments, are presented for each types of MRE.

Comparison of *NoField01* and *NoField02*

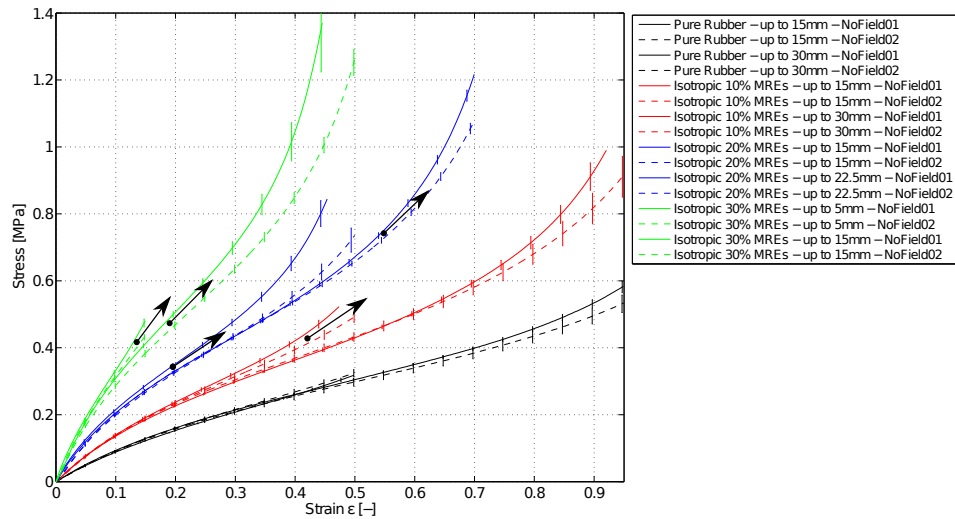


Figure E.6: Comparison between *NoField01* and *NoField02* tension tests. The third loading part of pure rubber and isotropic MREs with 10% to 30% iron content is shown. Each type of MRE is stretched to two different displacements (Table 5.7). The arrows indicate the points of divergence (Table 5.12).

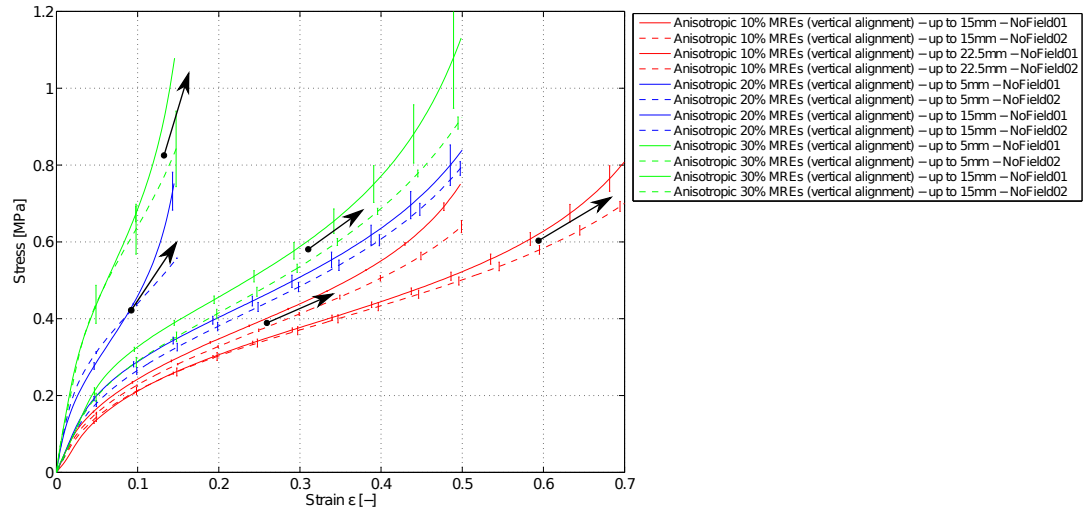


Figure E.7: Comparison between *NoField01* and *NoField02* tension tests. The third loading part of anisotropic MREs with 10% to 30% iron content with vertical particle alignment is shown. Each type of MRE is stretched to two different displacements (Table 5.7). The arrows indicate the points of divergence (Table 5.12).

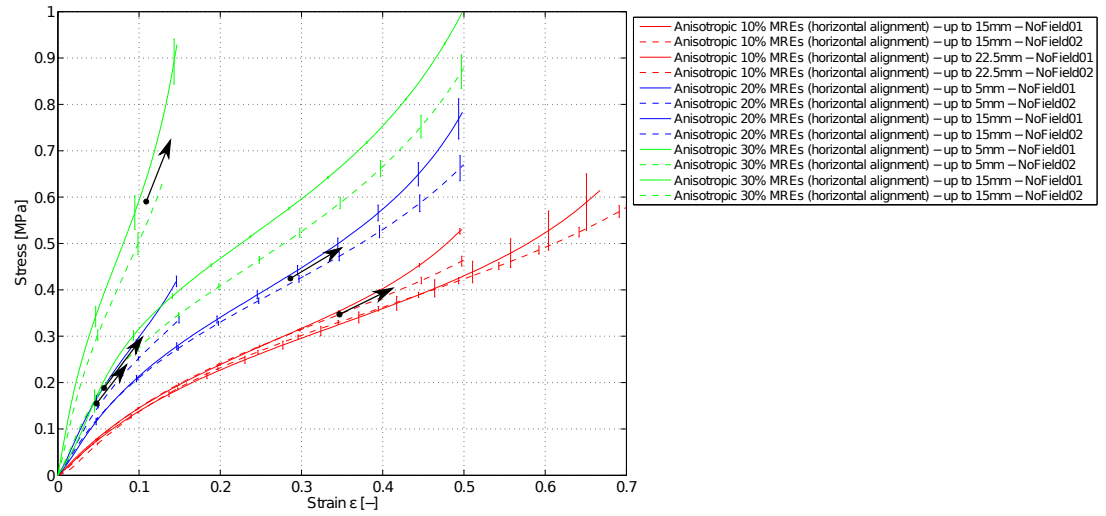


Figure E.8: Comparison between *NoField01* and *NoField02* tension tests. The third loading part of anisotropic MREs with 10% to 30% iron content with horizontal particle alignment is shown. Each type of MRE is stretched to two different displacements (Table 5.7). The arrows indicate the points of divergence (Table 5.12).

Comparison of different magnetic field strengths

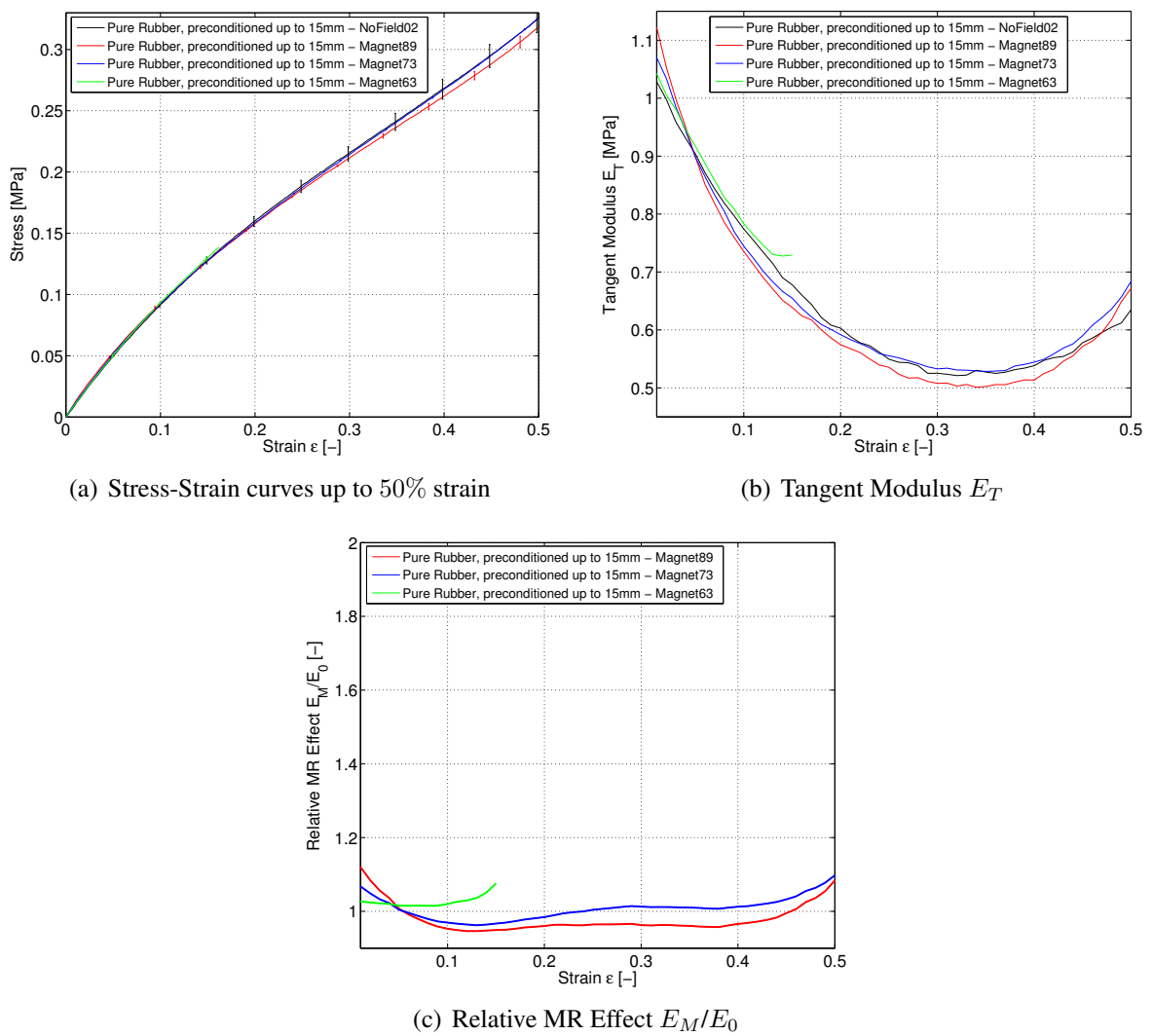
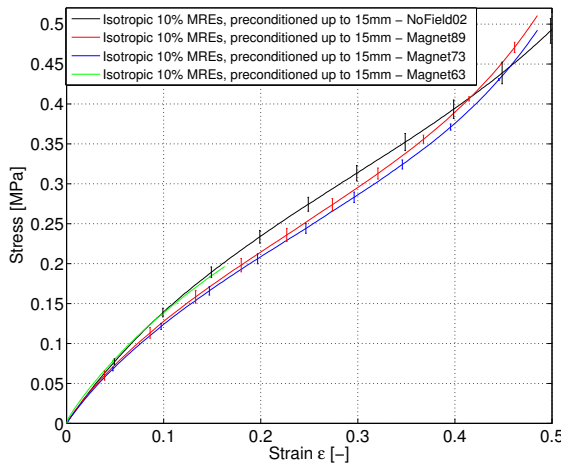
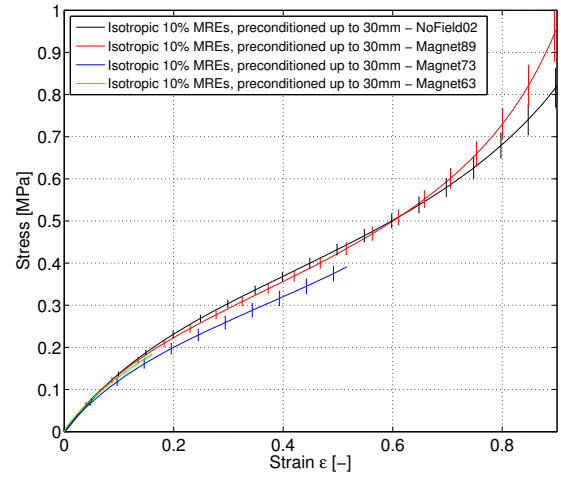


Figure E.9: Pure Rubber, preconditioned up to 15 mm (50% strain) in uniaxial tension. Stress-strain curves, the tangent moduli, and the relative MR effects are presented.



(a) Stress-Strain curves up to 50% strain



(b) Stress-Strain curves up to 100% strain

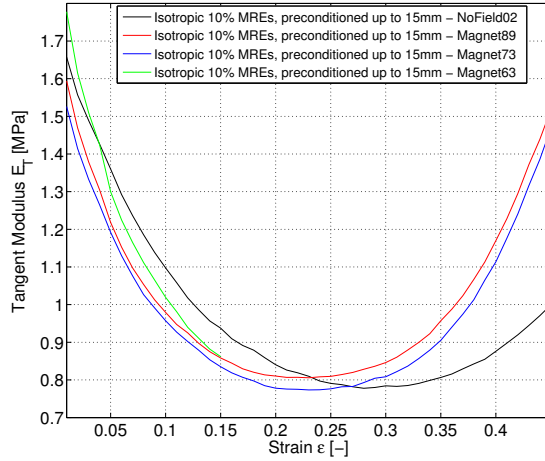
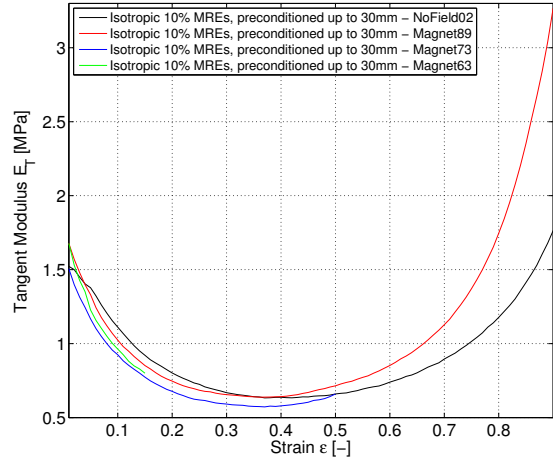
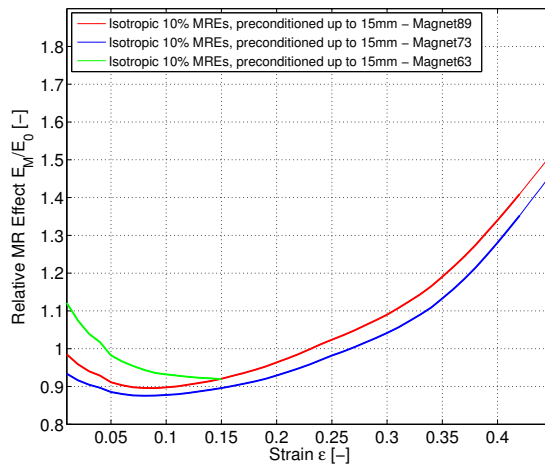
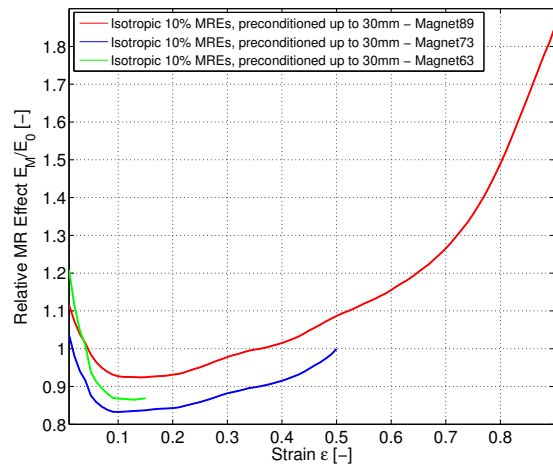
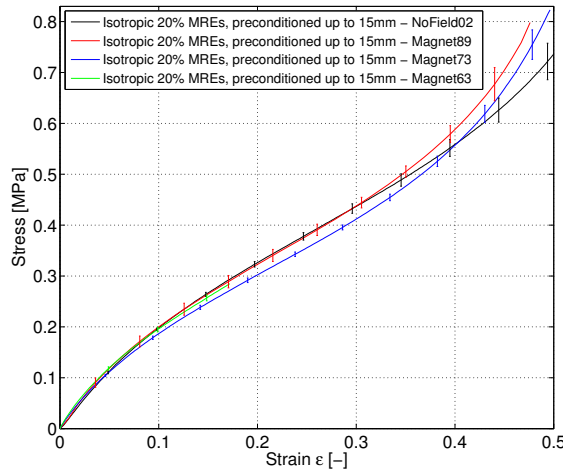
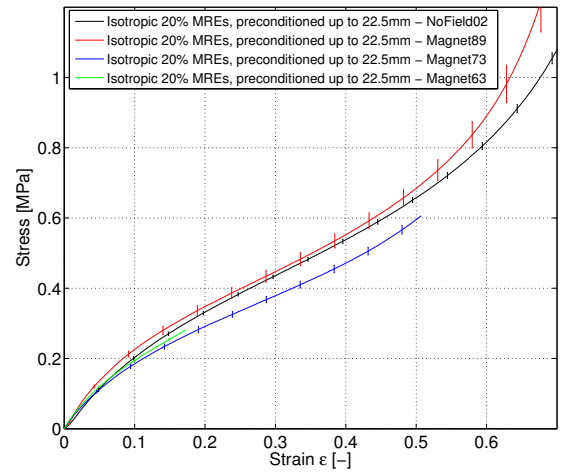
(c) Tangent Modulus E_T (d) Tangent Modulus E_T (e) Relative MR Effect E_M/E_0 (f) Relative MR Effect E_M/E_0

Figure E.10: Isotropic MREs with 10% CIP content tested in uniaxial tension: (left) preconditioned up to 15 mm (50% strain), (right) up to 30 mm (100% strain). Stress-strain curves, the tangent moduli, and the relative MR effects are presented.



(a) Stress-Strain curves up to 50% strain



(b) Stress-Strain curves up to 75% strain

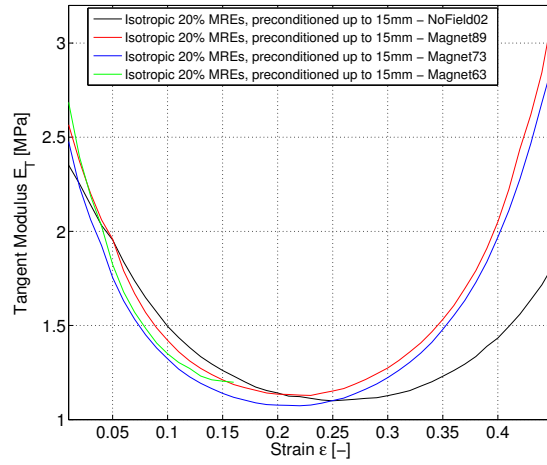
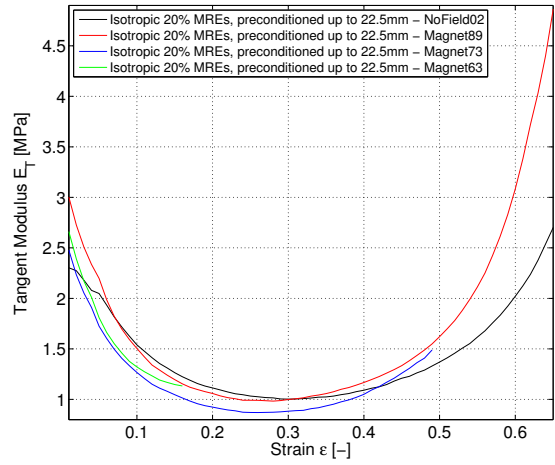
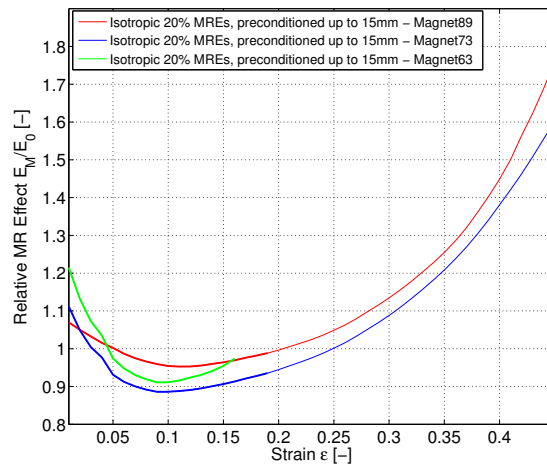
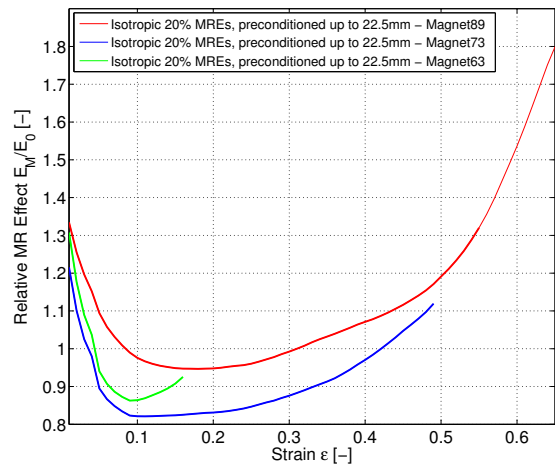
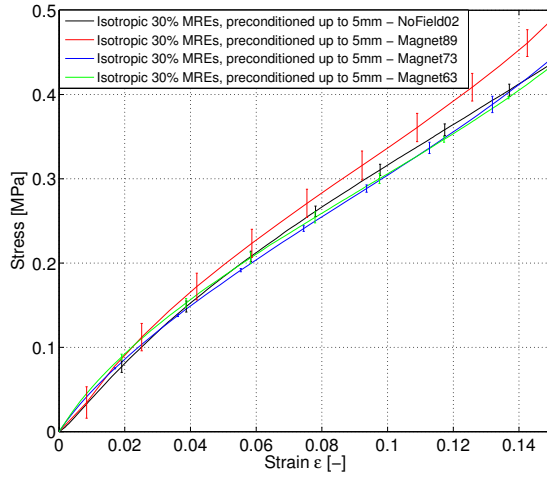
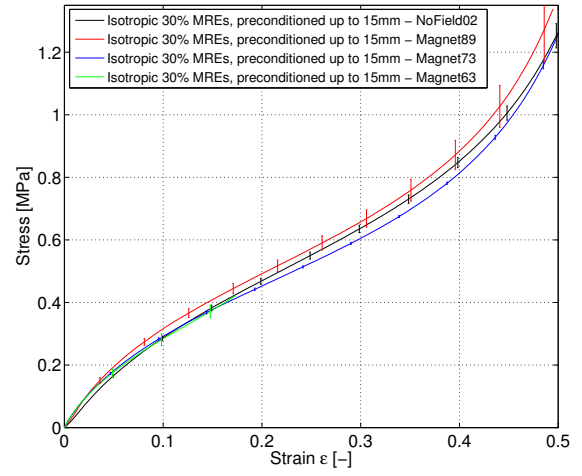
(c) Tangent Modulus E_T (d) Tangent Modulus E_T (e) Relative MR Effect E_M/E_0 (f) Relative MR Effect E_M/E_0

Figure E.11: Isotropic MREs with 20% CIP content tested in uniaxial tension: (left) preconditioned up to 15 mm (50% strain), (right) up to 22.5 mm (75% strain). Stress-strain curves, the tangent moduli, and the relative MR effects are presented.



(a) Stress-Strain curves up to 15% strain



(b) Stress-Strain curves up to 50% strain

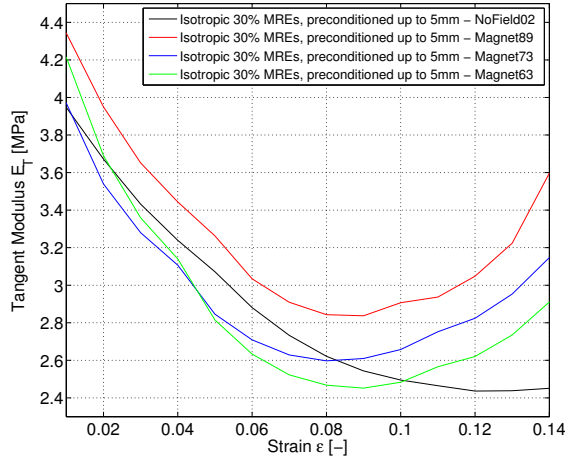
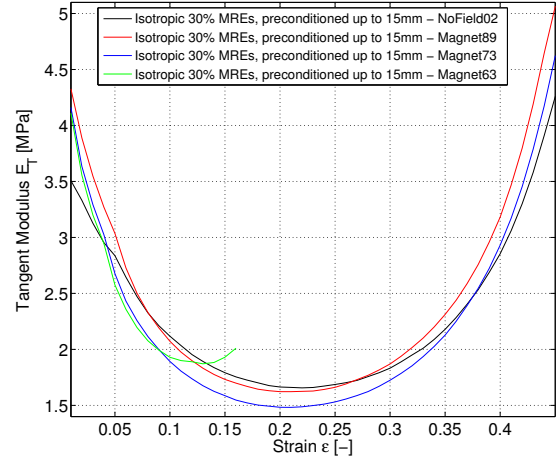
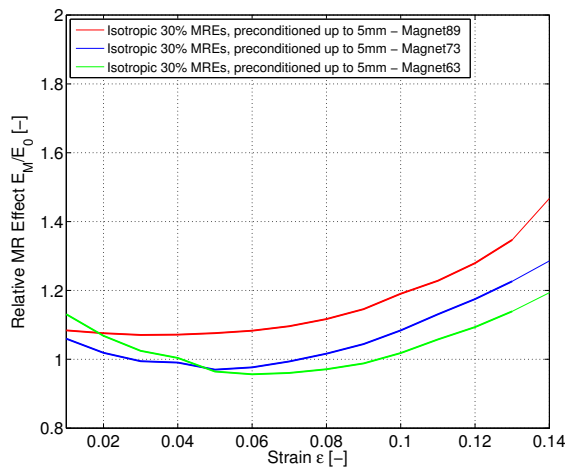
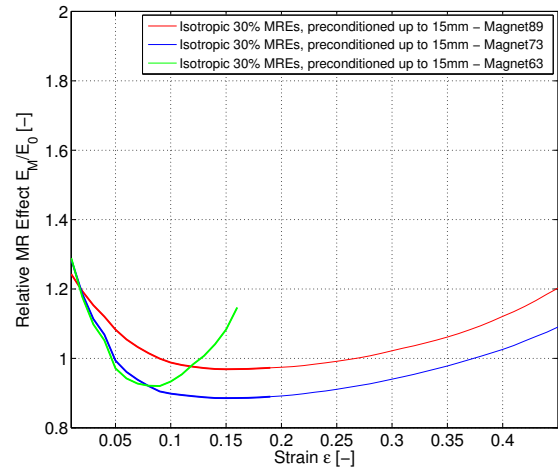
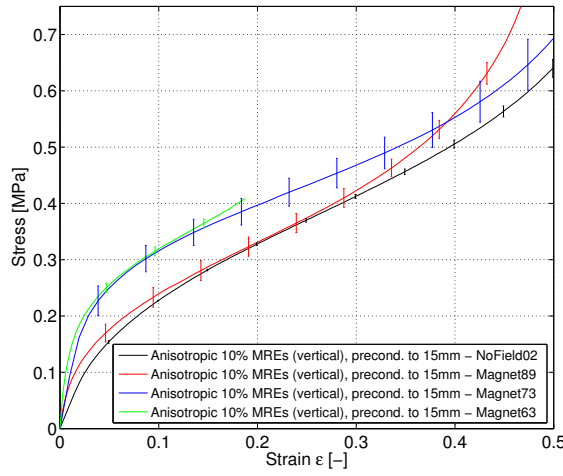
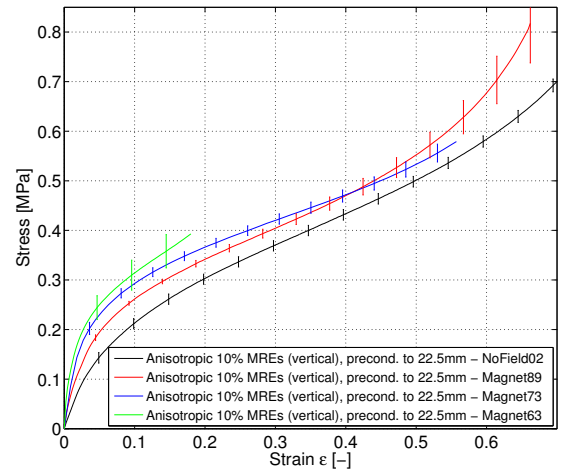
(c) Tangent Modulus E_T (d) Tangent Modulus E_T (e) Relative MR Effect E_M/E_0 (f) Relative MR Effect E_M/E_0

Figure E.12: Isotropic MREs with 30% CIP content tested in uniaxial tension: (left) preconditioned up to 5 mm (15% strain), (right) up to 15 mm (50% strain). Stress-strain curves, the tangent moduli, and the relative MR effects are presented.



(a) Stress-Strain curves up to 50% strain



(b) Stress-Strain curves up to 75% strain

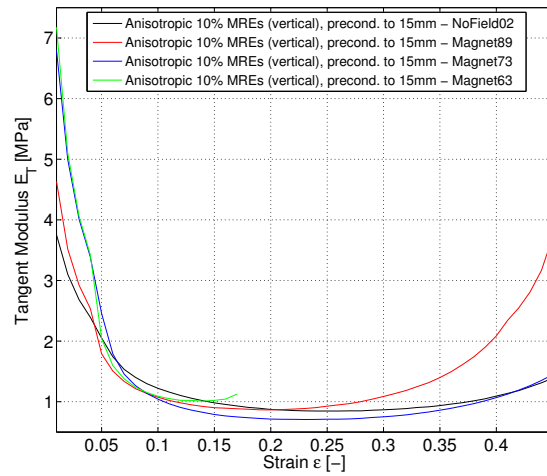
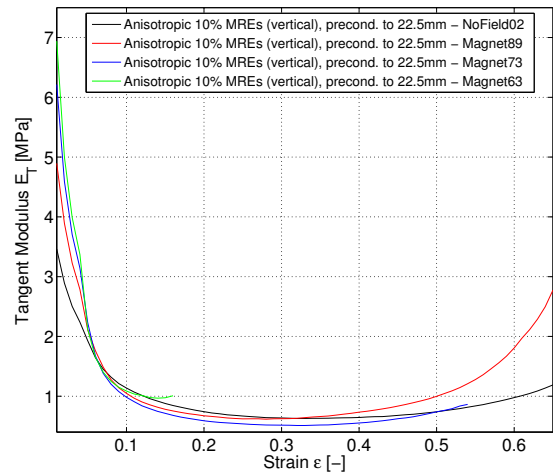
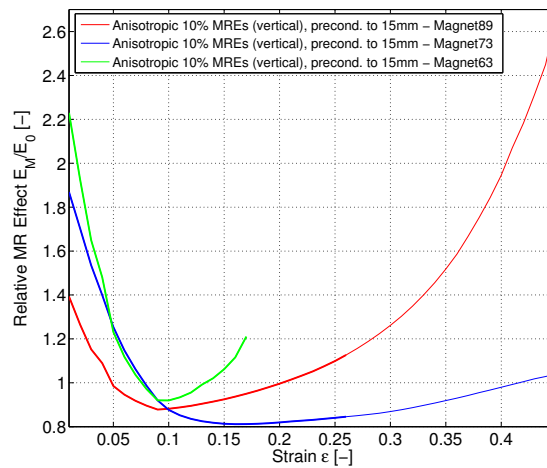
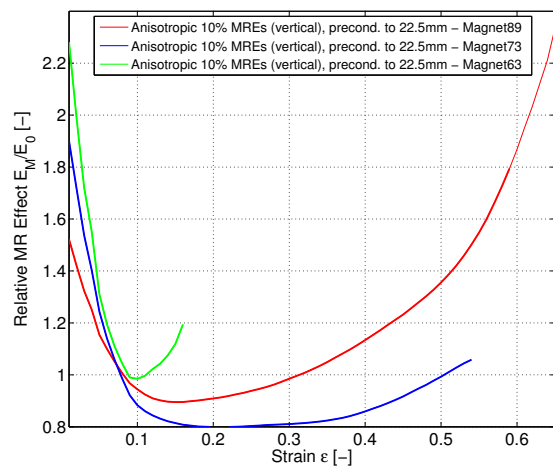
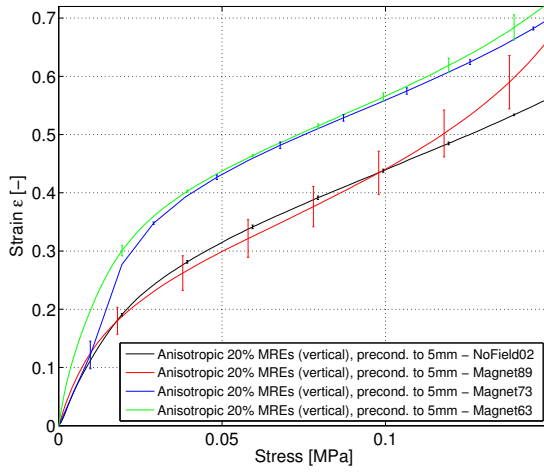
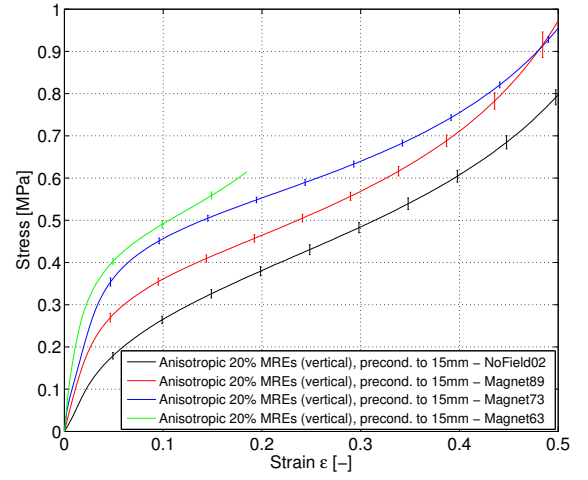
(c) Tangent Modulus E_T (d) Tangent Modulus E_T (e) Relative MR Effect E_M/E_0 (f) Relative MR Effect E_M/E_0

Figure E.13: Anisotropic MREs with vertical particle alignment with 10% CIP content tested in uniaxial tension: (left) preconditioned up to 15 mm (50% strain), (right) up to 22.5 mm (75% strain). Stress-strain curves, the tangent moduli, and the relative MR effects are presented.



(a) Stress-Strain curves up to 15% strain



(b) Stress-Strain curves up to 50% strain

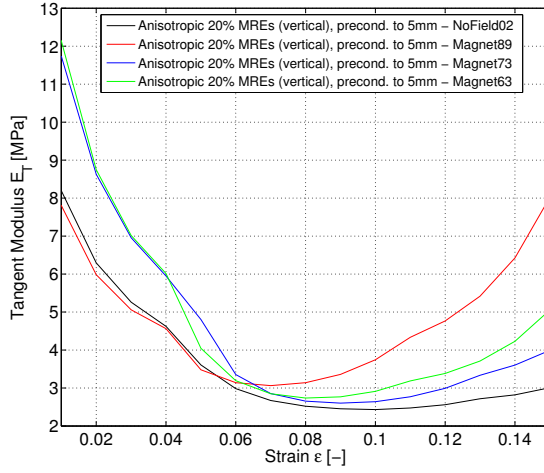
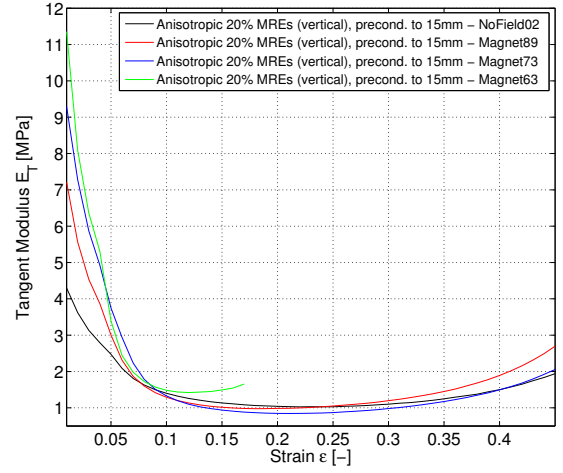
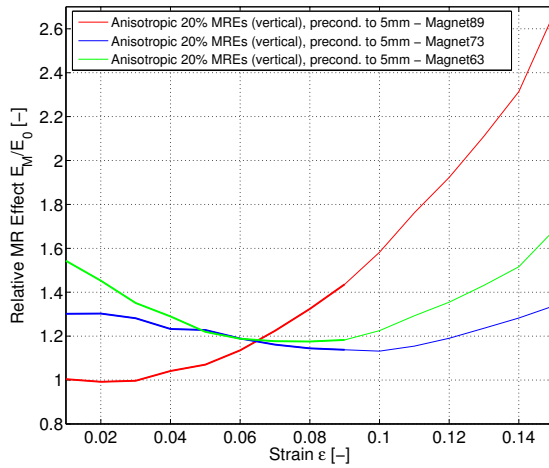
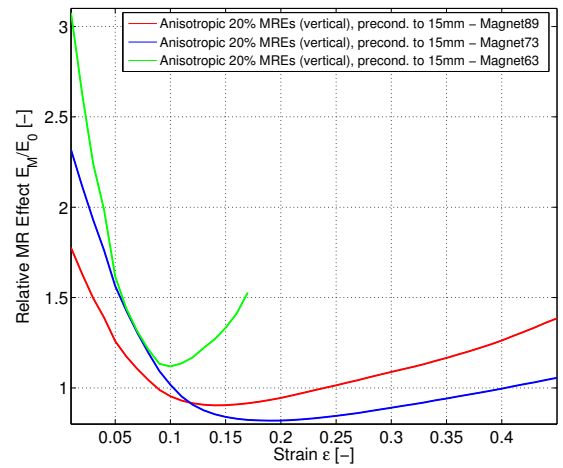
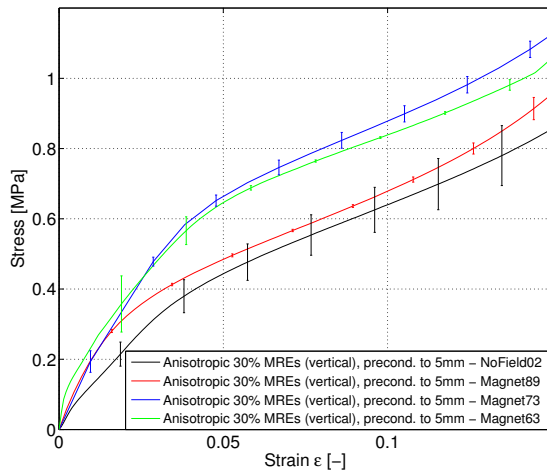
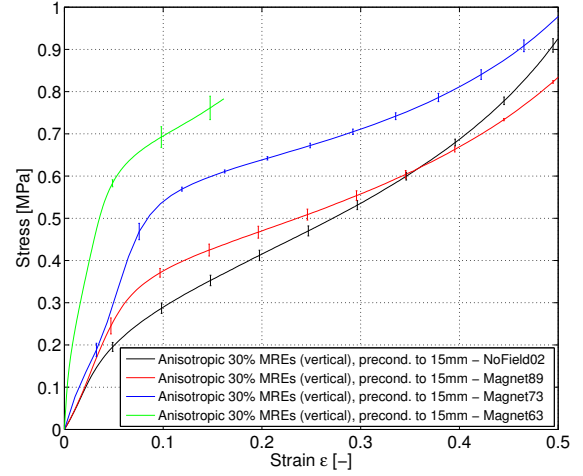
(c) Tangent Modulus E_T (d) Tangent Modulus E_T (e) Relative MR Effect E_M/E_0 (f) Relative MR Effect E_M/E_0

Figure E.14: Anisotropic MREs with vertical particle alignment with 20% CIP content tested in uniaxial tension: (left) preconditioned up to 5 mm (15% strain), (right) up to 15 mm (50% strain). Stress-strain curves, the tangent moduli, and the relative MR effects are presented.



(a) Stress-Strain curves up to 15% strain



(b) Stress-Strain curves up to 50% strain

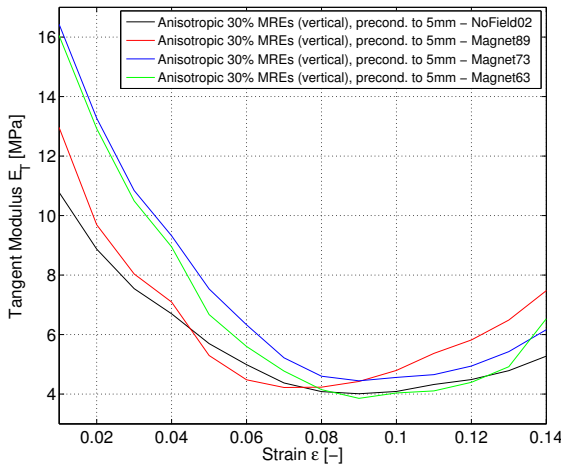
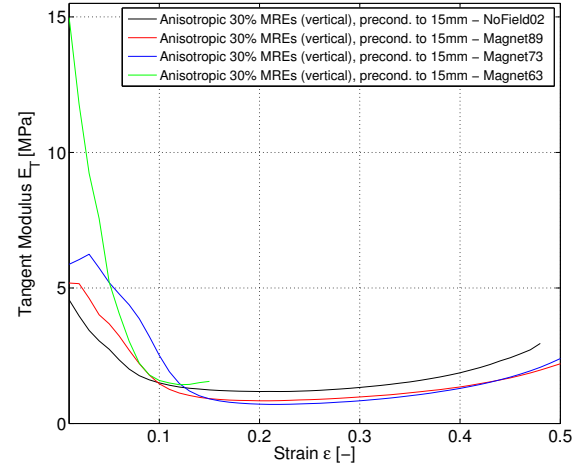
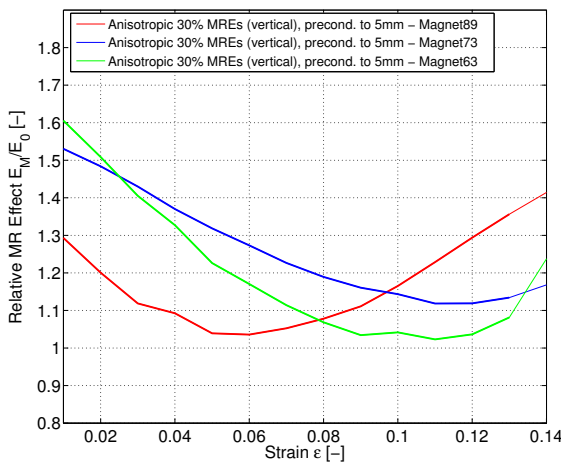
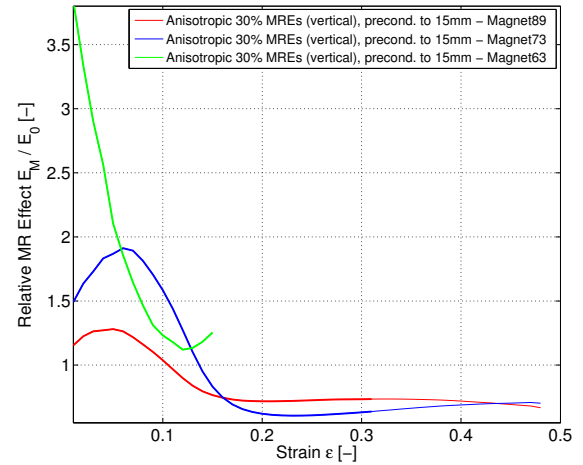
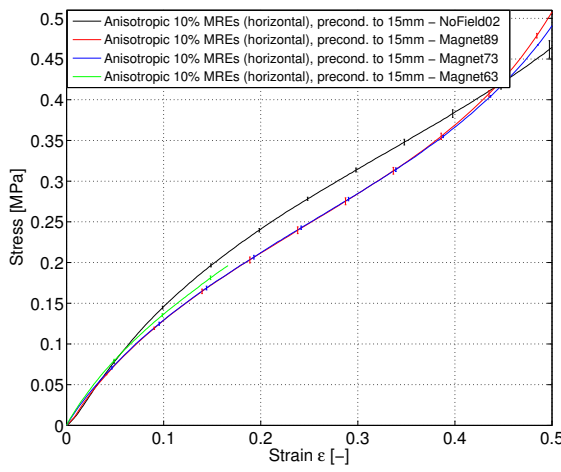
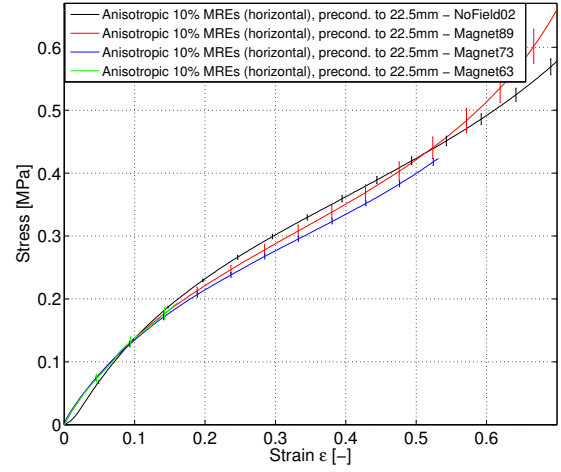
(c) Tangent Modulus E_T (d) Tangent Modulus E_T (e) Relative MR Effect E_M/E_0 (f) Relative MR Effect E_M/E_0

Figure E.15: Anisotropic MREs with vertical particle alignment with 30% CIP content tested in uniaxial tension: (left) preconditioned up to 5 mm (15% strain), (right) up to 15 mm (50% strain). Stress-strain curves, the tangent moduli, and the relative MR effects are presented.



(a) Stress-Strain curves up to 50% strain



(b) Stress-Strain curves up to 75% strain

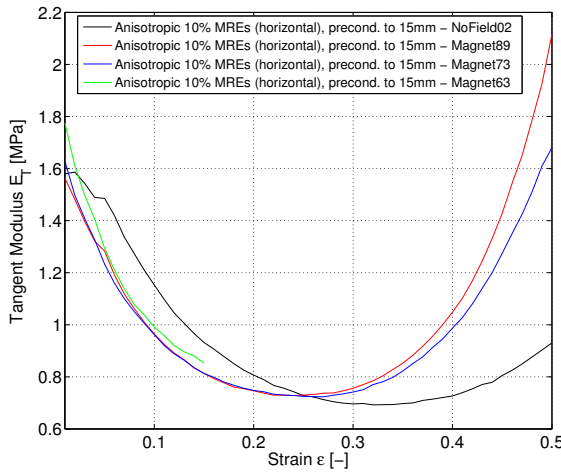
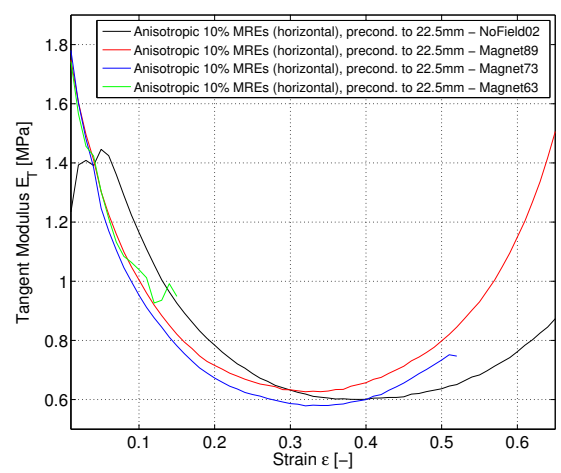
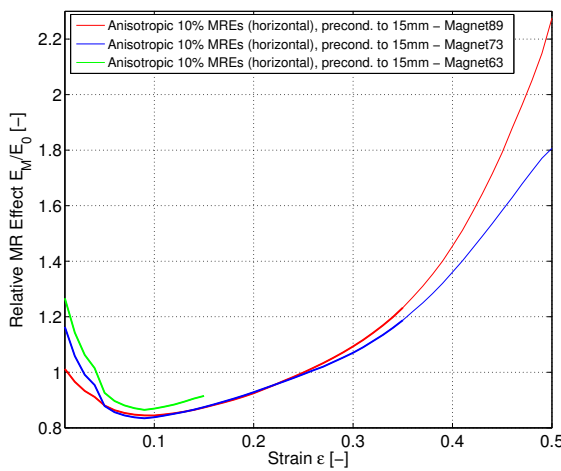
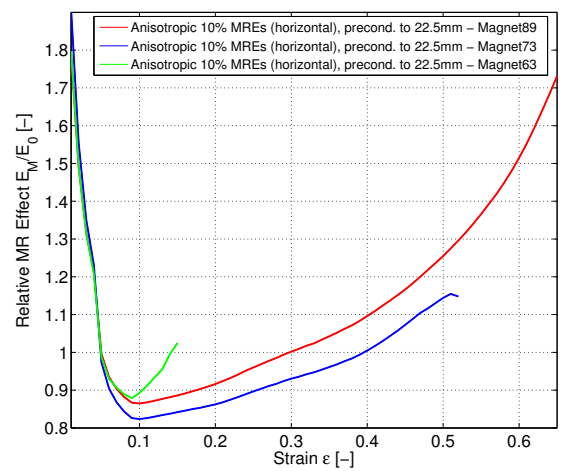
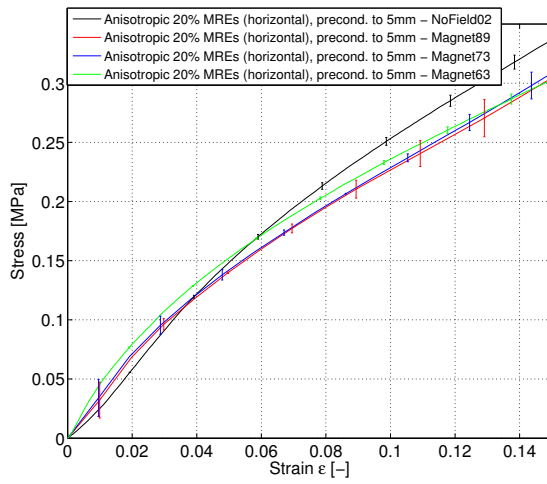
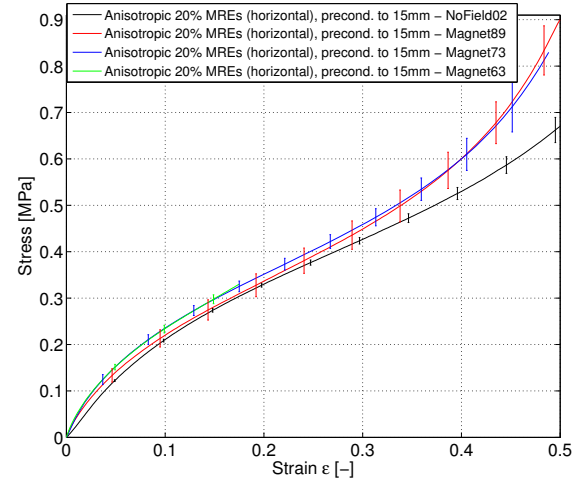
(c) Tangent Modulus E_T (d) Tangent Modulus E_T (e) Relative MR Effect E_M/E_0 (f) Relative MR Effect E_M/E_0

Figure E.16: Anisotropic MREs with horizontal particle alignment with 10% CIP content tested in uniaxial tension: (left) preconditioned up to 15 mm (50% strain), (right) up to 22.5 mm (75% strain). Stress-strain curves, the tangent moduli, and the relative MR effects are presented.



(a) Stress-Strain curves up to 15% strain



(b) Stress-Strain curves up to 50% strain

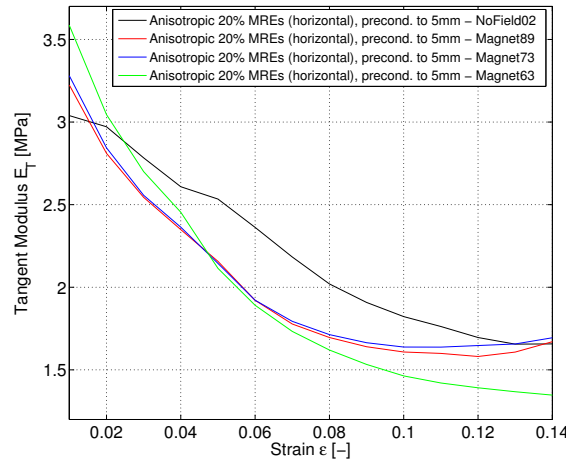
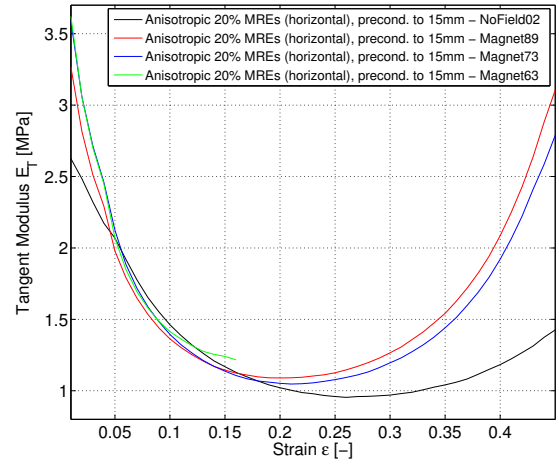
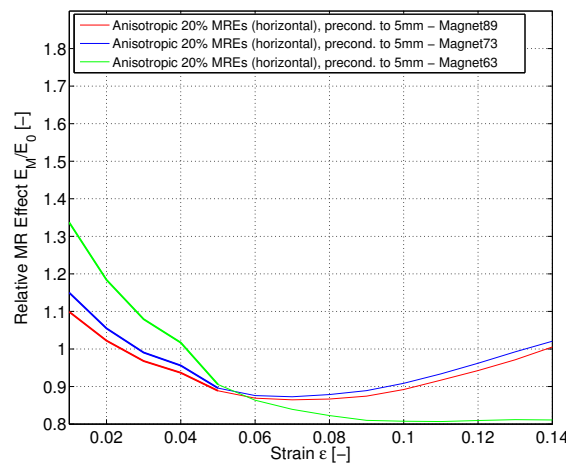
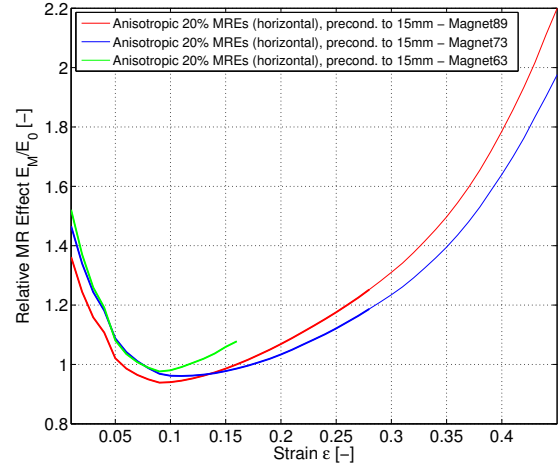
(c) Tangent Modulus E_T (d) Tangent Modulus E_T (e) Relative MR Effect E_M/E_0 (f) Relative MR Effect E_M/E_0

Figure E.17: Anisotropic MREs with horizontal particle alignment with 20% CIP content tested in uniaxial tension: (left) preconditioned up to 5 mm (15% strain), (right) up to 15 mm (50% strain). Stress-strain curves, the tangent moduli, and the relative MR effects are presented.

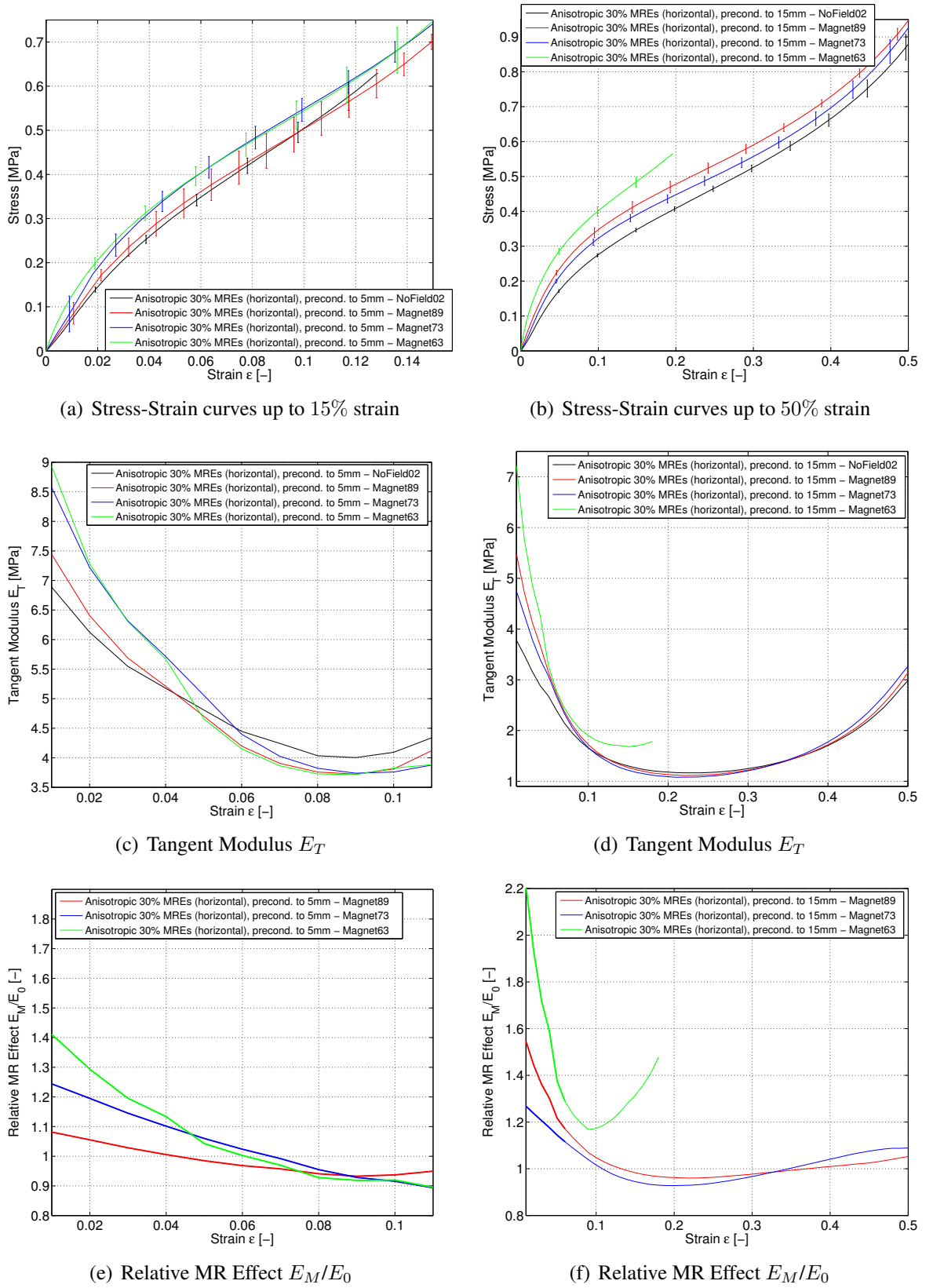


Figure E.18: Anisotropic MREs with horizontal particle alignment with 30% CIP content tested in uniaxial tension: (left) preconditioned up to 5 mm (15% strain), (right) up to 15 mm (50% strain). Stress-strain curves, the tangent moduli, and the relative MR effects are presented.

E.3 Pure shear tests

Pure shear tests were described in Section 5.4. Tests without and with an applied magnetic induction of 290 mT (*Magnet53*) were performed. Pure rubber, isotropic, and anisotropic MREs with vertically and horizontally aligned particles, containing 10% to 30% volume particle concentration, were stretched up to two different displacements (5.17). Three samples of each type, and up to each preconditioning level were tested, and mean values and standard deviations of the third loading cycle are shown. The tests without an applied magnetic induction were discussed in Section 5.4.4. The comparison between *NoField01* and *NoField02* stress-strain curves is illustrated in this Appendix. The tangent moduli, E_T , were used to describe the non-linear behaviour of different types of MREs. The MR effects were discussed in Section 5.4.5. The stress-strain curves and the tangent moduli comparing the *NoField02* with the magnetic tests of all types of MREs tested up to two different displacement are illustrated in this Appendix. The relative MR effects, calculated with the tangent moduli of 1% stress-strain increments, are presented for each types of MRE.

Comparison of *NoField01* and *NoField02*

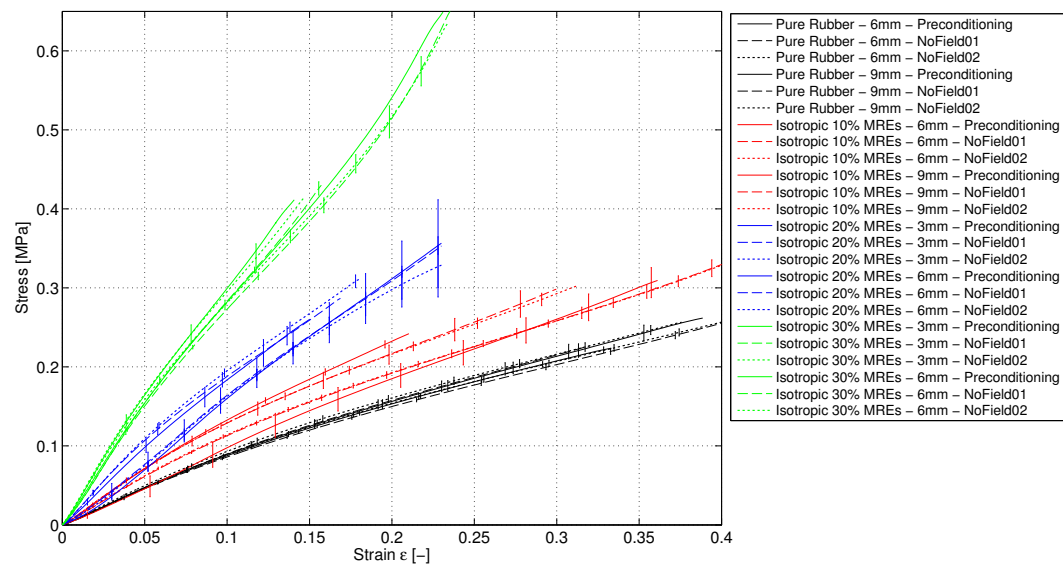


Figure E.19: Comparison between *Preconditioning*, *NoField01* and *NoField02* pure shear tests. The third loading part of pure rubber and isotropic MREs with 10% to 30% iron content is shown. Each type of MRE is stretched to two different displacements as listed in Table 5.17.

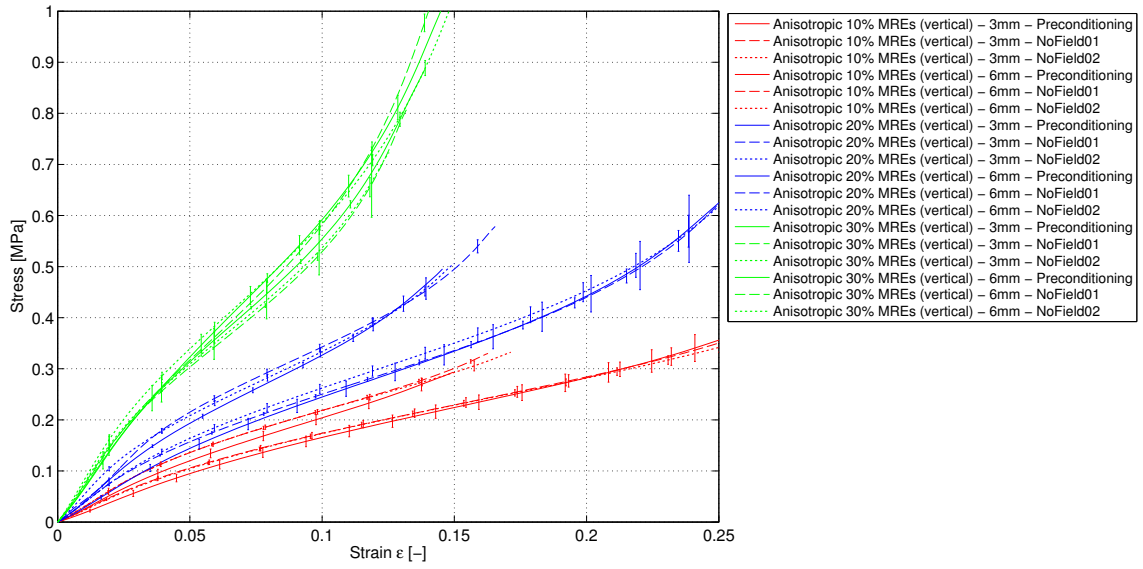


Figure E.20: Comparison between *Preconditioning*, *NoField01* and *NoField02* pure shear tests. The third loading part of anisotropic MREs with 10% to 30% vertical aligned iron particles is shown. Each type of MRE is stretched to two different displacements as listed in Table 5.17.

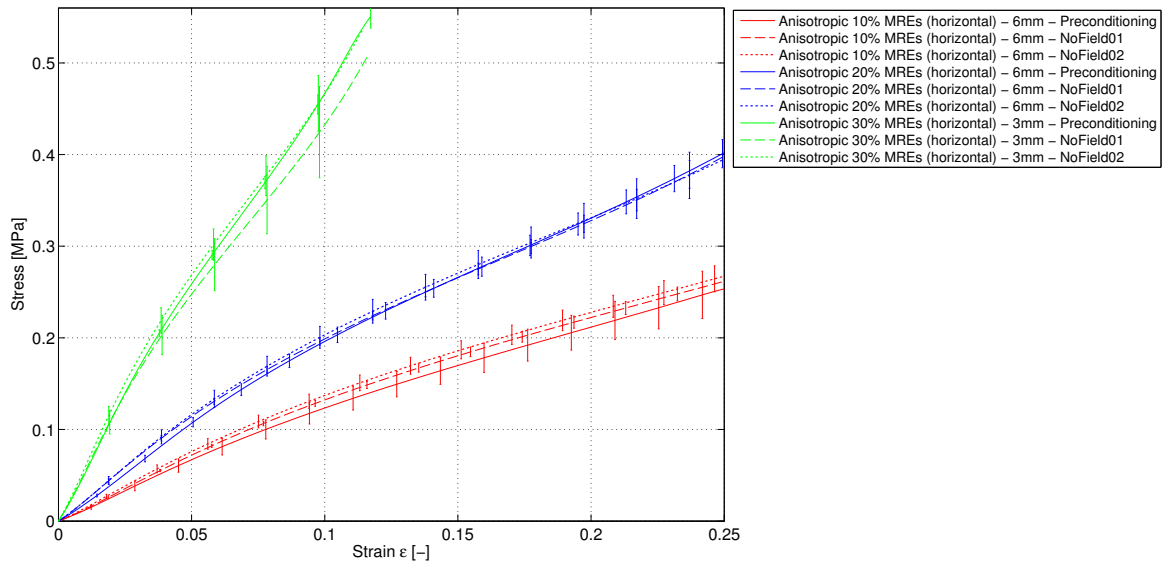


Figure E.21: Comparison between *Preconditioning*, *NoField01*, and *NoField02* pure shear tests. The third loading part of anisotropic MREs with 10% to 30% horizontal aligned iron particles is shown. Each type of MRE is stretched to two different displacements as listed in Table 5.17.

Comparison of different magnetic field strengths

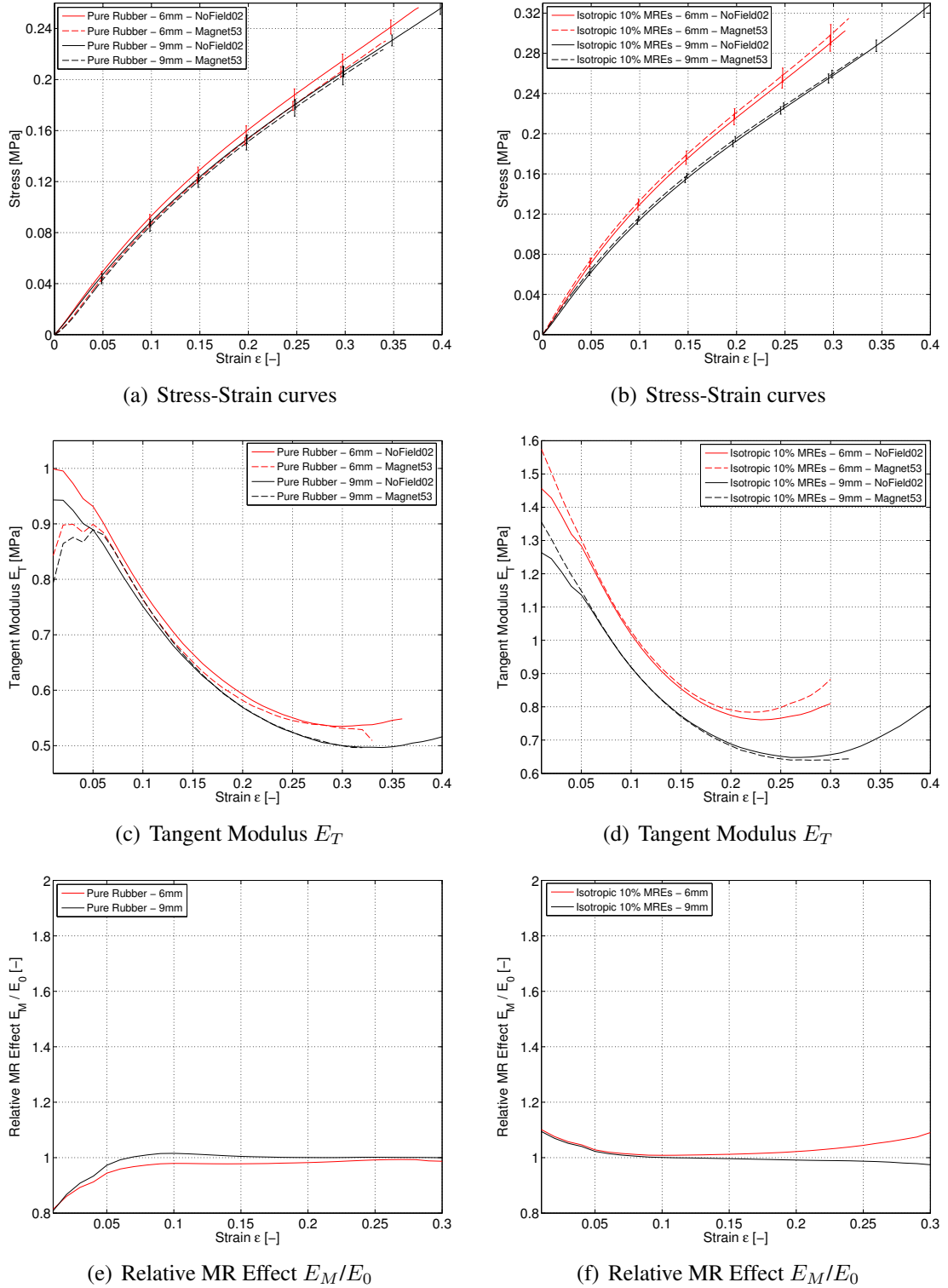
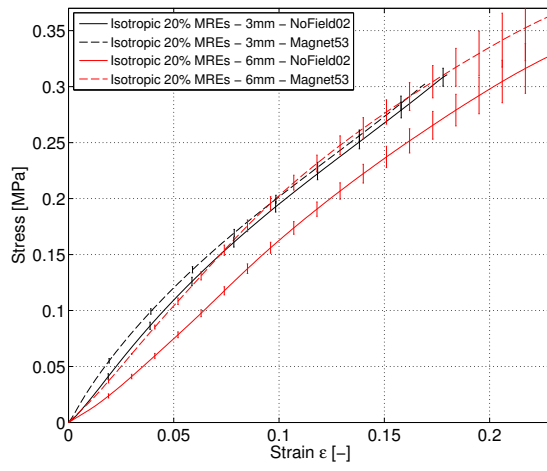
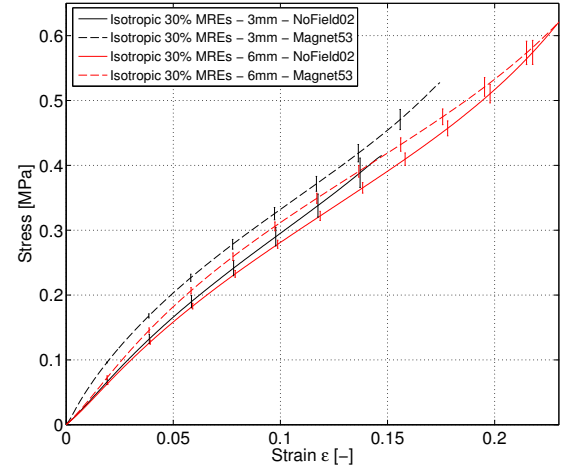


Figure E.22: Pure rubber and isotropic MREs with 10% CIP content tested in pure shear: (left) Pure rubber preconditioned up to 6 mm and 9 mm, (right) isotropic 10% MREs preconditioned up to 6 mm and 9 mm. Stress-strain curves, the tangent moduli, and the relative MR effects are presented.



(a) Stress-Strain curves



(b) Stress-Strain curves

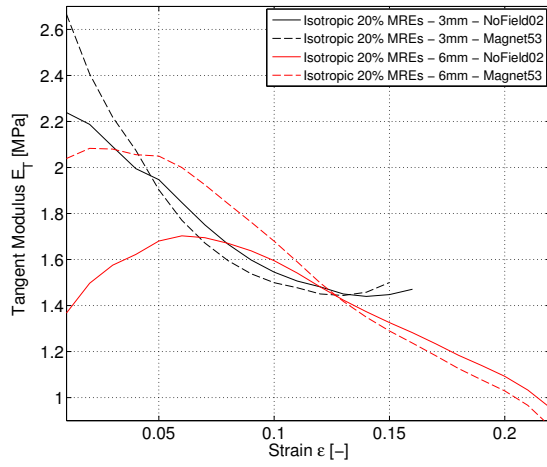
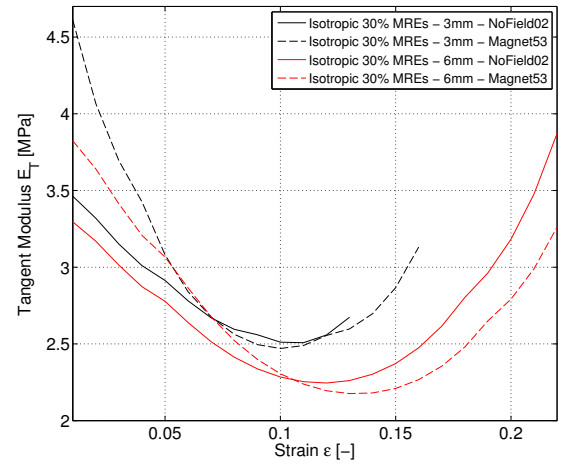
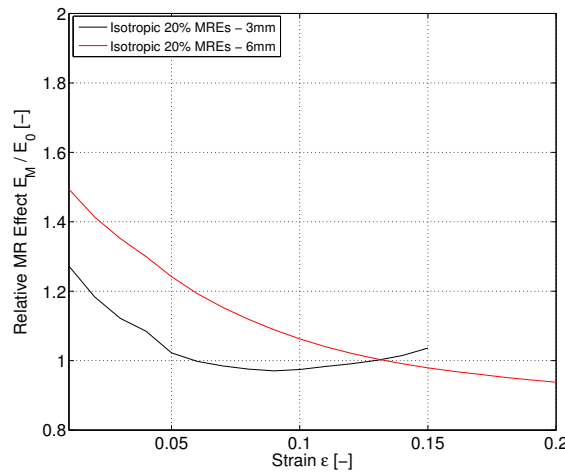
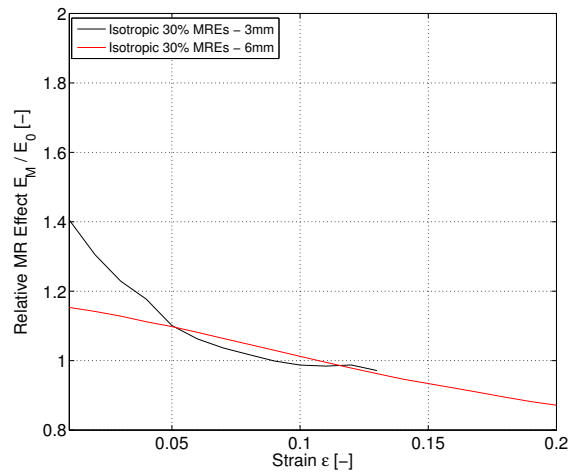
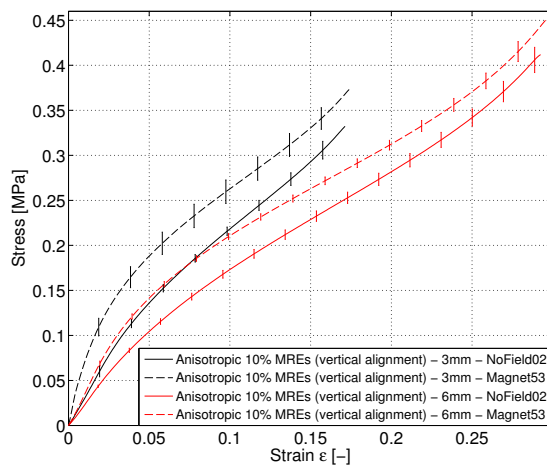
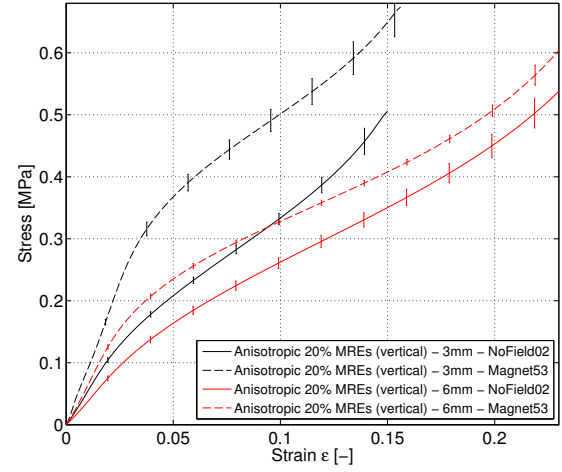
(c) Tangent Modulus E_T (d) Tangent Modulus E_T (e) Relative MR Effect E_M/E_0 (f) Relative MR Effect E_M/E_0

Figure E.23: Isotropic MREs with 20% and 30% CIP content tested in pure shear: (left) Isotropic 20% MREs preconditioned up to 3 mm and 6 mm, (right) isotropic 30% MREs preconditioned up to 3 mm and 6 mm. Stress-strain curves, the tangent moduli, and the relative MR effects are presented.



(a) Stress-Strain curves



(b) Stress-Strain curves

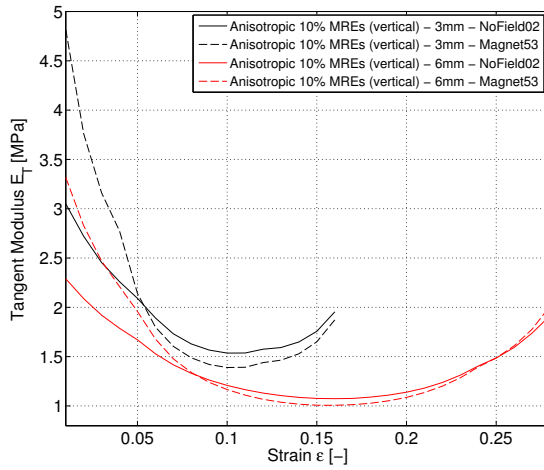
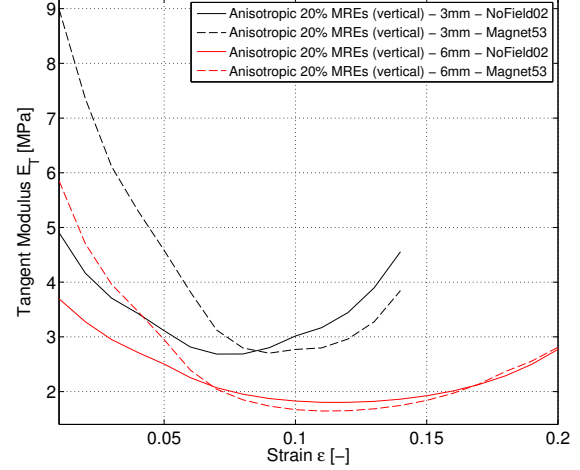
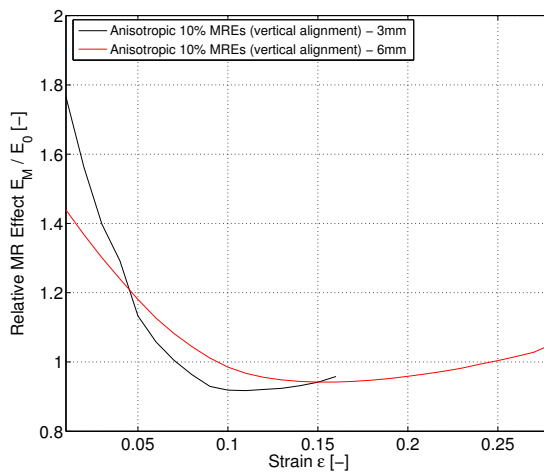
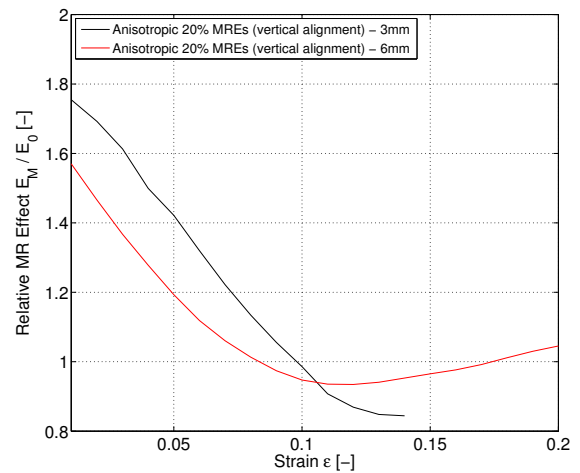
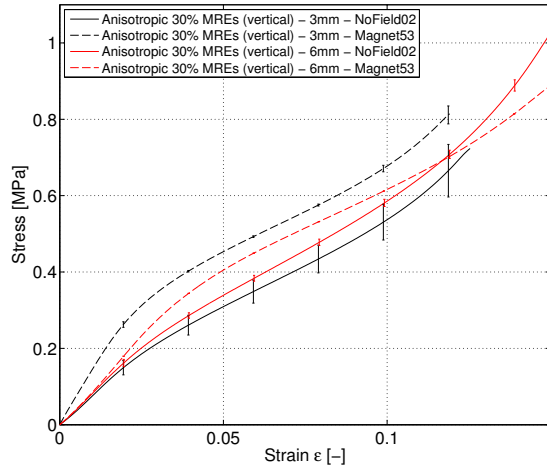
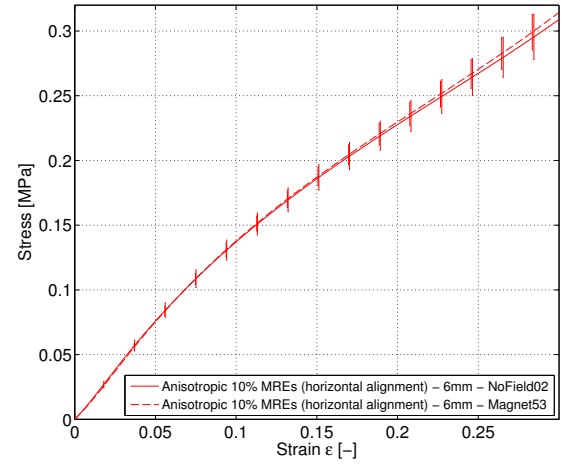
(c) Tangent Modulus E_T (d) Tangent Modulus E_T (e) Relative MR Effect E_M/E_0 (f) Relative MR Effect E_M/E_0

Figure E.24: Anisotropic MREs with 10% and 20% vertically aligned particles tested in pure shear: (left) Anisotropic 10% MREs (vertical) preconditioned up to 3 mm and 6 mm, (right) anisotropic 20% MREs (vertical) preconditioned up to 3 mm and 6 mm. Stress-strain curves, the tangent moduli, and the relative MR effects are presented.



(a) Stress-Strain curves



(b) Stress-Strain curves

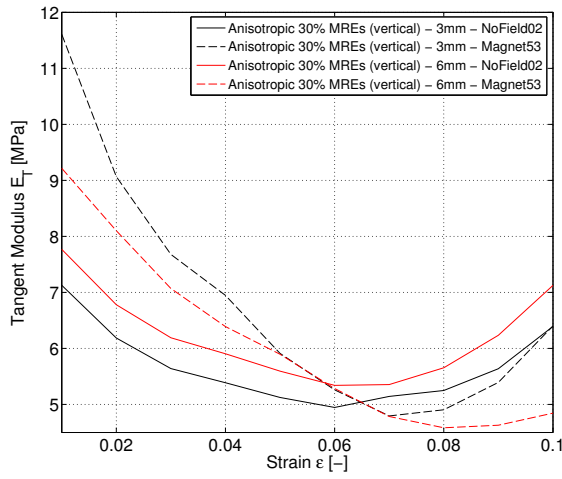
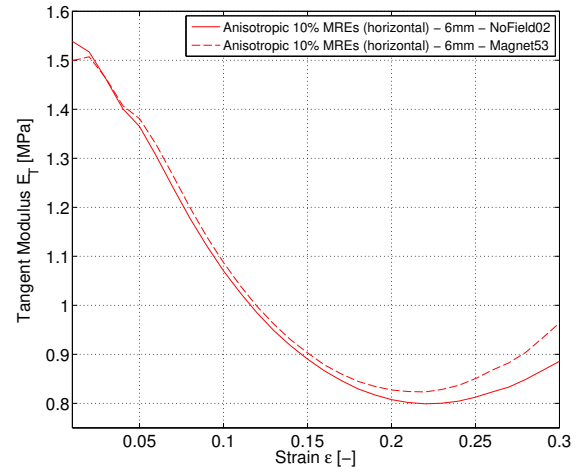
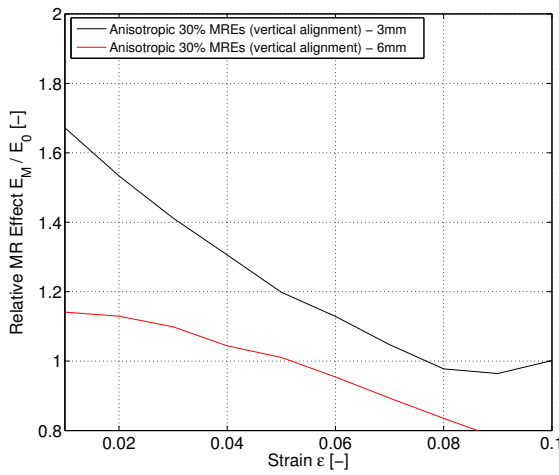
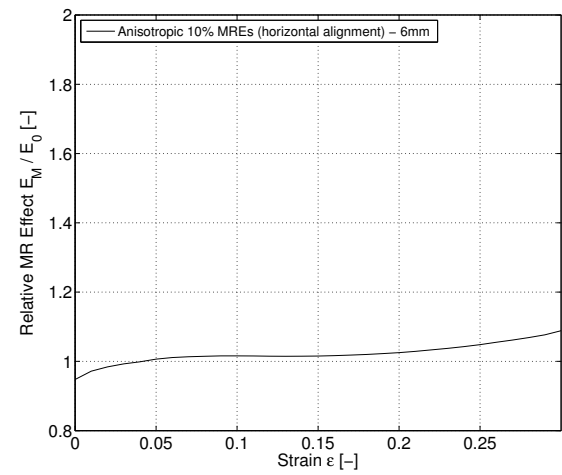
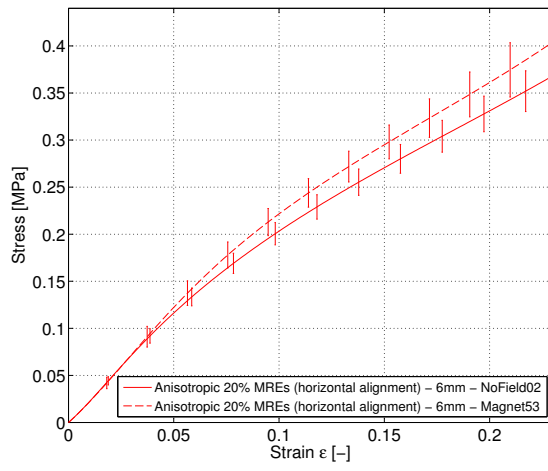
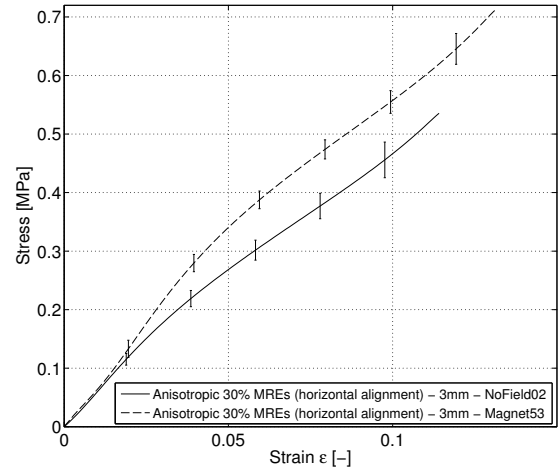
(c) Tangent Modulus E_T (d) Tangent Modulus E_T (e) Relative MR Effect E_M/E_0 (f) Relative MR Effect E_M/E_0

Figure E.25: Anisotropic MREs with 30% vertically and 10% horizontally aligned particles tested in pure shear: (left) Anisotropic 30% MREs (vertical) preconditioned up to 3 mm and 6 mm, (right) anisotropic 10% MREs (horizontal) preconditioned up to 6 mm. Stress-strain curves, the tangent moduli, and the relative MR effects are presented.



(a) Stress-Strain curves



(b) Stress-Strain curves

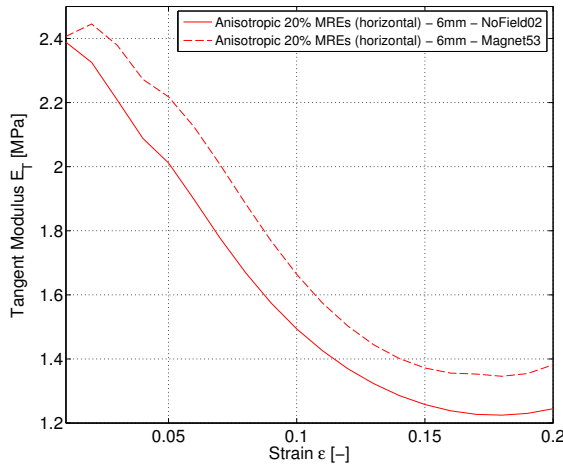
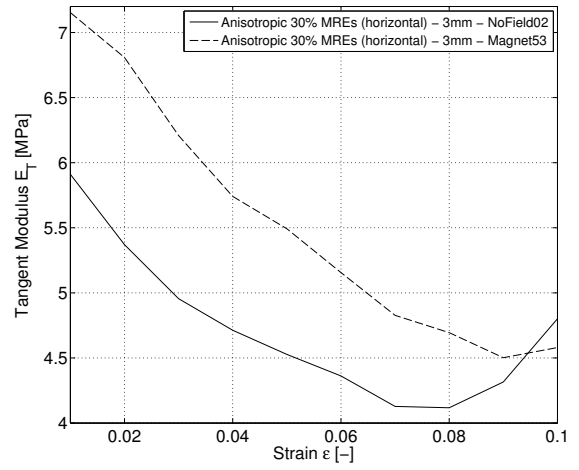
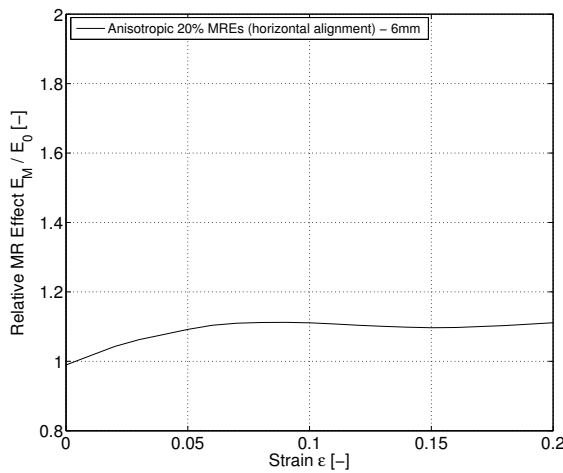
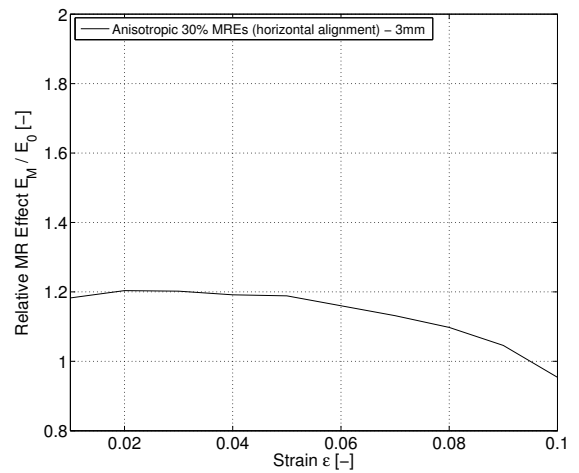
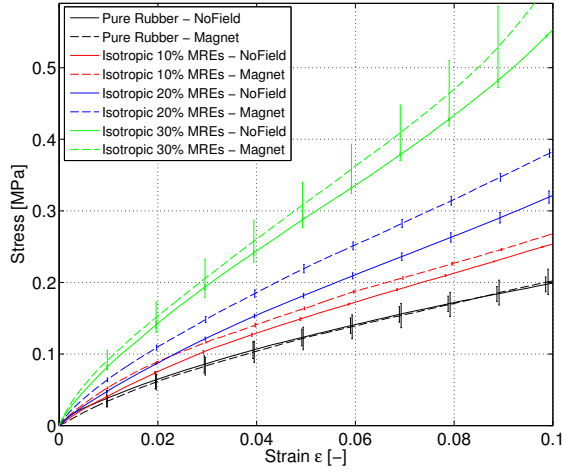
(c) Tangent Modulus E_T (d) Tangent Modulus E_T (e) Relative MR Effect E_M/E_0 (f) Relative MR Effect E_M/E_0

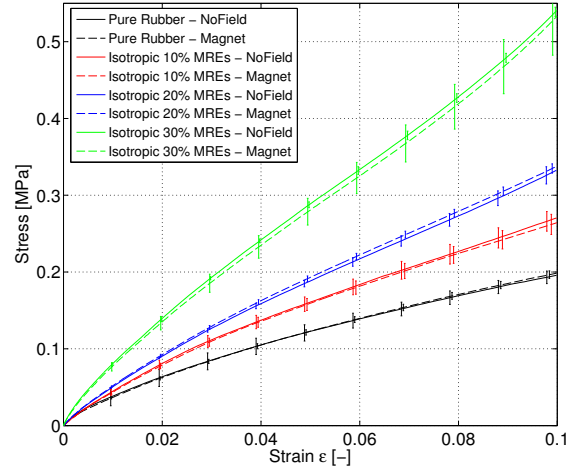
Figure E.26: Anisotropic MREs with 20% and 30% horizontally aligned particles tested in pure shear: (left) Anisotropic 20% MREs (horizontal) preconditioned up to 6 mm, (right) anisotropic 30% MREs (horizontal) preconditioned up to 3 mm. Stress-strain curves, the tangent moduli, and the relative MR effects are presented.

E.4 Equi-biaxial tension tests

Equi-biaxial tension tests were described in Section 5.5. Tests without and with an applied magnetic induction of 67.5 mT were performed. Pure rubber, isotropic, and anisotropic MREs with their particle alignment both parallel and perpendicular to the applied magnetic induction, containing 10% to 30% volume particle concentration, were stretched up to 10% strain. Three samples of each type were tested, and mean values and standard deviations of the third loading cycle are shown. The tests without an applied magnetic induction were discussed in Section 5.5.5. The tangent moduli, E_T , were used to describe the non-linear behaviour of the different types of MREs. The MR effects were discussed in Section 5.5.6. The stress-strain curves and the tangent moduli comparing the no-magnetic tests with the magnetic tests of all types of MREs tested are illustrated in this Appendix. The relative MR effects, calculated with the tangent moduli of 1% stress-strain increments are presented.



(a) Stress-Strain curves in x-direction



(b) Stress-Strain curves in y-direction

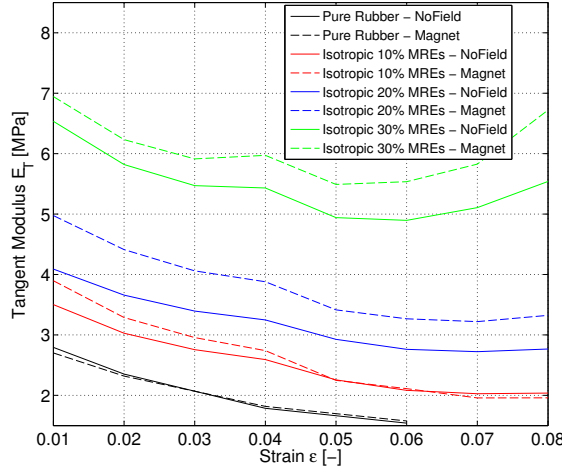
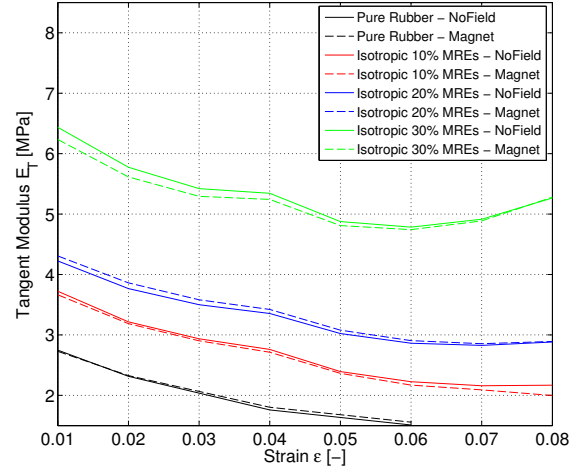
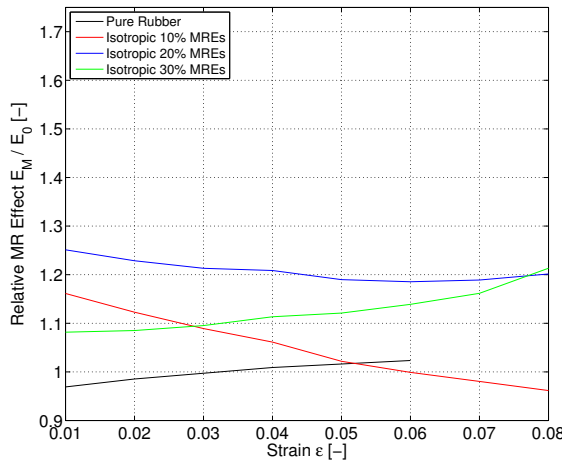
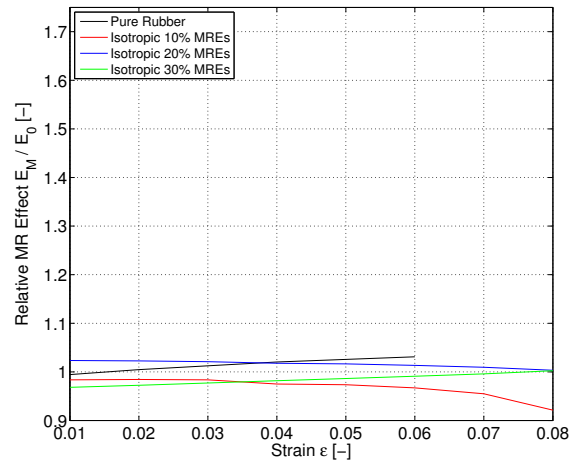
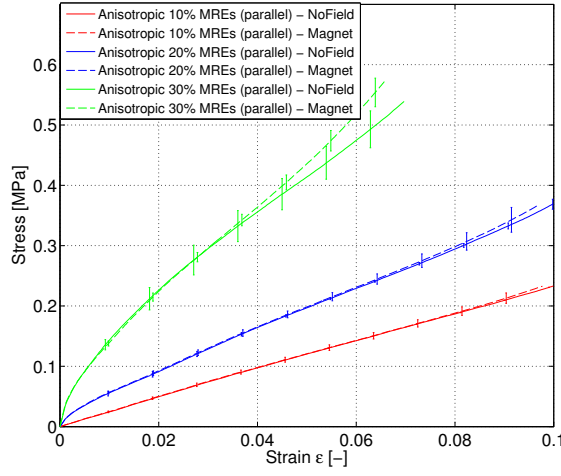
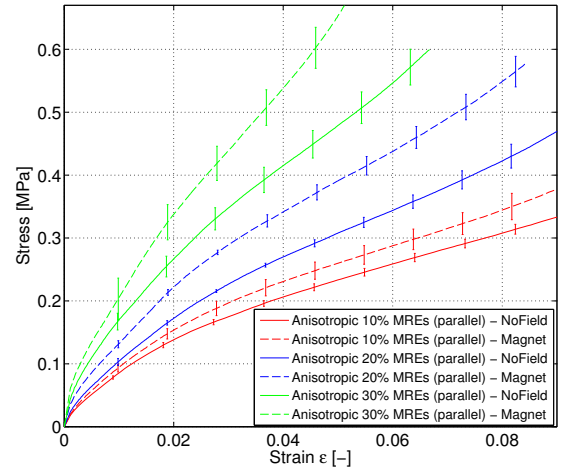
(c) Tangent Modulus E_T in x-direction(d) Tangent Modulus E_T in y-direction(e) Relative MR Effect E_M/E_0 in x-direction(f) Relative MR Effect E_M/E_0 in y-direction

Figure E.27: Pure rubber and isotropic MREs tested in equi-biaxial tension: (left) in the direction of the applied magnetic induction (x-direction), and (right) perpendicular to the applied magnetic induction (y-direction). Stress-strain curves, the tangent moduli, and the relative MR effects are presented.



(a) Stress-Strain curves in x-direction



(b) Stress-Strain curves in y-direction

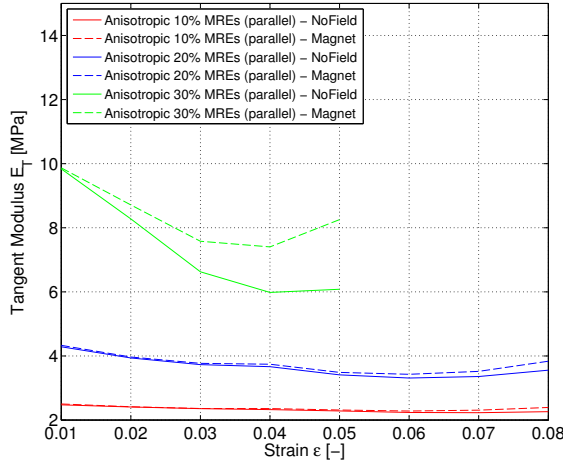
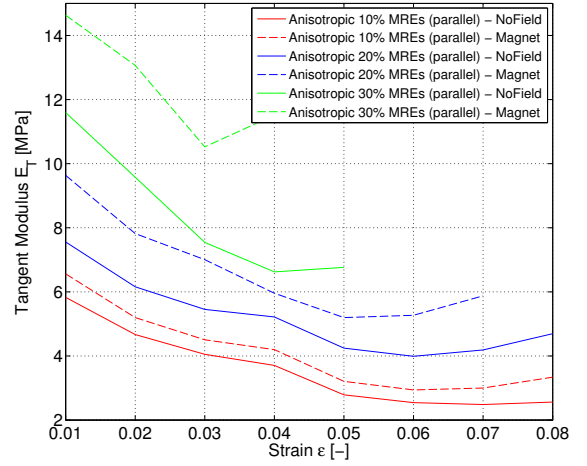
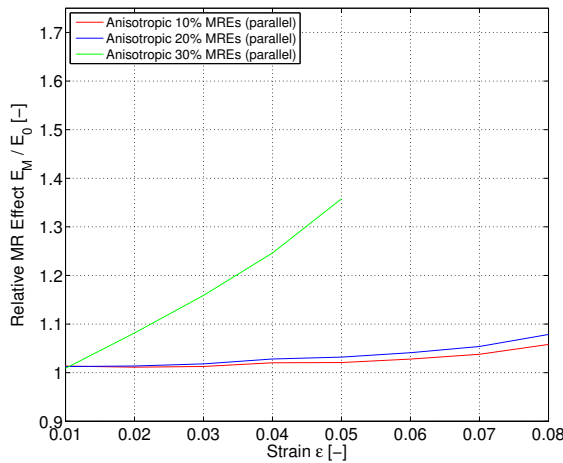
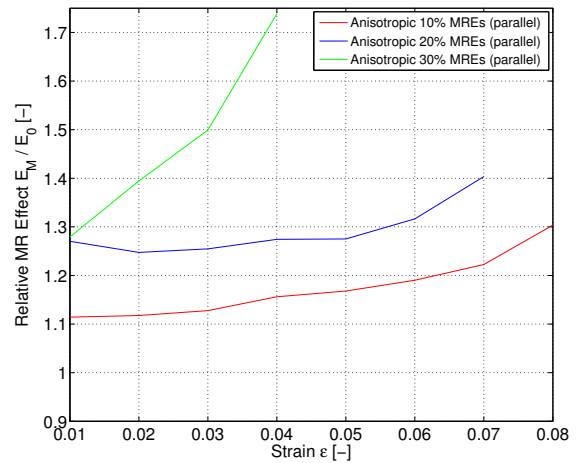
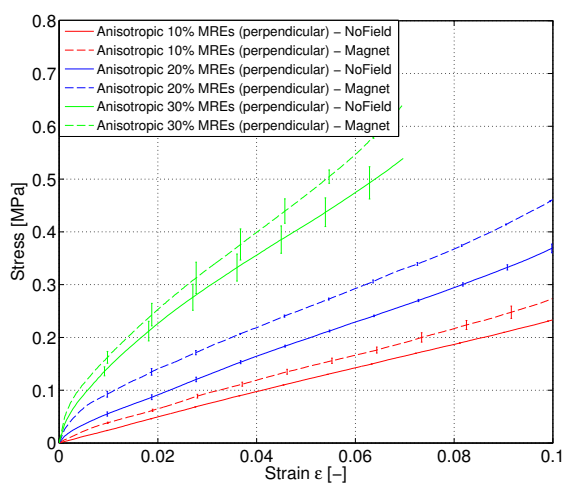
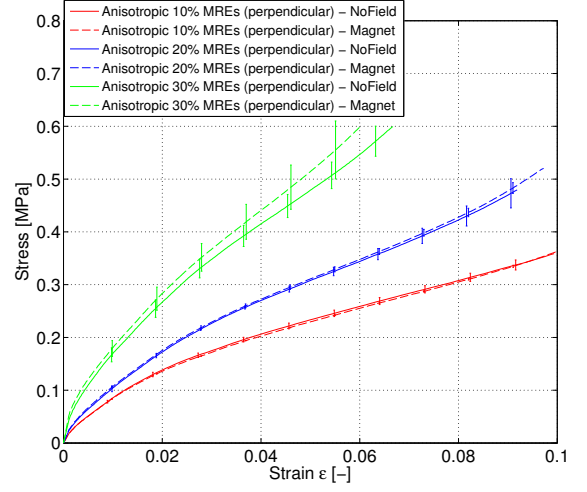
(c) Tangent Modulus E_T in x-direction(d) Tangent Modulus E_T in y-direction(e) Relative MR Effect E_M/E_0 in x-direction(f) Relative MR Effect E_M/E_0 in y-direction

Figure E.28: Anisotropic MREs with the applied magnetic induction parallel to the particle alignment direction tested in equi-biaxial tension: (left) perpendicular to the applied magnetic induction (x-direction), and (right) in the direction the applied magnetic induction (y-direction). Stress-strain curves, the tangent moduli, and the relative MR effects are presented.



(a) Stress-Strain curves in x-direction



(b) Stress-Strain curves in y-direction

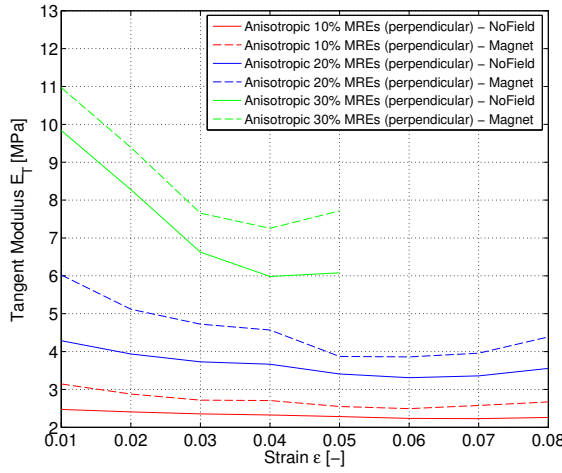
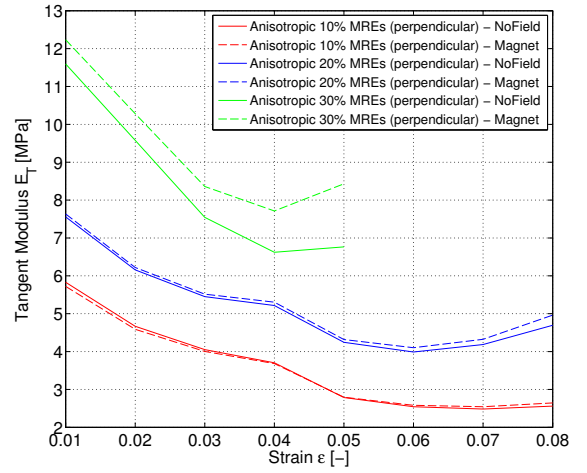
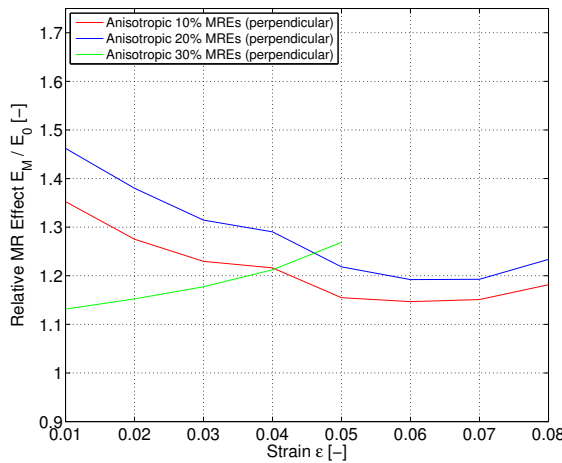
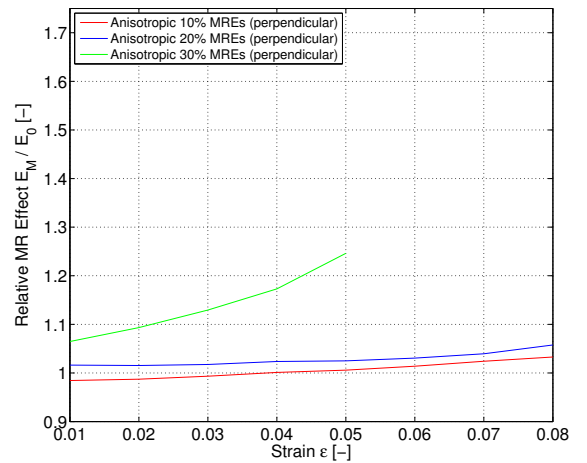
(c) Tangent Modulus E_T in x-direction(d) Tangent Modulus E_T in y-direction(e) Relative MR Effect E_M/E_0 in x-direction(f) Relative MR Effect E_M/E_0 in y-direction

Figure E.29: Anisotropic MREs with the applied magnetic induction perpendicular to the particle alignment direction tested in equi-biaxial tension: (left) in the direction of the applied magnetic induction (x-direction), and (right) perpendicular to the applied magnetic induction (y-direction). Stress-strain curves, the tangent moduli, and the relative MR effects are presented.

Appendix F

Results of Constitutive Modelling

F.1 Isotropic MREs

Isotropic MREs were modelled with the *Ogden Model* for incompressible isotropic rubber-like materials, the theory of which was presented in Sections 6.1 and 6.3.1. The data fitting procedure was described in Section 6.3.2. The results of isotropic MREs, for all deformation modes, and combinations thereof, is described in Sections 6.3.3 and 6.3.5. In this Appendix the determined model parameters, α_p and μ_p , are summarised. The strain energy function of the *Ogden Model* is defined as a function of the principal stretches

$$\Psi = \Psi(\lambda_1, \lambda_2, \lambda_3) = \sum_{p=1}^N \frac{\mu_p}{\alpha_p} (\lambda_1^{\alpha_p} + \lambda_2^{\alpha_p} + \lambda_3^{\alpha_p} - 3)$$

where λ_a are the principal stretches, μ_p and α_p are the model parameters, and $N = 1, 2, 3$ is the order of the *Ogden Model*. The modulus, μ , of the *Neo-Hookean* model can be calculated with

$$\mu = \frac{1}{2} \sum_{p=1}^N \mu_p \alpha_p.$$

The given 2-Norm and the coefficient of determination R_2 are defined as follows, both interpret the quality of the fit.

$$\|\cdot\|_2 = \|\mathfrak{G}(\lambda, \mathbf{mp}) - \tau\|_2 = \sqrt{\sum_{i=1}^m [\mathfrak{G}(\lambda_i, \mathbf{mp}) - \tau_i]^2}$$

$$R_2 = 1 - \frac{\sum_{i=1}^m [\mathfrak{G}(\lambda_i, \mathbf{mp}) - \tau_i]^2}{\sum_{i=1}^m [\tau_i - \bar{\tau}]^2}$$

Test	Sample	μ_1 [Pa]	α_1 [—]	μ_2 [Pa]	α_2 [—]	μ_3 [Pa]	α_3 [—]	μ [MPa]	R_2	$\ \cdot\ _2$
Compression	Pure Rubber	3.0648e+05	1.5311e+00	7.5072e+02	1.5310e+00	-1.6977e+02	-8.8141e+00	0.2359	0.999986	0.011948
	10% MREs	9.6811e+05	5.8200e-01	-1.3654e-02	-3.0302e+01	8.3622e-11	4.9200e+00	0.2817	0.999868	0.037122
	20% MREs	4.6889e+06	1.5212e-01	-1.3766e-05	-4.7352e+01	5.8219e-13	5.6125e+00	0.3566	0.999645	0.069570
	30% MREs	1.0760e+06	9.6458e-01	2.3645e-04	4.8438e-08	1.1813e-05	4.8942e-08	0.5189	0.999353	0.066381
Tension	Pure Rubber (100%)	-3.9418e+05	-1.6587e+00	9.2042e+03	5.8653e+00	3.4299e-04	2.7069e+01	0.3539	0.999996	0.011245
	Pure Rubber (50%)	-4.7985e+05	-1.4550e+00	-3.0848e+04	-2.2204e-14	2.3066e+03	9.5359e+00	0.3601	0.999995	0.004660
	10% MREs (100%)	-2.7553e+05	-4.0272e+00	3.2001e+03	7.9471e+00	1.0240e-03	2.7607e+01	0.5675	0.999994	0.002577
	10% MREs (50%)	-1.8426e+05	-6.3079e+00	7.8540e+03	4.2768e+00	7.3561e+00	2.2123e+01	0.5980	0.999998	0.011856
	20% MREs (75%)	-3.1787e+05	-5.3322e+00	-1.0626e+02	-3.2907e+01	1.6822e+01	4.1119e-14	0.8492	0.999875	0.066462
	20% MREs (50%)	-2.8265e+05	-5.9999e+00	3.3667e-14	1.0586e+00	2.8335e-14	9.2083e-01	0.8479	0.999710	0.027350
	30% MREs (50%)	-3.9200e+05	-6.2730e+00	2.6098e-04	2.1181e-07	1.2504e-05	2.1536e-05	1.2295	0.999059	0.070770
	30% MREs (15%)	-3.1067e+05	-9.1222e+00	1.2810e-03	2.4586e-09	2.6467e-08	2.0139e-05	1.4170	0.999545	0.034799
Pure Shear	Pure Rubber (70%)	2.8080e+07	1.7996e-02	6.1445e+02	6.0039e-02	2.6250e+01	1.9482e+01	0.2529	0.999939	0.012717
	Pure Rubber (47%)	2.0568e+09	8.6132e-05	2.0568e+09	8.6132e-05	2.0568e+09	8.6132e-05	0.2657	0.999864	0.011855
	10% MREs (67%)	1.7566e+08	3.6314e-03	1.6315e-01	3.6433e+01	2.6098e-04	8.2249e-08	0.3189	0.999511	0.039909
	10% MREs (45%)	2.3847e+09	1.0049e-04	2.3847e+09	1.0049e-04	2.3847e+09	1.0049e-04	0.3595	0.998623	0.053193
	20% MREs (45%)	2.4215e+05	3.7492e+00	4.6449e+01	2.2204e-14	1.9341e+01	1.2104e-12	0.4539	0.996082	0.089310
	20% MREs (23%)	2.9341e+09	1.2486e-04	2.9339e+09	1.2739e-04	2.9338e+09	1.2808e-04	0.5579	0.998281	0.046245
	30% MREs (45%)	4.5022e+08	3.5944e-03	1.4316e+00	5.3984e+01	2.6098e-04	8.2249e-08	0.8092	0.999345	0.096959
	30% MREs (23%)	3.5662e+09	1.6069e-04	3.5662e+09	1.6069e-04	3.5662e+09	1.6069e-04	0.8596	0.998929	0.059699
Equi-Biaxial	Pure Rubber	1.5989e+05	5.9413e+00	1.1514e+02	4.2115e-14	4.3250e-11	1.2302e-01	0.4750	0.977173	0.162066
	10% MREs	2.0246e+05	6.0836e+00	7.8482e-05	1.5383e-07	3.4347e-05	1.5196e-08	0.6159	0.990950	0.154271
	20% MREs	2.2644e+05	6.5926e+00	2.3072e-03	2.0072e-13	7.6290e-04	3.5659e-09	0.7464	0.997607	0.094185
	30% MREs	2.9326e+05	8.5125e+00	4.8216e-03	1.6636e+02	1.7066e-03	6.7894e-09	1.2482	0.998225	0.142994

Table F.1: Identified model parameters of the *Ogden Model* ($N = 3$) to uniaxial compression, uniaxial tension, pure shear and equi-biaxial tension test data of pure rubber and isotropic MREs. The experimental data were presented in Sections 5.2, 5.3, 5.4, and 5.5, and the data fitting of the *Ogden* model to single deformation modes was presented in Section 6.3.3.1. The model parameters, α_p and μ_p , the modulus, μ , the coefficient of determination, R_2 , and the 2-Norm, $\|\cdot\|_2$, are provided.

	μ_1 [Pa]	$\alpha_1[-]$	μ_2 [Pa]	$\alpha_2[-]$	μ_3 [Pa]	$\alpha_3[-]$	μ [MPa]	R_2	$ \cdot _2$
SP1	6.3000e+05	1.3000e+00	1.2000e+03	5.0000e+00	-1.0000e+04	-2.0000e+00	0.2359	0.999986	1.194816410456e-2
MP1	3.0723e+05	1.5311e+00	-1.6977e+02	-8.8141e+00	-5.4865e+01	-7.1366e-03	0.2359	0.999986	1.194816394403e-2
SP2	1.0000e+00	1.0000e+00	1.0000e+00	1.0000e+00	1.0000e+00	1.0000e+00	0.2359	0.999986	1.194816394403e-2
MP2	3.0720e+05	1.5311e+00	-1.6977e+02	-8.8142e+00	3.3885e+01	1.5377e+00	0.2359	0.999986	1.194816394403e-2
SP3	1.0000e+02	1.0000e+00	1.0000e+02	1.0000e+00	1.0000e+02	1.0000e+00	0.2359	0.999986	1.194816394497e-2
MP3	3.0723e+05	1.5311e+00	-1.6975e+02	-8.8143e+00	6.8449e-01	1.5391e+00	0.2359	0.999986	1.194816394392e-2
SP4	1.0000e+04	1.0000e+00	1.0000e+04	1.0000e+00	1.0000e+04	1.0000e+00	0.2359	0.999986	1.194816394392e-2
MP4	3.0723e+05	1.5311e+00	-1.3115e+04	-6.2144e-08	-1.6977e+02	-8.8141e+00	0.2359	0.999986	1.194816394392e-2
SP5	1.0000e+06	1.0000e+00	1.0000e+06	1.0000e+00	1.0000e+06	1.0000e+00	0.2359	0.999986	1.194816394775e-2
MP5	3.0723e+05	1.5311e+00	-5.0607e+02	-2.0200e-05	-1.6977e+02	-8.8141e+00	0.2359	0.999986	1.194816394775e-2
SP6	1.0000e+08	1.0000e+00	1.0000e+08	1.0000e+00	1.0000e+08	1.0000e+00	0.2153	0.999540	6.861058682224e-2
MP6	4.8005e+07	8.5287e-03	2.5852e+07	7.7830e-04	2.5851e+07	4.2333e-05	0.2359	0.999986	1.194816395198e-2
SP7	1.0000e+00	1.0000e+01	1.0000e+00	1.0000e+01	1.0000e+00	1.0000e+01	0.2359	0.999986	1.194816394649e-2
MP7	3.0723e+05	1.5310e+00	-1.6973e+02	-8.8145e+00	2.0705e+00	1.5343e+00	0.2359	0.999986	1.194816394383e-2
SP8	1.0000e+02	1.0000e+01	1.0000e+02	1.0000e+01	1.0000e+02	1.0000e+01	0.2359	0.999986	1.194816394364e-2
MP8	3.0711e+05	1.5311e+00	-1.6976e+02	-8.8143e+00	1.2468e+02	1.5284e+00	0.2359	0.999986	1.194816394364e-2
SP9	1.0000e+04	1.0000e+01	1.0000e+04	1.0000e+01	1.0000e+04	1.0000e+01	0.2359	0.999986	1.194816394364e-2
MP9	3.0648e+05	1.5311e+00	7.5072e+02	1.5310e+00	-1.6977e+02	-8.8141e+00	0.2359	0.999986	1.194816394383e-2
SP10	1.0000e+06	1.0000e+01	1.0000e+06	1.0000e+01	1.0000e+06	1.0000e+01	0.2359	0.999986	1.194816394383e-2
MP10	3.0723e+05	1.5311e+00	3.9920e+04	1.4944e-08	-1.6977e+02	-8.8141e+00	0.2359	0.999986	1.194816394383e-2
SP11	1.0000e+08	1.0000e+01	1.0000e+08	1.0000e+01	1.0000e+08	1.0000e+01	0.2359	0.999986	1.194816394394e-2
MP11	3.0476e+05	1.5311e+00	2.4649e+03	1.5310e+00	-1.6977e+02	-8.8141e+00	0.2359	0.999986	1.194816394394e-2
SP12	1.0000e+00	1.0000e+02	1.0000e+00	1.0000e+02	1.0000e+00	1.0000e+02	0.2359	0.999986	1.194816395187e-2
MP12	3.0723e+05	1.5311e+00	-1.6975e+02	-8.8143e+00	1.4171e+00	1.6531e+00	0.2359	0.999986	1.194816395187e-2

Table F.2: Identified model parameters of *Ogden Model* ($N = 3$) to uniaxial compression test data of pure rubber. Different sets of start parameters and resulting identified model parameters are listed. The model parameters, α_p and μ_p , the shear modulus, μ , the coefficient of determination, R_2 , and the 2-Norm, $|| \cdot ||_2$, are provided. The set of parameters number 9 is the final solution with the smallest 2-Norm.

Sample	Combination	μ_1 [Pa]	α_1 [-]	μ_2 [Pa]	α_2 [-]	μ_3 [Pa]	α_3 [-]	μ [MPa]	R_2	$\ \cdot\ _2$
Pure Rubber	C-T15-PS6	7.9012e+04	3.2854e+00	7.4901e+04	3.2854e+00	-3.0553e+00	-1.2566e+01	0.2529	0.9728	0.5434
	C-T15-PS6-EB	1.5598e+05	3.2550e+00	-5.9552e-09	-4.7577e+01	2.5588e-10	4.8185e-01	0.2539	0.1559	1.6997
	C-T15-PS6-EB with weight factors	8.0117e+05	8.4076e-01	1.7253e+00	2.4822e+01	-1.9262e-01	-2.1476e+01	0.3368	0.9618	0.2801
		$w_c = 0.6814$ $w_{ps} = 0.7842$ $w_{eb} = 1.2592$						0.2295 0.2641 0.4241		
Isotropic 10% MREs	C-T15-PS6	4.7809e+04	4.4678e+00	4.7733e+04	4.4678e+00	4.7554e+04	4.4678e+00	0.3197	0.9118	1.1714
	C-T15-PS6-EB	4.9539e+04	4.3595e+00	4.9405e+04	4.3595e+00	4.9029e+04	4.3595e+00	0.3225	0.1540	2.9256
	C-T15-PS6-EB with weight factors	2.9956e+06	3.4021e-01	2.9280e-02	4.0093e+01	-1.7121e-06	-5.1135e+01	0.5096	0.9784	0.4263
		$w_c = 0.5448$ $w_{ps} = 0.7045$ $w_{eb} = 1.0599$						0.2776 0.3590 0.5401		
Isotropic 20% MREs	C-T15-PS6	7.4844e+04	5.5720e+00	7.4582e+04	5.5720e+00	1.4264e-20	4.9987e+01	0.4163	0.5489	1.3880
	C-T15-PS6-EB	1.2019e+05	5.0578e+00	4.9135e+04	5.0578e+00	7.3386e-18	6.8359e+01	0.4282	0.1352	3.2280
	C-T15-PS6-EB with weight factors	6.6621e+06	2.2085e-01	9.7399e+05	9.2600e-14	1.3872e-04	8.8860e+01	0.7357	0.9904	0.4994
		$w_c = 0.4868$ $w_{ps} = 0.6522$ $w_{eb} = 0.8816$						0.3582 0.4798 0.6486		
Isotropic 30% MREs	C-T15-PS6	1.7566e+08	1.0896e-18	-1.8947e+05	-1.0102e-15	1.5796e+05	7.9755e+00	0.6299	0.7983	2.1653
	T5-EB	8.6626e+05	2.6529e+00	5.1782e+01	2.6574e+00	-3.4298e-03	-8.6353e+01	1.1491	0.9867	0.3849
	C-T15-PS6-EB	3.2662e+05	4.7005e+00	3.1938e+03	1.1133e-05	3.7262e-08	1.2986e+02	0.7676	0.3510	5.3436
	C-T15-PS6-EB with weight factors	4.8026e+06	4.3722e-01	-3.0157e+06	-5.9862e-08	8.0256e-02	6.9194e+01	1.0499	0.9888	0.6916
		$w_c = 0.4817$ $w_{ps} = 0.7755$ $w_{eb} = 1.0386$						0.5057 0.8142 1.0904		

Table F.3: Identified model parameters of the *Ogden Model* ($N = 3$) to combined deformation modes of pure rubber and isotropic MREs without and with the use of weight factors. The results were presented in Section 6.3.3.2. The model parameters, α_p and μ_p , and the moduli, μ , the coefficient of determination, R_2 , and the 2-Norm, $\|\cdot\|_2$, are provided. When combining all deformation modes with weight factors, the model parameters represent the tension mode, and the resulting moduli for the other deformation modes are calculated.

Sample	Strain Level [%]	μ_1 [Pa]	α_1 [—]	μ_2 [Pa]	α_2 [—]	μ_3 [Pa]	α_3 [—]	μ [MPa]	R_2	$\ \cdot\ _2$
Pure Rubber	50	7.9012e+04	3.2854e+00	7.4901e+04	3.2854e+00	-3.0553e+00	-1.2566e+01	0.2529	0.9728	0.5434
	10	9.1954e+09 $w_c = 0.5825$	5.5943e-16 0.5825	6.9935e+09	7.8591e-16	-2.8144e+05	-2.5408e+00	0.3575 0.2083	0.5255	0.5020
Isotropic 10% MREs	50	1.9823e+05 $w_c = 0.8753$	3.6280e+00 0.8753	-8.2999e+00	-1.5129e+01	-5.8092e+00	-1.5129e+01	0.3597 0.3148	0.9413	1.0789
	10	-6.8731e+08 $w_c = 0.5179$	-1.5728e-15 0.5179	-6.8588e+08	-1.5763e-15	7.0908e+05	1.5694e+00	0.5564 0.2882	0.7172	0.3908
Isotropic 20% MREs	50	1.8401e+09 $w_c = 0.9094$	1.3175e-15 0.9094	1.9145e+05	4.7627e+00	1.2953e+02	4.7629e+00	0.4562 0.4149	0.6540	1.2321
	10	-3.4149e+09 $w_c = 0.6394$	-1.5336e-15 0.6394	-1.5313e+06	-5.6582e-12	9.2578e+05	1.4500e+00	0.6712 0.4292	0.9630	0.2747
Isotropic 30% MREs	50	4.0038e+05 $w_c = 0.7215$	3.9470e+00 0.7215	-2.8235e-01	-3.0687e-01	1.3860e-07	1.2702e+02	0.7901 0.5701	0.8719	1.1249
	10	3.6153e+05 $w_c = 0.6672$	3.3938e+00 0.6672	3.2436e+05	3.3938e+00	-3.5590e-02	-7.4506e+01	1.1639 0.7765	0.9736	0.4928

Table F.4: Identified model parameters of the *Ogden Model* ($N = 3$) to combined deformation modes obtained from tests up to 50% and 10% strain of pure rubber and isotropic MREs. The results were presented in Section 6.3.5. The model parameters, α_p and μ_p , the moduli, μ , the coefficient of determination, R_2 , and the 2-Norm, $\|\cdot\|^2$, are provided.

F.2 Anisotropic MREs

Anisotropic MREs were modelled with the *Qui-Pence*, the *Merodio-Ogden*, the *Holzappel-Gasser*, and the *Guo* models, all models that characterise transversely isotropic materials. The theory was presented in Sections 6.4.1 and 6.4.2. The fitting procedure was described in Section 6.4.3. Results of data fitting to each deformation (fitted to both data sets obtained with the loading parallel and perpendicular to the direction of particle alignment) were presented in Section 6.4.4, but only the results of the *Qui-Pence* model were discussed in the main text. In this appendix, the results of the *Merodio-Ogden*, *Holzappel-Gasser*, and *Guo* models are presented. The predictions of the models are compared with the experimental data of anisotropic MREs with 10%, 20% and 30% MREs. The model parameters, Young's moduli, E_1 and E_2 , and coefficients of determination, R_2 , are listed in the tables.

Merodio-Ogden model

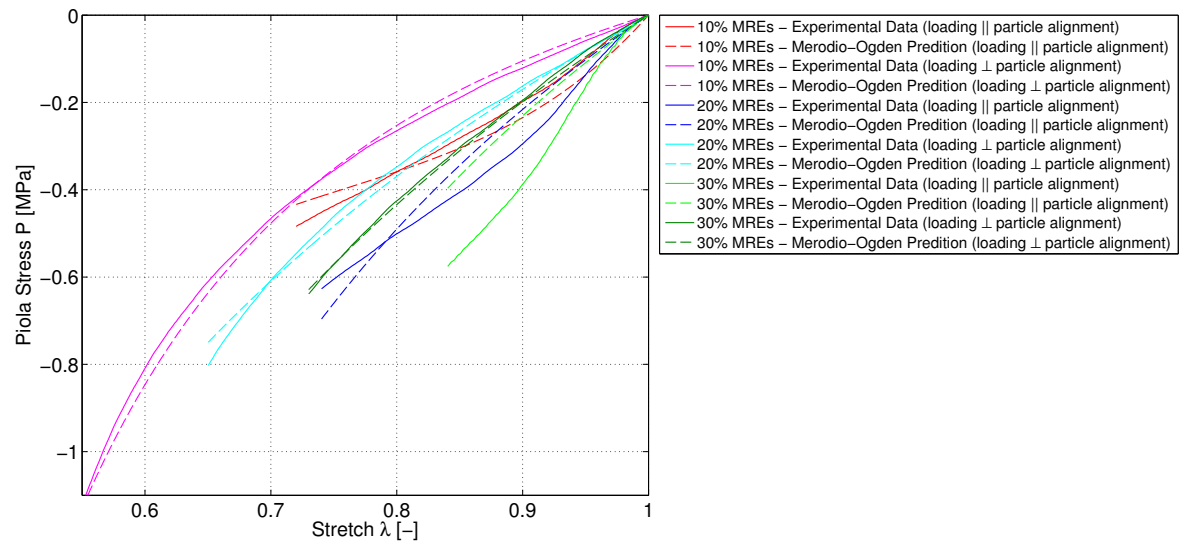


Figure F.1: Predictions of the *Merodio-Ogden* model fitted to uniaxial compression data with both loading parallel and perpendicular to the direction of particle alignment are compared to experimental data from anisotropic MREs with 10%, 20%, and 30% CIP content.

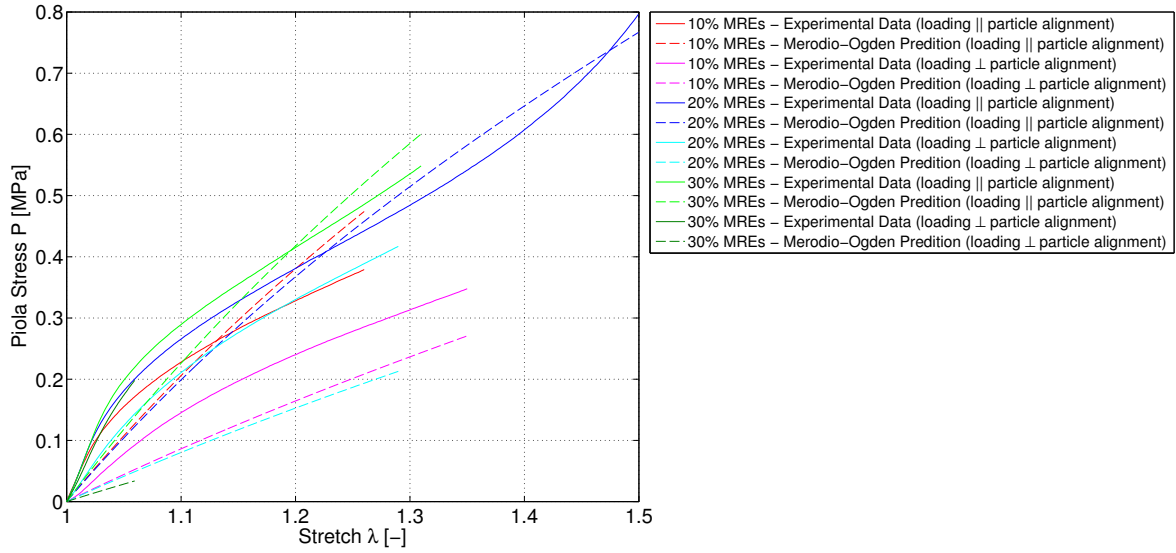


Figure F.2: Predictions of the *Merodio-Ogden* model fitted to uniaxial tension data with both loading parallel and perpendicular to the direction of particle alignment are compared to experimental data from anisotropic MREs with 10%, 20%, and 30% CIP content.

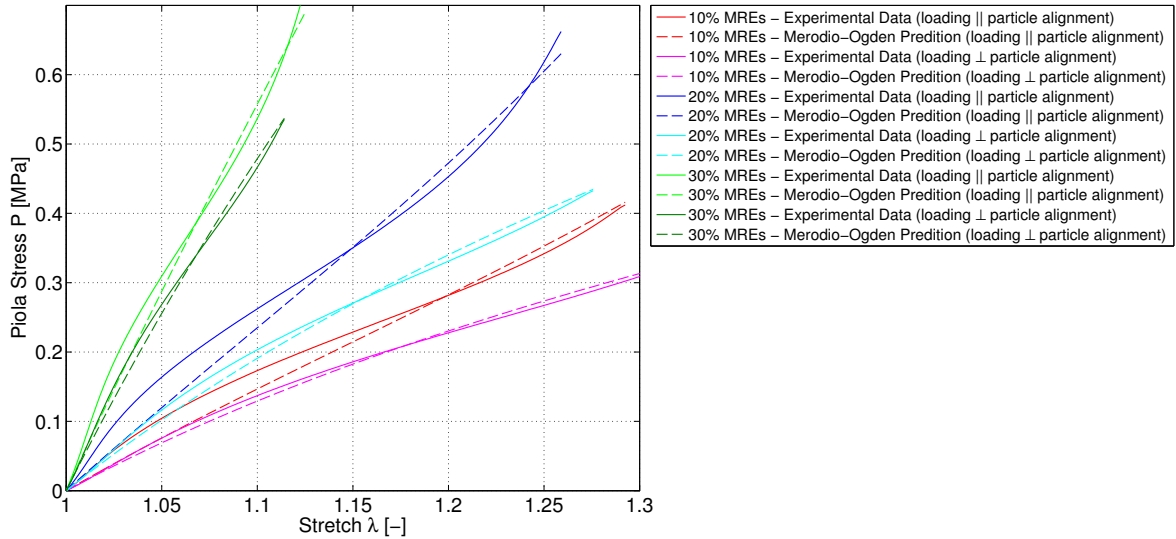


Figure F.3: Predictions of the *Merodio-Ogden* model fitted to pure shear data with both loading parallel and perpendicular to the direction of particle alignment are compared to experimental data from anisotropic MREs with 10%, 20%, and 30% CIP content.

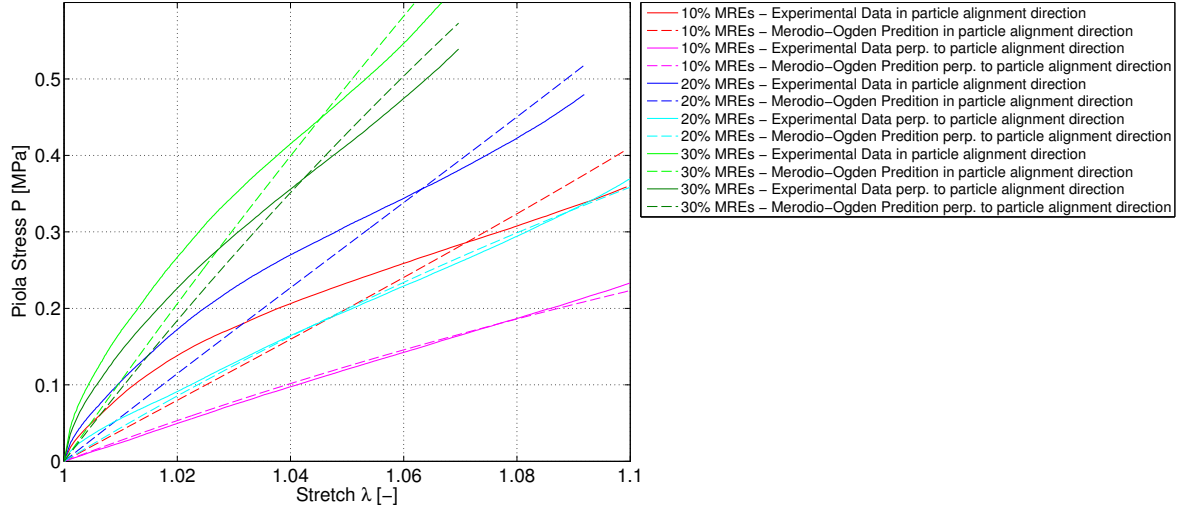


Figure F.4: Predictions of the *Merodio-Ogden* model fitted to equi-biaxial tension data are compared to experimental data from anisotropic MREs with 10%, 20%, and 30% CIP content. Predictions and experimental data are illustrated for both directions, parallel and perpendicular to the direction of particle alignment.

	MRE	μ [MPa]	γ [-]	E_1 [MPa]	E_2 [MPa]	R_2
Compression	Anisotropic 10% MREs	0.7523	4.0817e-18	2.2568	2.2568	0.5496
	Anisotropic 20% MREs	0.7266	8.7986e-18	2.1799	2.1799	0.7161
	Anisotropic 30% MREs	0.8263	6.5707e-18	2.4789	2.4789	0.8814
Tension	Anisotropic 10% MREs	0.2109	7.7597e-1	3.2509	0.7922	0.9560
	Anisotropic 20% MREs	0.6398	2.9783e-3	1.9500	1.9271	0.9256
	Anisotropic 30% MREs	0.6895	1.7466e-16	2.0684	2.0684	0.5253
Pure Shear	Anisotropic 10% MREs	0.3707	1.8959e-2	1.5953	1.4829	0.9724
	Anisotropic 20% MREs	0.5474	3.2605e-2	2.4754	2.1898	0.9769
	Anisotropic 30% MREs	1.3733	2.3171e-2	6.0021	5.4930	0.9862
Equi-Biaxial Tension	Anisotropic 10% MREs	0.4660	1.6250e-1	4.0080	2.7963	0.8169
	Anisotropic 20% MREs	0.7482	1.1154e-1	5.8244	4.4891	0.8982
	Anisotropic 30% MREs	1.6110	3.8882e-2	10.6680	9.6658	0.9127

Table F.5: The parameters μ and γ of the *Merodio-Ogden* model fitted to data of each deformation mode (fitted to tests with both the loading parallel and perpendicular to the particle alignment direction), are listed. The Young's moduli, E_1 parallel, and E_2 perpendicular to the direction of particle direction can be compared with the experimentally determined moduli (Tables 5.5, 5.13, 5.20, and 5.23).

Holzapfel-Gasser model

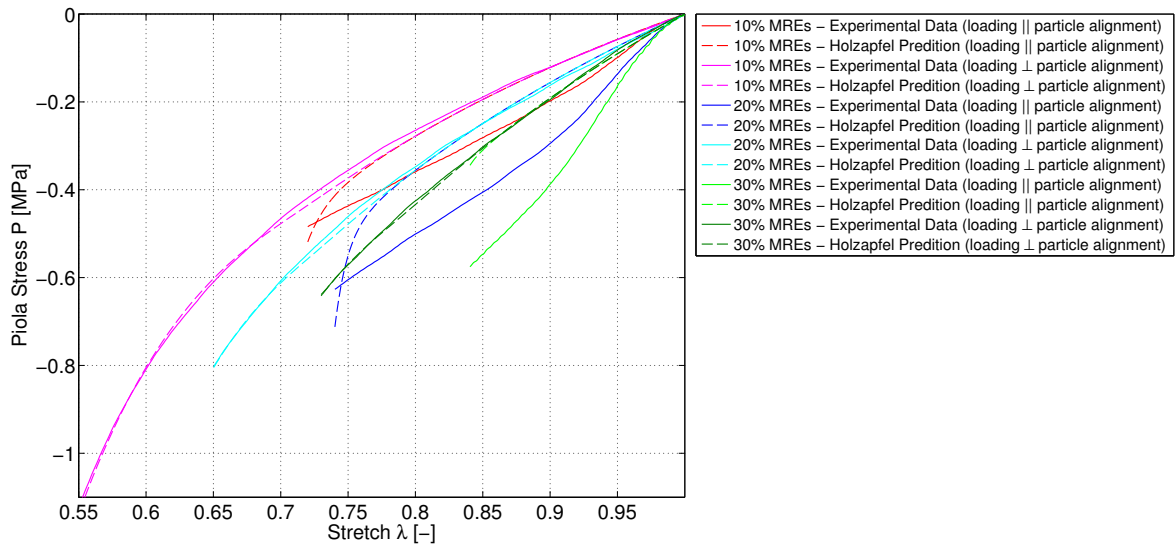


Figure F.5: Predictions of the *Holzapfel-Gasser* model fitted to uniaxial compression data with both loading parallel and perpendicular to the direction of particle alignment are compared to experimental data from anisotropic MREs with 10%, 20%, and 30% CIP content.

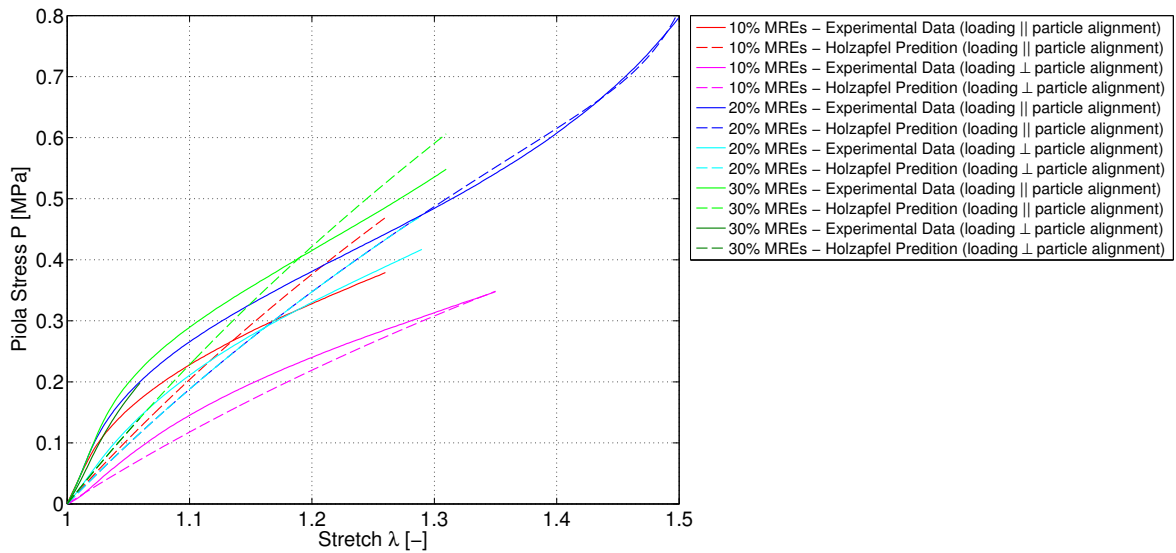


Figure F.6: Predictions of the *Holzapfel-Gasser* model fitted to uniaxial tension data with both loading parallel and perpendicular to the direction of particle alignment are compared to experimental data from anisotropic MREs with 10%, 20%, and 30% CIP content.

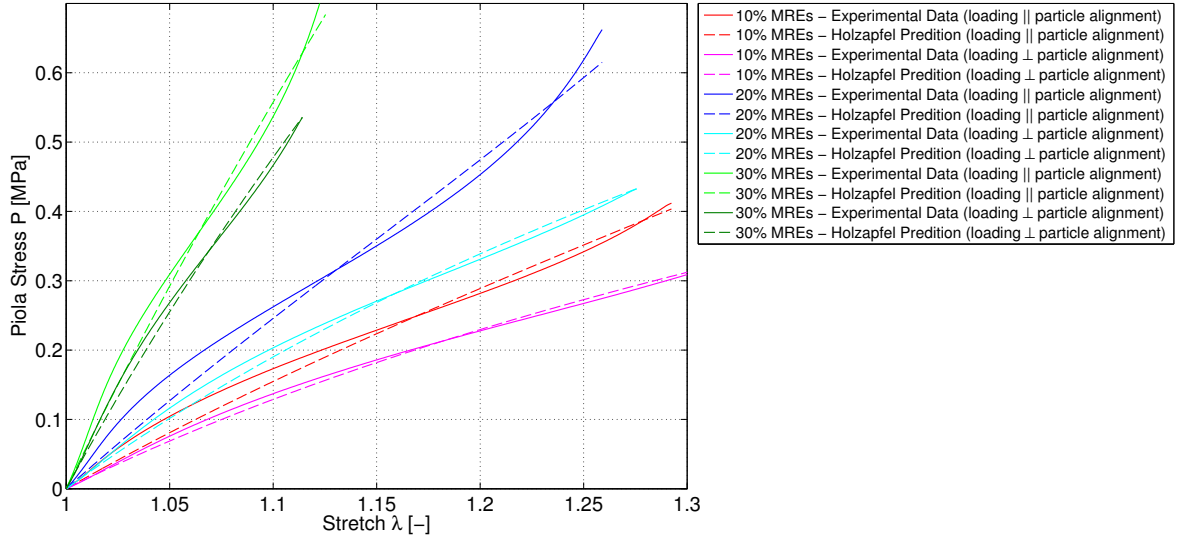


Figure F.7: Predictions of the *Holzapfel-Gasser* model fitted to pure shear data with both loading parallel and perpendicular to the direction of particle alignment are compared to experimental data from anisotropic MREs with 10%, 20%, and 30% CIP content.

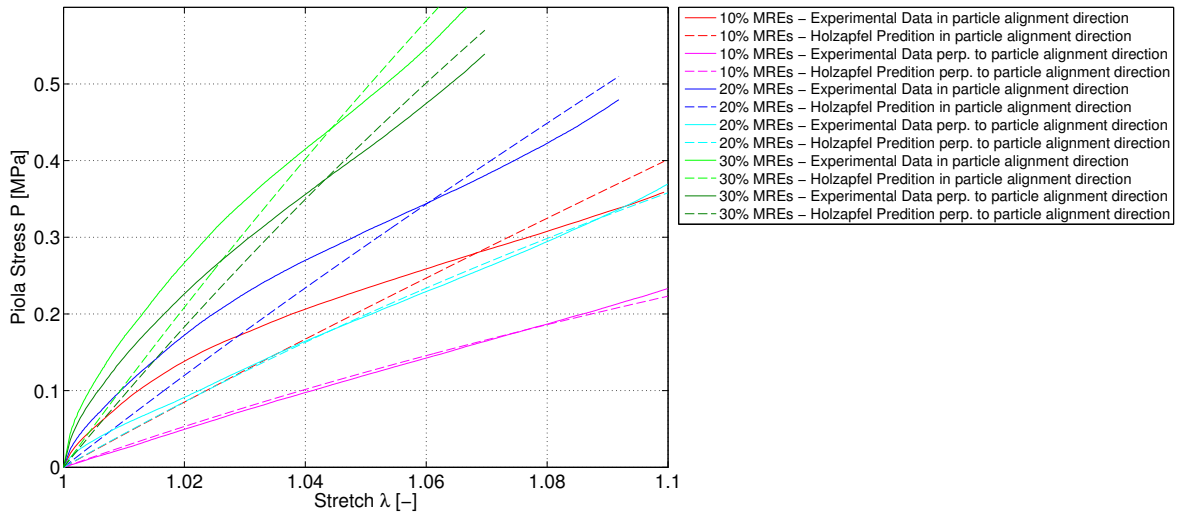


Figure F.8: Predictions of the *Holzapfel-Gasser* model fitted to equi-biaxial tension data are compared to experimental data from anisotropic MREs with 10%, 20%, and 30% CIP content. Predictions and experimental data are illustrated for both directions, parallel and perpendicular to the direction of particle alignment.

	MRE	μ [MPa]	k_1 [MPa]	k_2 [–]	E_1 [MPa]	E_2 [MPa]	R_2
Compression	10% MREs	0.7444	7.8149e–13	6.0377e0	2.2331	2.2331	0.7868
	20% MREs	0.6872	2.6286e+1	4.3127e0	2.0617	2.0617	0.9468
	30% MREs	0.8342	1.7571e–10	3.0352e0	2.5025	2.5025	0.5616
Tension	10% MREs	0.3645	5.4251e–1	5.2828e+1	1.0934	1.0934	0.7759
	20% MREs	0.4663	1.9090e–2	8.1232e+1	1.3990	1.3990	0.5686
	30% MREs	0.5723	1.6298e–1	1.4112e+2	1.7170	1.7170	0.2159
Pure Shear	10% MREs	0.3695	5.6036e+4	1.8150e–16	1.7023	1.4782	0.9840
	20% MREs	0.5452	1.1794e+5	4.3931e–1	2.6527	2.1810	0.9821
	30% MREs	1.3704	1.7236e+5	4.6976e–13	6.1712	5.4818	0.9877
Equi-Biaxial Tension	10% MREs	0.4658	3.8612e+5	1.8468e–12	4.3391	2.7947	0.8583
	20% MREs	0.7473	4.1807e+5	2.0423e–13	6.1562	4.4839	0.9192
	30% MREs	1.6028	3.0939e+5	4.4131e–13	10.8542	9.6166	0.9185

Table F.6: The parameters μ , k_1 , and k_2 of the *Holzappel-Gasser* model fitted to data of each deformation mode (fitted to tests with both the loading parallel and perpendicular to the particle alignment direction), are listed. The Young's moduli, E_1 parallel, and E_2 perpendicular to the direction of particle direction can be compared with the experimentally determined moduli (Tables 5.5, 5.13, 5.20, and 5.23).

Guo model

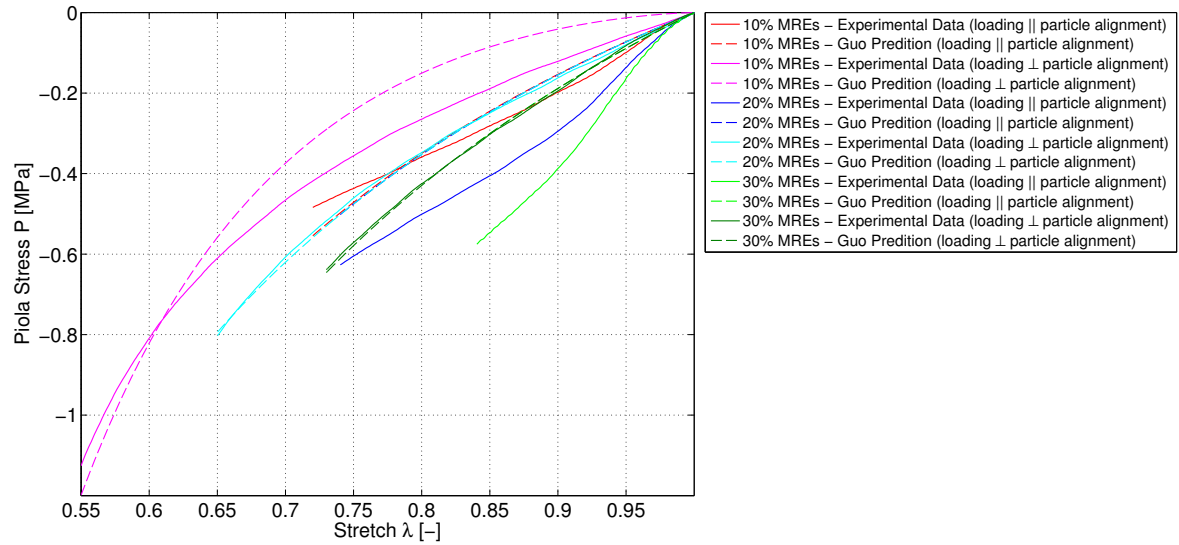


Figure F.9: Predictions of the *Guo* model fitted to uniaxial compression data with both loading parallel and perpendicular to the direction of particle alignment are compared to experimental data from anisotropic MREs with 10%, 20%, and 30% CIP content.

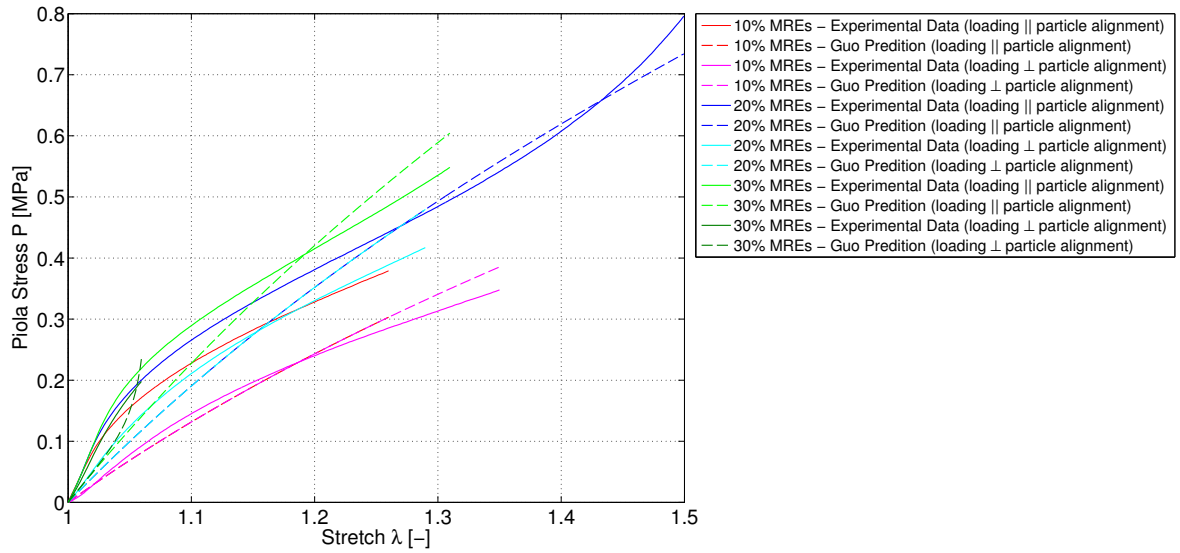


Figure F.10: Predictions of the *Guo* model fitted to uniaxial tension data with both loading parallel and perpendicular to the direction of particle alignment are compared to experimental data from anisotropic MREs with 10%, 20%, and 30% CIP content.

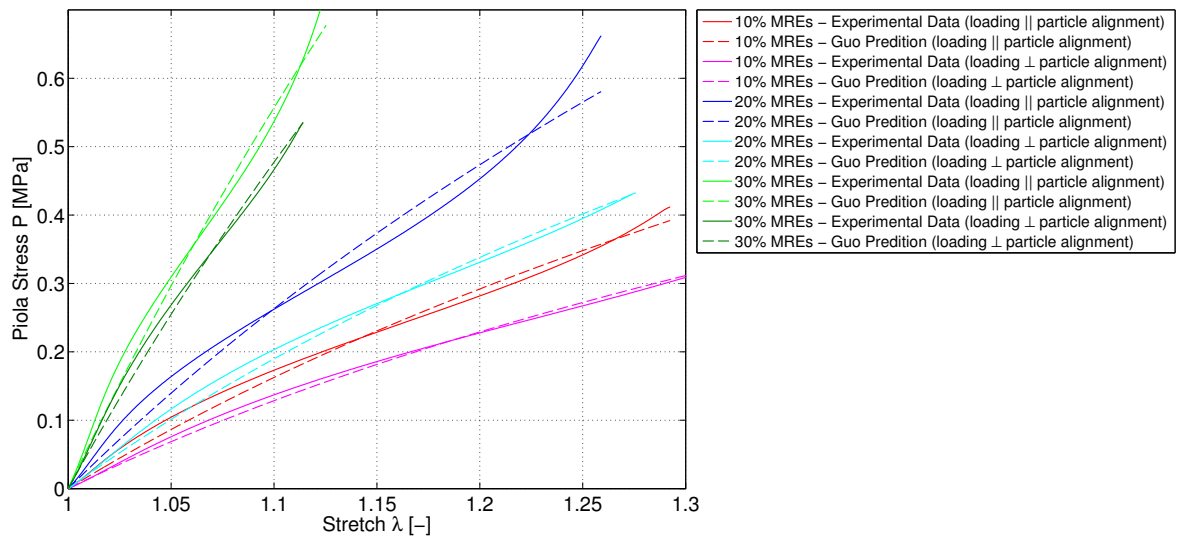


Figure F.11: Predictions of the *Guo* model fitted to pure shear data with both loading parallel and perpendicular to the direction of particle alignment are compared to experimental data from anisotropic MREs with 10%, 20%, and 30% CIP content.

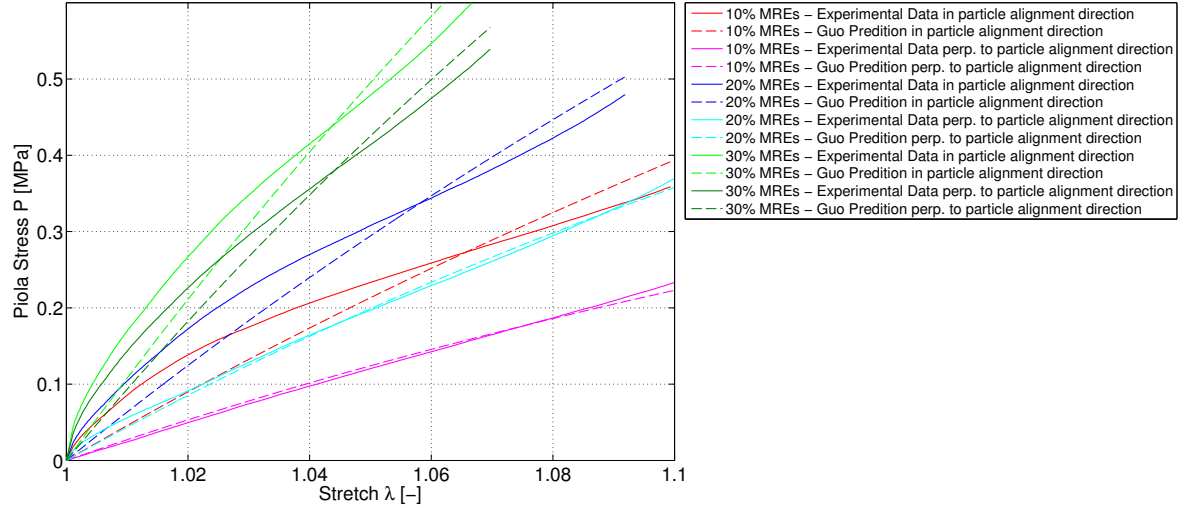


Figure F.12: Predictions of the *Guo* model fitted to equi-biaxial tension data are compared to experimental data from anisotropic MREs with 10%, 20%, and 30% CIP content. Predictions and experimental data are illustrated for both directions, parallel and perpendicular to the direction of particle alignment.

	MRE	μ [MPa]	β [-]	E_1 [MPa]	E_2 [MPa]	R_2
Compression	Anisotropic 10% MREs	0.4809	5.3286e-13	1.4428	1.4428	0.2250
	Anisotropic 20% MREs	0.6961	7.0042e-13	2.0884	2.0884	0.9377
	Anisotropic 30% MREs	0.0775	9.7281e0	2.4948	0.3007	0.7966
Tension	Anisotropic 10% MREs	0.0000	1.3568e+4	1.3761	0.0001	0.9430
	Anisotropic 20% MREs	0.4626	4.8684e-13	1.3878	1.3878	0.5209
	Anisotropic 30% MREs	0.5633	9.9733e-13	1.6900	1.6900	0.1773
Pure Shear	Anisotropic 10% MREs	0.3688	3.3700e-1	1.8480	1.4751	0.9901
	Anisotropic 20% MREs	0.5441	4.9252e-1	2.9806	2.1766	0.9799
	Anisotropic 30% MREs	1.3689	2.1241e-1	6.3479	5.4756	0.9887
Equi-Biaxial Tension	Anisotropic 10% MREs	0.4656	1.3407e0	4.6658	2.7933	0.8896
	Anisotropic 20% MREs	0.7466	8.9321e-1	6.4803	4.4797	0.9353
	Anisotropic 30% MREs	1.5959	3.0616e-1	11.0414	9.5756	0.9237

Table F.7: The parameters μ and β of the *Guo* model fitted to data of each deformation mode (fitted to tests with both the loading parallel and perpendicular to the particle alignment direction), are listed. The Young's moduli, E_1 parallel, and E_2 perpendicular to the direction of particle direction can be compared with the experimentally determined moduli (Tables 5.5, 5.13, 5.20, and 5.23).